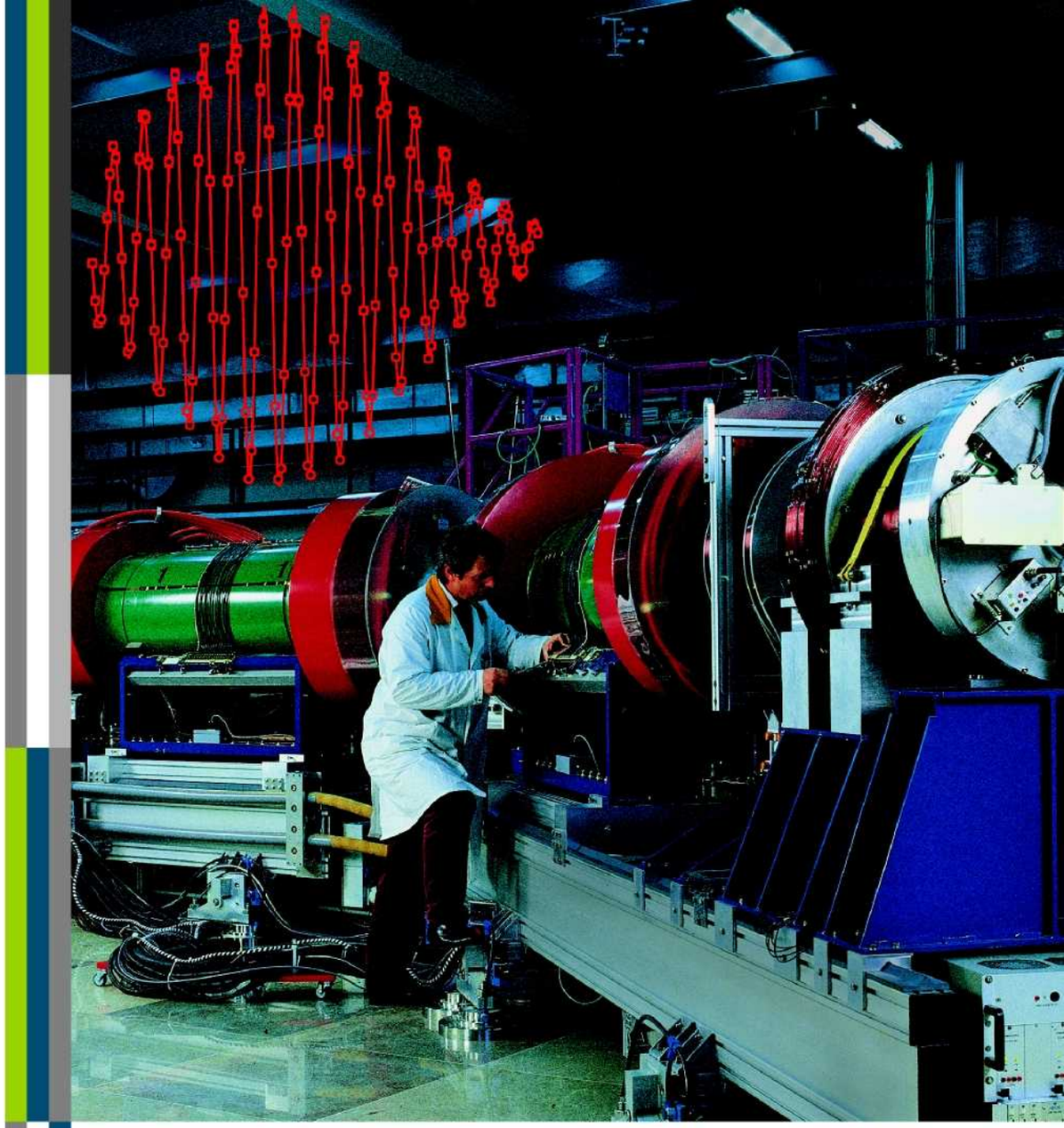


Laboratory Course

# Neutron Scattering

Lectures

Thomas Brückel, Gernot Heger,
Dieter Richter and Reiner Zorn (Editors)

RWTH Aachen
University of Münster

JÜLICH
FORSCHUNGSZENTRUM

Mitglied der Helmholtz-Gemeinschaft

Schriften des Forschungszentrums Jülich
Reihe Schlüsseltechnologien / Key Technologies Band / Volume 5

Forschungszentrum Jülich GmbH
Institut für Festkörperforschung (IFF)
Neutronenstreuung (IFF-5)

Thomas Brückel, Gernot Heger, Dieter Richter and Reiner Zorn (Editors)

# Neutron Scattering

Lectures of the JCNS Laboratory Course held at
Forschungszentrum Jülich and the research reactor
FRM II of TU Munich
In cooperation with
RWTH Aachen and University of Münster

Schriften des Forschungszentrums Jülich
Reihe Schlüsseltechnologien / Key Technologies Band / Volume 5

ISSN 1866-1807 ISBN 978-3-89336-532-6

Bibliographic information published by the Deutsche Nationalbibliothek.
The Deutsche Nationalbibliothek lists this publication in the Deutsche Nationalbibliografie; detailed bibliographic data are available in the Internet at http://dnb.d-nb.de.

| | |
|---|---|
| Publisher and Distributor: | Forschungszentrum Jülich GmbH<br>Zentralbibliothek, Verlag<br>D-52425 Jülich<br>phone:+49 2461 61-5368 · fax:+49 2461 61-6103<br>e-mail: zb-publikation@fz-juelich.de<br>Internet: http://www.fz-juelich.de/zb |
| Cover Design: | Grafische Medien, Forschungszentrum Jülich GmbH |
| Printer: | Grafische Medien, Forschungszentrum Jülich GmbH |
| Copyright: | Forschungszentrum Jülich 2008 |

Schriften des Forschungszentrums Jülich
Reihe Schlüsseltechnologien / Key Technologies Band / Volume 5

ISSN 1866-1807
ISBN 978-3-89336-532-6

The complete volume is freely available on the Internet on the Jülicher Open Access Server (JUWEL) at http://www.fz-juelich.de/zb/juwel

Neither this book nor any part may be reproduced or transmitted in any form or by any means, electronic or mechanical, including photocopying, microfilming, and recording, or by any information storage and retrieval system, without permission in writing from the publisher.

# Contents


| | | |
|---|---|---|
| I | **Fourier Transform** | R. Zorn |
| II | **Basic Assumptions of Quantum Mechanics and the Born Approximation – A Brief Tutorial** | D. Richter |
| III | **Symmetry in Crystals** | G. Heger |
| 1 | **Neutron Sources** | A. Ioffe |
| 2 | **A neutron primer: Elastic scattering and the properties of the neutron** | Th. Brückel |
| 3 | **Polarized neutron scattering** | W. Schweika |
| 4 | **Correlation Functions Measured by Scattering Experiments** | R. Zorn, D. Richter |
| 5 | **Continuum Description: Grazing Incidence Neutron Scattering** | O.H. Seeck, E. Kentzinger |
| 6 | **Applications of neutron scattering** | Th. Brückel |
| 7 | **Diffractometer** | G. Heger |
| 8 | **Small-Angle Scattering** | H. Frielinghaus |
| 9 | **Inelastic Crystal Spectrometers** | J. Wuttke |
| 10 | **Time-of-flight spectrometers including NSE** | M. Monkenbusch |
| 11 | **Structure determination** | G. Heger |
| 12 | **Inelastic neutron scattering: phonons and magnons** | M. Braden |
| 13 | **Structure of Complex Fluids and Macromolecules** | H. Frielinghaus |
| 14 | **Dynamics of Macromolecules** | D. Richter |
| 15 | **Correlated electrons in complex transition metal oxides** | Th. Brückel |

# I

# Fourier Transform

Reiner Zorn

# I. Fourier Transform

Reiner Zorn

In this lecture a short introduction to Fourier transforms (FTs), their application, and useful theorems will be given. Emphasis will be put on the application for scattering problems although some of the theorems have more widespread importance. The proofs of the theorems will mostly only be sketched. For the mathematically more inclined reader refs. 1–3 are recommended.

## I.1 Definitions

The most straightforward definition of Fourier transforms (FTs) is that given by the Fourier sine and cosine transform, respectively[1]:

$$F_{\mathrm{c}}(X) = \int_0^\infty f(x)\cos(2\pi X x)\mathrm{d}x\,, \tag{I.1}$$

$$F_{\mathrm{s}}(X) = \int_0^\infty f(x)\sin(2\pi X x)\mathrm{d}x\,. \tag{I.2}$$

Here, we will preferentially use the exponential two-sided Fourier transform which results from combining the sine and cosine FT using the Euler formula, $\exp(\mathrm{i}z) = \cos z + \mathrm{i}\sin z$ with $\mathrm{i} = \sqrt{-1}$:

$$F(X) = \int_{-\infty}^\infty f(x)\exp(\mathrm{i}Xx)\mathrm{d}x\,. \tag{I.3}$$

The advantage of this definition is that once the exponential FT is known the sine and cosine FT can be obtained as the imaginary and real part. Also it turns out that the integral in (I.3) is often easier to calculate than those containing trigonometric functions. Of course, the imaginary part has to be considered with some care in physical applications. Its significance depends on the context in which the the exponential FT occurs.

[1] Wherever no physical meaning is associated with the functions and variables, we will write the original function and argument in lowercase letters, e.g. $f(x)$, and the Fourier transformed function and argument by its uppercase counterparts, e.g. $F(X)$.

In classical applications where it is just a completion of the cosine FT it may be discarded. In quantum-mechanical calculations it usually represents the phase of a quantity like the wave function which is not observable. Nevertheless, it has its importance when calculating interference phenomena.

Wherever possible we will use the functional notation

$$\mathcal{F}_{X|x}[f(x)] = \int_{-\infty}^{\infty} f(x)\exp(\mathrm{i}Xx)\mathrm{d}x\,. \tag{I.4}$$

to abbreviate the Fourier integral.

The inversion of the FT (I.3) is:

$$f(x) = \mathcal{F}^{-1}_{x|X}[F(X)] = \frac{1}{2\pi}\int_{-\infty}^{\infty} F(X)\exp(-\mathrm{i}Xx)\mathrm{d}X\,. \tag{I.5}$$

The proof that (I.5) is the inverse of (I.3) is not simple and can be found in ref. 1.

Note that the inverted FT (iFT) is not much different from the FT, in shorthand:

$$\mathcal{F}^{-1}_{X|x} = \frac{1}{2\pi}\mathcal{F}_{-X|x}\,. \tag{I.6}$$

In order to make this symmetry more obvious, some authors include $2\pi$ in the argument of the exponential or "symmetrise" the pre-factors in equations (I.3) and (I.5) to $1/\sqrt{2\pi}$. In both variant definitions the iFT is just the FT at negative argument $-X$. Also it is clear at this point that the FT may have a minus sign in the argument of the exponential instead of the iFT without any change of their relation. This variant is also often found in the literature.

The so-called near-equivalence expressed by (I.6) has the consequence that most of the theorems derived hold in similar ways for FT and iFT, at most only differing in a factor $2\pi$ or a minus sign.

If one of the functions, say $f(x)$, is periodic, i.e. $f(x+a) = f(x)$, it can be expressed as a Fourier series

$$f(x) = \sum_{K=-\infty}^{\infty} F_K \exp(-2\pi\mathrm{i}Kx/a)\,. \tag{I.7}$$

This means that the Fourier transform $F(X)$ reduces to a sequence of complex numbers $F_K$. These coefficients $F_K$ result from the relation

$$F_K = \frac{1}{a}\int_{-a/2}^{a/2} f(x)\exp(2\pi\mathrm{i}Kx/a)\mathrm{d}x\,. \tag{I.8}$$

A third variant is the completely discrete FT where both $f_k$ and $F_K$ are sequences of complex numbers. In this case the FT is

$$F_K = \frac{1}{N} \sum_{k=0}^{N-1} f_k \exp(2\pi \mathrm{i} K k/N) \tag{I.9}$$

with the inverse

$$f_k = \sum_{K=0}^{N-1} F_K \exp(-2\pi \mathrm{i} K k/N)\,. \tag{I.10}$$

(Again, different definitions with $1/N$ for the iFT or $1/\sqrt{N}$ for both may be found in the literature.)

A straightforward generalisation of the FT is that to multiple dimensions. The most important case of three dimensions is:

$$F(X,Y,Z) = \int_{-\infty}^{\infty} \mathrm{d}x \int_{-\infty}^{\infty} \mathrm{d}y \int_{-\infty}^{\infty} \mathrm{d}z \exp(\mathrm{i}Xx) \exp(\mathrm{i}Yy) \exp(\mathrm{i}Zz) f(x,y,z)\,. \tag{I.11}$$

The arguments of the exponentials can be grouped together and replaced by the scalar product of the vector $\underline{r} = (x,y,z)$ and the 'reciprocal space' vector $\underline{R} = (X,Y,Z)$:

$$F(\underline{R}) = \int \exp(\mathrm{i}\underline{R} \cdot \underline{r}) f(\underline{r}) \mathrm{d}^3 r\,. \tag{I.12}$$

The inversion is obviously

$$f(\underline{r}) = \frac{1}{(2\pi)^3} \int \exp(-\mathrm{i}\underline{R} \cdot \underline{r}) F(\underline{R}) \mathrm{d}^3 r \tag{I.13}$$

with one $1/2\pi$ pre-factor for each of the individual coordinates' transform.

An important special case of the 3D FT is that of isotropic functions, where the functions only depend on the absolute values $r = \|\underline{r}\| = \sqrt{x^2+y^2+z^2}$ and $R = \|\underline{R}\|$. In spherical polar coordinates (I.12) reads:

$$F(R) = \int_0^{\infty} \mathrm{d}r \int_0^{\pi} \mathrm{d}\theta \int_0^{2\pi} \mathrm{d}\phi\, r^2 \sin\theta \exp(\mathrm{i}\underline{R} \cdot \underline{r}) f(\underline{r}) =$$

Because of the symmetry one can assume $\underline{R} = (0,0,R)$ without loss of generality[2]. Then $\underline{R} \cdot \underline{r} = Rr\cos\theta$. In addition, because $f(\underline{r})$ does not depend on $\phi$ the integral over this angle can be carried out: $\int_0^{2\pi} \mathrm{d}\phi = 2\pi$. With this we get:

$$= \int_0^{\infty} \mathrm{d}r \int_0^{\pi} \mathrm{d}\theta\, 2\pi r^2 \sin\theta \exp(\mathrm{i}Rr\cos\theta) f(r) =$$

[2] German: ohne Beschränkung der Allgemeinheit

Here, we substitute $\cos\theta \to t$ with the consequence that $\mathrm{d}t = -\sin\theta \mathrm{d}\theta$:

$$= -\int_0^\infty \mathrm{d}r\ 2\pi r^2 \int_1^{-1} \mathrm{d}t \exp(\mathrm{i}Rrt) f(r) =$$

Because only $\exp(\mathrm{i}Rrt)$ depends on $t$ the integration can be carried out resulting in

$$= \int_0^\infty \frac{\sin(Rr)}{Rr} f(r) 4\pi r^2 \mathrm{d}r = \frac{4\pi}{R} \int_0^\infty f(r) r \sin(Rr) \mathrm{d}r\,. \tag{I.14}$$

From the definition of the exponential FT and relation (I.71) shown later one can see that alternatively the FT of an isotropic function can be written as

$$F(R) = -\frac{2\pi\mathrm{i}}{R} \mathcal{F}_{R|r}[rf(|r|)] = \frac{2\pi}{R} \frac{\mathrm{d}}{\mathrm{d}R} \mathcal{F}_{R|r}[f(|r|)]\,. \tag{I.15}$$

Similarly it can be shown that the inverse FT is

$$f(r) = \frac{1}{2\pi^2 r} \int_0^\infty F(R) R \sin(Rr) \mathrm{d}R\,. \tag{I.16}$$

Finally, the Laplace transform (LT) which is closely related to the FT should be mentioned in passing:

$$\mathcal{L}_{X|x}[f(x)] = \int_0^\infty f(x) \exp(-Xx) \mathrm{d}x\,. \tag{I.17}$$

It can be seen that with the change of variables $X \to -\mathrm{i}X$ this becomes the one-sided variant of the exponential FT. The inverse of the Laplace transform is

$$\mathcal{L}^{-1}_{x|X}[F(X)] = \frac{1}{2\pi\mathrm{i}} \int_{\gamma-\mathrm{i}\infty}^{\gamma+\mathrm{i}\infty} F(X) \exp(Xx) \mathrm{d}X \tag{I.18}$$

where $\gamma$ is chosen such that all singularities of $F(X)$ lie to the left of the integration line. Because of the similarity between FT and LT some of the rules mentioned in the following (e.g. the convolution theorem) hold in an only slightly modified way for the LT too.

## I.2 Motivation from Physics

### I.2.1 Fraunhofer diffraction

For light scattering the situation that light source and detection are both in a sufficient distance that for the incident as well as the scattered light plane waves can be assumed, is called *Fraunhofer diffraction*. For the set-up shown in Fig. I.1 we will show that then the diffraction pattern visible on the screen basically is the squared Fourier transform of

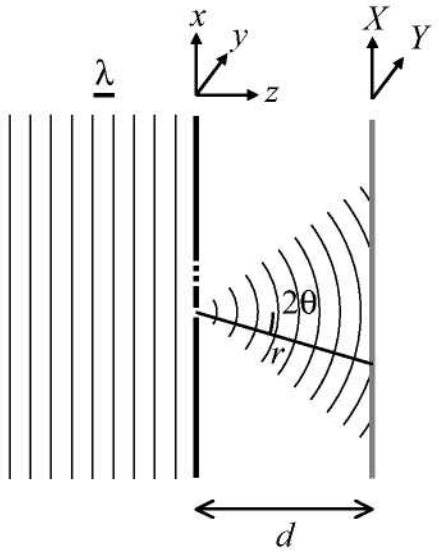



Figure I.1: Fraunhofer diffraction. For simplicity only one partial wave is shown.

the pattern in the object plane. In this discussion we will neglect the vector character of the electromagnetic field but just deal with a scalar field $a(\underline{r}, t)$.

Let the amplitude in the object plane be $f(x, y)$, e.g. by variation of the transparency of the screen. Then the amplitude of the partial wave starting at $(x, y)$ in the observation plane at $(X, Y)$ is proportional to $f(x, y)/r$ where $r = \sqrt{(X-x)^2 + (Y-y)^2 + d^2}$. Because the object screen is illuminated by wave fronts parallel to it all partial waves start with the same phase but arrive in the observation plane with phase

$$\delta = 2\pi \frac{r}{\lambda} = \frac{2\pi}{\lambda} \sqrt{(X-x)^2 + (Y-y)^2 + d^2}\,. \tag{I.19}$$

(The frequency of the waves be $\nu$ and the wave length $\lambda = c/\nu$.) The situation of Fraunhofer diffraction requires that $x, y \ll X, Y \ll d$. The first conditions lead to the approximation

$$\delta \approx \frac{2\pi}{\lambda} \sqrt{X^2 - 2Xx + Y^2 - 2Yy + d^2} \tag{I.20}$$

and the second allows the square root to be approximated:

$$\delta = \frac{2\pi d}{\lambda} \sqrt{1 + \frac{X^2}{d^2} - \frac{2Xx}{d^2} + \frac{Y^2}{d^2} - \frac{2Yy}{d^2}} \approx \frac{2\pi d}{\lambda} \left(1 + \frac{X^2}{2d^2} - \frac{Xx}{d^2} + \frac{Y^2}{2d^2} - \frac{Yy}{d^2}\right)\,. \tag{I.21}$$

The field in the observation plane at $(X, Y)$ is the integral over the contributions of all

partial waves:

$$\begin{aligned} a(X,Y,t) &= \int_{-\infty}^{\infty} \mathrm{d}x \int_{-\infty}^{\infty} \mathrm{d}y \frac{f(x,y)}{r} \cos(\delta + 2\pi\nu t) \\ &= \Re \int_{-\infty}^{\infty} \mathrm{d}x \int_{-\infty}^{\infty} \mathrm{d}y \frac{f(x,y)}{r} \exp(\mathrm{i}(\delta + 2\pi\nu t)) \end{aligned} \tag{I.22}$$

In first order approximation $r \approx d$ and one can insert the approximation (I.21) for $\delta$ to obtain

$$\begin{aligned} a(X,Y,t) &= \Re \frac{1}{d} \exp\left(\mathrm{i}\left(2\pi\nu t + \frac{2\pi d}{\lambda}\left(1 + \frac{X^2}{2d^2} + \frac{Y^2}{2d^2}\right)\right)\right) \\ &\quad \times \int_{-\infty}^{\infty} \mathrm{d}x \int_{-\infty}^{\infty} \mathrm{d}y\, f(x,y) \exp\left(-\mathrm{i}\frac{2\pi}{\lambda d}(Xx + Yy)\right) . \end{aligned} \tag{I.23}$$

We note that this is still a simple oscillating field

$$a(X,Y,t) = \Re A \exp(\mathrm{i}2\pi\nu t) \tag{I.24}$$

with a complex amplitude $A = A' + \mathrm{i}A''$

$$A = \frac{1}{d} \exp\left(\frac{2\pi\mathrm{i}d}{\lambda}\left(1 + \frac{X^2}{2d^2} + \frac{Y^2}{2d^2}\right)\right) \mathcal{F}_{2\pi X/\lambda d, 2\pi Y/\lambda d \,|\, x,y}[f(x,y)] \tag{I.25}$$

proportional to the two-dimensional FT of $f(x,y)$. The target value of the FT, $Q_{[x,y]} = 2\pi[X,Y]/\lambda d$ is the small-angle approximation of the scattering vector which for higher angles is $Q = \frac{4\pi}{\lambda}\sin\theta$ where $\theta$ is half the angle between the incident and the scattered beam.

The observed intensity is the average of the squared field, i.e.

$$I(X,Y) = \nu \int_0^{1/\nu} a^2(X,Y,t)\mathrm{d}t\,. \tag{I.26}$$

By inserting (I.24) one obtains

$$\begin{aligned} I(X,Y) &= \nu \int_0^{1/\nu} \left(A'\cos(2\pi\nu t) - A''\sin(2\pi\nu t)\right)^2 \mathrm{d}t \\ &= A'^2\nu \int_0^{1/\nu} \cos^2(2\pi\nu t)\mathrm{d}t \\ &\qquad -2A'A''\nu \int_0^{1/\nu} \cos(2\pi\nu t)\sin(2\pi\nu t)\mathrm{d}t + A''^2\nu \int_0^{1/\nu} \sin^2(2\pi\nu t)\mathrm{d}t \\ &= \frac{A'^2 + A''^2}{2} = \frac{|A|^2}{2} \end{aligned} \tag{I.27}$$

Because $|\exp(\mathrm{i}x)| = 1$ for any real $x$ inserting $A$ from (I.25) simply yields:

$$I(X,Y) = \frac{1}{2d^2}\left|\mathcal{F}_{2\pi X/\lambda d, 2\pi Y/\lambda d \,|\, x,y}[f(x,y)]\right|^2 . \tag{I.28}$$

This result—that the scattered intensity pattern is the squared FT of the scattering object density—is a general feature of scattering processes (light, neutrons, x-rays...).

### I.2.2 Complex conductance

To give a non-scattering example too we will consider the derivation of the complex conductance in electronics. For a simple resistor Ohm's law states that

$$I = G \cdot U \tag{I.29}$$

where $G = 1/R$ is the reciprocal value of the resistance, the conductance. For a simple resistor this equation remains valid if current $I$ and voltage $U$ are replaced by time-dependent quantities $i(t)$ and $u(t)$.

This is not more the case if the resistor is replaced by a two-terminal circuit which contains capacitors and inductors. In this case by virtue of the charges of capacitors and fields in the coils the circuit has a "memory" which allows past voltages to affect the current at a certain time. Despite this more complex behaviour the circuit often still responds *linear*, i.e. the current resulting from a sum of voltages $u_1(t) + u_2(t)$ is simply the sum of the currents resulting from each of the single stimuli: $i_1(t) + i_2(t)$. In this case the response current to an arbitrary voltage signal $u(t)$ can be expressed as

$$i(t) = \int_{-\infty}^{t} g(t, \tilde{t}) u(\tilde{t}) \mathrm{d}\tilde{t}\,. \tag{I.30}$$

The idea behind this expression is that one can decompose $u(t)$ into individual pulses. $g(t, \tilde{t})$ describes the current at time $t$ resulting from a unit pulse at time $\tilde{t}$. Because of linearity all the contributions to the current can be simply summed up. The response of the circuit usually does not depend on the absolute time. Therefore, $g$ does only depend on the time difference $t - \tilde{t}$ in most cases:

$$i(t) = \int_{-\infty}^{t} g(t - \tilde{t}) u(\tilde{t}) \mathrm{d}\tilde{t} = \int_{0}^{\infty} g(\hat{t}) u(t - \hat{t}) \mathrm{d}\hat{t}\,. \tag{I.31}$$

The integrals can be extended to infinity if one defines $g(t) = 0$ for $t < 0$.

The most interesting practical case is that the voltage depends sinusoidally on time, $u(t) = U_0 \cos(\omega t)$. Inserting this into equation (I.31) yields:

$$\begin{aligned} i(t) &= \int_{-\infty}^{\infty} g(\hat{t}) U_0 \cos(\omega(t - \hat{t})) \mathrm{d}\hat{t} \\ &= \int_{-\infty}^{\infty} g(\hat{t}) U_0 \Re \exp(-\mathrm{i}\omega(t - \hat{t})) \mathrm{d}\hat{t} \\ &= U_0 \Re \exp(-\mathrm{i}\omega t) \int_{-\infty}^{\infty} g(\hat{t}) \exp(\mathrm{i}\omega \hat{t}) \mathrm{d}\hat{t} \end{aligned}$$

$$= U_0 \Re\left(\exp(-\mathrm{i}\omega t) G(\omega)\right) . \tag{I.32}$$

Here, $G(\omega)$ emerges naturally as the FT of the response function $g(t)$. It is in general complex. Denoting the real and complex parts with primes and double-primes one obtains

$$i(t) = U_0(G'(\omega)\cos(\omega t) + G''(\omega)\sin(\omega t)) . \tag{I.33}$$

Thus, $i(t)$ is sum of a sine and a cosine function (i.e. phase shifted with respect to $u(t)$ ) $I'_0\cos(\omega t) + I''_0\sin(\omega t)$ with

$$I'_0 = G'(\omega)\cdot U_0 \text{ and } I''_0 = G''(\omega)\cdot U_0 \tag{I.34}$$

which is the analogue of Ohm's law for AC conductance.

## I.3 Some examples

Only two concrete examples of FTs will be presented here, the exponential/Lorentzian FT pair and the Gaussian function. Interestingly, together with clever use of the rules and the delta function presented in the following sections these may cover 90 % of all physical problems. If there is really the necessity to obtain the FT of other functions they may be found in table books as [4]. In some cases it may even be more effective to look up the Fourier integrals (I.1–I.3) in a table of definite integrals. The (according to the experience of the author) most extensive compilation of such integrals can be found in [5].

*Exponential decay:* Because the exponential $\exp(-ax)$ diverges for $x$ going to negative infinity one cannot FT it with the two-sided transform. One has either to use a one sided transform or define a function

$$f(x) = \begin{cases} 0 & \text{for } x < 0 \\ \exp(-ax) & \text{for } x > 0 \end{cases} \tag{I.35}$$

which is cut-off at $x = 0$. This makes also sense in most of the physical contexts, e.g. thinking of the current of a capacitor which is discharged by closing a circuit with a resistor at time zero. The Fourier integral (I.3) becomes then

$$\int_0^\infty \exp(\mathrm{i}Xx)\exp(-ax)\mathrm{d}x = \int_0^\infty \exp((\mathrm{i}X - a)x)\mathrm{d}x = \tag{I.36}$$

The indefinite integral of the exponential is known, $\int \exp(Ax) = \exp(Ax)/A$, thus one continues the calculation

$$= \frac{\exp((\mathrm{i}X - a)x)}{\mathrm{i}X - a}\bigg|_0^\infty = \frac{1}{a - \mathrm{i}X} = \frac{a}{a^2 + X^2} + \frac{X}{a^2 + X^2}\,\mathrm{i}\,.$$

The real part (which is usually the physically relevant) is a so-called Lorentzian function which peaks at $X = 0$ and has a full width at half maximum of $2a$. Reverting to the interpretation as a decay in time, $a$ is related to the time constant by $a = 1/\tau$. This means that the decay time and the width of the Lorentzian in frequency are inversely proportional.

*Gaussian:* The bell-shaped curve of the Gaussian (or 'normal') distribution

$$f(x) = \frac{1}{\sqrt{2\pi}\sigma} \exp\left(-\frac{x^2}{2\sigma^2}\right) \tag{I.37}$$

decays to both sides rapidly enough and can thus be FTed two-sidedly. The Fourier integral is:

$$\int_{-\infty}^{\infty} \exp(\mathrm{i}Xx) \frac{1}{\sqrt{2\pi}\sigma} \exp\left(-\frac{x^2}{2\sigma^2}\right) \mathrm{d}x = \frac{1}{\sqrt{2\pi}\sigma} \int_{-\infty}^{\infty} \exp\left(\mathrm{i}Xx - \frac{x^2}{2\sigma^2}\right) \mathrm{d}x =$$

In order to simplify the integral we are going to 'complete the square'[3] inside the exponential by adding $\sigma^2 X^2/2$ and compensating this by a factor in front of the integral:

$$\begin{aligned} &= \frac{1}{\sqrt{2\pi}\sigma} \exp\left(-\frac{\sigma^2 X^2}{2}\right) \int_{-\infty}^{\infty} \exp\left(-\frac{x^2}{2\sigma^2} + \mathrm{i}Xx + \frac{\sigma^2 X^2}{2}\right) \mathrm{d}x \\ &= \frac{1}{\sqrt{2\pi}\sigma} \exp\left(-\frac{\sigma^2 X^2}{2}\right) \int_{-\infty}^{\infty} \exp\left(-\frac{(x - \mathrm{i}\sigma^2 X)^2}{2\sigma^2}\right) \mathrm{d}x = \end{aligned}$$

The definite integral of the Gaussian distribution always fulfills the normalisation property $(1/\sqrt{2\pi}\sigma) \int_{-\infty}^{\infty} \exp(-(x - A)^2/2\sigma^2)\mathrm{d}x = 1$, irrespectively of its centre $A$. Therefore, the simple result is:

$$= \exp\left(-\frac{\sigma^2 X^2}{2}\right). \tag{I.38}$$

This means that the FT of a Gaussian is a Gaussian, a property which is called 'self-reciprocity'. It is shared by all Hermite functions of which the Gaussian is the simplest [2]. Nevertheless, the Fourier transform is not the *same* Gaussian but one with the reciprocal standard deviation $1/\sigma$ of the original Gaussian. Also the FT is not normalised to one but its maximum is fixed to one. This in turn causes that the area under the FT Gaussian is $\int_{-\infty}^{\infty} \exp(-\sigma^2 X^2/2)\mathrm{d}x = \sqrt{2\pi}/\sigma$.

[3] German: quadratische Ergänzung

## I.4 The delta 'function'

We are now coming to a topic which may create nausea to mathematicians because we are going to define a function with infinite value. This may be justified by the mathematical concept of *distributions* (in contrast to functions). But because this lecture is addressed to physicists we will simply define the delta function as the following limit:

$$\delta(x) = \lim_{a\to 0} \begin{cases} 1/a & \text{for } |x| < a/2 \\ 0 & \text{everwhere else} \end{cases} . \tag{I.39}$$

When the limit is carried out the delta function is everywhere zero except for $x = 0$ where it has an infinite value. What is important is that the area under the function is always one during the whole limiting process. Therefore, we conclude that $\int_{-\infty}^{\infty} \delta(x)\mathrm{d}x = 1$. This integral condition and the fact that only the value at $x = 0$ does not vanish is the only characteristics of the delta function. Therefore, different definitions by limits are possible, e.g. by narrowing Gaussian functions, equation (I.37) with $\sigma \to 0$. It is somehow justified to say that the delta function is the Black Hole of mathematics, where every individuality of the function is lost as that of a star when it collapses.

The property making the delta function interesting is that it is able to pull out a single value of a function from a definite integral:

$$\int_{-\infty}^{\infty} \delta(x) f(x)\mathrm{d}x = \lim_{a\to 0} \frac{1}{a} \int_{-a/2}^{a/2} f(x)\mathrm{d}x =$$

Because in the limit of small $a$ the function does not vary much over the interval $[-a/2, a/2]$ it can be replaced by its value at the centre, $f(0)$:

$$= \lim_{a\to 0} \frac{1}{a} a f(0) = f(0) . \tag{I.40}$$

Formally, it is also possible to use derivatives of the delta function in integrals which are calculated by application of the rule of integration by parts:

$$\int_{-\infty}^{\infty} \delta'(x) f(x)\mathrm{d}x = \delta(x) f(x)|_{-\infty}^{\infty} - \int_{-\infty}^{\infty} \delta(x) f'(x)\mathrm{d}x = -f'(0) . \tag{I.41}$$

(The product $\delta(x)f(x)$ vanishes for any $x \neq 0$ therefore also in the limit $x \to \pm\infty$) This means that the derivatives of the delta function have the characteristic property to pick the derivatives of a function at $x = 0$ below an integral.

From the basic property of the delta function (I.40) follows that the FT as the integral (I.3) is

$$\mathcal{F}_{X|x}[\delta(x)] = \int_{-\infty}^{\infty} \exp(\mathrm{i}Xx)\delta(x)\mathrm{d}x = 1\,, \tag{I.42}$$

i.e. the FT of the delta function is the constant function $F(X) = 1$. By writing down the inversion formula (I.5) one obtains that the iFT of a constant is a delta function:

$$\mathcal{F}^{-1}_{x|X}[1] = \frac{1}{2\pi}\int_{-\infty}^{\infty} \exp(-\mathrm{i}Xx)\mathrm{d}x = \delta(x)\,. \tag{I.43}$$

(At this point it is important not to forget the $2\pi$!) Because in the last two formulae $\mathrm{i}Xx$ can be replaced by $-\mathrm{i}Xx$ it is of course also true that the iFT of the delta function is a constant $(1/2\pi)$ and the FT of a constant a delta function:

$$\mathcal{F}^{-1}_{x|X}[\delta(X)] = \frac{1}{2\pi}\,, \tag{I.44}$$

$$\mathcal{F}_{X|x}[1] = 2\pi\delta(x)\,. \tag{I.45}$$

As a typical application we will now use the delta function to show that the Fourier series is a special case of the continuous FT. Let $F(X)$ be a function which consists of delta functions at discrete values $X = 2\pi K/a$, $K \in \mathbb{Z}$ with 'weights' $2\pi F_K$:

$$F(X) = \sum_{K=-\infty}^{\infty} 2\pi F_K \delta\left(X - \frac{2\pi K}{a}\right)\,. \tag{I.46}$$

The iFT of this function is

$$\begin{aligned} f(x) &= \frac{1}{2\pi}\int_{-\infty}^{\infty}\sum_{K=-\infty}^{\infty} 2\pi F_K \delta\left(X - \frac{2\pi K}{a}\right)\exp(-\mathrm{i}Xx)\mathrm{d}x \\ &= \sum_{K=-\infty}^{\infty} F_K \int_{-\infty}^{\infty}\delta\left(X - \frac{2\pi K}{a}\right)\exp(-\mathrm{i}Xx)\mathrm{d}x \\ &= \sum_{K=-\infty}^{\infty} F_K \exp\left(-\frac{2\pi\mathrm{i}Kx}{a}\right) \end{aligned} \tag{I.47}$$

which is just the Fourier series (I.7).

Without demonstrating this we mention that in a similar way the completely discrete FT (I.9) can be derived from the continuous FT.

## I.5 Some useful theorems

### I.5.1 Linearity

From the definition it is clear that the FT is a linear operation, i.e.:

$$\mathcal{F}_{X|x}[af(x)] = a\mathcal{F}_{X|x}[f(x)] \tag{I.48}$$

$$\mathcal{F}_{X|x}[f(x)+g(x)] = \mathcal{F}_{X|x}[f(x)] + \mathcal{F}_{X|x}[g(x)]\,. \tag{I.49}$$

Obviously, this is also true for the iFT. The physical significance of this property is that (in a linear medium) waves superimpose without influencing each other.

### I.5.2 Scaling theorem

Let $a$ be a non-zero real number. Then

$$\mathcal{F}_{X|x}[f(ax)] = \frac{1}{|a|}\mathcal{F}_{X/a|x}[f(x)]\,. \tag{I.50}$$

Proof: If $a > 0$ we write out the left-hand FT as an integral and substitute $ax \to t$:

$$\int_{-\infty}^{\infty} \exp(\mathrm{i}Xx) f(ax)\mathrm{d}x = \int_{-\infty}^{\infty} \exp(\mathrm{i}Xt/a) f(t)\frac{\mathrm{d}t}{a} = \frac{1}{a}\int_{-\infty}^{\infty} \exp(\mathrm{i}(X/a)t) f(t)\mathrm{d}t\,.$$

If $a < 0$ we have to multiply the infinite bounds by a negative number effectively exchanging them and thus introducing a minus sign:

$$\int_{-\infty}^{\infty} \exp(\mathrm{i}Xx) f(ax)\mathrm{d}x = \int_{\infty}^{-\infty} \exp(\mathrm{i}Xt/a) f(t)\frac{\mathrm{d}t}{a} = -\frac{1}{a}\int_{-\infty}^{\infty} \exp(\mathrm{i}(X/a)t) f(t)\mathrm{d}t\,.$$

It is clear that both cases are represented if the absolute value $|a|$ is used in the denominator.

The physical phenomenon related to this property of the FT is the change of diffraction patterns with the change of the scattering object. If an object is scaled down affinely the diffraction pattern becomes larger in an inverse proportional way without changing its shape but just by a scaling factor.

An important special case of the scaling theorem is that of $a = -1$ and a real function $f(x) \in \mathbb{R}$:

$$\mathcal{F}_{X|x}[f(-x)] = \mathcal{F}_{-X|x}[f(x)] = \left(\mathcal{F}_{X|x}[f(x)]\right)^* \tag{I.51}$$

where the star denotes the complex conjugate defined as $(a+b\mathrm{i})^* = a-b\mathrm{i}$. In words: The Fourier transform of the mirror image of a *real* function is the complex conjugate of the original function.

### I.5.3 Shifting theorem

The shifting theorem can be written in two ways:

$$\mathcal{F}_{X|x}[f(x+a)] = \exp(-\mathrm{i}Xa)\mathcal{F}_{X|x}[f(x)] \quad \text{and} \tag{I.52}$$

$$\mathcal{F}_{X+A|x}[f(x)] = \mathcal{F}_{X|x}[\exp(\mathrm{i}xA)f(x)]\,. \tag{I.53}$$

The proof of the second relation is trivial by insertion into the definition. To prove the first line, which is the more common statement, one has to substitute $x+a \rightarrow t$ in the Fourier integral.

Because $|\exp(-\mathrm{i}Xa)| = 1$ this implies that the complex absolute of a FT does not change if its argument function $f(x)$ is shifted. For scattering experiments, which usually only observe the absolute value but not the phase, this means that the diffraction pattern is not changed when the sample is displaced within the beam.

### I.5.4 Symmetries

If a function shows certain symmetries its FT may have properties reflecting that symmetry. One example is the periodicity (or translational symmetry) of $f(x)$ which—as shown above—causes the FT to be a sum of equidistant delta functions. Others are mirror symmetries which cause the FT to be purely real or imaginary. In summary, the symmetry

relations for one-dimensional FT are:

| $f(x)$ | $F(X)$ |
|---|---|
| periodic: $f(x+a) = f(x)$ | discrete, stepsize $\Delta X = 2\pi/a$ |
| discrete, stepsize $\Delta x = 2\pi/A$ | periodic: $F(X+A) = F(X)$ |
| real: $\forall_{x\in\mathbb{R}} f(x) \in \mathbb{R}$ | $F(-X) = F^*(X)$ |
| $f(-x) = f^*(x)$ | real: $\forall_{X\in\mathbb{R}} F(X) \in \mathbb{R}$ |
| especially: | |
| real and even | real and even |
| real and odd | imaginary and odd |
| imaginary and even | imaginary and even |
| imaginary and odd | real and odd |

A consequence is that if $f(x)$ and $F(X)$ are both real functions (which has to be the case if both have a physically observable meaning) both have to be even functions. In this case it makes not much difference whether one uses the one-sided cosine FT (I.1) or the two-sided exponential FT (I.3) because they only differ by a constant factor of two.

A more subtle case of "symmetry" arises if a function is not mirrored at zero but cut-off. Such functions are called *causal* because in physics they usually describe the response of a system to a stimulus at time zero, e.g. the electric displacement $\underline{D}(t)$ for a electric field pulse $\underline{E}(t) = \delta(t)$ (or $g(t)$ in the example of subsection I.2.2). If one does not believe in precognition, clairvoyance or related effects one may safely assume that the past remains unaffected by the stimulus at $t = 0$ and thus the response function vanishes for $t < 0$. The FT of the response function

$$F(\omega) = \int_0^\infty f(t) \exp(\mathrm{i}\omega t) \mathrm{d}t \tag{I.54}$$

is the *susceptibility*[4]. In the example above it is related to the dielectric constant by $\epsilon(\omega) = 1 + F(\omega)$. The susceptibility has both a real and an imaginary part because $f(t)$ is neither even nor odd. Nevertheless, from causality, $f(t) = 0$ for $t < 0$, follows that the real and imaginary part are not independent but can be calculated from each other via the Kramers-Kronig relations[11]. The sketch of the proof of the Kramers-Kronig

[4] Here, we specify $t$ and $\omega$ as arguments because only the interpretation as time and frequency make sense.

relations is as follows: Firstly, $F(\omega)$ is interpreted in the sense of complex analysis[5] as a function of complex argument. Because the integral in (I.54) is not extended to negative $t$ it converges for any $\omega$ with positive imaginary part. Thus, $F(\omega)$ is analytic in the upper half plane of $\omega$ values. For this reason Cauchy's theorem

$$F(\omega) = \frac{1}{2\pi \mathrm{i}} \oint_{\mathcal{C}} \frac{F(\tilde{\omega})}{\tilde{\omega} - \omega} \mathrm{d}\tilde{\omega} \tag{I.55}$$

can be invoked where $\mathcal{C}$ is a contour comprising the real $\omega$ axis and a semicircle at infinity in the upper half plane. By some straightforward mathematics follows that the real and imaginary part of $F(\omega) = F'(\omega) + F''(\omega)\mathrm{i}$ are related by

$$F'(\omega) = \frac{1}{\pi} \mathcal{P} \int_{-\infty}^{\infty} \frac{F''(\tilde{\omega})}{\tilde{\omega} - \omega} \mathrm{d}\tilde{\omega} \text{ and} \tag{I.56}$$

$$F''(\omega) = -\frac{1}{\pi} \mathcal{P} \int_{-\infty}^{\infty} \frac{F'(\tilde{\omega})}{\tilde{\omega} - \omega} \mathrm{d}\tilde{\omega} . \tag{I.57}$$

Here, $\mathcal{P}$ denotes the *(Cauchy) principal value* of the integral: Actually the integrand diverges at $\tilde{\omega} = \omega$ in a way that is not integrable. Nevertheless the limits

$$\lim_{\epsilon \to 0} \left( \int_{-\infty}^{\omega - \epsilon} \ldots \mathrm{d}\tilde{\omega} + \int_{\omega + \epsilon}^{\infty} \ldots \mathrm{d}\tilde{\omega} \right)$$

exist and are called principal values. Equations (I.56) and (I.57) are of not much use in the theoretical calculation of susceptibilities because it is much easier to calculate them as real and imaginary part of the FT (I.54). Nevertheless, they have some importance for experiments where only one of the quantities $F'(\omega)$ or $F''(\omega)$ is accessible and the other has to be calculated. For this purpose one usually invokes the symmetries resulting from the fact that $f(t)$ is a real function, $F'(-\omega) = F'(\omega)$ and $F''(-\omega) = -F''(\omega)$, and obtains:

$$F'(\omega) = \frac{2}{\pi} \mathcal{P} \int_{0}^{\infty} \frac{\tilde{\omega} F''(\tilde{\omega})}{\tilde{\omega}^2 - \omega^2} \mathrm{d}\tilde{\omega} . \tag{I.58}$$

$$F''(\omega) = -\frac{2\omega}{\pi} \mathcal{P} \int_{0}^{\infty} \frac{F'(\tilde{\omega})}{\tilde{\omega}^2 - \omega^2} \mathrm{d}\tilde{\omega} , \tag{I.59}$$

equations which only include the susceptibility at positive frequencies.

---

[5] German: Funktionentheorie

### I.5.5 Convolution theorem

The *convolution*[6] of two functions is defined as follows:

$$f \otimes g(x) = \int_{-\infty}^{\infty} f(t)g(x-t)\mathrm{d}t\,. \tag{I.60}$$

One of the most important occurrences of the convolution and its two- and three-dimensional generalisations in Physics is the consideration of limited instrumental resolution. E.g. if $f(x,y)$ is the ideal two-dimensional picture of a scene and $g(x,y)$ is the picture of a single light spot by a camera, then $f \otimes g(x,y)$ is the blurred picture of the scene you obtain from the camera. Actually, most of the "optical" effects included in programs like Adobe PhotoShop® are realised mathematically as convolutions.

One of the most important theorems on FTs is now that the FT of a convolution is the product of the individual FTs:

$$\mathcal{F}_{X|x}[f \otimes g(x)] = \mathcal{F}_{X|x}[f(x)] \cdot \mathcal{F}_{X|x}[g(x)] = F(X)G(X) \tag{I.61}$$

or vice versa:

$$\mathcal{F}_{X|x}[f(x)g(x)] = \mathcal{F}_{X|x}[f(x)] \otimes \mathcal{F}_{X|x}[g(x)] = F(X) \otimes G(X)\,. \tag{I.62}$$

Proof of relation (I.61): From the definition (I.3) follows straightforwardly:

$$\begin{aligned}
\mathcal{F}_{X|x}[f \otimes g(x)] &= \int_{-\infty}^{\infty} \exp(\mathrm{i}Xx) \left( \int_{-\infty}^{\infty} f(t)g(x-t)\mathrm{d}t \right) \mathrm{d}x \\
&= \int_{-\infty}^{\infty} \mathrm{d}x \int_{-\infty}^{\infty} \mathrm{d}t \exp(\mathrm{i}Xx) f(t)g(x-t) \\
&= \int_{-\infty}^{\infty} \mathrm{d}x \int_{-\infty}^{\infty} \mathrm{d}t \exp(\mathrm{i}X(x-t)) \exp(\mathrm{i}Xt) f(t)g(x-t) \\
&= \int_{-\infty}^{\infty} \mathrm{d}t \int_{-\infty}^{\infty} \mathrm{d}x \exp(\mathrm{i}X(x-t)) \exp(\mathrm{i}Xt) f(t)g(x-t)
\end{aligned} \tag{I.63}$$

Substituting $x - t \to x'$ leaves the infinite bounds of the first integral unchanged:

$$\begin{aligned}
&= \int_{-\infty}^{\infty} \mathrm{d}t \int_{-\infty}^{\infty} \mathrm{d}x' \exp(\mathrm{i}Xx') \exp(\mathrm{i}Xt) f(t)g(x') \\
&= \int_{-\infty}^{\infty} \exp(\mathrm{i}Xt) f(t)\mathrm{d}t \int_{-\infty}^{\infty} \exp(\mathrm{i}Xx') g(x')\mathrm{d}x' \\
&= \mathcal{F}_{X|x}[f(x)] \cdot \mathcal{F}_{X|x}[g(x)]
\end{aligned} \tag{I.64}$$

---

[6] German: Faltung (sometimes also used in English)

Note that the critical step of this proof is the exchange of integrations at line (I.63). For some "crazy" functions this may not be allowed and in consequence the convolution theorem does not hold. Nevertheless, for "physical" functions this is usually no issue.

In addition to numerous applications to derive FTs analytically—of which some will be discussed in section I.6—the convolution theorem is also exploited in numerical calculations, e.g.:

- Discretisation of (I.60) with $N$ points for $f$ and $g$ each means for a numerical calculation of $f \otimes g$ that $N$ sums of $N$ summands have to be calculated. Thus the complexity rises proportional to $N^2$ with the number of points. At the first glance it seems more complicated to use the convolution theorem, i.e. calculate the FTs of $f$ and $g$ first, multiply them, and Fourier backtransform the product. Nevertheless, because fast FT algorithms [6] have a complexity only proportional to $N \log N$ and only $N$ products have to be calculated the aggregate computational effort may be smaller via FT for sufficiently large $N$.

- With regard to the significance of the convolution as influence of the limited instrumental resolution it is clearly of interest to reconstruct the function $f(x)$ (physical quantity) from the convolution product $f \otimes g(x)$ (measured quantity) and $g(x)$ (instrumental resolution function). Because the inverse integral transform of (I.60) is usually not known it is not possible to calculate $f(x)$ directly. Nevertheless, using the convolution theorem it is easy to calculate $F(X)$ by dividing the FT of the measured quantity by that of the resolution function[7]:

$$F(X) = \frac{\mathcal{F}_{X|x}[f \otimes g(x)]}{\mathcal{F}_{X|x}[g(x)]} \,. \tag{I.65}$$

[7] It should be mentioned that if experimental errors are considered the result may be ambiguous, i.e. depend strongly on the particular realisation of errors. The inversion of (I.60) is an "ill-defined" problem, even a small difference in the errors of the measured quantity may cause a largely different $f(x)$. This means that in order to select a physically meaningful $f(x)$ one has to introduce additional criteria, e.g. smoothness of the result. This leads to various empirical techniques as indirect Fourier transform [7], Tikhonov regularisation [8, 9], or Maximum Entropy methods [10]

In principle, the thus obtained $F(X)$ could be back-transformed to yield $f(x)$ but the accumulation of numerical errors usually prohibits this in practice.

Closely related to the convolution is the correlator or correlation function of two functions:

$$\langle f(0)g(x)\rangle = \int_{-\infty}^{\infty} f(t)g(x+t)\mathrm{d}t\,. \tag{I.66}$$

By a substitution $t \rightarrow -t'$ it is easy to show that

$$\langle f(0)g(x)\rangle = f(-x) \otimes g(x) \tag{I.67}$$

so that the correlator is just the convolution with one of the functions mirrored. Using the convolution theorem and scaling theorem in succession, it follows that the FT of the correlation function is the product of the FTs of the correlated functions with one FT mirrored, i.e.

$$\mathcal{F}_{X|x}[\langle f(0)g(x)\rangle] = \mathcal{F}_{-X|x}[f(x)]\mathcal{F}_{X|x}[g(x)] = F(-X)G(X)\,. \tag{I.68}$$

For a real function $f(x)$ from (I.51) follows that the FT of the correlation function is the product of the complex conjugate of the FT of that function multiplied with the FT of the other function:

$$\mathcal{F}_{X|x}[\langle f(0)g(x)\rangle] = F^*(X)G(X)\,. \tag{I.69}$$

In physics the most important special case is the autocorrelation function where $f = g$:

$$\mathcal{F}_{X|x}[\langle f(0)f(x)\rangle] = F^*(X)F(X) = |F(X)|^2\,. \tag{I.70}$$

This relation, which expresses that the autocorrelation function $\langle f(0)f(t)\rangle$ and the power spectrum $|F(\omega)|^2$ of a signal $f(t)$ are related by a FT, is known as the Wiener-Khinchine theorem.

Note that the right-hand side is just the typical result for the scattered intensity as in (I.28). The Wiener-Khinchine theorem thus allows the scattered intensity to be calculated in two ways: (1) The object density can be FTed to obtain an amplitude of which subsequently the absolute squared is calculated. (2) One can construct the autocorrelation function of the object density (called Patterson function, pair correlation function, van-Hove function etc. depending on context) and FT it.

### I.5.6 Differentials, integrals

By differentiating (I.3) one obtains directly:

$$\begin{aligned}\frac{\mathrm{d}}{\mathrm{d}X}\mathcal{F}_{X|x}[f(x)] &= \frac{\mathrm{d}}{\mathrm{d}X}\int_{-\infty}^{\infty}\exp(\mathrm{i}Xx)f(x)\mathrm{d}x \\ &= \int_{-\infty}^{\infty}\mathrm{i}x\exp(\mathrm{i}Xx)f(x)\mathrm{d}x \\ &= \mathrm{i}\mathcal{F}_{X|x}[xf(x)]\,. \end{aligned} \tag{I.71}$$

Analogously, for the iFT holds:

$$\frac{\mathrm{d}}{\mathrm{d}x}\mathcal{F}^{-1}_{x|X}[F(X)] = -\mathrm{i}\mathcal{F}^{-1}_{x|X}[XF(X)]\,. \tag{I.72}$$

By FTing the last equation and inserting $F(X) = \mathcal{F}_{X|x}[f(x)]$ one obtains the more common form of the differentiation theorem:

$$\mathcal{F}_{X|x}\left[\frac{\mathrm{d}f}{\mathrm{d}x}\right] = -\mathrm{i}X\mathcal{F}_{X|x}[f(x)]\,. \tag{I.73}$$

Thus, the FT of the derivative is the FT of the original function multiplied by $-\mathrm{i}X$ [8].

In signal processing differentiation of a signal $f(t)$ is realised by a high pass filter. Expressed in frequency domain, $f(\omega)$, this filter has the effect of pronouncing the high frequencies and shifting the phase by 90°. This is exactly what is mathematically expressed by a multiplication with $-\mathrm{i}\omega$.

By induction[9] it is easy to prove that the FT of derivatives of arbitrary order $n$ can be easily calculated:

$$\mathcal{F}_{X|x}\left[\frac{\mathrm{d}^n f}{\mathrm{d}x^n}\right] = (-\mathrm{i}X)^n\mathcal{F}_{X|x}[f(x)]\,. \tag{I.74}$$

Since the integral is a kind of inverse operation to the derivative, similar theorems hold for integration. Namely, the definite integral of a FT is:

$$\begin{aligned}\int_A^X \mathcal{F}_{T|x}[f(x)]\mathrm{d}T &= \int_A^X \mathrm{d}T\int_{-\infty}^{\infty}\mathrm{d}x\exp(\mathrm{i}Tx)f(x) \\ &= \int_{-\infty}^{\infty}\mathrm{d}x\int_A^X \mathrm{d}T\exp(\mathrm{i}Tx)f(x)\end{aligned}$$

[8] Note that for alternative definitions of the FT this factor may by $+\mathrm{i}X$ or $\pm 2\pi\mathrm{i}X$.

[9] German: vollständige Induktion

$$= \int_{-\infty}^{\infty} \left( \frac{\exp(\mathrm{i}Xx)}{\mathrm{i}x} - \frac{\exp(\mathrm{i}Ax)}{\mathrm{i}x} \right) f(x)\mathrm{d}x$$
$$= \mathrm{i}\mathcal{F}_{A|x}\left[\frac{f(x)}{x}\right] - \mathrm{i}\mathcal{F}_{X|x}\left[\frac{f(x)}{x}\right] . \qquad \text{(I.75)}$$

With respect to $X$ the first term is a constant and therefore an indefinite integral or primitive[10] of a FT is

$$\int \mathcal{F}_{X|x}[f(x)]\mathrm{d}X = -\mathrm{i}\mathcal{F}_{X|x}\left[\frac{f(x)}{x}\right] , \qquad \text{(I.76)}$$

i.e. the FT of the function divided by $\mathrm{i}x$.

The corresponding theorem for the iFT is:

$$\int_a^x \mathcal{F}^{-1}_{t|X}[F(X)]\mathrm{d}t = \mathrm{i}\mathcal{F}^{-1}_{x|X}\left[\frac{F(X)}{X}\right] - \mathrm{i}\mathcal{F}^{-1}_{a|X}\left[\frac{F(X)}{X}\right] . \qquad \text{(I.77)}$$

As above, by FTing the last equation and inserting $F(X) = \mathcal{F}_{X|x}[f(x)]$ the FT of an integral is obtained:

$$\mathcal{F}_{X|x}\left[\int_a^x f(t)\mathrm{d}t\right] = \mathrm{i}\frac{F(X)}{X} - \mathrm{i}\mathcal{F}^{-1}_{a|X}\left[\frac{F(X)}{X}\right] 2\pi\delta(X)$$
$$= \mathrm{i}\frac{\mathcal{F}_{X|x}[f(x)]}{X} - 2\pi\mathrm{i}\mathcal{F}^{-1}_{a|X}\left[\frac{\mathcal{F}_{X|x}[f(x)]}{X}\right]\delta(X) \qquad \text{(I.78)}$$

This expression seems to be impracticably complicated. But one has to notice that the second term is just a delta function. Therefore, up to the value at $X = 0$ it can be omitted for the result. For the same reason the integration constant of the indefinite integral does not play a rôle except for the delta function strength at $X = 0$ and

$$\forall_{X\neq 0} \quad \mathcal{F}_{X|x}\left[\int f(x)\mathrm{d}x\right] = \mathrm{i}\frac{\mathcal{F}_{X|x}[f(x)]}{X} . \qquad \text{(I.79)}$$

Note that this result is included in the general expression (I.74) if the integration is interpreted as the $-1^{\text{th}}$ derivative[11].

Obviously, the integration corresponds to the low pass filter in signal processing as the derivative did for the high pass.

---

[10] German: Stammfunktion

[11] If the definitions of *fractional calculus* [12] are used rule (I.74) is even valid for any real $n$.

### I.5.7 Sum rules

The title of this subsection is actually a misnomer since it deals with infinite integrals over FTs which only in the discrete version can be expressed by sums. Nevertheless, it is the term most used in the Physics literature.

The simplest sum rule is that for the infinite integral of the FT itself:

$$\begin{aligned}\int_{-\infty}^{\infty} \mathcal{F}_{X|x}[f(x)]\mathrm{d}X &= \int_{-\infty}^{\infty} \mathrm{d}X \int_{-\infty}^{\infty} \mathrm{d}x \exp(iXx) f(x) \\ &= \int_{-\infty}^{\infty} f(x) 2\pi\delta(x)\mathrm{d}x = 2\pi f(0)\,. \end{aligned} \tag{I.80}$$

(We use that $\int_{-\infty}^{\infty} \mathrm{d}x \exp(iXx)$ is the FT of one, see (I.45).) Here again, we assume that the integrals over $X$ and $x$ are interchangeable which may cause problems for certain functions. Often (e.g. for a simple function as (I.35) ) it may be necessary to interpret the integral over $X$ as Cauchy principal value and handle discontinuities in $f(x)$ by imposing Dirichlet's condition, $f(a) = (\lim_{x\searrow a} f(x) + \lim_{x\nearrow a} f(x))/2$.

The complementary sum rule is even simpler to derive:

$$\mathcal{F}_{0|x}[f(x)] = \int_{-\infty}^{\infty} f(x) \exp(\mathrm{i}0x)\mathrm{d}x = \int_{-\infty}^{\infty} f(x)\mathrm{d}x\,. \tag{I.81}$$

We see that the infinite integral of a FT corresponds to the value of the original function at zero (up to a factor $2\pi$) and vice versa.

We define the equivalent width of a function $f(x)$ as

$$\Delta x = \frac{\int_{-\infty}^{\infty} f(x)\mathrm{d}x}{f(0)}\,. \tag{I.82}$$

i.e. by the area under the function reshaped into a rectangle of width $\Delta x$ and the height of the function at $x = 0$. If $F(X)$ is the FT of $f(x)$ using (I.81) one can write

$$\Delta x = \frac{F(0)}{f(0)}\,. \tag{I.83}$$

Analogously, with (I.80) one obtains

$$\Delta X = \frac{\int_{-\infty}^{\infty} F(X)\mathrm{d}X}{F(0)} = \frac{2\pi f(0)}{F(0)}\,. \tag{I.84}$$

Multiplying the last two equations yields

$$\Delta X \cdot \Delta x = 2\pi \tag{I.85}$$

which is the *uncertainty relation* of Fourier transforms. It expresses in a mathematically exact way the notion "If the function is narrower the FT is wider and vice versa." It is also the mathematical origin of the uncertainty relation in quantum mechanics. For scattering experiments its consequence is that an object of dimension $\Delta x$ causes a scattering pattern of size $\Delta Q = 2\pi/\Delta x$ where $Q = \frac{4\pi}{\lambda}\sin\theta$ is the scattering vector.

The sum rules (I.80) and (I.81) are a special case of general rules to calculate the moments of a FT. The $n^{\text{th}}$ moment of a function is defined as

$$[x^n]_f = \int_{-\infty}^{\infty} x^n f(x)\mathrm{d}x\,. \tag{I.86}$$

These moments are of special importance if $f(x)$ has the meaning of a probability distribution (e.g. in the example of a Gaussian (I.37) above). Then the moments enter into statistical quantities as average, variance, skewness, and kurtosis. Using the differentiation rule (I.74) the $n^{\text{th}}$ ($n \in \mathbb{N}$) moment of a FT can be calculated in a simple way:

$$[X^n]_F = \int_{-\infty}^{\infty} X^n F(X)\mathrm{d}X = \int_{-\infty}^{\infty} \mathrm{i}^n \mathcal{F}_{X|x}\left[\frac{\mathrm{d}^n f}{\mathrm{d}x^n}\right]\mathrm{d}X = 2\pi\mathrm{i}^n \left.\frac{\mathrm{d}^n f}{\mathrm{d}x^n}\right|_{x=0} \tag{I.87}$$

or complementarily:

$$[x^n]_f = (-\mathrm{i})^n \left.\frac{\mathrm{d}^n F}{\mathrm{d}X^n}\right|_{X=0} \tag{I.88}$$

This means that all moments of $f(x)$ are characterised by the behaviour of the FT, viz its derivatives, close to zero. For this reason the FT of a probability distribution is called *characteristic function* in probability theory.

There are also sum rules concerning quadratic expressions in the FTs. E.g. by integrating (I.69) and applying sum rule (I.80) one obtains

$$\int_{-\infty}^{\infty} F^*(X)G(X)\mathrm{d}X = \int_{-\infty}^{\infty} \mathcal{F}_{X|x}\left[\langle f(0)g(x)\rangle\right]\mathrm{d}X = 2\pi\langle f(0)g(0)\rangle = 2\pi\int_{-\infty}^{\infty} f(x)g(x)\mathrm{d}x\,.$$

One has to note that this equation is only valid for real $f(x)$ since (I.69) is restricted to this (in physics most important) case. Without proof we note that the generalisation to complex $f(x)$ (and $g(x)$ ) is

$$\int_{-\infty}^{\infty} F^*(X)G(X)\mathrm{d}X = 2\pi\int_{-\infty}^{\infty} f^*(x)g(x)\mathrm{d}x\,. \tag{I.89}$$

This is usually called the *power-* or *Plancherel's theorem* because if $f$ and $g$ are interpreted as voltage $u(t)$ and current $i(t)$ of a signal the right hand side is the electrical power of

that signal. The power theorem now states that the power can also be calculated by integrating the product of the voltage and current spectra, $U(\omega)$ and $I(\omega)$, over the whole frequency spectrum.

The special case $g(x) = f(x)$ is often better known as *Parseval's theorem*:

$$\int_{-\infty}^{\infty} |F(X)|^2 \mathrm{d}X = 2\pi \int_{-\infty}^{\infty} |f(x)|^2 \mathrm{d}x\,. \tag{I.90}$$

This means that the norm of a function remains unchanged by a FT except for a factor $2\pi$ [12].

## I.6 Application of theorems

### I.6.1 Diffraction by slits and gratings

Here a couple of freshman examples of optical diffraction (single and double slit, infinite and finite grating) will be re-examined. The emphasis will be put on the use of the convolution theorem to obtain the old results in a more simple and evident way.

The transmissivity of a single slit of width $a$ can be described by the "mesa" or "boxcar" function

$$f(x) = \begin{cases} 1 & \text{for } -a/2 < x < a/2 \\ 0 & \text{elsewhere.} \end{cases} \tag{I.91}$$

The FT of this function is

$$F_1(X) = \int_{-a/2}^{a/2} \exp(\mathrm{i}Xx)\mathrm{d}x = \left.\frac{\exp(\mathrm{i}Xx)}{\mathrm{i}X}\right|_{-a/2}^{a/2} = \frac{2}{X}\sin\frac{Xa}{2}\,. \tag{I.92}$$

Up to constant factors the intensity of the diffraction pattern is the absolute square, namely

$$I_1(X) = |F_1(X)|^2 = \frac{4}{X^2}\sin^2\frac{Xa}{2}\,. \tag{I.93}$$

We now consider two such slits in a distance $d$, i.e. centred at $x = -d/2$ and $x = d/2$. Using the shifting theorem (I.52) we can state the FT of each slit separately is

[12] This factor—which is especially annoying at that point—would not appear for certain alternative definitions of the FT.

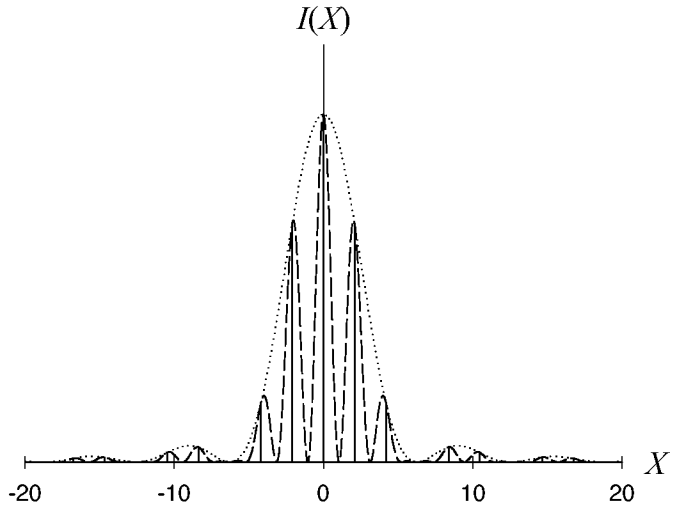



Figure I.2: Diffraction from a single slit (·····), a double slit (- - -), and an infinite array of slits (——). Slit width: $a = 1$, slit distance: $d = 3$.

$\exp(\pm \mathrm{i}Xd/2)F_1(X)$ and the sum

$$F_2(X) = 2\cos\frac{Xd}{2}\frac{2}{X}\sin\frac{Xa}{2}\,. \tag{I.94}$$

Thus the intensity is

$$I_2(X) = |F(X)|^2 = \frac{4}{X^2}\sin^2\frac{Xa}{2}\cos^2\frac{Xd}{2}\,. \tag{I.95}$$

(Fig. I.2) Alternatively, we can say that the transmissivity of a double slit is that of a single one convoluted with two delta functions in a distance $d$, $g(x) = \delta(x - d/2) + \delta(x + d/2)$, of which the FT is

$$G(X) = \exp(\mathrm{i}Xd/2) + \exp(-\mathrm{i}Xd/2) = 2\cos(Xd/2)\,. \tag{I.96}$$

The convolution theorem (I.61) states the the FT of the convolution is the product $F_1(X)G(X)$ which is exactly the same result as (I.94).

Analogously, one can derive the diffraction pattern of an infinite grid of slits with width $a$ and distance $d$. The function to be FTed here is the convolution $f(x) \otimes g(x)$ with $f(x)$ from (I.91) and

$$g(x) = \sum_{k=-\infty}^{\infty} \delta(x + kd)\,. \tag{I.97}$$

This is just the case of a periodic function discussed in section I.1 and from (I.8) the Fourier coefficients are constant $G_K = 1/d$. The FT itself is then a sum of delta functions apart by $2\pi K/d$ with these coefficients:

$$G(X) = \sum_{K=-\infty}^{\infty} \frac{1}{d}\delta\left(X - \frac{2\pi K}{d}\right) . \tag{I.98}$$

So the diffracted intensity from the infinite grating is

$$I_3(X) = |F(X)G(X)|^2 = \sum_{K=-\infty}^{\infty} \frac{4}{K^2}\sin^2\frac{Ka}{2d}\delta^2\left(X - \frac{2\pi K}{d}\right) . \tag{I.99}$$

So the scattering is concentrated into sharp peaks (which is a consequence of the translational symmetry) but the intensity is not constant but modulated by the scattering function of a single slit.

This is the simplest one-dimensional case of decomposition of the scattered intensity into *form factor* and *structure factor*. In scattering physics one often has the situation that the sample is an arrangement of identical individual particles (atoms, molecules, colloidal particles ...) where the fictitious scattering pattern of their centres-of-mass (corresponding to $G(X)$ in the above example) is known and called the structure factor $S(\underline{Q})$. Let the density of scatterers (electrons, nuclei ...) within a single particle be $\rho(\underline{r})$. Then the squared FT of that density $P(\underline{Q}) = \left|\mathcal{F}_{\underline{Q}|\underline{r}}[\rho(\underline{r})]\right|^2$ is called the form factor of the particle. From the convolution theorem follows that the total scattered intensity from the arrangement of particles is $I(\underline{Q}) = P(\underline{Q})S(\underline{Q})$, the product of form- and structure factor.

As a last example we will extend the considerations to a finite grating of size $l$. We can do this by multiplying with a mesa function masking out the desired part from an infinite grating:

$$h(x) = \begin{cases} 1 & \text{for } -l/2 < x < l/2 \\ 0 & \text{elsewhere.} \end{cases} \tag{I.100}$$

So the total function to be transformed is $(f(x) \otimes g(x)) \cdot h(x)$ where $f(x)$ is defined by (I.91) and $g(x)$ by (I.97). In analogy to (I.92) the FT of $h(x)$ is $H(X) = (2/X)\sin(Xl/2)$. Applying both versions of the convolution theorem one obtains:

$$\begin{aligned} F_4(X) &= (F(X)\cdot G(X)) \otimes H(X) \\ &= \left(\sum_{K=-\infty}^{\infty} \frac{2}{K}\sin\frac{Ka}{2d}\delta\left(X - \frac{2\pi K}{d}\right)\right) \otimes \frac{2}{X}\sin\frac{Xl}{2} \end{aligned}$$

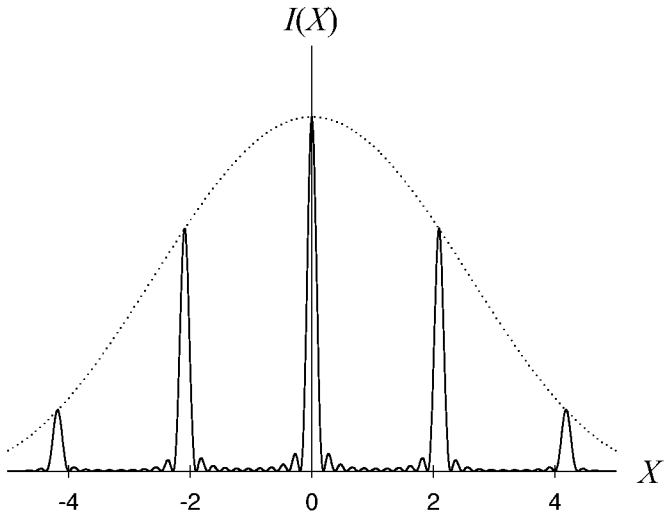



Figure I.3: Diffraction from a single slit (·····) and a finite array of slits (——). Slit width: $a = 1$, slit distance: $d = 3$, length of grating: $l = 33$ (this means 11 slits).

$$= \sum_{K=-\infty}^{\infty} \frac{2}{K} \sin\frac{Ka}{2d} \frac{2}{X - 2\pi K/d} \sin\frac{(X - 2\pi K/d)l}{2}. \qquad \text{(I.101)}$$

It turns out that a somewhat simpler result can be obtained if we think of the finite grating generated the other way around: We multiply $g(x)$ and $h(x)$ first to obtain a finite grid of infinitely narrow slits and then convolute this with $f(x)$ representing the slit of finite width: $f(x) \otimes (g(x) \cdot h(x))$ [3]. It is clear that this function has the same values as the one representing the grating before and therefore the FT is the same:

$$\begin{aligned} F_4(X) &= F(X) \cdot (G(X) \otimes H(X)) \\ &= \frac{2}{X} \sin\frac{Xa}{2} \sum_{K=-\infty}^{\infty} \frac{2}{X - 2\pi K/d} \sin\frac{(X - 2\pi K/d)l}{2} = \end{aligned} \qquad \text{(I.102)}$$

Note that the sum is now over a simpler expression. Indeed, it can be calculated in closed form now. If the grating has $n$ slits of distance $d$ there is some arbitrariness in the choice of $l$ cutting out this number of slits. We assume that $l = nd$ and note that $n$ has to be an odd number because of symmetry. Replacing $l$ by $nd$ one obtains:

$$\begin{aligned} &= \frac{2}{X} \sin\frac{Xa}{2} \sum_{K=-\infty}^{\infty} \frac{1}{Xnd/2 - \pi nK} \sin(Xnd/2 - \pi nK) \\ &= \frac{2}{X} \sin\frac{Xa}{2} \sum_{K=-\infty}^{\infty} \frac{1}{Xnd/2 - \pi nK} (-1)^K \sin(Xnd/2) \end{aligned}$$

$$= \frac{2}{X}\sin\frac{Xa}{2}\sin\frac{Xnd}{2}\sum_{K=-\infty}^{\infty}\frac{(-1)^K}{Xnd/2-\pi nK}$$

By applying a serial representation of the cosecant, $1/\sin x = \sum_{k=-\infty}^{\infty}(-1)^k/(x-\pi k)$ one finally gets

$$F_4(X) = \frac{2\sin(Xa/2)\sin(Xnd/2)}{nX\sin(Xd/2)} \tag{I.103}$$

and the corresponding intensity

$$I_4(X) = \frac{4\sin^2(Xa/2)\sin^2(Xnd/2)}{n^2X^2\sin^2(Xd/2)}\,. \tag{I.104}$$

It has to be conceded that the advantage of using the FT theorems to derive exact results as (I.104) is not so big if compared with a direct calculation. Nevertheless, the theorems allow a quick comprehension of how the result looks like without doing any calculation. E.g. here it is more important to see that because there is a convolution with $H(X)$ the result is that in each position where the infinite grating creates a sharp delta peak a copy of the FT of the cut-off function $h(x)$ is placed. To quickly assess such connections the researcher who works with scattering methods should always be aware of the FT theorems and their consequences.

### I.6.2 AC circuits

In subsection I.2.2 we have derived the complex conductance for a single frequency. Applying the convolution theorem (I.61) on (I.31) we see that for any voltage with the Fourier spectrum $U(\omega)$ the current spectrum $I(\omega)$ is given by

$$I(\omega) = G(\omega)\cdot U(\omega)\,. \tag{I.105}$$

It is more common to formulate this with the complex *impedance* $Z(\omega) = 1/G(\omega)$ which is the analogue of the resistance for AC:

$$Z(\omega) = \frac{U(\omega)}{I(\omega)}\,. \tag{I.106}$$

Obviously the complex impedance of a resistor is $Z(\omega) = R$. For the capacitor we have the time-dependent current given by the derivative of the voltage

$$i(t) = C\frac{\mathrm{d}u}{\mathrm{d}t}\,. \tag{I.107}$$

Application of the differentiation theorem yields

$$I(\omega) = -\mathrm{i}\omega C U(\omega) \Rightarrow Z_C(\omega) = \frac{\mathrm{i}}{\omega C}\,. \tag{I.108}$$

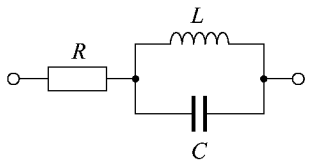
(Note that the signs here are opposite to those found in the electronics literature because we define the FT differently.) Analogously, for the inductor we have

$$u(t) = L\frac{\mathrm{d}i}{\mathrm{d}t} \tag{I.109}$$

resulting in

$$U(\omega) = \mathrm{i}\omega L I(\omega) \Rightarrow Z_L(\omega) = -\mathrm{i}\omega L\,. \tag{I.110}$$

The attractiveness of the concept of complex impedance lies in the possibility to simply calculate the response of complex linear electronic circuits. Even a simple circuit as




would require a system of equations and differential equations to be solved, viz

$$\begin{aligned} &i = i_1 + i_2,\ u = u_1 + u_2, \\ &u_1 = Ri,\ i_1 = C\frac{\mathrm{d}u_2}{\mathrm{d}t},\ u_2 = L\frac{\mathrm{d}i_2}{\mathrm{d}t} \end{aligned} \tag{I.111}$$

Instead of this, one can use the complex impedance in lieu of the resistance and treat the whole circuit using the rules for parallel and serial resistors:

$$Z(\omega) = R + \frac{1}{\frac{1}{Z_C} + \frac{1}{Z_L}} = R + \frac{1}{\frac{\omega C}{\mathrm{i}} - \frac{1}{\mathrm{i}\omega L}} = R + \frac{\omega L}{\omega^2 LC - 1}\mathrm{i}\,. \tag{I.112}$$

With this expression it is possible to calculate the behaviour of the circuit for any frequency $\omega$. Especially, it can be seen that $Z(\omega)$ diverges for $\omega = 1/\sqrt{LC}$ which is the resonance frequency.

# References


[1] K. B. Howell: "Principles of Fourier Analysis" (Chapman & Hall/CRC, Boca Raton, 2001).

[2] H. J. Weaver: "Theory of discrete and continuous Fourier analysis" (John Wiley & Sons, New York, 1988).

[3] J. Kauppinen, J. Partanen: "Fourier Transforms in Spectroscopy" (Wiley-VCH, Berlin, 2001).

[4] F. Oberhettinger: "Tables of Fourier Transforms and Fourier Transforms of Distributions" (Springer, Berlin, 1990).

[5] A. P. Prudnikov, Yu. A. Brychkov, O. I. Marichev: "Integrals and Series" (Gordon and Breach, New York 1986–1992).

[6] E. O. Brigham: "The fast Fourier transform and its applications" (Prentice Hall, London, 1988).

[7] O. Glatter: "The Inverse Scattering Problem in Small-Angle Scattering" in "Neutrons, X-rays and Light: Scattering Methods Applied to Soft Condensed Matter", eds. P. Lindner, Th. Zemb (North-Holland, Amsterdam, 2002).

[8] A. N. Tikhonov, V. Y. Arsenin: "Solutions of ill-posed problems" (Halsted Press, Washington, 1977).

[9] C. W. Groetsch: "The theory of Tikhonov Regularization for Fredholm Equations of the First Kind" (Pitman, Boston, 1984).

[10] J. Skilling (ed.): "Maximum Entropy and Bayesian Methods" (Kluwer, Dordrecht, 1989).

[11] section 7.10 in J. D. Jackson: "Classical Electrodynamics" (John Wiley & Sons, New York, 1975).

[12] S. G. Samko, A. A. Kilbas, O. I. Marichev: "Fractional Integrals and Derivatives" (Gordon and Breach, Yverdon, Switzerland, 1993).

# II

# Basic Assumptions of Quantum Mechanics and the Born Approximation – A Brief Tutorial

Dieter Richter

# II. Basic Assumptions of Quantum Mechamics and the Born Approximation – A Brief Tutorial

*D. Richter*

Institut für Festkörperforschung, Forschungszentrum Jülich, D-52425 Jülich, Germany

## II.1.1 Introductory remarks

This manuscript constitutes (i) a short revision course on some basic principles of quantum mechanics and (ii) it outlines the quantum mechanical treatment of scattering processes. Thereby it follows to some extend the excellent book on quantum mechanics by Claude Cohen-Tannoudji, Bernard Diu and Frank Laloe [1].

Quantum mechanics plays a fundamental role in the description and understanding of nature. In fact phenomena occurring on an atomistic scale cannot be described outside the frame of quantum mechanics (Q.M.). This concerns for example the existence and the properties of atoms, the chemical bond, the propagation of an electron in a crystal. But also in the macroscopic world there are many phenomena which reveal the quantum behavior of nature. It is in this sense, that it can be said that quantum mechanics is the basis of our present understanding of all natural phenomena including those traditionally treated in chemistry, biology, etc. Even in cosmology, e.g. questions after the origin of the universe, are subject to quantum mechanical treatment.

Historically the necessity of a quantum description of nature was first discovered, when dealing with black body radiation at the end of the 19's century. There it became clear that the energy spectrum emitted by a black body could not be explained by electromagnetic theory. This prompted Planck to suggest the hypothesis of a quantization of energy (1900). For an electromagnetic wave of frequency $\nu$ the only possible energies are integral multiples of the quantum $h\nu$, where h is the new fundamental constant.

Einstein generalized this hypothesis and proposed (1905) that light consists of a beam of photons each possessing an energy $h\nu$. In this way Einstein explained in a very simple way the sofar inexplicable characteristics of the photoelectric effect.

These considerations led to the conclusion: the interaction of an electromagnetic wave with matter occurs by means of elementary indivisible processes in which the radiation appears to be composed of particles, the photons. The particle parameters (energy $E$ and momentum $\underline{p}$ and wave parameters $\omega = 2\pi\nu$ and the wave vector $|\underline{k}| = 2\pi/\lambda$) are linked by the fundamental relations

$$E = h\nu \qquad \text{(II.1.1)}$$
$$\underline{p} = \hbar\underline{k}$$

where $\hbar = \frac{h}{2\pi}$ is defined in terms of the Planck constant $h = 6.62 \times 10^{-34}$ Js. Thus, light or electromagnetic radiation in general has also the character of particles.

The other key observation dealt with the wave character of particles: The study of atomic emission and absorption spectra uncovered a fundamental fact which classical physics was unable to explain. Such spectra are composed of narrow lines, an atom emits or absorbs only photons with well determined frequencies. This fact was interpreted assuming that the energies of an atom are quantisized and take certain discrete values $E_i$ ($i = 1, 2 \ldots n$). The emission or absorption of a photon is then accompanied by a jump in energy of the atom from one permitted energy level $E_i$ to another $E_j$. Conservation of energy implies that the photon must have a frequency $\nu_{ij}$ such that

$$h\nu_{ij} = |E_i - E_j| \qquad \text{(II.1.2)}$$

The existence of such discrete energy levels was confirmed independently by the Frank Herz experiment. Bohr interpreted these findings in terms of privileged electronic orbits and stated an empirical rule which permitted the calculation of these orbits for the hydrogen atom, but the fundamental origin of the quantization rules remained mysterious.

Finally in 1923 De Broglie stated the following hypothesis: *"Material particles just like photons can have a wave like aspect"*. With that hypothesis he derived the Bohr Sommerfeld quantization rules. Thereby the various energy levels appeared as analogous to the normal modes of a vibrating string. Electron diffraction experiments (Davisson and German, 1927) confirmed the existence of the wave like aspect of matter by showing that interference patterns could be obtained by particles such as electrons. Thus, a particle with mass having an energy $E$ and the momentum $p$ can be

associated with a wave of an angular frequency $\omega = 2\pi\nu$ and a wave vector $k$ which are given by the same relations as for the photons (Eq.[II.1.1]). In other words the wavelength of a particle is

$$\lambda = \frac{2\pi}{k} = \frac{h}{|\underline{p}|} \tag{II.1.3}$$

### II.1.2 Basic assumptions of quantum mechanics

**(1)** The classical concept of a trajectory is replaced by the notion of a time dependent wave function $\psi(\underline{r},t)$ which describes the state of a quantum mechanical system completely. E.g.

$$\psi(\underline{r},t) = \exp\left[\frac{i}{\hbar}\left(\underline{p}\cdot\underline{r} - Et\right)\right] \tag{II.1.4}$$

describes the state, where a particle with the mass $m$ displays a momentum $\underline{p}$ and an energy $E = p^2/2m$. Comment: The wave function $\psi$ contains all information which are possible to know about a Q.M. system.

**(2)** $\psi(\underline{r},t)$ is interpreted as a probability amplitude of the particle's presence. The possible positions of a particle form a continuum. Therefore the probability $dP(\underline{r},t)$ of a particle being at time t in a volume element $d^3r = dx\,dy\,dz$ situated at a point $\underline{r}$ being proportional to $d^3r$ $|\psi(\underline{r},t)|^2$ is then interpreted as the corresponding probability density with

$$dP(\underline{r},t) = C|\psi(\underline{r},t)|^2 d^3r \tag{II.1.5}$$

where $C$ is the normalization constant.

**(3)** For the wave functions a superposition principle is valid. If states $\psi_1(\underline{r},t)$ and $\psi_2(\underline{r},t)$ are possible then also

$$\psi(r,t) = C_1\psi_1(\underline{r},t) + C_2\psi_2(\underline{r},t) \tag{II.1.6}$$

is a possible state.

**(4)** The equation describing the evolution of $\psi(\underline{r},t)$ is a differential equation called Schrödinger equation. It assumes the form

$$i\hbar \frac{\partial}{\partial t} \psi(\underline{r},t) = -\frac{\hbar^2}{2m} \Delta\psi(\underline{r},t) + V(\underline{r},t)\, \psi(\underline{r},t) \qquad \text{(II.1.7)}$$

We note that this equation is linear and homogenous in $\psi$. Consequently the superposition principle which we have introduced under (3) is fulfilled. Together with the interpretation of $\psi$ as a probability amplitude, it is the source of the wave like effect. The differential equation is of first order with respect to time. This condition is necessary, if the state of the particle at a time $t_0$ is to determine its subsequent state.

**(5)** In quantum mechanics all dynamic variables are described by linear operators. E.g. the momentum $p$ becomes $\frac{\hbar}{i}$ grad. Considering the Hamilton function of a free particle $H = \frac{p^2}{2m}$ in quantum mechanics we arrive at $\hat{H} = -\frac{\hbar^2}{2m}(grad)^2$. Adding the potential energy the Schrödinger equation [II.1.7] can also be written as

$$\hat{H}\psi = +i\hbar \frac{\partial \psi}{\partial t} \qquad \text{(II.1.7a)}$$

Remembering that the Hamilton function is giving the total energy of a system, and following Eq.[II.1.7a] we may associate with the energy $E$ the operator $-\frac{\hbar}{i}\frac{\partial}{\partial t}$.

Note, there is an important difference between the concept of classical states and quantum states. The classical state of a particle at time $t$ is determined by the specification of six parameters: its positions and velocities. The quantum state of a particle is determined by the values of the wave function $\psi(\underline{r},t)$ describing the quantum state at the various points in space. The classical idea of a trajectory is substituted by the idea of the propagation of the wave associated with a particle.

### II.1.3 Example: free particle

We consider now a particle whose potential energy is zero or constant. The particle is thus not subjected to any force, therefore it is called free. With $V(\underline{r},t) = 0$ the Schrödinger equation [II.1.7] becomes

$$i\hbar \frac{\partial}{\partial t} \psi(\underline{r},t) = -\frac{\hbar^2}{2m} \Delta\psi(\underline{r},t) \tag{II.1.8}$$

This differential equation is obviously solved by

$$\psi(\underline{r},t) = A \exp\left[i(\underline{k}\,\underline{r} - \omega t)\right] \tag{II.1.9}$$

with $\omega = \left(\frac{\hbar^2 k^2}{2m}\right)$. Following the De Broglie relation 1.3, the energy and the momentum of the free particle are related by $E = \left(\frac{p^2}{2m}\right)$. With the probability interpretation of Eq.[II.1.5] we realize that such a wave function leads to a particle presence uniformly smeared throughout space $|\psi(r,t)|^2 = |A|^2$. The super position principle of Eq.[II.1.6] tells us that every linear combination of plane waves satisfying the proper relation between $\omega$ and k is also a solution of Eq.[II.1.8]. Such a superposition may be written as

$$\psi(r,t) = \frac{1}{(2\pi)^{3/2}} \int g(k) \exp\left[i(\underline{k}\,\underline{r} - \omega(k)t)\right] d^3k \tag{II.1.10}$$

($d^3k$ represents by definition the infinitesimal volume element in $\underline{k}$ space). $g(\underline{k})$ may be a complex function describing the distribution of $\underline{k}$. A wave function such as Eq.[II.1.10] is called a three dimensional wave packet. For simplicity we consider also the case of one dimensional wave packets which are obtained from the superposition of plane waves all propagating parallel to the x-axis. Then the wave function depends only on x and t.

$$\psi(x,t) = \frac{1}{\sqrt{2\pi}} \int_{-\infty}^{+\infty} g(k) \exp\left[i(kx - \omega(k)t)\right] dk \tag{II.1.11}$$

### II.1.4 Heisenberg uncertainty relation

We have seen that a plane wave $\exp(i(k_0x - \omega_0t))$ corresponds to a constant probability density for the particles presence along the $x$-axis for all values of $t$. We may also say that the uncertainty $\Delta x$ to find the particle along the $x$-axis is infinite. On the other hand only one angular frequency $\omega_0$ and only one wave vector $k_0$ are involved. Taking the De Broglie relations, this means that the energy and momentum of the particle are well defined: $E = \hbar\omega_0$ and $p = \hbar k_0$. Such a plane wave can be considered as a special case of Eq.[II.1.11] with

$$g(k) = \delta(k - k_0) \tag{II.1.12}$$

the corresponding uncertainty in $k$, $\Delta k$ is then 0.

This property may also be interpreted in the following manner. We may say that the particle at $t = 0$ $\psi(x,0) = A\exp(ikx)$ has a well determined momentum. A measurement of the momentum at this time will definitely lead to $p = \hbar k$. From this we may deduce that $\exp(ikx)$ characterizes an eigenstate of the wave function corresponding to $p = \hbar k$.

We now consider Eq.[II.1.11] at $t = 0$. $\psi(x,0)$ appears as a linear a superposition of the momentum eigenfunctions in which the coefficient of $\exp(ikx)$ is $g(k)$. We are thus lead to interpret $|g(k)|^2$ as a probability of finding $p = \hbar k$ if one measures at $t = 0$ the momentum of a particle whose state is described by $\psi(x,t)$. Keeping in mind the probability interpretation of the wave function we may just write

$$\psi(x,0) = \frac{1}{\sqrt{2\pi\hbar}} \int \psi(p) e^{\frac{ipx}{\hbar}} dp \tag{II.1.13}$$

The wave function in real space and momentum space are related to each other by a Fourier transformation. Now taking the distribution function as a Gaussian $g(k) \approx \exp\left(-k^2/2\Delta k^2\right)$ the wave function in real space becomes $\psi(x,0) \approx \exp\left(-x^2/\left(2/\Delta k^2\right)\right)$. Considering the two widths in momentum and real space we are led to the famous Heisenberg uncertainty principle

$$\Delta x \Delta k \geq 1 \quad or \quad \Delta x \Delta p \geq \hbar \tag{II.1.14}$$

Obviously the product of the uncertainty in the space and the momentum coordinate is at least $\hbar$ or we may say it is impossible to define at a given time both the position of the particle and its momentum to an arbitrary degree of accuracy. When we tried to increase the precision in momentum determination, then Eq.[II.1.14] tells us that the accuracy in the position determination will decrease and finally become infinite. There is nothing like that in classical mechanics. The limitation expressed in Eq.[II.1.14] arises from the fact that $h$ is not 0.

### II.1.5 Wave functions, operators: mathematical tools

The probabilistic interpretation of the wave function $\psi(\underline{r},t)$ requires that a total probability of finding a particle somewhere in space is equal to 1. So we must have

$$\int d^3r \left|\psi(\underline{r},t)\right|^2 = \underline{1} \tag{II.1.15}$$

where the integration extends over all space. Thus, the allowed wave functions are a set of square integrable functions. These are functions for which the integral II.1.15 converges. Mathematically this set is called $L^2$ and has the structure of a Hilbert space. From a physical point of view, it is clear that $L^2$ is too wide in scope. The wave functions have actually to possess the properties of regularity. We can only retain functions $\psi(\underline{r},t)$ which are everywhere defined, continuous and infinitely differentiable. It is also possible to confine ourselves to wave functions which are bounded. The particle can be found in a finite region of space for example the laboratory. We will not precise these requirements but we note that the functional space $F$, where our functions exist is a subspace of $L^2$. F satisfies all criteria of a vector space. For example, if $\psi_1(r)$ and $\psi_2(r,t)$ are element of $F$ then also

$$\psi(\underline{r}) = \lambda_1 \psi_1(\underline{r}) + \lambda_2 \psi_2(\underline{r}) \tag{II.1.16}$$

where $\lambda_1$, $\lambda_2$ are arbitrary complex numbers is an element of $F$ (can easily be shown via the integrability of the sum).

**Scalar product**

We now define a scalar product on $F$. $\varphi(r)$ and $\psi(\underline{r})$ are associated with a complex number denoted by $(\phi,\psi)$ which by definition is equal to

$$(\varphi,\psi) = \int d^3r\, \varphi^*(\underline{r})\psi(\underline{r}) \tag{II.1.17}$$

The following properties follow from Eq.[II.1.17]

$$(\varphi,\psi) = (\psi,\varphi)^* \tag{II.1.18}$$

$$(\varphi,\lambda_1\psi_1 + \lambda_2\psi_2) = \lambda_1(\varphi,\psi_1) + \lambda_2(\varphi,\psi_2)$$

$$(\lambda_1\varphi_1 + \lambda_2\varphi_2,\psi) = \lambda_1^*(\varphi_1,\psi) + \lambda_2^*(\varphi_2,\psi)$$

The scalar product is linear with respect to the second function and antilinear with respect to the first one. If $(\phi,\psi) = 0$ then the two functions orthogonal.

**Linear operators**

As we have outlined above in quantum mechanics dynamical variables or observables are described by linear operators. Linear operators are defined as a mathematical entity which associates with every function $\psi(\underline{r}) \in F$ another function $\psi'(\underline{r}) \in F$, the correspondence being linear.

$$\psi'(\underline{r}) = \hat{A}\psi(\underline{r}) \tag{II.1.19}$$

$$\hat{A}\left(\lambda_1\psi_1(\underline{r}) + \lambda_2\psi_2(\underline{r})\right) = \lambda_1\psi_1'(\underline{r}) + \lambda_2\psi_2'(\underline{r})$$

We now give a number of examples for linear operators

(i) the parity operator $\Pi$

$$\hat{\Pi}\psi(x,y,z) = \psi(-x,-y,-z) \tag{II.1.20}$$

(ii) the space operator $\hat{X}$ ($x$-component), which is defined by

$$\hat{X}\psi(x,y,z) = x\psi(x,y,z) \tag{II.1.21}$$

(iii) finally an operator which differentiates with respect to $x$. This we call $D_x$ (it relates to the momentum $P_x$ by $\hat{P}x = \frac{\hbar}{i} D_x$. It is defined by

$$\hat{D}_x \psi(x,y,z) = \frac{\partial}{\partial x} \psi(x,y,z) \tag{II.1.22}$$

If $\hat{A}$ and $\hat{B}$ are linear operators then their product $\hat{A}\hat{B}$ is defined by

$$\left(\hat{A}\hat{B}\right)\psi(\underline{r}) = \hat{A}\left[\hat{B}\psi(r)\right] \tag{II.1.23}$$

This equation means that $\hat{B}$ is first acting on $\psi$ and on the result of that the operator $\hat{A}$ is acting. In general we have $\hat{A}\hat{B} \neq \hat{B}\hat{A}$. We call the commutator of $\hat{A}$ and $\hat{B}$ the operator written $\left[\hat{A},\hat{B}\right]$. This is defined

$$\left[\hat{A},\hat{B}\right] = \hat{A}\hat{B} - \hat{B}\hat{A} \tag{II.1.24}$$

as an example we treat the commutator $\left[\hat{X},\hat{D}_x\right]$. With an arbitrary function $\psi(\underline{r})$ we have

$$\begin{aligned}
\left[\hat{X},\hat{D}_x\right]\psi(r) &= \left(x\frac{\partial}{\partial x} - \frac{\partial}{\partial x}x\right)\psi(\underline{r}) \\
&= x\frac{\partial}{\partial x}\psi(\underline{r}) - \frac{\partial}{\partial x}\left(\psi(r)\right) \qquad \text{(II.1.25)} \\
&= x\frac{\partial}{\partial x}\psi(\underline{r}) - \psi(\underline{r}) - x\frac{\partial}{\partial x}x\psi(\underline{r}) = -\psi(\underline{r})
\end{aligned}$$

This result is true for all functions $\psi$ therefore we have

$$\begin{aligned}
\left[\hat{X},\hat{D}_x\right] &= -1 \\
\left[\hat{X},\hat{p}\right] &= i\hbar
\end{aligned} \tag{II.1.26}$$

The most important linear operator in Q.M. is the Hamilton operator $\hat{H}$ which is derived from the Hamilton function of the corresponding classical system $H = {p^2}/{2m} + V(\underline{r})$. Transcription into Q.M. leads to

$$\hat{H} = \frac{\hat{p}^2}{2m} + V(r) \tag{II.1.27}$$

For a system with energy conservation $\frac{\partial \hat{H}}{\partial t} = 0$. Then space and time variables of the Schrödinger Eq.[II.1.7] may be separated yielding a stationary Schrödinger equation of the form

$$\hat{H}\psi(\underline{r}) = E\psi(\underline{r}) \tag{II.1.28}$$

where $E$ describes the possible energy states of the system

**Orthonormal basis in functional space**

Within the functional space $F$ we may define an orthonormal basis $\{u_i(\underline{r})\}$. We consider a countable set of functions of $F$ labeled by a discrete index $(i = 1, 2, \ldots n \ldots)$. The set $\{u_i(\underline{r})\}$ is orthonormal if

$$(u_i, u_j) = \int d^3r\, u_i^*(\underline{r})\, u_j(\underline{r}) = \delta_{ij} \tag{II.1.29}$$

where $\delta_{ij}$ is the Kronecker symbol. $\delta$ is equal to 1 for $i = j$ and 0 otherwise. The functions u constitute a basis, if every function $\psi(\underline{r}) \in F$ can be expanded in only one way in terms of the $\{u_i(\underline{r})\}$

$$\psi(\underline{r}) = \sum_i c_i u_i(\underline{r}) \tag{II.1.30}$$

The components $c_i$ of a wave function with respect to a basis function $u_i(\underline{r})$ is obtained by

$$c_i = (u_i, \psi) = \int d^3r\, u_i^*(\underline{r})\psi(\underline{r}) \qquad \text{(II.1.31)}$$

The component $c_i$ of $\psi(r)$ on $u_i(r)$ is therefore equal to the scalar product of $u_i(\underline{r})$ and $\psi(\underline{r})$. Once a basis is chosen it is equivalent to specify $\psi$ or the set of its components $c_i$ with respect to the basis functions. The set of numbers $c_i$ is said to represent $\psi(\underline{r})$ in the $\{u_i(\underline{r})\}$ basis.

**Bra and Ket vectors**

Dirac has generalized and formalized the above considerations in introducing so called ket and bra vectors. We characterize each quantum state of a particle by a state vector which belongs to an abstract space $E_r$ called the state space of the particle. Since $F$ is a subspace of $L^2$ also $E_r$ is a subspace of a Hilbert space. We are now going to define the notation and rules for vector calculations in $E_r$.

Any element or vector of $E_r$ space is called ket vector or most simply a ket. It is represented by the symbol $|\ \rangle$. Inside this symbol we place a sign which enables us to distinguish the corresponding ket from all others. For example $|\psi\rangle$. Note that now the symbol $\psi$ is not associated any more with the space coordinate $r$. The letter $\psi$ reminds us with which function the ket is associated with. $\psi(\underline{r})$ then is interpreted as a set of components of the ket vector $\psi$ in a particular basis $r$.

The scalar product between two kets is formally taken over from Eq.[II.1.18] associating a complex number with a pair of kets obeying the rules establish there. We now define so called bras which are associated with each ket in an antilinear fashion

$$\lambda_1|\varphi_1\rangle + \lambda_2|\varphi_2\rangle \Rightarrow \lambda_1^*\langle\varphi_1| + \lambda_2^*\langle\varphi_2| \qquad \text{(II.1.32)}$$

With this notion we may write the scalar product as

$$(|\varphi\rangle, |\psi\rangle) = \langle\varphi|\psi\rangle \qquad \text{(II.1.33)}$$

Note that the rules II.1.18 are naturally fulfilled by these definitions. The role of linear operators may be taken over from Eqs.[II.1.19] to [II.1.23]. Eq.[II.1.19] becomes

$$|\psi'\rangle = \hat{A}|\psi\rangle \tag{II.1.34}$$
$$\hat{A}\left(\lambda_1|\psi_1\rangle + \lambda_2|\psi_2\rangle\right) = \lambda_1 \hat{A}|\psi_1\rangle + \lambda_2 \hat{A}|\psi_2\rangle$$

with the definition of bra and ket vectors we may also define in terms of a scalar product so called matrix elements of an operator $\hat{A}$ between $|\varphi\rangle$ and $|\psi\rangle$

$$\langle\varphi|(A|\psi\rangle) \equiv \langle\varphi|A|\psi\rangle \tag{II.1.35}$$

**Eigenvalues and eigenvectors of an operator**

As stated above in quantum mechanics observables correspond to linear operators. The action of such an operator on the wave function results in possible realisations of the observable. Formally it is interesting to know which wave functions or kets correspond to a specific possible realisation of an observable and what are these realizations. Mathematically this corresponds to eigenvalue problem. The possible realisations are given by the eigenvalues of an operator and the corresponding wave functions are the eigenvectors. $|\psi\rangle$ is an eigenvector or eigenket of a linear operator $\hat{A}$ if

$$\hat{A}|\psi\rangle = a|\psi\rangle \tag{II.1.36}$$

where $a$ is a complex number. Eq.[II.1.36] is also called the eigenvalue equation of the linear operator $\hat{A}$. In general this equation possesses a solution only if $a$ takes certain values, called eigenvalues of $\hat{A}$. The set of the eigenvalues is called the spectrum of $\hat{A}$. Eigenvalues may be degenerate meaning that several linear independent eigenfunctions may be associated with the same eigenvalue. For the sake of simplicity, we will only consider the non-degenerate case.

Given a linear operator $\hat{A}$, how does one find all its eigenvalues and the corresponding eigenvectors? We shall consider the case, where the state space is of finite dimension $N$ and we shall assume that the results can be generalized to an infinite dimensional state space. Let us choose a basis, e.g. $\{|u_i\rangle\}$ and let us project the vector equation [II.1.36] onto the various orthonormal basis vectors $|u_i\rangle$

$$\left\langle u_i \middle| \hat{A} \middle| \psi \right\rangle = a \left\langle u_i | \psi \right\rangle \tag{II.1.37}$$

Inserting the closure relation $\sum_j |u_j\rangle\langle u_j| = \hat{1}$, where $\hat{1}$ is the unity operator, between $\hat{A}$ and $|\psi\rangle$ we obtain

$$\sum_j \left\langle u_i \middle| \hat{A} \middle| u_j \right\rangle \left\langle u_j | \psi \right\rangle = a \left\langle u_i | \psi \right\rangle^* \tag{II.1.38}$$

With the usual notations

$$\left\langle u_i | \psi \right\rangle = c_i \tag{II.1.39}$$

$$\left\langle u_i \middle| \hat{A} \middle| u_j \right\rangle = A_{ij}$$

Eq.[II.1.38] may be rewritten to

$$\sum_j \left[ A_{ij} - a\delta_{ij} \right] c_j = 0 \tag{II.1.40}$$

This equation can be considered to be a system of equations, where the unknowns are the $c_j$, the components of the eigenvector in the chosen representation. The system is linear and homogeneous. Eq.[II.1.40] has nontrivial solutions, if and only if the determinant of the coefficients is zero. This condition is written as

$$Det\left[ \underline{\underline{A}} - a\underline{\underline{I}} \right] = 0 \tag{II.1.41}$$

where $\underline{\underline{A}}$ is the N × N matrix of the elements $a_{ij}$ and $\underline{\underline{I}}$ is the unit matrix. Solutions of Eq.[II.1.41] gives us the eigenvalues or the spectrum of $\hat{A}$. After having obtained the eigenvalues, the eigenvectors are found by inserting the respective eigenvalues into Eq.[II.1.40] and solving for $c_j$.

Note that observables in quantum mechanics are always associated with Hermetian linear operators $\hat{A}$. These operators have the additional property that $A^+ = A$. It can be shown that the eigenvalues of Hermetian operators are real. Furthermore, eigenvectors of Hermetian operators corresponding to

*The projector $\sum_j |u_j\rangle\langle u_j|$ provides a complete projection of ψ on the various base function $|u_j\rangle$.

different eigenvalues are orthogonal. In a space of finite dimension $N$ a Hermetian operator always has $N$ linearly independent eigenvectors forming a base with respect to the operator $\hat{A}$.

### II.1.6 Heisenberg and Schrödinger pictures

**Time evolution operator**

The Schrödinger equation [II.1.7] is of first order in time. From this it follows that given the initial state $|\psi(t_0)\rangle$ the state $|\psi(t)\rangle$ at any subsequent time is uniquely determined. There is no indeterminacy in the time evolution of quantum systems. The transformation of $|\psi(t_0)\rangle$ into $|\psi(t)\rangle$ is linear. Therefore in general there exists a linear operator $\hat{U}(t,t_0)$ such that

$$|\psi(t)\rangle = \hat{U}(t,t_0)|\psi(t_0)\rangle \tag{II.1.42}$$

$\hat{U}(t,t_0)$ is also called the evolution operator of the system. Since the ket $|\psi(t_0)\rangle$ is arbitrary, it is clear from Eq.[II.1.42] that

$$\hat{U}(t_0,t_0) = 1 \tag{II.1.43}$$

$\hat{U}(t_0,t_0)$ is the unity operator. We now substitute Eq.[II.1.42] into the Schrödinger equation. With that we obtain

$$i\hbar \frac{\partial}{\partial t} \hat{U}(t,t_0)|\psi(t_0)\rangle = \hat{H}(t)\,\hat{U}(t,t_0)|\psi(t_0)\rangle \tag{II.1.44}$$

Since $|\psi\rangle$ is arbitrary we have

$$i\hbar \frac{\partial}{\partial t} \hat{U}(t,t_0) = \hat{H}(t)\,\hat{U}(t,t_0) \tag{II.1.45}$$

The first order differential equation completely defines $\hat{U}(t,t_0)$, if we take the initial condition [II.1.43] into account.

It is easily shown that $U$ is unitary

$$\hat{U}^{+}(t,t') = \hat{U}^{-1}(t,t') = \hat{U}(t',t) \tag{II.1.46}$$

Thus, the transformation $\hat{U}$ conserves the norm of vectors, on which it acts. I.e. the norm of the state vector does not change over time.

We now consider the special case of a conservative system, where $\hat{H}$ does not depend explicitly on time. Then Eq.[II.1.45] may easily be integrated and we obtain

$$\hat{U}(t,t_0) = e^{-i\hat{H}(t-t_0)/\hbar} \tag{II.1.47}$$

**The Heisenberg picture**

Up to now we have been discussing in general time independent operators, which correspond to the observables of the system. For example the position, the momentum and the kinetic energy operators of a particle do not depend on time. The evolution of the system is entirely contained in that of the state vector $|\psi(t)\rangle$ and this time evolution is obtained from the Schrödinger equation. This is why this approach is called the Schrödinger picture. With the unitary transformations we have been discussing above, it is now also possible to define a unitary transformation, acting on ket and bra vectors such, that they become time independent and that all the time dependence is contained in the operators. We call this approach the Heisenberg picture. In order to distinguish both approaches, we will systematically assign an index $S$ to the kets and operators in the Schrödinger picture, while an index $H$ will be used for those in the Heisenberg picture.

From Eq.[II.1.42] we know that the state vector at an instant $t$ may be expressed in terms of the state vector at an instant $t_0$ by the relation

$$|\psi_s(t)\rangle = \hat{U}(t,t_0)\,|\psi_s(t_0)\rangle \tag{II.1.48}$$

Since $\hat{U}$ is unitary we may perform the unitary transformation associated with the operator $U^{+}(t,t_0)$ to obtain a constant transformed vector $|\psi_H\rangle$.

$$|\psi_H\rangle = \hat{U}^+(t,t_0)|\psi_s(t)\rangle \tag{II.1.49}$$

$$= \hat{U}^+(t,t_0)\,\hat{U}(t,t_0)|\psi_S(t_0)\rangle = |\psi_S(t_0)\rangle \tag{II.1.50}$$

In the Heisenberg picture the state vector is constant and equal to $|\psi_S(t)\rangle$ at time $t_0$. The transform $\hat{A}_H(t)$ of an operator $\hat{A}_S$ is given by

$$\hat{A}_H(t) = \hat{U}^+(t,t_0)\;\hat{A}_S(t)\,\hat{U}(t,t_0) \tag{II.1.51}$$

$\hat{A}_H(t)$ generally depends on time even if $\hat{A}_S$ does not. There exists an interesting special case in which, if $\hat{A}_S$ is time independent, the same is true of $\hat{A}_H$. This occurs if a system is conservative and $\hat{A}_S$ commutes with $\hat{H}_S$ (or $\hat{A}_S$ is the constant of motion). Then since $\hat{U}$ is given by Eq.[II.1.47] if $\hat{A}_S$ commutes with $\hat{H}_S$ it also commutes with $\hat{U}(t,t_0)$. So that

$$\hat{A}_H(t) = \hat{U}^+(t,t_0)\;\hat{U}(t,t_0)\hat{A}_S = \hat{A}_S \tag{II.1.52}$$

The operators $\hat{A}_S$ and $\hat{A}_H$ are thus simply equal. In particular $\hat{H}_S = \hat{H}_H$ the Hamilton operator for a conservative system is identical in the Schrödinger and the Heisenberg picture. For an arbitrary operator $\hat{A}_S(t)$ the evolution of the operator $\hat{A}_H(t)$ is obtained from Eq.[II.1.51] in combination with the equation for the time dependence of the time evolution operator (Eq.[II.1.45]). Differentiating [II.1.51] and inserting [II.1.45] we obtain

$$\frac{d}{dt}\hat{A}_H(t) = -\frac{1}{i\hbar}\hat{U}^+(t,t_0)\,\hat{H}_S(t)\,\hat{A}_S(t)\,\hat{U}(t,t_0)$$

$$+\hat{U}^+(t,t_0)\,\frac{d\hat{A}_S(t)}{dt}\,\hat{U}(t,t_0) \tag{II.1.53}$$

$$+\frac{1}{i\hbar}\hat{U}^+(t,t_0)\;\hat{A}_S(t)\hat{H}_S(t)\,U(t,t_0)$$

If we insert in the first and last term of this expression between $\hat{A}_S$ and $\hat{H}_S$ the product $\hat{U}(t,t_0)$ $\hat{U}^+(t,t_0)$ which is equal to the identity operator, then Eq.[II.1.53] may be reduced to

$$i\hbar\frac{d}{dt}\hat{A}_H(t) = \left[\hat{A}_H(t),\, \hat{H}_H(t)\right] + i\hbar\left[\frac{d}{dt}\, A_S(t)\right]_H \qquad \text{(II.1.54)}$$

Eq.[II.1.54] is the basic equation of motion for operators in the Heisenberg picture. For operators which in the Schrödinger picture are not explicitly depending on time, the evolution of an operator in the Heisenberg picture is just given by its commutator with the Hamilton operator. The considerations of the Heisenberg picture will become important later, when the correlation functions in terms of the van Hove picture are derived.

## II.2. Scattering theory

Scattering experiments in condensed matter consist of directing a beam onto a target composed of matter and studying the resulting scattering pattern: i.e. the direction and the energy of the scattered particles at various scattering angles $\theta_1$ and $\theta_2$ (see Fig.2.1). From the interaction of the incoming beam – in our case neutrons – with the target detailed information about the microscopic materials properties are sought. In this chapter we first will introduce a number of definitions and then formulate the scattering problem and its general solutions in terms of stationary scattering states. Then, we will give a general calculation of the cross section. Thereafter the Born approximation will be introduced and finally the Fermi pseudo potential will be discussed.

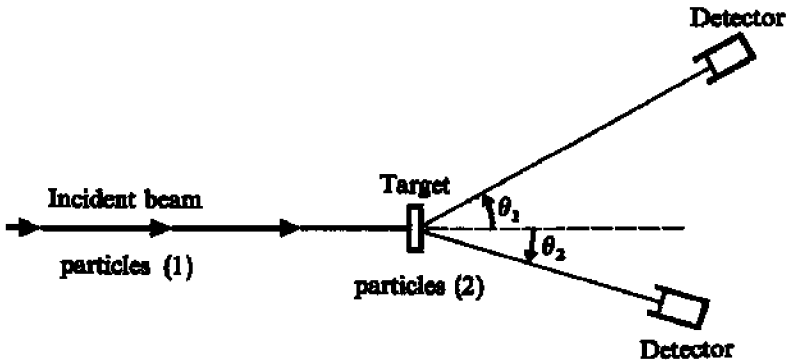



**Figure 2.1:** Schematic sketch of a scattering experiment.

For our treatment we make a number of assumptions, in order to simplify the problem.

(i) We shall suppose that the spin does not play a role.

(ii) We will assume that the scattering is elastic, i.e. that the final energy of the scattered particles is identical to that of the incoming particles. This assumption however can be generalized straight forwardly.

(iii) We will discuss only scattering processes on a single nucleus and thus, not discuss coherent effects which will be subject of later lectures.

(iv) We shall assume that the interactions between the incoming beam and the target can be described by a potential energy $V(\underline{r}_1 - \underline{r}_2)$ which depends only on the relative position $\underline{r} = \underline{r}_1 - \underline{r}_2$ of the particles. In that case a center of mass reference frame of the two particles may be used, which reduces the problem to the study of the scattering of the single particle by a potential $V(r)$.

**Definition of the scattering cross section**

Let the $z$ direction be the direction of the incident particles (Fig.2.2).

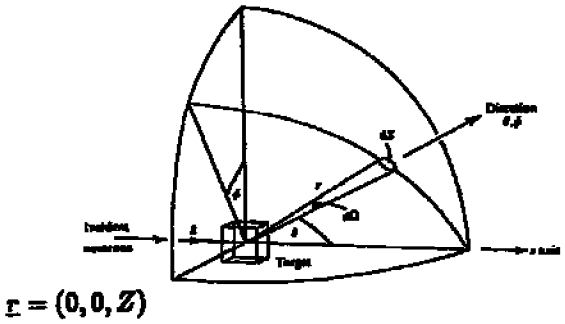



**Figure 2.2:** Scattering geometry for an incident plane wave scattered at a target.

The potential $V(r)$ is localized around the origin of the coordinate system. We shall designate by $F_i$ the flux of the particles in the incident beam, i.e. the number of particles per unit time, which traverse the unit surface perpendicular to the $z$ direction.

We place a detector far from the region under the influence of the potential (or the target). In the direction fixed by the polar angles $\theta$ and $\varphi$ with an opening facing the target and spanning a solid angle $d\Omega$. In such an arrangement we can count the number $dn$ of particles scattered per unit time into the solid angle $d\Omega$ around the direction $(\theta,\varphi)$. $dn$ is obviously proportional to $d\Omega$ and to the incident flux $F_i$. We define $d\sigma(\theta,\varphi)$ to be the coefficient of proportionality between $dn$ and $F_i\, d\Omega$

$$dn = F_i d\sigma(\theta,\varphi) d\Omega \qquad \text{(II.2.1)}$$

The dimensions of $dn$ and $F_i$ are respectively $t^{-1}$ and $(\ell^2 t)^{-1}$, where $t$ is the time and $\ell$ is a length defining the cross section of the incident beam. $d\sigma(\theta,\varphi)$ therefore has the dimension of a surface. It is called the differential scattering cross section in the direction $(\theta,\varphi)$. Cross sections are commonly measured in barns.

$$1\ barn = 10^{-24} cm^2 \qquad \text{(II.2.2)}$$

The definition II.2.1 may be interpreted in the following way. The number of particles per unit time which reach the detector is equal to the number of particles which would cross a surface $\sigma(\theta,\varphi)\, d\Omega$

placed perpendicular to the $z$ direction in the incident beam. Similarly the total scattering cross section $\sigma$ is defined by the formula

$$\sigma = \int d\sigma(\theta,\varphi)\, d\Omega \tag{II.2.3}$$

**II.2.1 Formulation of the scattering problem; stationary scattering states**

In order to describe in quantum mechanical terms the scattering of a given incident particle by the potential $V(r)$ it is necessary to study the time evolution of a wave packet representing the state of the incoming particle. Each of such wave packages at large negative times were $V(r)$ is not yet active, may be described as a superposition of stationary states (see Eq.[II.1.11]), which we are going to treat here. Thus, we have to study the eigenvalue equation for the Hamiltonian

$$H = H_0 + V(\underline{r}) \text{ with } H_0 = \frac{p^2}{2\mu} \tag{II.2.4}$$

Here p describes the momentum and $\mu$ the reduced mass of the incoming particle. Schrödingers equation describing the evolution of the particle in the potential $V(\underline{r})$ is satisfied by solutions associated with a well defined energy $E$ (stationary states).

$$\Psi(\underline{r},t) = \varphi(\underline{r})\ e^{-iEt/\hbar} \tag{II.2.5}$$

where $\varphi(r)$ is the solution of the eigenvalue equation

$$\left[-\frac{\hbar^2\Delta}{2\mu} + V(\underline{r})\right]\varphi(\underline{r}) = E\varphi(\underline{r}) \tag{II.2.6}$$

In the following we assume that the potential $V(r)$ decreases faster than $1/r$ as $r$ approaches infinity. We shall be concerned with solutions with Eq.[II.2.6] associated with a positive energy $E$ equal to the kinetic energy of the incident particle before it reaches the zone of influence of the potential. Defining

$$E = \frac{\hbar^2 k^2}{2\mu} \tag{II.2.7}$$

$$V(\underline{r}) = \frac{\hbar^2}{2\mu} U(\underline{r})$$

allows us to rewrite Eq.[II.2.6]

$$\left[\Delta + k^2 - U(\underline{r})\right] \varphi(\underline{r}) = 0 \qquad \text{(II.2.8)}$$

For each value of $k$ Eq.[II.2.8] can be satisfied by an infinite number of solutions (the positive eigenvalues of the Hamiltonian $H$ are infinitely degenerate). Among these large number of possible solutions we have to choose that, which satisfies the physical problem. We will now specify the conditions that must be imposed on the solutions of Eq.[II.2.8] if they are to be used in the description of the scattering process. We shall call the eigenstates of the Hamiltonian which satisfy these conditions stationary scattering states and we shall designate by $\psi_k(r)$ the associated wave functions.

For large negative values of t the incident particle is free and its state must be presented in form of plane wave $e^{ikz}$, where k is the constant which appears in Eq.[II.2.8]. In the region of the potential the evolution of the incoming wave is complicated. However, for large positive values of t, when the scattered particle has left the region of influence of the potential, once again we have to have a simple form. Now, the wave will be splitted into a transmitted wave which continues to propagate along the $z$ direction and the scattered wave. The wavefunction $\psi_k(r)$ will be obtained from a superposition of the plane wave $e^{ikz}$ and a scattered wave.

The structure of the scattered wave obviously depends on the potential. However, its asymptotic form is simple. By analogy with wave optics, the scattered wave must present the following characteristics at large $r$

(i) In a given direction $(\theta,\varphi)$ its radial dependence is of the form $e^{ikr}/r$. The outgoing wave has the same energy as the incident wave. The factor $1/r$ ensures that Eq.[II.2.8] is satisfied. (In optics the factor $1/r$ insures that the total flux of energy passing through a sphere of radius $r$ is independent of $r$ for large $r$. In quantum mechanics it is the probability flux passing through the sphere that does not depend on $r$.)

(ii) Since the scattering is generally not isotropic the amplitude of the outgoing wave depends on the direction $\theta,\varphi$ which is considered. The asymptotic form of $\psi_k$ thus becomes

$$\Psi_k(r) \underset{r\to\infty}{\sim} e^{ikz} + f_k(\theta,\varphi)\frac{e^{ikr}}{r} \tag{II.2.9}$$

The function $f_k(\theta,\varphi)$ is called the scattering amplitude. It is the only function which depends on the potential $V(r)$.

**Calculation of the cross section in terms of probability currents**

We want to calculate the contributions of the incident wave and the scattered wave to the probability current in a stationary scattering state. The expression for the current $J(r)$ associated with a wave function $\varphi(r)$ is

$$J(r) = \frac{1}{\mu}\,\mathrm{R_e}\left[\varphi^*(r)\frac{\hbar}{i}\nabla\varphi(r)\right] \tag{II.2.10}$$

The incident current $J_i$ is obtained from 2.10 by replacing $\varphi(k)$ by the plane wave $e^{ikz}$. $J_i$ is therefore directed belong the positive $z$ direction. Its expectation value is

$$|J_i| = \frac{\hbar k}{\mu} \tag{II.2.11.}$$

Since the scattered wave is expressed in spherical coordinates we will calculate the components of the scattered current $J_d$ along the local axis defined by this coordinate system. We recall that the corresponding components of the operator $\nabla$ are

$$(\nabla)_r = \frac{\partial}{\partial r} \tag{II.2.12}$$

$$(\nabla)_\theta = \frac{1}{r}\frac{\partial}{\partial\theta}$$

$$(\nabla)_\varphi = \frac{1}{r\sin\theta}\frac{\partial}{\partial\varphi}$$

If we replace $\varphi(r)$ in Eq.[II.2.10] by the function $f_k(\theta,\varphi)e^{ikr}/r$ we easily obtain the scattered current in the asymptotic region

$$
\begin{aligned}
(J_d)_r &= \frac{\hbar k}{\mu}\frac{1}{r^2}\left|f_k(\theta,\varphi)\right|^2 \\
(J_d)_\theta &= \frac{\hbar}{\mu}\frac{1}{r^3}\ \mathrm{Re}\left[\frac{1}{i}f_k^*(\theta,\varphi)\frac{\partial}{\partial\theta}f_k(\theta,\varphi)\right] \\
(J_d)_\varphi &= \frac{\hbar}{\mu}\frac{1}{r^3\sin\theta}\ \mathrm{Re}\left[\frac{1}{i}f_k^*(\theta,\varphi)\frac{\partial}{\partial\varphi}f_k(\theta,\varphi)\right]
\end{aligned}
\qquad \text{(II.2.13)}
$$

Since r is large $(J_d)_\theta$ and $(J_d)_\varphi$ are negligible compared to $(J_d)_r$ i.e. the scattered current is practically radial.

In order to go to the flux, we note that sending a great number of particles on a target the same experiment is repeated a large number of times. Therefore flux and current are proportional. Similarly, the number $dn$ of particles hitting a detector at $\theta,\varphi$ per unit time is proportional to the flux of the vector $J_d$ across the detector surface $d$s of the opening. The proportionality constants are the same in both cases. Thus, we have

$$
\begin{aligned}
dn = C\,J_d\,dS &= C(J_d)_r\ r^2\ d\Omega \\
&= C\frac{\hbar k}{\mu}\left(f_k(\theta,\varphi)\right)^2\ d\Omega
\end{aligned}
\qquad \text{(II.2.14)}
$$

We see that $dn$ is independent of r for sufficiently large $r$. If we substitute Eq[II.2.11] and Eq.[II.2.14] into Eq.[II.2.1] we obtain

$$
d\sigma(\theta,\varphi) = \left|f_k(\theta,\varphi)\right|^2 \qquad \text{(II.2.15)}
$$

The differential cross section is simply the square of the scattering amplitude.

### II.2.2 Calculation of the cross section

We now address the more formal solution of the scattering Eq.[II.2.6]. In order to do so, we introduce the integral scattering equation, whose solutions are precisely the stationary scattering state wave functions. We go back to the eigenvalue equation [2.6] and put it in a different form.

$$\left(\Delta + k^2\right) \varphi(\underline{r}) = U(\underline{r})\, \varphi(\underline{r}) \tag{II.2.16}$$

For the moment let us assume that there exist a function $G(\underline{r})$ such that

$$\left(\Delta + k^2\right) G(\underline{r}) = \delta(\underline{r}) \tag{II.2.17}$$

$G(\underline{r})$ is called the Green function of the operator $\Delta + k^2$. Then any function $\varphi(\underline{r})$ which satisfies

$$\varphi(\underline{r}) = \varphi_0(\underline{r}) + \int d^3r'\, G(\underline{r} - \underline{r}')\, U(\underline{r}')\, \varphi(\underline{r}') \tag{II.2.18}$$

where $\varphi_0(r)$ is a solution of the homogenous equation

$$\left(\Delta + k^2\right) \varphi_0(\underline{r}) = 0 \tag{II.2.19}$$

is a solution of the differential equation [II.2.16]

In order to show this, we apply the operator $\Delta + k^2$ to both sides of Eq.[II.2.18]. Taking II.2.19 into account. This gives

$$\left(\Delta + k^2\right) \varphi(\underline{r}) = \left(\Delta + k^2\right) \int d^3r'\, G(\underline{r} - \underline{r}')\, U(\underline{r}')\, \varphi(r') \tag{II.2.20}$$

Assuming that we can move the operator inside the integral - it will only act on the variable $r$ and following II.2.17 we get

$$\left(\Delta + k^2\right) \varphi(\underline{r}) = \int d^3r'\, \delta(\underline{r} - \underline{r}')\, U(\underline{r}')\, \varphi(\underline{r}') = U(\underline{r})\, \varphi(\underline{r}) \tag{II.2.21}$$

Inversely, it can also be shown that any solution of Eq.[II.2.16] satisfies Eq.[II.2.18]. In practical terms it is often easier to use the integral equation. Its principal advantage derives from the fact that by choosing $\varphi_0(\underline{r})$ and $G(\underline{r})$ correctly one can incorporate into the equation the desired asymptotic behavior. Thus, the integral equation called the integral scattering equation becomes the equivalent of the differential equation [II.2.16] together with the asymptotic conditions.

Now we have first have to construct the Green function defined in Eq.[II.2.17]. We show, that the functions

$$G_{\pm}(\underline{r}) = -\frac{1}{4\pi}\frac{e^{\pm ikr}}{r} \tag{II.2.22}$$

precisely fulfill the conditions of Eq.[II.2.16]. We may write

$$\Delta G_{\pm}(\underline{r}) = e^{\pm ikr}\,\Delta\left(\frac{-1}{4\pi r}\right) - \frac{1}{4\pi r}\Delta\left(e^{\pm ikr}\right) + 2\left(\nabla\left(-\frac{1}{4\pi r}\right)\right)\left(\nabla e^{\pm ikr}\right) \tag{II.2.23}$$

A simple calculation gives

$$\Delta G_{\pm}(\underline{r}) = -k^2\, G_{\pm}(\underline{r}) + \delta(\underline{r}) \tag{II.2.24}$$

which is what we wanted to prove. $G_+$ and $G_-$ are called respectively outgoing and incoming Green functions. The actual form of the desired asymptotic behavior (Eq.[II.2.9]) suggest the choice of the incident plane wave $e^{ikz}$ for $\varphi_0(\underline{r})$ and the choice of the outgoing Green function $G_+(\underline{r})$ for $G(\underline{r})$. We will now show that the integral scattering equation may be written as

$$\psi_k(\underline{r}) = e^{ikz} + \int d^3r'\, G_+(\underline{r} - \underline{r}')\, U(\underline{r}')\, \psi_k(\underline{r}') \tag{II.2.25}$$

To do so, we place ourselves at a point $M$ (position $\underline{r}$) very far from the various points (position $\underline{r}'$) of the target, with a linear dimension of the order $L^*$ (Fig.2.3).

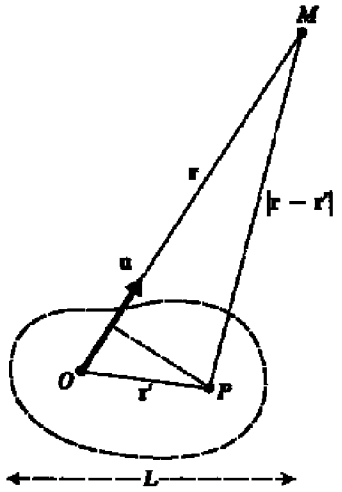



**Figure 2.3:** Approximate calculation of the distance $|r - r'|$ between a point $M$ very far from $O$ and a point $P$ situated in the zone of influence of the potential (the dimensions of this zone of influence are of the order of $L$).

Since the angle between $MO$ and $MP$ is very small the length $MP$ (that is $|\underline{r} - \underline{r}'|$) is equal within a good approximation to the projection of $MP$ on $MO$.

$$|\underline{r} - \underline{r}'| \approx r - \underline{u}\,\underline{r}' \tag{II.2.26}$$

where $\underline{u}$ is the unit vector in the $\underline{r}$ direction. Thus, for large $r$

$$G_+(\underline{r} - \underline{r}') = -\frac{1}{4\pi}\frac{e^{ik|\underline{r}-\underline{r}'|}}{|\underline{r} - \underline{r}'|} \sim -\frac{1}{4\pi}\frac{e^{ikr}}{r}\,e^{-ik\underline{u}\underline{r}'} \tag{II.2.27}$$

substituting back this expression into Eq.[II.2.25] we obtain the asymptotic behavior of $\psi_k(\underline{r})$.

$$\psi_k(\underline{r})_{r\to\infty} \sim e^{ikz} - \frac{1}{4\pi}\frac{e^{ikr}}{r}\int d^3r'\, e^{ik\underline{u}\underline{r}'}\,U(\underline{r}')\,\psi_k(\underline{r}') \tag{II.2.28}$$

which is indeed of the form II.2.9. Setting

$$f_k(\theta,\varphi) = -\frac{1}{4\pi}\int d^3r'\, e^{ik\underline{u}\underline{r}'}\,U(\underline{r}')\psi_k(\underline{r}') \tag{II.2.29}$$

we arrive at an expression which is identical to II.2.9. At the end of this paragraph we introduce a number of further definitions. We define the incident wave factor $k_i$ as a vector of modulus $k$, directed along the $z$ direction of the beam such that

$$e^{ikz} = e^{i\underline{k}_i \underline{r}} \tag{II.2.30}$$

In the same way the vector $k_d$ which has the same value as the incident wave vector but whose direction is fixed by the angles $\theta$ and $\varphi$ is called the scattered wave vector in the direction $(\theta,\varphi)$

$$\underline{k}_f = k\underline{u} \tag{II.2.31}$$

Finally, the scattering wave vector in the direction $(\theta,\varphi)$ is a difference between $k_f$ and $k_i$ (Fig.2.4)

$$\underline{Q} = \underline{k}_f - \underline{k}_i \tag{II.2.32}$$

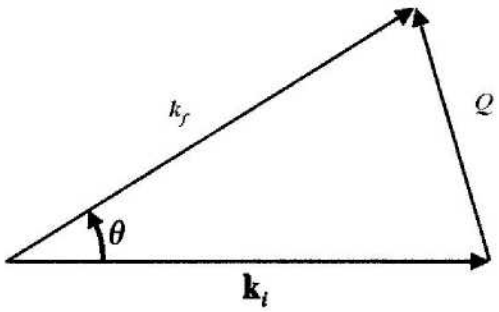



**Figure 2.4:** Scattering triangle with the incident wave vector $\underline{k}_i$ the scattered wave vector $\underline{k}_f$ and the transferred wave vector $\underline{Q}$.

### II.2.3 The Born approximation

We now are trying to solve the scattering Eq.[II.2.18] by iteration.

$$\psi_k(\underline{r}') = e^{i\underline{k}_I\underline{r}'} + \int d^3\underline{r}''\, G_+(\underline{r}'-\underline{r}'')\, U(\underline{r}'')\, \psi_k(\underline{r}'') \tag{II.2.33}$$

We insert this equation into Eq.[II.2.25] yielding

$$\begin{aligned}\psi_k(\underline{r}) = {} & e^{i\underline{k}_I\underline{r}} + \int d^3r'\, G_+(\underline{r}-\underline{r}')\, U(\underline{r}')\, e^{i\underline{k}_I\underline{r}'} \\ & + \int d^3r' \int d^3r''\, G_+(\underline{r}-\underline{r}')\, U(\underline{r}')\, G_+(\underline{r}'-\underline{r}'')\, U(\underline{r}'')\, \psi_k(\underline{r}'')\end{aligned} \tag{II.2.34}$$

There the first two terms on the right hand side are known. Only the third contains the unknown function $\psi_k(\underline{r})$. The procedure may be repeated in the next step yielding

$$\begin{aligned}\psi_k(r) = {} & e^{ik_Ir} + \int d^3r' G_+(\underline{r}-\underline{r}')\, U(\underline{r}')\, e^{i\underline{k}_I\underline{r}} \\ & + \int d^3r' \int d^3r''\, G_+(\underline{r}-\underline{r}')\, U(\underline{r}') G_+(\underline{r}'-\underline{r}'')\, U(\underline{r}'') e^{i\underline{k}_I\underline{r}''} \\ & + \int d^3r' \int d^3r'' \int d^3r'''\, G_+(\underline{r}-\underline{r}')\, U(\underline{r}') G_+(\underline{r}'-\underline{r}'')\, U(\underline{r}'') \\ & \times G_+(\underline{r}''-\underline{r}''')\, U(\underline{r}''')\ \psi_k(\underline{r}''')\end{aligned} \tag{II.2.35}$$

where now the first three terms are known. The unknown function $\psi_k(r)$ has been pushed back to the fourth term. In this way we may construct step by step what is called the Born approximation of the stationary scattering wave function. We note that each term of this expansion brings one higher power of the potential than the preceding one. Thus, if the potential is weak, each successive term is smaller than the preceding one. If one pushes the expansion far enough, then one can neglect the last term on the right hand side and thus obtains $\psi_k(\underline{r})$ entirely in terms of known quantities.

If we now substitute this expansion of $\psi_k(\underline{r})$ into the expression for the scattering amplitude (II.2.29) then we obtain the Born approximation of the scattering amplitude. In particular if we limit ourselves to the first order in the potential all what we need to do is to replace $\psi_k(\underline{r}')$ by $e^{i\underline{k}\underline{r}'}$ on the right hand side of Eq.[II.2.29]. This is called the first Born approximation.

$$f_k^{(B)}(\theta,\varphi) = -\frac{1}{4\pi}\int d^3r'\, e^{-ik\underline{u}\underline{r}'}\, U(\underline{r}')\, e^{i\underline{k}_i\underline{r}'}$$

$$= -\frac{1}{4\pi}\int d^3r'\, e^{-i(\underline{k}_f-\underline{k}_i)\underline{r}'}\, U(\underline{r}') \qquad \text{(II.2.36)}$$

$$= -\frac{1}{4\pi}\int d^3r'\, e^{-i\underline{Q}\underline{r}'}\, U(\underline{r}')$$

where $Q$ is the scattering vector defined in Eq.[II.2.32]. The scattering cross section in the first Born approximation is thus very simply related to the Fourier transformation of the potential. For the cross section this implies (Eq.[II.2.7], [II.2.15] and [II.2.36])

$$d\sigma_k^{(B)}(\theta,\varphi) = \frac{\mu^2}{4\pi^2\hbar^4}\left|\int d^3r\, e^{-\underline{Q}\underline{r}}V(\underline{r})\right|^2 \qquad \text{(II.2.37)}$$

Let us try to give a very simple physical interpretation of Eq.[II.2.34]. We draw a formal analogy between quantum mechanics and wave optics. Let us consider the target area to be a scattering medium whose density is proportional to $U(\underline{r})$. The function $G_+(\underline{r}-\underline{r}')$ represents the amplitude at the point $\underline{r}$ of a wave radiated by a point source situated at $\underline{r}'$. Consequently the first two terms in Eq.[II.2.34] describes the total wave at a point r as a result of the superposition of the incident wave $e^{i\underline{k}_i\underline{r}}$ and an infinite number of waves coming from secondary sources induced in the scattering medium by the incident wave. The amplitude of each of these sources is indeed proportional to the incident wave and the density of the scattering material ($U(\underline{r}')$) evaluated at the corresponding point $r'$. This interpretation is symbolized by Fig.2.5 recalling Huygen's principle in wave optics. Formula 2.34 includes a third term. We can interpret in an analogous fashion also the successive terms of the Born expansion. Since the scattering medium extends over a certain area, a given secondary source is excited not only by the incident waves but also by scattered waves coming from other secondary sources inducing multiple scattering.

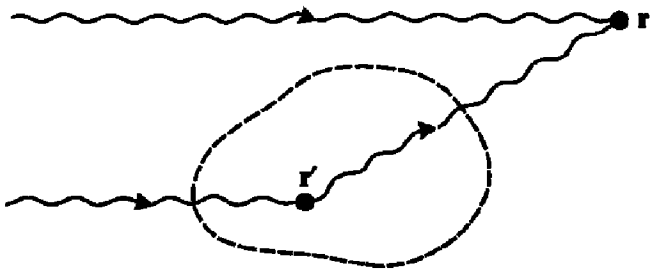



**Figure 2.5:** Schematic representation of the Born approximation: we only consider the incident wave and the waves scattered by one interaction with the potential.

Fig.2.6 represents symbolically the third term of the Born expansion. If the scattering medium has a very low density, we can neglect the influence of the secondary sources on each other.

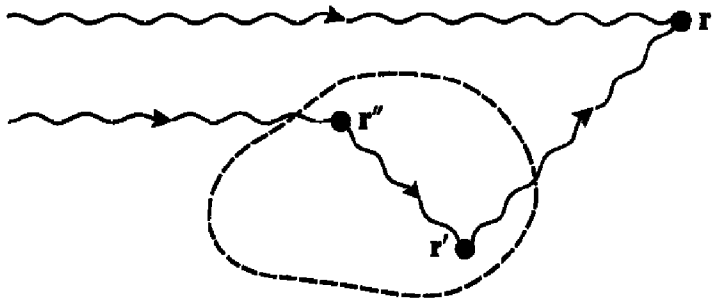



**Figure 2.6:** Schematic representation of the second-order term in the Born expansion: here we consider waves which are scattered twice by the potential.

Comment: The first Born approximation is valid for weak potentials ($\sigma/a^2\pi << 1$), where a is the size of the scattering object. For neutron scattering on a single nucleus this estimation gives about $10^{-7}$ and the Born approximation is well fulfilled. We note one important exception. The dynamic scattering theory which considers the scattering problem close to a Bragg reflection in a crystal. Then multiple beam interferences are important and the Born approximation ceases to apply. For most practical purposes however in neutron scattering the Born approximation is valid.

### II.2.4 The Fermi pseudo potential

The interaction of the neutron with a nucleon occurs under the strong interaction on a length scale of $1.5 \cdot 10^{-15}$m. For that process, the Born criterion is not fulfilled and for the scattering process on a single nucleus the Born series would have to be summed up. Fortunately, this is a problem of nuclear physics and for the purposes of neutron scattering a phenomenological approach suffices. Considering that the wavelengths of thermal neutrons are in the order of $10^{-10}$m, we realize that they are much larger than the dimension of a nucleus of about $10^{-15}$m. Therefore, for any scattering event the scattering cannot dependent on the shape of the object and must be isotropic (we may perform a separation into partial waves and consider only the isotropic *S*-wave scattering formally). Such scattering processes may be described by one parameter the scattering length $b = b_1 + i \cdot b_2$. Thereby $b_1$ describes scattering, while $b_2$ is the absorption part. For thermal neutrons the scattering potential of a single nucleus becomes (Fermi pseudo potential).

$$V(\underline{r}) = \frac{2\pi \ \hbar^2}{m_n} \ b\delta \ \ (\underline{r} - \underline{R}) \tag{II.2.38}$$

The scattering lengths $b$ have been measured as a function of neutron energy. For thermal and lower energies the real parts of these scattering lengths are constant and depend in an non-systematic way on the number of nucleons (see Fig.2.7).

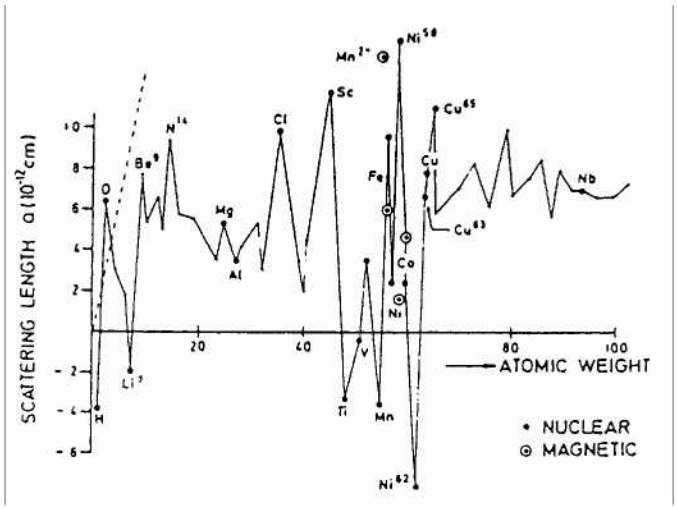



**Figure 2.7:** Scattering length of nuclei for thermal neutrons as a function of atomic weight.

We realize, that there are positive as well as negative scattering lengths. Following a convention most of the scattering lengths are positive. In this case, we have potential scattering with a phase shift of 180° between the incoming and scattered wave. Negative values result from resonance scattering where the neutrons penetrate the nuclei and create a compound nucleus. Then the emitted neutrons do not undergo a phase shift. We also realize strong differences in the scattering lengths for some isotopes. In particular important is the difference in scattering length between hydrogen and deuterium ($b_h$ = -0.374, $b_d$ = +0.667). This significant difference in scattering length is the basis of all contrast variation experiments in soft condensed matter research as well as in biology (see later lectures). We also note, that the scattering lengths may depend on the relative orientation of the neutron spin with respect to the spin of the scattering nucleus. Again a very prominent example is the hydrogen. There the scattering length for the triplet state - neutron and hydrogen spins are parallel - amounts to $b_{triplet} = 1.04 \cdot 10^{-12}$cm while the scattering length for the singlet situation - neutron and hydrogen spins are antiparallel - is $b_{singlet} = -0.474 \cdot 10^{-12}$cm.

References:

[1] Quantum Mechanics, Eds. Claude Cohen Tannoudji, Bernhard Diu and Frank Laloe, Wiley, New York (1977)

# III

# Symmetry in Crystals

Gernot Heger

# III. Symmetry of Crystals

G. Heger

## III.1 Introduction

The term "crystal" comes from the Greek κρύσταλλος, which was first used as description of ice and later on - more general - of transparent minerals with regular morphology (regular crystal faces and edges).



Fig. 1. Example: rock crystal – quartz ($SiO_2$), mineral from the Gotthard-Massif.

Matter is usually classified into three states: gaseous – liquid – solid. Crystals are representatives of the solid state. **Crystalline solids are thermodynamically stable** in contrast to glasses and are **characterised by a regular three-dimensional periodic arrangement of atoms (ions, molecules) in space**.

## III.2 Crystal lattices

The three-dimensional periodicity of crystals can be represented by the so-called crystal lattice. The repeat unit in form of a parallelepiped - known as the **unit cell** – is defined by 3 non-linear basis vectors $\underline{a}$, $\underline{b}$, and $\underline{c}$, whose directions form the reference axes X, Y, and Z of the corresponding right-handed crystallographic coordination system. The 6 lattice parameters are given as the lengths of the basis vectors $a = |\underline{a}|$, $b = |\underline{b}|$, $c = |\underline{c}|$ and the angles between the basis vectors: angle $(\underline{a},\underline{b}) = \gamma$, angle $(\underline{b},\underline{c}) = \alpha$, angle $(\underline{c},\underline{a}) = \beta$. The faces of the unit cell are named as face $(\underline{a},\underline{b})$ = C, face $(\underline{b},\underline{c})$ = A, face $(\underline{c},\underline{a})$ = B.

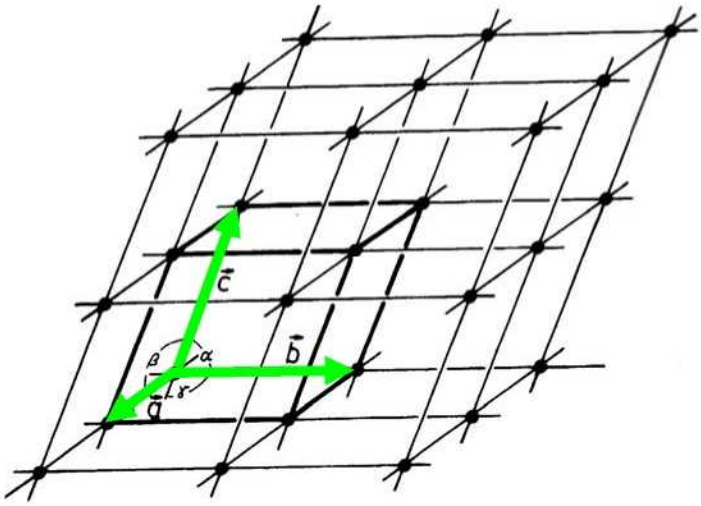



Fig. 2. Notation for a unit cell and a point lattice.

If the vertices of all repeat units (unit cells) are replaced by points, there results the crystal lattice in the form of a **point lattice**. Each lattice point is given by a vector $\underline{\tau} = u\underline{a} + v\underline{b} + w\underline{c}$, with u, v, w being integers. As a symmetry operation of parallel displacement, $\underline{\tau}$ - also known as **translation vector** – maps the atomic arrangement of the crystal (crystal structure) onto itself.

A **lattice point** is named "uvw", according to the coefficients (integers) of the translation vector $\underline{\tau} = u\underline{a} + v\underline{b} + w\underline{c}$ from the origin to the lattice point. A **lattice direction** - given by the symbol [uvw] - is defined by the direction of the corresponding translation vector.

A plane passing through three lattice points is known as a **lattice plane**. Since all lattice points are equivalent (by translation symmetry) there will be infinitely many parallel planes passing through all the other points of the lattice. Such a set of equally spaced planes is known as a **set of lattice planes**. If the first plane from the origin of a set of lattice planes makes intercepts a/h, b/k, c/l on the X, Y, Z axes, respectively, where h, k, l are integers, then the **Miller indices** of this set of lattice planes are (hkl), the three factors h, k, l being enclosed in parentheses.

The equation of lattice planes can be written in intercept form as

$$(hx/a) + (ky/b) + (lz/c) = n, \qquad (1)$$

where n is an integer. If n = 0 the lattice plane passes through the origin; if n = 1 the plane makes intercepts a/h, b/k, c/l on the X, Y, Z axes respectively; if n = 2 the intercepts are 2a/h, 2b/k, 2c/l; and so on.

The line of intersection of any two non-parallel lattice planes is a row of lattice-points common to both planes. This lattice point row defines a lattice direction [uvw] which is known as **zone axis**. All lattice planes intersecting in a common lattice-point row are said to lie in the same **zone**. The condition for lattice planes to be parallel to a lattice vector $\underline{\tau} = u\underline{a} + v\underline{b} + w\underline{c}$ is the **zone equation**

$$uh + vk + wl = 0 \qquad (2)$$

The zone axis symbol [uvw] for the zone containing the two planes $(h_1k_1l_1)$ and $(h_2k_2l_2)$ is obtained by solving the simultaneous equations $uh_1 + vk_1 + wl_1 = 0$ and $uh_2 + vk_2 + wl_2 = 0$,

$$[uvw] = [k_1l_2\text{-}k_2l_1,\ l_1h_2\text{-}l_2h_1,\ h_1k_2\text{-}h_2k_1]. \qquad (3)$$

### III.3 Crystallographic coordinate systems

The description of a crystal structure consists first of the choice of a unit cell as smallest repeat unit of the crystal with its basis vectors. In this way a crystal-specific coordinate system is defined which is used to localize all the atoms in the unit cell. Whereas in physics and chemistry usually cartesian coordinate systems are used, in crystallography quite different systems are applied. The conventional crystallographic coordinate systems are based on the symmetry of the crystals. In three dimensions there exists 7 different crystal systems and hence 7 crystallographic coordinate systems:

| name of system | minimum symmetry | conventional unit cell |
|---|---|---|
| triclinic | 1 or $\bar{1}$ | $a \neq b \neq c;\ \alpha \neq \beta \neq \gamma$ |
| monoclinic (unique axis b) | one diad – 2 or m ( $\parallel$ Y) | $a \neq b \neq c;\ \alpha=\gamma=90°,\ \beta>90°$ |
| orthorhombic | three mutually perpendicular diads – 2 or m ( $\parallel$ X, Y and Z) | $a \neq b \neq c;\ \alpha=\beta=\gamma=90°$ |
| tetragonal | one tetrad – 4 or $\bar{4}$ ( $\parallel$ Z) | $a = b \neq c;\ \alpha=\beta=\gamma=90°$ |
| trigonal (hexagonal cell) | one triad – 3 or $\bar{3}$ ( $\parallel$ Z) | $a = b \neq c;\ \alpha=\beta=90°,\ \gamma=120°$ |
| hexagonal | one hexad – 6 or $\bar{6}$ ( $\parallel$ Z) | $a = b \neq c;\ \alpha=\beta=90°,\ \gamma=120°$ |
| cubic | four triads – 3 or $\bar{3}$ ( $\parallel$ space diagonals of cube) | $a = b = c;\ \alpha=\beta=\gamma=90°$ |

The choice of the origin of the coordinate system is free in principle, but for convenience it is usually chosen in a centre of symmetry (inversion centre), if present, otherwise in a point of high site symmetry of the space group.

In order to complete the symmetry conventions of the coordinate systems it is necessary to add to the 7 so-called primitive unit cells of the crystal systems (primitive lattice types with only one lattice point per unit cell) 7 centred unit cells with two, three or four lattice points per unit cell (centred lattice types). These centred unit cells are consequently two, three or four times larger than the smallest repeat units of the crystals. The resulting 14 **Bravais lattice types** with their centring conditions are collected in Fig. 3.

A set of lattice planes (hkl) is separated by a characteristic interplanar spacing d(hkl). According to the different crystallographic coordinate systems these d(hkl) values are calculated in a specific manner:

For the cubic lattice ($a = b = c$, $\alpha = \beta = \gamma = 90°$), ex. NaCl

$$d(hkl) = a \cdot \left(h^2 + k^2 + l^2\right)^{-\frac{1}{2}}$$

For the hexagonal lattice ($a = b$, $c$, $\alpha = \beta = 90°$, $\gamma = 120°$), ex. Graphite

$$d(hkl) = \left(\frac{4}{3}\frac{h^2 + k^2 + hk}{a^2} + \frac{l^2}{c^2}\right)^{-\frac{1}{2}}$$

For the tetragonal lattice ($a = b$, $c$, $\alpha = \beta = \gamma = 90°$)

$$d(hkl) = \left(\frac{h^2 + k^2}{a^2} + \frac{l^2}{c^2}\right)^{-\frac{1}{2}}$$

For the orthorhombic lattice ($a$, $b$, $c$, $\alpha = \beta = \gamma = 90°$)

$$d(hkl) = \left(\frac{h^2}{a^2} + \frac{k^2}{b^2} + \frac{l^2}{c^2}\right)^{-\frac{1}{2}}$$

For the monoclinic lattice ($a$, $b$, $c$, $\alpha = \gamma = 90°$, $\beta > 90°$)

$$d(hkl) = \left(\frac{h^2}{a^2\sin^2\beta} + \frac{k^2}{b^2} + \frac{l^2}{c^2\sin^2\beta} - \frac{2hl\cos\beta}{ac\sin^2\beta}\right)^{-\frac{1}{2}}$$

For the triclinic lattice ($a$, $b$, $c$, $\alpha$, $\beta$, $\gamma$), the most general case,

$$d(hkl) = \left(1 - \cos^2\alpha - \cos^2\beta - \cos^2\gamma + 2\cos\alpha \cdot \cos\beta \cdot \cos\gamma\right)^{\frac{1}{2}}$$

$$\left(\begin{array}{l} \frac{h^2}{a^2}\sin^2\alpha + \frac{k^2}{b^2}\sin^2\beta + \frac{l^2}{c^2}\sin^2\gamma \\ + \frac{2kl}{bc}\left(c \cdot \cos^2\beta - \cos\alpha\right) + \frac{2lh}{ca}\left(c \cdot \cos^2\gamma - \cos\beta\right) + \frac{2hk}{ab}\left(c \cdot \cos^2\alpha - \cos\gamma\right) \end{array}\right)^{-\frac{1}{2}} \qquad (4)$$

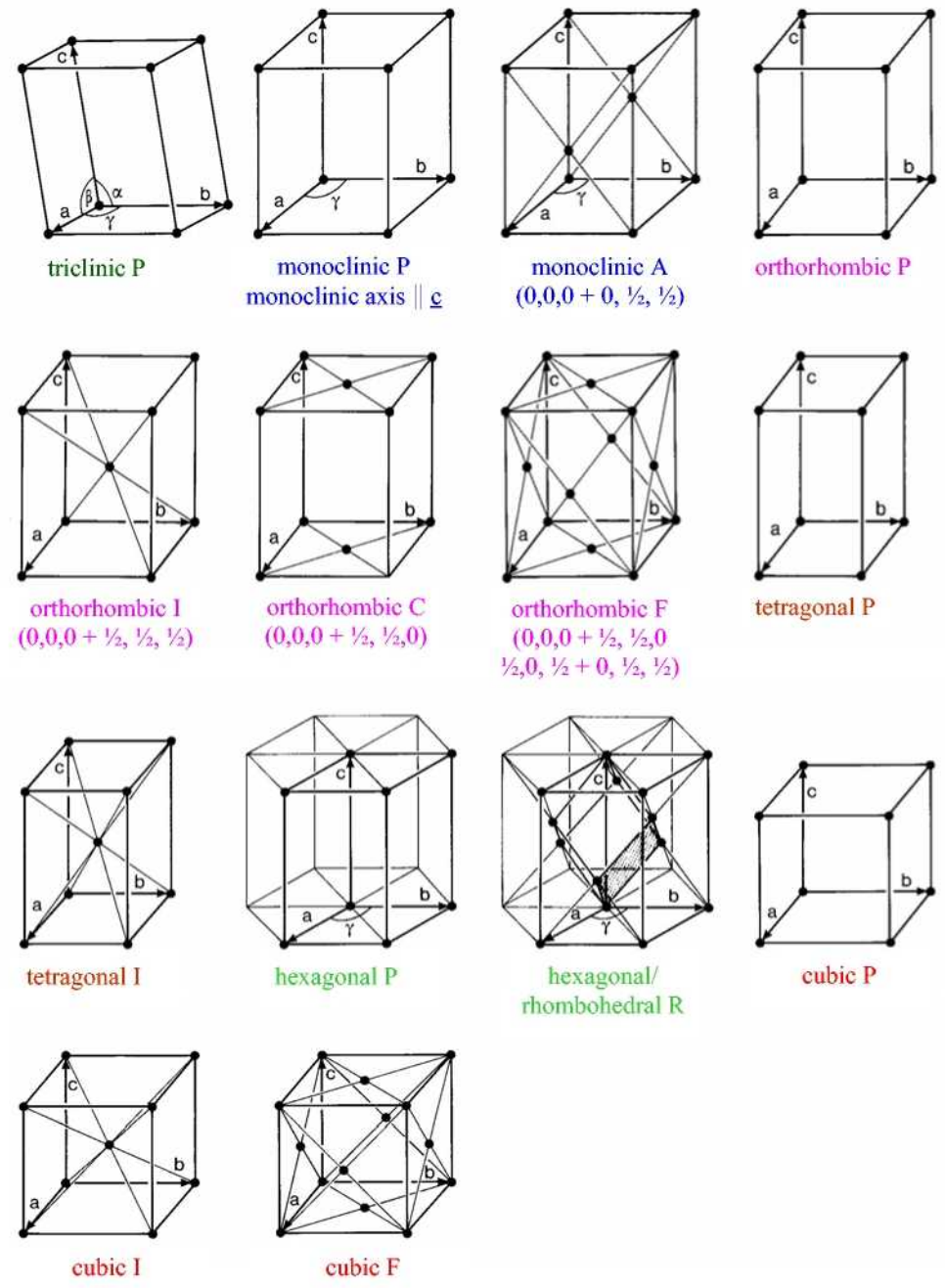



Fig. 3. The 14 Bravais lattices consisting of the 7 primitive lattices **P** for the 7 crystal systems with only one lattice point per unit cell + the 7 centred (multiple) lattices **A**, **B**, **C**, **I**, **R** and **F** with 2, 3 and 4 lattice points per unit cell.

### III.4 Crystallographic symmetry operations and symmetry elements

The **symmetry operations** of a crystal are isometric transformations or motions, i.e. mappings which preserve distances and, hence, also angles and volumes. An object and its transformed object superpose in a perfect manner, they are indistinguishable.

The simplest crystallographic symmetry operation is the **translation**, which is a parallel displacement of the crystal by a translation vector $\underline{\tau}$ (see chapt. X.2). There is no fixed point, the entire lattice is shifted and therefore, theoretically, the crystal lattice is considered to be infinite.

Crystallographic **rotations** n around an axis by an angle $\varphi = 360°/n$ (n-fold rotations) and **rotoinversions** (combination of rotations and inversions) $\bar{n}$ are called point symmetry operations because they leave at least one point of space invariant (at least one fixed point). An important fact of crystallographic symmetry is the restriction of the rotation angles by the three-dimensional crystal lattice to $\varphi = 360°$ (n = 1), 180° (n = 2), 120° (n = 3), 90° (n = 4), 60° (n = 6). Only for these crystallographic rotations the space can be covered completely without gaps and overlaps. The rotoinversion $\bar{n} = \bar{1}$ is an **inversion** in a point, $\bar{n} = \bar{2} \equiv m$ (mirror) describes a **reflection** across a plane.

The combination of n-fold rotations with $m/n \cdot \underline{\tau}$ translation components ($m < n$) $\parallel$ to the rotation axis leads to the so-called **screw rotations** $n_m$, e.g. $2_1$, $3_2$, $4_2$, $6_5$. These symmetry operations have no fixed points.

The combination of a reflection through a plane (glide plane) with translation components (glide vectors) of $\underline{a}/2$, $\underline{b}/2$, $\underline{c}/2$, $(\underline{a}+\underline{b})/2$, … $\parallel$ to this plane are known as **glide reflections** a, b, c, n, …, d. Again no fixed points exist for these symmetry operations.

In addition to the symmetry operations which represent isometric motions of an object, symmetry can also be described in (static) geometrical terms by **symmetry elements**. They form the geometrical locus, oriented in space, on which a symmetry operation is performed (line for a rotation, plane for a reflection, point for an inversion) together with a description of this operation. Symmetry elements are mirror planes, glide planes, rotation axes, screw axes, roto-inversion axes and inversion centres. The geometrical descriptions of the crystallographic symmetry operations are illustrated in Figs. 4-6.

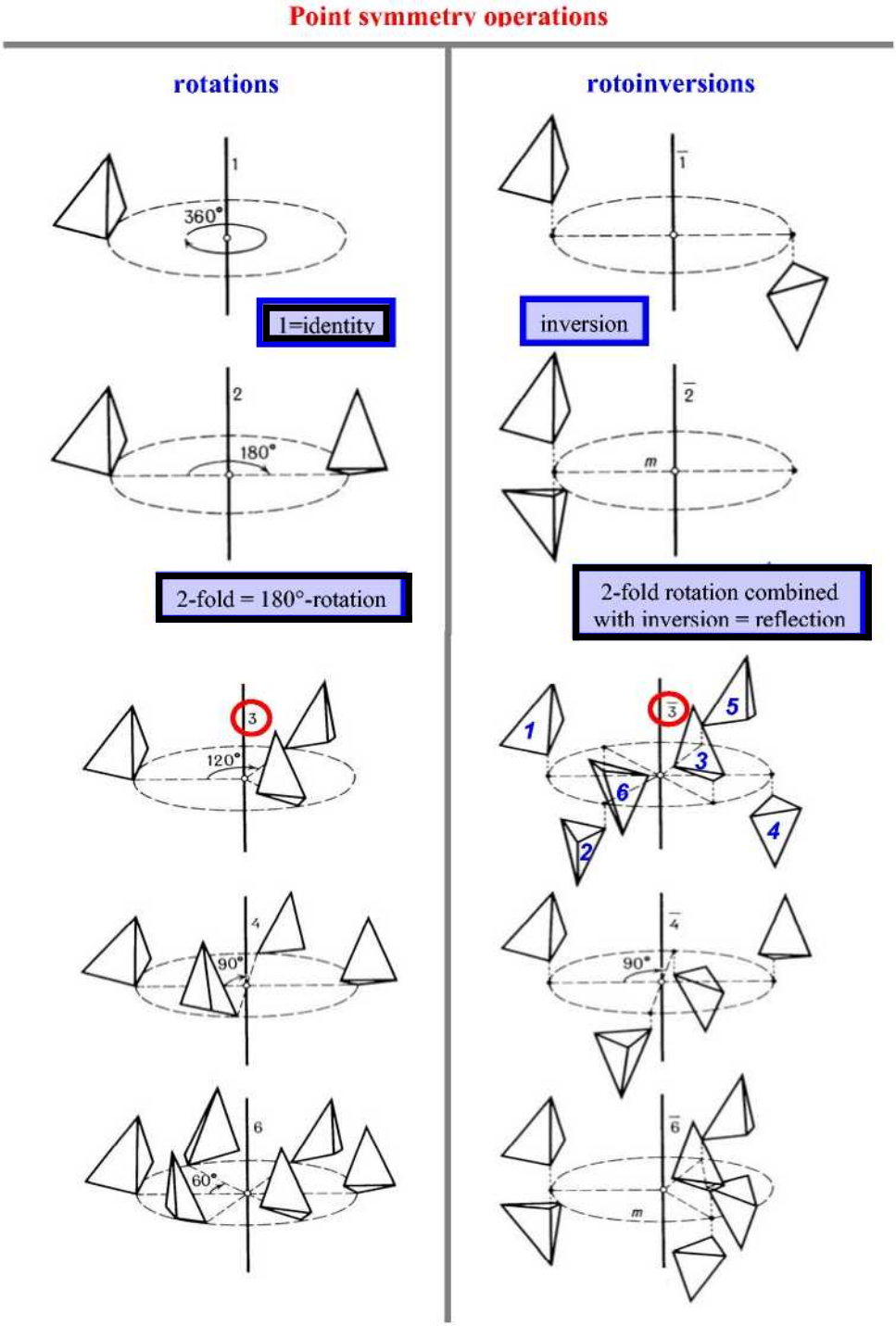



Fig. 4. Rotations: n=1 (identity), n=2 (rotation angle 180°), n=3 (120°), n=4 (90°), n=6 (60°)
Rotoinversions: $\bar{1}$ (inversion), $\bar{2} \equiv$ m (reflection), $\bar{3} = 3 + \bar{1}$, $\bar{4}$, $\bar{6} = 3/m$.

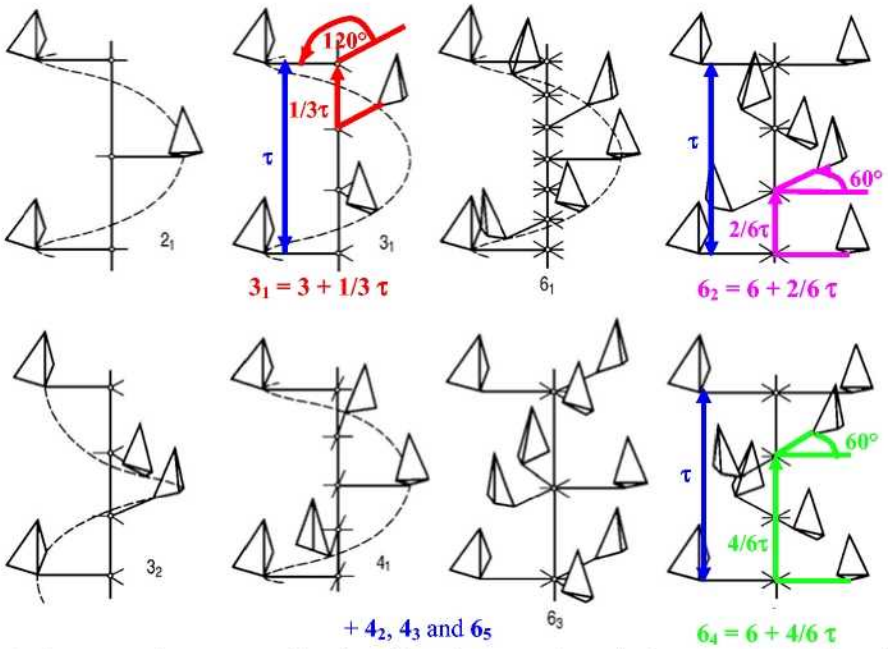
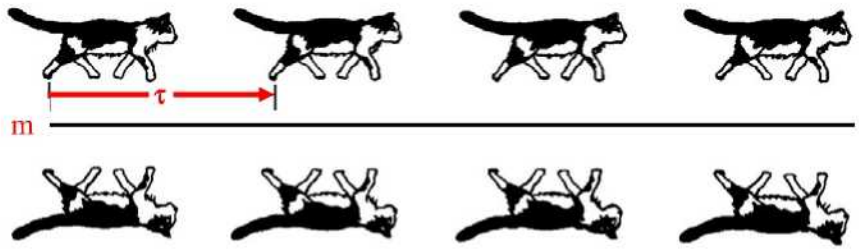
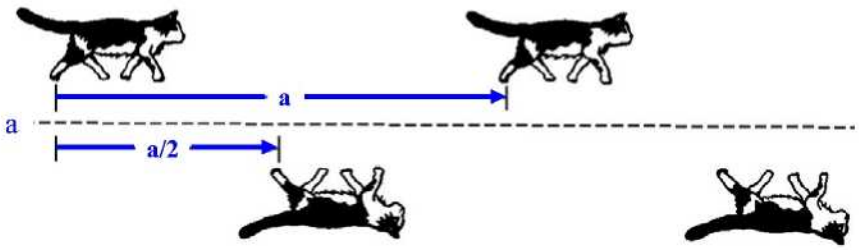



Fig. 5. Screw rotations $n_m$: combination of rotations n and translation components m/n·τ || to the rotation axis.




reflection: mirror plane m ⊥ image plane (plane of the paper)




glide reflection: glide plane a ⊥ with glide vector **a**/2

Fig. 6. Examples of reflections and glide reflections.

A symmetry operation transforms a point X with coordinates x, y, z (according to a position vector $\underline{X} = x\underline{a} + y\underline{b} + z\underline{c}$) into a symmetrically equivalent point X' with coordinates x', y', z' mathematically by the linear equations

$$\begin{aligned} x' &= W_{11}x + W_{12}y + W_{13}z + w_1 \\ y' &= W_{21}x + W_{22}y + W_{23}z + w_2 \\ z' &= W_{31}x + W_{32}y + W_{33}z + w_3 \end{aligned} \qquad (5)$$

or, in matrix notation:

$$\begin{pmatrix} x' \\ y' \\ z' \end{pmatrix} = \begin{pmatrix} W_{11} & W_{12} & W_{13} \\ W_{21} & W_{22} & W_{23} \\ W_{31} & W_{32} & W_{33} \end{pmatrix} \circ \begin{pmatrix} x \\ y \\ z \end{pmatrix} + \begin{pmatrix} w_1 \\ w_2 \\ w_3 \end{pmatrix}; \quad \underline{X}' = \mathbf{W} \circ \underline{X} + \mathbf{w} = (\mathbf{W}, \mathbf{w}) \circ \underline{X}. \qquad (6)$$

The (3×3) matrix **W** is the rotation part and the (3×1) column matrix **w** the translation part of the symmetry operation. The two parts **W** and **w** can be assembled into an augmented (4×4) matrix $\boldsymbol{W}$ according to

$$\begin{pmatrix} x' \\ y' \\ z' \\ 1 \end{pmatrix} = \begin{pmatrix} W_{11} & W_{12} & W_{13} & w_1 \\ W_{21} & W_{22} & W_{23} & w_2 \\ W_{31} & W_{32} & W_{33} & w_3 \\ 0 & 0 & 0 & 1 \end{pmatrix} \circ \begin{pmatrix} x \\ y \\ z \\ 1 \end{pmatrix} = \boldsymbol{W} \circ \boldsymbol{X} \qquad (7)$$

Since every symmetry transformation is a "rigid-body" motion, the determinant of all matrices **W** and $\boldsymbol{W}$ is $\det \mathbf{W} = \det \boldsymbol{W} = \pm 1$ (+ 1: preservation of handedness; - 1:change of handedness of object).

The sequence of two symmetry operations (successive application) is given by the product of their matrices $\boldsymbol{W_1}$ and $\boldsymbol{W_2}$:

$$\boldsymbol{W_3} = \boldsymbol{W_1} \circ \boldsymbol{W_2}, \qquad \text{whereby } \boldsymbol{W_3} \text{ is again a symmetry operation.} \qquad (8)$$

### III.5 Crystallographic point groups and space groups

The symmetry of a crystal and of its crystal structure can be described by mathematical group theory. The symmetry operations are the group elements of a crystallographic group G and the combination of group elements is the successive execution of symmetry operations. All possible combinations of crystallographic point-symmetry operations in three-dimensional space lead to exactly 32 crystallographic point groups (≡ crystal classes) which all are of finite order (the maximum order is 48 for the cubic crystal class $m\bar{3}m$). For the different crystal systems they are represented by stereographic projections in Fig. 7. There are two types of

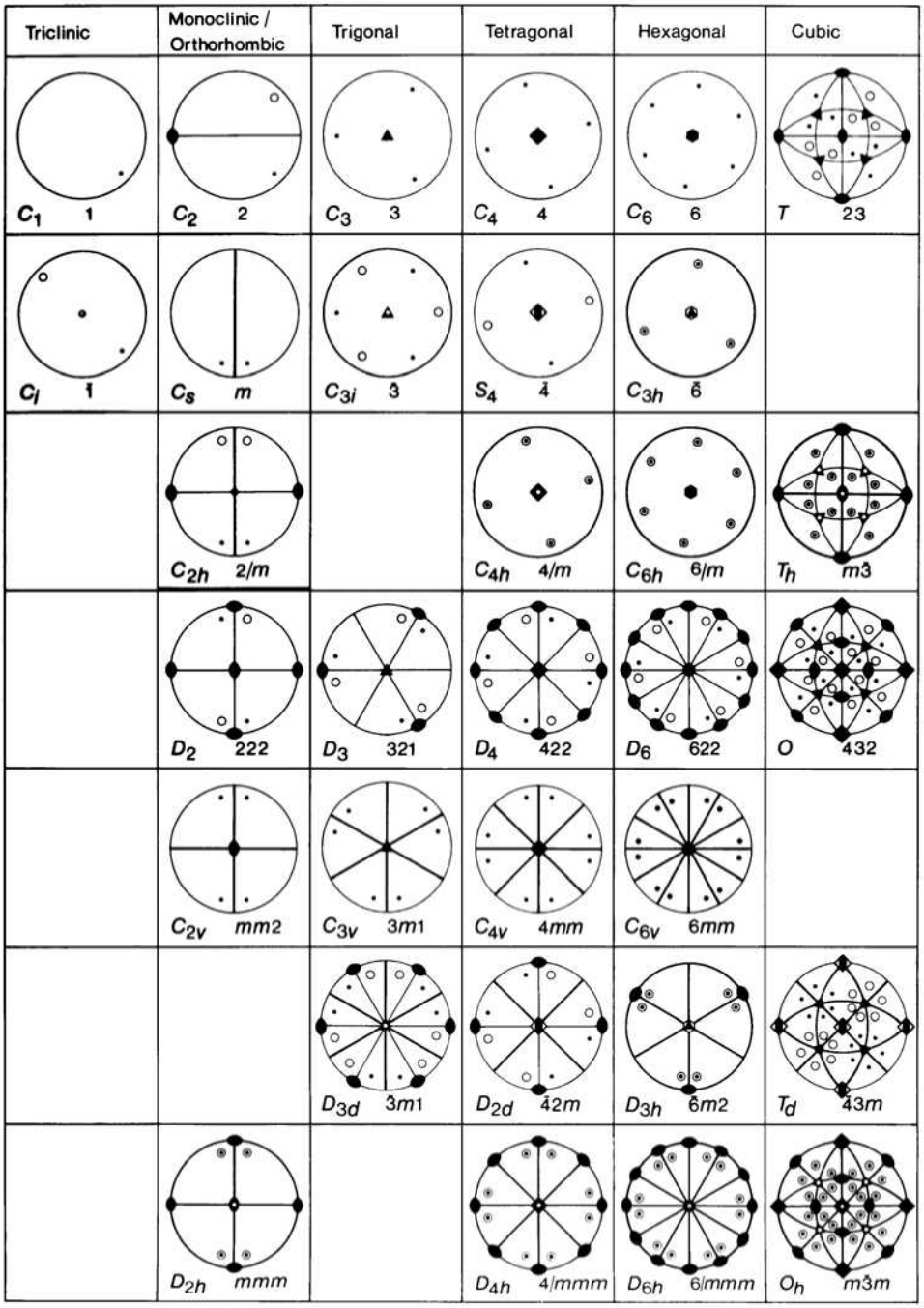



Fig. 7. The 32 crystallographic point groups (crystal classes) in three-dimensional space represented by their stereographic projections. The group symbols are given according to Schoenflies (bottom left) and to Hermann-Mauguin (bottom right).

group symbols in use: for each crystal class the corresponding Schoenflies symbol is given at the bottom left and the Hermann-Mauguin (international) symbol at the bottom right. A maximum of 3 independent main symmetry directions ("Blickrichtungen") is sufficient to describe the complete symmetry of a crystal. These Blickrichtungen are specifically defined for the 7 crystal systems (Hermann-Mauguin symbols). As an example the Blickrichtungen of the cubic system are shown in Fig. 8.

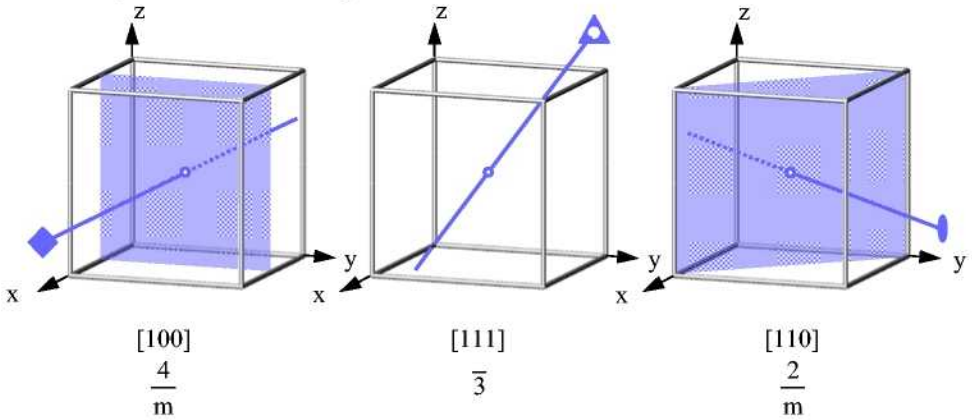



Fig. 8. Symmetry directions ("Blickrichtungen") of the cubic lattice (a=b=c, α=β=γ=90°)
Along [100]: 4/m, along [111]: $\bar{3}$, along [110]: 2/m.

The point-group symmetries determine the anisotropic (macroscopic) physical properties of crystals, i. e. mechanical, electrical, optical and thermal properties. By diffraction methods normally only the 11 centrosymmetric Laue classes can be determined:

| crystal system | Laue class |
|---|---|
| triclinic | $\bar{1}$ |
| monoclinic | 1 2/m 1 = 2/m |
| orthorhombic | 2/m 2/m 2/m = m m m |
| tetragonal | 4/m<br>4/m 2/m 2/m = 4/m m m |
| trigonal | $\bar{3}$<br>$\bar{3}$ 2/m = $\bar{3}$ m |
| hexagonal | 6/m<br>6/m 2/m 2/m = 6/m m m |
| cubic | 2/m $\bar{3}$ = m $\bar{3}$<br>4/m $\bar{3}$ 2/m = m $\bar{3}$ m |

In three dimensions all possible combinations of the point symmetries of the 32 crystallographic point groups with the lattice translations of the 14 Bravais lattices lead to exactly 230 space groups, all of infinite order. As already mentioned, there result new symmetry operations: screw rotations and glide reflections. The conventional graphical symbols for the symmetry elements according to the International Tables for Crystallography Vol. A (ITA, 2002 [1]) are shown in Fig. 9.

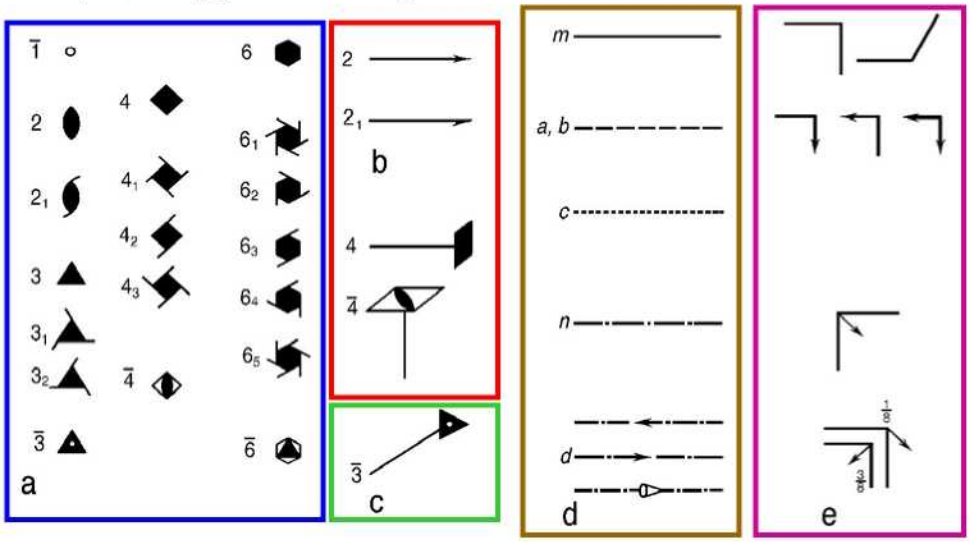



Fig. 9. Conventional graphical symbols for symmetry elements:

- symmetry axes (a) perpendicular, (b) parallel, and (c) inclined to the image plane
- symmetry planes (d) perpendicular and (e) parallel to the image plane.

In the International Tables for Crystallography Vol. A [1] all space groups are described in detail with their Hermann-Mauguin symbols and corresponding crystal classes, the relative locations and orientations of the symmetry elements with respect to a chosen origin and the crystal-specific basis vectors, a listing of the general and all special positions (with their symmetrically equivalent points) and the related reflection conditions.

### III.6 Example of the crystal structure description of $YBa_2Cu_3O_{7-\delta}$ using the ITA

The crystal structure determination with atomic resolution is achieved by diffraction experiments with X-rays, electron or neutron radiation. As an example, the results of a structure analysis by neutron diffraction on a single crystal of the ceramic high-$T_C$ superconductor $YBa_2Cu_3O_{7-\delta}$ with $T_C$ = 92 K are presented. The atomic arrangement of the orthorhombic structure, space group Pmmm, and the temperature-dependent electrical resistivity is shown in Fig. 10.

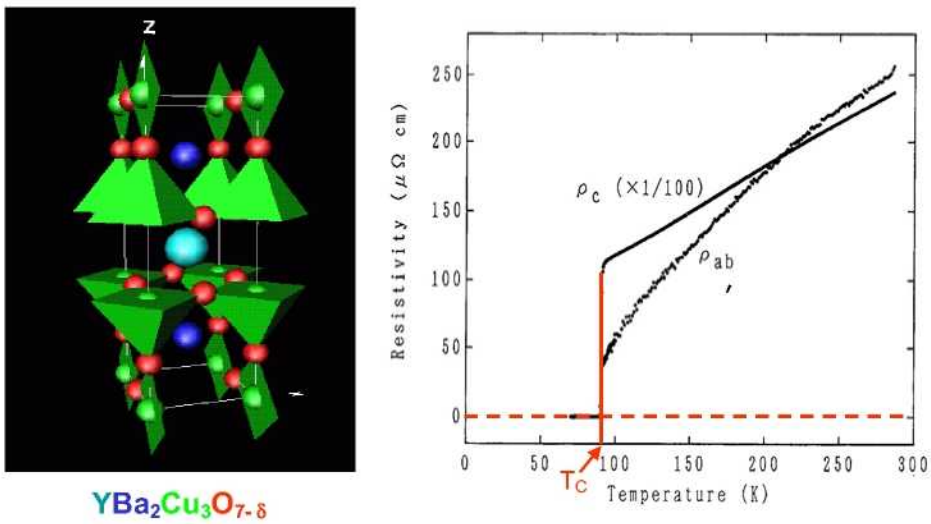



Fig. 10. Crystal structure (unit cell) of $YBa_2Cu_3O_{7-\delta}$ with the $CuO_x$-polyhedra (left) and the electrical resistivity as a function of temperature $\parallel$ and $\perp$ to the [001] direction.

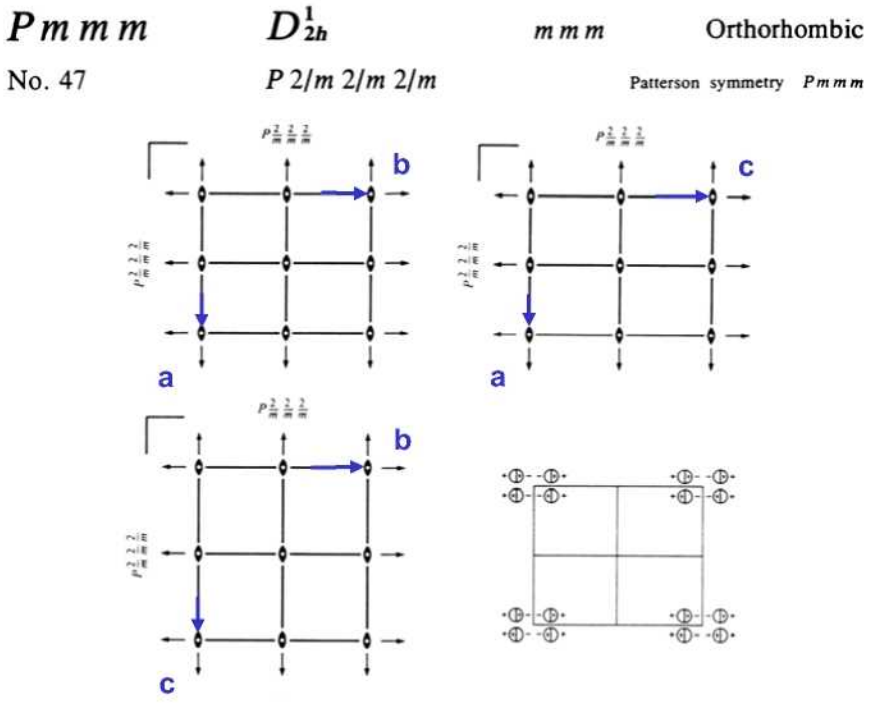



Fig. 11. Description of the orthorhombic space group Pmmm in ITA (2002).

Information from ITA on the relative locations and orientations of the symmetry elements (symmetry operations 1, $2_z$, $2_y$, $2_x$, $\bar{1}$, $m_z$, $m_y$, $m_x$) of the orthorhombic space group Pmmm, together with the choice of the origin (in an inversion centre), is shown in Fig. 11. The general position (site symmetry 1) of multiplicity 8 and all special positions with their site symmetries are listed in Fig. 12. There are no special reflection conditions for this space group.

CONTINUED $YBa_2Cu_3O_{7-\delta}$ No. 47 *Pmmm*

**Generators selected** (1); $t(1,0,0)$; $t(0,1,0)$; $t(0,0,1)$; (2); (3); (5)

**Positions**

| Multiplicity, Wyckoff letter, Site symmetry | | | Coordinates | | | | Reflection conditions |
|---|---|---|---|---|---|---|---|
| 8 | $\alpha$ | 1 | (1) $x,y,z$ | (2) $\bar{x},\bar{y},z$ | (3) $\bar{x},y,\bar{z}$ | (4) $x,\bar{y},\bar{z}$ | General: |
| | | | (5) $\bar{x},\bar{y},\bar{z}$ | (6) $x,y,\bar{z}$ | (7) $x,\bar{y},z$ | (8) $\bar{x},y,z$ | no conditions |
| | | | | | | | Special: no extra conditions |
| 4 | $z$ | $..m$ | $x,y,\frac{1}{4}$ | $\bar{x},\bar{y},\frac{1}{4}$ | $\bar{x},y,\frac{3}{4}$ | $x,\bar{y},\frac{3}{4}$ | |
| 4 | $y$ | $..m$ | $x,y,0$ | $\bar{x},\bar{y},0$ | $\bar{x},y,0$ | $x,\bar{y},0$ | |
| 4 | $x$ | $.m.$ | $x,\frac{1}{4},z$ | $\bar{x},\frac{1}{4},z$ | $\bar{x},\frac{1}{4},\bar{z}$ | $x,\frac{1}{4},\bar{z}$ | |
| 4 | $w$ | $.m.$ | $x,0,z$ | $\bar{x},0,z$ | $\bar{x},0,\bar{z}$ | $x,0,\bar{z}$ | |
| 4 | $v$ | $m..$ | $\frac{1}{4},y,z$ | $\frac{1}{4},\bar{y},z$ | $\frac{1}{4},y,\bar{z}$ | $\frac{1}{4},\bar{y},\bar{z}$ | |
| 4 | $u$ | $m..$ | $0,y,z$ | $0,\bar{y},z$ | $0,y,\bar{z}$ | $0,\bar{y},\bar{z}$ | |
| 2 | $t$ | $mm2$ | $\frac{1}{4},\frac{1}{4},z$ | $\frac{1}{4},\frac{1}{4},\bar{z}$ | | | |
| 2 | $s$ | $mm2$ | $\frac{1}{4},0,z$ | $\frac{1}{4},0,\bar{z}$ | | | |
| 2 | $r$ | $mm2$ | $0,\frac{1}{4},z$ | $0,\frac{1}{4},\bar{z}$ | | | |
| 2 | $q$ | $mm2$ | $0,0,z$ | $0,0,\bar{z}$ | | | |
| 2 | $p$ | $m2m$ | $\frac{1}{4},y,\frac{1}{4}$ | $\frac{1}{4},\bar{y},\frac{1}{4}$ | | | |
| 2 | $o$ | $m2m$ | $\frac{1}{4},y,0$ | $\frac{1}{4},\bar{y},0$ | | | |
| 2 | $n$ | $m2m$ | $0,y,\frac{1}{4}$ | $0,\bar{y},\frac{1}{4}$ | | | |
| 2 | $m$ | $m2m$ | $0,y,0$ | $0,\bar{y},0$ | | | |
| 2 | $l$ | $2mm$ | $x,\frac{1}{4},\frac{1}{4}$ | $\bar{x},\frac{1}{4},\frac{1}{4}$ | | | |
| 2 | $k$ | $2mm$ | $x,\frac{1}{4},0$ | $\bar{x},\frac{1}{4},0$ | | | |
| 2 | $j$ | $2mm$ | $x,0,\frac{1}{4}$ | $\bar{x},0,\frac{1}{4}$ | | | |
| 2 | $i$ | $2mm$ | $x,0,0$ | $\bar{x},0,0$ | | | |
| 1 | $h$ | $mmm$ | $\frac{1}{4},\frac{1}{4},\frac{1}{4}$ | | | | |
| 1 | $g$ | $mmm$ | $0,\frac{1}{4},\frac{1}{4}$ | | | | |
| 1 | $f$ | $mmm$ | $\frac{1}{4},\frac{1}{4},0$ | | | | |
| 1 | $e$ | $mmm$ | $0,\frac{1}{4},0$ | | | | |
| 1 | $d$ | $mmm$ | $\frac{1}{4},0,\frac{1}{4}$ | | | | |
| 1 | $c$ | $mmm$ | $0,0,\frac{1}{4}$ | | | | |
| 1 | $b$ | $mmm$ | $\frac{1}{4},0,0$ | | | | |
| 1 | $a$ | $mmm$ | $0,0,0$ | | | | |

Fig. 12. General and special positions (coordinates of all symmetrically equivalent positions) of space group Pmmm with their site symmetries and multiplicities as well as reflection conditions. The special positions of the $YBa_2Cu_3O_{7-\delta}$ structure are indicated by frames.

The atomic parameters of the structure refinement of $YBa_2Cu_3O_{6.96}$ at room temperature [2] are given in the following Table:

| **Atomic positions of $YBa_2Cu_3O_{6.96}$**<br>orthorhombic, space group type P *2/m 2/m 2/m*<br>a = 3.858 Å, b = 3.846 Å, c = 11.680 Å (at room temperature) | | | | | |
|---|---|---|---|---|---|
| **atom/ion** | **multiplicity** | **site symmetry** | **x** | **y** | **z** |
| $Cu1/Cu^{2+}$ | 1 | *2/m 2/m 2/m* | 0 | 0 | 0 |
| $Cu2/Cu^{2+}$ | 2 | *m m 2* | 0 | 0 | 0.35513(4) |
| $Y/Y^{3+}$ | 1 | *2/m 2/m 2/m* | ½ | ½ | ½ |
| $Ba/Ba^{2+}$ | 2 | *m m 2* | ½ | ½ | 0.18420(6) |
| $O1/O^{2-}$ | 2 | *m m 2* | 0 | 0 | 0.15863(5) |
| $O2/O^{2-}$ | 2 | *m m 2* | 0 | ½ | 0.37831(2) |
| $O3/O^{2-}$ | 2 | *m m 2* | ½ | 0 | 0.37631(2) |
| $O4/O^{2-}$ | 1 | *2/m 2/m 2/m* | 0 | ½ | 0 |

**References**


[1] International Tables for Crystallography Vol. A, Space-group Symmetry, edited by Th. Hahn, Dordrecht: Kluwer Academic Publishers (5. Edition, 2002).

[2] P. Schweiss, W. Reichardt, M. Braden, G. Collin, G. Heger, H. Claus, A. Erb, Phys. Rev. **B49**, 1387 – 1396 (1994).

# 1

# Neutron Sources

Alexander Ioffe

# 1. Neutron Sources

Alexander Ioffe

## 1.1 Introduction

Neutron scattering is a very important tool for studies of fundamental properties of condensed matter as well as material research. It has a special stand among other kinds of radiation as light, X-rays or synchrotron radiation, electrons or ions because of electrical neutrality of neutrons, its large magnetic moment and low kinetic energy. Due to these unique properties of neutrons they became irreplaceable for the investigations of static and dynamic properties of condensed matter, magnetic properties and living biological objects.

The performance of neutron scattering instruments, i.e. the precision of carried out experiments, is primarily determined by the recorded intensity of the scattered beam. The latter is proportional to the unit scattering power of a sample (the scattering cross-section), to its volume and to the incident neutron flux. A general tendency in modern science is to investigate smaller samples (such as nanostructures, biological objects, etc.) and weaker effects, so that the flux at the neutron scattering instrument becomes an ultimate parameter that defines the quality of the experiment.

Usually, under the neutron source one understands a nuclear installation emitting neutrons. However, from the point of view of neutron scattering the neutron source should be considered more generally, including also a spectrum transformer, tailoring the neutron spectrum according to the parameters of the neutron scattering instruments and the neutron transport system that delivers neutrons to the instrument sites. In this lecture we will discuss all these three components in more details.

## 1.2 Nuclear reactions

In nature neutrons are strongly bound in the atomic nuclei. Therefore, despite the fact that neutrons constitute about a half of each atom so that nature for a half is comprised of neutrons, it is rather difficult to set them free. Therefore, the only way to free neutrons from the nuclear confinement is to break a nucleus apart by means of a nuclear reaction. Further we will consider two types of such reactions – fission and spallation nuclear reactions – that are used in modern continuous and pulsed neutron sources, respectively.

### 1.2.1 Nuclear fission reaction

Namely by this way, bombarding the beryllium nuclei with of $\alpha$-particles obtained from decay of natural polonium, Chadwick has produced the first free neutrons in 1932. However, the neutron flux available from such sources was far away from being useful for the condensed matter investigation. The

breakthrough happened in the 40$^{ies}$, when nuclear reactors using the nuclear fission reactions have been constructed. Although these reactors have been primarily developed for purposes of the nuclear weapon industry, a by-product of their operation - an enormous for that time neutron flux, about $10^7$ neutrons per square centimetre per second (n/cm$^2$ s) at the CP-1 reactor in USA - was immediately used for first neutron scattering experiments. Developments in technology of fission reactors during the next 30 years resulted in a tremendous, by 8 orders of magnitude increase of the neutron flux of nuclear research reactors that approached $10^{15}$ n/cm$^2$ s for the high-flux reactor of the Institut-Laue-Langevin (Grenoble, France) in 1972.

These reactors are using the fission of the uranium isotope $^{235}$U. Following the capture of a slow neutron, this nucleus is deformed and is split into two fragments, simultaneously releasing 2 or 3 (on average 2.5) "prompt" neutrons with energies $E_T \approx 1.29$ MeV (Fig. 1):

$$^{235}\text{U} + \text{neutron} \rightarrow \text{fission fragments} + 2.52\ \text{neutrons} + 180\ \text{MeV}. \qquad (1)$$

Each of these practically instantly (within 10 ns) emitted neutrons can cause the fission of another 2-3 nuclei, so that each of them will also emit 2 to 3 neutrons, and so on (see Fig. Chain). This process is called the chain reaction, where the amount of fissile material needed to sustain the chain reaction is called critical mass. If the mass of fissile material is more than critical, the number of neutrons will increase exponentially and the reaction will become uncontrollable very quickly, leading to a huge energy release. If the mass of fissile material is less than critical, it will be impossible to sustain a chain reaction: the number of neutrons will decrease over time.

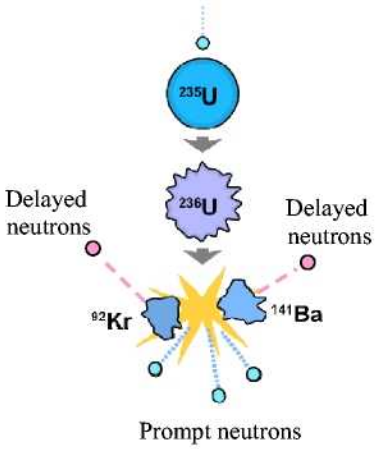



Fig. 1. Schematic representation of the fission process of U235.

However, the fission fragments are also rich in neutrons and emit neutrons (as a part of their radioactive decay), which can also contribute to the fission of any U-235 nucleus they strike. These so-called "delayed" neutrons are extremely important because they are emitted with the average time delay of the order of seconds and thanks to them the chain reaction can be controlled. Practically one runs a reactor sub-critically as far as only prompt neutrons are concerned, i.e. neutron multiplication is suppressed, so that the chain reaction vanishes. The delayed neutrons come a moment later but just in time to sustain the chain reaction when it is going to die out, thus allowing to reach criticality. More precisely, the neutrons in the reactor are moderated to decrease their energy and to increase their absorption by control roads that are made of a neutron absorbing material (usually containing boron). When inserted in the reactor core, these roads will reduce the number of slow neutrons to the amount just as necessary for the self–sustaining chain reaction and may be adjusted, so that the reaction remains critical only with the inclusion of the delayed neutrons. Thus, a simple and reliable mechanical control system can be used for the control of the chain reaction in the nuclear reactor. Another inherent safety factor is the so-called negative coefficient of reactivity. A mass of a fissile material that is exactly critical at room temperature becomes sub-critical if it is warmed. Intrinsically, fission becomes less probable as the fuel temperature increases due to more intense fission, and the chain reaction dies out.

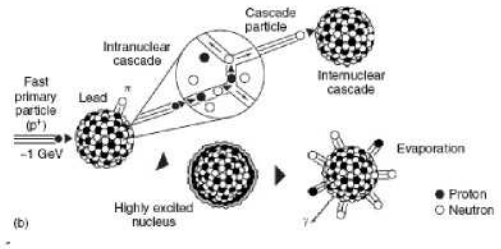



Fig. 2. Schematic representation of the spallation process.

### 1.2.2 Spallation reaction

The fission is not the only nuclear reaction allowing us to obtain free neutrons. Another kind of nuclear reactions that can be used for neutron production is the spallation reaction (Fig. 2.), where extremely high energy particles (e.g. protons) hit the target made of a neutron-rich material, "breaking" a heavy nucleus into highly excited fragments. In contrast to the fission reaction, the de Broglie wavelength

$$\lambda = \sqrt{h^2/2mE} \tag{2}$$

of the bombarding particles is shorter than the size of the nuclei, and collisions can take place with individual nuclides in the nucleus rather than with the nucleus as a whole. Indeed, a large amount of energy is transferred to the nuclides, which in turn can hit other nuclides in the same nucleus. As the result of this so-called intranuclear cascade, energy is more or less evenly distributed over the nucleus, bringing it to a highly excited state, so that the excited nucleus will "evaporate" neutrons and a smaller amount of protons. However, some energetic particles can escape from the nucleus and either hit another one (internuclear cascade) or just escape from the target. The energy of these neutrons is extended up to the energy of the incident particles (i.e. up to 1 GeV).

The spallation process is very short and ends within less than $10^{-15}$ s after the nucleus is hit. Thus, the time distribution of the spallation neutrons is entirely determined by the time distribution of the driving particle pulse, generally provided by a linear accelerator. This pulse that can be made either rather long, about 5 ms (called the long pulse spallation source (LPSS)), or rather short, about 10 μs (called the short pulse spallation source (SPSS)), by compressing charged particles in a compressor ring.

The most intense up-to-day spallation neutron source ISIS at Chilton (Great Britain) provides instantaneous thermal neutron fluxes over $10^{16}$ n/cm$^2$ s with short pulse lengths of ~50 μs. Next generation of pulsed neutron sources – SNS in USA and JHP in Japan - with fluxes more than $10^{17}$ n/cm$^2$ s are currently under construction. The European project of 5MW spallation source ESS with flux more than $10^{17}$ n/cm$^2$s is expected to take off within the next years.

Comparing possible nuclear reactions that can be used for neutron production (see Table 1), one should pay attention not only to their efficiency. The heat deposition that accompanies the neutron production results in the cooling problem, which is the real limiting factor for all kinds of neutron sources. From this point of view, fusion is the most attractive process, although it is still a technique of a far future.

Table 1. Neutron yields and deposited heat for selected neutron-producing reactions.

| Reaction | Energy/event | Yield (neutron/event) | Deposited heat (MeV/neutron) |
|---|---|---|---|
| (T,d) fusion | | ~1 neutron/fusion | 3 |
| $^{235}$U fission | | ~1 neutron/fission | 200 |
| Pb spallation | 1 GeV | ~20 neutron/proton | 23 |
| $^{238}$U spallation | 1 GeV | ~40 neutron/proton | 50 |

**1.3 Neutron spectrum and spectrum transformation**

To be useful for condensed matter investigations neutrons wavelength $\lambda$ should be about few Angstroms, that corresponds to the meV energy range. However, the energy spectrum of neutrons produced by fission or spallation nuclear reactions is in the range of 1 MeV, i.e. the spectrum transformation aiming an energy shift of several orders of magnitude is required. Let us express the neutron energy in the terms of the mean temperature $T$ of the neutron ensemble as $E=kT$, where $k$ *is* the conversion coefficient $k = 11600$ K/eV (the Boltzmann constant): then one can say that required energy shift can be achieved by cooling the neutrons down to a much lower temperature. For this purpose neutrons should be brought into the thermal equilibrium with a cold body (moderator): such thermalization process is accomplished by the moderation of neutrons via their multiple inelastic collisions with the light atoms of the moderator.

Depending on the type of neutron source the moderator should provide either the highest possible flux in the largest possible volume for continuous neutron sources or in the shortest possible time for pulsed neutron sources. This can be achieved by using water or heavy water moderators. Neutrons are slowing down and achieving thermal equilibrium with the moderator within $10^{-6}$ s. The neutron energy spectrum is given by the Maxwellian distribution

$$\Phi(E) = \frac{2\sqrt{E}}{\sqrt{\pi k^3 T^3}} \exp\left\{-\frac{E}{kT}\right\} \tag{3}$$

where $T$ is the moderator temperature. Practically, moderators are big (light or heavy) water volumes (also serving as a biological shielding) surrounding the reactor core or the spallation target and are generally kept at the room temperature of $T \approx 300$ K. Because of this reason the corresponding neutrons are called thermal neutrons, with a maximum peak flux around $\lambda \approx 1$ Å.

Tables 2 and 3 contains some neutron properties and useful relations between different parameters of neutrons.

Table 2. Neutron properties

| | |
|---|---|
| Mass | $m = 1.675 \cdot 10^{-27}$ kg |
| Electrical charge | $q = 0$ |
| Magnetic dipole moment | $\mu_n = -1.913\ \mu_B$ ($\mu_B$ – nuclear magneton) |
| Life time | $t_{1/2} = 820$ s |

Table 3. Useful relations.

| | |
|---|---|
| $\lambda(\text{Å}) = \frac{h}{mv} = \frac{3956}{v(m/s)} = \frac{0.286}{\sqrt{E(eV)}}$ | $v(m/s) = \frac{h}{m\lambda} = \frac{3956}{\lambda(\text{Å})}$ |

**1.4 Nuclear reactor and spallation source**

Now we can consider the construction of a neutron source. In all cases its heart is a core where the nuclear fission reaction takes plays. In the case of the nuclear reactor a set of uranium $^{238}$U fuel elements (or a complex single fuel element) is enriched by the isotope $^{235}$U. One distinguishes between high-enriched (~95%) and low-enriched (~20%) uranium: because the amount of fission material necessary to support the chain reaction is predetermined (the critical mass), the enrichment of

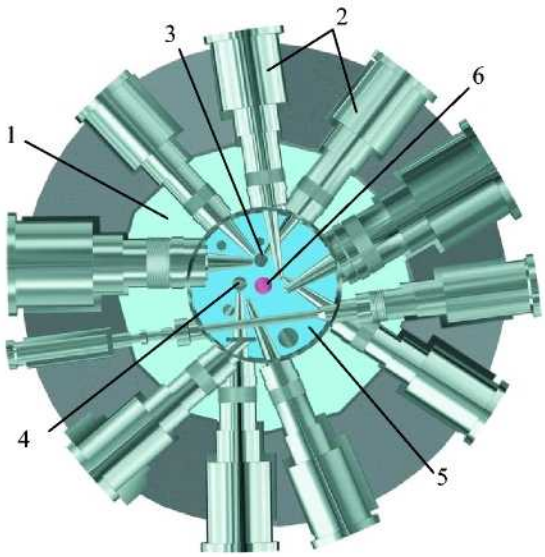



Fig. 3. Horizontal section through the reactor pool of the FRM-2 reactor in Garching, Germany. The reactor tank with internal diameter approx. 5m is filled with light water (1). In the centre of the arrangement the reactor core is situated. The experimental installations as horizontal beam tubes (2), a cold (3) and a hot (4) neutron source are arranged in the heavy water tank (5) around the fuel element (6).

the used uranium fuel actually defines the volume of the core and the neutron flux density. Compact cores made of high-enriched uranium at the reactors of the Institut-Laue-Langevin (Grenoble, France) and the Maier-Leibnitz Neutron Source (FRM-2) (Garching, Germany) provide the highest flux density and therefore, the highest neutron source luminosity achievable up to this day.

The reactor core is surrounded by (heavy) water (T=300 K) that plays the role of the moderator of high-energy fission neutrons (Fig. 3). Obviously, the full thermalization of these neutrons requires some time necessary for a few collisions with hydrogen (or deuterium) atoms, so that the density of thermal neutrons increases with the distance $r$ from the core. On the other hand, the neutron absorption is inverse proportional to the neutron velocity, so that the flux of already thermalized neutrons decreases with $r$. As the result of these two competing processes, the thermal neutron flux density achieves its maximum at a certain distance of $r$ = 10-15 cm from the core. Obviously, to extract thermal neutrons from the reactor, the entrance of a neutron beam tube should be placed exactly in this position. Aiming the decrease in undesirable background of fast (i.e. still not thermalized) neutrons and $\gamma$-rays from the core, one should avoid the direct view of the core through the neutron beam tube. All together, it leads to the conclusion that the optimal arrangement of beam tubes is tangential to the reactor core (see Fig. 3).

In case of the spallation source, the role of the reactor core plays a target made of heavy metal as Bi, Pb or Hg. The proton beam is obtained from negatively charged hydrogen ions produced by powerful ion sources (Fig. 4). These ions are accelerated in a linear accelerator (linac) by a number of

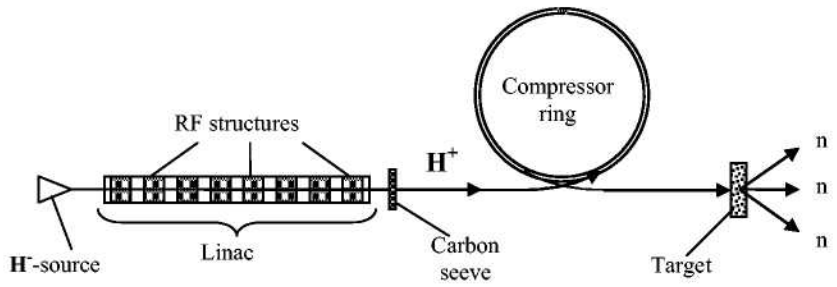



Fig. 4. Layout of the neutron spallation source

subsequent radio-frequency cavities with strong electro-magnetic fields, thus achieving kinetic energies in the GeV range (i.e. about 90% of the speed of light). When these hydrogen ions leave the linac, they are stripped off all their electrons by passing through a thin carbon sieve, so that the negative hydrogen ions become protons. Now, depending on the design of the spallation source, LPSS or SPSS (see Chapter 2) the protons are either sent to the target directly or through a compressor ring, respectively. The latter collects the protons from a large number of successive bunches from the linac into a single very high-intensity proton pulse. It is achieved by an assembly of magnets that send each accelerated proton bunch into a circular orbit of such a large diameter (~50–100 m), so that the

travelling time is equal to the time interval between the bunches. Indeed, the next bunch of protons arrives exactly when the previous has made a full turn and both of them are sent around again. When about 1000 bunches are piled up by such a procedure, sufficient intensity is accumulated and the full proton pulse with a pulse length of about 1 μs is sent to the target. The target is normally a liquid metal (mercury or a lead–bismuth eutectic mixture), placed in special materials to consume the beam power of a few megawatts. The proton pulse repetition rate on the target should be about 10–100 Hz to achieve an optimal use of neutrons in time-of-flight scattering experiments.

Thus, there are two kinds of neutron sources and certainly the question arises, which of them is better answering future trends. These trends, as discussed in the Ch.1 require a significant increase in the luminosity of neutron sources in order to improve the counting statistics of neutron scattering experiments. However, the evolution of nuclear reactors that was very impressive some decades ago, shows no progress since 1972, when the high-flux reactor at the ILL, Grenoble became operative. The reason for this is clearly the technical difficulty of removing the heat from the reactor core.

Let us make some rough estimations. As it was mentioned in Table 1, the deposited heat amounts to 200 Mev/fission with the yield of 1 neutron from 2.5 to be extracted for neutron scattering experiments. Using the relation 1 eV = $1.6 \cdot 10^{-19}$ J, we obtain the source strength (i.e. the number of neutrons emitted per second) $Q = 3 \cdot 10^{16}$ n/s per MW of the reactor power to be removed. However, this is a kind of a "point neutron source" that immersed into the moderator to slow neutrons down till thermal energies (see Ch. 2). Indeed, all neutrons emitted by the point source will be spread over the moderator surface of about 2000 $cm^2$ ($r$ =10-15 cm), so that the thermal neutron flux will amount to 0.0005 of Q, i.e. about $1.5 \cdot 10^{13}$ $n/s \cdot cm^2$ per MW of reactor power. Thus, for the 57 MW reactor at the ILL, one may expect the thermal flux of $1 \cdot 10^{15}$ $n/s \cdot cm^2$ to be compared with the actual value of $2 \cdot 10^{15}$ $n/s \cdot cm^2$ .

Thus, a further increase in the thermal neutron flux from nuclear reactors will require a significant increase in their power. However, such an increase will also require a very sophisticated reactor cooling and result in even stronger radiation damage of the reactor vessel components (beam tube noses, cold source, etc.). Experience gained at the ILL reactor shows that their service time is seven years. Already now new reactors are being designed in a way allowing for a regular exchange of the beam tube noses. Tenfold increase of the reactor power will result in a rather unpractical service time of these elements. Another problem is the worldwide concern about a potential risk associated with nuclear fission installations. On the other hand, pulsed sources are inherently safer because of the absence of any critical configuration that is potentially explosive. The deposited heat is 10 times less with the simultaneous significantly large neutron output (see Table 1) allows for a high peak flux about 50 times higher than the one for the ILL reactor (Table 2). Losses in the average thermal neutron flux will be compensated by the opportunities offered for neutron scattering instrumentation by the

time-structured neutron beams, when the instrument performance depends on the peak flux in the pulse rather than on the time-averaged flux.

Therefore, it is not surprising that all new sources under construction, SNS in USA and JHP in Japan as well as planned new European neutron source ESS, are spallation neutron sources. However, SNS and JHP are 1–2 MW spallation sources designed to create rather short neutron pulses of about 100 μs and further increase in their power level is rather problematic due to possible target problems. In contrast to this, ESS is planned as 5MW spallation source because it will create neutron pulses of a few milliseconds duration. It was demonstrated that such long pulse provides significant advantages for certain categories of neutron scattering instruments. Although target problems for LPSS also become increasingly severe with the increase of power, nevertheless it seems realistic to approach the ultimate limit of 20MW (i.e. 20 mA proton current at 1 GeV).

### 1.5 Cold, thermal and hot neutrons

As it was shown in the previous Chapter, the energies of neutrons produced by neutron sources cover many orders of magnitude. Depending on their energy $E$, neutrons are classified by commonly used names (see Table 2). Neutrons with $E < 1$ keV are called slow neutrons; in turn they are classified in 6 groups, but the most relevant for purposes of neutron scattering are hot, thermal and cold neutrons –energy ranges corresponding to these groups that are presented in Table 3. The maximum of the spectrum of thermal neutrons is defined by room temperature of the water moderator and is about $\lambda \approx 1$ Å (see Ch. 3 ). As one can see from Fig. 5, most of the neutrons are concentrated around this wavelength in the range of (0.8÷2) Å. These neutron wavelengths perfectly match the interatomic distances in solids and therefore, are extensively used for the studies of structure and dynamics of crystalline.

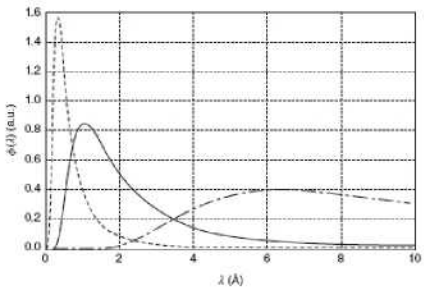



Fig. 5. Neutrons wavelength distribution from cold (dot dashed line, T=50 K), thermal (solid line, T=300K) and hot (dashed line, T=1000 K) moderators.

However, it also means that the amount of hot or cold neutrons in the thermal neutron spectrum is very small, so that any scattering experiment which requires hot or cold neutrons will

suffer from enormous flux losses. To enhance the hot or cold neutron flux one has to transform the thermal neutron spectrum shifting it towards high or low energies: in other words by heating or cooling the thermal neutron spectrum.

To achieve a significant gain factor by such spectrum transformations, the moderator temperature should be as high as 2000K and as low as 20K, respectively. Obviously, it is unrealistic to heat or to cool the whole water in the reactor vessel - tens of cubic meters – to such temperatures. The trick that is used to solve this problem is to insert other small local moderators inside the water and to set their temperatures accordingly. These devices are called hot and cold sources.

The hot source is usually made of a graphite block heated up to T=2400 K, when the cold sources is usually a vessel filled with liquid $H_2$ or $D_2$ or their mixture cooled down to 20 K. Hot and cold neutron spectra are shown in Fig. 5. Each of them allows for a significant, up to 20 times gain in the corresponding neutron flux. By choosing the adequate neutron spectrum scattering experiments can be optimally tailored to particular experimental requirements.

Finally, in Table 2 we present the basic properties of the neutron, as well as some useful relations.

**1.6 Neutron beam transport**

However, it is not enough to produce neutrons in the moderator – they still have to be transported to a neutron scattering instrument. As it was already mentioned in Ch. 4, neutrons are extracted from the moderator by neutron beam tubes, inserted in a heavy biological shielding surrounding the reactor tank and necessary because neutrons are isotropically emitted from the moderator.

The angular acceptance of a neutron beam tube is defined by its diameter (~10 cm) and length (~5m). Thus, the beam divergence of a beam tube is about ~1°, so that the neutron flux available at its output is drastically reduced by about six orders of magnitude, in comparison to the core flux.

This situation can be significantly improved by using neutron optical devices called neutron guides. The principle of their operational is rather similar to the one of light guides, where the light propagating in an optically dense media (i.e. with the refraction index n >1) is totally reflected from the glass air-interface due to the effect of total external reflection (the refraction index of air is equal to unity). In contrast to light, the refraction index of glass for neutrons is n <1, so that the effect of the total external reflection will take place on the air-glass interface. However, in case of neutrons this phenomenon takes place only for incident angles, i.e. less than the critical angle $\theta_c$ which is given by

$$\theta_c = \lambda\sqrt{\frac{2\rho b_c}{\pi}},$$

where $\rho$ and $b_c$ are the density and the coherent scattering length of the wall material, respectively. To increase $\theta_c$ the Ni coating with the critical angle $0.1° \cdot \lambda$ is used. Moreover, the wall of the neutron guide can be coated with so-called supermirrors, with the critical angle up to three times as much as the nickel's one. Indeed, the neutron guide is made as a hollow glass tube, Ni or supermirror coated from the inside (Fig. 5). Because the intensity at the neutron guide output is proportional to $\theta_c^2$, they provide an order of magnitude flux increase as compared to a beam tube.

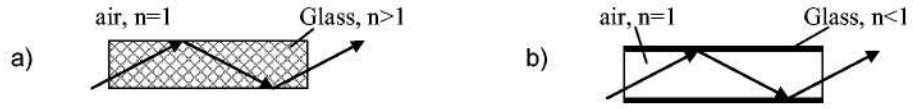



Fig. 5. To principle of the operation of light guides (a) and neutron guides (b)

Moreover, neutron guides can be bent or shaped. Bent neutron guides allow to avoid direct sight-of-view of the reactor core, drastically reducing γ- and neutron background at the instrument position. The parabolic or elliptic shaping of neutron guides opens exciting possibilities for the concentrating (focusing) of neutrons on a sample, thus providing additional increase in intensity at the position of neutron scattering instruments.

References:

1. G.R. Bauer (1993) Neutron sources. In: A.Furrer (ed.) *Neutron Scattering*, pp. 331–357. PSI-Proceedings No. 93-01, ISSN 1019-6447, Paul Scherrer Institute, Villigen.
2. J.M. Carpenter and W.B. Yelon (1986) Neutron sources. In: K. Sköld and D.L. Price (eds.) *Methods of Experimental Physics*, vol. 23A, pp. 99–196. London: Academic Press.
3. K. Clausen (2001) *Neutron sources*. Office for Official Publications of the European Communities, Luxembourg, ISBN 92-894-0037-4.

# 2

# A neutron primer: Elastic scattering and the properties of the neutron

Thomas Brückel

# 2. A neutron primer: Elastic scattering and the properties of the neutron

Thomas Brückel, IFF, Forschungszentrum Jülich

## 2.1 Introduction

After we have learnt how neutrons are produced in neutron sources, we will explain in this chapter, how neutrons can be used to study the atomic structure and dynamics of condensed matter systems. We will give a basic introduction into scattering methods in general and then introduce the special properties of neutrons, which make them an invaluable probe for condensed matter research. Neutrons tell us, where the atoms are, how the atoms move and what their atomic magnetic moments do.

Our present understanding of the properties and phenomena of condensed matter science is based on atomic theories. The first question we pose when studying any condensed matter system is the question concerning the internal structure: what are the relevant building blocks (atoms, molecules, colloidal particles, ...) and how are they arranged? The second question concerns the microscopic dynamics: how do these building blocks move and what are their internal degrees of freedom? For magnetic systems, in addition we need to know the arrangement of the microscopic magnetic moments due to spin and orbital angular momentum and their excitation spectra. In principle, the macroscopic response and transport properties, such as specific heat, thermal conductivity, elasticity, viscosity, susceptibility, magnetization etc., which are the quantities of interest for applications, result from the microscopic structure and dynamics. To determine these macroscopic properties from the microscopic information provided by experiment represents a huge challenge to condensed matter theory as we are dealing with an extreme many body problem with typically $10^{23}$ particles involved. It is a true masterly achievement of mankind that for many solid state systems, such microscopic theories could be developed, based on quantum mechanics and statistical physics.

For the development of modern condensed matter research, the availability of probes to study the structure and dynamics on a microscopic level is therefore essential. Modern scattering techniques can provide all the required information. Radiation, which has a rather weak interaction with the sample under investigation, provides a non-invasive, non-destructive probe for the microscopic structure and dynamics. This has been shown for the first time by W. Friedrich, P. Knipping and M. von Laue in 1912, when interference of x-ray radiation scattered from a single crystal was observed. Max von Laue received the Nobel Prize for the interpretation of these observations. One cannot overestimate this discovery: it was the first definite proof that atoms as the elementary building blocks of condensed matter are arranged in a periodic manner within a crystal. The overwhelming part of our present-day knowledge of the atomic structure of condensed matter is based on x-ray structure investigations. The method has developed rapidly since 1912. With the advent of modern synchrotron x-ray sources, the source brilliance has since then increased by 18 orders of magnitude. Currently X-ray Free Electron Lasers, e. g. the XFEL project (http://xfel.desy.de/), are being realized which will increase this brilliance by another 10 orders of magnitude. Nowadays the structure of highly complex biological macromolecules, like the crystal structure of the ribosome, can be determined with atomic resolution. Extremely weak phenomena such as magnetic x-ray scattering can be exploited successfully at modern synchrotron radiation sources. In soft condensed matter research, where one is interested in the dynamics on larger lengths scales,

such as of colloidal particles in solution, light scattering is an important tool besides x-ray scattering. Finally, intense neutron beams have properties, which make them an excellent probe for condensed matter investigations. Neutron scattering is a unique tool to solve magnetic structures and determine magnetic excitations and fluctuations. In soft matter and life science, neutrons excel due to the possibility to apply contrast variation techniques by selective deuteration of molecules or molecular subunits. Neutrons give access to practically all lengths scales relevant in condensed matter investigations from the sub-atomic level of some pm up to about 1000 nm. They are particularly well suited for investigations of the movement of atoms and molecules. As with x-rays, the experimental techniques are in rapid evolution, mainly due to the advent of new neutron optical devices, but also of new sources. The new spallation sources, such as the American Spallation Neutron Source SNS (http://www.sns.gov/) or the proposed European Spallation Source ESS (http://neutron.neutron-eu.net/n_ess) will increase the capabilities of neutron investigations in condensed matter science drastically in the years to come.

This lecture is organized as follows: First we give a very basis introduction into elementary scattering theory for elastic scattering, which is valid for any probe. Then a more rigorous derivation in the framework of the Born series follows. We will introduce the concepts of coherence and pair correlation functions. Then we will discuss, which probes are most relevant for condensed matter investigations and present in some detail the interaction of neutrons with matter leading to the absorption and scattering cross-sections. More details can be found in [1 - 4].

We will frequently make use of the particle-wave dualism of quantum mechanics, which tells us that the radiation used in the scattering process can be described in a wave picture, whenever we are interested in interference phenomena, and in a particle picture, when the interaction with matter is relevant, e. g. for the detection process.

## 2.2 Elementary scattering theory: Elastic scattering

Throughout this lecture we assume that the atoms within our sample are rigidly fixed on equilibrium positions in space. Therefore we only look at those processes, in which the recoil is being transferred to the sample as a whole so that the energy change for the radiation is negligible and the scattering process appears to be elastic. In subsequent lectures, this restriction will be dropped and so-called inelastic scattering processes will be discussed. These are due to excitations or internal fluctuations in the sample, which give rise to an energy change of the radiation during the scattering process.

A sketch of the scattering experiment is shown in Figure 2.1.

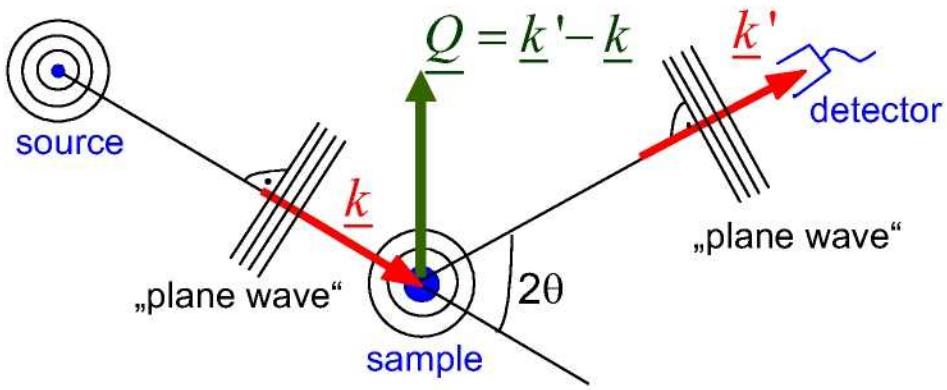



***Fig. 2.1**: A sketch of the scattering process in the Fraunhofer approximation in which it is assumed that plane waves are incident on sample and detector due to the fact that the distances source-sample and sample-detector, respectively, are significantly larger than the size of the sample.*

Here we assume the so-called *Fraunhofer approximation*, where the size of the sample is much smaller than the distance between sample and source and the distance between sample and detector, respectively. This assumption holds in all cases discussed in this lecture. In addition we assume that the source emits radiation of one given energy, i. e. so-called *monochromatic* radiation. Then the wave field incident on the sample can be considered as a plane wave, which is completely described by a wave vector $\underline{k}$. The same holds for the wave incident on the detector, which can be described by a vector $\underline{k}'$. In the case of elastic scattering (diffraction) we have

$$k = |\underline{k}| = |\underline{k}'| = k' = \frac{2\pi}{\lambda} \tag{2.1}$$

Let us define the so-called *scattering vector* by

$$\underline{Q} = \underline{k}' - \underline{k} \tag{2.2}$$

$\hbar\underline{Q}$ represents the momentum transfer during scattering, since according to de Broglie, the momentum of the particle corresponding to the wave with wave vector $\underline{k}$ is given by $\underline{p}=\hbar\underline{k}$. The magnitude of the scattering vector can be calculated from wavelength $\lambda$ and scattering angle $2\theta$ as follows

$$Q = |\underline{Q}| = \sqrt{k^2 + k'^2 - 2kk'\cos 2\theta} \Rightarrow Q = \frac{4\pi}{\lambda}\sin\theta \tag{2.3}$$

A scattering experiment comprises the measurement of the intensity distribution as a function of the scattering vector. The scattered intensity is proportional to the so-called *cross section*, where the proportionality factors arise from the detailed geometry of the experiment. For a definition of the scattering cross section, we refer to Figure 2.2.

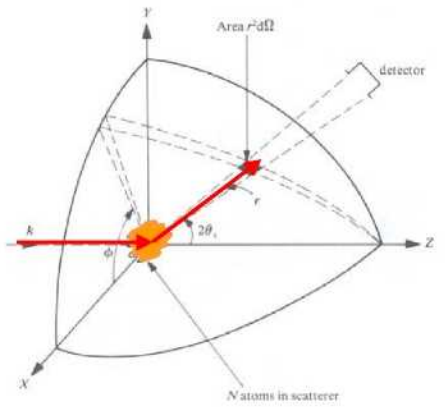



***Fig. 2.2**: Geometry used for the definition of the scattering cross section.*

If n' particles are scattered per second into the solid angle dΩ seen by the detector under the scattering angle 2θ and into the energy interval between E' and E' + dE', then we can define the so-called *double differential cross section* by:

$$\frac{d^2\sigma}{d\Omega dE'} = \frac{n'}{j d\Omega dE'} \tag{2.4}$$

Here j refers to the incident beam flux in terms of particles per area and time. If we are not interested in the change of the energy of the radiation during the scattering process, or if our detector is not able to resolve this energy change, then we will describe the angular dependence by the so-called *differential cross section:*

$$\frac{d\sigma}{d\Omega} = \int_0^\infty \frac{d^2\sigma}{d\Omega dE'} dE' \tag{2.5}$$

Finally the so-called *total scattering cross section* gives us a measure for the total scattering probability independent of changes in energy and scattering angle:

$$\sigma = \int_0^{4\pi} \frac{d\sigma}{d\Omega} d\Omega \tag{2.6}$$

Therefore our task is to determine the arrangement of the atoms in the sample from the knowledge of the scattering cross section $d\sigma/d\Omega$. The relationship between scattered intensity and the structure of the sample is particularly simple in the so-called *Born approximation*, which is often also referred to as *kinematic scattering approximation*. In this case, refraction of the beam entering and leaving the sample, multiple scattering events and the extinction of the primary beam due to scattering within the sample are being neglected. Following Figure 2.3, the phase difference between a wave scattered at the origin of the coordinate system and at position $\underline{r}$ is given by

$$\Delta\Phi = 2\pi \cdot \frac{\left(\overline{AB} - \overline{CD}\right)}{\lambda} = \underline{k}' \cdot \underline{r} - \underline{k} \cdot \underline{r} = \underline{Q} \cdot \underline{r} \tag{2.7}$$

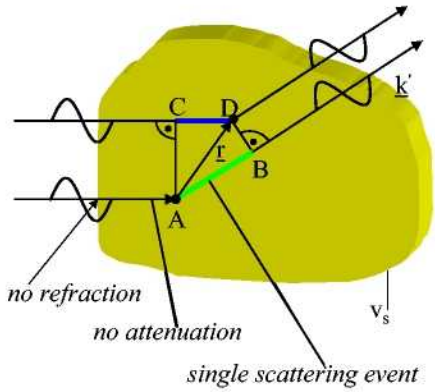



***Fig. 2.3:*** *A sketch illustrating the phase difference between a beam scattered at the origin of the coordinate system and a beam scattered at the position* $\underline{r}$.

The scattered amplitude at the position $\underline{r}$ is proportional to the scattering density $\rho_s(\underline{r})$ at that position. $\rho_s$ depends on the type of radiation used and the interaction of this radiation with the sample. In fact, $\rho_s$ is directly proportional to the interaction potential, as will be shown in the next chapter. Assuming a laterally coherent beam, the total scattering amplitude is given by a coherent superposition of the scattering from all points within the sample, i. e. by the integral

$$A = A_0 \cdot \int_{V_S} \rho_S(\underline{r}) \cdot e^{i\underline{Q}\,\underline{r}} d^3r \qquad (2.8)$$

Here $A_0$ denotes the amplitude of the incident wave field. (2.8) demonstrates that the scattered amplitude is connected with the scattering density $\rho_s(\underline{r})$ by a simple Fourier transform. Knowledge of the scattering amplitude for all scattering vectors $\underline{Q}$ allows us to determine via a Fourier transform the scattering density uniquely. This is the complete information on the sample, which can be obtained by the scattering experiment. Unfortunately, nature is not so simple. On one hand, there is the more technical problem that one is unable to determine the scattering cross section for <u>all</u> values of momentum transfer $\hbar\underline{Q}$. The more fundamental problem, however, is that normally the amplitude of the scattered wave is not measurable. Instead only the scattered intensity

$$I \sim |A|^2 \qquad (2.9)$$

can be determined. Therefore the phase information is lost and the simple reconstruction of the scattering density via a Fourier transform is no longer possible. This is the so-called *phase problem* of scattering. There are ways to overcome the phase problem, i.e. by use of reference waves. Then the scattering density becomes directly accessible. The question, which information we can obtain from a scattering experiment despite the phase problem will be addressed below.

Which wavelength do we have to choose to obtain the required real space resolution? For information on a length scale L, a phase difference of about $Q \cdot L \approx 2\ \pi$ has to be achieved. Otherwise according to (2.7) $\underline{k}'$ and $\underline{k}$ will not differ significantly. According to (2.3) $Q \approx 2\pi/\lambda$ for typical scattering angles ($2\theta \sim 60°$). Combining these two estimates, we end up with the requirement that the wavelength $\lambda$ has to be in the order of the real space length scale L under investigation. To give an example: with the wavelength in the order of 0.1 nm, atomic resolution can be achieved in a scattering experiment.

## 2.3 Fundamental scattering theory: The Born series

In this chapter, we will give a simple formulation of scattering theory. Our purpose is to derive (2.8) from fundamental principles. The conditions under which (2.8) holds and the limitations of kinematical scattering theory will thus become clearer. The derivation will be done for particle beams – in particular neutrons - for which the Schrödinger equation holds. Beginners can skip this chapter and continue with 2.4.

In quantum mechanics, neutrons are described as particle wave fields through the Schrödinger equation:

$$H\Psi = \left( -\frac{\hbar^2}{2m_n}\Delta + V \right)\Psi = i\hbar\frac{\partial}{\partial t}\Psi \tag{2.10}$$

$\psi$ is the probability density amplitude, V the interaction potential. In case of purely elastic scattering E = E', the time dependence can be described by the factor $\exp\left(-i\frac{E}{\hbar}t\right)$. Assuming this time dependence, a wave equation for the spatial part of the probability density amplitude $\psi$ can be derived from (2.10):

$$\Delta\Psi + k^2(\underline{r})\Psi = 0 \tag{2.11}$$

In (2.11) we have introduced a spatially varying wave vector with the magnitude square:

$$k^2(\underline{r}) = \frac{2m_n}{\hbar^2}\left(E - V(\underline{r})\right) \tag{2.12}$$

Solutions of (2.10) in empty space can be guessed immediately. They are given by plane waves $\Psi = \Psi_0 \exp\left[i\left(\underline{k}\cdot\underline{r} - \frac{E}{\hbar}t\right)\right]$ with $k^2 = \frac{2m_n}{\hbar^2}E$. The relations between magnitude of the wave vector, wave length and energy of the neutron E can be written in practical units:

$$\begin{aligned} k\left[\text{Å}^{-1}\right] &\approx 0.695\sqrt{E[meV]} \\ \lambda\left[\text{Å}\right] &\approx 9.045/\sqrt{E[meV]} \\ E[meV] &\approx 81.8/\lambda^2\left[\text{Å}\right] \end{aligned} \tag{2.13}$$

To give an example, neutrons of wavelength $\lambda$ = 2.4 Å = 0.24 nm have an energy of 14.2 meV with a magnitude of the neutron wave vector of k = 2.6 $Å^{-1}$.

To obtain solutions of the wave equation (2.11) in matter, we reformulate the differential equation by explicitly separating the interaction term:

$$\left(\Delta + k^2\right)\Psi = \frac{2m_n}{\hbar^2}V\cdot\Psi =: \chi \tag{2.14}$$

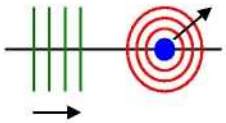
Here $\underline{k}$ denotes the wave vector for propagation in empty space. The advantage of this formulation is that the solutions of the left hand side are already known. They are the plane waves in empty space. Equation (2.14) is a linear partial differential equation, i. e. the superposition principle holds: the general solution can be obtained as a linear combination of a complete set of solution functions. The coefficients in the series are determined by the boundary conditions. To solve (2.14) one can apply a method developed for inhomogeneous linear differential equations. For the moment, we assume that the right hand side is fixed (given as $\chi$). We define a *Greens-function* by:

$$\left(\Delta + k^2\right)G(\underline{r},\underline{r}') = \delta(\underline{r} - \underline{r}') \tag{2.15}$$

A solution of (2.15) is given by:

$$G(\underline{r},\underline{r}') = \frac{e^{ik|\underline{r}-\underline{r}'|}}{4\pi|\underline{r}-\underline{r}'|} \tag{2.16}$$

The meaning of (2.16) is immediately clear: the scattering from a point-like scatterer (δ-potential) gives an emitted spherical wave. In a schematic graphical representation:

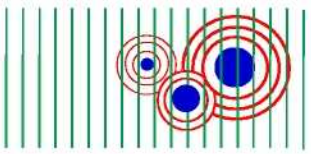


Using the Greens-function G(r,r'), we can write down a formal solution of the wave equation (2.14):

$$\Psi = \Psi^o + \int G(\underline{r},\underline{r}')\chi(\underline{r}')d^3r' \tag{2.17}$$

Here, we have taken the initial conditions of an incident plane wave $\psi^0$ into account. (2.17) is indeed a solution of (2.14) as can be easily verified by substituting (2.17) into (2.14). If we finally substitute the definition of $\chi$, one obtains the so-called *Lippmann-Schwinger* equation:

$$\Psi(\underline{r}) = \psi^\circ(\underline{r}) + \frac{2m_n}{\hbar^2}\int G(\underline{r},\underline{r}')V(\underline{r}')\Psi(\underline{r}')d^3r' \tag{2.18}$$



(2.18) has a simple interpretation: the incident plane wave $\psi^0(\underline{r})$ is superimposed by spherical waves emitted from scattering at positions r'. The intensity of these spherical waves is proportional to the interaction potential V(r') and the amplitude of the wave field at the position r'. To obtain the total scattering amplitude, we have to integrate over the entire sample volume.

However, we still have not solved (2.14): our solution $\psi$ appears again in the integral in (2.18). In other words, we have transformed differential equation (2.14) into an integral equation. The advantage is that for such an integral equation, a solution can be found by iteration. In the zeroth approximation, we neglect the interaction V completely. This gives $\psi = \psi^0$. The next higher order approximation for a weak interaction potential is obtained by substituting this solution in the right hand side of (2.18). The first non-trivial approximation can thus be obtained:

$$\Psi^1(\underline{r}) = e^{i\underline{k}\cdot\underline{r}} + \frac{2m_n}{\hbar^2}\int \frac{\exp(ik|\underline{r}-\underline{r}'|)}{4\pi|\underline{r}-\underline{r}'|}V(\underline{r}')e^{i\underline{k}\underline{r}'}d^3r' \tag{2.19}$$

(2.19) is nothing else but a mathematical formulation of the well-known *Huygens principle* for wave propagation.

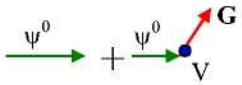
The approximation (2.19) assumes that the incident plane wave is only scattered once from the potential V(r'). For a stronger potential and larger sample, multiple scattering processes will occur. Again, this can be deduced from the integral equation (2.18) by further iteration. For simplification we introduce a new version of equation (2.18) by writing the integral over the "Greens function" as operator **G**:

$$\psi = \psi^o + \mathbf{G}V\psi \tag{2.20}$$

The so-called *first Born approximation*, which gives the *kinematical scattering theory* is obtained by substituting the wave function $\psi$ on the right hand side by $\psi^0$:

$$\psi^1 = \psi^o + \mathbf{G}V\psi^o \tag{2.21}$$

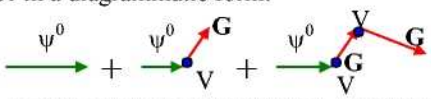
This first approximation can be represented by a simple diagram as a sum of an incident plane wave and a wave scattered once from the potential V:




The second approximation is obtained by substituting the solution of the first approximation (2.21) on the right hand side of equation (2.20):

$$\psi^2 = \psi^o + \mathbf{G}V\psi^1 = \psi^o + \mathbf{G}V\psi^o + \mathbf{G}V\mathbf{G}V\psi^o \tag{2.22}$$

Or in a diagrammatic form:




I. e. in the second approximation, processes are being taken into account, in which the neutron is scattered twice by the interaction potential V. In a similar manner, all higher order approximations can be calculated. This gives the so-called *Born series*.[1] For weak potential and small samples, this series converges rather fast. Often, the first approximation, the *kinematic scattering theory*, holds very well. This is especially the case for neutron scattering, where the scattering potential is rather weak, as compared to x-ray- or electron- scattering. Due to the strong Coulomb interaction potential, the probability for multiple scattering processes of electrons in solids is extremely high, making the interpretation of electron diffraction experiments very difficult. But even for neutrons, the kinematic scattering theory can break down, for example in the case of Bragg scattering from large ideally perfect single crystals, where the Born series does not converge. The wave equation has to be solved exactly under the boundary conditions given by the crystal geometry. For simple geometries, analytical solutions can be obtained. This is then called the *dynamical scattering theory*. Since for neutrons, the kinematical theory holds in most cases, or multiple scattering events can often be corrected for, we will no longer discuss dynamical theory in what follows and refer to [3, 5].

Let us return to the first Born approximation (2.19). In a further approximation, the Fraunhofer approximation, we assume that the size of the sample is significantly smaller than the distance sample-detector. The geometry to calculate the far field limit of (2.19) is given in Figure 2.4. Under the assumption $|\underline{R}| >> |\underline{r}'|$, we can deduce from Figure 2.4 the following approximation for the emitted spherical wave:

$$\frac{\exp\left(ik\left|\underline{r}-\underline{r}'\right|\right)}{\left|\underline{r}-\underline{r}'\right|} \approx \frac{\exp\left(ik\left(R-\underline{r}'\cdot\hat{\underline{R}}\right)\right)}{R} \approx \frac{\exp(ikR)}{R}\cdot e^{-i\underline{k}'\underline{r}'} \tag{2.23}$$

The probability density amplitude for the scattered wave field in the limit of large distances from the sample is thus given by:

$$\Rightarrow \psi^1\left(\underline{R}\right) = e^{i\underline{k}\underline{R}} + \frac{2m_n}{\hbar^2}\frac{e^{ikR}}{4\pi R}\int V\left(\underline{r}'\right)e^{i\underline{Q}\underline{r}'}d^3r' \tag{2.24}$$

[1] Note that Born approximation or the Born series violates energy conservation: scattered waves are created without weakening of the incident plane wave. Born series can therefore only be applied in the limit of very weak scattering potentials.

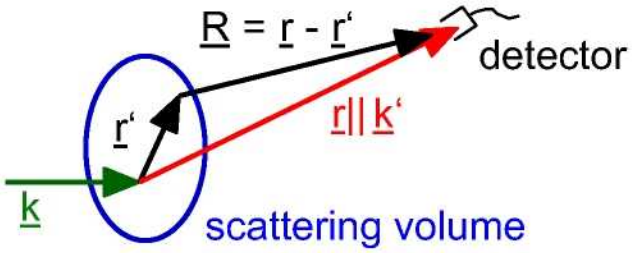



***Fig. 2.4**: Scattering geometry for the calculation of the far field limit at the detector. In the Fraunhofer approximation, we assume that |R| >> |r'|.*

This is just the sum of an incident plane wave and a spherical wave emitted from the sample as a whole. The amplitude of the scattered wave is given according to (2.24):

$$A(\underline{Q}) = \frac{m_n}{2\pi\hbar^2}\int V(\underline{r})e^{i\underline{Q}\cdot\underline{r}}d^3r \sim F\left[V(\underline{r})\right] \tag{2.25}$$

The integral in the above equation is nothing but the transition matrix element of the interaction potential V between the initial and final plane wave states, therefore:

$$\frac{d\sigma}{d\Omega} = \left(\frac{m_n}{2\pi\hbar^2}\right)^2 \left|\langle \underline{k}'|V|\underline{k}\rangle\right|^2 \tag{2.26}$$

This formula corresponds to *Fermi's Golden Rule* from time-dependent perturbation theory, where the transition probability per time interval from state k to states k' is given by:

$$W_{k'k} = \frac{2\pi}{\hbar}\left|\langle k'|V|k\rangle\right|^2 \cdot \rho(E_{k'}) \tag{2.27}$$

Here, $\rho(E_{k'})$ denotes the density of states for the final states k'.

With this exact derivation of the scattering cross section, we can now deduce by comparison with (2.8) that the scattering density in the simple derivation of chapter 2.2 is just $\rho_S(\underline{r}) = \frac{m_n}{2\pi\hbar^2}V(\underline{r})$ for particle beams governed by the Schrödinger equation.

We now allow for inelastic processes, where the sample undergoes a charge of its state from $\alpha$ to $\alpha'$ ($\alpha$ denotes a set of quantum numbers characterizing an eigenstate of the sample). In this case, due to the different length of the wavevectors for incoming and outgoing waves, we have to introduce factors k' and k, which arise from the density of states factor in (2.27). Since the scattering event must fulfill energy and momentum conservation, we arrive at the double differential cross section:

$$\frac{d^2\sigma}{d\Omega d\omega} = \frac{k'}{k}\left(\frac{m_n}{2\pi\hbar^2}\right)^2 \sum_{\alpha} p_\alpha \sum_{\alpha'}\left|\langle \underline{k}', \alpha'|V|\underline{k}, \alpha\rangle\right|^2 \cdot \delta(\hbar\omega + E_\alpha - E_{\alpha'}) \tag{2.28}$$

The first summation is carried out over all possible initial states $\alpha$ of the system, weighted with their thermodynamic occupation probability $p_\alpha$. The sum over $\alpha'$ is the sum over all final states allowed by energy conservation, which is guaranteed through the $\delta$-function. $\hbar\omega$ denotes the energy transfer of the neutron to the system. This double differential cross section will be discussed in the following lectures on inelastic scattering.

## 2.4 Coherence

In the above derivation, we assumed plane waves as initial and final states. For a real scattering experiment, this is an unphysical assumption. In the incident beam, a wave packet is produced by collimation and monochromatization. This wave packet can be described as a superposition of plane waves. As a consequence, the diffraction pattern will be a superposition of patterns for different incident wavevectors $\underline{k}$ and the question arises, which information is lost due to these non-ideal conditions. This *instrumental resolution* is intimately connected with the *coherence* of the beam. Coherence is needed, so that the interference pattern is not significantly destroyed. Coherence requires a phase relationship between the different components of the beam. Two types of coherence can be distinguished.

• *Temporal or longitudinal coherence* due to a wavelength spread.
A measure for the longitudinal coherence is given by the length, on which two components of the beam with largest wavelength difference ($\lambda$ and $\lambda + \Delta\lambda$) become fully out of phase. According to the following figure, this is the case for $l_{\parallel} = n \cdot \lambda = \left(n - \frac{1}{2}\right)(\lambda + \Delta\lambda)$.

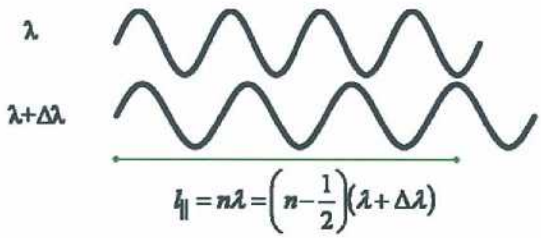



***Fig. 2.5**: A sketch illustrating the longitudinal coherence due to a wavelength spread.*

From this, we obtain the *longitudinal coherence length* $l_{\parallel}$ as

$$l_{\parallel} = \frac{\lambda^2}{2\Delta\lambda} \tag{2.29}$$

• *Transversal coherence* due to source extension
Due to the extension of the source (transverse beam size), the phase relation is destroyed for large source size or large divergence. According to the following figure, a first minimum occurs for $\frac{\lambda}{2} = d \cdot \sin\theta \approx d \cdot \theta$.

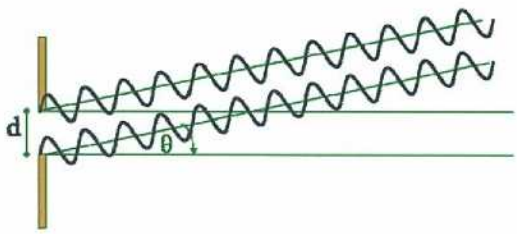



***Fig. 2.6**: A sketch illustrating the transverse coherence due to source extension.*

From this, we obtain the *transversal coherence length* $l_\perp$ as

$$l_\perp = \frac{\lambda}{2\Delta\theta} \tag{2.30}$$

Here $\Delta\theta$ is the divergence of the beam. Note that $l_\perp$ can be different along different spatial directions: in many instruments, the vertical and horizontal collimations are different.

Together, the longitudinal and the two transversal coherence lengths define a *coherence volume*. This is a measure for a volume within the sample, in which the amplitudes of all scattered waves superimpose to produce an interference pattern. Normally, the coherence volume is significantly smaller than the sample size, typically a few 100 Å for neutron scattering, up to µm for synchrotron radiation. Scattering between different coherence volumes within the sample is no longer coherent, i. e. instead of the amplitudes the intensities of the contributions to the scattering pattern have to be added. This limits the real space resolution of a scattering experiment to the extension of the coherence volume.

## 2.5 Pair correlation functions

After having clarified the conditions under which we can expect a coherent scattering process, let us now come back to the question, which information is accessible from the intensity distribution of a scattering experiment. From (2.9) we see that the phase information is lost during the measurement of the intensity. For this reason the Fourier transform of the scattering density is not directly accessible in most scattering experiments (note however that phase information can be obtained in certain cases).

Substituting (2.8) into (2.9), we obtain for the magnitude square of the scattering amplitude, a quantity directly accessible in a scattering experiment:

$$I \sim \left| A(\underline{Q}) \right|^2 \sim \int d^3r' \rho_s(\underline{r}') e^{i\underline{Q}\cdot\underline{r}'} \int d^3r\, \rho_s^*(\underline{r})\, e^{-i\underline{Q}\cdot\underline{r}} = \iint d^3r' d^3r\, \rho_s(\underline{r}') \rho_s^*(\underline{r})\, e^{i\underline{Q}\cdot(\underline{r}'-\underline{r})}$$
$$= \iint d^3R d^3r \rho_s(\underline{R}+\underline{r}) \rho_s^*(\underline{r})\, e^{i\underline{Q}\cdot\underline{R}} \tag{2.31}$$

This shows that the scattered intensity is proportional to the Fourier transform of a function $P(\underline{R})$:

$$I(\underline{Q}) \sim \int d^3R\, P(\underline{R})\, e^{i\underline{Q}\cdot\underline{R}} \tag{2.32}$$

This function denotes the so-called *Patterson function* in crystallography or more general the *static pair correlation function:*

$$P(\underline{R}) = \int d^3r\, \rho_s^*(\underline{r})\, \rho_s(\underline{r}+\underline{R}) \tag{2.33}$$

$P(\underline{R})$ correlates the value of the scattering density at position $\underline{r}$ with the value at the position $\underline{r}+\underline{R}$, integrated over the entire sample volume. If, averaged over the sample, no correlation exists between the values of the scattering densities at position $\underline{r}$ and $\underline{r}+\underline{R}$, then the Patterson function $P(\underline{R})$ vanishes. If, however, a periodic arrangement of a pair of atoms exists in the sample with a difference vector $\underline{R}$ between the positions, then the Patterson function will have an extremum for this vector $\underline{R}$. Thus the Patterson function reproduces all the vectors connecting one atom with another atom in a periodic arrangement.

Quite generally, in a scattering experiment, pair correlation functions are being determined. In a coherent inelastic scattering experiment, we measure the *scattering law* $S(Q,\omega)$, which is the Fourier transform with respect to space and time of the spatial and temporal pair correlation function:

$$\frac{d^2\sigma}{d\omega d\Omega} \sim S(\underline{Q},\omega) = \frac{1}{2\pi\hbar}\int_{-\infty}^{+\infty} dt\, e^{-i\omega t}\int d^3r\, e^{i\underline{Q}\underline{r}} G(\underline{r},t) \tag{2.34}$$

While the proportionality factor between the double differential cross section and the scattering law depends on the type of radiation and its specific interaction potential with the system studied, the spatial and temporal pair correlation function is only a property of the system studied and independent of our probe:

$$G(\underline{r},t) = \frac{1}{N}\sum_{ij}\int d^3r' \left\langle \delta(\underline{r}' - \underline{r}_j(0)) \cdot \delta(\underline{r}' + \underline{r} - \underline{r}_i(t)) \right\rangle = \frac{1}{N}\int d^3r' \left\langle \rho(\underline{r}',0)\rho(\underline{r}'+\underline{r},t) \right\rangle \tag{2.35}$$

Here, the pair correlation function is once expressed as a correlation between the position of N point-like particles (expressed by the delta function) and once by the correlation between the densities at different positions in the sample for different times. In a magnetic system, we scatter from the atomic magnetic moments, which are vector quantities. Therefore, the scattering law becomes a tensor - the Fourier transform of the spin pair correlations:

$$\mathbf{S}^{\alpha\beta}(\underline{Q},\omega) = \frac{1}{2\pi}\sum_{l}\int dt\, e^{i\left[\underline{Q}(\underline{R}_l - \underline{R}_0) - \omega t\right]} \left\langle S_0^{\alpha}(0) S_l^{\beta}(t) \right\rangle \tag{2.36}$$

$\alpha$, $\beta$ denote the Cartesian coordinates $x$, $y$, $z$; $\underline{R}_0$ and $\underline{R}_l$ are the spatial coordinates of a reference spin $0$ and a spin $l$ in the system.

## 2.6 Form-factor

So far we have not specified the nature of our sample. Now we assume an assembly on N scatterers of finite size, see Figure 2.7.

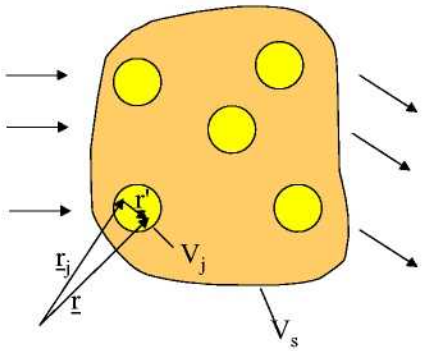



***Fig. 2.7:*** *Sketch showing the assembly of N scatterers of finite size and defining the quantities needed for the definition of the form factor.*

These could be atoms in a solid or colloidal particles in a homogeneous solution. In what follows, we will separate the interference effects from the scattering within one such a particle from the interference effects arising from scattering from different particles. With the decomposition of the vector $\underline{r}$ into the centre-of-gravity-vector $\underline{r}_j$ and a vector $\underline{r}'$ within the particle, the scattering amplitude can be written as (all particles are assumed to be identical):

$$\begin{aligned} A &\propto \int_{V_S} d^3r\, \rho_S(\underline{r}) e^{i\underline{Q}\underline{r}} = \sum_{j=1}^{N}\int_{V_j} d^3r\, \rho_S(\underline{r}) e^{i\underline{Q}\underline{r}} \\ &= \sum_{j=1}^{N} e^{i\underline{Q}\underline{r}_j}\int_{V_j^0} d^3r'\, \rho_S(\underline{r}') e^{i\underline{Q}\underline{r}'} =: \sum_{j=1}^{N} e^{i\underline{Q}\underline{r}_j}\rho_j^{tot} f_j(\underline{Q}) \end{aligned} \tag{2.37}$$

With (2.37), we have separated the scattering from within the single particles from the interference between different particles. $\rho_j^{tot}$ denotes the total scattering power of the particle. The *form-factor f(Q)* is defined as the normalized amplitude of scattering from within one particle[2] (it describes the "form" of the particle):

$$f(\underline{Q}) \equiv \frac{\int_{V_j^0} d^3r' \, \rho_s(\underline{r}') \, e^{i\underline{Q}\cdot\underline{r}'}}{\int_{V_j^0} d^3r' \, \rho_s(\underline{r}')} \tag{2.38}$$

For a homogeneous sphere

$$\rho_S(\underline{r}) = \begin{cases} 0 & |\underline{r}| > R \\ 1 & |\underline{r}| \le R \end{cases} \tag{2.39}$$

, the form-factor can be calculated by using spherical co-ordinates:

$$\Rightarrow f(Q) = 3 \cdot \frac{\sin QR - QR \cdot \cos QR}{(QR)^3} \tag{2.40}$$

The function (2.40) is plotted in Figure 2.8. In forward direction, there is no phase difference between waves scattered from different volume elements within the sample (note: we assume the Fraunhofer approximation and work in a far field limit). The form-factor takes its maximum value of one. For finite scattering angles $2\theta$, the form-factor drops due to destructive interference from various parts within one particle and finally for large values of the momentum transfer shows damped oscillations around $0$ as a function of $QR$.

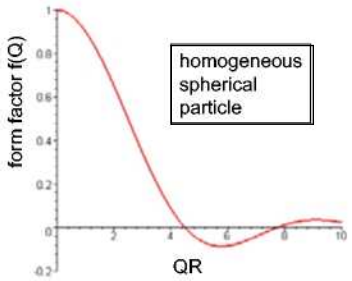



***Fig. 2.8**: Form-factor for a homogeneous sphere according to (2.40).*

## 2.7 Scattering from a periodic lattice in three dimensions

As an example for the application of (2.8) and (2.9), we will now discuss the scattering from a three dimensional lattice of point-like scatterers. As we will see later, this situation corresponds to the scattering of thermal neutrons from a single crystal. More precisely, we will restrict ourselves to the case of a Bravais lattice with one atom at the origin of the unit cell. To each atom we attribute a "scattering power" $\alpha$[3]. The single crystal is finite with N, M and P periods along the basis vectors a, b and c. The scattering density, which we have to use in (2.8) is a sum over δ-functions for all scattering centers:

[2] For simplicity we now drop the index j

[3] We will later see that this „ scattering power" is connectedto the so-called scattering length of the atom.

$$\rho_s(\underline{r}) = \sum_{n=0}^{N-1}\sum_{m=0}^{M-1}\sum_{p=0}^{P-1} \alpha \cdot \delta\left(\underline{r} - \left(n\cdot\underline{a} + m\cdot\underline{b} + p\cdot\underline{c}\right)\right) \tag{2.41}$$

The scattering amplitude is calculated as a Fourier transform:

$$A(\underline{Q}) \sim \alpha \sum_{n=0}^{N-1} e^{in\underline{Q}\cdot\underline{a}} \sum_{m=0}^{M-1} e^{im\underline{Q}\cdot\underline{b}} \sum_{p=0}^{P-1} e^{ip\underline{Q}\cdot\underline{c}} \tag{2.42}$$

Summing up the geometrical series, we obtain for the scattered intensity:

$$I(\underline{Q}) \sim \left|A(\underline{Q})\right|^2 = \left|\alpha\right|^2 \cdot \frac{\sin^2\frac{1}{2}N\underline{Q}\cdot\underline{a}}{\sin^2\frac{1}{2}\underline{Q}\cdot\underline{a}} \cdot \frac{\sin^2\frac{1}{2}M\underline{Q}\cdot\underline{b}}{\sin^2\frac{1}{2}\underline{Q}\cdot\underline{b}} \cdot \frac{\sin^2\frac{1}{2}P\underline{Q}\cdot\underline{c}}{\sin^2\frac{1}{2}\underline{Q}\cdot\underline{c}} \tag{2.43}$$

The dependence on the scattering vector $\underline{Q}$ is given by the so-called *Laue function*, which factorizes according to the three directions in space. One factor along one lattice direction $\underline{a}$ is plotted in Figure 2.9.

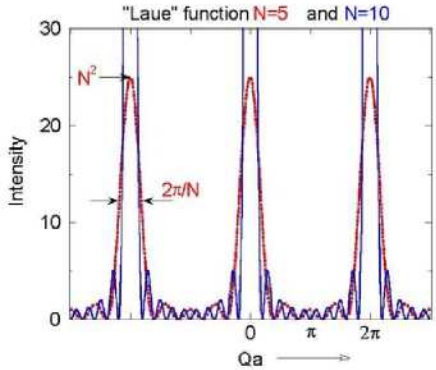



***Fig. 2.9:*** *Laue function along the lattice direction $\underline{a}$ for a lattice with five and ten periods, respectively.*

The main maxima occur at the positions $Q = n \cdot 2\pi/a$. The maximum intensity scales with the square of the number of periods $N^2$, the half width is given approximately by $\Delta Q = 2\pi/(N\cdot a)$. The more periods contribute to coherent scattering, the sharper and higher are the main peaks. Between the main peaks, there are $N-2$ side maxima. With increasing number of periods $N$, their intensity becomes rapidly negligible compared to the intensity of the main peaks. The main peaks are of course the well known *Bragg reflections*, which we obtain for scattering from a crystal lattice. From the position of these Bragg peaks in momentum space, the metric of the unit cell can be deduced (lattice constants $a, b, c$ and unit cell angles $\alpha, \beta, \gamma$). The width of the Bragg peaks is determined by the size of the coherently scattering volume (parameters $N$, $M$, and $P$) - and some other factors for real experiments (resolution, mosaic distribution, internal strains, ...).

## 2.8 Probes for scattering experiments in condensed matter science

In this chapter, we will discuss which type of radiation is suitable for condensed matter investigations. For neutron beams, we will then discuss the relevant interaction processes with matter in detail.

A list of requirements for the type of radiation used in condensed matter investigations looks as follows:

(1) The achievable spatial resolution should be in the order of the inter-particle distances, which implies (see section 2.2) that the wavelength $\lambda$ is in the order of the inter-particle distance $L$.
(2) If we want to study volume effects, the scattering has to originate from the bulk of the sample, which implies that the radiation should be at most weakly absorbed within matter.
(3) For a simple interpretation of the scattering data within the Born approximation (see section 2.2), multiple scattering effects should be negligible, i. e. the interaction of the radiation with matter should be weak.
(4) For the sake of simplicity, the probe should have no inner degrees of freedom, which could be excited during the scattering process (i. e. avoid beams of molecules, which have internal vibrational or rotational degrees of freedom).
(5) To study magnetic systems, we need a probe which interacts with the atomic magnetic moments in the sample.
(6) If, in addition to structural studies, we want to investigate elementary excitations, we would like the energy of the probe to be in the order of the excitation energies, so that the energy change during the scattering process is easily measurable.

This list of requirements leads us to some standard probes in condensed matter research. First of all, electromagnetic radiation governed by the Maxwell equations can be used. Depending on the resolution requirements, we will use x-rays with wavelength $\lambda$ about 0.1 nm to achieve atomic resolution or visible light ($\lambda \sim 350$ - 700 nm) to investigate e. g. colloidal particles in solution. Besides electromagnetic radiation, particle waves can be used. It turns out that thermal neutrons with a wavelength $\lambda \sim 0.1$ nm are particularly well adapted to the above list of requirements. The neutron beams are governed by the Schrödinger equation of quantum mechanics. An alternative is to use electrons, which for energies of around 100 keV have wavelengths in the order of 0.005 nm. As relativistic particles, they are governed by the Dirac equation of quantum mechanics. The big drawback of electrons as a condensed matter probe is the strong Coulomb interaction with the electrons in the sample. Therefore neither absorption, nor multiple scattering effects can be neglected. However the abundance of free electrons and the relative ease to produce optical elements makes them very suitable for imaging purposes (electron microscopy). Electrons, but also atomic beams are very powerful tools for surface science: due to their strong interaction with matter, both types of radiation are very surface sensitive. Low Energy Electron Diffraction LEED and Reflection High Energy Electron Diffraction RHEED are both used for in-situ studies of the crystalline structure during thin film growth, e.g. with Molecular Beam Epitaxy MBE. In what follows we will concentrate on neutron scattering as one of the probes, which is best suited for bulk studies on an atomic scale. We will introduce the properties of the neutron, discuss the absorption of neutrons in matter and derive the scattering cross sections for the main interaction processes with matter.

## 2.9 Properties of the neutron

We mentioned in the introduction that neutron beams provide a particularly useful probe for condensed matter investigations. The neutron is an elementary particle, a nucleon, consisting of three valance quarks, which are hold together by gluons. It thus has an internal structure, which, however, is irrelevant for condensed matter physics, since the energy scales involved in internal excitations are much too high. Keeping in mind the difference in lengths scales (diameter of an atom: about 0.1 nm = $10^{-10}$ m; diameter of a neutron: about 1 fm = $10^{-15}$ m),

we can safely consider the neutron as a point-like particle without internal structure for our purposes. Due to the weak interaction, the neutron is not a stable particle. A free neutron undergoes a β-decay after an average lifetime of about 15 minutes:

$$n \xrightarrow{15\,\mathrm{min}} p + e^- + \bar{\nu} \tag{2.44}$$

This leaves ample time for scattering investigations. In contrast to the mass less photon, the neutron has a mass m of about one atomic mass unit ~ $1.675 \cdot 10^{-27}$ kg. The finite neutron mass is comparable to the mass of a nucleus and thus an appreciable amount of energy can be transferred during the scattering process. The neutron is a charge less particle and thus does not show the strong Coulomb interaction with matter. This results in large penetration depths. Finally, the neutron has a nuclear spin 1/2 giving rise to a magnetic dipolar moment of

$$\mu_n = \gamma \mu_N; \quad \gamma = 1.91; \quad \mu_N = 5.05 \cdot 10^{-27}\, J/T \tag{2.45}$$

Due to this magnetic moment, the neutron can interact with the magnetic field of unpaired electrons in a sample leading to *magnetic scattering*. Thus magnetic structures and excitations can be studied by neutron scattering.

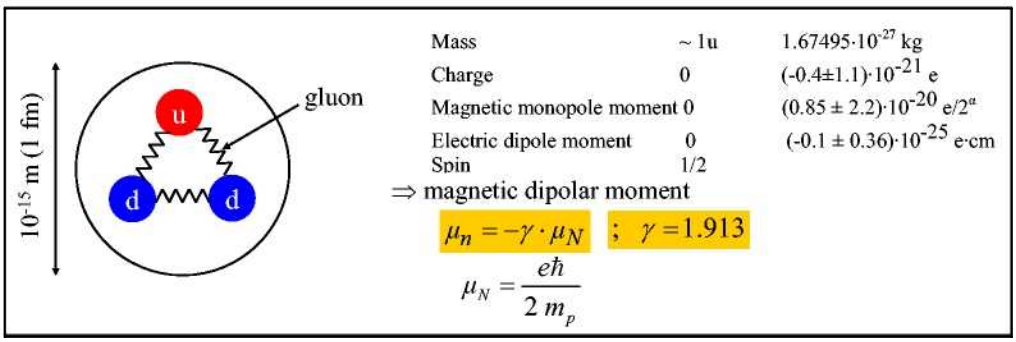



***Fig. 2.10:*** *Schematics of the neutron being composed of three quarks and gluons and the main quantities characterizing the neutron as a particle.*

To calculate the interference effects during the scattering process, a neutron has to be described as a matter wave with momentum

$$\underline{p} = m \cdot \underline{v} = \hbar \underline{k}; \; p = h/\lambda \tag{2.46}$$

and energy

$$E = \frac{1}{2} m v^2 = \frac{\hbar^2 k^2}{2m} = \frac{h^2}{2m\lambda^2} \equiv k_B T_{eq} \tag{2.47}$$

Here $\underline{v}$ is the velocity of the neutron and $T_{eq}$ defines the temperature equivalent of the kinetic energy of the neutron. In practical units:

$$\lambda[nm] = \frac{400}{v[m/s]}$$
$$E[meV] = \frac{0.818}{\lambda^2[nm]} \tag{2.48}$$

Let us consider the example of so-called *thermal neutrons* from a moderator at ambient temperature corresponding to a temperature equivalent of $T_{eq}$ ~ 300 K. According to (2.47), their wavelength is 0.18 nm, matching perfectly the distance between atoms. The energy of thermal neutrons is around 25 meV, which matches well the energy of elementary excitations, such as spin waves (magnons) or lattice vibrations (phonons). Together with the usually large penetration depths (charge = 0) and the magnetic interaction, these properties make neutrons so extremely useful for condensed matter investigations.

In the elementary scattering theory of chapter 2.3, we saw that the relevant quantity is the interaction potential V(r) of the probe with the system from which the probe is scattered. This potential enters in the cross-section in kinematical theory derived either from Born approximation or from Fermi's golden rule. To determine this interaction potential, we will look in more detail at the interaction of neutrons with matter. For neutrons there exist two dominant interactions: the interaction of the neutron with nuclei and its interaction with the magnetic field in the sample. The nuclear interaction results from the so-called strong interaction of particle physics, which is also responsible for the binding of neutrons and protons in the atomic nuclei. The interaction with the magnetic field is nothing but the magnetic dipole interaction of the neutron due to its dipolar moment with the magnetic field of unpaired electrons. There are other interactions, which are significantly weaker. One is the interaction of the neutron with the electric fields in the sample due to the neutrons magnetic dipole moment. This is a purely relativistic effect. Another is the magnetic dipole interaction of the neutron with the magnetic field produced by the nuclei. Since such interactions are several orders of magnitude weaker than the nuclear and magnetic interaction, they can usually be neglected and we will not discuss them further in this lecture.

## 2.10 Nuclear interaction: Scattering and absorption

To evaluate the cross section (2.26) for nuclear scattering, we have to specify the interaction potential with the nucleus. To derive this interaction potential from first principles is one of the fundamental challenges of nuclear physics. Fermi has proposed a phenomenological potential based on the argument that the wavelength of thermal neutrons is much larger than the nuclear radius. This means that the nuclei are point-like scatterers which leads to isotropic, Q-independent, (so-called s-wave) scattering. We will therefore use the so-called *Fermi-pseudo-potential:*

$$V(\underline{r}) = \frac{2\pi\hbar^2}{m} b\delta(\underline{r} - \underline{R}) \tag{2.49}$$

to evaluate the cross section (2.26).

Note, that despite the fact that the strong interaction of high energy physics is responsible for the scattering of the neutron with the nucleus, the scattering probability is small due to the small nuclear radius. Therefore, we can apply the first Born approximation. The quantity b introduced in (2.49) is a phenomenological quantity describing the strength of the interaction potential and is referred to as the *scattering length*. Tabulated values of b can be found in [6]. The total cross section of a given nucleus is $\sigma = 4\pi|b|^2$, corresponding to the surface area of a sphere with radius b. Since the interaction potential obviously depends on the details of the nuclear structure, b is different for different isotopes of the given element and also for different nuclear spin states. This fact gives rise to the appearance of so-called *coherent* and *incoherent scattering*, see section 2.12. Figure 2.11 shows the variation of the scattering amplitude as a function of atomic weight throughout the periodic table. The scattering length is mostly positive but can also adopt negative values. Since -1 = exp(iπ) this negative sign corresponds to a phase shift of π (or 180°) during the scattering process. The scattering length roughly follows the dashed line labeled *potential scattering* contribution, despite the fact that there are rather large excursions from this line.

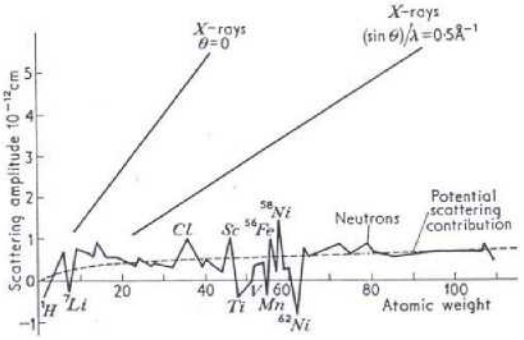



***Fig. 2.11:*** *Scattering length as a function of atomic weight throughout the periodic table.*

In the simplest one dimensional model, we can describe the nucleus as a rectangular potential well, see Figure 2.12.

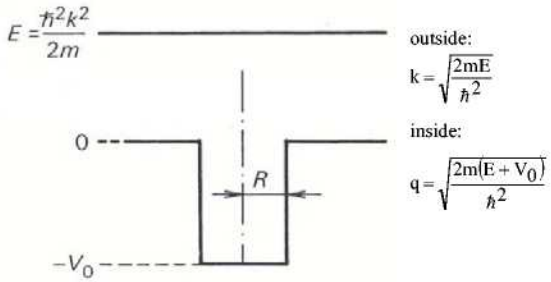



***Fig. 2.12:*** *The nucleus described as a potential well of radius R and depth $-V_0$, while the neutron has the kinetic energy* $E = \frac{\hbar^2 k^2}{2m}$.

The wave function of the neutron being scattered from such a potential well can be written as:

$$\Psi(\underline{r}) \sim e^{i\underline{kr}} + \frac{f}{r} e^{ikr} \tag{2.50}$$

Here the first term describes the incident plane wave and the second term describes a spherical wave emitted from the nucleus. f describes the scattering amplitude. In the limit of a hard sphere, the wave function on the surface of the nucleus has to vanish since the neutron cannot penetrate inside the nucleus. Mathematically this is described by the condition $\psi(R) = 0$ or $-f = R$. The scattering length is defined as $b: = -f$, so that its value is positive for most nuclei. Therefore for pure potential scattering, where the nucleus is assumed to be a hard sphere, $b$ attains the value of the nuclear radius $b = R$, which is plotted in Figure 2.11 as a dashed line: the *potential scattering* contribution. The marked deviations from this overall behavior are due to so-called *resonance scattering*. In a simplified picture, such resonances occur, when the neutron energy is such that absorption of the neutron in the nucleus produces a bound excited state. This can lead to a resonant absorption process, but it can also lead to resonance scattering, a typical second order perturbation process: in the initial state, the nucleus is in its ground state and the interaction with the neutron can be described as a virtual transition into an excited state of the compound nucleus and back with a re-emission of the neutron, where the nucleus decays back from the excited compound system into its ground state. This process $n+K \rightarrow C^* \rightarrow K+n$ has a cross-section given by the famous *Breit-Wigner-formula*:

$$\sigma_R = 4\pi \left| R + \frac{const}{E - E_R + \frac{1}{2} i\Gamma} \right|^2 \qquad (2.51)$$

Here R is the radius of the nucleus, E the neutron energy, $E_R$ the resonance energy and $\Gamma$ a damping term connected with the life-time of the excited state. As one can see, this formula describes very strong energy dependence with a pronounced maxima, when the neutron energy equals the resonance energy. Moreover, the resonance amplitude has an imaginary part, which describes the *resonance absorption*. In the resonant absorption process, the neutron is captured by the nucleus, leading to a compound nucleus in an excited state, containing one more neutron then the original nucleus. In a subsequent nuclear reaction, the compound nucleus gets rid of its excess energy. Examples for such absorption reactions will be given in the subsequent section. Finally the Breit-Wigner-formula gives an indication that the scattering length can be negative whenever the resonant term is negative (i. e. $E < E_R$), and its magnitude is larger than the contribution from potential scattering.

## 2.11 Neutron absorption

As explained above, neutron absorption can occur during nuclear reactions. Far away from the resonance, the absorption cross section is given by

$$\sigma_a \sim \lambda \sim \frac{1}{v} \qquad (2.52)$$

This proportionality to the wavelength $\lambda$ or the inverse velocity is a result of the density of states appearing in Fermi's golden rule. One can argue that wavelength and neutron velocity v are inversely proportional and thus, for longer wavelength i. e. smaller velocity, the neutron remains correspondingly longer close to the nucleus, which leads to a higher absorption cross-section. Table 2.1 gives examples for neutron absorption processes connected with nuclear reactions.

| Examples: | | |
|---|---|---|
| $\sigma_a$ (25 meV) [barn] | | |
| 5333 | $n + {}^3He \rightarrow {}^4He^* \rightarrow p + {}^3T$ | neutron detection |
| 940 | $n + {}^6Li \rightarrow {}^7Li^* \rightarrow {}^3T + {}^4He$ | |
| 3837 | $n + {}^{10}B \rightarrow {}^{11}B^* \rightarrow {}^4He + {}^7Li + \gamma$ | |
| 681 | $n + {}^{235}U \rightarrow$ fission | |

***Tab. 2.1*** *Examples for neutron absorption processes due to nuclear reactions. The absorption cross-section is given for neutrons of energy 25 meV in barn = $10^{-28}$ $m^2$ = 100 $fm^2$.*

As an example, there is a high probability of neutrons to be absorbed by $^3$He nuclei, because the $^4$He or $\alpha$-particle is very stable, since it corresponds to a closed nuclear shell. However, during the absorption of the neutron, the $^4$He nucleus is produced in an excited state. It gets rid of its surplus energy by decay into a proton and a triton $^3$T[4]. Since these two particles have very high energies of about 0.5 MeV due to the nuclear reaction, charged particles are created during this decay, which can be used for neutron detection in a proportional counter. In a similar manner, the reaction with $^6$Li, $^{10}$B or $^{235}$U can be used to build neutron detectors. It should be mentioned, however, that the neutron absorption in $^3$He is very strongly dependent on the relative orientation of the nuclear spins of both particles. While for anti parallel spin direction, the absorption cross-section is 6000 barn, it reduces to 2 barn for parallel spin

[4] The triton $^3$T nucleus is a hydrogen isotope with one proton and 2 neutrons.

direction. This effect can be used to build efficient neutron polarization filters. By optical pumping with laser light, the nuclear moment of the $^3$He nuclei can be aligned along one direction (so-called hyperpolarized $^3$He gas). If an unpolarized neutron beam passes a filter cell filled with hyperpolarized $^3$He, the neutrons with spin moment anti parallel to the nuclear moment of the $^3$He have a high probability to be absorbed, while neutrons with the other spin direction have a high probability to be transmitted. For an appropriate thickness of the filter cell, a very high neutron beam polarization can be achieved in this manner.

Another class of absorption processes are so-called *(n, γ)-resonances*. Examples are given in Table 2.2. In these processes, a nucleus is produced, which contains one additional neutron and this compound nucleus decays into the ground state by emission of γ-radiation. Prominent (n,γ)-resonances occur for Cadmium or Gadolinium where, depending on the isotope, the absorption cross-section can be very high, see Table 2.2. These metals are often used as neutron absorbers in shieldings or diaphragms, which define the size of the neutron beam. One should, however, be aware that in these reactions, γ-radiation of very high energy is being released, which requires additional lead shielding for radiation protection.

| | nucleide | $\sigma_\gamma$[barn] | $E_{resonance}$[meV] |
|---|---|---|---|
| (n, γ)-resonances: | $^{113}$Cd | 20600 | 178 |
| | $^{151}$Eu | 9200 | 321 |
| | $^{155}$Gd | 60900 | 26.8 |
| | $^{157}$Gd | 254000 | 31.4 |

***Tab. 2.2*** *Examples for (n, γ)-resonances with the cross-section in barn and the resonance energy in meV.*

As described by the Breit-Wigner-Formula, these resonance absorption cross-sections have very strong energy dependence. The simple proportionality to the wavelength given in equation (2.52) no longer holds close to the resonance energies. As an example, we show the energy dependence of the absorption cross-section for Cadmium in Figure 2.13. Such data can be found in the compilation [7].

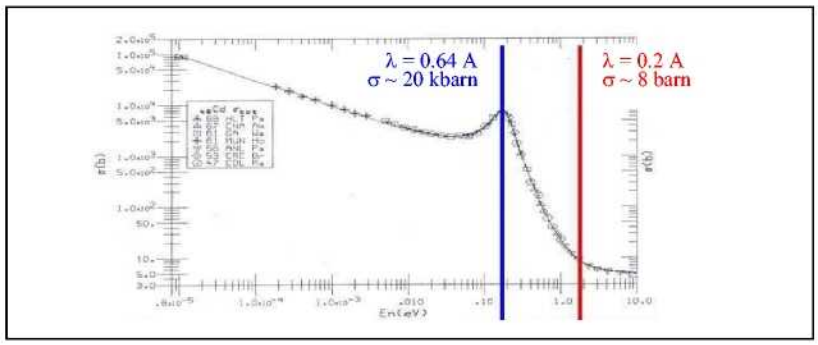



***Fig. 2.13:*** *Absorption cross-section of the element Cadmium as a function of energy in a double logarithmic representation.*

Figure 2.13 shows that for lower energies, i. e. long wavelengths, the proportionality of the absorption cross-section to the wavelength holds to very good approximation. However, there is a strong resonance for a wavelength of 0.64 Å, where the cross-section attains a maximum of about 20 kbarn. Above this energy, i. e. for shorter wavelengths, the absorption cross-section drops drastically. At a wavelength of 0.2 Å, it attains a value of only 8 barn. This shows that in the thermal energy range, Cadmium can be used as an efficient neutron absorber. However, one has to be careful and not use it for the same purpose in case of hot neutrons, where Cadmium becomes virtually transparent. There are many more resonances for higher neutron energies, which are not relevant for neutron scattering, where only hot, thermal and cold neutrons are being used.

Similar strong energy dependence occurs for the element Gadolinium. Usually, neutron scatterers try to avoid samples containing Gadolinium since it is the most absorbing element, especially the isotope $^{157}$Gd. However, the resonances lay right in the thermal neutron energy range. If the scattering experiment is performed with hot neutrons, the absorption cross-section of Gadolinium becomes much smaller and scattering experiments become feasible[5].

## 2.12 Coherent and incoherent scattering

As mentioned above, the nuclear interaction potential depends on the details of the nuclear structure and thus, the scattering length b is different for different isotopes of a given element and also for different nuclear spin states. In this section, we will discuss the effects of these special properties of the interaction of neutrons and nuclei for the scattering from condensed matter.

Let us assume an arrangement of atoms with scattering lengths $b_i$ on fixed positions $\underline{R}_i$. For this case, the scattering potential writes:

$$V(\underline{r}) = \frac{2\pi\hbar^2}{m_n} \sum_i b_i \delta(\underline{r} - \underline{R}_i) \tag{2.53}$$

The scattering amplitude is obtained from a Fourier transform:

$$A(\underline{Q}) = \sum_i b_i e^{i\underline{Q}\cdot\underline{R}_i} \tag{2.54}$$

When we calculate the scattering cross section, we have to take into account that the different isotopes are distributed randomly over all sites. Also the nuclear spin orientation is random, except for very low temperatures in external magnetic fields. Therefore, we have to average over the random distribution of the scattering length in the sample:

$$\frac{d\sigma}{d\Omega}(\underline{Q}) \sim \left|A(\underline{Q})\right|^2 = \left\langle \sum_i b_i \; e^{i\underline{Q}\cdot\underline{R}_i} \cdot \sum_j b_j^* e^{-i\underline{Q}\underline{R}_j} \right\rangle \tag{2.55}$$

In calculating the expectation value of the product of the two scattering lengths at sites i and j, we have to take into account that according to the above assumption, the distribution of the scattering length on the different sites is completely uncorrelated. This implies that for $i \neq j$, the expectation value of the product equals to the product of the expectation values. Only for $i = j$ a correlation occurs, which gives an additional term describing the mean quadratic deviation from the average:

[5] Another possibility is to use isotope enriched Gadolinium. While the isotope $^{157}$Gd with natural abundance 15.7% has a thermal absorption cross section of 259000 barn, the isotope $^{158}$Gd, which, with 24.8%, is the most abundant, has an absorption cross section of only 2.2 barn.

$$\left\langle b_i b_j \right\rangle = \begin{cases} \langle b \rangle \langle b \rangle = \langle b \rangle^2 & i \neq j \\ \left\langle b^2 \right\rangle = \langle b \rangle^2 + \left\langle (b - \langle b \rangle)^2 \right\rangle & i = j \end{cases}$$

The line for i = j results from the identity:

$$\left\langle (b - \langle b \rangle)^2 \right\rangle = \left\langle b^2 - 2b\langle b \rangle + \langle b \rangle^2 \right\rangle = \left\langle b^2 \right\rangle - \langle b \rangle^2 \tag{2.56}$$

Therefore, we can write the cross section in the following form:

$$\frac{d\sigma}{d\Omega}(\underline{Q}) = \langle b \rangle^2 \left| \sum_i e^{i\underline{Q}\cdot\underline{R}_i} \right|^2 \quad \text{"coherent"} \qquad + N\left\langle (b - \langle b \rangle)^2 \right\rangle \quad \text{"incoherent"} \tag{2.57}$$

The scattering cross section is as a sum of two terms. Only the first term contains the phase factors $e^{i\underline{Q}\cdot\underline{R}}$, which result from the coherent superposition of the scattering from pairs of scatterers. This term takes into account interference effects and is therefore named *coherent scattering*. The scattering length averaged over the isotope- and nuclear spin- distribution enters this term. The second term in (2.57) does not contain any phase information and is proportional to the number N of atoms (and not to $N^2$!). This term is not due to the interference of scattering from different atoms. As we can see from (2.56) (line i = j), this term corresponds to the scattering from single atoms, which subsequently superimpose in an incoherent manner (adding intensities, not amplitudes!). This is the reason for the intensity being proportional to the number N of atoms. Therefore the second term is called *incoherent scattering*. Coherent and incoherent scattering are illustrated in Figure 2.14.

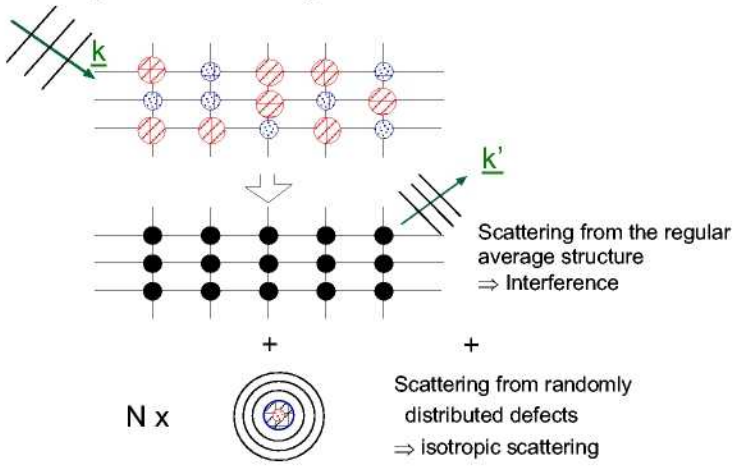



***Fig. 2.14:*** *Two-dimensional schematic illustration of the scattering process from a lattice of N atoms of a given chemical species, for which two isotopes (small dotted circles and large hatched circles) exist. The area of the circle represents the scattering cross section of the single isotope. The incident wave (top part of the figure for a special arrangement of the isotopes) is scattered coherently only from the average structure. This gives rise to Bragg peaks in certain directions. In the coherent scattering only the average scattering length is visible. Besides these interference phenomena, an isotropic background is observed, which is proportional to the number N of atoms and to the mean quadratic deviation from the average scattering length. This incoherent part of the scattering is represented by the lower part of the figure.*

The most prominent example for *isotope incoherence* is elementary nickel. The scattering lengths of the nickel isotopes are listed together with their natural abundance in Table 2.3 [6]. The differences in the scattering lengths for the various nickel isotopes are enormous. Some isotopes even have negative scattering lengths. This is due to resonant bound states, as compared to the usual potential scattering.

| Isotope | Natural Abundance | Nuclear Spin | Scattering Length [fm] |
|---|---|---|---|
| $^{58}$Ni | 68.27 % | 0 | 14.4(1) |
| $^{60}$Ni | 26.10 % | 0 | 2.8(1) |
| $^{61}$Ni | 1.13 % | $^3/_2$ | 7.60(6) |
| $^{62}$Ni | 3.59 % | 0 | -8.7(2) |
| $^{64}$Ni | 0.91 % | 0 | -0.37(7) |
| Ni | | | 10.3(1) |

**Tab. 2.3** *The scattering lengths of the nickel isotopes and the resulting scattering length of natural $_{28}$Ni [6].*

Neglecting the less abundant isotopes $^{61}$Ni and $^{64}$Ni, the average scattering length is calculated as:

$$\langle b \rangle \approx [0.68 \cdot 14.4 + 0.26 \cdot 2.8 + 0.04 \cdot (-8.7)] fm \approx 10.2\, fm \tag{2.58}$$

, which gives the total coherent cross section of:

$$\Rightarrow \sigma_{coherent} = 4\pi \langle b \rangle^2 \approx 13.1\, barn\ (exact: 13.3(3) barn) \tag{2.59}$$

The incoherent scattering cross section per nickel atoms is calculated from the mean quadratic deviation:

$$\sigma_{incoherent}^{Isotope} = 4\pi \left[ 0.68 \cdot (14.4 - 10.2)^2 + 0.26 \cdot (2.8 - 10.2)^2 + 0.04 \cdot (-8.7 - 10.2)^2 \right] fm^2 \tag{2.60}$$
$$\approx 5.1 barn\ (exact: 5.2(4) barn)$$

Values in parentheses are the exact values taking into account the isotopes $^{61}$Ni and $^{64}$Ni and the nuclear spin incoherent scattering (see below). From (2.59) and (2.60), we learn that the incoherent scattering cross section in nickel amounts to more than one third of the coherent scattering cross section.

The most prominent example for *nuclear spin incoherent scattering* is elementary hydrogen. The nucleus of the hydrogen atom, the proton, has the nuclear spin I = ½. The total nuclear spin of the system H + n can therefore adopt two values: J = 0 and J = 1. Each state has its own scattering length: $b_-$ for the singlet state (J = 0) and $b_+$ for the triplet state (J = 1) - compare Table 2.4.

| **Total Spin** | **Scattering Length** | **Abundance** |
|---|---|---|
| J = 0 | $b_-$ = - 47.5 fm | $\frac{1}{4}$ |
| J = 1 | $b_+$ = 10.85 fm | $\frac{3}{4}$ |
| <b> = - 3.739(1) fm | | |

**Tab. 2.4** *Scattering lengths for hydrogen [6].*

As in the case of isotope incoherence, the average scattering length can be calculated:

$$\langle b \rangle = \left[ \frac{1}{4}(-47.5) + \frac{3}{4} \cdot (10.85) \right] fm = -3.74\, fm \tag{2.61}$$

This corresponds to a coherent scattering cross section of about ≈ 1.76 barn [6]:

$$\Rightarrow \sigma_{coherent} = 4\pi \langle b \rangle^2 = 1.7568(10)\, barn \tag{2.62}$$

The nuclear spin incoherent part is again given by the mean quadratic deviation from the average:

$$\sigma_{incoherent}^{nuclear\ spin} = 4\pi \left[ \frac{1}{4}(-47.5+3.74)^2 + \frac{3}{4}(10.85+3.74)^2 \right] fm^2 = 80.2\, barn$$

$$(exact:\ 80.26(6)\, barn) \tag{2.63}$$

Comparing (2.62) and (2.63), it is immediately clear that hydrogen scatters mainly incoherently. As a result, we observe a large background for all samples containing hydrogen. We should avoid all hydrogen containing glue for fixing our samples to a sample stick. Finally, we note that deuterium with nuclear spin I = 1 has a much more favorable ratio between coherent and incoherent scattering:

$$\sigma_{coh.}^{D} = 5.592(7) barn; \quad \sigma_{inc.}^{D} = 2.05(3) barn \tag{64}$$

The coherent scattering lengths of hydrogen (-3.74 fm) and deuterium (6.67 fm) are significantly different. This can be used for contrast variation by isotope substitution in all samples containing hydrogen, i. e. in biological samples or soft condensed matter samples, see corresponding chapters.

A further important element, which shows strong nuclear incoherent scattering, is vanadium. Natural vanadium consists to 99,75 % of the isotope $^{51}$V with nuclear spin 7/2. By chance, the ratio between the scattering lengths $b_+$ and $b_-$ of this isotope are approximately equal to the reciprocal ratio of the abundances. Therefore, the coherent scattering cross section is very small and the incoherent cross section dominates [6]:

$$\sigma_{coh}^{V} = 0.01838(12)\, barn; \quad \sigma_{incoh}^{V} = 5.08(6)\, barn \tag{2.65}$$

For this reason, Bragg scattering of vanadium is difficult to observe above the large incoherent background. However, since incoherent scattering is isotropic, the scattering from vanadium can be used to calibrate multi-detector arrangements.

Here, we will not discuss scattering lengths for further elements and refer to the values tabulated in [6].

## 2.13 Magnetic neutron scattering

So far, we have only discussed the scattering of neutrons by the atomic nuclei. Apart from nuclear scattering, the next important process is the scattering of neutrons by the magnetic moments of unpaired electrons. This so-called magnetic neutron scattering comes about by the magnetic dipole-dipole interaction between the magnetic dipole moment of the neutron and the magnetic field of the unpaired electrons, which has spin and orbital angular momentum contributions. This magnetic neutron scattering allows us to study the magnetic properties of a sample on an atomic level, i. e. with atomic spatial- and atomic energy- resolution. In what follows, we will give an introduction into the formalism of magnetic neutron scattering, restricting ourselves to the case of elastic magnetic scattering. Inelastic magnetic scattering will we discussed in subsequent lectures.

To derive the magnetic scattering cross section of thermal neutrons, we consider the situation shown in Figure 2.15: a neutron with the nuclear moment $\mu_n$ is at position $\underline{R}$ with respect to an electron with spin $\underline{S}$, moving with a velocity $\underline{v}_e$.

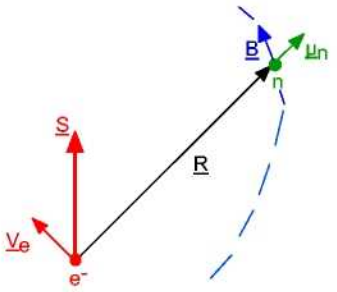



***Fig. 2.15**: Geometry for the derivation of the interaction between neutron and electron.*

Due to its magnetic dipole moment, the neutron interacts with the magnetic field of the electron according to:

$$\mathbf{V}_m = -\underline{\mu}_n \cdot \underline{B} \tag{2.66}$$

Here, the magnetic moment of the neutron is given by:

$$\underline{\mu}_n = -\gamma_n \mu_N \cdot \underline{\sigma} \tag{2.67}$$

$\underline{\sigma}$ denotes the spin operator, $\mu_N$ the nuclear magneton and $\gamma_N = -1.913$ the gyromagnetic factor of the neutron. The magnetic field $\underline{B}$ of an electron is due to a spin- and orbital- part $\underline{B} = \underline{B}_S + \underline{B}_L$. The dipole field of the spin moment is given by:

$$\underline{B}_S = \underline{\nabla} \times \left( \frac{\underline{\mu}_e \times \underline{R}}{R^3} \right) \quad ; \quad \underline{\mu}_e = -2\mu_B \cdot \underline{S} \tag{2.68}$$

The field due to the movement of the electron is given according to Biot-Savart:

$$\underline{B}_L = \frac{-e}{c} \frac{\underline{v}_e \times \underline{R}}{R^3} \tag{2.69}$$

The magnetic scattering cross section for a process, where the neutron changes its wave vector from $\underline{k}$ to $\underline{k}'$ and the projection of its spin moment to a quantization axis z from $\sigma_z$ to $\sigma_z'$ can be expressed within the first Born approximation:

$$\frac{d\sigma}{d\Omega} = \left( \frac{m_n}{2\pi\hbar^2} \right)^2 \left| \langle \underline{k}' \sigma_z' | \mathbf{V}_m | \underline{k} \sigma_z \rangle \right|^2 \tag{2.70}$$

As mentioned, we only consider the single differential cross section for elastic scattering. Introducing the interaction potential from (2.66) to (2.69) in (2.70) we obtain after some algebra [1, 4]:

$$\frac{d\sigma}{d\Omega} = (\gamma_n r_0)^2 \left| -\frac{1}{2\mu_B} \left\langle \sigma_z' \left| \underline{\sigma} \cdot \underline{M}_\perp(\underline{Q}) \right| \sigma_z \right\rangle \right|^2 \tag{2.71}$$

The pre-factor $\gamma_n r_0$ has the value $\gamma_n r_0 = 0.539 \cdot 10^{-12}$ cm = 5.39 fm. Here, $\underline{M}_\perp(\underline{Q})$ denotes the component of the Fourier transform of the sample magnetization, which is perpendicular to the scattering vector $\underline{Q}$ (see Figure 2.16):

$$\underline{M}_\perp(\underline{Q}) = \hat{\underline{Q}} \times \underline{M}(\underline{Q}) \times \hat{\underline{Q}} \tag{2.72}$$

$$\underline{M}(\underline{Q}) = \int \underline{M}(\underline{r}) e^{i\underline{Q}\cdot\underline{r}} d^3 r \tag{2.73}$$

The total magnetization is given as a sum of the spin- and orbital-angular- momentum part according to:

$$\underline{M}(\underline{r}) = \underline{M}_S(\underline{r}) + \underline{M}_L(\underline{r})$$
$$\underline{M}_S(\underline{r}) = -2\mu_B \cdot \underline{S}(\underline{r}) = -2\mu_B \sum_i \delta(\underline{r} - \underline{r}_i)\underline{S}_i \qquad (2.74)$$

(2.71) tells us that with magnetic neutron scattering, we are able to determine the magnetization $\underline{M}(\underline{r})$ in microscopic atomic spatial co-ordinates $\underline{r}$. This gives a lot more information than a simple macroscopic measurement, where we obtain the ensemble average of the magnetization over the entire sample. We also see from (2.71) that the orientation of the nuclear spin momentum of the neutron (represented by $\sigma_z$) plays an important role in magnetic scattering. This is not surprising, since magnetism is a vector property of the sample and obviously there should be an interaction with the vector property of the neutron, its nuclear magnetic moment. Therefore, the analysis of the change of the direction of the neutron nuclear moment in the scattering process should give us valuable additional information as compared to a determination of the change of energy and momentum direction of the neutron alone. These so-called polarization analysis experiments are discussed in the following lecture. Finally, to obtain an idea of the size of magnetic scattering relative to nuclear scattering, we can replace the matrix element in (2.71) for a spin ½ particle by the value 1 $\mu_B$. This gives us an "equivalent" scattering length for magnetic scattering of 2.696 fm for a spin ½ particle. This value corresponds quite well to the scattering length of cobalt, which means that magnetic scattering is comparable in magnitude to nuclear scattering.
In contrast to nuclear scattering, we obtain for magnetic scattering a directional term: neutrons only "see" the component of the magnetization perpendicular to the scattering vector (see Figure 2.16).

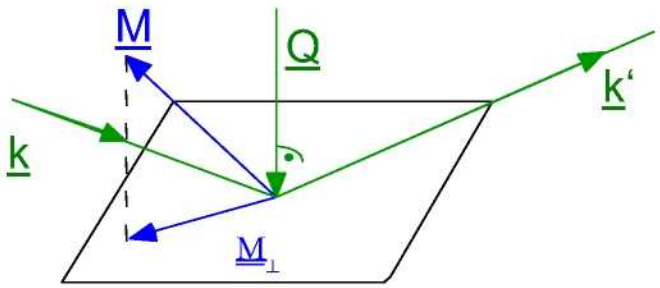



***Fig. 2.16:*** *For magnetic neutron scattering, only the component $\underline{M}_\perp$ of the magnetization perpendicular to the scattering vector $\underline{Q}$ is of relevance.*

A second specialty of magnetic scattering as compared to nuclear scattering is the existence of the *magnetic form factor*. How the form factor comes about is most easily understood in the simple case of pure spin scattering, i. e. for atoms with spherical symmetric (L = 0) ground state, such as $Mn^{2+}$ or $Fe^{3+}$. Moreover, the derivation is simplified for ionic crystals, where the electrons are located around an atom. We denote the spin operators of the electrons of atom i with $\underline{s}_{ik}$. The spatial co-ordinates of the electron number *k* in atom *i* are $\underline{r}_{ik} = \underline{R}_i + \underline{t}_{ik}$, where $\underline{R}_i$ denotes the position vector to the nucleus of atom i. Now we proceed to separate the intra-atomic quantities. We can write the operator for the magnetization density as:

$$\underline{M}_S(\underline{r}) = -2\mu_B \sum_{ik} \delta(\underline{r} - \underline{r}_{ik}) \cdot \underline{s}_{ik} \qquad (2.75)$$

The Fourier transform of this magnetization density is calculated to:

$$\underline{M}(\underline{Q}) = \int \underline{M}_S(\underline{r}) e^{i\underline{Q}\cdot\underline{r}} d^3r = \sum_{ik} e^{i\underline{Q}\cdot\underline{r}_{ik}} \underline{s}_{ik} = \sum_i e^{i\underline{Q}\cdot\underline{R}_i} \sum_k e^{i\underline{Q}\cdot\underline{t}_{ik}} \cdot \underline{s}_{ik} \qquad (2.76)$$

To calculate the scattering cross section, we now have to determine the expectation value of this operator for the quantum mechanical state of the sample averaged over the thermodynamic ensemble. This leads to

$$\underline{M}(\underline{Q}) = -2\mu_B \cdot f_m(\underline{Q}) \cdot \sum_i e^{i\underline{Q}\cdot\underline{R}_i} \cdot \underline{S}_i \tag{2.77}$$

The single differential cross section for elastic scattering is thus given by:

$$\frac{d\sigma}{d\Omega} = (\gamma_n r_0)^2 \left| f_m(\underline{Q}) \sum_i S_{i\perp} e^{i\underline{Q}\underline{R}_i} \right|^2 \tag{2.78}$$

Here, $f_m(\underline{Q})$ denotes the form factor, which is connected with the spin density of the atom via a Fourier transform:

$$f_m(\underline{Q}) = \int_{Atom} \rho_s(\underline{r}) e^{i\underline{Q}\cdot\underline{r}} d^3r \tag{2.79}$$

With the form (2.78), we have expressed the cross section in simple atomic quantities, such as the expectation values of the spin moment $\underline{S}_i$ at the various atoms. The distribution of the spin density within an atom is reflected in the magnetic form factor (2.79).

For ions with spin and orbital angular momentum, the cross section takes a significantly more complicated form [4]. Under the assumption that spin- and orbital- angular momentum of each atom couple to the total angular momentum $\underline{J}_i$ (L/S-coupling) and for rather small momentum transfers (the reciprocal magnitude of the scattering vector has to be small compared to the size of the electron orbits), we can give a simple expression for this cross section in the so-called *dipole approximation*:

$$\frac{d\sigma}{d\Omega} = (\gamma_n r_o)^2 \cdot \left| \frac{g_J}{2} f_m(Q) \sum_i J_{i\perp} e^{i\underline{Q}\cdot\underline{R}_i} \right|^2 \tag{2.80}$$

Here the magnetic form factor writes:

$$f_m(Q) = \langle j_o(Q) \rangle + C_2 \langle j_2(Q) \rangle \tag{2.81}$$

$g_J$ denotes the Lande g-factor, $C_2 = \frac{2}{g_J} - 1$ and

$$\langle j_l(Q) \rangle = 4\pi \int_0^\infty j_l(Qr) R^2(r) r^2 dr \tag{2.82}$$

are the spherical transforms of the radial density distributions *R(r)* with the spherical Bessel functions $j_l(Qr)$. For isolated atoms, the radial part *R(r)* has been determined by Hartree-Fock-calculations and the functions $\langle j_0(Q) \rangle$ and $\langle j_2(Q) \rangle$ in (2.82) have been tabulated [8].

Since the distribution of the magnetic field for spin and orbital angular momentum is completely different, different Q-dependencies of the corresponding form factors result. Moreover, because only the outer electrons in open shells contribute to magnetic scattering, the magnetic form factor also differs from the x-ray form factor introduced above, see Figure 2.17.

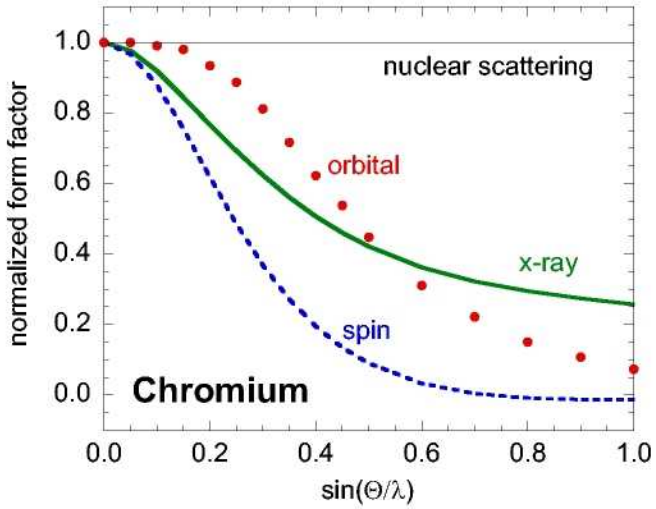



***Fig. 2.17:*** *Form-factor of Cr [9, 10]. Due to the different distribution of the magnetic field for S and L, a more rapid decrease of the scattering amplitude as a function of momentum transfer results for the spin momentum. For the x-ray form factor, the inner electrons play an important role, too. Therefore, the x-ray form factor drops slower as compared to the magnetic form factor. On the Å length scale of the thermal neutron wavelength, the nucleus is point-like. Therefore, nuclear scattering is independent of the momentum transfer. Finally, we want to mention that the magnetic form factor can in general be anisotropic, if the magnetization density distribution is anisotropic.*

## 2.14 Comparison of probes

In this lecture, we have so far introduced the elementary formalism to describe the scattering process and discussed the interaction of neutrons with matter. We now want to ask the questions, for which problems in condensed matter research, neutrons can be utilized successfully also in comparison to other probes, such as x-ray scattering or electron microscopy and electron scattering. To answer these questions, we have to look at the ranges of energies, wavelength or scattering vector, which can be covered by various probes as well as the different contrast mechanisms.

Figure 2.18 shows a double logarithmic plot of the dispersion relation "wavelength versus energy" for the three probes neutrons, electrons and photons. The plot demonstrates, how thermal neutrons of energy 25 meV are ideally suited to determine interatomic distances in the order of 0.1 nm, while the energy of x-rays or electrons for this wavelength is much higher. However with modern techniques at a synchrotron radiation source, energy resolutions in the meV-region become accessible even for photons of around 10 keV corresponding to a relative energy resolution $\Delta E/E \approx 10^{-7}$! The graph also shows that colloids with a typical size of 100 nm are well suited for the investigation with light of energy around 2 eV. These length scales can, however, also be reached with thermal neutron scattering in the small angle region. While Figure 18 thus demonstrates for which energy-wave-length combination a certain probe is particularly useful, modern experimental techniques extend the range of application by several orders of magnitude.

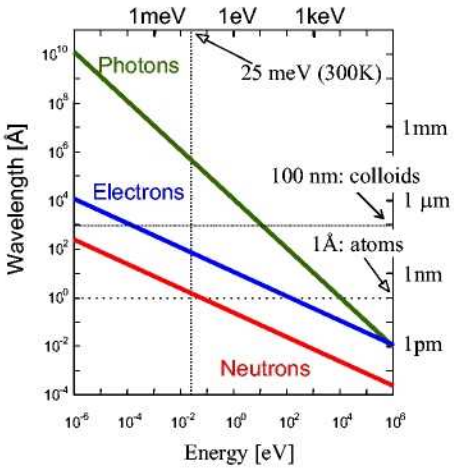



***Fig. 2.18:*** *Comparison of the three probes - neutrons, electrons and photons - in a double logarithmic energy-wavelength diagram.*

It is therefore useful to compare the scattering cross sections as it is done in Figure 2.19 for x-rays and neutrons. Note that the x-ray scattering cross sections are in general a factor of 10 larger as compared to the neutron scattering cross sections. This means that the signal for x-ray scattering is stronger for the same incident flux and sample size. But caution has to be applied that the conditions for kinematical scattering are fulfilled. For x-rays, the cross section depends on the number of electrons and thus varies in a monotonic fashion throughout the periodic table. Clearly it will be difficult to determine hydrogen positions with x-rays in the presence of heavy elements such as metal ions. Moreover, there is a very weak contrast between neighboring elements as can be seen from the transition metals Mn, Fe and Ni in Figure 2.19. However, this contrast can be enhanced by anomalous scattering, if the photon energy is tuned close to the absorption edge of an element. Moreover, anomalous scattering is sensitive to the anisotropy of the local environment of an atom. For neutrons the cross section depends on the details of the nuclear structure and thus varies in a non-systematic fashion throughout the periodic table. As an example, there is a very high contrast between Mn and Fe. With neutrons, the hydrogen atom is clearly visible even in the presence of such heavy elements as Uranium. Moreover there is a strong contrast between the two Hydrogen isotopes H and D. This fact can be exploited for soft condensed matter investigations by selective deuteration of certain molecules or functional groups. This will vary the contrast within the sample.

Finally, both neutrons and x-rays allow the investigation of magnetism on an atomic scale. Magnetic neutron scattering is comparable in strength to nuclear scattering, while non-resonant magnetic x-ray scattering is smaller than charge scattering by several orders of magnitude[6]. Despite the small cross sections, non-resonant magnetic x-ray Bragg scattering from good quality single crystals yields good intensities with the brilliant beams at modern synchrotron radiation sources. While neutrons are scattered from the magnetic induction within the sample, x-rays are scattered differently from spin and orbital momentum and thus allow one to measure both form factors separately. Inelastic magnetic scattering e.g. from magnons or so called quasielastic magnetic scattering from fluctuations in disordered magnetic systems

[6] Typically between 6 to 9 orders of magnitude.

is a clear domain of neutron scattering and cannot be done with x-rays up to now. Finally, resonance exchange scattering XRES allows one not only to get enhanced intensities, but also to study magnetism with element- and band sensitivity [11].

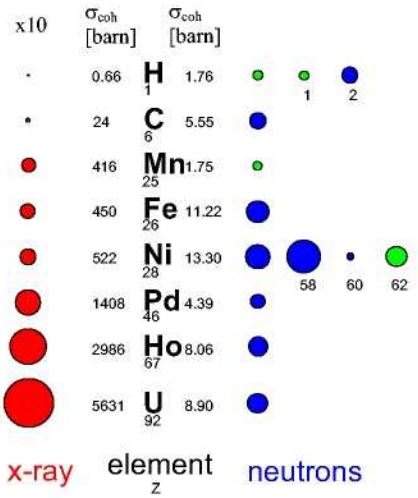



***Fig. 2.19:*** *Comparison of the coherent scattering cross-sections for x-rays and neutrons for a selection of elements. The area of the colored circles represent the scattering cross section, where in the case of x-rays a scale factor 10 has to be applied. For neutrons, the blue and green circles distinguish the cases where the scattering occurs with or without a phase shift of $\pi$.*

With appropriate scattering methods, employing neutrons, x-rays or light, processes in condensed matter on very different time and space scales can be investigated. Which scattering method is appropriate for which region within the "scattering vector Q - energy E plane" is plotted schematically in Figure 2.20. A scattering vector Q corresponds to a certain length scale, an energy to a certain frequency, so that the characteristic lengths and times scales for the various methods can be directly determined from the Figure. Examples for applications and information on instrumentation will follow in subsequent lectures.

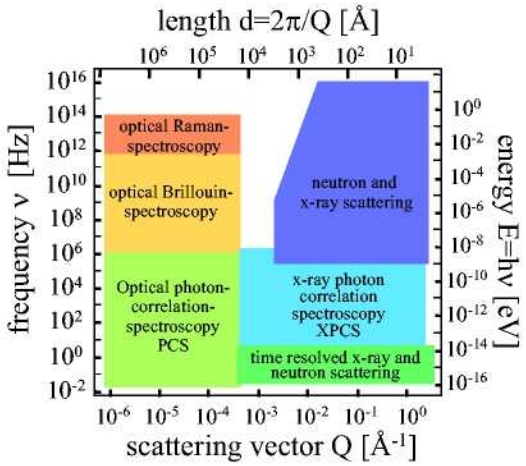



***Fig. 2.20***: *Regions in frequency ν and scattering vector Q or energy E and length d plane, which can be covered by various scattering methods.*

**References**


[1] G. L. Squires "Introduction to the Theory of Thermal Neutron Scattering" Dover 1997

[2] K. Sköld, D. Price (Eds.) "Methods of Experimental Physics" Neutron Scattering Part A-C Academic Press 1987

[3] J. M. Cowley "Diffraction Physics" North Holland, Amsterdam 1995

[4] S. W. Lovesey "Theory of neutron scattering from condensed matter" Clarendon Press, Oxford, 1987

[5] B. W. Batterman, H. Cole "Dynamical Diffraction of X-Rays by Perfect Crystals" Rev. Mod. Phys. 36 (1964), 681 - 717.

[6] A. Dianoux, G. Lander (Eds.) "Neutron Data Booklet", Institute Laue-Langevin (2002) - see also [8] -

[7] D. E. Garber, R. R. Kinsey "Neutron Cross-Section II" BNL-Report (1976)

[8] E. Price (Ed.) "International Tables for Crystallography, Volume C" International Union of Crystallography (2004) - see also [6] -

[9] J. Strempfer et al. Eur. Phys. J B **14** (2000), 63 - 72

[10] J. Strempfer et al. Physica B **267 - 268** (1999), 56 - 59

[11] Th. Brückel "Scattering Techniques II: Magnetic X-Ray Scattering" Schriften des Forschungszentrum Jülich, Materie und Material **26** (2006), B5.1 - B5.34

# 3

# Polarized neutron scattering

Werner Schweika

# 3. Polarized neutron scattering

Werner Schweika

The neutron's magnetic moment is an ideal probe to study magnetic structures and excitations in condensed matter physics. Many physical properties of a system can be inferred from the energy and momentum transfer in the scattering process. Specific magnetic properties and correlations may be identifiable that way or by parametric studies with temperature or magnetic field variation. However, it might be intuitively clear that polarization analysis gives valuable additional information on vector properties involving spin and orbital momentum. Neutron scattering is a low flux technique which is particularly true when polarization of neutrons is involved. This is not a concern for structure determination from measured Bragg scattering but for scattering due to magnetic fluctuations, spin-correlations in the disordered paramagnetic phase or spin excitations, where scattering is typically weak. However, the benefit of such effort of polarization analysis is not only the separation of scattering, it may also reveal new unique and most detailed information on correlations involving magnetic fluctuations. The lecture will give an introduction to neutron polarization analysis including most recent advances, and will discuss as an example for applications the spin correlations in highly frustrated spin systems, the scattering from a complex chiral structure, and an application to the local structure in soft matter materials.

## 3.1 Neutron spins in magnetic fields

### 3.1.1 Precession of neutron spins

Neutrons are fermions with spin 1/2 and have a magnetic moment $\boldsymbol{\mu} = -1.91\mu_N$ in terms of the nuclear Bohr magneton $\mu_N$. The characteristic motion of the neutron magnetic moment in a magnetic field is Larmor precession, which for simplicity can be considered in a classical treatment[1]. In fact, even the quantum mechanical treatment, which introduces Pauli spin matrices $\hat{\boldsymbol{\sigma}}$ into the Schrödinger equation, is effectively a classical treatment considering the origin of these matrices. They result from the problem of mapping three

dimensions onto two by introducing a complex component and were treated by Cayley and Klein (1897) [2] describing the classical problem of a spinning top.

Classical mechanics shows that a torque exerted on a magnetic moment $\boldsymbol{\mu}$ by a magnetic feld $\mathbf{H}$ inclined at an angle $\theta$ relative to the magnetic moment causes the magnetic moment of the neutron to precess about the direction of the feld with the *Larmor* frequency $\omega_L$. The precession frequency is independent of the angle of inclination $\theta$. Different to the motion of a spinning top in a gravity feld the neutron's motion shows no nutation, its angular momentum $\mathbf{L} = \hbar\mathbf{S}$ and its energy is a constant of motion. $S = \frac{1}{2}$ denotes the spin quantum number of the neutron and $\hbar$ is Planck's constant divided by $2\pi$. The ratio of angular momentum $\mathbf{L}$ and magnetic moment $\boldsymbol{\mu}$ defnes the *gyromagnetic ratio* $\gamma$, $\boldsymbol{\mu} = \gamma\mathbf{L}$. An applied magnetic feld will tend to align this magnetic moment and exerts a torque. No force is exerted by a homogeneous feld, therefore, the resulting equation of motion

$$\dot{\mathbf{L}} = -\gamma\,\mathbf{L} \times \mathbf{H} \tag{1}$$

simply describes a precession of the magnetic moment around the magnetic feld, see Fig.1, in which $L_z$ and hence the polarization along the feld axis is a constant of motion.

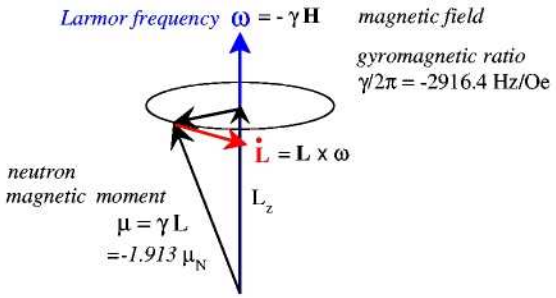



Figure 1: Larmor precession: the motion of the neutron in a constant magnetic feld.

### 3.1.2 Motion in time dependent fields

Thermal neutrons move with a speed of thousands of meters per second. When passing through magnetic felds, the neutrons experience time-depedent changes in the feld. Replacing $\mathbf{H}$ by $\mathbf{H}(t)$, the differential equation Eq. (1) can be used to calculate numerically

the effect of all relevant field variations in a n experimental set-up. Besides the precession in constant fields, in practice however, it is usually possible to work at least within two simple limiting cases of either **(i) slow adiabatic field variation**, in which the non-precessing spin component parallel to the fe ld smoothly follows the field direction, or of **(ii) sudden field reversal**, in which the non-precessing spin component has no time to reorient itself, when traversing abruptly from a parallel to anti-parallel field or vice versa. Slow field variation means that the field $\mathbf{H}$ changes or rotates in the coordinate system of the neutron with a frequency that is small compared to the Larmor frequency.

### 3.1.3 Polarized neutron beams

Polarization of a neutron beam is defined by the average over the neutron spin operators $\mathbf{S}$

$$\mathbf{P} = \langle 2\mathbf{S} \rangle \tag{2}$$

Polarization will be measured with respect to a magnetic field defining a quantization axis and any device for polarization analysis will take the projection of the spins in up- and down state state, $n_\uparrow$ and $n_\downarrow$ respectively,

$$\mathrm{P} = \frac{n_\uparrow - n_\downarrow}{n_\uparrow + n_\downarrow}, \tag{3}$$

Typical neutron beams have a cross-section of a few $cm^2$. In order to preserve the beam polarization $\mathbf{P}$ one could try to avoid and screen any disturbing magnetic fields, however, it is more convenient to use magnetic fields to guide the polarization $\mathbf{P}$, fields which may show even smooth field variations. When working with a precessing polarization $\mathbf{P}$, however, there are more stringent requirements for field homogeneity in direction and magnitude to keep the neutron spins in phase.

## 3.2 Experimental set-up for neutron polarization analysis

### 3.2.1 The DNS instrument

The diffuse neutron scattering spectrometer DNS (now being transferred from Jülich to the new research reactor at Munich FRM2 in Munich) is equipped with polarization analysis and is particularly devoted to elastic and inelastic diffuse scattering that may

arise from spin correlations and magnetic disorder and ordering in materials. A layout of the instrument is shown in Fig. 2. DNS is a time-of-flight instrument[3] with a multi-detector system similar to the D7 instrument at the ILL[4]. The monochromatic incident beam is polarised with a focusing supermirror bender, xyz-field coils allow to change the polarization at the sample, and the polarisation analysis is performed with supermirror analysers in focusing arrangement in front of each detector.

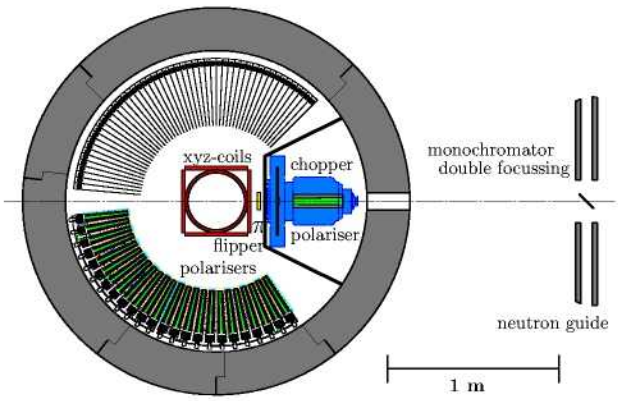



Figure 2: Scheme of the DNS instrument.

### 3.2.2 Polarization analyzers

The most common methods to polarize neutrons are (i) using the total reflection from magnetic multi-layers, (ii) using Bragg reflection of polarizing single crystals (typically Heusler crystals) and (iii) polarized He-3 filters, in which for anti-parallel spins the (n,$^3$He)-compound has a large absorption cross-section while all neutrons with parallel spins may pass the filter cell. The first two methods use an interference effect of nuclear and magnetic scattering amplitudes having the same absolute value.

The polarization analysis at the DNS is performed with supermirrors using total reflection. The angle of total reflection for a single ferromagnetic (FM) layer is given by

$$\Theta_c^{\pm} = \lambda\sqrt{n(b-p)/\pi}. \tag{4}$$

Here $n$ denotes the particle density and $b$ and $p$ the nuclear and magnetic scattering lengths, respectively. However, the critical angle can be further increased by artificial multi-layers (supermirrors) of alternating FM and non-magnetic layers of varying thickness [5]. The alternating layers of the DNS polarizers consist of the materials $Fe_{50}Co_{48}V_2$ / $TiN_x$, with critical angles up to $\Theta_c = 0.3^o \times \lambda/\text{Å}$. The degree of polarization that can be achieved is rather high, typically 98%.

Both the polarizer in the initial flight-path and the polarization analyzers in front of the detectors are made out of supermirrors being curved to avoid any direct flight path without reflection, and in addition the curvature is such that neutrons are focussed on the sample. The common polarization axis of initial and final polarizers is vertical.

### 3.2.3 Guide-fields

A magnetic *guide field* is used to maintain the direction of the spin and the polarization of the neutron beam. The guide field preserves the quantization axis to which the neutron moments have align either parallel or anti-parallel. Guide fields are typically weak so that the sample magnetization is not significant ly influenced, but sufficiently stronger than for instance the magnetic field of the earth or any other stray magnetic fields from the surrounding. In the DNS instrument the polarizers and polarization analyzers are kept in a permanent vertical field that is not screened. This vertical stray-field is used as a guide field throughout the instrument. At the sample position its strength is still about 5 Gauss.

### 3.2.4 $\pi$ and $\pi/2$-Flipper

The purpose of a $\pi$-flipper is to reverse the polarization and to detect whether the sample causes spin-flip scattering.

When applying a magnetic field perpendicular to the polarized neutron beam, the polarization immediately starts its Larmor precession. A flipper that reverses the neutron polarization with respect to the guide field has to induce a well-defined field pulse that the polarization precesses by an angle $\pi$. Therefore, one can use the homogenous field of a long rectangular coil, see Fig.3.2.4. Neutrons see a sudden field change when they enter

and exit the coil, in between they precess around the flipping field, whose magnitude is tuned with respect to the time of flight that the neutrons spent inside the coil.

In the DNS set-up the initial polarization is along the vertical guide field. In a combination of two perpendicular coils, one is used to compensate the guide field and the second is used for flipping. (To give an example for typical flipping fields, a $\pi$-flip is achieved by 17 Gauss for neutrons with a wave length of $\lambda = 4$Å and a flight path of 1 cm through the coil.)

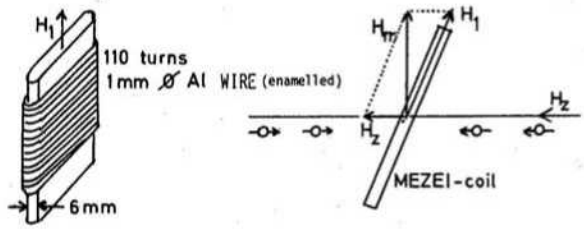



Figure 3: Principle of a neutron $\pi$-spin flipper. The neutrons perform half of a Larmor-precession inside a long rectangular coil. The field $\underline{H}_\pi$ is perpendicular to spin orientation and to the travel direction of the neutron and has to be adjusted to the speed of the neutrons. Here the flipper is tilted to compensate the guide field inside the flipper coil (Fig. from [1]).

A $\boldsymbol{\pi}$ **/2-flip** of the polarization can also be performed with the same flipper coils and will initiate Larmor precessions along the further flight path. A precessing polarization is used for instance in high resolution Neutron Spin Echo spectroscopy (see D.6 Monkenbusch). On the DNS instrument, a precessing neutron polarization technique is used for spherical polariation analysis. Scattering of complex magnetic structures, for example may cause a rotation of $90^o$ and may put the polarization back into a non-precessing mode that can be analyzed.

### 3.2.5 xyz-coils

In order to set the polarization into any desired direction at the sample position, there is (in the simplest version) a set-up of three orthogonal pairs so-called xyz-coils. Fig.3.2.5 illustrates the field setting along x-directio n. One can see that the z-coil has been used

to compensate the guide field at the sample position, and that the x-coils produce a field of a few Gauss. The field is sufficiently strong that the neutron polarization can follow adiabatically the smooth variation of the field, finally turning back into the z-direction of the guide field around the xyz-coils.

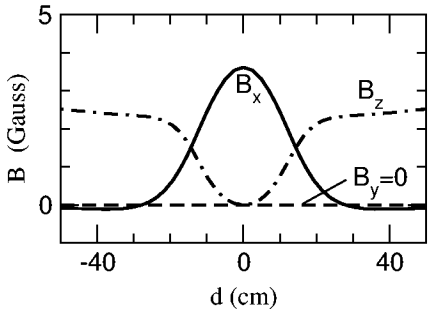



Figure 4: Magnetic field setting by the xyz-coils for an adiabatic nutation of the polarization in x-direction at the sample.

When after a $\pi/2$ flip the polarization is precessing perpendicular to the guide field, the same field conditions that nutate the polarization as shown in Fig.3.2.5 will also turn now adiabatically the precession plane. For an applied field in x-direction the polarization precesses in the yz-plane, and its precession angle at the sample is determined by the total field integral along its flight path and can be tuned in phase by the applied field.

## 3.3 Scattering and polarization

### 3.3.1 Interaction of neutrons with matter

The interaction of neutrons with matter and neutron scattering amplitudes have been introduced before (D.1 Brückel). We briefly recall basics results and discuss effects of scattering events on the polarization (see also textbooks [6, 7]). The total scattering amplitude consists of two parts, a nuclear and magnetic term, that are often comparable in magnitude

$$F_Q = N_{\mathbf{Q}} + \hat{\boldsymbol{\sigma}} \cdot \mathbf{M}_{\mathbf{Q}}^{\perp}. \tag{5}$$

The **nuclear interaction** can be described by a point-like Fermi potential, which is

isotope-specific. The interaction is spin-dependent if the scattering nuclei have a non-zero spin $\mathbf{I}$. Since nuclear spins are usually randomly oriented, this leads to spin-incoherent scattering. In contrast to coherent nuclear scattering, spin-incoherent scattering effects the neutron polarization. As shown in detail in the Appendix, the component of $\mathbf{I}$ parallel to $\mathbf{P}$, say $I_z \parallel P_z$, does not affect $\mathbf{P}$, but the two perpendicular components $I_x$ and $I_y$ change $P_z$ to $-P_z$ upon scattering. Therefore, two thirds of the spin-incoherent scattering is spin-flip scattering, and the final polarisation $\mathbf{P}' = -\frac{1}{3}\mathbf{P}$, has changed in sign, is reduced magnitude, but shows no inclination towards $\mathbf{P}$.

Therefore, we can distinguish three contributions of the nuclear scattering

$$\sigma^N_{\mathbf{Q}} = |N_{\mathbf{Q}}|^2, \text{ with } N_{\mathbf{Q}} = \sum_j b_j e^{i\mathbf{Q}\cdot\mathbf{R}_j} \tag{6}$$
$$\sigma^N_{\mathbf{Q}} = \sigma^N_{\mathbf{Q},coh} + \sigma^N_{isotop-inc} + \sigma^N_{spin-inc}.$$

The coherent part of the nuclear scattering can be separated from the spin-incoherent scattering by measuring spin-flip and non-spin-flip scattering.

The **magnetic interaction** arises from the scattering potential $-\mu \cdot \mathbf{H}$ describing the dipole-dipole interaction between the magnetic moment of the neutron $\mu$ and a magnetic field $\mathbf{H}$ that is due to the spins $\mathbf{s}_j$ of the unpaired electrons $j$ and their orbital momentum $\mathbf{p}_j = -i\nabla_j$. The Fourier transform of the interacting magnetic moments is given by

$$\mathbf{M}_{\mathbf{Q}} = r \int d\tau \psi^*_b(\tau) \sum_j e^{i\mathbf{Q}\cdot\mathbf{R}_j}(\mathbf{s}_j - i(\mathbf{Q} \times \mathbf{p}_j))\psi^*_a(\tau) \tag{7}$$

where $r = |\gamma|e^2/mc^2$ is the magnetic scattering length of an electron and $e^2/mc^2$ is the classical electron radius. As illustrated in Fig. 5 the component of a magnetic dipole field parallel to the scattering vector $\mathbf{Q}$ cancels out. Therefore, in contrast to the spin-incoherent scattering, magnetic scattering is anisotropic with respect to $\mathbf{Q}$ and only $\mathbf{M}^{\perp}_{\mathbf{Q}}$, the component perpendicular to $\mathbf{Q}$ can be observed. The transition matrix elements for magnetic interaction also show the same dependence for the neutron spin operators when applied to components of $\mathbf{M}^{\perp}_{\mathbf{Q}}$ (see Appendix), which is illustrated in Fig. 6. These selection rules including the $\mathbf{Q}$-dependence provide another simple rule: If $\mathbf{P} \parallel \mathbf{Q}$, all magnetic scattering will be spin-flip.

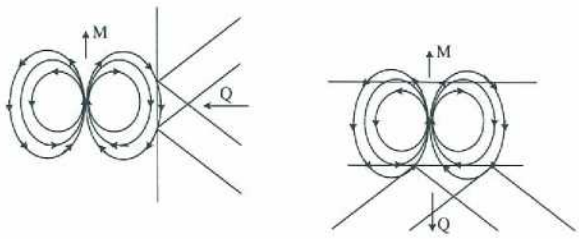



Figure 5: Illustration why only $\mathbf{M}_{\mathbf{Q}}^{\perp}$ is measured. Magnetic field amplitudes of the dipole field show for a) $\mathbf{M} \perp \mathbf{Q}$ constructive interference; and for b) $\mathbf{M} \parallel \mathbf{Q}$ destructive interference.

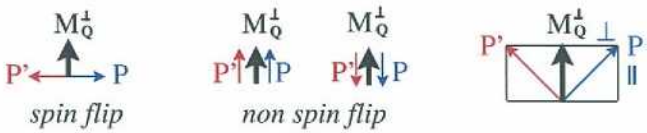



Figure 6: Polarization $\mathbf{P}$ perpendicular to $\mathbf{M}_{\mathbf{Q}}^{\perp}$ reverses sign but not the component parallel to $\mathbf{M}_{\mathbf{Q}}^{\perp}$.

### 3.3.2 Scattering cross-section for polarized neutrons

A theoretical description of neutron scattering including magnetic interactions has been derived by Blume [8] and Maleyev [9]. The scattering process can be completely described by two master equations, (i) for the scattering cross-section $\sigma$ and (ii) for $\mathbf{P}'\sigma$, where $\mathbf{P}'$ denotes the final polarization.

$$\begin{aligned} \sigma_{\mathbf{Q}} &= \sigma^{N}_{\mathbf{Q},coh} + \sigma^{N}_{isotop-inc} + \sigma^{N}_{spin-inc} \\ &\quad + |\mathbf{M}_{\mathbf{Q}}^{\perp}|^2 + \mathbf{P}(N_{-\mathbf{Q}}\mathbf{M}_{\mathbf{Q}}^{\perp} + \mathbf{M}_{-\mathbf{Q}}^{\perp}N_{\mathbf{Q}}) + i\mathbf{P}(\mathbf{M}_{-\mathbf{Q}}^{\perp} \times \mathbf{M}_{\mathbf{Q}}^{\perp}) \end{aligned} \tag{8}$$

$$\begin{aligned} \mathbf{P}'\sigma_{\mathbf{Q}} &= \mathbf{P}\sigma^{N}_{\mathbf{Q},coh} + \mathbf{P}\sigma^{N}_{isotop-inc} - \frac{1}{3}\mathbf{P}\sigma^{N}_{spin-inc} \\ &\quad + \mathbf{M}_{\mathbf{Q}}^{\perp}(\mathbf{P}\mathbf{M}_{-\mathbf{Q}}^{\perp}) + \mathbf{M}_{-\mathbf{Q}}^{\perp}(\mathbf{P}\mathbf{M}_{\mathbf{Q}}^{\perp}) - \mathbf{P}\mathbf{M}_{\mathbf{Q}}^{\perp}\mathbf{M}_{-\mathbf{Q}}^{\perp} \\ &\quad + \mathbf{M}_{\mathbf{Q}}^{\perp}N_{-\mathbf{Q}} + \mathbf{M}_{-\mathbf{Q}}^{\perp}N_{\mathbf{Q}} + i\mathbf{M}_{\mathbf{Q}}^{\perp} \times \mathbf{M}_{-\mathbf{Q}}^{\perp} + i(\mathbf{M}_{\mathbf{Q}}^{\perp}N_{-\mathbf{Q}} - \mathbf{M}_{-\mathbf{Q}}^{\perp}N_{\mathbf{Q}}) \times \mathbf{P} \end{aligned} \tag{9}$$

The first equation shows that for unpolarized neutrons, $\mathbf{P}$=0, one can measure the square of $N_{\mathbf{Q}}$ and the square of $\mathbf{M}_{\mathbf{Q}}^{\perp}$ but some of the scattering terms are not detectable. These terms are related to *nuclear-magnetic interference* and the cross-products of $\mathbf{M}_{\mathbf{Q}}^{\perp}$ to *chiral*

*correlations* $\langle \mathbf{s}_i \times \mathbf{s}_j \rangle$ that can be found in many more complex magnetic materials; as follows from the second equation, due to such terms, polarization can be created in a scattering process.

For $\mathbf{P} = 0$, the scattering contribution due to the interference term of nuclear and magnetic scattering amplitudes as well as the chiral term vanish. On the other hand, polarization may be created by Bragg scattering with nuclear-magnetic interference. For example, for $\mathbf{P} = 0$ and vanishing chiral terms, one obtains

$\sigma_{\mathbf{Q}} = |N_{\mathbf{Q}}|^2 + |\mathbf{M}^{\perp}_{\mathbf{Q}}|^2$ and $\mathbf{P}'\sigma_{\mathbf{Q}} = \mathbf{M}^{\perp}_{\mathbf{Q}} N_{-\mathbf{Q}} + \mathbf{M}^{\perp}_{-\mathbf{Q}} N_{\mathbf{Q}}$, yielding a polarization

$\mathbf{P}' = \frac{\mathbf{P}'\sigma_{\mathbf{Q}}}{\sigma_{\mathbf{Q}}} = \frac{\mathbf{M}^{\perp}_{\mathbf{Q}} N_{-\mathbf{Q}} + \mathbf{M}^{\perp}_{-\mathbf{Q}} N_{\mathbf{Q}}}{|N_{\mathbf{Q}}|^2 + |\mathbf{M}^{\perp}_{\mathbf{Q}}|^2} = 1$, if $N_{\mathbf{Q}} = \mathbf{M}^{\perp}_{\mathbf{Q}}$.

Polarization creation is also possible from scattering of chiral structures, with $\mathbf{P}' = \frac{i\mathbf{M}^{\perp}_{\mathbf{Q}} \times \mathbf{M}^{\perp}_{-\mathbf{Q}}}{\mathbf{M}^{\perp}_{\mathbf{Q}} \cdot \mathbf{M}^{\perp}_{-\mathbf{Q}}}$, and it can be seen also that scattering is sensitive to the sign of the chirality, for instance the helicity of a magnetic spiral.

In general, polarization analysis demands to measure an arbitrary rotation and a change in magnitude of the polarization in a scattering process. The relationship between initial and final polarization vectors, $\mathbf{P}$ and $\mathbf{P}'$ can be conveniently described by a tensor equation

$$P'_i = P_{ij} P_j + P''_i, \tag{10}$$

defining a 3 $\times$ 3 polarization matrix $P_{ij}$ that rotates the initial polarization $\mathbf{P}$, while $\mathbf{P}''$ is the polarization that is created by the scattering process. The polarization matrix $P_{ij}$ and $\mathbf{P}''$ can be determined experimentally.

### 3.3.3 Spin-flip and non-spinflip scattering

One interesting application of polarized neutron scattering is the separation of coherent and spin-incoherent scattering. Typical soft matter samples contain hydrogen which causes a huge spin-incoherent background in the wide-angle scattering that contains information about local correlations. Here, a precise determination of coherent scattering, ideally combined with the method of contrast variation, can be achieved by measuring spin-flip and non-spin-flip scattering. Fig.3.3 .3 shows the separated coherent scattering of a polymer glass. Such results can be compared to those obtained in molecular dynamics simulations of theoretical polymer models [10]. A recent application to water also showed

that the simplest type of polarization analyis provides a new, unprecedented quality of data and a better insight into local correlations in water [11].

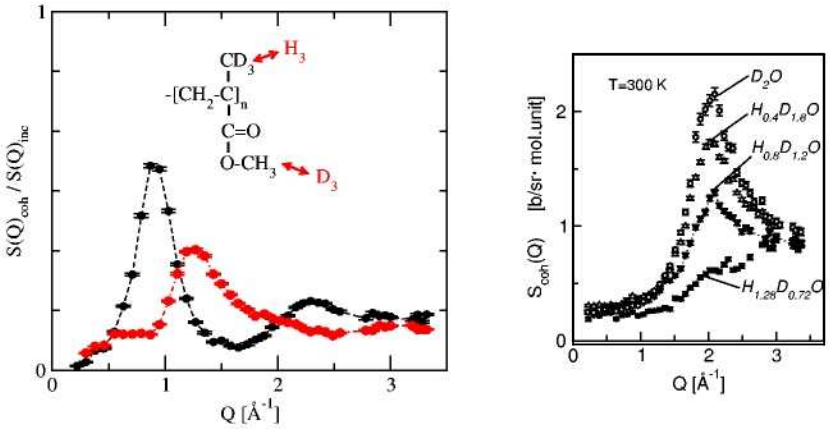



Figure 7: Neutron polarisation analysis separates coherent scattering from spin-incoherent scattering which is typically a disturbing large background in materials that contain hydrogen. The examples show results for the coherent scattering of (left) a polymer glasses [10] and (right) water [11]. Both experiments also show the effect of H/D contrast.

### 3.3.4 xyz-polarization analysis

In order to separate magnetic scattering, one needs a polarization analysis with directional dependence. The standard technique has been developed by Moon, Riste and Koehler in a seminal paper[12], and is usually called longitudinal polarization analysis (LPA). In LPA the change of polarization is measured with respect to an applied field, and allows one to determine the trace of the (3×3) polarization matrix. This method cannot identify all magnetic scattering contributions; scattering with chirality and magnetic-nuclear interference may change the direction of the polarization and appear as an apparent depolarization. However, paramagnetic scattering and scattering from collinear magnetic structures can be separated from nuclear scattering by measuring both with polarization parallel and perpendicular to **Q**. The difference retains only magnetic scattering contributions [13]. This principle is also used in the method of xyz-polarization analysis [14], where the polarization is set into three orthogonal directions. This requires an ad-

ditional measurement, however, it also applies for larger area- or multi-detectors, when $\mathbf{P} \parallel \mathbf{Q}$ cannot be achieved simultaneously. A measurement with $\mathbf{P}$ along z-direction is perpendicular to the scattering plane and thus to $\mathbf{Q}$; measurements with $\mathbf{P}$ along the x- and y-direction in the scattering plane comprise the sum of the intensities with initial polarization parallel and perpendicular to $\mathbf{Q}$. Hence, the paramagnetic scattering or the scattering of anti-ferromagnetic powder samples is given by [14]:

$$\frac{d\sigma}{d\Omega}_{pm} = 2\left(\frac{d\sigma}{d\Omega_{\mathrm{x}}}^{SF} + \frac{d\sigma}{d\Omega_{\mathrm{y}}}^{SF} - 2\frac{d\sigma}{d\Omega_{\mathrm{z}}}^{SF}\right) = -2\left(\frac{d\sigma}{d\Omega_{\mathrm{x}}}^{NSF} + \frac{d\sigma}{d\Omega_{\mathrm{y}}}^{NSF} - 2\frac{d\sigma}{d\Omega_{\mathrm{z}}}^{NSF}\right), \quad (11)$$

Any nuclear scattering will be eliminated by these differences. An application of xyz-polariation analysis to magnetic spin-fluctu ations in a geometrically frustrated lattice is given below.

### A highly frustrated spin system: the kagome anti-ferromagnet

The topology of many crystal structures has an important influence on the collective behavior of interacting magnetic moments. In lattices with triangular networks, the anti-ferromagnetic (AF) coupling between all spins can not be satisfied simultaneously owing to geometrical frustration that strongly reduces the ordering temperature and disturbs the settling of the system into a long range ordered state. A typical signature of geometrical frustration is the appearance of non-collinear and chiral spin configurations. In addition, ordering is particularly difficult in lower dimensions. According to the Mermin-Wagner theorem, the Heisenberg AF does not order in 2D lattices at any finite temperature.
We shall discuss such an example of high spin frustration and show recent results on low-temperature spin correlations in a new oxide material, the compound $Y_{0.5}Ca_{0.5}BaCo_4O_7$, that exhibits a layering of Co-atoms in a kagomé lattice, see Fig. 8. The ground state of kagomé AF exhibits an infinite degeneracy, with a co mpetition between two different chiral structural motifs, depicted in Fig. 9. Diffuse neutron scattering experiments with xyz-polarization analysis performed on the DNS instrument achieved a separation of magnetic scattering from nuclear coherent spin-incoherent background.
The temperature dependence of the magnetic scattering, see Fig. 8, does not show long range order at low T, although according to susceptibility measurements, the Curie-Weiss temperature (the mean-field estimate of the ordering temperature) is about 2000

K. Furthermore, the asymmetric shape of the diffuse peak is characteristic for 2-D spin correlations.

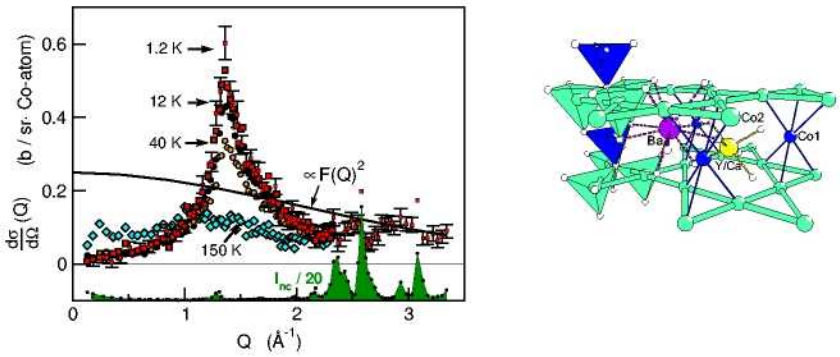



Figure 8: *(left)* Temperature dependence of the diffuse magnetic scattering; data are calibrated by the spin-incoherent scattering of Co (0.382 b/sr); the separated nuclear coherent scattering, $I_{nc}$, has been rescaled and shifted (bottom part). *(right)* The $Y_{0.5}Ca_{0.5}BaCo_4O_7$ crystal structure. Thicker bonds between the Co2 atoms highlight the kagomé layers.

The magnetic scattering can be described in terms of the Fourier transform of the spin pair-correlations [16]

$$\frac{d\sigma}{d\Omega}_{mag}(Q) = \frac{2}{3} r_0^2 F_Q^2 \sum_r \langle \underline{S}_0 \cdot \underline{S}_r \rangle \frac{\sin Qr}{Qr}, \tag{12}$$

where $Q$ is the modulus of the scattering vector, $r_0 = -0.54 \times 10^{-12}$cm the magnetic scattering length, $S$ the spin quantum number of the scattering ion, and $F_Q$ the magnetic scattering form-factor of a single $Co^{2+}$ ion. By this quantitative description it is possible to determine the average Co spin moment. The most plausible explanation is a Co high spin state 3/2 in the kagomé layers and a low spin S=0 state in the intermediate layers, which explains the 2-D character by a decoupling of the kagomé layers. The low-T data has been normalized to $S(Q) = \sum_r \langle \hat{S}_0 \cdot \hat{S}_r \rangle \sin Qr/(Qr)$, where $\hat{S}$ are unit length spins, see Fig. 9. Spin correlations $\langle \hat{S}_0 \cdot \hat{S}_r \rangle$ based on the two competing chiral structures have been modeled with a suitable asymptotic spatial decay function ($\propto r^{-\eta}$, $\eta$ 0.6) and reveal a clear preference for the $\sqrt{3} \times \sqrt{3}$ structure. One can also obtain the spin correlations by Fourier analysis, using a linear least squares refinement, see Fig. 9. Compared to the model of the $\sqrt{3} \times \sqrt{3}$ structure, a peak (at $\mathbf{q}_{\sqrt{3}}$) is missing in the data, indicating an

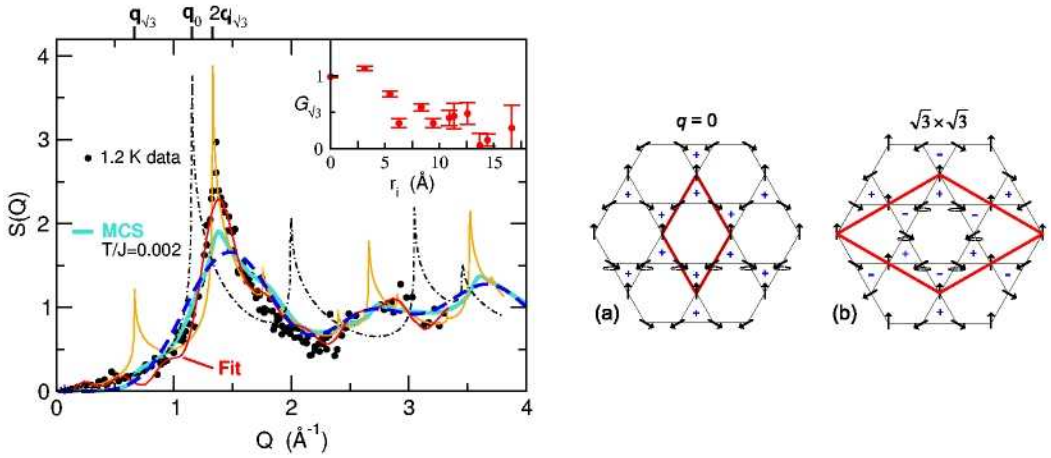



Figure 9: Modeling of 1.2 K scattering data. (i) power law decay of spin correlations (thin lines, dashed dotted and solid) in the $q_0$ and $\sqrt{3} \times \sqrt{3}$ structures respectively; (ii) Fourier analysis (Fit), yielding $G_{\sqrt{3}}$ (inset) spin correlations normalized to those of the $\sqrt{3} \times \sqrt{3}$ structure with ideal staggered chirality; (iii) Monte Carlo simulation (MCS) data (thick line) for a classical Heisenberg AF at $T/J = 0.002$ [17]; (iv) hexagon spin mode (dashed line) see also Fig. 10.

incompletely ordered ground state of the system in agreement with earlier Monte Carlo simulations [17].

The $\sqrt{3} \times \sqrt{3}$ structure is entropically favored, because of local degeneracies of the spin alignments on hexagon. Spins on hexagons gather in a collective local rotations, a characteristic feature of the disorder at low T, on one side. On the other side, this dynamic correlation is a robust feature driving the structural formation, a reason why the selectionof the $\sqrt{3} \times \sqrt{3}$ structure has been called an *order by disorder phenomenon.* The hexagon mode can still be seen in the quasi-elastic paramagnetic scattering at intermediate temperatures, see Fig. 10,

### 3.3.5 Spherical polarization analysis

Spherical polarization analysis is a recent development, which allows to determine complex magnetic structures that cannot be uniquely identifed by other standard techniques. The method has been successfully applied to anti-ferromagnets with propagation vector $\mathbf{q} = 0$,

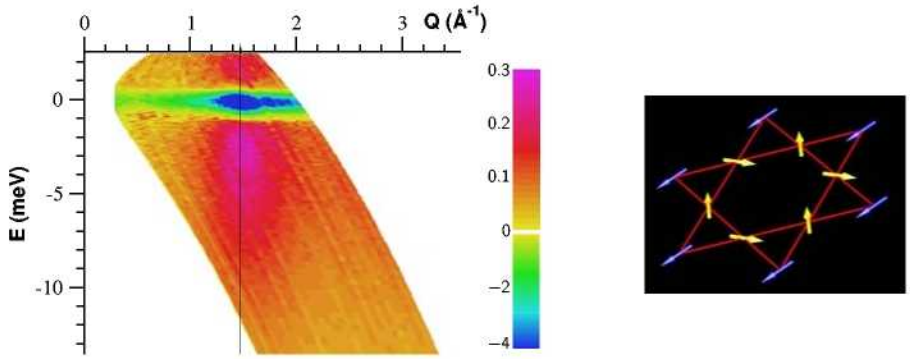



Figure 10: Quasi-elastic broadening due to thermal spin fluctuations. The difference of S(Q,$\omega$) measured at 150 K and 40 K in time-of-flight mode reveals a loss of elastic intensity (blue) and a relaxation response (red) with a Q-dependence consistent with hexagon spin modes (right).

where the magnetic and nuclear structure has the same unit cell size and structure factors are in phase quadrature, to spiral structures, systems with magnetic domains, and to systems in which ferro-electricity couples to magnetism, etc. All these examples cause a change of polarization in the scattering process, such that the final polarization will be tilted from the initial polarization. Using standard LPA and applying a magnetic field, the final polarization starts to precess and only the projection to the field is measured. The transverse precessing components have been (falsely) believed to depolarize rapidly and to be lost. Therefore, one has built zero-field chambers, using superconducting Meissner screens, best known is the device CryoPAD developed at the ILL. Clearly zero-field avoids any precession of the polarization, and the polarization of the scattered intensity can be realigned by a flipper-coil parallel to the ex ternal field guiding the polarization to the analyzer.

Of course, it is also possible to work with precessing polarization and this is used in diverse neutron instruments. Very recently, spherical polarization analysis has been developed with a new precession technique on the DNS instrument [20, 21]. Therefore, one starts with a precessing initial polarization analyzing only the non-precessing final polarization. A simulation is shown in Fig. 3.3.5 and an experimental verification can be seen in Fig. 12.

One of the early successful examples of spherical polarization analysis solving a com-

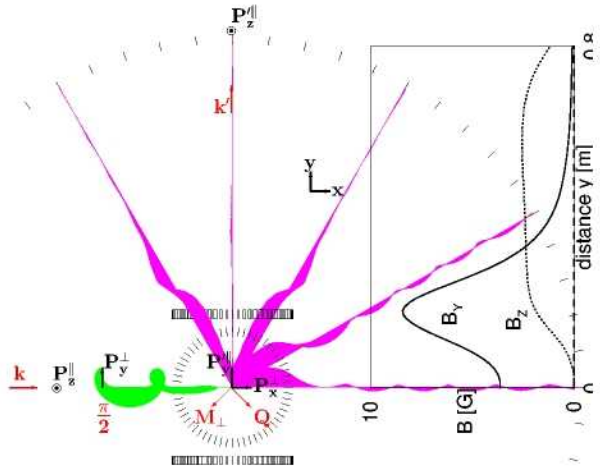



Figure 11: Simulation of precessing neutron polarisation analysis for typical parameters of the DNS instrument. Neutrons with wave-vector $\underline{k}$ are polarized in $P_z$ undergo a $\pi/2$-flip into $P_y$, then precess to the sample into $P_x$ in a field turning the normal vector of the precessing plane from z to y. Scattering is simulated for five different scattering angles, and in each case the final polarization turns up adiabatically from $P_y$ to $P_z$. The inset shows the field variation for 90 $^o$ scattering.

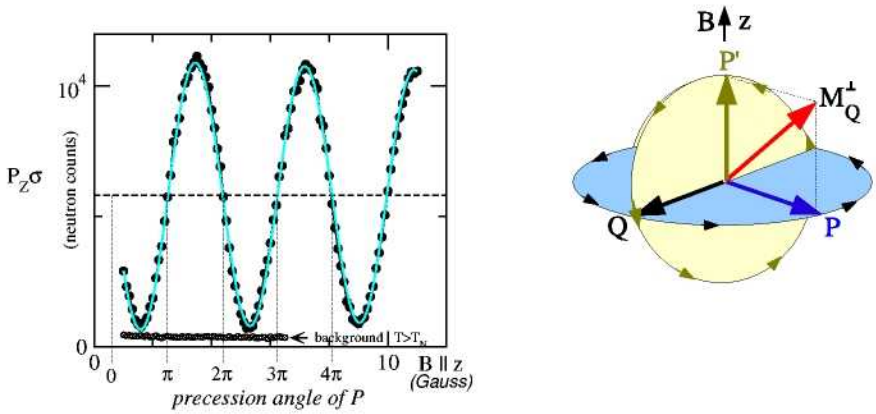



Figure 12: $\mathbf{P}'\sigma$ versus a precessing initial polarization $\mathbf{P}$ for magnetic Bragg scattering of $MnF_2$, with moments inclined by 45°. (The precision in phase is 0.5 degrees keeping up to 98% of the polarization).

plex antiferromagnetic structure is the study of $U_{14}Au_{51}$ (with zero-field polarimetry on CryoPAD-2)[22]. It is a magnetic structure with zero propagation vector, for which nuclear and magnetic Bragg peaks coincide. We repeated the experiment on DNS with the new precession technique. Fig. 13 illustrates the identification of nuclear and magnetic scattering for the (201) Bragg peak. The crystal is oriented vertically with its b-axis parallel to z. The spins are ordered within the a-b plane with a hexagonal star-like structure. The nuclear scattering is confirmed by a measurement above the Neel temperature at 30K and remains independent of the polarisation. Maxima are found for a rotation of the polarisation from the z to the y direction. For an initial polarisation along x (which is set parallel to the scattering vector) only spin-flip scattering is observed for the magnetic scattering, as it must be. For all cases, when taking nuclear scattering into account, an effective depolarisation is observed. These results are in excellent agreement with the results obtained with CryoPAD [22].

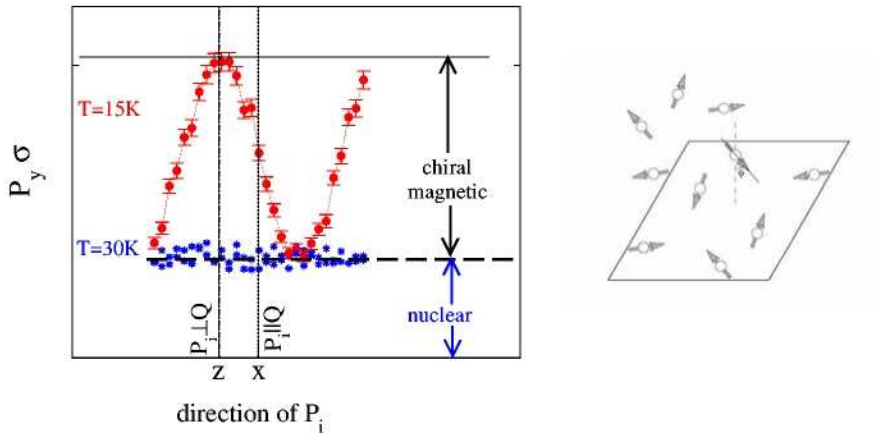



Figure 13: Spherical polarisation analysis on the (201) Bragg peak of $U_{14}Au_{51}$. Initially the polarisation precesses perpendicular to the applied field in y-direction. At 30 K there is only a nuclear Bragg component which continues to precess after the scattering event. At lower temperatures, T=15 K, there is an additional magnetic contribution for which the neutron polarisation changes from $P_i \parallel z$ to $P_f \parallel y$.

## 3.4 Final remarks

In this lecture we have considered only a few applications of polarized neutron scattering. Interested readers are referred to the literature [23, 24] and references therein. Plakhty has given a recent review on chiral scattering[25] which exhibit critical exponents that belong to new universality classes. Such experiments demand single crystalline samples with a preference for one of the usually two occuring domains with left and right handed screws.

Considering instrumentation for polarization analysis, such as the DNS instrument or the similar instrument D7 (ILL), there has been an enormous gain in efficiency compared to the original set-up of Moon, Riste and Koehler. There are new developments in progress, for instance the so-called Pastis set-up at the ILL Grenoble, a He-3 filter cell best suited for polarization analysis of thermal neutrons, which are needed to investigate higher energy excitations. The He-3 polarizer which will also cover more efficiently a larger solid angle for detection. However,, requirements for field homogeneity are very challenging.

The new precessing technique for spherical neutron polarization analysis has the great advantage compared to zero-field methods, that it is not necessary anymore to align the final polarization with respect to the guide field. Apart from avoiding complicated cryogenic sample enviroments and zero-field restrict ions, the more important progress is that $\mathbf{P}'$ can be simultaneously measured independent of momentum and energy transfer, and the realization of spherical polarization analysis on a multi-detector and time-of-flight instrument. Hence, this method will have a great future potential for the diffuse scattering involving magnetic fluctuations and may reveal new insights in correlations between magnetic fluctuations and structural or lattice fluctuations, for example, in high $T_c$ superconductors and in the recently discovered multi-ferroica. Complex and chiral spin ordering is characteristic for these materials where electric fields couple to magnetic properties. Strongly coupled magnetic moments that do not settle into stable ordering because of geometrical frustration or because of low dimensionality of space can be influenced and determined by rather subtle higher order interaction terms. Hence unexpected and promising rich and interesting complex phenomena may emerge. Magnetic fluctuations are considered to be of fundamental importance for the mechanism of unconventional superconductivity. For example, alternatively to the common picture of collinear stripes with sinusoidal AF

spin correlations fluctuations from a spiral spin phase ground state have been proposed recently [26] explaining the inelastic magnetic response; in order to test such a interesting hypothesis, tools of neutron polarization analysis will be required.

## Appendix

### Nuclear scattering

The interaction of thermal and cold neutrons with the nuclei of of scattering system is given by the sum of Fermi potentials $V(r) = \frac{2\pi\hbar^2}{m_N} b\delta(r)$, where b is a scalar complex parameter called scattering length. Tabulated values comprise average scattering lengths for each element, with further distinction of scattering lengths of isotopes[27]. The interaction potential depends also on the spin of the scattering compound of nucleus and neutron. Therefore, if the nucleus has a non-zero spin, one can distinguish further the scattering lengths $b_+$ and $b_-$ for parallel and anti-parallel spin alignment. If the nucleus has zero spin, there is of course no spin-dependent interaction potential.

In general, we can decompose the nuclear scattering into two parts, the average coherent nuclear scattering and the spin-dependent and spin-incoherent scattering. The reason why the latter part is incoherent, except for some unusual cases, is because the orientation of nuclear spins is given by a random distribution.

Therefore, in general, the scattering length needs to be replaced by the scattering length operator $\mathbf{b} = A + B\,\boldsymbol{\sigma}\cdot\mathbf{I}$ with $A = \frac{(I+1)\,b_+ + I\,b_-}{2I+1}$ and $B = \frac{b_+ - b_-}{2I+1}$ where $\mathbf{I}$ denotes the nuclear spin operator. One may calculate the transition probability from the initial spin state $|S\rangle$ to the final spin state $\langle S'|$, which yields the scattering amplitude $\mathrm{A}_{\mathbf{Q}}$, assuming an arbitrary orientation of the neutron spin, say along z-direction,

$$\mathrm{A}_{\mathbf{Q}} = \langle S'_{(z)}|A + B\boldsymbol{\sigma}\cdot\mathbf{I}|S_{(z)}\rangle = \begin{cases} A + B\mathrm{I}_z & \left\{ \begin{array}{l} + \rightarrow + \\ - \rightarrow - \end{array} \right\} NSF \\ B(\mathrm{I}_x + \mathrm{i}\mathrm{I}_y) & \left\{ \begin{array}{l} + \rightarrow - \\ - \rightarrow + \end{array} \right\} SF \end{cases} \tag{13}$$

Thermal averaging yields, for random orientation of nuclear spins $\langle \mathrm{I}_x \rangle = \langle \mathrm{I}_y \rangle = \langle \mathrm{I}_z \rangle = 0$, so that the (coherent) scattering amplitude is given only by the non-spin flip matrix

element equal to $A \equiv b_{coh} = \bar{b}$ and the coherent nuclear scattering is proportional to the square of $\bar{b}^2$

$$\frac{d\sigma}{d\Omega}^{(NSF)}_{coherent} = \bar{b}^2 \sum_{\mathbf{r},\mathbf{r}'} \mathrm{e}^{\mathrm{i}\mathbf{Q}\cdot(\mathbf{r}'-\mathbf{r})}. \tag{14}$$

*The coherent nuclear scattering does not change the polarization of the neutrons.*

We have used that the neutron spin operator $\sigma$ can be described by the Pauli-spin matrices $\underline{\underline{\sigma}}_\alpha$

$$\underline{\underline{\sigma}}_{\mathrm{x}} = \begin{pmatrix} 0 & 1 \\ 1 & 0 \end{pmatrix}, \underline{\underline{\sigma}}_{\mathrm{y}} = \begin{pmatrix} 0 & -\mathrm{i} \\ \mathrm{i} & 0 \end{pmatrix}, \underline{\underline{\sigma}}_{\mathrm{z}} = \begin{pmatrix} 1 & 0 \\ 0 & -1 \end{pmatrix} \tag{15}$$

When applied to spin-up and down states $|+\rangle = \begin{pmatrix} 1 \\ 0 \end{pmatrix}$ and $|-\rangle = \begin{pmatrix} 0 \\ 1 \end{pmatrix}$ respectively, one obtains the following relations:

$$\begin{aligned} \underline{\underline{\sigma}}_{\mathrm{x}}|+\rangle &= \ |-\rangle \quad , \quad \underline{\underline{\sigma}}_{\mathrm{x}}|-\rangle = \ \ |+\rangle \\ \underline{\underline{\sigma}}_{\mathrm{y}}|+\rangle &= \mathrm{i}\,|-\rangle \quad , \quad \underline{\underline{\sigma}}_{\mathrm{y}}|-\rangle = -\mathrm{i}\,|+\rangle \\ \underline{\underline{\sigma}}_{\mathrm{z}}|+\rangle &= \ |+\rangle \quad , \quad \underline{\underline{\sigma}}_{\mathrm{z}}|-\rangle = \ -|-\rangle\,. \end{aligned} \tag{16}$$

The incoherent scattering intensity is determined only by the thermal average of the squares of the matrix elements. With $\langle \mathrm{I}_{\mathrm{x}}^2 \rangle = \langle \mathrm{I}_{\mathrm{y}}^2 \rangle = \langle \mathrm{I}_{\mathrm{z}}^2 \rangle = \frac{1}{3}\mathrm{I}\langle |\mathrm{I}+1\rangle$ and Eq. (13), the spin-incoherent scattering (per atom)

$$\frac{d\sigma}{d\Omega}^{(\substack{+-+ \\ --},NSF)}_{spin-incoherent} = (\bar{b^2} - \bar{b}^2)^{NSF} = \frac{1}{3}\langle B^2 \mathrm{I}(\mathrm{I}+1)\rangle \tag{17}$$

$$\frac{d\sigma}{d\Omega}^{(\substack{+-- \\ --+},SF)}_{spin-incoherent} = (\bar{b^2} - \bar{b}^2)^{SF} = \frac{2}{3}\langle B^2 \mathrm{I}(\mathrm{I}+1)\rangle \tag{18}$$

*The result is that 1/3 of the spin-incoherent part of the nuclear scattering is non-spin flip scattering and 2/3 of it is spin-flip scattering, and it is independent of the (direction) of an external field* $\mathbf{H}$.

### Magnetic scattering

For pure magnetic scattering we consider the interaction of the neutron magnetic moment $\boldsymbol{\mu}_N$ with the magnetic feld of the electrons $\mathbf{B} = \mathbf{B}_{spin} + \mathbf{B}_{orbital}$ due to spin and orbital

momentum. The magnetic interaction potential $V_m = -\mu_n \cdot \mathbf{B}$ defines the magnetic scattering amplitude

$$A_{\mathbf{Q}} = \langle S'_z | \frac{-\gamma_n r_o}{2\mu_B} \boldsymbol{\sigma} \cdot \mathbf{M}^{\perp}_{\mathbf{Q}}) | S_z \rangle = \frac{-\gamma_n r_o}{2\mu_B} \sum_{\alpha} \langle S'_z | \underline{\sigma}_{\alpha} | S_z \rangle \, M_{\alpha,\mathbf{Q}} \, . \tag{19}$$

Here $\gamma_n = -1.913$ denotes the magnetic dipole moment of the neutron expressed in nuclear magnetons $\mu_N = 5.051 \cdot 10^{-27} J/T$, and $r_0 = e^2/(m_e c^2)$ is the classical electron radius. Inserting the relations of Eq.(16) into Eq. (19) we obtain the matrix elements (scattering amplitudes) for spin-flip and non-spin flip scattering:

$$A_{\mathbf{Q}} = \frac{-\gamma_n r_o}{2\mu_B} \times \begin{cases} \mathbf{M}^{\perp}_{z,\mathbf{Q}} \\ -\mathbf{M}^{\perp}_{z,\mathbf{Q}} \\ (\mathbf{M}^{\perp}_{x,\mathbf{Q}} - i\mathbf{M}^{\perp}_{y,\mathbf{Q}}) \\ (\mathbf{M}^{\perp}_{x,\mathbf{Q}} + i\mathbf{M}^{\perp}_{y,\mathbf{Q}}) \end{cases} \text{for} \begin{cases} + \rightarrow + \quad \text{(NSF)} \\ - \rightarrow - \quad \text{(NSF)} \\ + \rightarrow - \quad \text{(SF)} \\ - \rightarrow + \quad \text{(SF)} \end{cases} \tag{20}$$

Different to the coherent nuclear scattering now we can also observe "spin-flip" processes that reverse the neutron spin direction. Recall that $\mathbf{M}^{\perp}_{\mathbf{Q}}$ is the perpendicular component of $\mathbf{M}_{\mathbf{Q}}$ with respect to the scattering vector $\mathbf{Q}$, and the neutron polarization has been chosen parallel to an external field $\mathbf{H}_z$. We obtain two rules for the magnetic scattering:

*The "spin-flip" processes are observed for the component* $\mathbf{M}^{\perp}_{\mathbf{Q}}$ *that is perpendicular to the neutron polarization. The "non-spin flip" processes are observed for the component of* $\mathbf{M}^{\perp}_{\mathbf{Q}}$ *that is parallel to the neutron polarization.*

# References


[1] O. Schärpf, in *Neutron Spin Echo* Lecture Notes in Physics **128**, Ed. F. Mezei, Springer (1980) 27-52.

[2] F. Klein, *The mathematical theory of the top*, Princeton 1897; see also H. Goldstein, *Klassische Mechanik*, Akademische Verlagsges. Frankfurt am Main (1974).

[3] W. Schweika and P. Böni, Physica B **297**, 155 (2001).

[4] O. Schärpf, Physica B **182** (1992) 376.

[5] O. Schärpf, J. Physics E: Sci. Instrum. **8** (1975) 268; F. Mezei, Commun. Phys. **1** (1976) 81; P. Böni, J. Neutron Research **5** (1996) 63.

[6] G.L. Squires, *Introduction to the theory of thermal neutron scattering*, Cambridge University Press, Cambridge (1978).

[7] S.W. Lovesey, *Theory of neutron scattering from condensed matter*, Volume 2: Polarization and magnetic scattering, Clarendon Press, Oxford (1987).

[8] M. Blume, Phys. Rev. **130** (1963) 1670; Phys. Rev. **133** (1964) A1366.

[9] S.V. Maleyev, Zh. Eksperim. i Teor. Fiz. **33** (1958) 129 [English Translation: Soviet Phys.-JETP **34** (1958) 89]; S.V. Maleev, Zh. Eksperim. i Teor. Fiz. **40** (1961) 1224 [English Translation: Soviet Phys.-JETP **13** (1961) 860].

[10] A. C. Genix *et. al.* Macromolecules **39** (2006) 3947.

[11] L. Temleitner, L. Pusztai, and W. Schweika, J. Phys. Cond. Mat., accepted (2007).

[12] R.M. Moon, T. Riste, W.C. Koehler, Phys. Rev. **181** (1969) 920.

[13] G. Shirane, Y.J. Uemura, J.P.Wicksted, Y. Endoh, Y. Ishikawa, Phys. Rev. B **31** (1985) 1227.

[14] Th. Brückel, *Dissertation* Tübingen (1988); O. Schärpf, H. Capellmann, Phys. Stat. Sol. (a) **135** (1993) 359.

[15] W. Schweika, M. Valldor, P. Lemmens, Phys. Rev. Lett. **98**, 067201 (2007).

[16] Eq.12 holds in the limit $|J| \gg T$.

[17] J. N. Reimers and A. J. Berlinsky, Phys. Rev. B **48** (1993) 9539.

[18] F. Tasset, Physica B **156-157** (1989) 627; F. Tasset, Physica B **241-243** (1998) 177.

[19] P. J. Brown, J. B. Forsyth, and F. Tasset, Proc. Roy. Soc. London A 442 (1993) 147; P.J. Brown, *Polarimatric Neutron Scattering*, in lecture notes on *Polarized Neutron Scattering* (Eds. Th. Brückel and W. Schweika), Schriften des Forschungszentrums Jülich, Series Matter and Materials Vol.12, Forschungszentrums Jülich (2002).

[20] W. Schweika, Physica B **335** (1-4), (2003) 157-163.

[21] W. Schweika, S. Easton, and K.-U. Neumann, Neutron News **16** (2005) 14.

[22] P. J. Brown, J. Crangle, K.-U. Neumann, J. G. Smith, and K. R. A. Ziebeck, J. Phys.: Cond. Mat. **9** (1997) 4729.

[23] J. R. Stewart, K. H. Andersen, R. Cywinski, and A. P. Murani, J. Appl. Phys. **87** (2000) 5425.

[24] B. Roessli, P. Böni, cond-mat/0012180.

[25] V. P. Plakhty *et al.*, Physica B **385-386** (2006) 441-451.

[26] P.-A. Lindgard, Phys. Rev. Lett. **95** (2005) 217001.

[27] V. F. Sears, Neutron News **3** (1992).

# 4

# Correlation Functions Measured by Scattering Experiments

Reiner Zorn and Dieter Richter

# 4. Correlation Functions Measured By Scattering Experiments

Reiner Zorn, Dieter Richter

In this lecture static and dynamic correlation functions will be introduced. We will start by introducing probability densities, relate those to the scattering cross section and define the pair correlation function. Two examples will be given, one from the physics of liquids and one from polymer physics. The concept of dynamic correlation functions will be explained firstly by the example of correlation spectroscopy. Then the Van Hove correlation function will be introduced which is the basis for the calculation of the double differential scattering cross section. Finally, the concept will be applied to the example of an ideal gas.

## 4.1 Probability Densities

We start by considering a homogeneous monatomic liquid with $N$ atoms in a volume $V$. We denote the probability to find a certain atom in a volume element $\mathrm{d}^3r$ at $\underline{r}$ by $P(\underline{r})\mathrm{d}^3r$. Because of the homogeneity $P(\underline{r})$ is constant and evidently

$$P(\underline{r}) = \frac{1}{V}\,. \tag{4.1}$$

Then the number density of atoms at $\underline{r}$ is

$$\rho(\underline{r}) = NP(\underline{r}) = \frac{N}{V} \equiv \rho_0\,. \tag{4.2}$$

We call the probability density to find a certain atom at $\underline{r}_1$ and another at $\underline{r}_2$ $P(\underline{r}_1, \underline{r}_2)$. This function fulfills the basic relations

$$P(\underline{r}_1, \underline{r}_2) = P(\underline{r}_2, \underline{r}_1) \text{ and} \tag{4.3}$$

$$\int_V \mathrm{d}^3r_2 P(\underline{r}_1, \underline{r}_2) = P(\underline{r}_1)\,. \tag{4.4}$$

If there is no interaction between the atoms $P(\underline{r}_1, \underline{r}_2)$ factorizes into

$$P(\underline{r}_1, \underline{r}_2) = P(\underline{r}_1)P(\underline{r}_2)\,. \tag{4.5}$$

In real liquids however usually an interaction exists which depends (only) on the distance of the atoms $\underline{r}_{12} = \underline{r}_2 - \underline{r}_1$. We express the deviation from (4.5) by a pair correlation function defined by

$$g(\underline{r}_{12}) \equiv \frac{P(\underline{r}_1, \underline{r}_2)}{P(\underline{r}_1)P(\underline{r}_2)} \,. \tag{4.6}$$

With the pair distribution function $n(\underline{r}_1, \underline{r}_2) = N(N-1)P(\underline{r}_1, \underline{r}_2)$ which expresses the probability density for any pair of atoms to occupy positions $\underline{r}_1$ and $\underline{r}_2$ we obtain

$$g(\underline{r}_{12}) = \frac{n(\underline{r}_1, \underline{r}_2)}{{\rho_0}^2} \tag{4.7}$$

because in the limit of large $N$ we have $N(N-1) \approx N^2$.

The qualitative features of the pair correlation function are shown in figure 4.1. For $r \to 0$ one finds $g(r) = 0$ because two atoms cannot be at the same position. Usually, this is also true for distances $r < r_0$ because the atoms cannot penetrate each other and have a "hard core" radius $r_0$. For $r \to \infty$ the limit is $g(r) = 1$ because the interactions decay with distance and the $P(\underline{r}_1, \underline{r}_2)$ reverts to its default value 4.5. At intermediate distances $g(r)$ shows a peak because the probability density which is lacking at $r < r_0$ must be compensated. Its location is usually close to the minimum of the interatomic potential, i.e. close to the average next neighbour distance $r_{\mathrm{nn}}$.

Using the pair correlation function one can formulate the differential neutron cross section for a monatomic liquid[1]

$$\left(\frac{\mathrm{d}\sigma}{\mathrm{d}\Omega}\right)_{\mathrm{coh}} = |\overline{b}|^2 \left\langle \sum_{i,j=1}^{N} \exp\left(\mathrm{i}\underline{Q} \cdot \left(\underline{r}_i - \underline{r}_j\right)\right) \right\rangle \,. \tag{4.8}$$

Here $(\mathrm{d}\sigma/\mathrm{d}\Omega)_{\mathrm{coh}}$ denotes the angle dependent coherent scattering cross section and $\overline{b}$ is the average scattering length of the liquid atoms. $\underline{Q}$ is the scattering vector, i.e. the difference between incoming and scattered wave vector of the radiation, $\underline{Q} = \underline{k} - \underline{k}'$. The average in the expression can be evaluated using the pair correlation function (4.7):

$$\left(\frac{\mathrm{d}\sigma}{\mathrm{d}\Omega}\right)_{\mathrm{coh}} = |\overline{b}|^2 \left(1 + \left\langle \sum_{i \neq j}^{N} \exp\left(\mathrm{i}\underline{Q} \cdot \left(\underline{r}_i - \underline{r}_j\right)\right) \right\rangle\right)$$

[1] Exactly speaking, this expression is valid only for mon*isotopic* liquids. Otherwise, there would be an additional incoherent term like the one discussed for the dynamic correlation function in section 4.3. Nevertheless, this term is just a constant and therefore only visible as a flat background in the experiment. The $Q$ dependent (coherent) part of the cross section is still correctly represented by (4.8).

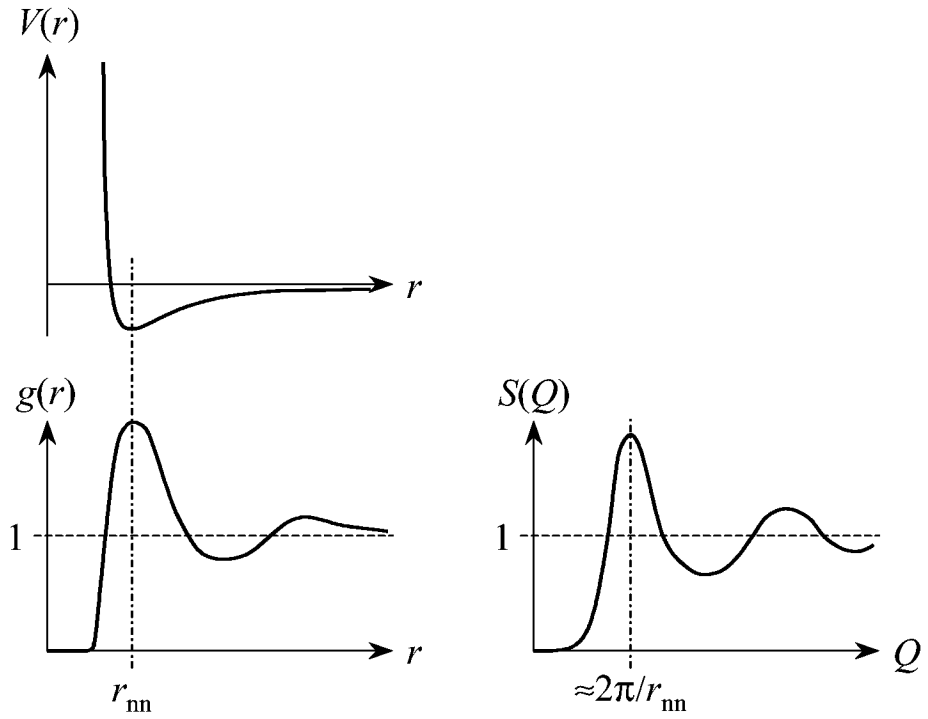



Figure 4.1: Schematic representation of interaction potential $V(r)$, pair correlation function $g(r)$, and scattering function $S(Q)$.

$$\begin{aligned} &= |\bar{b}|^2 \left( N + \int_V \mathrm{d}^3 r_1 \int_V \mathrm{d}^3 r_2 n(\underline{r}_1, \underline{r}_2) \exp\left(\mathrm{i}\underline{Q} \cdot (\underline{r}_1 - \underline{r}_2)\right)\right) \\ &= |\bar{b}|^2 \left( N + {\rho_0}^2 V \int_V \mathrm{d}^3 r_{12} g(\underline{r}_{12}) \exp\left(\mathrm{i}\underline{Q} \cdot \underline{r}_{12}\right)\right) \\ &= |\bar{b}|^2 N \left( 1 + \rho_0 \int_V \mathrm{d}^3 r_{12} g(\underline{r}_{12}) \exp\left(\mathrm{i}\underline{Q} \cdot \underline{r}_{12}\right)\right) . \end{aligned} \tag{4.9}$$

This equation states that the scattering cross section can be represented as the Fourier transform of the pair correlation function. Assuming isotropy (as is found in the homogeneous liquid discussed here) one can replace $g(\underline{r}_{12})$ by the radial correlation function $g(r)$:

$$\left(\frac{\mathrm{d}\sigma}{\mathrm{d}\Omega}\right)_{\mathrm{coh}} = |\bar{b}|^2 N \left( 1 + 4\pi\rho_0 \int_0^\infty r^2 \mathrm{d}^3 r g(r) \frac{\sin Qr}{Qr} \right) \tag{4.10}$$

Equation (4.10) follows from (4.9) by radial averaging of $\exp\left(\mathrm{i}\underline{Q} \cdot \underline{r}_{12}\right)$ (i.e. an average over all possible orientations of $\underline{r}_{12}$).

The term in big parentheses of equations (4.9) and (4.10)

$$S(\underline{Q}) \equiv 1 + \rho_0 \int_V \mathrm{d}^3 r_{12} g(\underline{r}_{12}) \exp\left(\mathrm{i}\underline{Q} \cdot \underline{r}_{12}\right) \tag{4.11}$$

is usually called structure factor or scattering law[2]. $S(Q)$ is solely determined by the properties of the sample and does not depend on the radiation used in examining the sample.

For $Q \to \infty$, $\exp\left(\mathrm{i}\underline{Q} \cdot \underline{r}_{12}\right)$ becomes a rapidly oscillating function and the integral vanishes. Then one has

$$\lim_{Q\to\infty} S(Q) = 1\,. \tag{4.12}$$

For $Q \to 0$, $S(Q)$ measures only the overall density fluctuation, i.e. the fluctuation of the particle number:

$$\lim_{Q\to 0} S(Q) = \frac{V^2\langle\delta\rho^2\rangle}{N} = \frac{\langle N^2\rangle - \langle N\rangle^2}{\langle N\rangle} = \rho_0 k_\mathrm{B} T \kappa_T\,. \tag{4.13}$$

Here, $k_\mathrm{B}$ denotes the Boltzmann factor, $T$ the temperature and $\kappa_T$ the isothermal compressibility. At intermediate $Q$, the structure factor of liquids shows a diminishing series of broad peaks, remainders of the Bragg peaks of a crystalline structure. The first peak occurs at a scattering vector roughly corresponding to the next neighbour distance by $Q_\mathrm{max} = 2\pi/r_\mathrm{nn}$.

[2] The usual definition of the structure factor found in the literature is

$$S'(\underline{Q}) \equiv 1 + \rho_0 \int_V \mathrm{d}^3 r_{12}\,(g(\underline{r}_{12}) - 1) \exp\left(\mathrm{i}\underline{Q} \cdot \underline{r}_{12}\right)$$

subtracting the long distance limit 1 from $g(r)$. Because the Fourier transform of the constant 1 is the delta function the two definitions differ only by a delta function, $S(Q) = S'(Q) + \rho_0\delta(Q)$. This means that apart from the unobservable scattering at zero angle ($Q = 0$) both are the same.

The reason for this alternative definition is to avoid the singularity. Another way to accomplish this is to use the density fluctuation $\delta\rho(\underline{r}) = \rho(\underline{r}) - \rho_0$ from the start (equation (4.2)). From this approach it becomes clear that the structure factor at $Q \neq 0$ depends only on the fluctuation of the density but not on its absolute level.

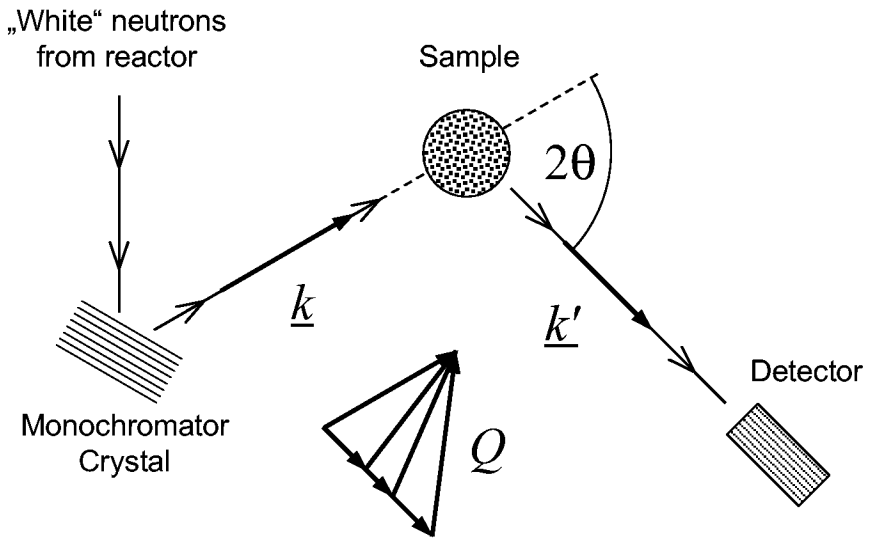



Figure 4.2: Schematic set-up of a diffraction experiment. The inset shows the relation between incident and final wave vectors $k$, $k'$ and the scattering vector $Q$.

## 4.2 Experimental Examples: Static Scattering

### 4.2.1 Placzek corrections

Figure 4.2 shows the schematics of a scattering experiment for the determination of $S(Q)$. By using a monochromator the incident neutron energy or the wave vector $k$ is fixed. After scattering the intensity is recorded as a function of the scattering angle $2\theta$ without energy discrimination. This means that the diffraction setup fixes only the direction of $\underline{k}_\mathrm{f}$ but not its magnitude. Therefore, for a given angle different scattering vectors $Q$ are mixed as figure 4.3 shows.

Strictly speaking, this invalidates the relation $(\mathrm{d}\sigma/\mathrm{d}\Omega)_\mathrm{coh} = |\overline{b}|^2 N S(Q)$ between (angle) differential cross section and structure factor.

Nevertheless, for high incident energies it is an excellent approximation as long as the energy transfer due to inelastic scattering is small compared to the incident energy $E$. This condition is always fulfilled for x-ray scattering because the incident energy lies in the keV range there and the inelasticity of scattering is limited mainly to thermal energies $k_\mathrm{B}T$ which are of the order of meV.

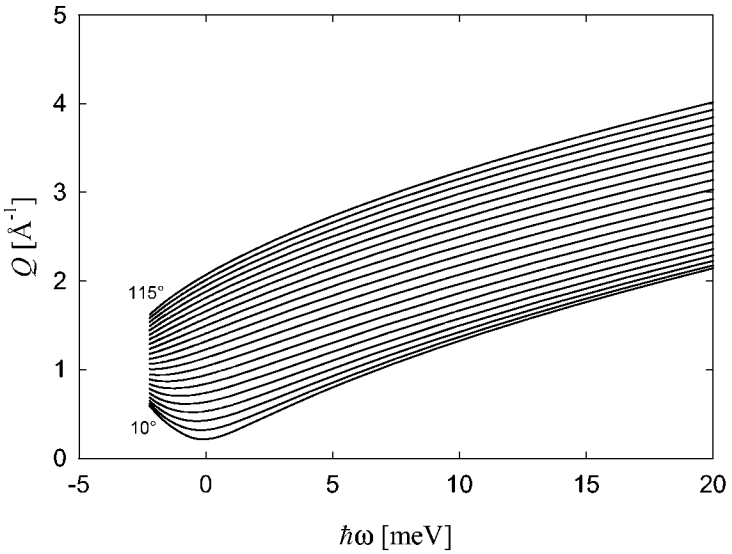



Figure 4.3: Scattering vectors $Q$ accessed by a diffraction experiment with the detector at scattering angles $2\theta = 10 \ldots 115°$ vs. the energy transfer $\hbar\omega$ (incident wavelength $\lambda_\mathrm{i} = 5.1$ Å).

For neutrons on the other hand, incident energies are just in the latter range. Fortunately, the errors which occur due to neglect of inelasticity are still not too large. Therefore, it is possible to derive a correction formula by expanding the true differential cross section under constant angle into a series in the ratio of the mass of the scattering nucleus and the neutron mass $m_\mathrm{n}/m_\mathrm{sc}$. In this way one obtains to first order[3]:

$$\left(\frac{\mathrm{d}\sigma}{\mathrm{d}\Omega}\right)_{2\theta} = |\bar{b}|^2 N \left(S(Q) + f_\mathrm{P}(Q)\right) \text{ with } f_\mathrm{P}(Q) = \frac{m_\mathrm{n}}{m_\mathrm{sc}} \left(\frac{k_\mathrm{B}T}{E} - \left(\frac{Q}{k}\right)^2\right) . \qquad (4.14)$$

Here, $E$ is the incident energy and $k = \sqrt{2m_\mathrm{n}E}/\hbar$ the respective wave vector.

[3] This formula is actually the specification of Placzek's original result [6] to the case of a detector which is equally sensitive for all neutron energies ("black" detector). As pointed out in [7] the correction depends strongly on the energy dependence of the sensitivity. Therefore, except for low $Q$ values, formula (4.14) is not the one which is used in practical applications.

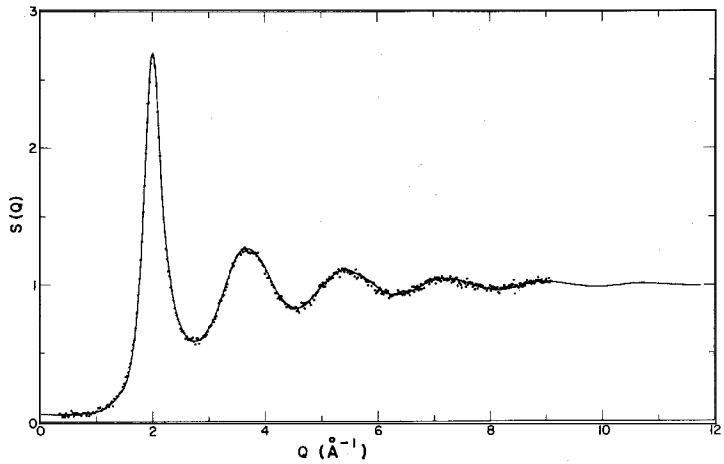



Figure 4.4: Structure factor $S(Q)$ of liquid $^{36}$Ar at 85 K. The points are from a neutron scattering experiment, the curve is generated by a molecular dynamics calculation using a Lennard-Jones potential [7].

### 4.2.2 Experiments on Liquid Argon

As an example of the structure factor $S(Q)$ of a monatomic liquid we consider the neutron scattering results of Yarnell et al. [7] from liquid Argon. The result of the experiment is shown in figure 4.4. The wavelength of the incident neutrons was $\lambda = 0.978$ Å. Under this condition the Placzek corrections vary between 0.0012 near $Q = 0$ and $-0.0426$ at $Q = 9.08\,\text{Å}^{-1}$. The pair correlation function $g(r)$ was obtained by numerical inverse Fourier transform of $S(Q) - 1$ and is shown in figure 4.5. The oscillations at small $r$ are a consequence of cut-off effects on the Fourier transform. They occur below the atomic diameter $r_0$ and therefore do not impede the interpretation. The determination of $g(r)$ is important for the calculation of equilibrium properties of the liquid and allows scrutinization of theoretical models for the interatomic forces.

Two methods of theory based calculation of $g(r)$ have to be emphasized: (1) In Monte Carlo (MC) calculations a large number of possible atomic configurations is created. Their probability is determined by the Boltzmann factor on the basis of interatomic potentials. Finally, the ensemble average is calculated. (2) In Molecular Dynamics (MD) calculations one starts from an initial configuration and solves (numerically) the equations

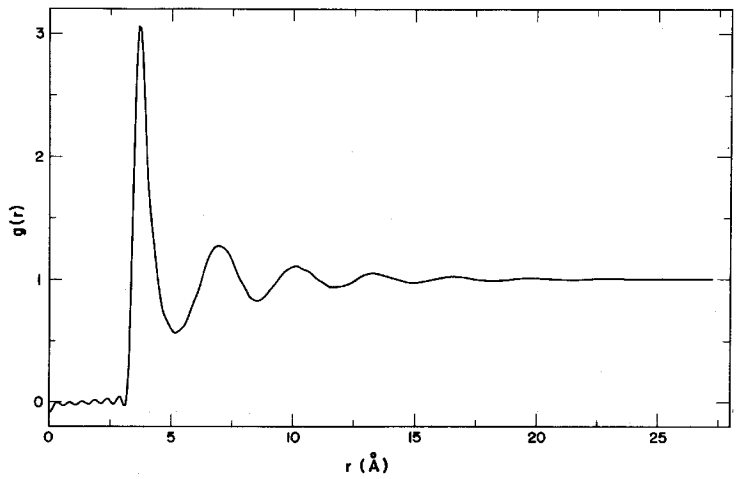



Figure 4.5: The pair correlation function $g(r)$ of liquid Argon calculated by inverse Fourier transform from the data in figure 4.4 [7].

of motions using the interatomic forces. These calculations yield the time average[4]. The solid curve in figure 4.5 shows the result of an MD calculation with a Lennard-Jones-Potential ($V(r) \propto (\sigma/r)^{12} - (\sigma/r)^6$)—the agreement is excellent.

Unfortunately, the pair correlation function is comparatively insensitive to details of the pair potential. To obtain exact information on $V(r)$ it is necessary to do extremely accurate measurements with errors in the per mille range.

### 4.2.3 Scattering from a Polymer Chain

We consider a polymer, i.e. a long chain molecule consisting of equal building blocks, the monomers. In the melt the spatial arrangement of the monomers is simply given by a random walk[5]. The mean squared distance between monomers $i$ and $j$ for such a coiled chain is proportional to the difference of indices

$$\langle {r_{ij}}^2 \rangle = \ell^2 |i - j| \tag{4.15}$$

[4] The ergodic hypothesis ensures that the results of both methods are the same.

[5] This is a result by no means trivial. It was actually confirmed for the first time by the neutron scattering results shown here.

where $r_{ij}$ denotes the monomer distance and $\ell$ is the characteristic monomer length. This is the same expression as for a random walk but with the time $t$ replaced by $|i-j|$. Because for not too small distances $r_{ij}$ is the sum of many random variables the central limit theorem is applicable and the final distribution of the distance is a Gaussian:

$$g(r_{ij}) = \left(\frac{3}{2\pi\langle {r_{ij}}^2\rangle}\right)^{3/2} \exp\left(-\frac{3{r_{ij}}^2}{2\langle {r_{ij}}^2\rangle}\right) . \tag{4.16}$$

Application of equation (4.8) (radially averaged as (4.10)) yields the so-called form factor[6] of the monomer

$$P(Q) = \frac{1}{\mathcal{N}^2}\sum_{i,j=1}^{\mathcal{N}} 4\pi \int {r_{ij}}^2 \mathrm{d}^3 r_{ij} \frac{\sin Qr_{ij}}{Qr_{ij}} g(r_{ij}) = \sum_{i,j=1}^{\mathcal{N}} \exp\left(-\frac{Q^2}{6}|i-j|\ell^2\right) \tag{4.17}$$

where $\mathcal{N}$ is now the number of monomers. Analogous to the preceding derivation of (4.9) we take the diagonal part out of the sum and convert the double sum into a single sum over all differences $k \equiv |i-j|$:

$$P(Q) = \frac{1}{\mathcal{N}}\left(1 + 2\sum_{k=1}^{\mathcal{N}}\left(1-\frac{k}{\mathcal{N}}\right)\exp\left(-\frac{Q^2}{6}k\ell^2\right)\right) . \tag{4.18}$$

Here it is taken account that in contrast to (4.9) not all pairs are equally probable but an index distance $k$ occurs $2(\mathcal{N}-k)$ times in the chain. Converting this sum into an integral one obtains

$$P(Q) = \frac{2}{z^2}\left(\mathrm{e}^{-z} - 1 + z\right) \equiv D(z) \text{ with } z = \frac{Q^2 N\ell^2}{6} . \tag{4.19}$$

The expression $D(z)$ is usually called the Debye function. It describes the scattering of a single polymer coil in the melt which is labeled e.g. by isotopic contrast. Figure 4.6 shows the scattering cross section of protonated polystyrene in a deuterated polystyrene matrix. The solid curve represents a fit with equation (4.19). At large scattering vectors the leading asymptotic term of $D(z)$ is $2/z$ and $P(Q)$ becomes proportional $1/Q^2$—characteristic for a Gaussian random walk. In a so-called Kratky plot ($Q^2 \cdot \mathrm{d}\sigma/\mathrm{d}\Omega$ vs. $Q$) one expects a plateau at high scattering vector $Q$. Figure 4.7 shows this plateau for polystyrene. At very large $Q$ values deviations occur again which signalize the breakdown of Gauss statistics for small distances.

[6] Here the monomers are simply considered as "big atoms" neglecting their inner structure. One has to keep in mind that the thus obtained results only represent the actual scattering law for small scattering vector when $2\pi/Q$ is larger than the size of a monomer.

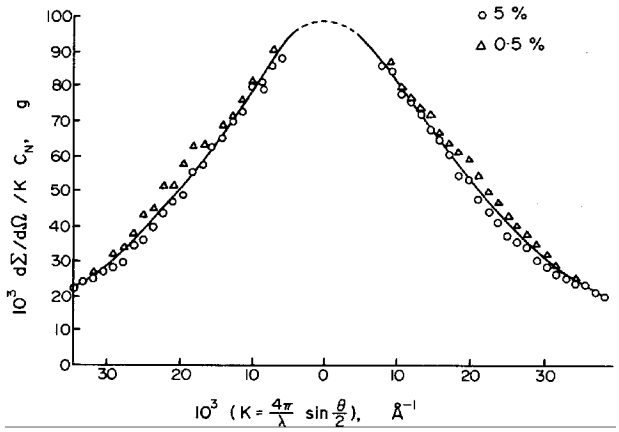



Figure 4.6: Partial differential cross section for protonated polystyrene in a deuterated polystyrene matrix [8]. The concentration of the protonated component is 5% (o) and 0.5% (Δ) respectively. The curve is a fit with the Debye function.

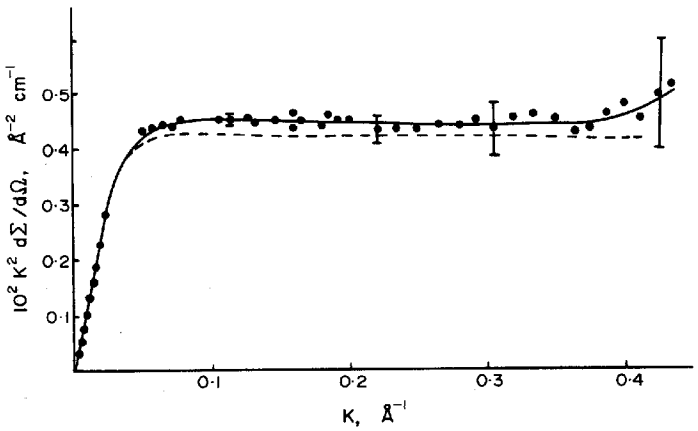



Figure 4.7: Kratky plot of the data from figure 4.6.

## 4.3 Dynamical Correlation Function

### 4.3.1 Correlation Spectroscopy

We consider an observable $A$ of a system which fluctuates randomly because of the thermal motion of the system. $A$ could be e.g. the pressure on the wall exerted by a gas in a cylinder or the particle density in a liquid. Figure 4.8 shows exemplarily the time-dependent value of a quantity $A$ fluctuating around its average value $\langle A \rangle$.

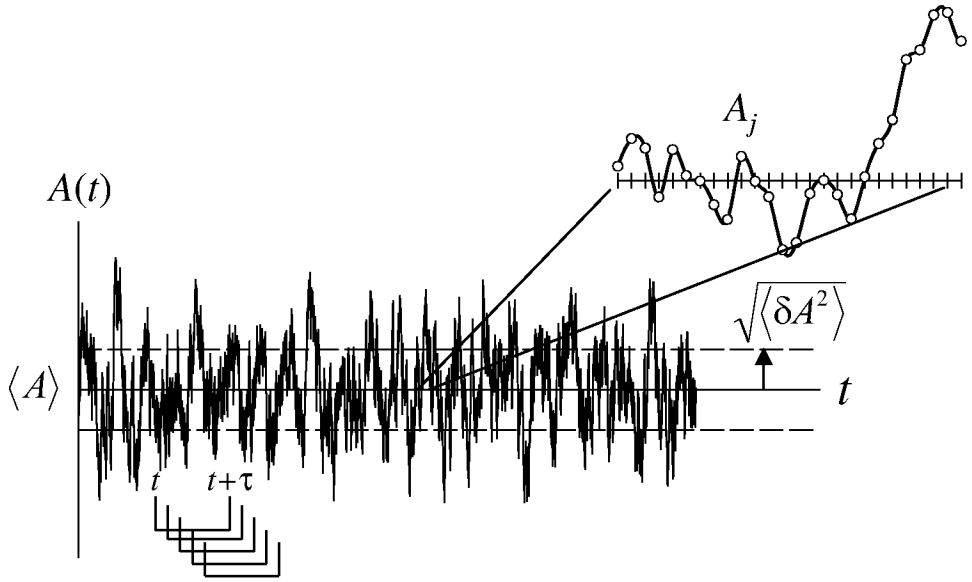



Figure 4.8: Fluctuating observable $A(t)$ of an ensemble of molecules as a function of time. The time axis is subdivided into discrete intervals of length $\Delta t$.

If one takes a time average over a long time interval as compared with the fluctuation periods one obtains a stationary result which is independent of the start of the time interval

$$\lim_{T\to\infty} \frac{1}{T} \int_{t_0}^{t_0+T} \mathrm{d}t A(t) = \text{const.} \equiv \langle A \rangle \tag{4.20}$$

but in general $A(t+\tau) \neq A(t)$. If $\tau$ is very small compared to typical times of the system $A(t+\tau)$ approaches the value of $A(t)$ which means that the both are correlated in time. As a measure of this correlation the autocorrelation function is introduced:

$$\langle A(0)A(\tau) \rangle = \lim_{T\to\infty} \frac{1}{T} \int_{t_0}^{t_0+T} \mathrm{d}t A(t)A(t+\tau)\,. \tag{4.21}$$

This function correlates the observable $A$ with itself in a certain time displacement $\tau$ and then averages over all starting times.

In a real experiment (figure 4.8) this can be done by sampling values $A_i$ at equidistant times $t_i = i\delta t$. Let $j$ denote the index of the starting time ($t = j\delta t$), $n$ the distance counted in time intervals ($\tau = n\delta t$), and $N$ the number of intervals to be averaged ($T = N\delta t$).

Then equation (4.21) can be converted into a sum:

$$\langle A(0)A(\tau)\rangle = \lim_{N\to\infty} \frac{1}{N} \sum_{j=1}^{N} A_j A_{j+n} \,. \tag{4.22}$$

In optical correlation spectroscopy sums like (4.22) are calculated from the photodetector signal by special purpose computers. In this case $A$ is the number of photons detected per time interval, i.e. the light intensity.

It is easy to see that the autocorrelation function has the following properties

$$\langle A(0)A(\tau)\rangle \leq \langle A(0)A(0)\rangle \equiv \langle A^2\rangle \tag{4.23}$$

$$\lim_{\tau\to\infty} \langle A(0)A(\tau)\rangle = \langle A\rangle^2 \,. \tag{4.24}$$

Figure 4.9 shows a simulation of data of a light scattering experiment. Such data could arise e.g. from scattering of polystyrene spheres in an aqueous dispersion.

The correlation function usually decays following a simple exponential law:

$$\langle A(0)A(\tau)\rangle = \langle A\rangle^2 + \left(\langle A^2\rangle - \langle A\rangle^2\right) \exp\left(-\tau/\tau_r\right) \tag{4.25}$$

where $\tau_r$ is the correlation time of the system. In general, also more complicated decays, e.g. involving multiple characteristic times, are possible. But the decay always takes places between the limits given by (4.23) and (4.24).

Alternatively, one can consider the fluctuations $\delta A(t) = A(t) - \langle A\rangle$, i.e. the deviations of the observable from its average. For its autocorrelation function follows:

$$\begin{aligned} \langle \delta A(0)\delta A(t)\rangle &= \langle A(0)A(\tau)\rangle - \langle A\rangle^2 \\ &= \langle \delta A^2\rangle \exp\left(-\tau/\tau_r\right) \,. \end{aligned} \tag{4.26}$$

The general result is that the fluctuation autocorrelation function decays starting from the variance of the observable, $\langle \delta A^2\rangle = \langle A^2\rangle - \langle A\rangle^2$ to zero.

The time-dependent autocorrelation function describes the temporal fluctuation behaviour of the system. In the case presented here of a polymer colloid the characteristic time is directly connected to the diffusion constant: ${\tau_r}^{-1} = DQ^2$.

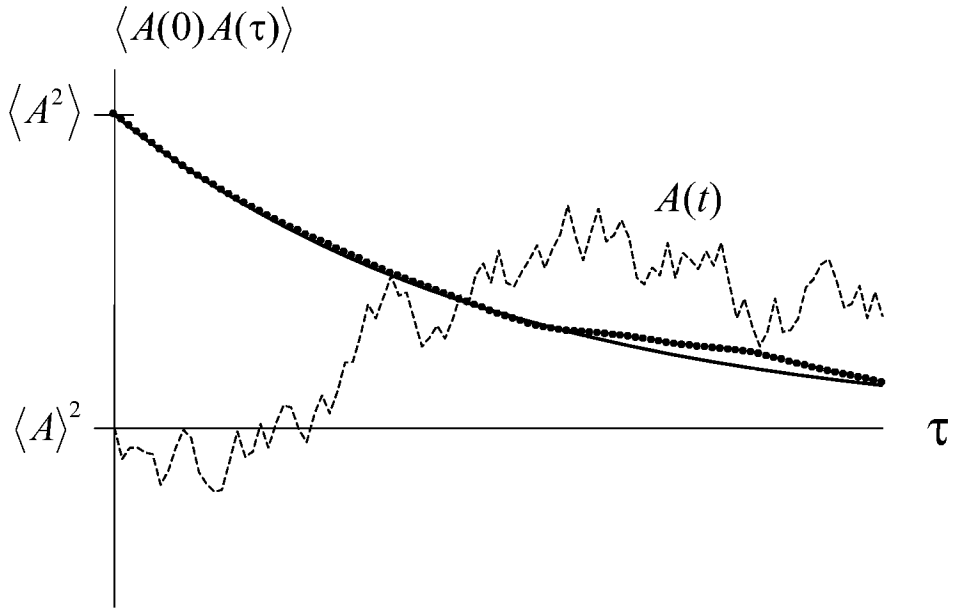



Figure 4.9: Simulated result of a dynamic light scattering experiment. The circular dots show the output of the correlator electronics. The continuous curve is the expected exponential decay (4.25). The dashed line shows the underlying fluctuating intensity.

### 4.3.2 The Van Hove Correlation Function

In order to consider inelastic scattering the differential cross section $\mathrm{d}\sigma/\mathrm{d}\Omega$ is generalized with respect to its dependence on the energy transfer $\hbar\omega$. This leads to the double differential cross section in quantum mechanical notation:

$$\frac{\partial^2\sigma}{\partial\Omega\partial\omega} = \frac{k'}{k}\sum_{\lambda,\sigma} P_\lambda P_\sigma \sum_{\lambda',\sigma'} \left|\sum_i \langle\lambda',\sigma'|b_i \exp(\mathrm{i}\underline{Q}\cdot\underline{\mathbf{r}}_i)|\lambda,\sigma\rangle\right|^2 \delta\left(\hbar\omega + E_\lambda - E_{\lambda'}\right) . \qquad (4.27)$$

Here, $\lambda$ and $\sigma$ describe the relevant space and spin quantum number respectively in the initial state of the scattering system and $\lambda'$ and $\sigma'$ those in the final state. $P_\lambda$ and $P_\sigma$ are the respective probabilities for the initial states $\lambda$ and $\sigma$. The inner sum refers to all particles with scattering lengths $b_i$ and single-particle coordinate operators $\underline{\mathbf{r}}_i$. $k$ and $k'$ are the wave vectors of the incident and scattered neutrons. The delta function expresses energy conservation: the energy transfer of the neutron $\hbar\omega$ is exactly compensated by the energy change of the quantum state of the scattering system $E_{\lambda'} - E_\lambda$. In the following we will neglect the spin coordinates for the sake of simplicity. We also do not consider

magnetic neutron scattering which would give rise to an additional term in the matrix element.

The route from expression (4.27) to the Van Hove correlation function starts with an integral representation of the delta function:

$$\delta\left(\hbar\omega + E_\lambda - E_{\lambda'}\right) = \frac{1}{2\pi\hbar}\int_{-\infty}^{\infty} \mathrm{d}t \exp\left(-\mathrm{i}\left(\omega + \frac{E_\lambda - E_{\lambda'}}{\hbar}\right)t\right) \tag{4.28}$$

which results from the fact that the delta function is the Fourier transform of a constant one. With this expression the matrix element in equation (4.27) can be written as a Fourier transform in time:

$$\begin{aligned}
&\left|\sum_i \langle\lambda'|b_i \exp(\mathrm{i}\underline{Q}\cdot\underline{\mathbf{r}}_i)|\lambda\rangle\right|^2 \delta\left(\hbar\omega + E_\lambda - E_{\lambda'}\right) \\
= \;& \frac{1}{2\pi\hbar}\int_{-\infty}^{\infty} \mathrm{d}t \exp(-\mathrm{i}\omega t) \exp\left(-\mathrm{i}\frac{E_\lambda}{\hbar}t\right) \exp\left(-\mathrm{i}\frac{E_{\lambda'}}{\hbar}t\right) \\
& \qquad \sum_i b_i \langle\lambda'|\exp(\mathrm{i}\underline{Q}\cdot\underline{\mathbf{r}}_i)|\lambda\rangle \sum_j b_j^* \langle\lambda|\exp(-\mathrm{i}\underline{Q}\cdot\underline{\mathbf{r}}_j)|\lambda'\rangle \\
= \;& \frac{1}{2\pi\hbar}\int_{-\infty}^{\infty} \mathrm{d}t \exp(-\mathrm{i}\omega t) \sum_{i,j} b_i b_j^* \langle\lambda|\exp(-\mathrm{i}\underline{Q}\cdot\underline{\mathbf{r}}_j)|\lambda'\rangle \\
& \qquad \langle\lambda'|\exp(\mathrm{i}E_{\lambda'}t/\hbar)\exp(\mathrm{i}\underline{Q}\cdot\underline{\mathbf{r}}_i)\exp(-\mathrm{i}E_\lambda t/\hbar)|\lambda\rangle
\end{aligned} \tag{4.29}$$

If $\mathbf{H}$ is the Hamiltonian of the scattering system, the fact that $|\lambda\rangle$ are energy eigenstates is expressed by

$$\mathbf{H}|\lambda\rangle = E_\lambda|\lambda\rangle\,. \tag{4.30}$$

Iterating this equation $n$ times yields:

$$\mathbf{H}^n|\lambda\rangle = {E_\lambda}^n|\lambda\rangle\,. \tag{4.31}$$

By expanding the exponential into a power series one finally obtains from this relation

$$\exp(\mathrm{i}\mathbf{H}t/\hbar)|\lambda\rangle = \exp(\mathrm{i}E_\lambda t/\hbar)|\lambda\rangle\,. \tag{4.32}$$

With this result and the analogous one for $\lambda'$ it is possible to replace the eigenvalues $E_\lambda$ in (4.29) by the Hamiltonian $\mathbf{H}$:

$$\ldots\langle\lambda'|\exp(\mathrm{i}\mathbf{H}t/\hbar)\exp(\mathrm{i}\underline{Q}\cdot\underline{\mathbf{r}}_i)\exp(-\mathrm{i}\mathbf{H}t/\hbar)|\lambda\rangle\,. \tag{4.33}$$

In the picture of time dependent Heisenberg operators the application of the operator $\exp(\mathrm{i}\mathbf{H}t/\hbar)$ and its conjugate just means a propagation by time $t$:

$$\exp\left(\mathrm{i}\underline{Q}\cdot\underline{\mathbf{r}}_i(t)\right) = \exp(\mathrm{i}\mathbf{H}t/\hbar)\exp(\mathrm{i}\underline{Q}\cdot\underline{\mathbf{r}}_i(0))\exp(-\mathrm{i}\mathbf{H}t/\hbar) \tag{4.34}$$

where we can arbitrarily set $\underline{\mathbf{r}}_i = \underline{\mathbf{r}}_i(0)$ because of translation of time invariance. Using this result the final expression for the double differential cross section is obtained:

$$\begin{aligned}\frac{\partial^2\sigma}{\partial\Omega\partial\omega} &= \frac{k'}{k}\frac{1}{2\pi\hbar}\int_{-\infty}^{\infty}\mathrm{d}t\,\exp(-\mathrm{i}\omega t) \\ &\quad \sum_\lambda P_\lambda \sum_{i,j} b_i b_j^* \left\langle \lambda \left| \exp(-\mathrm{i}\underline{Q}\cdot\underline{\mathbf{r}}_j(0))\exp(\mathrm{i}\underline{Q}\cdot\underline{\mathbf{r}}_i(t)) \right| \lambda \right\rangle . \end{aligned} \tag{4.35}$$

(Here, the sum over $\lambda'$ vanishes because of the completeness relation $\sum_{\lambda'}|\lambda'\rangle\langle\lambda'| = 1$.) This equation averages over the scattering length distribution (which may depend on the spin orientation distribution with respect to the incident neutron's spin). This produces coherent and incoherent scattering as explained in lecture 1. In addition the initial states of the scattering system are averaged weighted with the probability of their occurrence $P_\lambda$. The latter is given by the Boltzmann distribution

$$P_\lambda = \frac{1}{Z}\exp\left(-E_\lambda/k_\mathrm{B}T\right) \text{ with } Z = \sum_\lambda \exp\left(-E_\lambda/k_\mathrm{B}T\right) . \tag{4.36}$$

We now denote this thermal average by angular brackets $\langle\ldots\rangle$ while that over the scattering lengths be written as an overline $\overline{\ldots}$ . Keeping in mind that for equal indices $b_i b_i^* = |b_i|^2$ has to be averaged while for unequal indices the scattering lengths itself will be averaged we end up with the usual separation into incoherent and coherent part:

$$\begin{aligned}\frac{\partial^2\sigma}{\partial\Omega\partial\omega} &= \sum_\lambda P_\lambda \\ &\quad \frac{k'}{k}\frac{\overline{|b|^2}-|\bar{b}|^2}{2\pi\hbar}\int_{-\infty}^{\infty}\mathrm{d}t\,\exp(-\mathrm{i}\omega t)\sum_i \left\langle \lambda \left| \exp(-\mathrm{i}\underline{Q}\cdot\underline{\mathbf{r}}_i(0))\exp(\mathrm{i}\underline{Q}\cdot\underline{\mathbf{r}}_i(t)) \right| \lambda \right\rangle \\ &\quad + \frac{k'}{k}\frac{|\bar{b}|^2}{2\pi\hbar}\int_{-\infty}^{\infty}\mathrm{d}t\,\exp(-\mathrm{i}\omega t)\sum_{i,j} \left\langle \lambda \left| \exp(-\mathrm{i}\underline{Q}\cdot\underline{\mathbf{r}}_i(0))\exp(\mathrm{i}\underline{Q}\cdot\underline{\mathbf{r}}_j(t)) \right| \lambda \right\rangle . \end{aligned} \tag{4.37}$$

The first term is the incoherent scattering. It involves the coordinate vector operators of the *same* atom at different times. The second, the coherent term correlates also *different* atoms at different times. The material dependent parts are now defined as the scattering functions

$$S_\mathrm{inc}(Q,\omega) \equiv \frac{1}{2\pi\hbar N}\int_{-\infty}^{\infty}\mathrm{d}t\,\exp(-\mathrm{i}\omega t)\sum_i \langle \exp(-\mathrm{i}\underline{Q}\cdot\underline{\mathbf{r}}_i(0))\exp(\mathrm{i}\underline{Q}\cdot\underline{\mathbf{r}}_i(t))\rangle \tag{4.38}$$

$$S_\mathrm{coh}(Q,\omega) \equiv \frac{1}{2\pi\hbar N}\int_{-\infty}^{\infty}\mathrm{d}t\,\exp(-\mathrm{i}\omega t)\sum_{i,j} \langle \exp(-\mathrm{i}\underline{Q}\cdot\underline{\mathbf{r}}_i(0))\exp(\mathrm{i}\underline{Q}\cdot\underline{\mathbf{r}}_j(t))\rangle . \tag{4.39}$$

In terms of the scattering functions the double differential cross section can be written as

$$\frac{\partial^2\sigma}{\partial\Omega\partial\omega} = \frac{k'}{k}N\left(\left(\overline{|b|^2}-|\bar{b}|^2\right)S_\mathrm{inc}(\underline{Q},\omega) + |\bar{b}|^2 S_\mathrm{coh}(\underline{Q},\omega)\right) . \tag{4.40}$$

In addition it is often useful to define the intermediate scattering function which denotes the time dependent parts of definitions (4.38) and (4.39) before Fourier transform:

$$S_{\mathrm{inc}}(\underline{Q},t) \equiv \frac{1}{N}\sum_i \langle \exp(-\mathrm{i}\underline{Q}\cdot\underline{\mathbf{r}}_i(0))\exp(\mathrm{i}\underline{Q}\cdot\underline{\mathbf{r}}_i(t))\rangle \tag{4.41}$$

$$S_{\mathrm{coh}}(\underline{Q},t) \equiv \frac{1}{N}\sum_{i,j} \langle \exp(-\mathrm{i}\underline{Q}\cdot\underline{\mathbf{r}}_i(0))\exp(\mathrm{i}\underline{Q}\cdot\underline{\mathbf{r}}_j(t))\rangle\,. \tag{4.42}$$

If one compares this result with the definition of the structure factor (4.8–4.11) one recognizes that $S_{\mathrm{coh}}(Q,\omega)$ is in an analogous way the Fourier transform in space and time of a dynamical pair correlation function $G(\underline{r},t)$:

$$G(\underline{r},t) = \left(\frac{1}{2\pi}\right)^3 \int \mathrm{d}^3Q \exp\left(-\mathrm{i}\underline{Q}\cdot\underline{r}\right) \frac{1}{N}\sum_{i,j}\left\langle \exp\left(-\mathrm{i}\underline{Q}\cdot\underline{\mathbf{r}}_i(0)\right)\exp\left(\mathrm{i}\underline{Q}\cdot\underline{\mathbf{r}}_j(t)\right)\right\rangle\,. \tag{4.43}$$

The derivation of the relation between the coherent dynamical structure factor $S_{\mathrm{coh}}(Q,\omega)$ and the generalized pair correlation function requires a strict quantum mechanical calculation. This problem results from the fact that the coordinate vector operators commute only at identical times. Therefore, in all algebraic manipulations the order of $\underline{\mathbf{r}}_i(0)$ and $\underline{\mathbf{r}}_i(t)$ must not be interchanged.

To begin, one writes the operator $\exp\left(-\mathrm{i}\underline{Q}\cdot\underline{\mathbf{r}}_i(0)\right)$ as the Fourier transform of the delta function:

$$\exp\left(-\mathrm{i}\underline{Q}\cdot\underline{\mathbf{r}}_i(0)\right) = \int \mathrm{d}^3r' \delta\left(\underline{r}' - \underline{\mathbf{r}}_i(0)\right)\exp(-\mathrm{i}\underline{Q}\cdot\underline{r}')\,. \tag{4.44}$$

Using this expression equation (4.43) can be rewritten as

$$\begin{aligned} G(\underline{r},t) &= \left(\frac{1}{2\pi}\right)^3 \frac{1}{N}\sum_{i,j}\Bigg\langle \int \mathrm{d}^3r' \delta\left(\underline{r}' - \underline{\mathbf{r}}_i(0)\right) \\ &\qquad \underbrace{\int \mathrm{d}^3Q \exp\left(-\mathrm{i}\underline{Q}\cdot\underline{r} - \mathrm{i}\underline{Q}\cdot\underline{r}' + \mathrm{i}\underline{Q}\cdot\underline{\mathbf{r}}_j(t)\right)}_{=(2\pi)^3\delta\left(\underline{r}+\underline{r}'-\underline{\mathbf{r}}_j(t)\right)}\Bigg\rangle \\ &= \frac{1}{N}\sum_{i,j}\int \mathrm{d}^3r' \left\langle \delta\left(\underline{r}-\underline{r}'+\underline{\mathbf{r}}_i(0)\right)\delta\left(\underline{r}'-\underline{\mathbf{r}}_j(t)\right)\right\rangle \end{aligned} \tag{4.45}$$

without changing the order of the operators at different times.

Now the particle density operator is introduced as a sum over delta functions at the particle position operators:

$$\boldsymbol{\rho}(\underline{r},t) \equiv \sum_i \delta\left(\underline{r} - \underline{\mathbf{r}}_i(t)\right)\,. \tag{4.46}$$

With this definition the pair correlation function can be written as time-dependent density-density correlation function:

$$G(\underline{r},t) = \frac{1}{N}\int \mathrm{d}^3r' \left\langle \boldsymbol{\rho}(\underline{r}'-\underline{r},0)\boldsymbol{\rho}(\underline{r}',t)\right\rangle \ . \tag{4.47}$$

With this form of the dynamic pair correlation function the dynamical structure factor can be—analogously to equation (4.11)—written as the double Fourier transform of the correlator of the particle density:

$$S_{\mathrm{coh}}(\underline{Q},\omega) = \int_{-\infty}^{\infty} \mathrm{d}t \exp(-\mathrm{i}\omega t) \int \mathrm{d}^3r \int \mathrm{d}^3r' \exp\left(\mathrm{i}\underline{Q}\cdot\underline{r}\right) \left\langle \boldsymbol{\rho}(\underline{r}'-\underline{r},0)\boldsymbol{\rho}(\underline{r}',t)\right\rangle \ . \tag{4.48}$$

We now define the density operator in reciprocal space as the Fourier transform of (4.46):

$$\boldsymbol{\rho}_{\underline{Q}}(t) \equiv \sum_i \exp\left(\mathrm{i}\underline{Q}\cdot\underline{\mathbf{r}}_i(t)\right) \tag{4.49}$$

and obtain for the dynamic structure factor

$$S_{\mathrm{coh}}(\underline{Q},\omega) = \frac{1}{2\pi\hbar N}\int_{-\infty}^{\infty} \mathrm{d}t \exp(-\mathrm{i}\omega t) \left\langle \boldsymbol{\rho}_{\underline{Q}}(0)\boldsymbol{\rho}_{-\underline{Q}}(t)\right\rangle \ . \tag{4.50}$$

Correspondingly, the intermediate scattering function is

$$S_{\mathrm{coh}}(\underline{Q},t) = \frac{1}{N}\left\langle \boldsymbol{\rho}_{\underline{Q}}(0)\boldsymbol{\rho}_{-\underline{Q}}(t)\right\rangle \tag{4.51}$$

which after insertion of (4.49) turns out to be equivalent to (4.42).

Analogously, one can define a self correlation function by setting $i = j$ in the preceding equations leading to

$$G_{\mathrm{s}}(\underline{r},t) = \frac{1}{N}\sum_i \int \mathrm{d}^3r' \left\langle \delta\left(\underline{r}-\underline{r}'+\underline{\mathbf{r}}_i(0)\right)\delta\left(\underline{r}'-\underline{\mathbf{r}}_i(t)\right)\right\rangle \tag{4.52}$$

as the equivalent of (4.45).

The pair correlation function has some general properties:

1. For spatially homogeneous systems the integrand in (4.47) is independent of $\underline{r}'$ which can be arbitrarily set to the origin $\underline{0}$:

$$G(\underline{r},t) = \frac{V}{N}\left\langle \boldsymbol{\rho}(-\underline{r},0)\boldsymbol{\rho}(\underline{0},t)\right\rangle = \frac{1}{\rho_0}\left\langle \boldsymbol{\rho}(\underline{0},0)\boldsymbol{\rho}(\underline{r},t)\right\rangle \ . \tag{4.53}$$

2. The pair correlation function has the following asymptotic behaviour: For fixed distance and $t \to \infty$ or fixed time and $r \to \infty$ the averages in equation (4.47) can be executed separately and in consequence

$$G(\underline{r},t) \to \frac{1}{N}\int \mathrm{d}^3r' \left\langle \boldsymbol{\rho}(\underline{r}'-\underline{r},0)\right\rangle \left\langle \boldsymbol{\rho}(\underline{r}',t)\right\rangle = \rho_0\,. \tag{4.54}$$

3. For $t = 0$ the operators commute and the convolution integral of equation (4.47) can be carried out:

$$G(\underline{r},0) = \frac{1}{N}\sum_{i,j}\left\langle \delta\left(\underline{r}+\underline{\mathbf{r}}_i(0)-\underline{\mathbf{r}}_j(0)\right)\right\rangle\,. \tag{4.55}$$

For indistinguishable particles the relation to the static pair correlation function as defined in (4.6) can be drawn. Because of the identity of the particles we can set $i = 1$ in (4.55) and drop the average over $i$:

$$G(\underline{r},0) = \sum_j \left\langle \delta\left(\underline{r}+\underline{\mathbf{r}}_1(0)-\underline{\mathbf{r}}_j(0)\right)\right\rangle = \delta(\underline{r}) + \sum_{j\neq 1}\left\langle \delta\left(\underline{r}+\underline{\mathbf{r}}_1(0)-\underline{\mathbf{r}}_j(0)\right)\right\rangle\,. \tag{4.56}$$

We now consider the average number of particles $\delta N(\underline{r})$ in a volume $\delta V$ at a vector distance $\underline{r}$ from a given particle at $\underline{r}_1$. It is obviously given by the integral over the second term in the preceding expression which for small $\delta V$ can be written as

$$\delta N(\underline{r}) = \delta V \sum_{j\neq 1}\left\langle \delta\left(\underline{r}+\underline{\mathbf{r}}_1(0)-\underline{\mathbf{r}}_j(0)\right)\right\rangle\,. \tag{4.57}$$

Using the definition (4.6) and the expression for the number density in homogeneous fluids (4.2) one can relate $\delta N(\underline{r})$ also to the static pair correlation function:

$$\delta N(\underline{r}) = \rho_0 g(\underline{r})\delta V\,. \tag{4.58}$$

Finally, by comparison of the last three equations we get a relation between the dynamic correlation function at time zero and its static counterpart:

$$G(\underline{r},0) = \delta(\underline{r}) + \rho_0 g(\underline{r})\,. \tag{4.59}$$

This equation expresses the fact that the diffraction experiment ($g(r)$) gives an average snapshot picture ($G(r,0)$) of the sample.

In the classical approximation the operators commute always, especially also at different times. Then the integrals of equations (4.45) and (4.52) can be carried out and yield

$$G^{\mathrm{cl}}(\underline{r},t) = \frac{1}{N}\sum_{i,j}\delta(\underline{r}-\underline{r}_j(t)+\underline{r}_i(0)) \text{ and} \tag{4.60}$$

$$G_{\mathrm{s}}^{\mathrm{cl}}(\underline{r},t) = \frac{1}{N}\sum_{i}\delta(\underline{r}-\underline{r}_i(t)+\underline{r}_i(0))\,, \tag{4.61}$$

respectively. The former equation expresses the probability to find *any* particle at a time $t$ in a distance $\underline{r}$ from another at time 0. The latter equation denotes this probability for the *same* particle. It therefore depends only on the particle's displacement during a time interval $\Delta\underline{r}_i(t) = \underline{r}_i(t) - \underline{r}_i(0)$ leading to a simple expression for the intermediate incoherent scattering function:

$$S_{\mathrm{inc}}^{\mathrm{cl}}(\underline{Q}, t) = \frac{1}{N} \sum_i \left\langle \exp\left(-\mathrm{i}\underline{Q} \cdot \Delta\underline{r}_i(t)\right) \right\rangle . \tag{4.62}$$

In certain cases this expression can be further simplified using the "Gaussian approximation"[7]:

$$S_{\mathrm{inc}}^{\mathrm{Gauss}}(Q, t) = \exp\left(-\frac{1}{6} Q^2 \langle \Delta r^2(t) \rangle\right) . \tag{4.63}$$

Here $\langle \Delta r^2(t) \rangle$ is the average mean squared displacement which often follows simple laws, e.g. $\langle \Delta r^2(t) \rangle = 6Dt$ for simple diffusion. Because one of the prerequisites of the Gaussian approximation is that all particles move statistically in the same way (dynamic homogeneity) the particle average and the index $i$ vanish. An analogous expression can be derived for the coherent scattering.

In order to decide whether the classical approximation can be used the following rule has to be taken into account: Quantum effects play a rôle if the distance of two particles is of the order of the DeBroglie wavelength $\lambda_{\mathrm{B}} = \hbar/\sqrt{2m_{\mathrm{sc}}k_{\mathrm{B}}T}$ or if the times considered are smaller than $\hbar/k_{\mathrm{B}}T$.

Figure 4.10 schematically shows on the left side the behaviour of the correlation functions $G(r, t)$ and $G_{\mathrm{s}}(r, t)$ for a simple liquid (in classical approximation). On the right side the corresponding intermediate scattering functions $S_{\mathrm{coh}}(Q, t)$ and $S_{\mathrm{inc}}(Q, t)$ are displayed:

- For $t = 0$ the self correlation function is given by a delta function at $r = 0$. The pair correlation function follows the static correlation function $g(r)$. The intermediate scattering functions are constant one for the incoherent and the static structure factor for the coherent.

- For intermediate times the self correlation function broadens to a bell-shaped function while the pair correlation function loses its structure. The intermediate scat-

[7] For solids the long-time limit of this equation is called the Lamb-Mößbauer factor. Its coherent counterpart is the Debye-Waller factor.

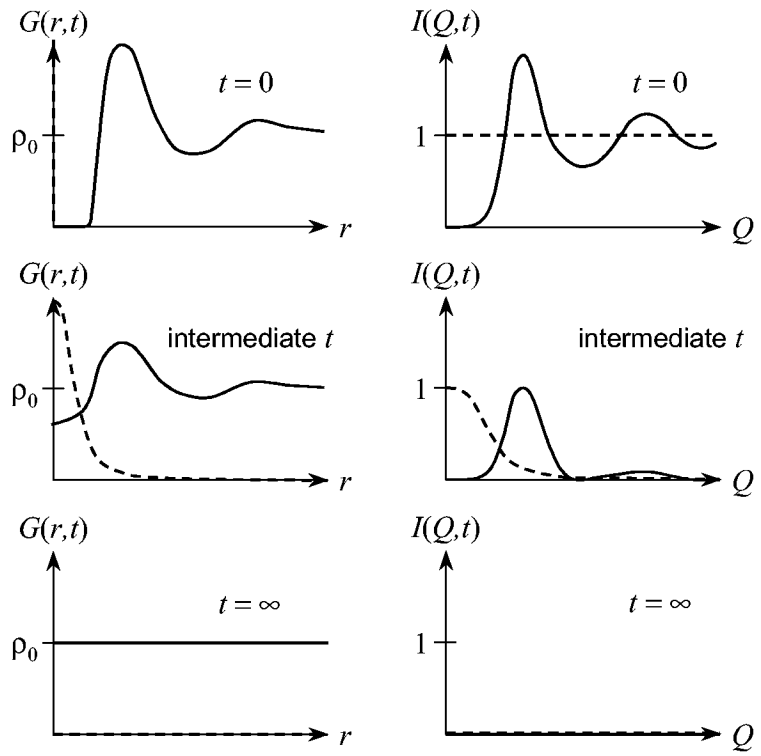



Figure 4.10: Schematic Comparison of the correlation functions $G(r,t)$, $G_s(r,t)$ and the intermediate scattering functions $S_{coh}(Q,t)$, $S_{inc}(Q,t)$ for a simple liquid at different times. The solid lines denote the coherent case, the dashed lines the self/incoherent.

tering functions decay with respect to the $t = 0$ value. The decay is faster for higher $Q$ and (in the coherent case) less pronounced at the structure factor maximum.

- The long time limit of the pair correlation function is the average density $\rho_0$ while the self correlation simply vanishes (in a liquid). In consequence both the coherent and the incoherent intermediate scattering function decay to zero for long times and any $Q$.

## 4.4 Scattering from an Ideal Gas

We consider a gas of $N$ atoms in a volume $V$ neglecting the spin coordinates $\sigma$ and assume that all scattering lengths are identical $b_i = 1$. The wave function of a free atom confined

to a volume $V$ is simply a plane wave with wave vector $\underline{\kappa}$:

$$\Psi_{\underline{\kappa}}(\underline{r}) = \langle \underline{r}|\underline{\kappa}\rangle = \frac{1}{\sqrt{V}} \exp(\mathrm{i}\underline{\kappa}\cdot\underline{r})\,. \tag{4.64}$$

Using this expression, the matrix element in the double differential cross section (4.27) can immediately be calculated:

$$\langle \underline{\kappa}'|\exp \mathrm{i}\underline{Q}\cdot\underline{\mathbf{r}}|\underline{\kappa}\rangle = \frac{1}{V}\int_V \mathrm{d}^3 r \exp(\mathrm{i}(\underline{Q}+\underline{\kappa}-\underline{\kappa}')\cdot\underline{r}) = \delta(\underline{Q}+\underline{\kappa}-\underline{\kappa}')\,. \tag{4.65}$$

The resulting delta function expresses the momentum conservation. Only if momentum is conserved the matrix element is 1—otherwise zero.

In the second step we have to consider energy conservation. The energy of the atom with wave vector $\kappa$ is

$$E_\kappa = \frac{\hbar^2}{2m_{\mathrm{sc}}}\kappa^2 \tag{4.66}$$

where $m_{\mathrm{sc}}$ is the mass of the scattering atom. For the evaluation of the delta function in (4.27) we need the energy difference between the states $\kappa$ and $\kappa'$. Because of the delta function factor (4.65) only such states with $\underline{\kappa}' = \underline{\kappa} - \underline{Q}$ have to be considered and for those the energy difference is:

$$E_\kappa - E_{\kappa'} = -\frac{\hbar}{2m_{\mathrm{sc}}}\left(Q^2 + 2\underline{Q}\cdot\underline{\kappa}\right)\,. \tag{4.67}$$

With this result one can calculate the scattering function:

$$S(Q,\omega) = \sum_{\underline{\kappa}} P_{\underline{\kappa}}\delta\left(\hbar\omega - \frac{\hbar}{2m_{\mathrm{sc}}}\left(Q^2 + 2\underline{Q}\cdot\underline{\kappa}\right)\right)\,. \tag{4.68}$$

In the limit of a large volume $V$, $\underline{\kappa}$ becomes a continuous variable. In addition only the component of $\underline{\kappa}$ parallel to $Q$ is relevant. Therefore, (4.68) can be written as a one-dimensional integral:

$$S(Q,\omega) = \int_{-\infty}^{\infty} \mathrm{d}\kappa P_\kappa \delta\left(\hbar\omega - \frac{\hbar}{2m_{\mathrm{sc}}}\left(Q^2 + 2Q\kappa\right)\right)\,. \tag{4.69}$$

The probability of a momentum state $\kappa$ follows from the Boltzmann distribution:

$$P_\kappa = \frac{1}{Z}\exp\left(-\frac{\hbar^2\kappa^2}{2m_{\mathrm{sc}}k_{\mathrm{B}}T}\right) \tag{4.70}$$

with the state sum being

$$Z = \int_{-\infty}^{\infty} \mathrm{d}\kappa \exp\left(-\frac{\hbar^2\kappa^2}{2m_{\mathrm{sc}}k_{\mathrm{B}}T}\right) = \frac{\sqrt{2\pi m_{\mathrm{sc}}k_{\mathrm{B}}T}}{\hbar}\,. \tag{4.71}$$

Insertion of this result into (4.69) yields:

$$S(Q,\omega) = \frac{\hbar}{\sqrt{2\pi m_{\rm sc} k_{\rm B} T}} \int_{-\infty}^{\infty} {\rm d}\kappa \exp\left(-\frac{\hbar^2\kappa^2}{2m_{\rm sc}k_{\rm B}T}\right) \delta\left(\hbar\omega - \frac{\hbar}{2m_{\rm sc}}\left(Q^2 + 2Q\kappa\right)\right) . \quad (4.72)$$

Substitution of $w \equiv \hbar\omega - \frac{\hbar}{2m_{\rm sc}}\left(Q^2 + 2Q\kappa\right)$ into this integral allows the evaluation of the delta function:

$$\begin{aligned} S(Q,\omega) &= \frac{\hbar}{\sqrt{2\pi m_{\rm sc} k_{\rm B} T}} \\ &\qquad \int_{-\infty}^{\infty} {\rm d}w \frac{m_{\rm sc}}{\hbar^2 Q} \exp\left(-\frac{\hbar^2}{2m_{\rm sc}k_{\rm B}T}\left(\frac{m_{\rm sc}}{\hbar^2 Q}(\hbar\omega - w) - \frac{Q}{2}\right)^2\right) \delta(w) \\ &= \sqrt{\frac{1}{4\pi E_{\rm r} k_{\rm B} T}} \exp\left(-\frac{(\hbar\omega - E_{\rm r})^2}{4E_{\rm r}k_{\rm B}T}\right) \end{aligned} \quad (4.73)$$

with $E_{\rm r} = \hbar^2 Q^2/2m_{\rm sc}$ being the recoil energy experienced by the atom during the scattering event. Thus, the dynamical structure factor of an ideal gas is a Gaussian centred around the recoil energy for a given $Q$. The width of the Gaussian $\sqrt{2E_{\rm r}k_{\rm B}T} = \sqrt{k_{\rm B}T/m_{\rm sc}}\hbar Q$ increases with temperature and scattering vector $Q$.

Double inverse Fourier transform with respect to $\omega$ and $Q$ gives the correlation function $G(r,t)$:

$$\begin{aligned} S(Q,t) &= \hbar \int_{-\infty}^{\infty} {\rm d}\omega \exp({\rm i}\omega t) \sqrt{\frac{1}{4\pi E_{\rm r} k_{\rm B} T}} \exp\left(-\frac{(\hbar\omega - E_{\rm r})^2}{4E_{\rm r}k_{\rm B}T}\right) \\ &= \exp\left(-\frac{Q^2}{2m_{\rm sc}}\left(k_{\rm B}Tt^2 - {\rm i}\hbar t\right)\right) , \end{aligned} \quad (4.74)$$

$$\begin{aligned} G(r,t) &= \left(\frac{1}{2\pi}\right)^3 \int {\rm d}^3 Q \exp(-{\rm i}\underline{Q}\cdot\underline{r}) \exp\left(-\frac{Q^2}{2m_{\rm sc}}\left(k_{\rm B}Tt^2 - {\rm i}\hbar t\right)\right) \\ &= \left(\frac{m_{\rm sc}}{2\pi k_{\rm B}Tt(t - {\rm i}\hbar/k_{\rm B}T)}\right)^{3/2} \exp\left(-\frac{m_{\rm sc}r^2}{2k_{\rm B}Tt(t - {\rm i}\hbar/k_{\rm B}T)}\right) . \end{aligned} \quad (4.75)$$

Because of the quantum mechanical nature of the underlying dynamics both $S(Q,t)$ and $G(r,t)$ have an imaginary part.

The same result can be obtained via the Van Hove correlation function. For this route we start with equation (4.39) for which we have to calculate $\exp({\rm i}\underline{Q}\cdot\underline{\mathbf{r}}(t))$ for a free atom. This can be done using the equation of motion

$${\rm i}\hbar\frac{\rm d}{{\rm d}t}\exp({\rm i}\underline{Q}\cdot\underline{\mathbf{r}}(t)) = \left[\exp({\rm i}\underline{Q}\cdot\underline{\mathbf{r}}(t)), \mathbf{H}\right] \quad (4.76)$$

where

$$\mathbf{H} = \frac{1}{2m_{\rm sc}}\mathbf{p}^2 \quad (4.77)$$

is the Hamiltonian of a free atom and $\mathbf{p}$ the momentum operator. In the following the time dependent operator $\exp(\mathrm{i}\underline{Q}\cdot\underline{\mathbf{r}}(t))$ shall be calculated. This is done using the equation of motion

$$\mathrm{i}\hbar\frac{\mathrm{d}}{\mathrm{d}t}\exp(\mathrm{i}\underline{Q}\cdot\underline{\mathbf{r}}(t)) = \left[\exp(\mathrm{i}\underline{Q}\cdot\underline{\mathbf{r}}(t)), \mathbf{H}\right] . \tag{4.78}$$

Here, the bracket on the right hand side is the commutator. In analogy to equation (4.34)

$$\frac{1}{2m_{\mathrm{sc}}}\left[\exp(\mathrm{i}\underline{Q}\cdot\underline{\mathbf{r}}(t)), \mathbf{p}^2\right] = \frac{1}{2m_{\mathrm{sc}}}\exp(\mathrm{i}t\mathbf{H})\left[\exp(\mathrm{i}\underline{Q}\cdot\underline{\mathbf{r}}(t)), \mathbf{p}^2\right]\exp(-\mathrm{i}t\mathbf{H}) \tag{4.79}$$

holds. The commutator at equal times on the right hand side of the last equation can easily be calculated. For this purpose one uses the coordinate representation $\underline{\mathbf{p}} = -\mathrm{i}\hbar\underline{\nabla}$. By calculation of the derivatives

$$\left[\exp(\mathrm{i}\underline{Q}\cdot\underline{\mathbf{r}}(t)), \mathbf{p}^2\right] = -\hbar\exp(\mathrm{i}\underline{Q}\cdot\underline{\mathbf{r}}(0))\left(\hbar Q^2 + 2\underline{Q}\cdot\underline{\mathbf{p}}\right) \tag{4.80}$$

follows. Since $\underline{\mathbf{p}}$ commutes with the Hamiltonian in the equation of motion the Hamiltonian can be applied directly on $\underline{\mathbf{r}}(0)$:

$$\mathrm{i}\hbar\frac{\mathrm{d}}{\mathrm{d}t}\exp(\mathrm{i}\underline{Q}\cdot\underline{\mathbf{r}}(t)) = -\frac{\hbar}{2m_{\mathrm{sc}}}\exp(\mathrm{i}\underline{Q}\cdot\underline{\mathbf{r}}(0))\left(\hbar Q^2 + 2\underline{Q}\cdot\underline{\mathbf{p}}\right) \tag{4.81}$$

This differential equation can be solved immediately and one obtains for the time dependent operator:

$$\exp(\mathrm{i}\underline{Q}\cdot\underline{\mathbf{r}}(t)) = \exp(\mathrm{i}\underline{Q}\cdot\underline{\mathbf{r}}(0))\exp\left(\frac{\mathrm{i}t}{2m_{\mathrm{sc}}}\left(\hbar Q^2 + 2\underline{Q}\cdot\underline{\mathbf{p}}\right)\right) . \tag{4.82}$$

With this result the correlator in the scattering function (4.39) can be calculated:

$$\left\langle\exp(-\mathrm{i}\underline{Q}\cdot\underline{\mathbf{r}}(0))\exp(\mathrm{i}\underline{Q}\cdot\underline{\mathbf{r}}(t))\right\rangle = \exp\left(\frac{\mathrm{i}\hbar Q^2}{2m_{\mathrm{sc}}}\right)\left\langle\exp\left(\frac{\mathrm{i}\hbar\underline{Q}\cdot\underline{\mathbf{p}}}{2m_{\mathrm{sc}}}\right)\right\rangle . \tag{4.83}$$

As in equation (4.72) the average is taken by using the Boltzmann factor yielding

$$\left\langle\exp\left(\frac{\mathrm{i}\hbar\underline{Q}\cdot\underline{\mathbf{p}}}{2m_{\mathrm{sc}}}\right)\right\rangle = \exp\left(-\frac{t^2Q^2k_{\mathrm{B}}T}{2m_{\mathrm{sc}}}\right) . \tag{4.84}$$

Insertion into (4.83) gives

$$\left\langle\exp(-\mathrm{i}\underline{Q}\cdot\underline{\mathbf{r}}(0))\exp(\mathrm{i}\underline{Q}\cdot\underline{\mathbf{r}}(t))\right\rangle = \exp\left(-\frac{Q^2}{2m_{\mathrm{sc}}}\left(t^2k_{\mathrm{B}}T - \mathrm{i}\hbar t\right)\right) . \tag{4.85}$$

identical to equation (4.74). Thus using the Van Hove correlation function we obtain the same result as was originally derived directly from the definition of the scattering function.

With this example we can also demonstrate that neglecting the operator character of the position vectors leads to a wrong result. If we write the scattering function using the classical expression (4.60)

$$S^{\mathrm{cl}}(Q,\omega) = \frac{1}{2\pi\hbar}\int_{-\infty}^{\infty} \mathrm{d}t \exp(-\mathrm{i}\omega t)\left\langle \exp\left(-\mathrm{i}\underline{Q}\cdot(\underline{r}(t)-\underline{r}(0))\right)\right\rangle \tag{4.86}$$

is obtained. For a free atom we have $\underline{r}(t) = \underline{r}(0) + t\underline{p}/m_{\mathrm{sc}}$. Inserting this expression into (4.86) and averaging leads to:

$$S^{\mathrm{cl}}(Q,\omega) = \sqrt{\frac{1}{4\pi E_{\mathrm{r}} k_{\mathrm{B}} T}} \exp\left(-\frac{\omega^2 m_{\mathrm{sc}}}{2k_{\mathrm{B}}TQ^2}\right). \tag{4.87}$$

Comparison with (4.73) shows that this result is wrong by neglecting the recoil energy term. Instead of being centred at $E_{\mathrm{r}}$ the expression (4.87) is symmetric with respect to $\omega = 0$.

# References


[1] G. E. Bacon: "Neutron Diffraction" (Clarendon Press, Oxford, 1975).

[2] G. E. Bacon (ed.): "Fifty Years Of Neutron Diffraction: The Advent Of Neutron Scattering" (Adam Hilger, Bristol, 1986).

[3] S. W. Lovesey: "Theory of Neutron Scattering from Condensed Matter" (Clarendon Press, Oxford, 1984).

[4] G. L. Squires: "Introduction to the theory of thermal neutron scattering" (Cambridge University Press, Cambridge, 1978).

[5] M. Bée: "Quasielastic neutron scattering" (Adam Hilger, Bristol, 1988).

[6] G. Placzek, *Phys. Rev.* **86** 377 (1952).

[7] J. L. Yarnell, M. J. Katz, R. G. Wenzel, S. H. Koenig, *Phys. Rev. A* **7** 2130 (1973).

[8] G. D. Wignall, D. G. H. Ballard, J. Schelten, *Eur. Polym. J.* **10** 861 (1973).

# 5

# Continuum Description: Grazing Incidence Neutron Scattering

Oliver H. Seeck and Emmanuel Kentzinger

# 5. Continuum description: Grazing Incidence Neutron Scattering

O.H. Seeck and E. Kentzinger

IFF-Streumethoden, FZ Jülich

## 5.1 Introduction

When studying solids or soft matter the explicit molecular structure is not always of particular importance. Quite often the properties investigated are long ranged and not directly connected with the atoms or their positions. One example is a material with a continuous ferromagnetic phase transition: Far below a well defined temperature (the critical temperature called Curie temperature) the material is in a complete ferromagnetic state. Far above no ferromagnetic behavior can be detected. Close to the critical temperature magnetic fluctuations appear. The typical width of the magnetic areas is in the range of several nanometers up to macroscopic distances depending on the temperature (see Fig. 5.1a). The width is basically independent of the lattice spacing or the particular kind of atoms. Therefore, the knowledge of the detailed molecular structure is not necessary to explain the physical properties of ferromagnets.

Other examples are surfaces or layer systems. The properties of the samples such as film thicknesses or in-plane correlation lengths are usually also long ranged compared to the atomic distances and the information about the exact atomic positions is not relevant (see Fig. 5.1b).

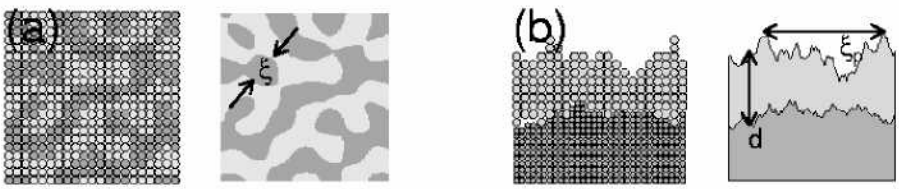



Figure 5.1: *Sketch of systems with relevant mesoscopic or macroscopic properties. (a) Ferromagnet close to the Curie temperature. Ordered regions with a correlation length* $\xi$ *exist. (b) Monolayer system. The layer thickness* d *and the in-plane correlation length of the rough surface* $\xi_p$ *are much larger than the atomic spacing. The left picture of each example shows the real atomic structure the right part the approximation as a continuous system.*

A straightforward method to investigate mesoscopic length scales without taking into account the exact molecular structure of the samples is the small angle scattering. 'Small angle' in this case means that the mean value of the wave vector transfer $|\underline{Q}|$ of the scattered beam is much smaller than the typical reciprocal spacing of the atoms in the sample (e.g., the reciprocal lattice vector $|\underline{a}^*|$ for a crystal with cubic symmetry). In this case the effects of the atomic structure on the scattered signal are negligible. This is schematically explained in Figure 5.2.

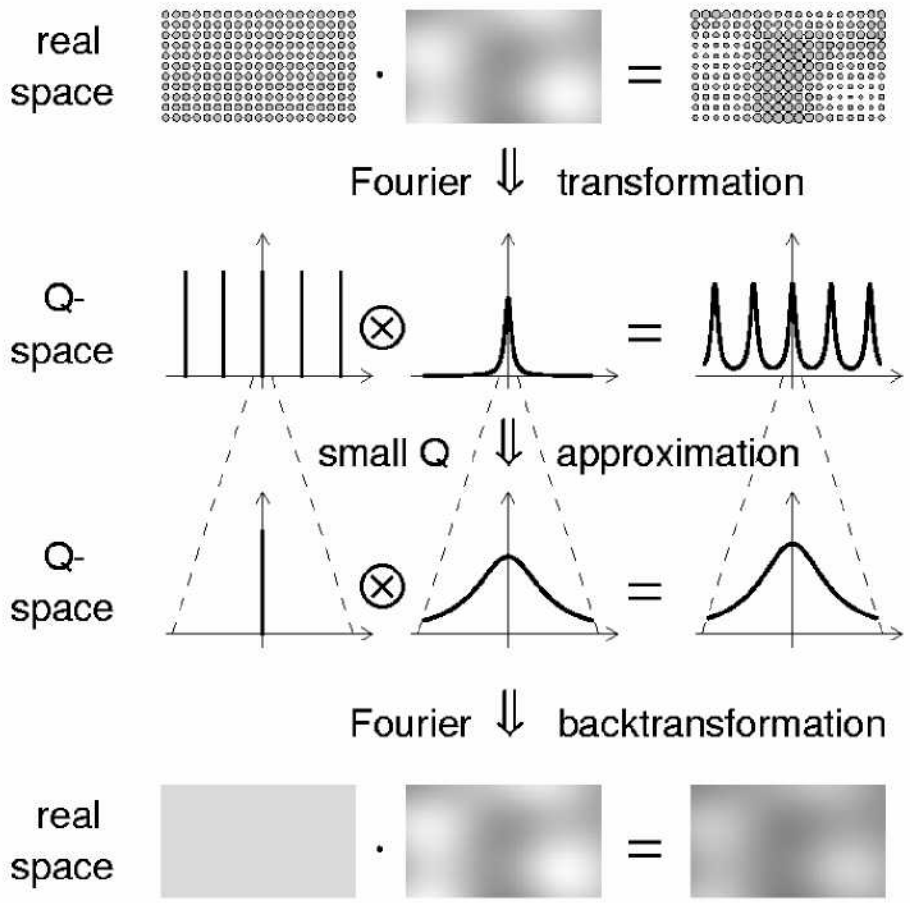



Figure 5.2: *Principles of small angle scattering. The method is not sensitive to the exact atomic structure but only to mesoscopic or macroscopic length scales. Therefore, samples can be treated as continuous systems. The operator* $\otimes$ *denotes the convolution of two functions. A more detailed explanation is given in the text.*

Starting point is the exact atomic structure of the sample. In this section a crystal with some density modulations is chosen (Fig. 5.2 top row). The potential $V(\underline{r})$ of such a system can be written as a product of the undisturbed infinite crystal lattice potential $V_{latt}(\underline{r})$ and the modulation $V_{mod}(\underline{r})$. As it was shown in previous sections in Born approximation the scattered intensity

$$I(\underline{Q}) \sim |A(\underline{Q})|^2 \sim \left|\int V(\underline{r}) \exp(i\underline{Q}\cdot\underline{r}) \mathrm{d}^3 r\right|^2 = \left|\int V_{latt}(\underline{r}) V_{mod}(\underline{r}) \exp(i\underline{Q}\cdot\underline{r}) d^3 r\right|^2 = |\mathbf{F}\{V_{latt}(\underline{r}) V_{mod}(\underline{r})\}(\underline{Q})|^2 \tag{5.1}$$

of the sample can be calculated by performing a Fourier transformation $\mathbf{F}\{V(\underline{r})\}$ of $V(\underline{r})$. The convolution theorem for Fourier transformations can be used to modify equation (5.1). This theorem states that the convolution $\otimes$ of two Fourier transformed functions $f_i = \mathbf{F}\{g_i\}$ gives the same result as the Fourier transformation of the product of both functions $g_i$. Thus,

$$\mathbf{F}\{g_1 \cdot g_2\} = \mathbf{F}\{g_1\} \otimes \mathbf{F}\{g_2\} = f_1 \otimes f_2 = \int f_1(\underline{q}) f_2(\underline{q} - \underline{Q}) \mathrm{d}^3 q \tag{5.2}$$

where the integral is the definition of the convolution.

It is also known from previous sections that for an infinite periodic crystal the lattice potential $V_{latt}(\underline{r})$ can be written as a sum of delta-functions weighted with the scattering length and located at the position of the atoms. The Fourier transformation of $V_{latt}(\underline{r})$ also yields delta-functions: the Bragg peaks at the reciprocal lattice positions. In contrast, the Fourier transformation of $V_{mod}(\underline{r})$ is usually a 'smooth' function which is strongly decreasing for large $|\underline{Q}|$. The result of the convolution is depicted in the second row of Figure 5.2.

By doing a small angle scattering experiment only wave vector transfers $\underline{Q}$ with a mean value close to 0 are considered. All other values are omitted. The result of the magnification around $\underline{Q}$=0 is shown in the third row of Figure 5.2. In good approximation it is identical to a convolution of just a **single** delta-function at $\underline{r}$=0 with the Fourier transformation of $V_{mod}(\underline{r})$. In real space (Fourier backtransformation) a single delta peak corresponds to an infinite sample with homogeneous potential which turns out to be the averaged value of $V_{latt}(\underline{r})$. The fourth row of Figure 5.2 proofs that no information about the atomic structure is necessary to explain a small angle scattering pattern.

To study the morphology of surfaces or interfaces of thin layer systems such as polymer films on silicon substrates or magnetic multilayer systems some specific kinds of small angle neutron (or x-ray) scattering experiments can be performed. Especially for buried interfaces these surface sensitive methods are the only way to investigate the film properties without destroying the sample. Therefore, they are very frequently applied and have an enormous impact on solid states and soft condensed matter physics in general.

The so-called **specular reflectivity** is a scan with a wave vector transfer $Q$ perpendicular to the sample surface which is defined as the $z$-direction in this section. Because of the missing $Q_x$- and $Q_y$-component the reflectivity is only sensitive to the thickness, the potential and the roughness of each film. In-plane properties of the interfaces such as lateral correlation lengths are accessible with different kinds of **diffuse scattering experiments** where at least one of the components $Q_x$ or $Q_y$ is not vanishing.

In the following, the specular reflectivity and the diffuse scattering are explained in more detail. The usual experimental setup will be shown and the basic theory of specular and diffuse scattering will be presented with some examples. Then, polarized neutron specular reflectivity and diffuse scattering for the study of magnetism will be introduced.

### 5.2 Experimental Principals of Surface Sensitive Neutron Scattering

A sketch of a typical neutron surface scattering experiment is displayed in Figure 5.3, a more detailed description is given in other sections. The direction of the primary beam is defined by some slits. Before the primary beam hits the sample the flux is usually monitored. The incident angle $\theta$ which is determined with respect to the sample surface is set by rotating the sample in the beam. The scattered beam is detected at an angle $\theta'$ (also with respect to the surface) which is determined by $\theta$ and the scattering angle $\phi=\theta'+\theta$. In the literature $\phi$ is sometimes called $2\theta$ (which is actually inaccurate because $\phi$ is not necessarily equal to $2\cdot\theta$).

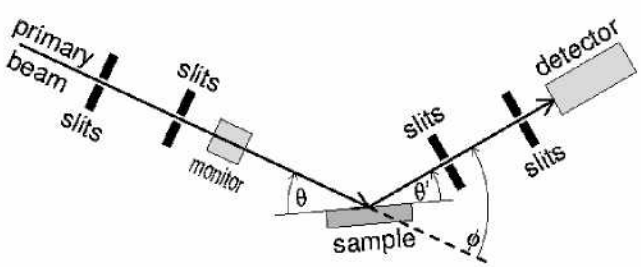



Figure 5.3: *Sketch of a typical surface sensitive neutron scattering experiment. The incident angle is denoted by* $\theta$, *the outgoing angle with respect to the surface by* $\theta'$. *The scattering angle is called* $\phi$.

For specular reflectivity measurements the condition θ=θ' holds which is usually not true for diffuse scattering experiments. The mean value of the wave vector transfer is given by

$$|\underline{Q}| = \frac{4\pi}{\lambda}\sin\left(\frac{\phi}{2}\right) \tag{5.3}$$

with the de Broglie wavelength of the neutrons $\lambda = h/(2mE)^{1/2}$. As it was mentioned before for a small angle scattering experiment $|\underline{Q}|$ has to be much smaller than the typical reciprocal distance of the atoms in the sample. Therefore, $\phi$ also has to be small. Depending on the chosen wavelength the angle $\phi$ is almost never larger than a few degrees. For a surface sensitive experiment, which is performed in reflection and not in transmission (see Fig. 5.4), this means that θ and θ' are also small and positive.

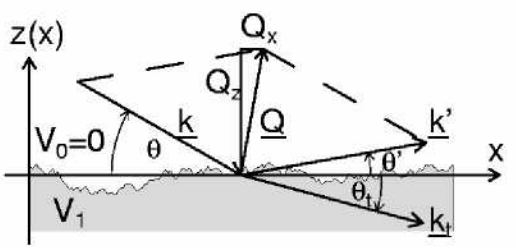



Fig. 5.4: *Sketch of the wave vectors for a surface sensitive experiment. The parameters of the transmitted beam are labeled with the index* t. *The potential of air is denoted by* $V_0$ *that one of the substrate with* $V_1$.

From simple geometrical considerations the components of the wave vector transfer can be deduced. They are defined by

$$Q_x = \frac{2\pi}{\lambda}(\cos\theta' - \cos\theta) \qquad Q_y = 0 \qquad Q_z = \frac{2\pi}{\lambda}(\sin\theta' + \sin\theta) \tag{5.4}$$

and can be used to estimate the accessible $Q$-range of surface sensitive experiments. At a typical wavelength of the neutrons of about 0.2nm=2Å and angles not larger than 1.0 degree $Q_z$ would always be less than $0.1\text{Å}^{-1}$. $|Q_x|$ would even be restricted to $5\cdot10^{-4}\text{Å}^{-1}$. For comparison: A simple cubic crystal with 3Å lattice spacing has a smallest reciprocal lattice vector of $2.1\text{Å}^{-1}$.

### 5.3 Specular Neutron Reflectivity in Born Approximation

For specular reflectivity measurements the exit angle θ' is always identical to the incident angle θ. Therefore, the $Q_x$-component is equal to zero and the reflectivity data does not contain any particular information about the in-plane structure of the sample. In first order Born approximation [1] the scattered intensity is given by

$$I(Q_z) \sim \frac{1}{Q_z^4}\left|\int \frac{\mathrm{d}V(z)}{\mathrm{d}z}\exp(-iQ_z z)\mathrm{d}z\right|^2 \tag{5.5}$$

which means, that the specular reflectivity is basically determined by the Fourier transformation of the gradient of the potential profile perpendicular to the sample surface. The averaged (continuous) potential of a particular material with $N$ components is defined by

$$V = \frac{2\pi\hbar^2}{m_n}\sum_{j=1}^{N} b_j \rho_j \tag{5.6}$$

where the $b_j$ are the scattering lengths and the $\rho_j$ are the particle number densities of the components. A one-component sample with a perfectly smooth and flat surface which is oriented in the $(x,y)$-plane would yield a step function for the $z$-dependent potential:

$$V(z) = \frac{2\pi\hbar^2 b\rho}{m_n}\left(\frac{1}{2} - \frac{1}{2}\Theta(z)\right) = \begin{cases} 0 & : \; z > 0 \\ 2\pi\hbar^2 b\rho / m_n & : \; z \le 0 \end{cases} \tag{5.7}$$

The derivative of $V(z)$ is a delta-function $dV(z)/dz \sim \delta(z)$. With Eq. (5.5) one gets $I(Q_z) \sim Q_z^{-4}$ because the Fourier transformation of a delta-function at $z=0$ is identical to 1.

However, a perfectly smooth and flat surface does not exist. Instead surface roughness or density gradients have to be taken into account [2,3]. As shown in Fig. 5.5 roughness means that the $z$-position of the surface is locally different from the mean position at $z=0$. Averaging the density in the $(x,y)$-plane at each $z$-coordinate gives a smooth profile $V(z)$ perpendicular to the surface. The exact shape of the profile depends on the actual physical and chemical properties close to the surface. For simple rough surfaces in good approximation an error-function

$$V(z) = \frac{V}{2} - \frac{V}{2}\mathrm{erf}\left(\frac{z}{\sqrt{2}\sigma}\right) \qquad \text{with} \qquad \mathrm{erf}(z) = \frac{2}{\sqrt{\pi}}\int_0^z \exp(-t^2)\mathrm{d}t \tag{5.8}$$

is sufficient to model the profile. The parameter σ is called rms-roughness and is a measure for the root mean square width of $V(z)$ given by the gaussian probability function

$$\frac{\mathrm{d}V(z)}{\mathrm{d}z} \sim P(z) = \frac{1}{\sqrt{2\pi}\sigma}\exp\left(-\frac{z^2}{2\sigma^2}\right). \tag{5.9}$$

Figure 5.5 also shows that the profile does not contain any information about the lateral structure of the rough surface. Therefore, the reflectivity is insensitive to different in-plane length scales $\xi_p$. It even cannot be used to distinguish between a rough interface and a density gradient caused by e.g., interdiffusion. It will be explained later that this can only be done by using diffuse scattering experiments.

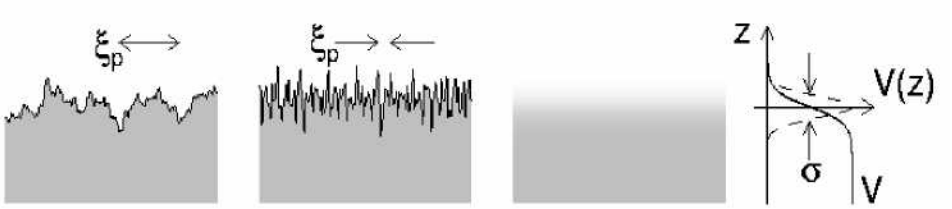



Figure 5.5: *Three different surfaces with the same rms-roughness σ determined by the root mean square width of the probability function (dashed line) of the profile* V(z) *(solid line). The in-plane structure is determined by the lateral correlation length* $\xi_p$ *which is large for the very left example quite small for the rough surface shown in the center and not defined for the density gradient example (right).*

The reflectivity of a rough surface with an error function profile can easily be calculated. The derivative of $V(z)$ is determined by the probability function P(z) [see Eq. (5.9)]. With Eq. (5.5) this yields $I(Q_z) \sim Q_z^{-4}\exp(-Q_z^2\sigma^2)$. Compared with the perfectly smooth surface the reflected intensity is damped by a Debye-Waller factor: The rougher the surfaces the less intensity is reflected at large $Q_z$ (see Figure 5.6 left).

Reflectivity scans are not only extremely sensitive to surfaces roughnesses but also to film thicknesses of layer systems. If a thin film with thickness $d$ and an averaged potential $V_1$ is deposited on a substrate with potential $V_2$ the density profile $V(z)$ is given by

$$V(z) = \begin{cases} 0 & : \quad z > d \\ 2\pi\hbar^2 b_1\rho_1 / m_n = V_1 & : \quad d \geq z > 0 \\ 2\pi\hbar^2 b_2\rho_2 / m_n = V_2 & : \quad 0 \geq z \end{cases} \tag{5.10}$$

if the interfacial rms-roughnesses $\sigma_1$ and $\sigma_2$ are neglected. The derivative yields two delta-functions: $dV(z)/dz \sim (b_2\rho_2 - b_1\rho_1)\delta(z) + b_1\rho_1\delta(z-d)$. Using Eq. (5.5), the specularily reflected intensity of a perfectly smooth monolayer system is given by

$$I(Q_z) \sim \frac{1}{Q_z^4}\left[\left(b_2\rho_2 - b_1\rho_1\right)^2 + \left(b_1\rho_1\right)^2 + 2\left(b_2\rho_2 - b_1\rho_1\right)\left(b_1\rho_1\right)\cos\left(Q_z d\right)\right]. \tag{5.11}$$

This means that films cause oscillations in the reflectivity. The period is determined by the film thickness the strength (usually called 'contrast') by the difference of the potentials $V_1$ and $V_2$ (see Fig. 5.6 right).

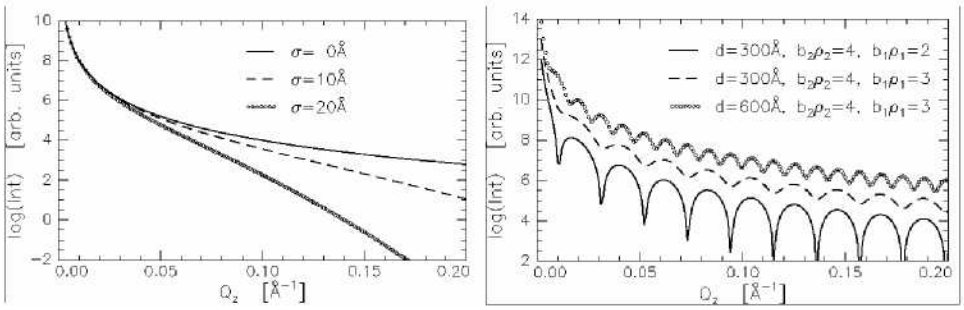



Figure 5.6: *The left graph displays the effect of the surface roughness on the specularily reflected intensity: the rougher the surface the less intensity is reflected at large* $Q_z$. *The right figure shows reflectivities of perfectly smooth monolayer systems. The curves are shifted in intensity for clarity. The thicker the film the smaller the distance of the so-called Kiessig fringes. The less the contrast (given by* $[b_2\rho_2\text{-}b_1\rho_1]$*) the less pronounced the oscillations are.*

In this way every additional layer appears as an oscillation in the reflectivity curve. Interface roughnesses can also quite easily be included in the theory and yield a typical damping of each oscillation. Multilayer systems with different parameters for each layer generally show very complicate reflectivities. They are usually difficult to analyze especially because of the so-called 'phase problem' which prevents an unambiguous solution of Eq. (5.5). The „ phase problem" appears when performing the mean square of the complex

function $\mathbf{F}\{dV(z)/dz\}$ to calculate the reflected intensity [see Eq. (5.5)]. The loss of the phase information may end up in identical reflectivities even though the potential profiles are different. E.g., using Eq. (5.11) it can easily be shown, that a monolayer system with $b_2\rho_2=4$ and $b_1\rho_1=3$ exactly results in the same reflectivity as $b_2\rho_2=4$ and $b_1\rho_1=1$, if the film thicknesses are identical.

### 5.4 Diffuse Neutron Scattering in Born Approximation

Performing a surface scattering experiment it turns out that some intensity is also scattered in directions with $\theta\neq\theta'$. In this case the wave vector transfer $\underline{Q}$ has a component in $Q_x$-direction (see Fig. 5.4). This off-specular signal is called diffuse scattering and is caused by lateral structures (in-plane, in the (x,y)-plane) of the sample [4]. If the samples are perfectly smooth or if there is no lateral structure (see Fig. 5.5 right) no diffuse scattering is expected.

In general, for rough layer systems the diffuse scattering is sensitive to the correlation function $C_{jk}(\underline{R})$ between two interfaces $j$ and $k$ where $\underline{R}$ is an in-plane vector $(x,y)$. The correlation function is defined by

$$C_{jk}(\underline{R}) = \int z_j(\underline{r}) z_k(\underline{r}+\underline{R}) \mathrm{d}^2 r \tag{5.12}$$

with the local deviation $z_j(\underline{r})$ from the averaged position of the interface $j$. The correlation function between two different interfaces is usually called 'cross-correlation'. If $j=k$ holds $C_{jk}(\underline{R})=C_{jj}(\underline{R})$ is called 'auto-correlation'. Qualitatively, $C_{jk}(\underline{R})$ is large if two areas of the interfaces $j$ and $k$, which are $\underline{R}$ apart from each other, 'look similar'. E.g., if the two interfaces contain a periodic structure with the same periodic distance $D$ the correlation function exhibits maxima at $D,2D,3D$ ... . For an auto-correlation function of a single rough surfaces one gets a monotone decreasing function: For very small distances the parts of the surface look similar, the larger the distance the more different they become. The width of the curve is connected to the lateral correlation length $\xi_p$ of the interface (see e.g., Fig 5.5) [5].

The diffuse scattering can be used to investigate periodic in-plane structures, in-plane correlation lengths of a single rough interface and correlations between two different interfaces. Figure 5.7 depicts some examples. The complete mathematical formalism to deduce the diffusely scattered intensity is quite complicate [6]. Therefore, the full theory is

omitted in this section. Instead, the diffuse scattering is explained using a simple monolayer system.

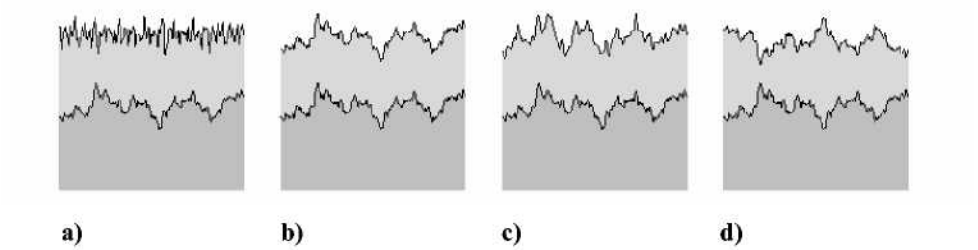



Figure 5.7: *Some examples of monolayer systems with rough surfaces. a) Both interfaces are not correlated at all. b) Perfect cross-correlation between the lower and the upper interface. c) A cross-correlation is visible but it is not perfect: The interfaces do not exactly look the same. d) Perfectly anti-correlated interfaces.*

In Born Approximation the diffusely scattered intensity of a monolayer system with the interfaces $j$=1,2 and the film thickness $d$ can be calculated by

$$I_{\text{diff}}(Q_x,Q_z) \sim \frac{1}{Q_z^2}\Big[(b_2\rho_2 - b_1\rho_1)^2 \exp\left(-Q_z^2\sigma_2^2\right)S_{22}(Q_x) + (b_1\rho_1)^2 \exp\left(-Q_z^2\sigma_1^2\right)S_{11}(Q_x) + 2(b_2\rho_2 - b_1\rho_1)(b_1\rho_1)\exp\left(-Q_z^2\left[\sigma_2^2+\sigma_1^2\right]/2\right)S_{12}(Q_x)\cos(Q_z d)\Big] \tag{5.13}$$

The rms-roughnesses are given by $\sigma_{1,2}$ and the so-called structure factor by

$$S_{jk}(Q_x) = \int\left(\exp\left[Q_z^2 C_{jk}(x)\right]-1\right)\exp\left(-iQ_x x\right)\mathrm{d}x. \tag{5.14}$$

Eq. (5.13) obviously looks similar to Eq. (5.11) which describes the specular reflectivity. The exponential Debye-Waller functions would also appear in Eq. (5.11) if roughness is taken into account, the only difference are the additional structure factors $S_{jk}(Q_x)$ which modify the scattering due to the in-plane structure of the interfaces.

Some examples of diffuse scattering experiments are depicted in Fig. 5.8. They show that the in-plane correlation length $\xi_p$ of a rough surface (see Fig 5.5) is directly connected with the width of the diffuse scattering in $Q_x$-direction. Furthermore, a $Q_z$-scan at fixed $Q_x$ contains the information about cross-correlations of two interfaces. If cross-correlations are present with $S_{jk}\neq 0$ for $j\neq k$ the last term of Eq. (5.13) leads to characteristic oscillations of the

diffuse scattering which are in-phase with the specular reflectivity in the case of correlated interfaces and out-of-phase in the case of anti-correlation.

Equation (5.13) also shows that the diffuse scattering can be detected in the whole $Q$-space even at $Q_x$=0 which is actually the position of the specularily reflected signal. This means that reflectivity measurements ($Q_z$-scans at $Q_x$=0) **always** contain both the specular reflectivity and the diffuse scattering at $Q_x$=0. To extract the specular reflectivity from the reflectivity measurement the diffuse scattering has to be subtracted. This is usually done by performing a $Q_z$-scan with a small offset $\Delta Q_x$ so that the specular condition is not exactly matched. This so-called longitudinal diffuse scan is subtracted from the measured reflectivity to get the true specular reflectivity.

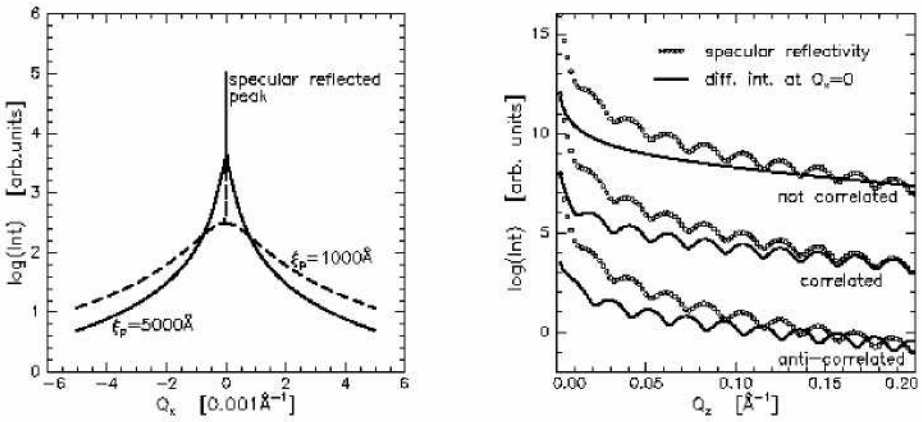



Figure 5.8: *Examples of diffuse scattering experiments. Left:* $Q_x$*-scan at fixed* $Q_z$ *from a single rough surface. The solid curve corresponds to a sample with an in-plane correlation length of* $\xi_p$*=5000Å the dashed line to* $\xi_p$*=1000Å. The peaks at the condition* $Q_x$*=0 (where* $\theta=\theta'$*) are* ***not*** *diffuse scattering but caused by the specular reflectivity. Right: Specular reflectivity (symbols) and diffuse scattering* $Q_z$*-scans at* $Q_x$*=0 (solid lines) of a monolayer system with* $d$*=300Å,* $b_2\rho_2$*=4,* $\sigma_2$*=5Å,* $b_1\rho_1$*=3 and* $\sigma_1$*=5Å. The diffuse scans show the effect of cross-correlations. The* ***measured*** *reflectivity is determined by the sum of the specular and the diffuse scan.*

Unfortunately, the intensity of the diffuse scattering is usually orders of magnitude smaller than the specularily reflected signal. To get good statistics and reliable data a very high primary flux is necessary. This can easily be achieved with synchrotron radiation x-ray sources but is hardly possibly for neutron sources (see section 5.6). Therefore, it is extremely difficult to extract quantitative information from the neutron diffuse scattering data.

## 5.5 The Regime of the Total External Reflection: Exact Solution of the Wave Equation

It is obvious that the Born approximation [Eqs. (5.5) and (5.13)] fails for $Q_z \to 0$ because the intensity would become infinite at $Q_z=0$. The reason is that multiple scattering processes are neglected within the Born approximation. For surface sensitive experiments multiple scattering processes become essential at very small angles [7]. An exact description of the scattered intensity can be deduced for a perfectly smooth surface from quantum theory.

Starting point is the Schrödinger equation

$$\left[-\frac{\hbar^2}{2m_n}\Delta + V(\underline{r})\right]\Psi(\underline{r}) = E\Psi(\underline{r}) \tag{5.15}$$

for the wave function of the neutrons $\Psi(\underline{r})$. The energy of the neutrons is given by $E = \hbar^2 k^2 / (2m_n)$ with the mean value $k=2\pi/\lambda$ of the wave vector $\underline{k}$ (the incident and the outgoing beam have identical $k$ because elastic scattering is assumed). For a homogeneous sample the potential is determined by Eq. (5.6), thus

$$\left[\Delta + \left(k^2 - 4\pi\Sigma_j b_j\rho_j\right)\right]\Psi(\underline{r}) = \left[\Delta + k^2\left(1 - \frac{\lambda^2}{\pi}\Sigma_j b_j\rho_j\right)\right]\Psi(\underline{r}) = \left[\Delta + k_t^2\right]\Psi(\underline{r}) = 0 \tag{5.16}$$

with the wave vector $k_t$ inside the medium (see Fig. 5.4). From Eq. (5.16) it is justified to introduce the refraction index $n_t=k_t/k$ of the material. In very good approximation one yields

$$n_t = 1 - \frac{\lambda^2}{2\pi}\sum_j b_j\rho_j = 1 - \delta_t \tag{5.17}$$

for the refraction index which is a number close to 1 for neutrons of approximate 1Å wavelength (the correction $\delta_t$ is called **dispersion** and is on the order of $10^{-5}...10^{-6}$)

By introducing the refraction index the basic principles of optics can be applied for all further considerations. First of all it is remarkable that for many materials $n_t$ is smaller than 1 (because $b_j$ is usually and $\rho_j$ always positive, thus $\delta_t$ is usually positive). This means that the transmitted beam is refracted towards the sample surface ($\theta_t<\theta$, see Fig. 5.4). For values of $\theta$ below the so-called **critical angle** $\theta_c$ the incoming beam cannot penetrate the sample surface

but is completely reflected. The critical angle can be estimated by $\theta_c \approx (2\delta_t)^{1/2}$ and is on the order of some 0.1 degree depending on the density, the scattering lengths of the atoms and the wavelength of the neutrons. For $\theta$ values beyond $\theta_c$ the beam can penetrate the sample and is only partly reflected. At the sample surface the reflection and transmission coefficients $r_f$ and $t_f$ are obtained by the Fresnel formulars

$$r_f = \frac{k_z - k_{t,z}}{k_z + k_{t,z}} \qquad \text{And} \qquad t_f = \frac{2k_z}{k_z + k_{t,z}} \tag{5.18}$$

with $k_z = k\sin\theta$ and $k_{t,z} = k_t \sin\theta_t = k(n_t^2 - \cos^2\theta)^{1/2}$ (see Fig. 5.4). The specular reflected intensity $I = |r_f|^2$ is determined by the absolute square of the reflection coefficient. It shows the typical plateau below the critical angle, the regime of the total external reflection, and the rapidly decreasing intensity beyond $\theta_c$. With appropriate approximations one gets $I \approx \delta_t^2/(4\sin^4\theta) \sim Q_z^{-4}$ for incident angles $\theta$ larger than $3\delta_t$ which is the confirmation of the Born approximation (see Fig. 5.9).

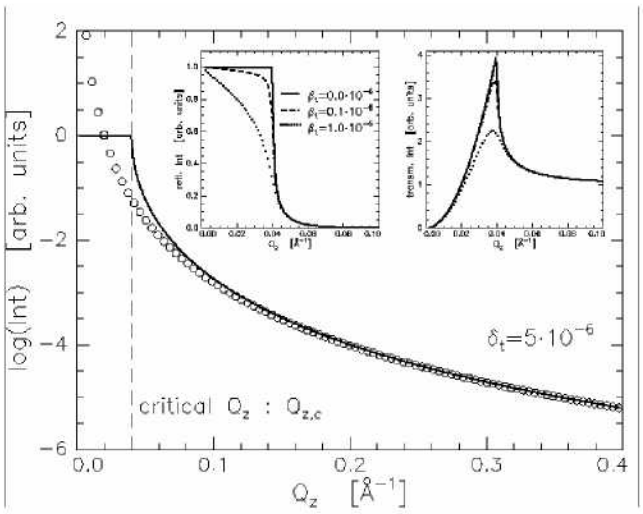



Figure 5.9: *Effect of the total external reflection. The large figure shows a reflectivity of a smooth surface in Born approximation (symbols) and the exact Fresnel form (solid line). The dashed line marks the critical* $Q_z$. *The left inset displays absorption effects in the reflectivity on a linear scale. The same is depicted for the transmitted intensity in the right inset.*

Not addressed yet in this section is the **absorption** $\beta_t$ of the neutrons inside the sample. For most materials such as silicon the absorption is negligible but this is not the case for e.g. cadmium or indium. Most straightforward, it can be introduced by including an imaginary part to the refraction index

$$n_t = 1 - \delta_t + i\beta_t . \tag{5.19}$$

The effect of the absorption is shown in Fig. 5.9. It basically smoothes the sharp features of the intensity close the critical angle and also restricts the penetration depth of the neutrons to finite values.

The diffuse scattering is also modified in the regime of the total external reflection [8,9]. In good approximation one gets

$$I_{\text{diff}}(Q_x, Q_z) \sim \left|t_f(\theta)\right|^2 Q_z^{-2} \exp\left(-Q_z^2\sigma_1^2\right) S_{11}(Q_x) \left|t_f(\theta')\right|^2 \tag{5.20}$$

for a single rough surface. For layer systems this expression becomes much more complicate. Eq. (5.20) shows, that the transmission functions of the incoming and the outgoing beam have to be taken into account. The transmission function $t_f$ exhibits a maximum at the critical angle (or the critical $Q_z$, respectively, see Fig. 5.9) because for incident angles $\theta = \theta_c$ an evanescent wave appears which runs parallel to the surface ($\theta' = 0$) [10]. Therefore, the diffuse scattering also has maxima called Yoneda wings at the positions $\theta=\theta_c$ and $\theta'=\theta_c$ (see Fig. 5.10).

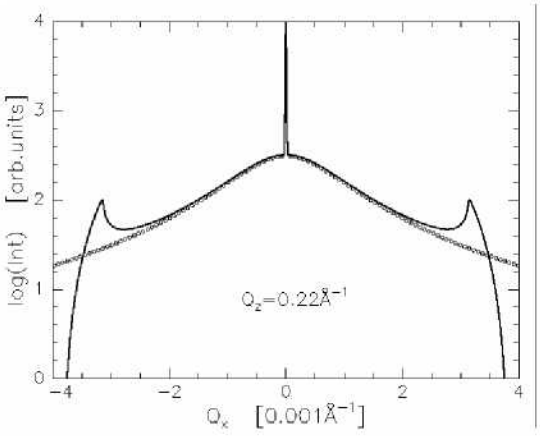



Figure 5.10: *Diffuse scattering scan at fixed* $Q_z$. *The symbols correspond to the Born approximation (dashed line in Fig. 5.8). The solid line displays the better approximation including the scattering effects due to the total external reflection at* $\theta=\theta_c$ *and* $\theta'=\theta_c$. *They are visible as the Yoneda-maxima at* $|Q_x|\approx 0.0032\text{Å}^{-1}$. *The peak at the center is the specular reflected intensity* ($\theta=\theta'$).

In summary, the optical properties of the sample affect the scattering only if the incident or the exit angle is comparable or smaller than the critical angle which is usually smaller than 0.4°. The full dynamical theory can only be deduced for the specular reflectivity. For the diffuse scattering no exact solution exists right now.

## 5.6 An Important Application of Neutron Reflectometry

For many standard scattering experiments on layer systems x-rays are much more suitable than neutrons because of the higher flux, the better collimation and the less divergence. In numbers: A standard synchrotron radiation source has a primary beam intensity of about $10^{10}$ counts/sec at a typical spot size of $(0.2\times1)\text{mm}^2$. The beam divergence which determines the $\underline{Q}$-space resolution is less than 1/100 of a degree. For a modern neutron source one gets less than $10^7$ counts/sec in an area of $(0.5\times20)\text{mm}^2$ with a divergence of larger than 0.02°.

However, for some topics of research neutron scattering is superior. One example is the investigation of materials which mainly contain hydrogen, carbon, nitrogen or oxygen such as organic molecules. In this case the electron density [which for x-rays replaces the potential $V(\underline{r})$] is very low and the x-ray contrast becomes very small. In contrast, for neutron $V(\underline{r})$ strongly depends on the isotope of the elements. Therefore, by using deuterated or hydrogenated organic materials the scattering contrast can easily be tuned without changing the chemical properties of the samples. Figure 5.11 shows an example of a polymer bilayer.

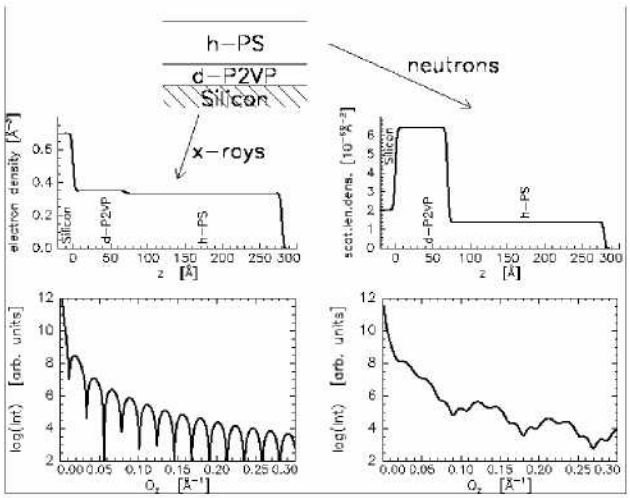



Figure 5.11: *Comparison of an x-ray (left column) and a neutron (right column) reflectivity of a polymer bilayer (210Å polystyrene [PS] on 70Å deuterated polyvinylpyrridine [d-P2VP] on a silicon substrate). The x-ray contrast between the two polymers given by the electron density is only about 5%.*

It can clearly be seen that the x-ray reflectivity only exhibits one significant oscillation period which is due to the whole film thickness. The x-ray contrast at the polymer interface is too small to modulate the intensity. Advanced analyzing methods have to be used to extract

the information of the polymer-polymer interface [11]. This is different for neutrons: By deuterating the bottom polymer the contrast is enhanced dramatically. The reflectivity shows separate oscillations: a long period due to the thin d-P2VP film and a short period which is caused by the h-PS film. The analysis is straightforward and usually very reliable.

**5.7 Polarized Neutron Methods – Introduction.**

The physical properties of magnetic multilayers and nanostructures, such as electron correlations, spin transport and molecular magnetism, do not depend only of the molecular structure of the layers but also on their nuclear and magnetic structure at the mesoscopic level [13]. In the following, we will concentrate on the investigation of the magnetisation density profiles and their in-plane fluctuations in multilayers using specular reflectivity and off-specular scattering of polarized neutrons.

The most popular laboratory techniques for the investigation of magnetism in multilayers, such as magnetic force microscopy (MFM) or Kerr microscopy, are surface or near surface techniques and can sometimes be disturbing. For example, the interaction of the MFM tip with the sample can disturb its magnetic field distribution inside it when it is made of a material of low magnetic coercivity. The magnetic and the nuclear interaction of neutrons with matter are very weak, making it a fully non-disturbing probe.

At and below the critical angle of total reflection $\theta_c$, the neutron wave is evanescent and has a small penetration depth, usually of the order of 100 to 200 Å at $\theta_c$. As the angle of incidence of the neutron increases from zero, the penetration increases. Just above $\theta_c$, the penetration depth shows a sharp increase and then further increases as θ increases. This dependency of the neutron penetration depth as a function of the angle of incidence makes therefore reflectometry and scattering under grazing incidence close to the critical angle of total reflection a unique probe to investigate in a depth-resolved way the nuclear and magnetisation profiles in thin films. We will exemplify this aspect in the example given later in this manuscript.

An important quantity to consider for the interpretation of specular reflectivity and off-specular scattering data is the projection $l_*$ of the coherence length of the neutron beam on the sample surface and its value with respect to the value of the lateral magnetic or nuclear correlation length. Within the coherence length, neutron waves can interfere, outside interference is not possible. If a sample is flat and homogeneous within $l_*$, no lateral

momentum $\boldsymbol{\kappa} = Q_x \mathbf{e}_x + Q_y \mathbf{e}_y$ can be transferred, and intensity is seen only in the specular direction. The measured specular reflectivity is the incoherent sum of the different reflectivities from all the illuminated coherence volumes of the sample. If the sample is not translational invariant in-plane on the length scale of $l_*$, lateral momentum transfer can occur and some intensity can be detected off-specular, i.e. at $\boldsymbol{\kappa} \neq 0$. The measured scattering cross section is then an average over the different scattering cross sections from the different coherence volumes of the sample. Usually, when spanning a whole range of θ and θ' values, off-specular signal ($\theta \neq \theta'$) coexists with specular reflectivity ($\theta = \theta'$). Specular reflectivity originates from the laterally averaged neutron-matter interaction potential and diffuse scattering from the fluctuations around this value.

In appropriate approximation the value of the lateral coherence length is given by the resolution of the in-plane component of the momentum transfer ($l_* \sim \delta Q_*$) and therefore depends of the wavelength resolution and on the collimation of the neutron beam. It typically ranges from a μm to several mm. It can therefore be greatly extended, leading to a high probability for coherent multiple scattering of the neutrons. In that case, the Born approximation fails to describe properly the measured diffuse scattering. The Distorted Wave Born Approximation (DWBA), already introduced in section 5.5, works usually quite well to reproduce the measured data.

### 5.9 Specular reflectivity of polarized neutron

We stay in the homogeneous and flat approximation, where the neutron-matter interaction potential is only depth depending. In the case of magnetic multilayers, the neutron-matter interaction in layer l can be separated into two parts, i.e. $\hat{V}_l = V_l^N \hat{1} + \hat{V}_l^M$ where $V_l^N$ is the neutron-nuclei interaction and $\hat{V}_l^M = -\mu_n \hat{\boldsymbol{\sigma}} \cdot \mathbf{B}_l$ is the magnetic dipole interaction operator between the neutron magnetic moment operator $\mu_n \hat{\boldsymbol{\sigma}}$ and the magnetic field $\mathbf{B}_l$. $\hat{\boldsymbol{\sigma}}$ is the vector of Pauli matrices, i.e. $\hat{\boldsymbol{\sigma}} = (\sigma_\perp, \sigma_z, \sigma_{//})$ with

$$\sigma_\perp = \begin{pmatrix} 0 & 1 \\ 1 & 0 \end{pmatrix} \quad \sigma_z = \begin{pmatrix} 0 & -i \\ i & 0 \end{pmatrix} \quad \sigma_{//} = \begin{pmatrix} 1 & 0 \\ 0 & -1 \end{pmatrix}. \qquad (5.21)$$

The magnetic interaction operator in the magnetic layer l can be decomposed into terms:

$$\hat{V}_l^M = -\mu_n \hat{\boldsymbol{\sigma}} \cdot [\mathbf{B}_0 + \mu_0 (1 - D)\mathbf{M}] \qquad (5.22)$$

where $\mathbf{B}_0$ is the applied field, $\mathbf{M}$ is the magnetisation inside the layer, D is the demagnetising factor. In the case of an infinite magnetic thin film, $(1-D)\mathbf{M}$ in Equ. (5.22) is equal to the in-plane component of the magnetisation [14]. It is only possible to measure the in-plane component of magnetisation.

The total interaction potential operator can be rewritten as

$$\hat{V}_l = \frac{2\pi\hbar^2}{m}\left(\rho_l^N \hat{1} + \rho_l^M \hat{\boldsymbol{\sigma}}\cdot\mathbf{b}_l\right) \qquad (5.23)$$

where $\rho_l^N$ and $\rho_l^M$ are respectively the nuclear and magnetic scattering length densities. $\mathbf{b}_l$ is the unit vector oriented along $\mathbf{B}_l$. It provides a quantization axis for the neutron spin. The eigenvectors $|+\rangle$ and $|-\rangle$ of the operator $\hat{\boldsymbol{\sigma}}\cdot\mathbf{b}_l$ with eigenvalues +1 and -1 respectively define states of the neutron with "up" and "down" spin projections along the quantization axis. The neutron state $|\Psi(\mathbf{r})\rangle$, solution of the Schrödinger equation in coordinates and spin space for the potential operator $\hat{V}_l$, is a linear combination of those two eigenvectors:

$$|\Psi(\mathbf{r})\rangle = \Psi^+(\mathbf{r})|+\rangle + \Psi^-(\mathbf{r})|-\rangle = \begin{pmatrix}\Psi^+(\mathbf{r})\\ \Psi^-(\mathbf{r})\end{pmatrix}. \qquad (5.24)$$

Before describing the interaction of the neutron dipole moment with the multilayer, we have to define one single quantization axis that will be fixed during the consideration of the whole interaction process. Usually the quantization axis is taken along the guiding magnetic field outside the sample and it is called the // axis. The states $|+\rangle$ and $|-\rangle$ representing spin up and spin down neutrons respectively are then the eigenvectors of the operator $\hat{\boldsymbol{\sigma}}\cdot\mathbf{b}_0 = \hat{\sigma}_{//}$ where $\mathbf{b}_0$ is the unit vector directed along the magnetic field outside the sample $\mathbf{B}_0$. The unit matrix $\hat{1}$ in (5.22) is the matrix that leaves those states unchanged.

Before the interaction with the sample and its surrounding magnetic field, the neutron can be considered as a plane wave with wave vector $\mathbf{k}_0$ and energy $\hbar^2 k_0^2/(2m)$. The interaction potential has no dependency along the lateral coordinate $\boldsymbol{\rho}$ of the sample and the neutron wave vector in layer l can be written as $|\Psi_l(\mathbf{r})\rangle = e^{i\boldsymbol{\kappa}.\boldsymbol{\rho}}|\Psi_l(z)\rangle$ where $\boldsymbol{\kappa}$ is the in-plane conserving component of the wave vector $\mathbf{k}_l = k_{z,l}.\mathbf{e}_z + \boldsymbol{\kappa}.\mathbf{e}_{\boldsymbol{\rho}}$. The three dimensional Schrödinger equation can therefore be reduced to a set of one dimensional equations:

$$\Psi''_{l,+}(z)+\left[k_{z,l}^2-4\pi\left(\rho_l^N+\rho_l^M b_{l,//}\right)\right]\Psi_{l,+}(z)-4\pi\rho_l^M b_{l,\perp}\Psi_{l,-}(z)=0$$
$$\Psi''_{l,-}(z)+\left[k_{z,l}^2-4\pi\left(\rho_l^N+\rho_l^M b_{l,//}\right)\right]\Psi_{l,-}(z)-4\pi\rho_l^M b_{l,\perp}\Psi_{l,+}(z)=0 \qquad (5.25)$$

The solutions of these coupled linear differential equations are of the form

$$\left|\Psi_l(z)\right\rangle=\left(e^{i\hat{k}_{z,l}(z-z_{l-1})}\hat{t}_l+e^{-i\hat{k}_{z,l}(z-z_{l-1})}\hat{r}_l\right)\left|\Psi_l(0)\right\rangle \qquad (5.26)$$

where

$$\hat{k}_{z,l}=\sqrt{k_{z,0}^2-4\pi\left(\rho_l^N+\rho_l^M\hat{\boldsymbol{\sigma}}\cdot\mathbf{b}_l\right)} \qquad (5.27)$$

is the component perpendicular to the sample surface of the incoming wave vector. Note that $\hat{k}_{z,l}$ is an operator in spin space, and has two different eigenvalues along the quantization axis: $k_{z,l}^{\pm}=\sqrt{k_{z,0}^2-4\pi\left(\rho_l^N\pm\rho_l^M\right)}$ where $k_{z,o}=(2\pi\sin\theta)/\lambda$ is the perpendicular component of the incoming wave vector in vacuum. $\hat{t}_l$ and $\hat{r}_l$ are the reflection and transmission operators in layer l. They are also operators in spin space, with two different eigenvalues.

The operators of reflection and transmission amplitude in each layer can be deduced recursively by considering the continuities of the wave function and its first derivative at the interfaces between two layers. If N is the number of layers in the system, the number of interfaces is N+1 and the continuity relations lead to 2(N+1) equations. Considering the vacuum on top of the system and the substrate, 2(N+2) reflection and transmission amplitudes operators have to be found. Two other conditions are added by considering that the transmission amplitude in the vacuum is equal to the unit matrix ($\hat{t}_0=\hat{1}$) and that the substrate, as a semi-infinite medium, has no reflection amplitude ($\hat{r}_{N+1}=\hat{0}$). The resolution of this system of equations is not complicated but lengthy. Its solution can be found in [15].

Four types of reflectivities follow, by projecting the reflection amplitude in vacuum on the bra and kets representing up and down neutrons. The measured reflectivity is then the modulus squared of the obtained number:

$$R^{\pm\pm}=\left|\left\langle\pm\left|\hat{r}_0\right|\pm\right\rangle\right|^2. \qquad (5.28)$$

The above equations have a clear physical meaning. From (5.25), it is clear that only the nuclear scattering length and the component of the in-plane magnetisation parallel to the external field ($B_{l,//}$) lead to non-spin-flip (NSF) reflectivities. The component of the in-plane magnetic induction perpendicular to the external field ($B_{l,\perp}$) lead to spin-flip (SF) reflectivities. By measuring both the SF and NSF reflectivities and comparing their relative

intensities it is therefore possible to get vector information on the magnetisations inside each layer.

Depending of the neutron spin orientation $\hat{k}_{k,l}$ has two different projections along the quantization axis. The transmitted part of the wave amplitude in layer l (first part of equ.5.26) will therefore be evanescent below two different values of $k_{z,0}$, leading to two different critical angles of total reflection $\theta_c^+$ and $\theta_c^-$ in the $R^{++}$ and the $R^{--}$ channels respectively.

The principle of a polarized neutron reflectivity measurement is depicted in fig. 5.12. A beam prepared with all neutrons having spin up or spin down projection along the quantization axis defined by the external field $\mathbf{B}_0$ impinge on the sample surface with wave vector **k** under a glancing angle θ. After reflection ($\theta = \theta'$) some neutrons have changed their spin projection and some have not. Each neutron is then spin analyzed and detected. In such an experiment four different reflectivities channels can therefore be recorded: $R^{++}, R^{--}, R^{-+}$ and $R^{+-}$. A practical realization of such an experiment can be found on the web site given in reference [16].

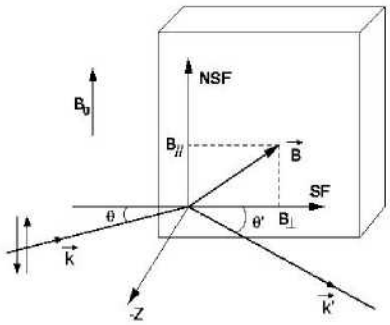



Fig 5.12: *Principle of a neutron specular reflectivity ($\theta = \theta'$) and off-specular scattering ($\theta \neq \theta'$) experiment.*

**5.10 Example: Layer-by-layer magnetometry in a remanent polarizing supermirror**

Polarizing supermirrors are commonly used for the polarization of cold neutron beams. They consist of a series of alternating ferromagnetic and non-magnetic layers with a gradient in the layer thickness.

The presented sample contains 100 $Fe_{50}Co_{48}V_2$ layers separated by 100 $TiN_x$ layers. $Fe_{50}Co_{48}V_2$ has been chosen for its large total scattering length density for up neutrons $\rho^+ = \rho^N + \rho^M$, leading to a large critical angle of total reflection and a strong contrast with $TiN_x$, whereas it does not reflect the down neutrons: $\rho^- = \rho^N - \rho^M < 0$. The content of

nitrogen in $TiN_x$ has been tuned such that the contrast between its scattering length density ($\rho_{TiN_x}$) and the scattering length density for down neutrons of $Fe_{50}Co_{48}V_2$ vanishes. ($\rho_{TiN_x} - \rho_- = 0$), leading to a strongly reduced reflectivity for down neutrons.

In order to further increase the range of angles for which the reflectivity for up neutrons stays close to 1, a gradient in the FeCoV/TiN bi-layer thicknesses has been introduced from the bottom to the top of the stack. It leads to a broadened multilayer Bragg peak spreading from the critical angle of total reflection for up neutrons to an angle defined by the bottom-most and thinnest bilayer. This arrangement permits to reflect an increased amount of neutrons coming from a non-collimated source of neutrons.

In remanent polarizing supermirrors, an uniaxial anisotropy allows to keep a remanent magnetisation after the magnetizing field is switched-off or even slightly reversed, putting the quantization axis of the neutrons anti-parallel to the magnetisations. In this state, the supermirror reflects neutrons with the spin opposite to the guiding field (i.e. spin down neutrons). This feature can be used to build an instrument providing both spin directions without the use of a spin flipper [17]. Those three different properties are schematized in fig. 5.13.

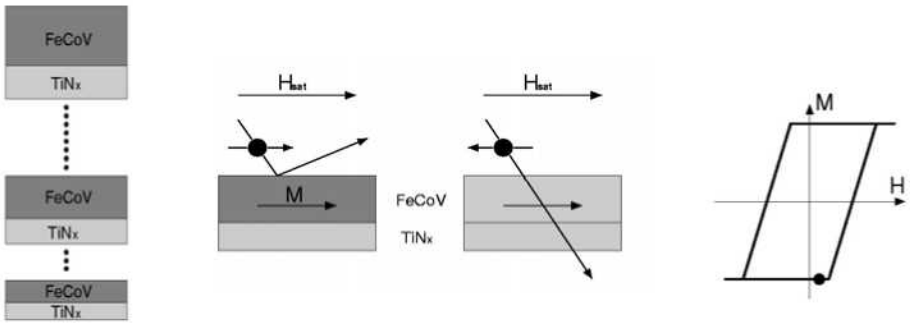



Fig. 5.13: *The three characteristics of a remanent (right) polarizing (center) supermirror (left picture)*

The remagnetization process of this system has been studied by reflectivity of polarized neutrons with polarization analysis. The measurements performed at several fields along the remagnetization curve are depicted in fig. 5.14. In (a) the measurements have been performed in the remanent state (no magnetisation has started to flip or to rotate); in (d) the measurements have been performed in the saturated state.

At saturation, all the layer magnetisations are aligned along the field: we observe a good reflectivity for up neutrons up to 20 mrad (the critical angle of total reflection for up neutrons of FeCoV is 8 mrad). The reflectivity for down neutrons is low. The measured spin flip reflectivities do not come from spin-flip processes happening in the sample. They are due to inefficiencies of the spin polarizing and analyzing devices. At remanence all the layer magnetisations are aligned against the field: the reflectivities in the $R^{++}$ and the $R^{--}$ channels are interchanged with respect to the saturation case.

One might expect that the remagnetization process proceed via a single flip of all the layers at the same coercive field or a simultaneous rotation of all the layers at the same range of fields. The specular reflectivity measurements shown in (b) and (c) along the remagnetization curve teach us that this is actually not the case. At $\mu_0 H$ = 3.8 and 5.6 mT, angular regions of strong $R^{++}$ and strong $R^{--}$ coexist. As the field is increased, the higher angular part of the strong $R^{--}$ reflectivity gets strongly reduced, while it is replaced by strong $R^{++}$ reflectivity. This shows that the thinnest FeCoV layers, contributing to the reflection at higher angles, have lower magnetic coercivity than the thicker ones, contributing to the reflection at lower angles. From the fits to the data using the formalism exposed in § 5.9, it was deduced that, out of the 100 FeCoV magnetisations, 48 of them have flipped along the field at 3.8 mT and 94 at 5.6 mT.

Another interesting point to notice is that, during the remagnetization process, no additional SF reflectivity has been observed, i.e. that the layer magnetisations never have any in-plane component perpendicular to the field. It means that the remagnetization process happen via sudden flips of the magnetisations from opposite to along the field, not via rotation.

This study is a good example of the power of polarized neutron reflectometry for depth-resolved investigations of the magnetisation configurations in a multilayer system.

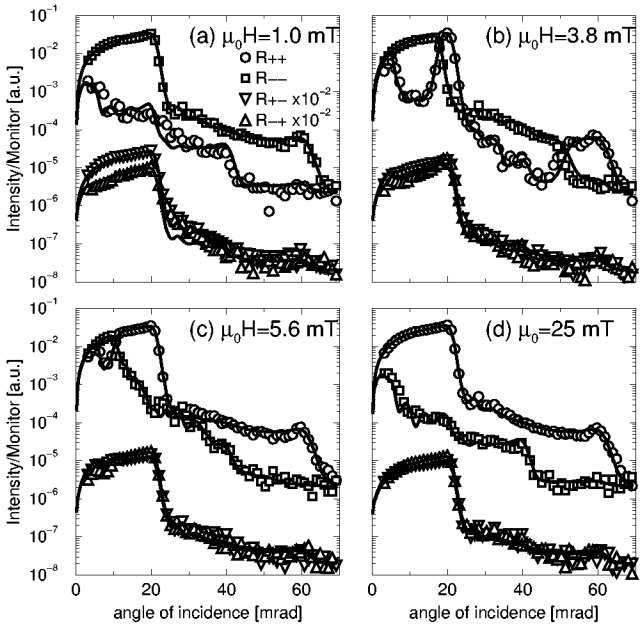



Fig. 5.14: *Polarized neutron reflectivity of a function of the angle of incidence $\theta$ on a remanent polarizing supermirror measured at four fields along the remagnetisation curve. The intensities have been plotted on a logarithmic scale. The measurements were performed at a neutron wavelength $\lambda$ = 4.52 Å. The lines are fits to the data.*

### 5.11 Off-specular scattering of polarized neutrons

If, on a length scale smaller than the projection of the coherence length of the neutron beam on the sample surface, in-plane fluctuations of the magnetisation are present, then some intensity can be collected off-specular ($\theta \neq \theta'$ in fig. 5.12).

The theoretical description of off-specular scattering of polarized neutrons with polarization analysis lies out of the scope of this school. A description within the DWBA can be found in references [18] and [19]. Let's mention however that its scattering cross section looks like the one in Equ. 5.29, and that birefringence effects due to the different spin projections on the quantization axis have also to be taken into account.

In Fig. 5.15 (a) we show the off-specular scattering measured together the specular reflectivity on the supermirror of the preceding section at $\mu_0 H$ = 3.8 mT. Along the main diagonal we recognize the specular reflectivity depicted in Fig. 5.14 (b). Off-diagonal, the diffuse scattering is very spin-polarized. The NSF off-specular signals result essentially from the scattering by interfacial roughness whose profile replicates itself from interface to interface. The SF diffuse scattering originates from in-plane magnetic fluctuations perpendicular to the applied field inside the layers that have not yet flipped along the field.

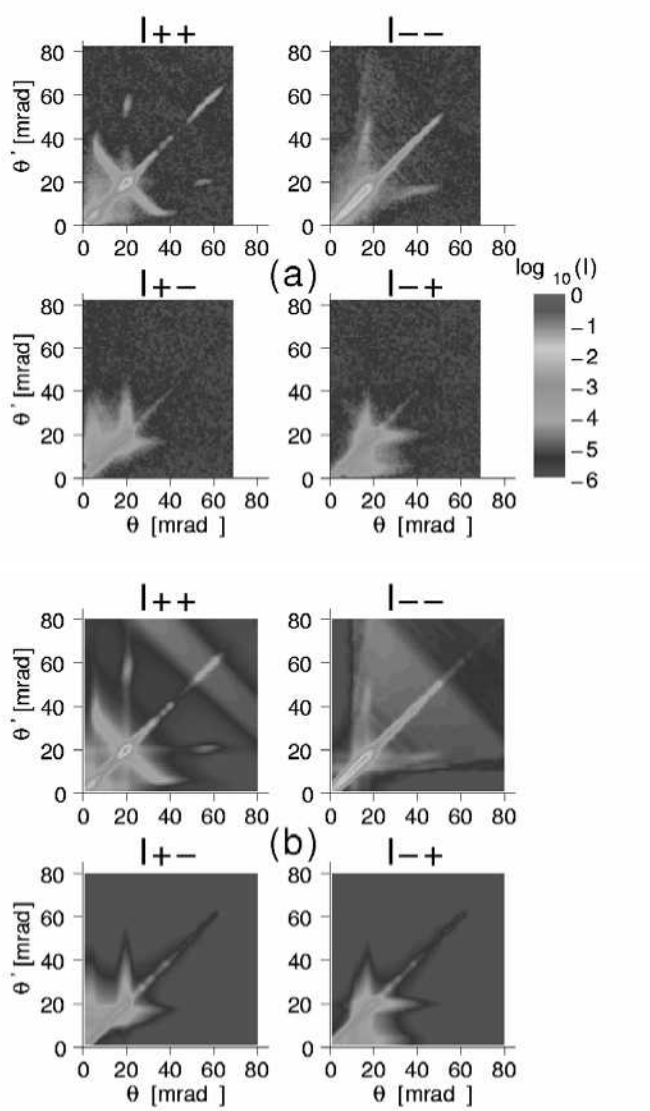



Fig. 5.15: *(a): Reflectivity and off-specular scattering of polarized neutrons with polarization analysis (all four channels I++, I--, I+- and I-+) from a remanent polarizing supermirror in a partially remagnetized state. θ is the angle of incidence with respect to the sample surface, θ' the outgoing angle. Along the main diagonal of each figure (θ = θ'), specular reflectivity is measured, giving access to laterally averaged information. Off-diagonal (θ ≠ θ'), off-specular scattering gives access to structural and magnetic correlations on length scales smaller than the in-plane projection of the coherence length of the neutron beam. (b): Simulation of the measured intensities within the DWBA.*

Those affirmations are confirmed by the simulations of the measured data within the DWBA shown in Fig. 5.15 (b)

Measuring off-specular scattering angular resolved leads therefore, in the same way as neutron specular reflectivity for the in-plane net magnetisations, to depth-resolved information on the in-plane magnetisation fluctuations.

**References**


[1] J. Als-Nielsen, *Topics in Current Physics. Structure and Dynamics of Surfaces* (Springer, Berlin, 1986).

[2] P. Beckmann, A. Spizzichino, *The Scattering of Electromagnetic Waves From Rough Surfaces* (Pergamon, New York, 1963).

[3] L. Névot, P. Croce, Revue de Physique appliqué **15**, 761 (1980).

[4] S.K. Sinha, E.B. Sirota, S. Garoff. H.B. Stanley, Phys. Rev. B **38**, 2297 (1988).

[5] A.L. Barabási, H.E. Stanley, *Fractal Concepts in Surface Growth* (Cambridge University Press, Cambridge, 1995).

[6] V. Holý, J. Kubena, I. Ohlídal, K. Lischka, W. Plotz, Phys. Rev. B **47**, 15896 (1993).

[7] J. Lekner, *Theory of Reflection* (Martinus Nijhoff, Dordrecht, Boston, 1987).

[8] S. Dietrich, A. Haase, Phys. Rep. **260**, 1 (1995).

[9] V. Holý, U. Pietsch, T. Baumbach, *X-Ray Scattering from Thin Films (High Resolution X-Ray Scattering from Crystalline Thin Films)* (Springer Tracts in Modern Physics, Vol. 149, Berlin, 1998).

[10] H. Dosch, *Critical Phenomena at Surfaces and Interfaces (Evanescent X-Ray and Neutron Scattering)* (Springer Tracts in Modern Physics, Vol. 126, Berlin, 1992).

[11] O.H. Seeck, I.D. Kaendler, M. Tolan, K. Shin, M.H. Rafailovich, J. Sokolov, R. Kolb, Appl. Phys. Lett. **76**, 2713 (2000).

[12] C.F. Majkrzak, J.F. Ankner, N.F. Berk, D. Gibbs, *Neutron and X-Ray Diffraction Studies of Magnetic Multilayers* (in: *Magnetic Multilayers*, World Scientific, Singapore, 1994).

[13] S. Blügel, T. Brückel, C.M. Schneider (Eds.), *Magnetism goes Nano*, Lecture Manuscripts of the 36$^{th}$ Spring School of the IFF, Forschungszentrum Jülich, Series "Matter and Materials" **26** (2005)

[14] C. Fermon, F. Ott and A. Menelle, "Neutron Reflectometry" in J. Daillant and A.

Gibaud (Eds), *X-ray and Neutron Reflectivity: Principles and Applications*, Springer (1999)

[15] E. Kentzinger, U. Rücker and B. Toperverg, Physica B **335**, 82 (2003)

[16] http://www.fz-juelich.de/iff/wns_hadas

[17] P. Böni, D. Clemens, M. Senthil Kumar, S. Tixier, Physica B **241-243**, 1060 (1998)

[18] B. Toperverg, Physica B **297**, 160 (2001)

[19] B. Toperverg, „ Polarized Neutron Reflection ad Off-Specular Scattering“ in T. Brückel and W. Schweika (Eds.), *Polarized Neutron Scattering*, Forschungszentrum Jülich, Series “Matter and Materials”, **12** (2002)

# 6

# Applications of neutron scattering

Thomas Brückel

# 6. Applications of neutron scattering

Thomas Brückel, IFF, Forschungszentrum Jülich

## 6.1 Introduction

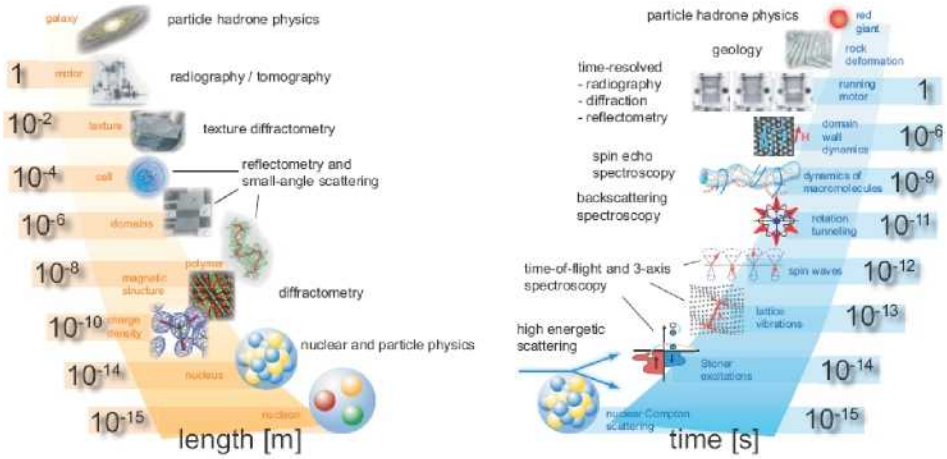



***Fig 6.1:*** *Length- and time scales covered by research with neutrons giving examples for applications and neutron techniques [1].*

Research with neutrons covers an extraordinary range of length- and time scales as depicted in figure 6.1. The very extremes of length scales - below $10^{-12}$ m - are the domain of nuclear and particle physics, where e. g. measurements of the charge or electric dipole moment of the neutron provide stringent tests of the standard model of particle physics without the need of huge and costly accelerators. On the other extreme, neutrons also provide information on length- and time scales relevant for astronomical dimensions, e. g. the decay series of radioactive isotopes produced by neutron bombardment give information on the creation of elements in the early universe. In this course, however, we are only concerned with neutrons as a probe for condensed matter research and therefore restrict ourselves to a discussion of neutron scattering. Still, the various neutron scattering techniques cover an area in phase space from picometers pm up to meters and femtoseconds fs up to hours, a range, which probably no other probe can cover to such an extend.

Different specialized neutron scattering techniques are required to obtain structural information on different length scales:

- With *wide angle neutron diffractometry*, magnetization densities can be determined within single atoms on a length scale of ca. 10 pm[1]. The position of atoms can be determined on a similar length scale, while distances between atoms lie in the 0.1 nm range[2].

[1] In this sense, neutrons are not only nanometer nm, but even picometer pm probes!
[2] In what follows, we use as "natural atomic unit" the Ångstrøm, with 1 Å=0.1 nm

- The sizes of large macromolecules, magnetic domains or biological cells lie in the range of nm to μm or even mm. For such studies of large scale structures, one applies *reflectometry* or *small angle scattering* techniques.
- Most materials relevant for engineering or geo-science occur neither in form of single crystals, nor in form of fine powders. Instead they have a grainy structure, often with preferred orientation of the grains. This so called texture determines the macroscopic strength of the material along different directions. *Texture diffractometry* as a specialized technique allows one to determine this grainy structure on length scales of up to mm.
- Finally, for even larger structures, one uses imaging techniques, such as neutron *radiography* or *tomography*, which give a 2dimensional projection or full 3-dimensional view into the interior of a sample due to the attenuation of the neutron beam, the phase shift or other contrast mechanisms.

In a similar way, different specialized neutron scattering techniques are required to obtain information on the system's dynamics on different time scales:

- *Neutron Compton scattering*, where a high energy neutron in the eV energy range makes a deep inelastic collision with a nucleus in so-called impulse approximation, gives us the momentum distribution of the atoms within the solid. Interaction times are in the femtosecond fs time range.
- In magnetic metals, there exist single particle magnetic excitations, so-called Stoner excitations, which can be observed with inelastic scattering of high energy neutrons using the so-called *time-of-flight spectroscopy* or the *triple axis spectroscopy* technique. Typically, these processes range from fs to several hundred fs.
- Lattice vibrations (phonons) or spin waves in magnetic systems (magnons) have frequencies in the picosecond ps time range. Again these excitations can be observed with *time-of-flight* or *triple axis spectroscopy*.
- Slower processes in condensed matter are the tunneling of atoms, for example in molecular crystals or the slow dynamics of macromolecules. Characteristic time scales for these processes lie in the nanosecond ns time range. They can be observed with specialized techniques such as *backscattering spectroscopy* or *spin-echo spectroscopy*.
- Even slower processes occur in condensed matter on an ever increasing range of length scales. One example is the growth of domains in magnetic systems, where domain walls are pinned by impurities. These processes may occur with typical time constants of microseconds μs. Periodic processes on such time scales can be observed with *stroboscopic neutron scattering* techniques.
- Finally, *kinematic neutron scattering* or imaging techniques, where data is taken in consecutive time slots, allow one to observe processes from the millisecond ms to the hour h range.

In this chapter, we will overview the various techniques used in neutron scattering and provide some examples for their application. We will start by repeating the properties of the different correlation functions, in order to be able to judge what kind of information we can obtain from a certain neutron scattering experiment. We will introduce neutron scattering techniques used to obtain information on "where the atoms are" (diffractometry) and "what the atoms do" (spectroscopy). We will finish by reviewing the range of applicability of various neutron scattering methods and compare them to other experimental techniques.

## 6.2 Scattering and correlation functions

In chapter 4 "Correlation Functions" it has been shown that the neutron scattering cross section for nuclear scattering can be expressed in the following form (for simplicity, we restrict ourselves to a mono-atomic system):

$$\frac{\partial^2\sigma}{\partial\Omega\partial\omega} = \frac{k'}{k}\cdot N\cdot\left[\left(\overline{|b|^2}-|\bar{b}|^2\right)S_{inc}(\underline{Q},\omega)+|\bar{b}|^2\,S_{coh}(\underline{Q},\omega)\right] \tag{6.1}$$

The cross section is proportional to the number N of atoms. It contains a kinematical factor $k'/k$, i. e. the magnitude of the final wave vector versus the magnitude of the incident wave vector, which results from the phase-space density. The scattering cross section contains two summands: one is the coherent scattering cross section, which depends on the magnitude square of the average scattering length density $|\bar{b}|^2$ and the other one is the incoherent scattering, which depends on the variance of the scattering length $\left(\overline{|b|^2}-|\bar{b}|^2\right)$. The cross section (6.1) has a very convenient form: it separates the interaction strength between probe (the neutrons) and sample from the properties of the system studied. The latter is given by the so-called scattering functions $S_{coh}(\underline{Q},\omega)$ and $S_{inc}(\underline{Q},\omega)$, which are completely independent of the probe and a pure property of the system under investigation [2]. The *coherent scattering function* $S_{coh}(\underline{Q},\omega)$ is a Fourier transform in space and time of the pair correlation function:

$$S_{coh}(\underline{Q},\omega) = \frac{1}{2\pi\hbar}\int G(\underline{r},t)e^{i(\underline{Q}\cdot\underline{r}-\omega t)}d^3r\,dt \tag{6.2}$$

Here the *pair correlation function* $G(\underline{r},t)$ depends on the time dependent positions of the atoms in the sample:

$$\begin{aligned} G(\underline{r},t) &= \frac{1}{N}\sum_{ij}\int\left\langle\delta(\underline{r}'-\underline{r}_i(0))\cdot\delta(\underline{r}'+\underline{r}-\underline{r}_j(t))\right\rangle d^3r' \\ &= \frac{1}{N}\int\left\langle\rho(\underline{r}',0)\cdot\rho(\underline{r}'+\underline{r},t)\right\rangle d^3r' \end{aligned} \tag{6.3}$$

Here $\underline{r}_i(0)$ denotes the position of atom i at time 0, while $\underline{r}_j(t)$ denotes the position of another atom j at time t. The angle brackets denote the thermodynamic ensemble average, the integral extends over the entire sample volume and the sum runs over all atom pairs in the sample. Instead of correlating the positions of two point-like scatterers at different times, one can rewrite the pair correlation function in terms of the particle density as given in the second line of (6.3). Coherent scattering arises from the superposition of the amplitudes of waves scattered from one particle at time 0 and a second particle at time t, averaged over the entire sample volume and the thermodynamic state of the sample. In contrast, incoherent scattering arises from the superposition of waves scattered from the same particle at different times. Therefore the *incoherent scattering function* $S_{inc}(\underline{Q},\omega)$ is given in the following form:

$$S_{inc}(\underline{Q},\omega) = \frac{1}{2\pi\hbar}\int G_s(\underline{r},t)e^{i(\underline{Q}\cdot\underline{r}-\omega t)}d^3r\,dt \tag{6.4}$$

, which is the Fourier transform in space and time of the *self correlation function* $G_S(\underline{r},t)$:

$$G_s(\underline{r},t) = \frac{1}{N}\sum_{j}\int\left\langle\delta(\underline{r}'-\underline{r}_j(0))\cdot\delta(\underline{r}'+\underline{r}-\underline{r}_j(t))\right\rangle d^3r' \tag{6.5}$$

We next define the *intermediate scattering function* $S(\underline{Q},t)$ as the purely spatial Fourier transform of the correlation function (here we have dropped the index "coh" and "inc",

respectively, as the intermediate scattering function can be defined for coherent as well as for incoherent scattering in the same way):

$$\begin{aligned} S(\underline{Q},t) &:= \int G(\underline{r},t)e^{i\underline{Q}\cdot\underline{r}}d^3r \\ &= S(\underline{Q},\infty)+S'(\underline{Q},t) \end{aligned} \tag{6.6}$$

For reasons, which will become apparent below, we have separated in the second line the intermediate scattering function for infinite time

$$S(\underline{Q},\infty)=\lim_{t\to\infty}S(\underline{Q},t) \tag{6.7}$$

from the time development at intermediate times. Given this form of the intermediate scattering function $S(\underline{Q},t)$, we can now calculate the scattering function as the temporal Fourier transform of the intermediate scattering function:

$$\begin{aligned} S(\underline{Q},\omega) &= \frac{1}{2\pi\hbar}\int_{-\infty}^{+\infty}S(\underline{Q},t)e^{-i\omega t}dt \quad = \frac{1}{2\pi\hbar}\int_{-\infty}^{+\infty}\left[S(\underline{Q},\infty)+S'(\underline{Q},t)\right]e^{-i\omega t}dt \\ &= \underbrace{\frac{1}{\hbar}\delta(\omega)S(\underline{Q},\infty)}_{\text{elastic scattering}} + \underbrace{\frac{1}{2\pi\hbar}\int_{-\infty}^{+\infty}S'(\underline{Q},t)e^{-i\omega t}dt}_{\text{inelastic scattering}} \end{aligned} \tag{6.8}$$

In this way, the scattering function has been separated into one term for frequency 0, i. e. vanishing energy transfer $\Delta E=\hbar\omega=0$ and one term for non-vanishing energy transfer. The first term is the purely elastic scattering, which is given by the correlation function at infinite times. Correlation at infinite times is obtained for particles at rest. A prominent example is the Bragg scattering from a crystalline material, which is purely elastic, while the scattering from liquids is purely inelastic, since the atoms in liquids are moving around freely and thus the correlation function vanishes in the limit of infinite time differences.

Often times the energy of the scattered neutron is not discriminated in the detector. In such experiments, where the detector is set at a given scattering angle, but does not resolve the energies of the scattered neutrons, we measure an *integral cross section* for a fixed direction $\hat{\underline{k}}'$ *of* $\underline{k}'$:

$$\left(\frac{d\sigma}{d\Omega}\right)_{coh,\text{int}} = \int\left.\frac{\partial^2\sigma}{\partial\Omega\partial\omega}\right|_{\hat{\underline{k}}'=const}\cdot d\omega \tag{6.9}$$

Momentum and energy conservation are expressed by the following kinematic equations of scattering:

$$\underline{Q}=\underline{k}'-\underline{k} \quad ; \quad \hbar\omega=E-E'=\frac{\hbar^2}{2m}\left(k^2-k'^2\right) \tag{6.10}$$

Due to these kinematic conditions, the scattering vector $\underline{Q}$ will vary with the energy of the scattered neutron $E'$ or the energy transfer $\hbar\omega$ as the integral in (6.9) is performed. The so-called *quasi-static approximation* neglects this variation and uses the scattering vector $Q_0$ for elastic scattering $(\hbar\omega=0)$ in (6.9). This approximation is valid only if the energy transfer is small compared to the initial energy. This means that the movements of the atoms are negligible during the propagation of the radiation wave front from one atom to the other. In this case, the above integral can be approximated as follows:

$$\begin{aligned} \left(\frac{d\sigma}{d\Omega}\right)_{coh,QSA} &= \frac{k'}{k}\frac{N}{2\pi\hbar}\int\left(\int G(\underline{r},t)e^{i(\underline{Q}_0\cdot\underline{r}-\omega\cdot t)}d^3rdt\right)d\omega \\ &= \frac{k'}{k}\frac{N}{2\pi\hbar}\int G(\underline{r},t)e^{i\underline{Q}_0\cdot\underline{r}}\delta(t)d^3rdt = \frac{k'}{k}\frac{N}{2\pi\hbar}\int G(\underline{r},0)e^{i\underline{Q}_0\cdot\underline{r}}d^3r \end{aligned} \tag{6.11}$$

, which shows that the integral scattering in quasi-static approximation depends on the *instantaneous spatial correlation function* only, i. e. it measures a snapshot of the arrangement of atoms within the sample. This technique is e. g. very important for the determination of short-range order in liquids, where no elastic scattering occurs (see above).

Our discussion on correlation functions can be summarized in a schematic diagrammatic form, see figure 6.2.

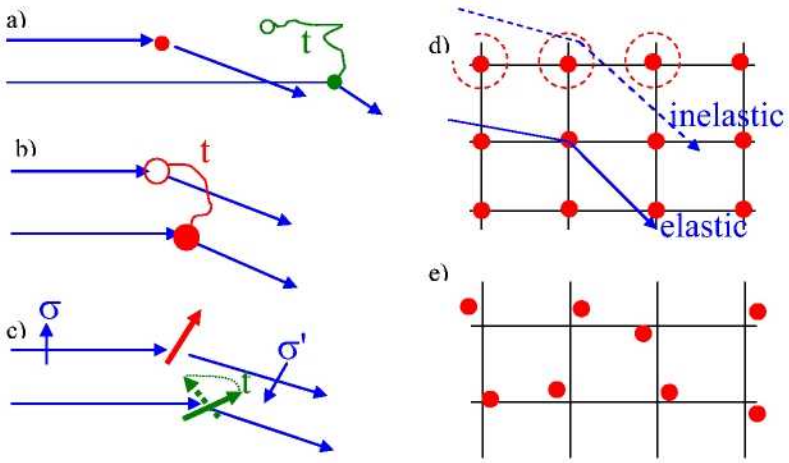



***Fig. 6.2:*** *Schematic diagrams depicting the various scattering processes: a) coherent scattering is connected with the pair correlation function in space-and time; b) incoherent scattering is connected with the self-correlation function; c) magnetic scattering is connected with the spin pair correlation function; d) elastic and inelastic scattering from a crystal measures average positions and movements of the atoms, respectively, e) inelastic scattering in quasistatic approximation sees a snapshot of the sample.*

Figure 6.2 shows that coherent scattering is related to the pair correlation between different atoms at different times (6.2a), while incoherent scattering relates to the one particle self correlation function at different times (6.2b). In analogy to nuclear scattering, magnetic scattering depends on the correlation function between magnetic moments of the atoms. If the magnetic moment is due to spin only, it measures the *spin pair correlation function*. Since the magnetic moment is a vector quantity, this correlation function strongly depends on the neutron polarization. For this reason, in magnetic scattering we often perform a polarization analysis as discussed in chapter 3. Figure 6.2d depicts elastic and inelastic scattering from atoms on a regular lattice. Elastic scattering depends on the infinite time correlation and thus gives us information on the time averaged structure. Excursions of the atoms from their time averaged positions due to the thermal movement will give rise to inelastic scattering, which allows one e. g. to determine the spectrum of lattice vibrations, see chapter 12 "inelastic neutron scattering". Finally, an experiment without energy analysis in quasi-static approximation will give us the instantaneous correlations between the atoms, see figure 6.2e. This schematic picture shows a snapshot of the atoms on a regular lattice. Their positions differ from the time averaged positions due to thermal movement.

## 6.3 The generic scattering experiment

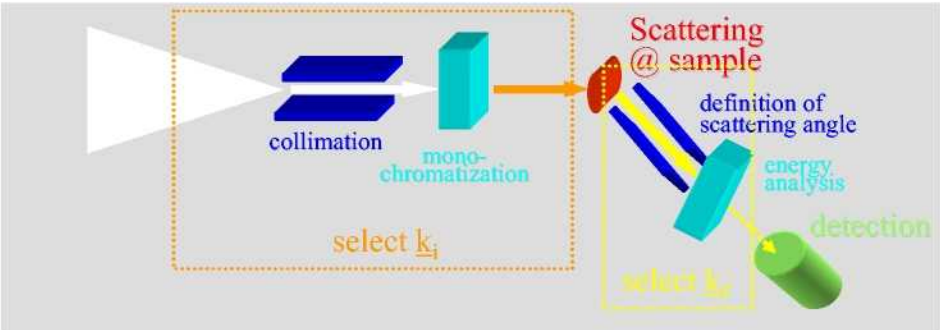



***Fig. 6.3:*** *Schematic diagram of a generic scattering experiment; the primary spectrometer in front of the sample serves to select an incident wave vector distribution by means of collimation and monochromatization; the secondary spectrometer after the sample selects a final wave vector; the number of neutrons for a given distribution of incident wave vector $\underline{k}_i$ and final wave vector $\underline{k}_f$ is counted in the detector.*

A generic scattering experiment is depicted schematically in figure 6.3. The incident beam is prepared by collimators, which define the direction of the beam and monochromators, which define the energy of the incident neutrons. Together these optical elements select an incident wave vector $\underline{k}_i$. In reality, since these neutron-optical elements are never perfect, a certain distribution of incident wave vectors around an average wave vector is selected in the primary spectrometer. In an analogous manner, a final wave vector - or better a distribution of final wave vectors - is being selected from all scattered waves after the sample by the secondary spectrometer. Finally the scattered neutrons are being counted in the detector. Since our neutron-optical elements are never perfect, the measured intensity in the detector is not simply proportional to the scattering function $S(\underline{Q},\omega)$ (or more general, the cross section), but it is proportional to the convolution of the scattering function (or cross section) with the *experimental resolution function R*:

$$I(\underline{Q}_0,\omega_0) \sim \iint S(\underline{Q},\omega)R(\underline{Q}_0-\underline{Q},\omega_0-\omega)d^3Qd\omega \qquad (6.12)$$

Here, the resolution function $R$ appears due to the limited ability of any experimental setup to define an incident or final wave vector $\underline{k}_i$ or $\underline{k}_f$, respectively. $R$ therefore depends purely on the instrumental parameters and not on the scattering system under investigation. The art of any neutron scattering experiment is to adjust the instrument - and with it the resolution function - to the problem under investigation. If the resolution of the instrument is too tight, the intensity in the detector becomes too small and counting statistics will limit the precision of the measurement. If, however, the resolution is too relaxed, the intensity will be smeared out and will not allow one to determine the scattering function properly.

The simplest way to collimate an incident beam is to put two slits with given openings in a certain distance in the beam path and thus define the angular spread of the incident beam. For monochromatization of a neutron beam, usually one of two different methods is applied:

- One can use the wave property of the neutron and diffract the neutron beam from a single crystal. According to Braggs' law $2d\sin\theta = \lambda$, a certain wave length $\lambda$ is being selected for a given lattice $d$-spacing under a scattering angle $2\theta$.
- One can use the particle property of the neutron and use the neutron time-of-flight to determine its velocity and thus its kinetic energy. How this is being done technically will be discussed in subsequent chapters.

Following our discussion of the correlation functions, we will now distinguish two principally different types of neutron scattering instruments:

- Diffractometers: these are scattering instruments, which either perform no energy analysis at all, or which measure only the truly elastic scattering. As discussed in chapter 6.2, the truly elastic scattering allows one to determine the time averaged structure. The prominent example is Bragg scattering from single crystals. If, however, no energy analysis is performed, one usually makes sure that one works in quasistatic approximation to facilitate the interpretation of the scattered intensity distribution. Quasistatic approximation corresponds to a snapshot of the scatterers in the sample and is important for example to determine short-range order in a liquid. Be it elastic scattering or integral scattering in quasistatic approximation, a diffraction experiment allows one to determine the position of the scatterers only. The movement of the scatterers is not accessible with such a diffraction experiment. Similarly, in a diffraction experiment for magnetic scattering, the arrangement of magnetic moments within the sample, i. e. its magnetic structure, can be determined, while the spin dynamics is not accessible in a diffraction experiment[3].
- Spectrometers: a neutron spectrometer is dedicated to measure inelastic scattering, e. g. to determine the change of the neutrons' kinetic energy $E = \frac{\hbar^2 k^2}{2m}$ during the scattering process. Such an experiment requires the analysis of the energy of the scattered neutrons, in contrast to a conventional diffractometer. Now the intensity measured in the detector depends on momentum- and energy- transfer and is proportional to the convolution of the double differential scattering cross section (6.1) with the resolution function of the instrument (6.12). Therefore a neutron spectrometer gives us information on the scattering functions (coherent or incoherent) and thus on the truly time dependent pair- or self correlation functions. This is why spectrometers are used to determine the dynamics of a system after its structure has been determined in a previous diffraction experiment[4].

[3] In fact there is a way to access also spin- or lattice- dynamics in a diffraction experiment: lattice vibrations will give rise to diffuse scattering around Bragg peaks, so-called thermal diffuse scattering, which can be modelled and thus the spectrum of excitations can be determined in an indirect, but not model-free direct way.

[4] Of course, spectrometers could also be used to determine the structure, but usually their resolution is not at all adapted to this purpose.

## 6.4 Diffractometers

### 6.4.1 Wide angle diffraction versus small angle scattering

According to (6.10), the momentum transfer during a scattering experiment is given by $\hbar\underline{Q} = \hbar\underline{k}' - \hbar\underline{k}$. Remembering that $k = \frac{2\pi}{\lambda}$, the magnitude of the scattering vector $Q$ can be expressed in terms of wavelength $\lambda$ and scattering angle $2\theta$ as:

$$Q = \frac{4\pi}{\lambda}\sin\theta \tag{6.13}$$

As we have seen in chapter 6.2, the scattering cross section is related to the Fourier transform of the spatial correlation function and therefore a reciprocal relation exists between characteristic real space distances $d$ and the magnitude of the scattering vector $Q$, for which intensity maxima appear:

$$\Delta Q \sim \frac{2\pi}{d} \tag{6.14}$$

Bragg scattering from crystals provides an example for this equation (compare chapter 4: "A neutron primer"): the distance between maxima of the Laue function is determined by $\Delta Q \cdot d = 2\pi$, where d is the corresponding real space periodicity. Reflectometry provides another example (see below): the Q-distance between Kiessig fringes is given by the relation $\Delta Q \cdot d \sim 2\pi$ (compare (6.19)), where d is the layer thickness.

(6.14) is central for the choice of an instrument or experimental set-up, since it tells us which Q-range we have to cover in order to get information on a certain length range in real space. (6.13) tells us, at which angles we will observe the corresponding intensity maxima for a given wavelength. This angle has to be large enough in order to separate the scattering event clearly from the primary beam. This is why we need different instruments to study materials on different length scales. Table 6.1 gives two examples.

| Example | d | ΔQ | 2θ (λ=1 Å) | 2θ (λ=10 Å) | Technique |
|---|---|---|---|---|---|
| Distance between atoms in crystals | 2 Å | 3.14 $Å^{-1}$ | 29° | "cut-off" | wide angle diffraction |
| Precipitates in metals (e.g. Co in Cu) | 400 Å | 0.016$Å^{-1}$ | 0.14° | 1.46° | small angle scattering |

***Tab. 6.1:*** *Examples for scattering from structures on different characteristic real space length scales d. $\Delta Q$ is the corresponding characteristic scattering vector according to (6.14), $2\theta$ the scattering angle according to (6.13), calculated for two different wavelength $\lambda$.*

1. The study of structures on atomic length scales is typically done with a wavelength of around 1 Å (comparable to the distance between the atoms) and the scattered intensity is observed at rather large angles between 5° and 175°. Therefore one speaks of *wide angle diffraction*, which is employed for the study of atomic structures.
2. For the study of large scale structures (precipitates, magnetic domains, macromolecules in solution or melt) on length scales of 10 up to 10,000 Å (1 up to 1000 nm), the

magnitude of the relevant scattering vectors as well as the corresponding scattering angles are small. Therefore one chooses a longer wavelength in order to expand the diffractogram. The suitable technique is *small angle scattering*, which is employed to study large scale structures.

In what follows we will first focus on the study of large scale structures. In the corresponding conceptually very simple instruments, some typical considerations for the design of an instrument can be exemplified. We will distinguish between small angle neutron scattering instruments and reflectometers, discuss the basic instrument concepts and list some possible applications. After having discussed how large scale structures can be studied with neutron diffraction, we will then introduce instruments for wide angle scattering and their possible applications.

### 6.4.2 Small angle neutron scattering SANS

As mentioned in chapter 6.4.1, small angle scattering is employed whenever structures on length scales between typically 10 Å and 10,000 Å (1 nm and 1,000 nm) are of interest. This range of real space lengths corresponds to a scattering vector of magnitude between about $10^{-1}$ Å$^{-1}$ and $10^{-4}$ Å$^{-1}$ (1 nm$^{-1}$ and $10^{-3}$ nm$^{-1}$). In order to observe the scattering events under reasonable scattering angles, one chooses a rather long wavelength. However, due to the moderator spectrum (see chapter 1 "Neutron Sources"), there is very little neutron flux at wavelengths above 20 Å. Therefore typically neutrons of wavelength between 5 and 15 Å are employed for small angle neutron scattering.

Two different principles of small angle neutron scattering will be distinguished in this chapter: the pinhole SANS and the focusing SANS depicted in figures 6.4 and 6.5, respectively. Other types of instruments, e.g. with multi-pinhole grid collimation, are variants of these techniques and will not be discussed here.

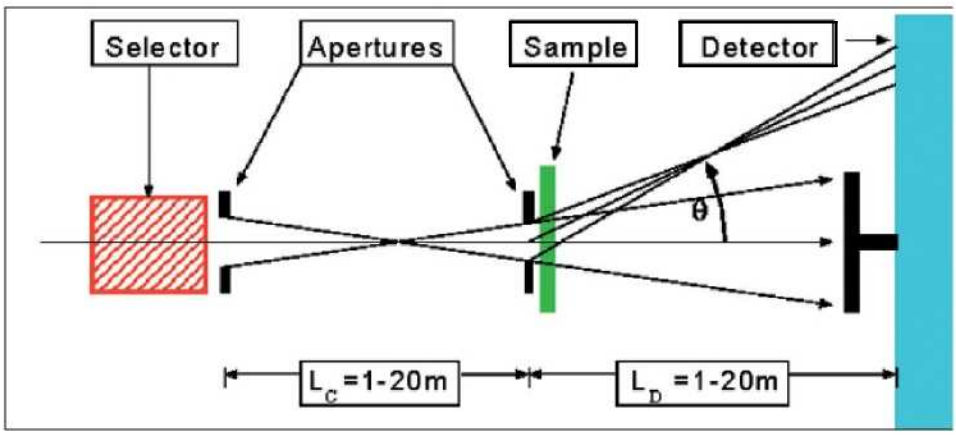



***Fig. 6.4***: *Schematics of a pinhole SANS, where the incident wave vector is defined through distant apertures (KWS-1 or KWS-2 of JCNS [3]).*

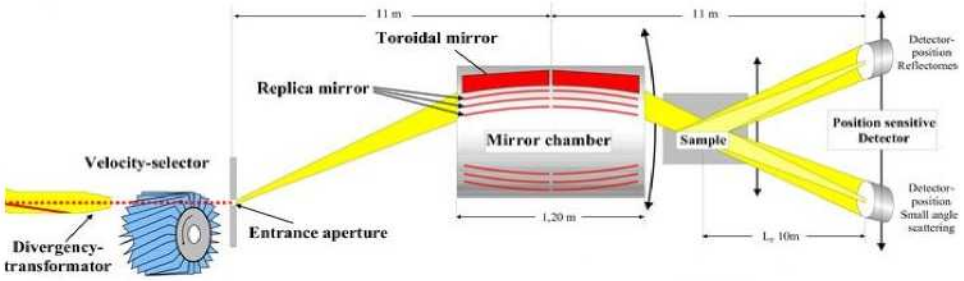



***Fig. 6.5***: *Schematics of a focusing SANS, where an image of the entrance aperture is produced on the detector by a focusing mirror (KWS-3 of JCNS [3]).*

For both instrument concepts, the wavelength band is usually defined by a so-called velocity selector. Figure 6.6 shows a photo of a velocity selector drum build in Jülich for the instrument KWS-3.



***Fig. 6.6***: *Drum of a velocity selector made from a light-weight, neutron absorbing alloy (MgLi). A velocity selector works on the "screw threat principle": it is rotating at high speeds and only neutrons in a certain velocity band can travel undisturbed in the channels between the absorbing partition walls; neutrons outside this velocity band are stopped in the walls. Thus only a certain velocity- or wavelength band can pass this device.*

In the pinhole SANS, the incident wave vector $\underline{k_i}$ is defined by two distant apertures of comparable size. The longer the distance between the diaphragms, the higher is the collimation for a given cross section of the beam. The sample is placed right next to the second aperture and the scattered neutrons are being recorded in a detector, which is at a large distance from the sample; typically the sample-detector distance is comparable to the collimation distance. The overall length of such an instrument can amount to 40 m, up to 80 m.

In contrast to the pinhole SANS, the focusing SANS uses a divergent incident beam and a focusing optical element produces an image of the entrance aperture on the detector. The sample is positioned directly behind the focusing element. Small angle scattering from the sample appears on the position-sensitive area detector around the primary beam spot. Such a set-up with a focusing element would be the natural solution in light optics, where focusing lenses are readily available. Due to the weak interaction of neutrons with matter, the index of refraction for neutrons is very close to one, and it is difficult to produce efficient focusing elements. In case of the focusing SANS realized by Forschungszentrum Jülich [4], a toroidal[5] mirror is employed as focusing element. Locally, the toroidal shape is a good approximation to an ellipsoid with its well-known focusing properties. The challenge in realizing such a

[5] A torus is a surface of revolution generated by revolving a circle about an axis coplanar with the circle, which does not touch the circle (examples: doughnuts, inner tubes).

device lies in the fact that small angle scattering from the focusing element has to be avoided i. e. the mirror has to be flat on an atomic scale (root-mean square roughness of about 3 Å !), which became possible due to the developments of optical industry for x-ray satellites.[6]

As an example of the considerations leading to the design of a neutron scattering instrument, we will now discuss the resolution of a pinhole SANS machine. In general terms, the resolution of an instrument denotes the smearing out of the signal due to the instruments' finite performance (6.12). As neutron scattering is a flux limited technique, there is need for optimization: the better the resolution of the instrument, i. e. the better the angular collimation $\Delta\theta$, the smaller the wavelength spread $\Delta\lambda$, the smaller is the intensity recorded on the detector. Therefore resolution has to be relaxed to such an extent that the features of interest are still measurable and not smeared out entirely by the resolution of the instrument, while at the same time the intensity is maximized. In order to determine the resolution of a SANS instrument, we start from (6.13): $Q = \frac{4\pi}{\lambda}\sin\theta$. The influence of angular- and wavelength spread can be determined by differentiation of this equation, where the different contributions have to be added quadratically:

$$\Delta Q^2 = \left(\frac{\partial Q}{\partial \theta}\right)^2 (\Delta\theta)^2 + \left(\frac{\partial Q}{\partial \lambda}\right)^2 (\Delta\lambda)^2 = \left(\frac{4\pi}{\lambda}\right)^2 \cos^2\theta (\Delta\theta)^2 + \left(\frac{4\pi \sin\theta}{\lambda^2}\right)^2 \Delta\lambda^2$$
$$\underset{\theta \to 0}{\overset{\uparrow}{=}} \left(\frac{4\pi}{\lambda}\right)^2 \left[ (\Delta\theta)^2 + \theta^2 \left(\frac{\Delta\lambda}{\lambda}\right)^2 \right] = \frac{k^2}{12} \left[ \left(\frac{d_D}{L_D}\right)^2 + \left(\frac{d_E}{L_C}\right)^2 + \left(\frac{d_S}{L_C} + \frac{d_S}{L_D}\right)^2 + \theta^2 \left(\frac{\Delta\lambda}{\lambda}\right)^2 \right] \qquad (6.15)$$

$\Delta Q^2$ is the variance of the scattering vector due to the finite collimation and monochromatization. An optimization can be achieved, if all terms in (6.15) contribute the same amount, which leads to the condition

$$L_D = L_C \;,\; d_E = d_D = 2d_S \qquad (6.16)$$

(6.16) shows that a pinhole SANS has to be designed such that sample-to-detector distance $L_D$ is equal to the collimation length $L_C$. Typical values are $L_D = L_C = 10$ m with openings of $d_E = 3$ cm for the entrance- and $d_S = 1.5$ cm for the sample aperture. Note that one can chose the opening of the entrance aperture to be twice as large as the opening of the sample aperture - or sample size - without sacrificing markedly in resolution, while gaining in neutron count rate! The detector needs a minimum pixel resolution $d_D \approx d_E$ ; A detector with a radius of about $R_D \approx 30$ cm is necessary to cover the required Q-range up to 0.05 $Å^{-1}$ at $L_D = 10$ m and for $\lambda = 8$ Å. Having defined the incident collimation, we can now determine the appropriate wavelength spread with the same argument as above: the last term in the sum in (6.15), corresponding to the wavelength spread, should contribute the same amount to the variance of the scattering vector as the corresponding terms for the collimation, i. e.:

$$\frac{\Delta\lambda}{\lambda} = \frac{d_E}{L_C} \cdot \frac{L_D}{r_D} \approx \frac{d_E}{r_D} \approx \frac{1}{10} = 10\% \qquad (6.17)$$

(6.17) demonstrates that in general for small angle scattering we don't need a very high degree of monochromatization. A 10 % wavelength band is acceptable, since for small angles the smearing due to the wavelength spread is quite comparable to the smearing due to the incident divergence. This is the reason why usually a velocity selector is employed as monochromatizing element for small angle scattering, as it lets a wavelength band of typically 10 % pass.

Let us now turn to applications of small angle scattering. One example is given in figure 6.7, which is concerned with the self-organization of crystalline amorphous diblock-copolymers

[6] It should be mentioned that nowadays focusing lenses for neutron scattering have also been realised. These have a very long focal distance, but can be employed to improve intensity or resolution in pinhole SANS.

[4]. Combining three different instruments, small angle scattering has been observed over ten orders of magnitude in cross section and nearly four orders of magnitude in momentum transfer. In different regions, different power laws apply, corresponding to different structures observed: the $Q^{-2}$ power law corresponds to 2d structures on the shortest length scale, the $Q^{-1}$ power law corresponds to the organization of rods in bundles, while the $Q^{-3}$ power law corresponds to a network of bundles with a mass fractal aspect and finally, correlations become visible in the very low Q-range.

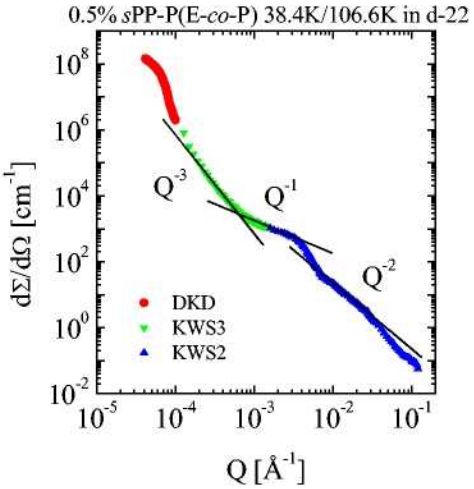



***Fig. 6.7:*** *SANS investigation of the self-organization of a crystalline-amorphous diblock-copolymer measured with three different instruments of different resolution: double crystal diffractometer, focussing SANS and pinhole SANS for the low, medium and larger Q range, respectively. Plotted is the cross section in absolute units versus the magnitude of the scattering vector. For details see [4].*

We will end this short introduction into the principles of small angle scattering by listing some examples for applications of small angle scattering in different fields of science:

- *soft matter*: polymers and colloids, e. g. micelles, dendrimers, liquid crystals, gels, reaction kinetics of mixed systems, …
- *materials science*: phase separation in alloys and glasses, morphologies of superalloys, microporosity in ceramics, interfaces and surfaces of catalysts
- *biological macromolecules*: size and shape of proteins, nucleic acids and of macromolecular complexes, biomembranes, drug vectors
- *magnetism*: ferromagnetic correlations and domains, flux line lattices in superconductors, …

### 6.4.3 Large scale structures: Reflectometry

As elaborated in chapter 6.4.2, neutron small angle scattering is applied to determine large scale structures, e. g. scattering length density fluctuations on length scales of some 100 Å in bulk material. There is another type of instruments, which is dedicated to the study of large scale structures in thin film systems, on surfaces and in multilayers. Such an instrument is called a *neutron reflectometer*. This conceptually simple instrument is depicted schematically in figure 6.8.

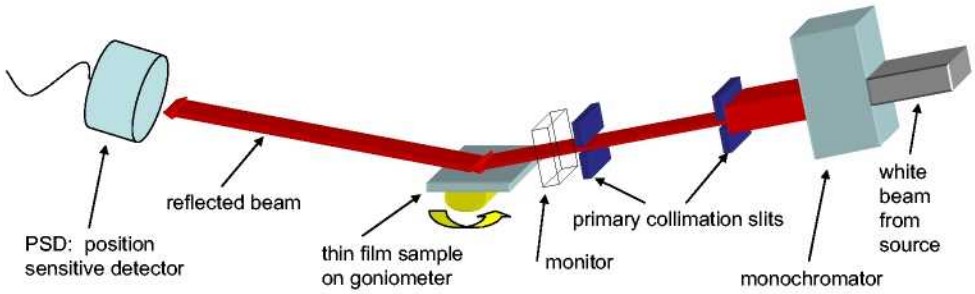



***Fig. 6.8**: Schematics of a neutron reflectometer. Monochromatization can be done in many different ways: by a velocity selector, by a crystal monochromator, or by a chopper in a time-of-flight instrument. Collimation slits define the direction of the incident beam. The monitor is a low efficient detector of high transmission, which measures the incident flux on the sample. The reflected neutrons are either detected in a position sensitive detector, or a secondary collimation track in front of a point detector selects the direction of the reflected beam. For magnetic samples, a polarizer, a polarization analyzer and guide fields can be inserted for polarization analysis experiments.*

Similar to a pinhole SANS instrument, the incident beam is collimated through a set of two well separated slits. However, since in reflectometry, one is mainly interested in the momentum transfer perpendicular to the planar sample surface, the collimation of a reflectometer is tight only in this direction. Along the sample surface the beam can be wide and have a larger divergence in order to gain intensity. This collimated beam impinges on the sample under a grazing angle (typically fractions of a degree up to a few degrees) and is reflected into a single point detector or a position sensitive detector. To define the angle of exit for a point detector, a secondary collimation is needed between sample and detector. The incident beam is monochromatized using different techniques, depending on the resolution requirements: velocity selector, time-of-flight chopper or crystal monochromator.

With such an instrument, the layer structure of a sample can be determined, such as layer composition, layer thickness and surface- or interfacial roughness, see chapter 5 "Continuum description". This information is obtained in so-called specular reflection, for which the incident angle is equal to the final angle like in a reflection from a perfect optical mirror. In this case, the momentum transfer of the neutrons is perpendicular to the surface of the sample and thus only laterally averaged information can be obtained. In order to determine lateral correlations within the layers, for example magnetic domain sizes, a momentum transfer within the layer has to occur, which implies that angle of incidence and final angle have to be different. Short range correlation within the layers will then give rise to so-called off specular diffuse scattering as well know in optics from a bad optical mirror. In fact, the theoretical description of neutron reflectometry follows exactly along the lines of conventional optics, except that for neutrons in most cases the index of refraction is smaller than one and thus external total reflection occurs for neutrons coming from vacuum towards matter[7]. Refraction and total reflection are described by the well-known Snell's Law of optics and the intensities of reflected and transmitted beam can be determined from the optical Fresnel equation as shown in chapter 5. Here we just want to demonstrate with very simple arguments how

[7] This is exactly what happens in neutron guides, evacuated tubes of usually rectangular cross section, where neutrons are totally reflected from the smooth glass side walls, often coated, e.g. with $^{58}$Ni, to enhance the angle of total reflection. Since for total reflection conditions, reflectivity is close to 100%, neutrons are transported nearly without loss from the source to the instruments by bouncing back- and forth from the guide side walls.

interference effects from layered structures arise and how the intensity modulation in Q-space are related to real space length scales. Figure 6.9 shows how interference can occur from a beam being reflected at the surface and at the internal interface of a double layer stack.

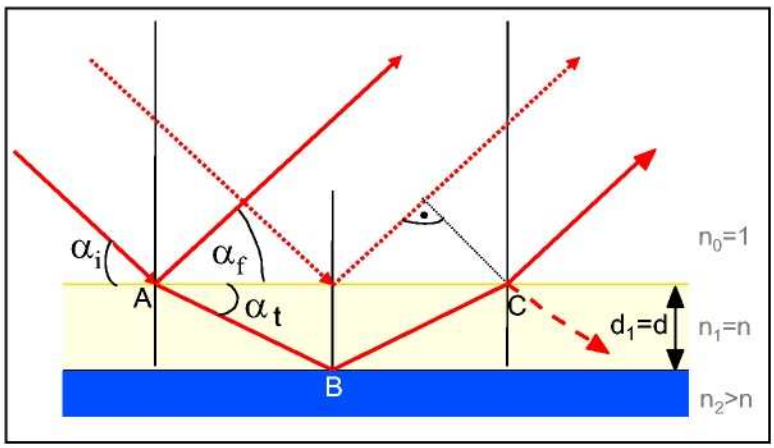



***Fig. 6.9***: *Schematics of the reflection of a neutron beam from a single layer on a substrate. There exists an optical path length difference Δ between the rays drawn with a solid line and those drawn with a dotted line.*

For simplicity we consider only the case of a specular reflection, i. e. the incident angle $\alpha_i$ is equal to the angle of exit $\alpha_f$: $\alpha_i = \alpha_f = \alpha$. Interference occurs between beams reflected from the surface (dotted line in Fig. 6.9) and those first transmitted into the layer, reflected from the interface between layer 1 and substrate and then leaving the layer into vacuum (solid line). To a good approximation, refraction at the top surface can be neglected for incident angles larger than about twice the critical angle of total reflection. In this case $\alpha_t = \alpha_i = \alpha_f = \alpha$ holds. Since the index of refraction for neutrons is very close to one, this approximation is valid even for rather small angles of incidence. Then the optical path length difference for the two beams is:

$$\Delta = 2d \sin\alpha \tag{6.18}$$

Here d is the thickness of the layer 1. We can now determine the distance between interference maxima from the condition that the path length difference has to differ by one wavelength: $\lambda = 2d \cdot \Delta(\sin\alpha) \approx 2d \cdot \Delta\alpha$. With $Q = \frac{4\pi}{\lambda}\sin\alpha \approx \frac{4\pi}{\lambda}\alpha$ we finally obtain:

$$\Delta Q \approx \frac{2\pi}{d} \tag{6.19}$$

Again we can see that the interference phenomena in Q-space are connected with real space length scales in a reciprocal way. (6.19) tells us that there will be a number of interference maxima at distances in Q of $\frac{2\pi}{d}$. These interference phenomena are called "*Kiessig fringes*" and are well known to us in conventional optics for example as the beautiful colors observed in soap bubbles. Figure 6.10 shows as an example the reflectivity of neutrons from a thin nickel layer on a glass substrate, which is nothing else but a section of a neutron guide employed to transport the neutrons from the source to the instrument over long distances by multiple total reflections. The Kiessig fringes are nicely visible in this example and the

thickness of the nickel layer can be determined from the distance between adjacent intensity maxima.

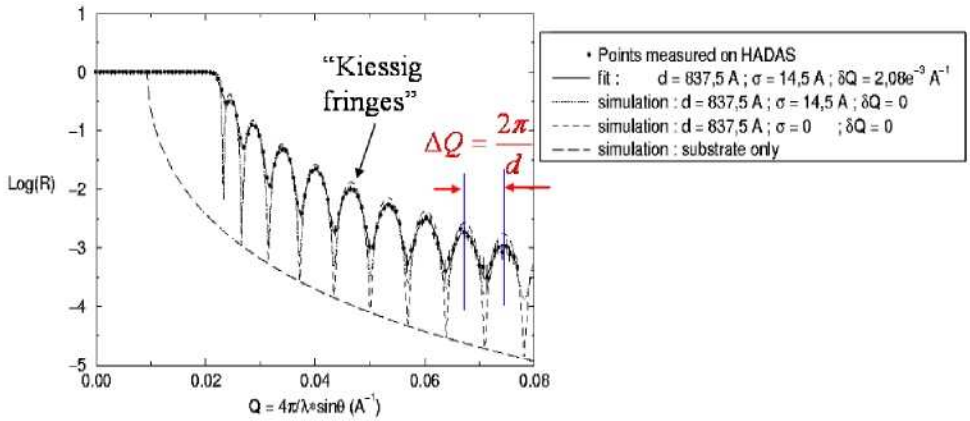



***Fig. 6.10**: Reflectivity of neutrons from a nickel layer on glass substrate on a logarithmic scale. Data points were measured on the HADAS reflectometer of the late FRJ-2 reactor. The solid line shows a fit, where the layer thickness was determined to be 837.5 Å with a route mean square roughness of 14.5 Å and where the resolution of the instrument of $\delta Q = 2.08 \cdot 10^{-3}\ Å^{-1}$ has been taken into account; the dotted line shows a simulation for the same structural parameters, but for an ideal instrument without resolution broadening; the short dashed line shows the simulation for the same layer thickness but without roughness; the long dashed line shows the simulation for the glass substrate only.*

Neutron reflectometry has many applications in different fields of science of which we can only list a few:

- *soft matter science*: thin films e. g. polymer films; polymer diffusion, self-organization of diblock copolymers; surfactants; liquid-liquid-interfaces, …
- *life science*: structure of biomembranes
- *materials science*: surface of catalysts; kinetic studies of interface evolution; structure of buried interfaces
- *magnetism*: thin film magnetism e. g. exchange bias, laterally structured systems for magnetic data storage, multilayers of highly correlated electron systems, …

### 6.4.4 Atomic structures: Single crystal and powder neutron diffraction

As explained in chapter 6.4.1, wide angle scattering with neutrons of wavelength typically 1 Å is applied for the determination of atomic structures. Due to the periodicity of the lattice, Bragg peaks appear under diffraction angles given by the Bragg equation (compare reflectometry: (6.18) and (6.19)!):

$$2d \sin\theta = \lambda \qquad (6.20)$$

The intensity of the Bragg peaks is governed by the arrangement of the atoms within the unit cell (structure factor) and the scattering from the single atom (form factor). By collecting a large set of scattered intensities for many Bragg peaks, modeling the atomic structure and

refining the parameters in order to get an optimum agreement between calculated and observed intensities, the arrangement of atoms within the unit cell as well as the arrangements of spins for magnetic samples can be determined. Figure 6.11 shows the schematics of a single crystal diffractometer.

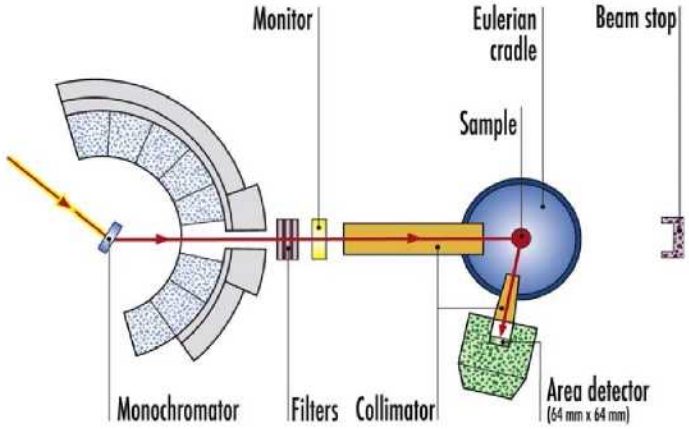



***Fig. 6.11***: *Schematics of a single crystal diffractometer. The drawing shows the layout of the diffractometer D9 at the Institute Laue-Langevin and has been taken from http://www.ill.eu/.*

In contrast to small angle scattering, where a broad wavelength band is employed to enhance the scattered intensity, a better monochromatization of typically $\frac{\Delta\lambda}{\lambda} \sim 1\%$ has to be achieved for wide angle scattering to avoid the broadening of the Bragg reflections due to the wavelength spread according to (6.20). This monochromatization is typically done by Bragg diffraction from a single crystal. The direction of the incident beam is determined by a set of slits. As Bragg reflections only occur when the corresponding lattice planes have a definite orientation with respect to the incident beam, the single crystal sample is usually mounted on a so-called Eulerian cradle, which allows one to orient the sample using the three Eulerian angles $\omega$, $\chi$ and $\phi$. Finally the scattered beam is detected in a point- or small area detector. Care must be taken to collect the entire integrated intensity for a scan through the Bragg reflection.

A conceptually simpler experiment for the determination of atomic structures is the neutron powder diffractometer. In this case, since the powder grains in the sample usually have random orientations with respect to the incident beam, there is no need for orienting the sample with respect to the beam. Scattering will always occur for some of the grains, which by chance fulfill the Bragg condition. As scattering occurs for all allowed Bragg reflections simultaneously, it would be very inefficient to detect it by a single point detector, which would have to be positioned recursively for the correct $2\theta$ values. Therefore in powder diffraction one usually uses a large linear - or even better area - position sensitive detector, which is arranged on a circular arch around the sample position.

While neutron powder diffraction is conceptually simple, it poses the problem that Bragg reflections will overlap for larger unit cells e. g. due to the finite peak width. Among other

factors, the peak width is determined by the resolution of the instrument. One can show that the resolution function for a neutron powder diffractometer on a beam being monochromized by a Bragg reflection from a monochromator crystal is given by the resolution function:

$$(\Delta 2\theta)^2 = U\tan^2\theta + V\tan\theta + W \qquad (6.21)$$

In such a situation, one cannot determine the intensities of the various Bragg reflections separately. The solution to the problem is the so-called *Rietveldt-* or profile refinement, where structural parameters (unit cell metric a,b,c,α,β,γ, atom positions and site occupations, the Debye-Waller-factors, etc) are refined together with the instrumental parameters (zero point of the scattering angle $2\theta_0$, parameters of the resolution function U, V, W, etc). Assuming a certain peak shape function, this allows one to model the entire powder diffractogram and determine the corresponding parameters from a refinement, which aims at minimizing the weighted sum of the quadratic deviations of calculated and observed intensities for all data points. Figure 6.12 shows an example of such a Rietveldt analysis for data taken from a colossal magnetoresistance manganite.

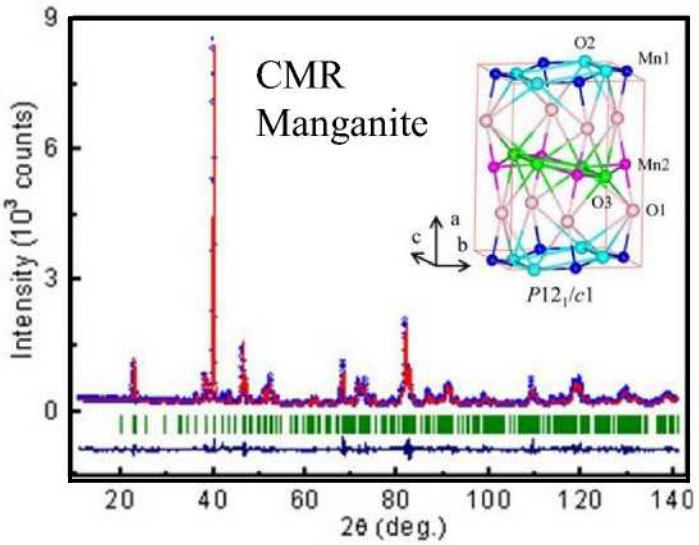



**Fig. 6.12**: *Powder neutron diffraction from a colossal magnetoresisance manganite. Points represent the measured intensities, the solid line the calculated profile function. The green bars below the diffractogram indicate the positions of the Bragg reflections and the line beneath shows the difference between observed and calculated intensities.*

As one can see, there is a very strong overlap of Bragg reflections, especially at larger scattering angles. Still, by using the above mentioned profile refinement technique, the atomic structure of the compound could be determined to a great position.

Applications of wide angle diffractions are manifold:

- *lifescience*: structure of biological macromolecules, e. g. Hydrogen (crystal water!) in protein structures
- *chemistry*: structure determination of new compounds, position of light atoms; time resolved reaction kinetics
- *materials science*: stress-strain determination; texture of materials

- *geo-science*: phase and texture analysis
- *solid state physics*: structure - function relations e. g. in high $T_C$ superconductors; magnetic structures and spin densities, e. g. in molecular magnets

### 6.5 Spectroscopy

So far, we have only explored the purely elastic - or the quasistatic correlation functions, which give us structural information on various length scales only. We will now turn to the general case of correlation functions in space and time, which allow us to determine in addition the microscopic dynamics of the sample under investigation. Again, different instrument types exist for different applications. First of all, if we consider the neutron as a particle, we can determine the time of flight it needs to travel from the sample to the detector and thus its velocity or energy after the scattering process. With the knowledge of the incident energy, the energy transfer during the scattering process can be determined. This kind of neutron spectrometer is called a *time-of-flight or TOF spectrometer*. A special case of the TOF spectrometer is the so-called *neutron spin echo spectrometer*, where the time-of-flight of each single neutron is being determined through the Larmor precession of the nuclear spin of the neutron in an external magnetic field. Neutron spin echo spectroscopy has the highest energy resolution and measures the intermediate scattering function directly. Therefore it is well suited to study slow relaxation processes. An alternative approach to spectroscopy is to determine the energy of the scattered neutrons by means of Bragg reflection from an analyzer crystal. Such an instrument is called a *crystal spectrometer* and if the selection of the incident wavelength is done by a crystal monochromator, it is called a *triple axis spectrometer*. A variant of a crystal spectrometer is the high resolution *backscattering spectrometer*. Of course there are various combinations of these techniques, which exist in particular at spallation sources. A discussion of all of the various instrument concepts goes well beyond the scope of this introductory chapter.

#### 6.5.1 Time-of-Flight or TOF spectrometry

Figure 6.13 depicts schematically a generic time-of-flight spectrometer.

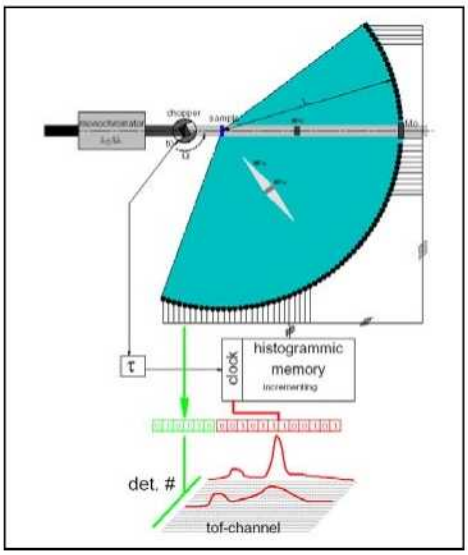



***Fig. 6.13**: Generic TOF spectrometer. The neutron beam is monochromatized, either by a crystal monochromator (X-TOF) or by time-of-flight (TOF-TOF) with choppers and / or the pulse from a spallation source. A chopper creates monochromatic neutron beam pulses incident on the sample. The scattered neutrons are collected in an array of detectors surrounding the sample. For each detector pixel, the neutrons are counted into a histogram as a function of their arrival time. These intensity – time histograms can be converted into the scattering function $S(Q,\omega)$ by using a reference sample for absolute calibration and simple kinematic relations between scattering angle and flight time on one hand and scattering vector and energy on the other hand.*

Neutrons are being monochromized either by reflection from a monochromator crystal or by time-of-flight techniques (X-TOF or TOF-TOF instruments). Monochromatic neutron pulses are produced by a chopper, which can be a fast rotating (up to e.g. 600 Hz) disc or drum made from neutron absorbing material, which has a slit that lets neutron pass only during a short time interval of typically some microseconds. This pulsed neutron beam impinges on the sample and is scattered under all possible scattering angles. Neutrons are recorded on a two dimensional position sensitive detector (nowadays, this is often an array of linear position sensitive $^3$He detector tubes) surrounding the sample typically on the surface of a cylinder. From the arrival time of the neutrons in the detector with respect to the starting time given by the opening of the chopper, an intensity spectrum can be recorded for each scattering angle separately as a function of the arrival time of the neutrons in the detector. Using simple kinematic equations for the neutron as a particle (see chapter 10 "Time-of-Flight Spectrometers") and a calibration obtained by measuring a reference sample, this time-of-flight spectrum can be converted into the scattering function S(Q,ω). Figure 6.14 illustrates the scattering process in a flight path versus time diagram.

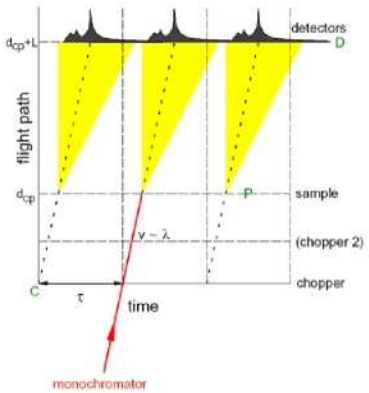



***Fig. 6.14:*** *Flight path versus time diagram for a generic time-of-flight instrument (see text). (Courtesy of Dr. M. Monkenbusch)*

In such a diagram, a monochromatic neutron beam has certain slope, which can be derived from the de Broglie equation $p = \frac{h}{\lambda} = m \cdot v = m \cdot \frac{s}{t}$:

$$t = \frac{m}{h} \cdot s \cdot \lambda \tag{6.22}$$

Typical velocities for thermal neutrons lie in the range of meter per millisecond. In figure 6.14, the neutrons coming from a monochromator enter the chopper with a certain slope in the path-vs.-time diagram corresponding to the velocity of the monochromatic neutrons. With a repetition rate of $1/\tau$ given by the chopper frequency, pulses of monochromatic neutrons leave the chopper. A second chopper can be applied to suppress higher order reflections. The neutron scattered from the sample can either gain energy, resulting in a steeper slope in the path-vs.-time diagram or loose energy resulting in a shallower slope. The number of neutrons entering the detector in a certain time interval is counted into a histogram with the elastic line usually being strongest and inelastic events being visible in neutron energy gain or -loss.

A nice example for a powder neutron time-of-flight spectrum is given by the excitation spectrum of a molecular magnet, namely $Mn_{12}$ acetat, see figure 6.15 [5]. Here the time-of-flight axis has been converted into an energy scale. Clearly visible are nicely separated excitations, which result in the energy level diagram depicted on the middle of figure 6.15. Transitions between these levels correspond to transitions between different values of the magnetic

quantum number of the total spin of the molecule. Modeling this energy level spectrum allows one to determine the magnetic interaction parameters, here mainly the magnetic anisotropy.

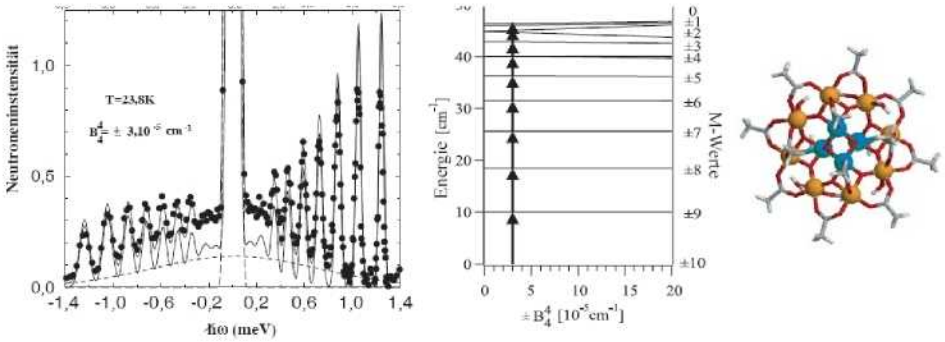



***Fig. 6.15**: Left: Time-of-flight spectrum of the molecular magnet $Mn_{12}$ acetat converted into an energy scale; middle: the corresponding energy level diagram; right: the magnetic molecule consisting of an outer ring of 8 Mn atoms with parallel coupled spins and an inner ring of 4 Mn atoms with opposite spin orientation. Taken from [5].*

Typical applications of time-of-flight spectroscopy can be found in various fields of science:

- *soft matter and biology*: dynamics of gels, proteins and biological membranes; diffusion of liquids, polymers; dynamics in confinement
- *chemistry*: vibrational states in solids and adsorbed molecules on surfaces; rotational tunneling in molecular crystals
- *materials science*: molecular excitations in materials of technological interest (e. g. zeolithes) and especially in diluted systems (matrix isolation); local and long range diffusion in superionic glasses, hydrogen-metal systems, ionic conductors
- *solid state physics*: quantum liquids; crystal field splitting in magnetic systems; spin dynamics in high $T_C$ superconductors; phase transitions and quantum critical phenomena; phonon density of states.

### 6.5.2 Triple axis spectroscopy

An alternative approach for the study of dynamics of condensed matter systems is the so-called *triple axis spectroscopy*. The schematic of a triple axis spectrometer is depicted in figure 6.16.

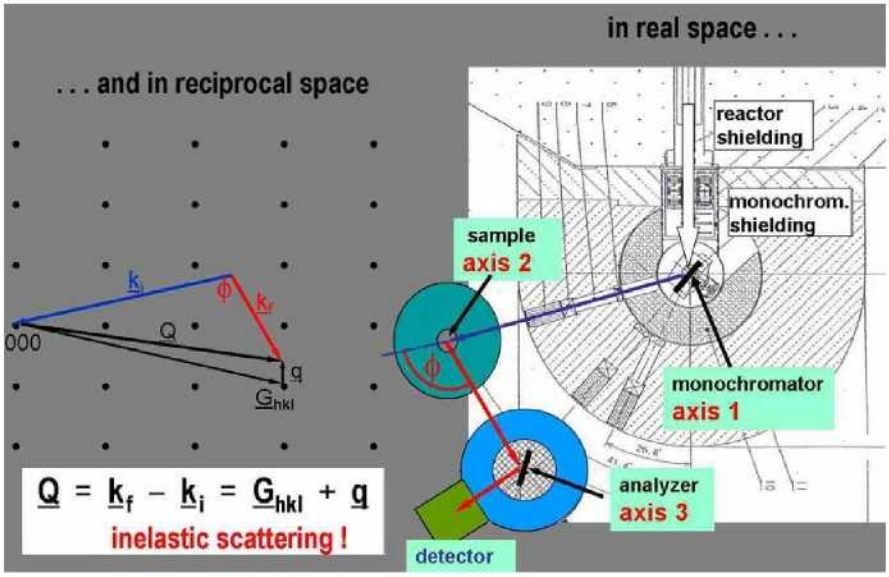



***Fig. 6.16***: *right: schematics of a triple axis spectrometer showing the three axes; left: scattering diagram in reciprocal space. (Courtesy of Dr. H. Conrad)*

In this case the energies of the incident and scattered neutrons are selected by means of a single crystal monochromator and - analyzer, respectively. Also the sample is usually in single crystalline form. These crystals are on rotation tables, which form axis 1, axis 2 and axis 3 of the triple axis spectrometer. If we compare this instrument with the time-of-flight spectrometer shown in figure 6.13, one difference becomes immediately clear: while the time-of-flight spectrometer with its large detector bank allows one to obtain an overview over the excitation spectrum in reciprocal space, the triple axis spectrometer is the instrument of choice, if a certain narrow region in $\underline{Q}$ and $\omega$ is of interest. This is the case, if sharp excitations like lattice vibrations (phonons) or spin waves (magnons) are being investigated. A propagation vector of such an excitation together with a certain energy transfer can be selected by setting monochromator, sample and analyzer to the corresponding values as depicted in the scattering diagram of figure 6.16, left. Here the energy transfer is given by $\Delta E = \frac{\hbar^2}{2m}(k_f^{\,2} - k_i^{\,2})$, while the momentum transfer is given as $\hbar\underline{Q} = \hbar\underline{k}_f - \hbar\underline{k}_i = \hbar\underline{G}_{hkl} + \hbar\underline{q}$.

Figure 6.17 shows as an example spin wave dispersion relations determined for the garnet $Fe_2Ca_3Ge_3O_{12}$ by triple axis spectroscopy.

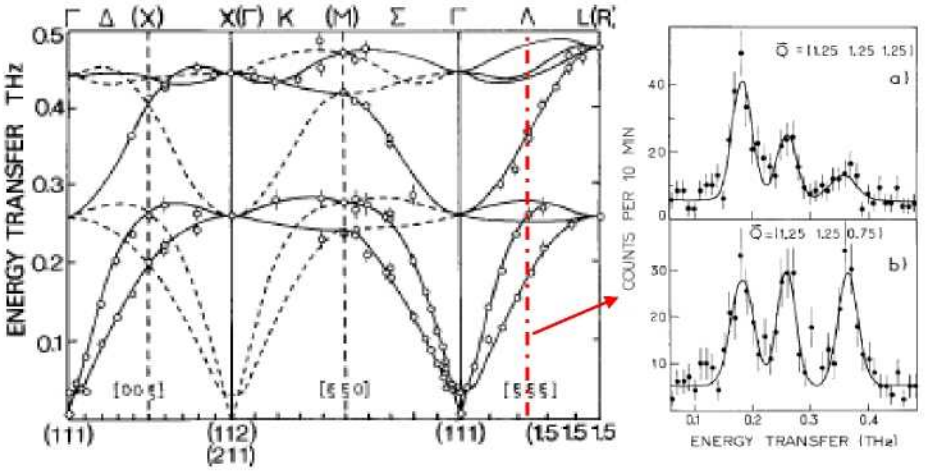



***Fig. 6.17**: Spin wave dispersion relations for the garnet $Fe_2Ca_3Ge_3O_{12}$ along main symmetry directions in reciprocal space. The data points are obtained from scans keeping the momentum transfer Q constant. The figure on the right shows examples of such "constant Q scans". The solid lines are model calculations, from which the interaction (exchange) parameters between the spins in the unit cells can be determined; figure taken from [6].*

Typical examples of triple axis spectroscopy lie mainly in solid state physics:

- phonon dispersions in crystalline material, from which the interatomic forces can be determined
- spin wave dispersions, which allow one to determine exchange and anisotropy parameters
- dynamics of biological model membranes
- lattice and spin excitations in quantum magnets, superconductors, …
- phase transitions: critical behavior.

### 6.5.3 High resolution spectroscopy

Both, time-of-flight and triple axis spectroscopy, have typical energy resolutions of a few percent of the incident neutron energy. While such energy resolutions are sufficient in many cases, there is need for higher energy resolutions, for example to investigate the rather slow movements of large macromolecules, the slow spin dynamics of frustrated spin systems, diffusion of atoms or tunneling processes in molecular crystals. In order to improve the energy resolution, one could just narrow the energy band width of the neutrons incident on the sample. However, such an improvement of resolution goes hand-in-hand with the decrease of the signal in the detector and is therefore not practicable. There are, however, alternative approaches to increase the energy resolution: *neutron spin echo spectroscopy* and *backscattering spectroscopy*.

Neutron spin echo spectroscopy can be understood as a further development of the time-of-flight spectroscopy, where the flight time of each single neutron is encoded and thus a broad wavelength band of incident neutron energies can be used. Encoding of the flight-time is done by the Larmor precession of the nuclear spin of the neutrons in an external magnetic field.

Loosely speaking "each neutron carries its own clock" to measure its individual time-of-flight. Figure 6.18 demonstrates the principle of neutron spin echo spectroscopy: the incident neutron beam with a broad wavelength band of typically 10 % is being polarized with the polarization along the neutron flight direction. A so-called $\frac{\pi}{2}$-flipper turns the neutron polarization into the vertical direction, just before the neutrons enter a strong magnetic field, which is designed in such a way that the field integral $\int \underline{B}(\underline{s})d\underline{s}$ is identical for all neutron flight paths. In the external filed, the nuclear magnetic moment of the neutron starts to precess in this field with a Larmor precession frequency determined by:

$$\frac{d\underline{s}}{dt} = \gamma \underline{s} \times \underline{B} \qquad (6.23)$$

Due to the different neutron velocities and thus different flight times in the magnetic field area, the neutron beam reaching the sample is entirely depolarized. Typical field integrals are in the range of 0.5 T·m giving rise to some 10,000 precessions of the neutron spin. At the sample, the polarization of each neutron is inverted by a so-called π-flipper. In the second arm of the neutron spin echo spectrometer, the scattered neutrons travel through an identical solenoid as on the incident side. If the neutrons are scattered elastically and the field integrals in the two coils are precisely identical, then the full polarization of the neutron beam will be restored and a full intensity will be recorded in the detector after a further $\frac{\pi}{2}$ flip and a polarization analyzer. This maximum intensity is called the spin echo. This spin echo is due to the fact that in the second coil, each neutron performs as many revolutions as in the first coil and thus has to end up with the initial spin direction. If an inelastic scattering event happens at the sample, the spin echo will be destroyed i. e. the intensity in the detector will be lowered. The echo signal can be measured by scanning the field of the second coil with respect to the field of the first coil. Since the echo signal depends directly on the time-of-flight which neutrons need to travel through the magnetic field region, the spin echo technique directly measures the intermediate scattering function $S(\underline{Q},t)$ instead of $S(\underline{Q},\omega)$. This type of spectroscopy is therefore well suited to measure slow relaxation processes like the magnetization dynamics in spin glasses or the dynamics of large macromolecules. This aspect will be detailed in lectures 10 and 14.

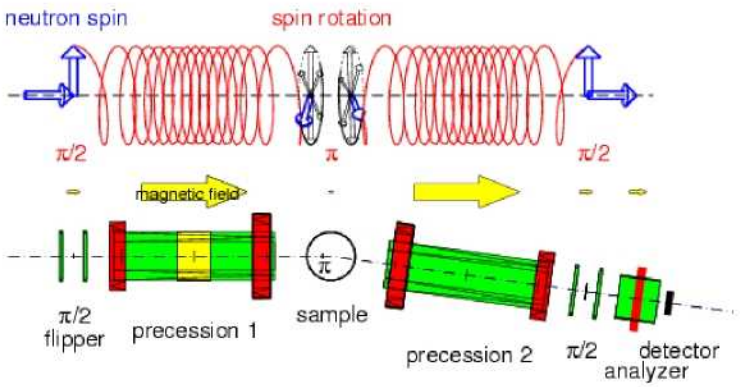



***Fig. 6.18**: Schematics of the neutron spin echo spectrometer of JCNS at the FRM II reactor in Munich [3]. The incident neutron beam has wavelength – or energy band of* $\Delta\lambda/\lambda = 10\%$.

Another instrument for high resolution spectroscopy, based on a crystal analyzer and thus related to the triple axis spectrometer, is the so-called neutron *backscattering instrument*. Starting from the Bragg equation $\lambda = 2d\sin\theta$ one can derive the wavelength spread of a Bragg reflection from a monochromator or analyzer crystal by simple derivation:

$$\Delta\lambda = \left(\frac{\partial\lambda}{\partial d}\right)^2 (\Delta d)^2 + \left(\frac{\partial\lambda}{\partial\vartheta}\right)^2 (\Delta\vartheta)^2 \Rightarrow \left(\frac{\Delta\lambda}{\lambda}\right)^2 = \left(\frac{\Delta d}{d}\right)^2 + \cot^2\vartheta\cdot(\Delta\vartheta)^2 \qquad (6.24)$$

(6.24) shows that the wavelength spread results from two factors: an uncertainty in the lattice d-spacing, which can be minimized for perfect crystals such as silicon or germanium and a term resulting from the divergence of the beam. For backscattering i. e. $2\theta = 180°$ or $\theta = 90°$ this latter contribution vanishes due to the cot(θ) dependence. Thus in backscattering, one can work with a very divergent beam and still achieve a very good wavelength- or energy-resolution – of course at the prize of a poor Q resolution. This principle is applied for backscattering instruments. An example of such a spectrometer from a neutron spallation source is shown in figure 6.19.

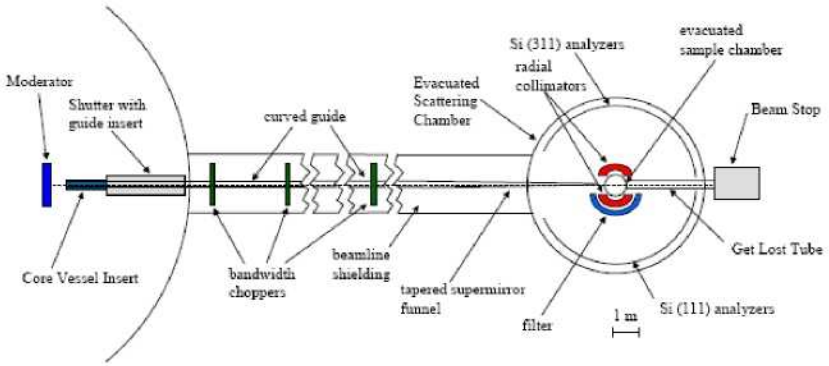



***Fig. 6.19**: Schematics of the neutron backscattering spectrometer BASIS at the Spallation Neutron Source SNS in Oak Ridge, USA, taken from [7].*

Neutron pulses are produced in the supercritical hydrogen moderator. These pulses have a width of about 45 μs for $\lambda = 6.267\,\text{Å}$ wavelength neutrons (this wavelength corresponds with silicon (111) backscattering analyzer). Bandwidth choppers are used to select a certain wavelength band from the pulsed white neutron beam. A long incident flight path of 84 m between moderator and sample allows one to define with great precision the wavelength of the incident neutrons arriving at the sample at a certain time after the initial neutron pulse. Neutrons are scattered from the sample onto Si (111) analyzers, reflected from these analyzers into detectors in a close-to-backscattering geometry. In this way the final neutron wavelength is fixed to 6.267 Å, while the incident neutron wavelength varies with time after the pulse and thus the energy transfer can be determined like in a time-of-flight instrument. An energy resolution of about 2.2 μeV can be achieved with the dynamic range of ± 250 μeV. Typical applications of such a backscattering spectrometer lie in the investigation of tunneling in molecular crystals, spin diffusion or slow spin relaxation in frustrated spin systems, or atomic diffusion processes.

## 6.12 Summary and conclusions

In this chapter we have given a rough overview over the different neutron scattering techniques and their applications. Many details will be discussed in the forthcoming chapters. In addition to the instrument concepts presented, there are many variants, which could not be discussed within the scope of this introduction. Besides neutron scattering there are of course many other techniques, which cover similar length and time scales for research in condensed matter. All these techniques are complementary since all of them can only access a certain range of length or time scales and since the contrast mechanisms are quite different for the different techniques. Figures 6.20 and 6.21 depict the relevant length and time scales accessible with the various neutron- and non-neutron techniques.

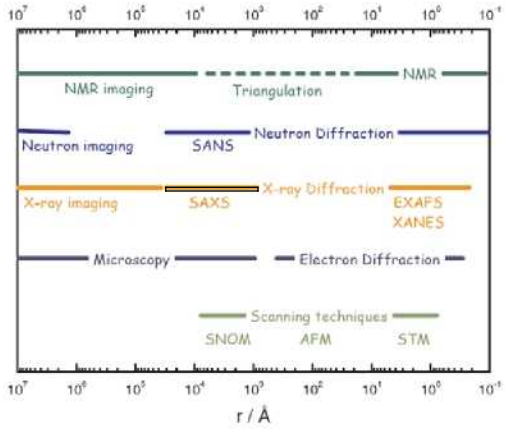



***Fig. 6.20***: *Experimental techniques with spatial resolution: neutron diffraction compared to other experimental techniques; taken from [8].*

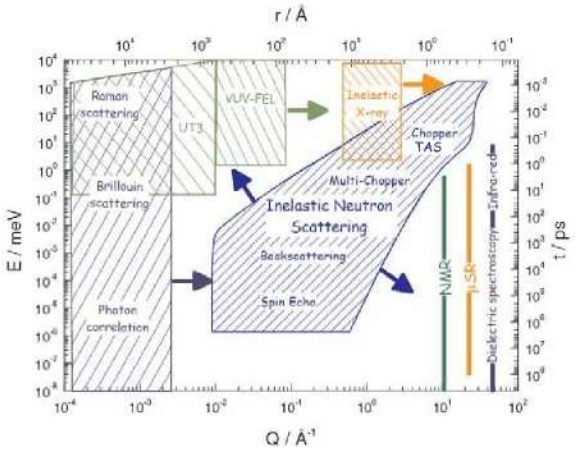



***Fig. 6.21***: *Experimental techniques with time and energy resolution, respectively: neutron spectroscopy compared to other experimental techniques; taken from [8].*

As these figures clearly demonstrate, neutron techniques cover a very large range of length and time scales relevant for research on condensed matter systems. Together with the typical assets of neutrons - sensitivity to magnetism, gentle non-destructive probe, sensitivity to light elements, contrast for neighboring elements etc. - it is clear why neutrons are such an important probe in many fields of research. Figure 6.22 shows how research with neutrons is relevant in many areas of fundamental research and how this in turn is highly relevant for many developments of modern technologies, which are the basis to solve current challenges of mankind.




**Fig. 6.22**: *Significance of research with neutrons in fundamental research and modern technologies, which finally shape our environment and help solve pressing problems of modern societies, like energy supply, transport or communication; taken from [8].*

**References:**


[1] Th. Brückel (Ed.) *Forschung mit Neutronen in Deutschland - Status und Perspektiven* Brochure of the German Committee for Research with Neutrons KFN; 2005 see also http://www.neutronenforschung.de

[2] G.L. Squires *Introduction to the Theory of Thermal Neutron Scattering* Dover Publications Inc.; Reprint 1997
or
S.W. Lovesey Theory *of Neutron Scattering from Condensed Matter: Vol. 1 & 2* (International Series of Monographs of Physics)
Clarendon Press; 1986

[3] http://www.jcns.info/jcns_instruments/

[4] A. Radulescu, E. Kentzinger, J. Stellbrink, L. Dohmen, B.Alefeld, U. Rücker, M. Heiderich, D. Schwahn, Th. Brückel, D. Richter; *KWS-3: The New (Very) Small-Angle Neutron Scattering Instrument Based on Focusing-Mirror-Optics*; Neutron News 16 (2005), 18 - 21

[5] R. Bircher, G. Chaboussant, A. Sieber, H.U. Güdel and H. Mutka; *Transverse magnetic anisotropy in $Mn_{12}$ acetate: Direct determination by inelastic neutron scattering*; Phys. Rev. B 70 (2004), 212413-6

[6] Th. Brückel, B. Dorner, A. Gukasov, V. Plakhty, W. Prandl, E. Shender, O. Smirnow; *Dynamical interaction of antiferromagnetic subsystems: a neutron scattering study of the spinwave spectrum of the garnet $Fe_2Ca_3(GeO_4)_3$*; Z. Phys. B 72 (1988), 477 - 485

[7] http://neutrons.ornl.gov/ ;
http://neutrons.ornl.gov/instrument_systems/beamline_02_basis/index.shtml

[8] ESS project reports 2003 and update 2004;
http://neutron.neutron-eu.net/n_documentation/n_reports/n_ess_reports_and_more

# 7

# Diffractometer

Gernot Heger

# 7. Diffractometer

G. Heger

## 7.1 Introduction

For pure elastic scattering the scattering function $S(\underline{Q},\omega)$ is reduced to the special case without energy transfer ($E_0 = E_1$ and $\hbar\varpi = E_0 - E_1 = 0$) and with equal length of the wave vectors of the incident and scattered beams: $|\underline{k_0}| = |\underline{k_1}|$. $S(\underline{Q}, \omega=0)$ and hence the scattering intensity is only depending on the scattering vector $\underline{Q} = \underline{k_0} - \underline{k_1}$. The coherent elastic neutron scattering (≡ neutron diffraction) yields information on the positions (distribution) of the atomic nuclei and the arrangement of the localised magnetic spins in crystalline solids, on the pair correlation function of liquids and glasses, and on the conformation of polymer chains.

Depending on the scientific problem to be investigated adequate diffraction methods may be quite different. For *fluids and glasses* diffraction data of high statistical relevance over a very large $|\underline{Q}|$ range are required. The direction of the scattering vector $\underline{Q}$ is not defined for these non-crystalline states and a good resolution $|\underline{\Delta Q}|/|\underline{Q}|$ is of no importance. In addition to the pure elastic scattering also inelastic contributions are involved.

Completely different are the needs for a diffraction study of *crystalline solids*. The diffraction by the crystal lattice gives rise to pure elastic scattering localised at the nodes of the so-called reciprocal lattice. The scattering vectors $\underline{Q}$ for the different "Bragg-reflections" are well defined. For the separation of reflections with similar $\underline{Q}$ values a good resolution $\underline{\Delta Q}/\underline{Q}$ is very important. A measured data set of Bragg-intensities (integrated intensities of Bragg-reflections), as complete as possible, over a large $|\underline{Q}|$ range is required. An experimental stability and accuracy leading to a precision of the intensity data of about 2% is desired and can be achieved.

Diffraction measurements on polycrystalline samples depend only on the length of the scattering vector $|\underline{Q}|$. Very small line widths (according to an excellent resolution $|\underline{\Delta Q}|/|\underline{Q}|$) combined with well defined reflection profiles are prerequisites for a quantitative line-profile analysis. The complete powder diagrams with their overlapping reflections are described and analysed by means of the Rietveld method.

For all diffraction methods the energy of the incident neutron beam (expressed alternatively as its wavelength or velocity) must be specified. In the case of angular dispersive diffraction, the 2-axes diffractometer (see Fig. 1) is equipped with a crystal monochromator to select a special

wavelengths band ($\lambda \pm \Delta\lambda/\lambda$) out of the "white" beam according to the Bragg condition for its scattering plane (*hkl*)

$$2d_{hkl} \cdot \sin\theta_{hkl} = \lambda, \qquad (1)$$

with the interplanar spacing $d_{hkl}$ and the monochromator scattering angle $2\theta_{hkl} = 2\theta_M$. The width of the wavelength band $\Delta\lambda/\lambda$, which is important for the Q-resolution, depends on the divergences of the beam before and after the monochromator (collimations $\alpha_1$ and $\alpha_2$), on the mosaic spread of the monochromator crystal $\Delta M$, and on the monochromator angle $2\theta_M$. In order to increase the intensity of the monochromatic beam at the sample position, the monochromator crystal is often bent in vertical direction perpendicular to the diffraction plane of the experiment. In this way the vertical beam divergence is increased leading to a loss of resolution in reciprocal space. The diffracted intensity from the sample is measured as a function of the scattering angle $2\theta$ and the sample orientation (the latter especially in case of a single crystal) and is:

for a single crystal $\rightarrow$ $I(\underline{Q})$, and for a polycrystalline sample $\rightarrow$ $I(|\underline{Q}|)$.

$2\theta$ is defined by the collimators $\alpha_2$ and $\alpha_3$. As there is no analysis of the energy of the

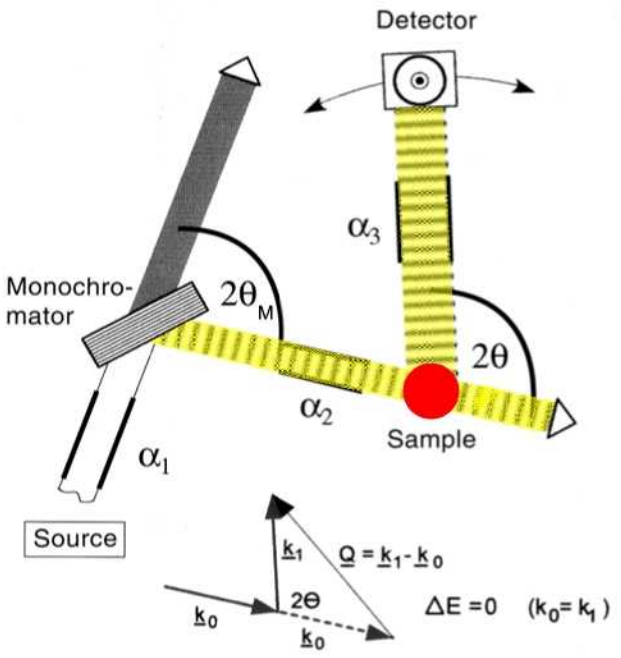



Fig. 1. Schematic representation of a 2-axes diffractometer.

scattered beam behind the sample, the energy resolution $\Delta E/E$ of a 2-axes diffractometer is not well defined (typically of the order of a few %). In addition to the dominant elastic scattering also some minor contributions from quasi-elastic and inelastic scattering are to be taken into account. The name 2-axes-diffractometer results from its two axes of rotation, the monochromator axis defining $2\theta_M$ and the sample axis ($2\theta$).

In the case of *energy-dispersive diffraction*, the time-of-flight diffractometer uses the complete energy spectrum of a pulsed neutron beam and the wavelengths of the scattered neutrons are determined by velocity analysis. The measurement of the neutron intensity as a function of velocity at fixed scattering angle $2\theta$ has to be calibrated according to the energy spectrum of the neutron beam. Assuming no energy transfer at the sample, the time-of-flight diffraction yields again $I(\underline{Q})$ (and for a polycrystalline sample $I(|\underline{Q}|)$.

### 7.2 Reciprocal lattice and Ewald construction

Bragg scattering (diffraction) means coherent elastic scattering of a wave by a crystal. The experimental information consists of the scattering function $S(\underline{Q},\omega = 0)$ with no change of energy or wavelength of the diffracted beam. For an ideal crystal and an infinite lattice with the basis vectors $\underline{a}_1$, $\underline{a}_2$, $\underline{a}_3$, there is only diffraction intensity $I(\underline{H})$ at the vectors

$$\underline{H} = h\underline{a}_1^* + k\underline{a}_2^* + l\underline{a}_3^* \qquad (2)$$

of the reciprocal lattice. *h,k,l* are the Miller indices and $\underline{a}_1^*$, $\underline{a}_2^*$, $\underline{a}_3^*$ the basis vectors of the reciprocal lattice, satisfying the two conditions

$$\underline{a}_1^* \cdot \underline{a}_1 = \underline{a}_2^* \cdot \underline{a}_2 = \underline{a}_3^* \cdot \underline{a}_3 = 1 \text{ and } \underline{a}_1^* \cdot \underline{a}_2 = \underline{a}_1^* \cdot \underline{a}_3 = \underline{a}_2^* \cdot \underline{a}_1 = \ldots = 0,$$

or in terms of the Kronecker symbol with i, j and k = 1, 2, 3:

$$\delta_{ij} = \underline{a}_i^* \cdot \underline{a}_j \text{ with } \delta_{ij} = 0 \text{ for } i \neq j \text{ and } \delta_{ij} = 1 \text{ for } i = j. \qquad (3)$$

The basis vectors of the reciprocal lattice can be calculated from those of the unit cell in real space

$$\underline{a}_i^* = (\underline{a}_j \times \underline{a}_k)/V_c, \qquad (4)$$

where $\times$ means the vector product, and $V_c = \underline{a}_1 \cdot (\underline{a}_2 \times \underline{a}_3)$ is the volume of the unit cell.

Here is a compilation of some properties of the reciprocal lattice:

- The reciprocal-lattice vectors are perpendicular to those in real space: $\underline{a}_i^* \perp \underline{a}_j$ and $\underline{a}_k$ $(i \neq j,k)$.
- The lengths of the reciprocal-lattice vectors are $|\underline{a}_i^*| = 1/V_c \cdot |\underline{a}_j| \cdot |\underline{a}_k| \cdot \sin\angle(\underline{a}_j,\underline{a}_k)$.
- Each point *hkl* in the reciprocal lattice refers to a set of planes (*hkl*) in real space.

• The direction of the reciprocal-lattice vector $\underline{H}$ is normal to the planes (*hkl*) and its length is reciprocal to the interplanar spacing $d_{hkl}$: $|\underline{H}| = 1/d_{hkl}$.

• Duality principle: The reciprocal lattice of the reciprocal lattice is the direct lattice.

From the positions of the nodes of the reciprocal lattice obtained by diffraction experiments one can determine directly the parameters of the unit cell of a crystal.

Although somewhat abstract, the concept of the reciprocal lattice provides a practical tool to express geometrically the condition for Bragg scattering in the so-called *Ewald construction*. In this way the different diffraction methods can be discussed.

We consider the reciprocal lattice of a crystal and choose its origin 000. In Fig. 2 the wave vector $\underline{k}_0$ (defined in the crystallographers' convention with $|\underline{k}_0| = 1/\lambda$) of the incident beam is marked with its end point at 000 and its origin P. We now draw a sphere of radius $|\underline{k}_0| = 1/\lambda$ around P passing through 000. Now, if any point *hkl* of the reciprocal lattice lies on the surface of this Ewald sphere, the diffraction condition for the lattice planes (*hkl*) is fulfilled: the wave vector of the diffracted beam $\underline{k}$ (with its origin also at P) for the set of planes (*hkl*) is of the same length as $\underline{k}_0$ ($|\underline{k}| = |\underline{k}_0|$), and the resulting vector diagram satisfies $\underline{k} = \underline{k}_0 + \underline{H}$. Introducing the scattering angle $2\theta$ (and hence the Bragg angle $\theta_{hkl}$), we can deduce immediately from $2|\underline{k}|\cdot\sin\theta = |\underline{H}|$ the Bragg equation:

$$2d_{hkl}\cdot\sin\theta_{hkl} = \lambda. \qquad (5)$$

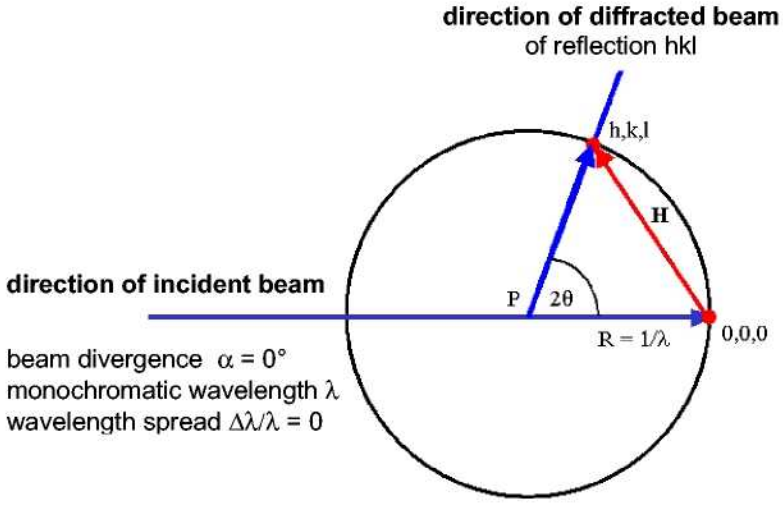



Fig. 2. Ewald construction in reciprocal space, showing the diffraction condition for the *hkl* reflection.

In the case of single-crystal diffraction, a rotation of the crystal and therefore also of the corresponding reciprocal lattice (which is rigidly attached to the crystal) is often used to set the diffraction conditions for the measurement of intensities $I(\underline{H})$.

If $|\underline{H}| > 2/\lambda$ (then $d_{hkl} < \lambda/2$) the reflection *hkl* cannot be observed. This condition defines the so-called *limiting sphere*, with center at 000 and radius $2/\lambda$: only the points of the reciprocal lattice inside the limiting sphere can be rotated into diffraction positions. Vice versa, if $\lambda > 2d_{max}$, where $d_{max}$ is the largest interplanar spacing of the unit cell, then the diameter of the Ewald sphere is smaller then $|\underline{H}|_{min}$. Under these conditions no node of the reciprocal lattice can intercept the Ewald sphere. That is the reason why diffraction of visible light (wavelength $\cong$ 5000 Å) can never be obtained from the atomic structure of crystals. $\lambda_{min}$ determines the amount of information available from a diffraction experiment. In ideal conditions, $\lambda_{min}$ should be short enough to measure all points of the reciprocal lattice with significant diffraction intensities.

For a real crystal of limited perfection and size, the infinitely sharp diffraction peaks (delta functions) are to be replaced by broadened line shapes. One reason is the local variation of the orientation of the crystal lattice (mosaic spread) implying some angular splitting of the vector $\underline{H}$. A spread of interplanar spacings $\Delta d/d$, which may be caused by inhomogeneities in the chemical composition of the sample, gives rise to a variation of its magnitude $|\underline{H}|$. The ideal geometry of the diffraction experiment, on the other hand, must also be modified. In a real experiment the primary beam has a finite divergence and wavelength spread. The detector aperture is also finite. A gain of intensity, which can be accomplished by increasing of the angular divergence and wavelengths bandwidth, has to be paid for by some loss of resolution and, hence, by a limitation of the ability to separate different Bragg reflections.

All of these influences can be studied by the *Ewald construction*. The influence of a horizontal beam divergence on the experimental conditions for a measurement of Bragg-intensities of a single crystal is illustrated in Fig. 3, where strictly monochromatised radiation (only one wavelength $\lambda$ with $\Delta\lambda/\lambda = 0$) is assumed. A so-called $\omega$-scan, where the crystal is rotated around the sample axis perpendicular to the diffraction plane, may be used for a reliable collection of integrated intensities by adapting the detector aperture $\Delta 2\theta$ as a function of the scattering angle $2\theta$. It is obvious that larger $\Delta 2\theta$-values will give rise to a higher background and may lead to difficulties for the separation of neighbouring reflections with similar $\underline{H}$-vectors in the reciprocal lattice. This example shows that a larger beam divergence with an increase in intensity can restrict the resolution conditions.

Bragg-intensities of single crystals are recorded in general by $\omega/n{\cdot}2\theta$-scans ($0 \le n \le 1$) with a coupled rotation of the sample and the detector. The mainly used bisecting special case consists of $\omega = \theta$. The horizontal and vertical detector apertures must be chosen in such a way as to avoid systematic errors from cutting off some intensity of a reflection. The pure $\omega$-scan (rocking-scan) records the intensity distribution of a reflection nearly perpendicular to the scattering vector $\underline{Q} = 2\pi\underline{H}$, almost corresponding to a transversal scan. The $\omega/2\theta$-scan ($n = 1$) represents a longitudinal scan in reciprocal space, recording reflection profiles along $\underline{H}$.

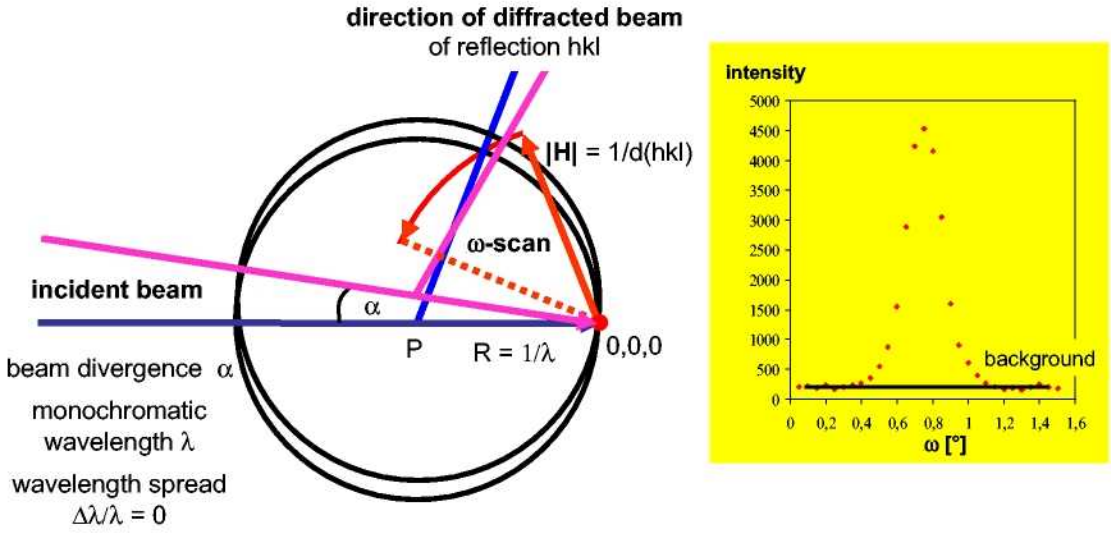



Fig. 3. Ewald-construction: influence of the horizontal beam divergence on the experimental conditions for the measurement of Bragg-intensities. The profile of a Bragg-reflection is shown in the yellow insert ($\omega$-scan).

*Powder diffraction* also may be discussed on the basis of the Ewald construction. An ideal polycrystalline sample is characterised by a very large number of arbitrarily oriented small crystallites. Therefore, for a powder without preferred orientation only $|\underline{H}|$ is defined. In Fig. 4 the corresponding sphere with radius $|\underline{H}| = 1/d_{hkl}$ is drawn around the origin of the reciprocal lattice at 000. For each Bragg-reflection the circle of intersection with the Ewald sphere yields a diffraction cone. All reflections with equal interplanar spacings $d_{hkl}$ are perfectly superimposed and cannot be separated.

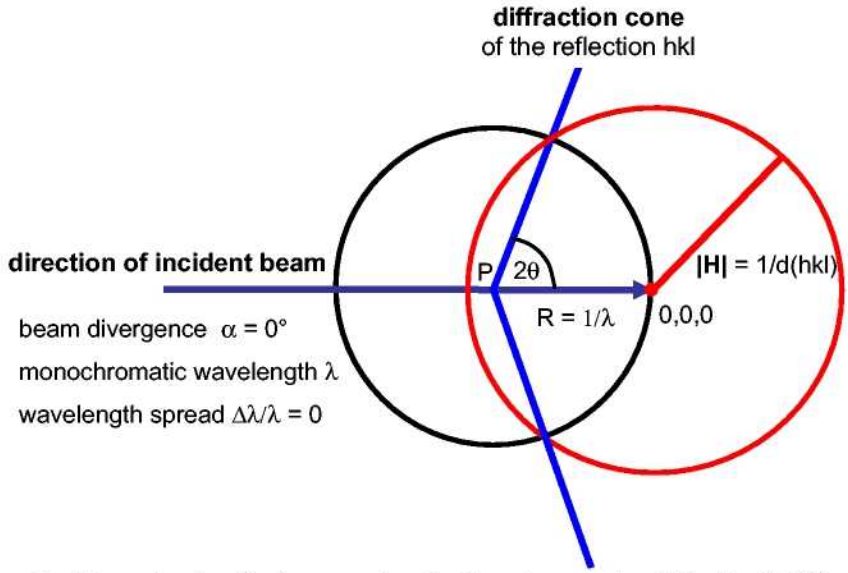



Fig. 4. Ewald-construction for the case of angle-dispersive powder diffraction (ADP).

**7. 3 Powder diffractometer**

There are two principally different powder diffraction techniques: the angular-dispersive ADP-method and the energy-dispersive EDP-method, the latter better known as time-of-flight method in the case of neutron diffraction. In the ADP-measurement the sample is irradiated by a monochromatic beam ($\lambda$ = const.). To each $d_{hkl}$ belongs a Bragg-angle $\theta_{hkl}$. Most of the neutron powder diffractometers at steady-state reactor sources work according to the *ADP-method* (e.g. the D2B-instrument at the HFR/ILL in Grenoble). The angular resolution of a powder-diffraction diagram depends on the beam divergence before and behind the monochromator, on the mosaic spread of the monochromator crystal, and on the monochromator's scattering angle $2\theta_M$. In Fig. 5 for several X-ray- and neutron powder diffractometers the half-width of powder lines (Bragg-reflections) $\Delta 2\theta$ is given as a function of the scattering angle $2\theta$. A large $2\theta_M$-value can be favourable for realising smaller line widths $\Delta 2\theta$ at higher diffraction angles, as can be seen for the D2B-instrument ($2\theta_M = 135°$).

The plan of the upgraded high-resolution D2B-instrument at the HFR/ILL in Grenoble is shown in Fig. 6. Its monochromator, composed of 28 Ge(115) crystals of 1 x 5 x 1 $cm^3$, has a relatively large overall mosaic spread of 20' to increase the neutron reflectivity. It is 300 mm high, focusing vertically onto about 50 mm; this large incident vertical divergence is matched by 200 mm high detectors and collimators. A complete diffraction pattern is obtained

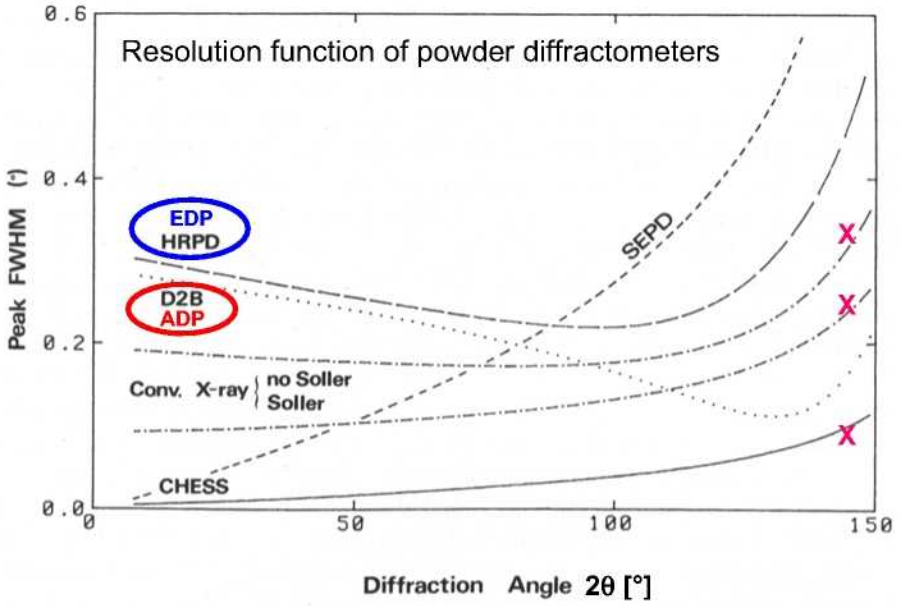



Fig. 5. Comparison of the half-widths of powder lines for selected neutron powder diffractometers: D2B at the HFR/ILL in Grenoble (F), HRPD at NBSR in Lucas Heights (USA), SEPD at ANL in Argonne (USA) – the time-of-flight data of this instrument with $\Delta d/d \approx 1.5 \cdot 10\text{-}3$ are converted to 2θ values – and X-ray powder diffractometers (marked with **X**): conventional and synchrotron facilities (CHESS, USA). All data are relatively old from 1993 [1].

after about 100 steps of 0.025° in 2θ, since the 64 detectors are spaced at 2.5° intervals. Such scans take typically 30 minutes; they can be repeated to optimise statistics.

D2B was also designed for work on magnetism and large d-spacings using wavelengths from 1 Å up to 6 Å. Wavelengths can easily be changed, since they are obtained by a simple rotation around the vertical zone axis $[1\,\bar{1}\,0]$ of the Ge-monochromator (see also Fig. 7):

| Ge(hhl)-reflecting plane | wavelength [Å] | neutron flux |
|---|---|---|
| (557) | 1.051 | |
| (337) | 1.277 | |
| (551) | 1.464 | |
| (335) | 1.594 (optimum λ) | high-resolution mode: $10^6$ n/s/cm²<br>high-intensity mode: $10^7$ n/s/cm² |
| (331) | 2.398 | |
| (113) | 3.152 | |

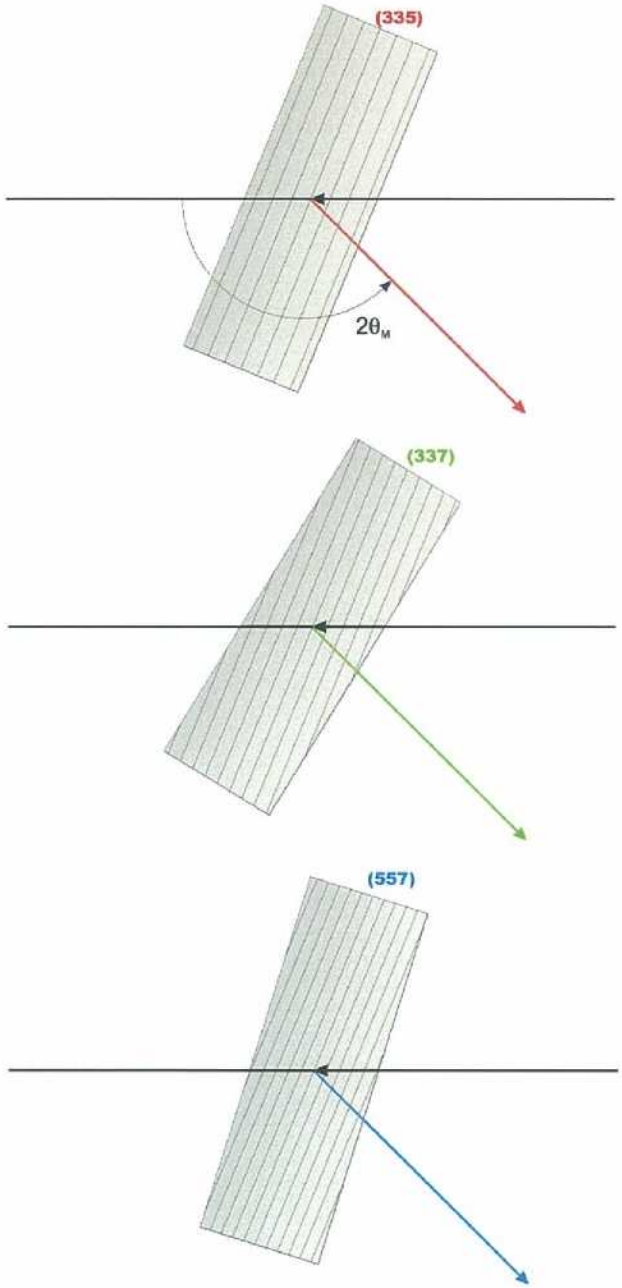



Fig. 7. Principle of the variation of wavelengths by rotation of the Ge-monochromator around the vertical zone axis $[1\bar{1}0]$. The Ge(hhl)-reflecting planes (335), (337) and (557) yield wavelengths of 1.594 Å, 1.277 Å and 1.051 Å, respectively, with a fixed monochromator angle $2\theta_M = 135°$.

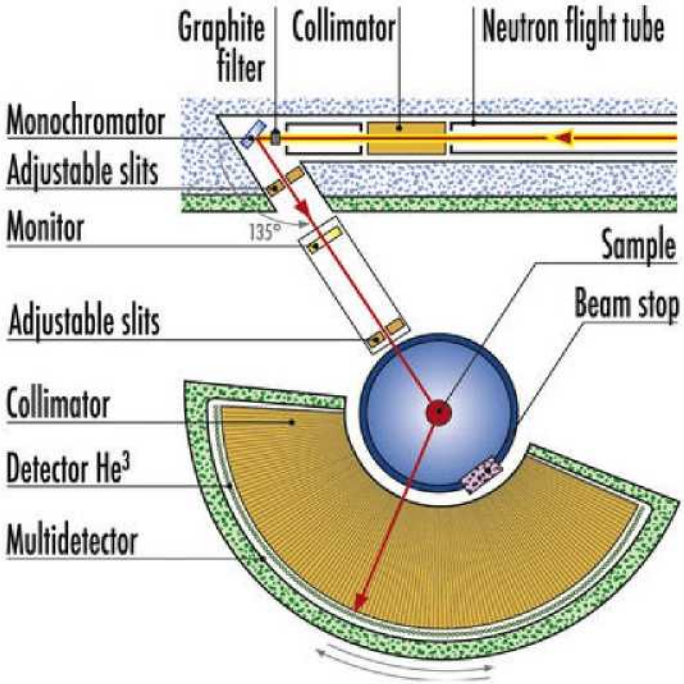



Fig. 6. Plan of the high-resolution powder diffractometer **D2B** at the HFR/ILL in Grenoble.

A large pyrolythic-graphite (PG) filter can be switched in to provide a very clean monochromatic beam at $\lambda = 2.4$ Å (to suppress $\lambda/2$ contamination) and a cold Be-filter can be used for longer wavelengths.

For an ADP-powder diffractometer the measuring time can be reduced substantially by the simultaneous use of many single detectors or of linear multidetector systems. As an example of a 2-axes diffractometer specially designed for the investigation of amorphous systems and liquids, the 7C2-instrument installed at the hot neutron source of the ORPHEE-reactor in Saclay (F) is shown in Fig. 8. With an exchange of monochromator crystals three different standard wavelengths are available: $\lambda$(Ge(111)) = 1.11 Å, $\lambda$(Cu(111)) = 0.7 Å, $\lambda$(Ge(311)) = 0.58 Å. The linear multidetector allows a continuous intensity measurement over a range in scattering angle of 128°. The angular resolution of this instrument is limited since there is no collimation between the sample position and the detector, but the $|\underline{Q}|$-range is very large. For the shortest wavelength $\lambda$(Ge(311)) = 0.58 Å, the accessible values extend up to $|\underline{Q}|_{max} = 2\pi|\underline{H}|_{max} = 20$ Å$^{-1}$.

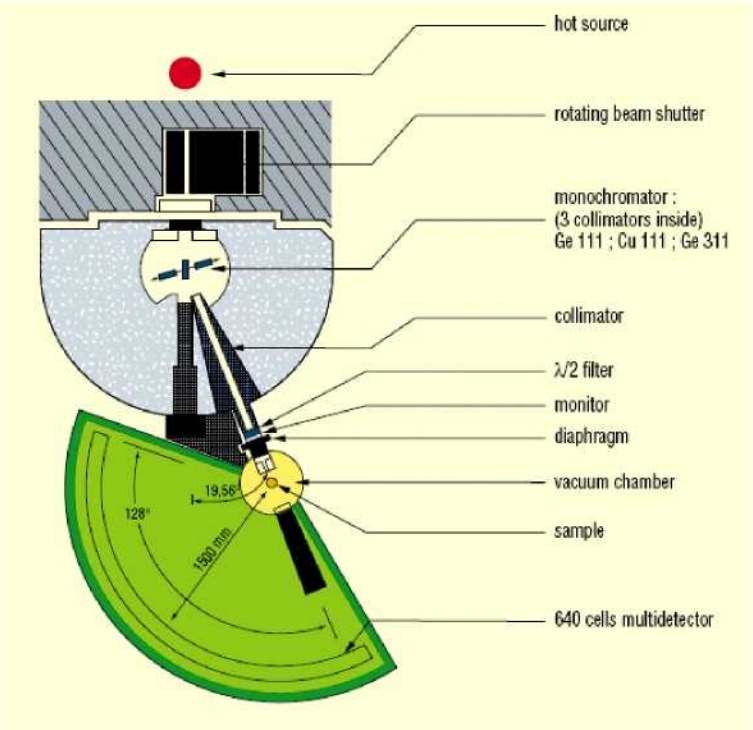



Fig. 8. Plan of the 2-axes diffractometer **7C2** at the hot source of the ORPHEE-reactor in Saclay (F).



Fig. 9. Large 1600-element microstrip detector of the 2-axes diffractometer **D20** at the HFR/ILL Grenoble (F).

To speed-up the measuring time down to the range of seconds and to improve the data statistics, e.g. for time-resolved experiments, the future of neutron diffraction instrumentation lies in the use of large multidetector systems. The 2-axes diffractometer D20 at the ILL in Grenoble is now equipped with a large 1600-element microstrip detector with a detection zone about 4 m long by 150 mm high, covering a 2θ-range of 153.6° (Fig. 9).

In the case of the *EDP-method* a polychromatic white beam is used with the scattering angle being fixed (2θ = const.). The $d_{hkl}$-values result from the time-of-flight measurement of the neutron velocities – converted to wavelengths - for the *hkl* reflections. This technique is especially suitable for pulsed neutron sources. Moreover, it offers some advantages for complex sample environments, such as extreme temperatures, magnetic fields, external pressures, etc. due to its fixed scattering geometry. The resolution of the time-of-flight analysis Δt/t depends on the wavelength-dependant pulse structure of the moderator, on the length of the flight path, and on the scattering angle 2θ (a back-scattering geometry is recommended). As there are normally also relatively short wavelengths in the beam, higher indexed reflections with shorter $d_{hkl}$-values may be reached too. Some typical technical data of the HRPD, installed at the spallation source ISIS/RAL in England, are shown in Fig. 10. A special feature of this instrument is the very long flight path of about 100 m. New fibre-optic-encoded ZnS scintillator detector modules have been developed (Fig. 11) which may cover large solid angle segments.

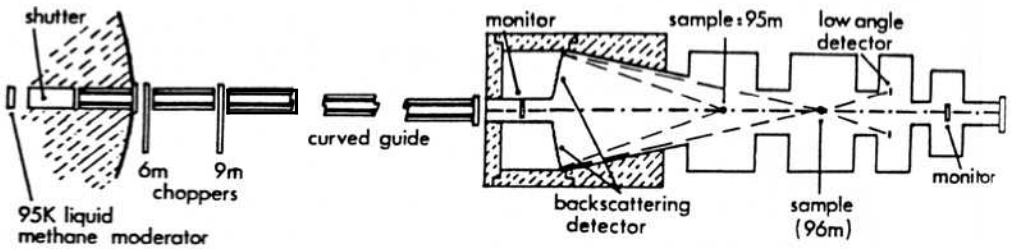



Fig. 10. **HRPD** (high-resolution powder diffractometer) at the spallation source ISIS/RAL, England. A resolution of $\Delta d/d \approx 4 \cdot 10^{-4}$ is achieved with a sample position at 95 m.

The excellent resolution of this time-of-flight diffractometer is demonstrated by sections of the powder diffractogram of benzene shown in Fig. 12. The complete rage of $0.5 \leq d \leq 2.0$ Å was analysed by means of the Rietveld profile method in order to refine the crystal structure of this molecular compound [2] (space group Pbca; lattice parameters: a = 7.3551 Å, b = 9.3712 Å, c = 6.6994 Å).

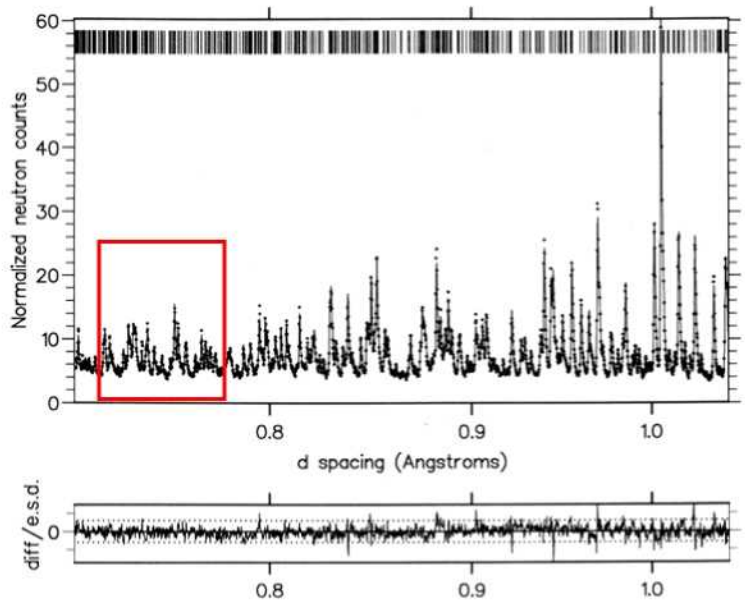



Fig. 12 (a). Powder diffractogram of benzene: section from 0.72 Å ≤ d ≤ 1.03 Å.

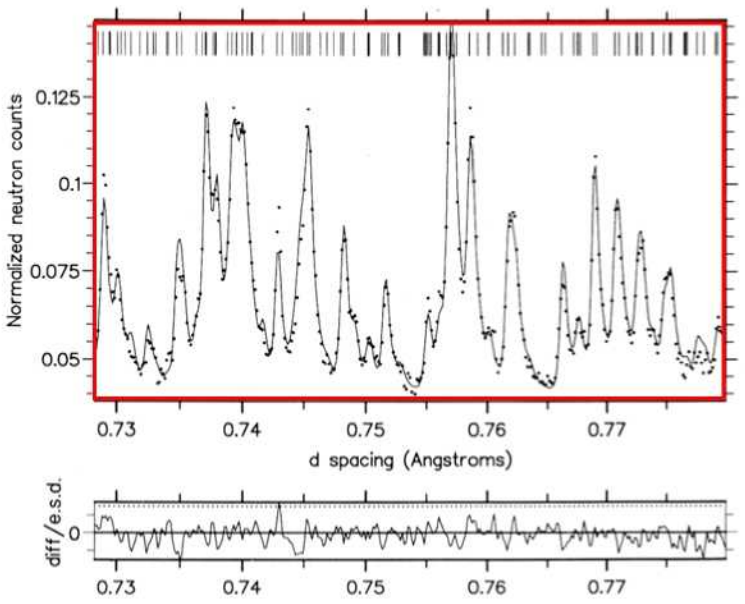



Fig. 12 (b). Powder diffractogram of benzene: enlarged section from 0.73 Å ≤ d ≤ 0.78 Å. The calculated $d_{hkl}$-values are indicated by the small lines at the top of the upper graphs. The quality of the refinement can be judged from the difference between experimental data and profile calculation in the lower graphs.



Fig. 11. One of the fibre-optic-encoded ZnS scintillator detector modules from the **HRPD** backscattering detector bank. The fully assembled bank comprises 8 modules which intersect the entire Debye-Scherrer rings over an angular range $160° < 2\theta < 176°$.

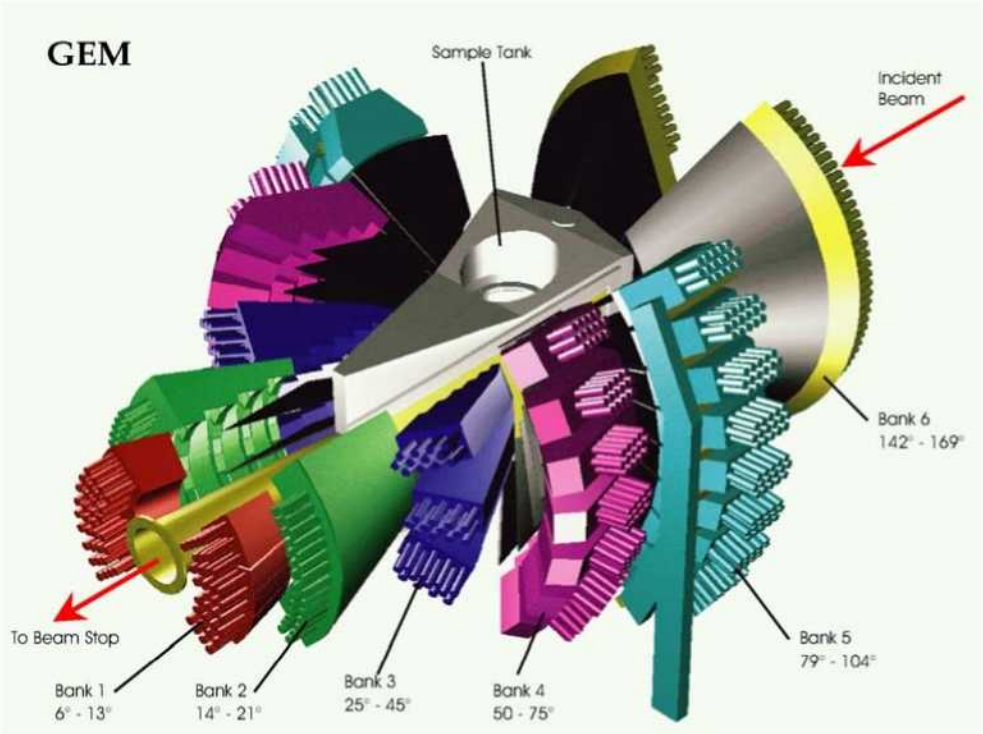



Fig. 13. Overview of the arrangement of the ZnS detector modules at **GEM**/ISIS. The detectors cover a very wide range in scattering angle from 1.1° to169.3°.

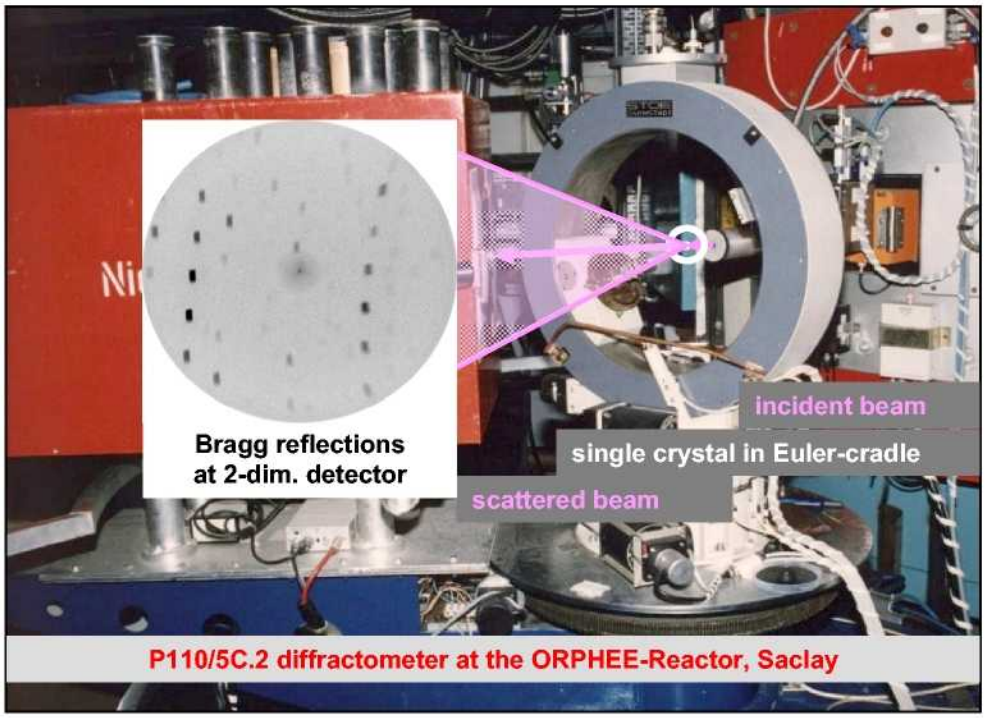
As a new generation neutron diffractometer with ZnS scintillator multi-detectors covering a huge solid angle of about 3.5 steradians the **Ge**neral **M**aterials Diffractometer (GEM) is recently constructed at the ISIS spallation source (Fig. 13). GEM has a total of 6550 detector elements in more than 77 modules. It is designed to be a high intensity, high resolution neutron diffractometer for structural studies of disordered materials and crystalline powders.

**7.4 Single-crystal diffractometer**

Neutron diffraction of single crystals is a domain of the structure analysis of complex structures with large unit cells. Moreover, Bragg-reflection intensity data over a large $\underline{Q}$-range are used for the determination of highly accurate structural parameters like atomic mean square displacements, for detailed investigations of phase transitions including twinning and for the analysis of magnetic ordering including the determination of spin densities. For neutron-diffraction studies on single crystals the Laue-method with 2-dim. positional sensitive detectors (e.g. LADI-instrument with an image-plate detector at HFR/ILL in Grenoble (F)) and 2-axes diffractometers with single detectors are in actual use. New developments with 2-dim. detection systems become more and more important.

To fulfil the diffraction condition for all vectors $\underline{H}$ of the reciprocal lattice (within $2\sin\theta/\lambda < |\underline{H}|_{max}$) single-crystal diffractometers are equipped with a special goniometer consisting of three independent rotations. The eularian cradle in Fig. 14 has in addition to the $\omega$-axis ($\perp$ to the diffraction plane) two further rotation axes $\chi$ and $\varphi$, which are perpendicular to each other. The $\chi$-axis is also perpendicular to the $\omega$-axis. Together with the $2\theta$-rotation axis of the detector ($\parallel$ to the $\omega$-axis) this mechanical unit is called 4-circle goniometer (leading to the name 4-circle diffractometer for this type of single-crystal diffractometers). The measurement of integrated intensities $I(\underline{H})$ of individual Bragg-reflections is performed according to the $\omega/n{\cdot}2\theta$-scan techniques described in chapter 7.2. For a computer-controlled automatic data collection a detailed knowledge of the crystal lattice is needed. Therefore, a single-crystal diffraction experiment starts with a systematic search of reflections by varying $\chi$ and $\varphi$, with the restriction $\omega = \theta$ (bisected condition). From the accurate angular positions of typically 20 indexed reflections the lattice constants and the orientation matrix are determined.

As an example for a single-crystal neutron diffractometer the P110/5C2-instrument installed at the hot neutron source of the ORPHEE-reactor in Saclay (F) is shown in Fig. 14. The monochromatic neutron flux at the sample position is increased by a monochromator system with vertical focussing. The use of small wavelengths allows the measurement of Bragg-intensities up to large $|\underline{H}|$-values ($|\underline{H}|_{max} = 2\sin\theta_{max}/\lambda = 2.8$ Å$^{-1}$).



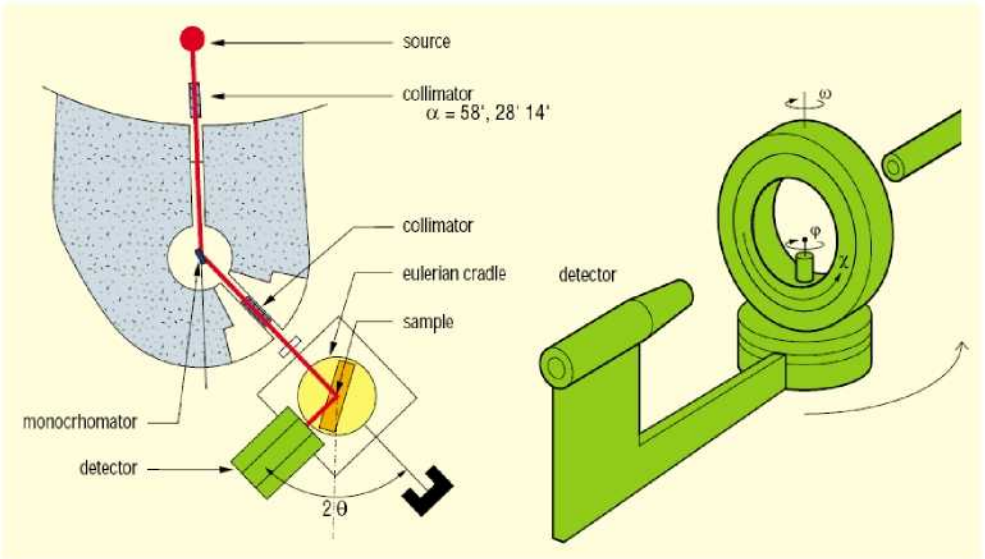




Fig. 14. Single-crystal diffractometer **P110/5C2** at the hot neutron source of the ORPHEE-reactor in Saclay (F).

**Attention:** The lengths of both, the vector $\underline{H}$ of the reciprocal lattice as used in crystallography and the scattering vector $\underline{Q}$ of solid state physics, are expressed in $Å^{-1}$. There is, however, a factor of $2\pi$ between both quantities, which means that $|\underline{H}| = 2.8\ Å^{-1}$ corresponds to $|\underline{Q}| = 17.6\ Å^{-1}$.

The influence of the primary collimation $\alpha_1$ on the half-width of Bragg-reflections of a perfect Ge crystal is shown in Fig. 15. The resolution curves for two different wavelengths $\lambda(Cu(420)) = 0.525$ Å and $\lambda(Cu(220)) = 0.831$ Å are plotted as a function of $\sin\theta/\lambda$.

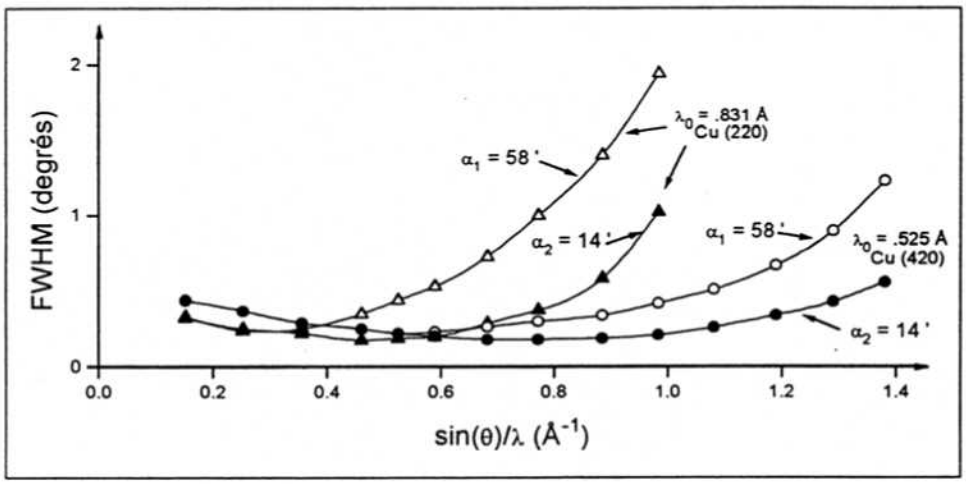



Fig. 15. Resolution curves of the single-crystal diffractometer **P110/5C2** at the hot neutron source of the ORPHEE-reactor in Saclay (F).

A new single-crystal diffractometer HEiDi has been constructed recently at the hot scource of the FRM-II reactor in Garching near Munich [3]. The monochromator exchange unit for three vertically focussable crystals, which can be adjusted independently of each other, and the Cu(220)-monochromator are shown in Fig.16. In combination with three possible monochromator angles $2\theta_M$, altogether 9 wavelengths are available between $\lambda_{min} = 0.280$ Å and $\lambda_{max} = 1.443$ Å:

| **monochomator crystals** | **Ge(311)** | **Cu(220)** | **Cu(420)** |
|---|---|---|---|
| **$2\theta_M$ [°]** | **wave lengths [λ]** | | |
| 20 | 0.593 | 0.443 | 0.280 |
| 40 | 1.168 | 0.870 | 0.552 |
| 50 | 1.443 | 1.079 | 0.680 |



Fig. 16. The monochromator exchange unit (left) and the Cu(220)-monochromator (right) of the single-crystal diffractometer **HEiDi** at the hot neutron source of the FRM-II reactor in Garching.

For the vertical focussing of the monochromatic beam the planar crystal segments of the monochromator are inclined to realise a quasi-curvature. The effect of focussing at the sample position is demonstrated in Fig.17 for the Cu(220)-monochromator with $2\theta_M = 40°$ (corresponding to $\lambda = 0.870$ Å). A minimum height of the homogeneous neutron beam of about 10 mm is obtained with a neutron flux of $4 \cdot 10^6$ n/s/cm².

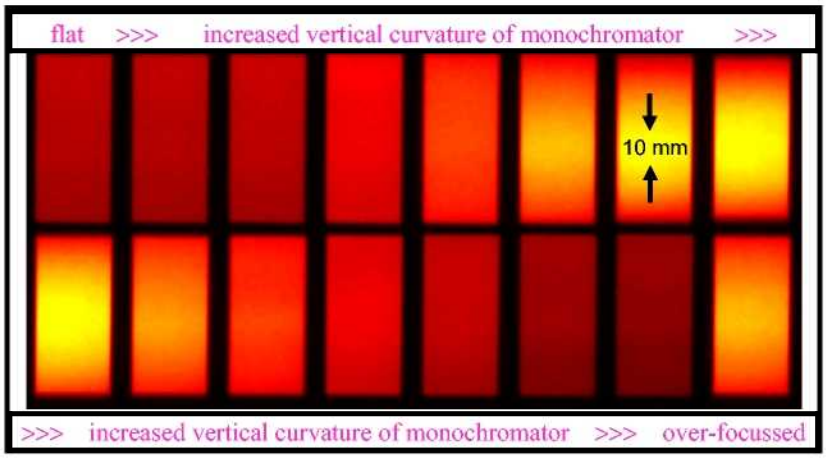



Fig. 17. Sequence of focussing with the Cu(220)-monochromator and $2\theta_M = 40°$ recorded with a CCD-camera at the sample position of HEiDi (size of each image 18*36 mm$^2$)

Single-crystal diffraction with polarized neutrons is employed for the analysis of complex magnetic structures and the determination of spin densities. The two-axes diffractometer 5C1 installed at the hot neutron source of the ORPHEE-reactor in Saclay is designed for so-called flipping-ratio measurements where the incident neutrons are polarized either parallel (+) or antiparallel (-) to a strong magnetic field applied to the sample. Fig. 18 shows the 5C1-instrument with its cryomagnet for H < 7.8 Tesla and lifting counter system.

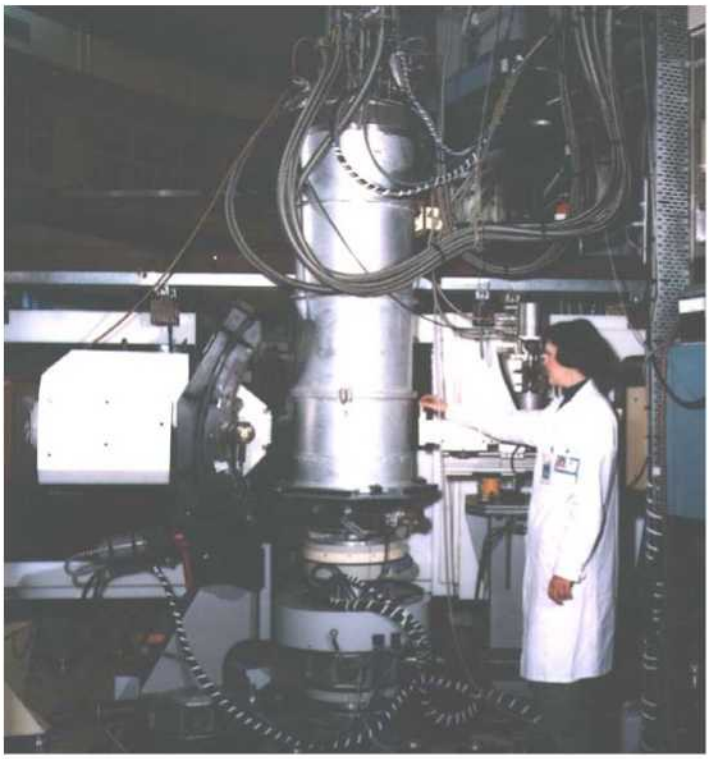


Fig. 18. 2-axes diffractometer **5C1** for polarized neutrons at the hot neutron source of the ORPHEE-reactor in Saclay (F).

**References**


[1] R. J. Hill, The Riedveld Method, ed. R. A. Young, Chap. 5, Oxford University Press (1993)

[2] W. I. F. David and J. D. Jorgensen, The Riedveld Method, ed. R. A. Young, Chap. 11, Oxford University Press (1993)

[3] M. Meven, V. Hutanu and G. Heger, Neutron News **18**, 19 (2007)

# 8

# Small-Angle Scattering

Henrich Frielinghaus

# 8. Small Angle Scattering

Henrich Frielinghaus

## 8.1. Introduction

Small angle scattering is used in conventional solid state physics and, nowadays, strongly in the field of soft matter research. This field embraces polymer melts, solutions, and rubbers, but also complex fluids such as microemulsions, colloidal dispersions, and micellar solutions. The similarity to biological systems brings biologists and physicists together at a small angle scattering machine. The measured magnitude of such a small angle scattering experiment is the intensity as a function of the momentum transfer Q:

$$Q = \frac{4\pi}{\lambda} \sin\Theta \tag{8.1}$$

with the scattering angle $2\Theta$ and the wavelength $\lambda$ of the neutrons. The momentum transfer $\vec{Q}$ is the difference of the momenta of the incoming and scattered neutrons. In an elastic scattering experiment the absolute momentum does not change, i.e. $|\vec{k}_i| = |\vec{k}_f| = 2\pi/\lambda$, since the observed objects are large and, therefore, move only slowly. The length scale of the observed objects is given by the momentum transfer $Q$, which is in the range of 0.3 to $10^{-4}$ Å$^{-1}$ due to the wavelength $\lambda$ = 5 to 20Å and the small angles. Thus, the considered length scales in real space $\ell = 2\pi / \lambda$ are of the order 10 to $10^5$Å (or 1nm to 10µm). The different instruments are optimized for different length scales; the technical realizations will be presented in this lecture. While the geometrical realizations of each instrument are discussed first, some components are discusses in the last sections in general. The discussed instruments are optimized for continuous radiations sources as the FRM-2. Spallation sources generate neutron pulses of different periodicity. Then, a whole spectrum of wavelengths is treated simultaneously, and the instruments need much quicker detectors for instance.

## 8.2. Absolute Intensity at Sample and Detector

The discussed conditions of a scattering experiment are depicted in Fig. 8.1 for a real space and a reciprocal space interpretation. In a realistic experiment the incoming and final neutrons have some uncertainty in direction (divergence) and wavelength. This detail is an issue of the resolution of the experiment, and will also be discussed below. The illuminated area of the sample is indicated by F.

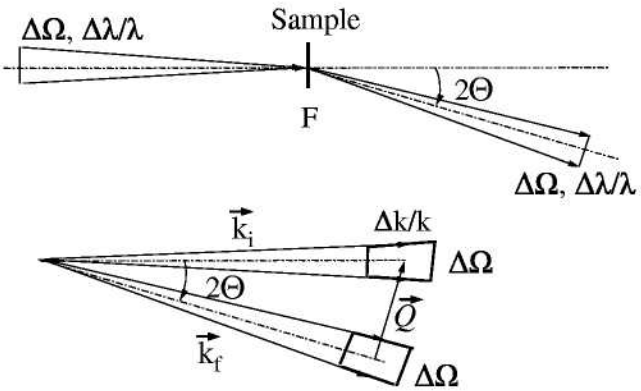



**Figure 8.1**: The changes of momentum due to the scattering process in a real space and a reciprocal space interpretation. The realistic experiment gives rise to uncertainties of the direction and wavelength, which will also be discussed in the context of the instrument resolution.

The intensity obtained by a reactor is characterized by the equilibrium of the neutrons with the moderator and/or the cold source. Thus, the neutrons are characterized by a certain temperature T or a typical wave vector $k_T = \sqrt{2m_n k_B T}/\hbar$ with $m_n$ being the neutron mass, and $k_B$ and $\hbar$ being the Boltzmann and Planck constants. The luminosity of the source is given by

$$L = \frac{\Phi}{2\pi}\left(\frac{k}{k_T}\right)^4 e^{-(k/k_T)^2}\frac{\Delta k}{k} \tag{8.2}$$

in units $cm^{-2}s^{-1}steradian^{-1}$. It is determined by the total thermal flux of the neutrons $\Phi$ and the selected wavelength band $\Delta k$ due to the monochromator, which can be freely adjusted to any wave vector $k$. The intensity at the sample is then given by:

$$\Delta I_0 = L \cdot F \cdot \Delta\Omega \tag{8.3}$$

This intensity is also called *primary intensity*, and is proportional to the irradiated area F and the divergence $\Delta\Omega$ due to an adjustable collimation. The interplay of intensity and resolution is discussed below.

For the scattered neutrons the first Born approximation is assumed to be valid. This means that each incoming neutron is scattered at most once. Practically, this means that only 10% of the neutrons are scattered coherently. Another large fraction (up to 40%) is scattered incoherently, and the remaining neutrons pass the sample unscattered. Within this approximation the scattered intensity can be related to the macroscopic cross section, according to:

$$\Delta I_D(\vec{Q}) = \Delta I_0 \cdot D \cdot T \cdot \frac{d\Sigma}{d\Omega}(\vec{Q}) \cdot \Delta\Omega_D \qquad (8.4)$$

The scattered intensity $\Delta I_D$ is detected at the detector in an element with the solid angle $\Delta\Omega_D$. The scattering vector $\vec{Q}$ is determined by the scattering angle $2\Theta$ and a polar angle. For isotropic samples the intensity is independent of the polar angle. The sample thickness $D$ and the transmission $T$, which is the ratio of the transmitted non-scattered and the primary intensities, determine the scattered intensity as well. The macroscopic cross section $d\Sigma/d\Omega$ is the experimental result given in absolute units [$cm^{-1}$]. It is free from most instrumental details, and, therefore, can be compared with other experiments or theoretical descriptions. Only resolution aspects remain inherent, which have to be treated separately as discussed below.

Since the primary intensity is too high to be measured by the detector directly, a secondary standard is usually used to measure the incident intensity indirectly. An incoherent scatterer (water or plexiglass) with a known macroscopic cross section delivers a constant intensity on the detector. The intensities of the sample and the standard are compared relatively, and the primary intensity cancels out. In this relative measurement the detector efficiency, which we did not treat explicitly here, is also removed from the final result.

### 8.3. Small Angle Scattering with Neutrons

The method of small angle neutron scattering (SANS) is frequently used for structural investigations in the nanometer scale. There are three different SANS techniques: The pin-hole SANS covers the conventional range of 1 to 100nm. This range is extended by the focusing SANS with either mirrors or lenses up to 1000nm. The double crystal (Bonse Hart) diffractometer reaches length scales in the µm range. While the pin-hole SANS is refurbished with an option of lenses at the JCNS in Garching, the conventional focusing mirror SANS runs in Garching as well. The double crystal diffractometer is not currently installed at the FRM-2, but such instruments exist at several institutions.

#### 8.3.1. Pin-Hole SANS

After thermalization in the cold source at ca. 30K (see §8.2) the neutrons are guided through neutron guides to the instrument. A scheme of a pin-hole SANS is shown in Fig. 8.2. The monochromator is a mechanical velocity selector with tilted lamellae on a rotating cylinder (see §8.4.2). Typically, neutrons are prepared with a wavelength $\lambda$ of 5 to 20Å and a relative distribution $\Delta\lambda_{FWHM}/\lambda$ (full width at half maximum) of 10 to 20%. One far aperture and the

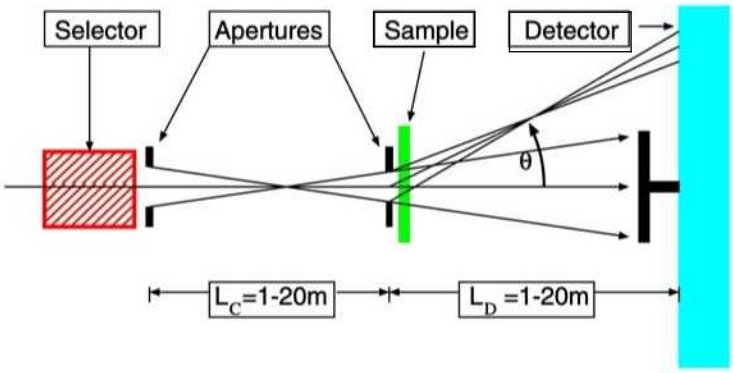



**Figure 8.2**: Scheme of a pin-hole SANS: The neutrons pass a velocity selector; the divergence is determined by two apertures in the collimation; then the neutrons hit the sample. The non-scattered neutrons are absorbed by the beam-stop. The scattered neutrons are collected by the position sensitive area detector.

sample aperture determine the divergence of the beam. The absorbing material contains usually boron (or even pure $^{11}B$) in the form of boron carbide; but cadmium is another option. Then the beam hits the sample. The non-scattered neutrons are absorbed at the beam-stop in front of the detector. A small monitor in the beam-stop allows to determine the transmitted intensity. The scattered neutrons are collected by the position sensitive area detector. From the position the angle $\Theta$ and the scattering vector $Q$ are obtained, to which the measured intensity is assigned.

The for the specific sample needed range of scattering vectors $Q$ is set by different detector distances $L_D$ between 1.3 and 20m, while the neutron wavelength (typically 7Å) is changed in extreme cases only. The typical $Q$-range is thus 0.3 to $10^{-3}$ Å$^{-1}$. The collimation length $L_C$ is usually set symmetrically, which means $L_C = L_D$. The varying distance between the monochromator and the entrance aperture is bridged by 1m segments of neutron guides. So the collimation length $L_C$ can only be varied in 1m steps. The shorter collimation distances $L_C$ for larger scattering angles $Q$ have the advantage, that the relaxed divergence conditions lead to higher intensities and thus to shorter measurement times. The intensity at the sample position as a function of the collimation length $L_C$ is shown in Fig. 8.3.

From the variation of eq. 8.1 the principal equation of the resolution correction can be obtained:

$$\left(\frac{\Delta Q}{Q}\right)^2 = \left(\frac{\Delta\Theta}{\Theta}\right)^2 + \left(\frac{\Delta\lambda}{\lambda}\right)^2 \qquad (8.5)$$

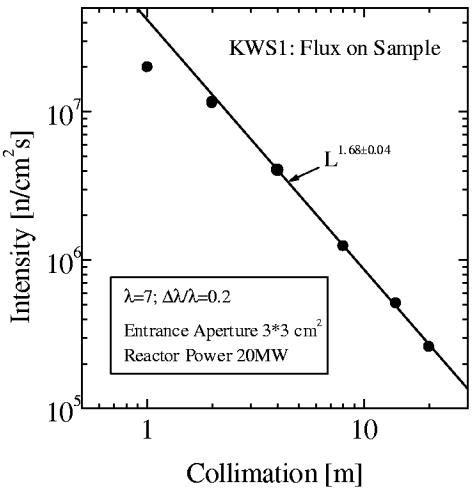



**Figure 8.3**: The intensity at the sample position for different collimation distances $L_C$. This dependence was measured at the instrument KWS-1 at the Jülich reactor FRJ-2. Higher intensities are expected for Garching. The saturation at small collimation lengths is due to the total angle of reflection of the Ni neutron guides.

The uncertainty of the scattering vector $\Delta Q$ is of interest for either deconvoluting the measured spectrum to an ideal spectrum, or for convoluting a theoretical function, which is fitted to the measured intensity. On the right hand side of eq. 8.5 the two independent contributions are listed: $\Delta\Theta$ is the collection of all angular uncertainties, which are due to the two collimation apertures and the finite size of the detector elements. $\Delta\lambda$ arises from the wavelength distribution of the selector.

As a first approach [4], all angular contributions can be assumed to be independent. This means that three terms arise from the entrance aperture with the diameter $d_E$, the sample aperture with the diameter $d_S$ and the detector elements with the diameter $d_D$:

$$\sigma_Q^2 = \frac{2}{12}k^2\left(\left(\frac{d_E}{L_C}\right)^2 + \left(\frac{d_S}{L_C}+\frac{d_S}{L_D}\right)^2 + \left(\frac{d_D}{L_D}\right)^2 + \Theta^2\left(\frac{\Delta\lambda}{\lambda}\right)^2\right) \qquad (8.6)$$

The left hand side of eq. 8.6 is solved for the variance $\sigma_Q$ of the scattering angle, while the $\Delta$-values represent full width at half maximum values. The additional factor 2 in eq. 8.6 with respect to reference [4] was added due to the 2-dimensional distribution of the intensity (at the detector). A more detailed study [5] includes the dependence of the angular uncertainty from the entrance and sample apertures. The final result reads:

$$\sigma_Q^2 = \frac{1}{8\ln 2} k^2 \left( (\Delta\beta)^2 + \left(\frac{d_D}{L_D}\right)^2 + \Theta^2 \left(\frac{\Delta\lambda}{\lambda}\right)^2 \right) \tag{8.7}$$

with:
$$\Delta\beta = \begin{cases} \dfrac{d_E}{L_C} - \dfrac{1}{4}\dfrac{d_S^2}{d_E}\dfrac{(L_C + L_D)^2}{L_C L_D^2} & \text{for } \dfrac{d_E}{L_C + L_D} \geq \dfrac{d_S}{L_D} \\ \left(\dfrac{d_S}{L_C} + \dfrac{d_S}{L_D}\right) - \dfrac{1}{4}\dfrac{d_E^2}{d_S}\dfrac{L_D}{L_C(L_C + L_D)} & \text{for } \dfrac{d_E}{L_C + L_D} < \dfrac{d_S}{L_D} \end{cases} \tag{8.8}$$

The first case of eq. 8.8 is the more common case, which means that the collimation aperture covers a larger angle than the sample aperture regarded back from the detector. The two prefactors of eqs. 8.6 and 8.7 are virtually identical.

As already mentioned, the instrument is usually set up symmetrically. Then, the optimized condition of the instrument – resolution-wise and intensity-wise – is obtained by:

$$L_C = L_D \qquad \text{and} \qquad d_E = d_D = 2 d_S \tag{8.9}$$

Arguing on the basis of eq. 8.6, all independent contributions should be equal. The refined analysis with eq. 8.7 leads to the same result, since $\Delta\beta$ is minimal then. Since the detector technique is highly developed, the single detector element $d_D$ is rather small, and generally can be neglected in the resolution consideration. The optimized intensity at the sample position is given by eq. 8.3, and reads:

$$\Delta I_0 = L_{\text{luminosity}} \cdot \frac{d_E^2}{L_C^2} \cdot \frac{d_S^2}{L_D^2} \cdot L_D^2 \quad \propto \quad L_{\text{luminosity}} \cdot \left(\frac{\Delta Q}{k}\right)^4 \cdot L_D^2 \tag{8.10}$$

The second part of this equation is just given without a precise prefactor, since the general dependence is more important: The intensity decreases with the power of 4 with a higher resolution, but longer instruments can compensate partially for this intensity loss. This is the reason, why typical SANS instruments are 40m long.

The quality of a SANS instrument can be judged by the primary neutron beam on the detector (with an attenuated direct beam). On the one hand the width of the beam can be compared with the theoretically expected width (eqs. 8.6 and 8.7), since the measured curve coincides with the resolution function at $Q = 0$. On the other hand the background intensity near the primary beam tells about the minimum detectable signal of a weakly scattering sample. An example measurement has been depicted in Fig. 8.4. The full width at half maximum is $\Gamma_{½}$, and the background is typically read off at $2\Gamma_{½}$. For good SANS instruments this background is in the range of $10^{-5}$ to $10^{-6}$, and the beam stop can be made as small as possible.

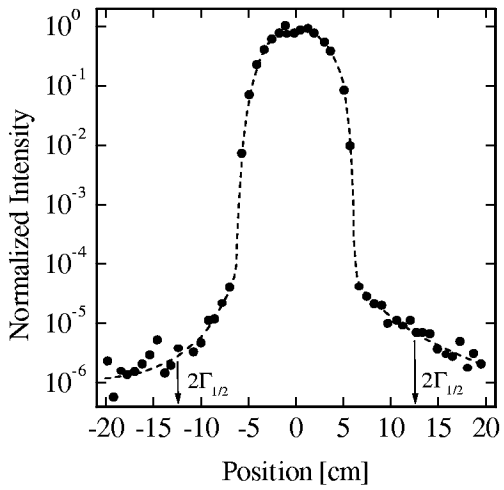



**Figure 8.4**: Semi-logarithmic intensity scan of the primary beam. This curve coincides with the resolution function at a scattering angle zero. The residual intensity next to the primary beam tells about the minimum signal detectable from a scattering sample. This background is typically read off at twice the full width at half maximum $\Gamma_{½}$.

### 8.3.2 Pin-hole SANS with focusing lenses

As we have seen with eqs. 8.6 and 8.7 and Fig. 8.4 the collimation aperture is imaged by the pin-hole SANS on the detector, and the sharpness of this image is connected with the resolution of the instrument. A simple improvement of the simple pin-hole SANS can be reached by placing a set of $MgF_2$ lenses right in front of the sample. This allows to open the sample aperture virtually infinitely while the imaged collimation aperture on the detector remains the same (or is even slightly improved). Regarding the sample intensity one obtains:

$$\Delta I_0 = L_{\text{luminosity}} \cdot \frac{d_E^2}{L_C^2} \cdot \frac{d_S^2}{L_D^2} \cdot L_D^2 \quad \propto \quad L_{\text{luminosity}} \cdot \left(\frac{\Delta Q}{k}\right)^2 \cdot \gamma_C^2 \cdot L_D^2 \qquad (8.11)$$

The collimation aperture is connected with the resolution, while the maximum sample aperture is limited by the transported divergence of the neutron guide, i.e. the total angle of reflection $\gamma_C$. There are two possible applications of the neutron lenses: (i) The resolution is kept constant, and the intensity is increased due to the smaller exponent 2 (instead of 4); (ii) the intensity is kept at a reasonable level, and the resolution is increased by choosing a smaller collimation aperture.

Some extremely well suited lenses are depicted in Fig. 8.5. These lenses are manufactured from $MgF_2$ and have a diameter of 5.2 cm. Due to the negative refractive index for neutrons



**Figure 8.5**: Aspherical $MgF_2$ lenses as focusing neutron device. The lenses are concave since the refractive index is smaller than unity for the neutrons. The lenses have a parabolic shape in order to reduce the spherical aberrations.

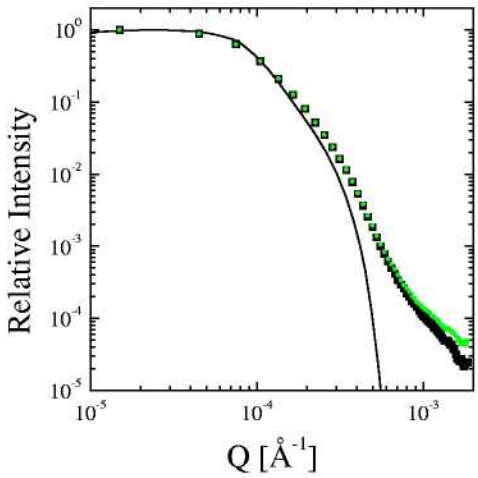



**Figure 8.6**: The primary beam of a pin-hole SANS instrument with 7 neutron lenses. The instrument setup was $L_C$ = 10m, $L_D$ = 10m, $d_E$ = 5mm, $d_S$ = 5cm, $d_D$ = 0.5mm, $\lambda$=19Å. The black squares were measured, while the solid line was computer simulated. The difference is due to scattering windows material. The small greed dots are the scattering signal of a sample.

the lenses are concave. Furthermore we chose a parabolic shape in order to reduce the spherical aberrations. Seven of these lenses have been successfully tested in a conventional pin-hole SANS machine. Since the maximum collimation and detector distances were 10m, we had to chose a neutron wavelength of $\lambda$ = 19Å to reach a focus of 5m. A high resolution detector with a spatial resolution of $d_D$ = 0.5mm was used. The measured primary beam, as

depicted in Fig. 8.6, agrees well with the computer simulations. Only some scattering of window material shows an additional signal at higher $Q$. A sample measured with these conditions shows considerable scattering at the higher $Q$, but a detailed analysis shows, that considerable differences are detectable down to $Q = 10^{-4}$Å$^{-1}$. In this way the neutron lenses proved to be successful in the high resolution application. The simpler high intensity application was not tested so far since the desired 28 lenses have not been manufactured so far, but a 10 times higher intensity is expected if the lenses are cooled down to 100 to 150K to reduce the thermal diffuse scattering.

The Q-resolution of a lens based SANS instrument can be found in reference [6]. The general problem is the chromatic aberration which is proportional to the selected wavelength band $\Delta\lambda$. This additional term slightly reduces the quality of this solution; and this problem is overcome with focusing mirrors.

### 8.3.3. Focusing SANS

Historically, the concepts of a focusing SANS instrument were developed for a mirror based solution. However, these concepts do not differ from the lens based instrument, as we will see. A scheme of this instrument is given in Fig. 8.7. The monochromatized neutrons enter the instrument through an aperture of $d_E \approx 2$mm. The focusing mirror is installed at a rather flat angle close to the total angle of reflection. To cover the full divergence of the neutron guide, the mirror has a quite large area (length up to 1.2m). The sample is placed directly behind the mirror, and the detector collects the scattered neutrons. The instrument is symmetric, i.e $L_C = L_D = 11$m, and the focus of the mirror is exactly in the middle $f = 5.5$m. The position sensitive detector has a spatial resolution of $d_D = 0.5$mm. With a typical wavelength of 15Å the instrument covers the typical $Q$-range between $10^{-3}$ and $10^{-4}$Å$^{-1}$, which is also typical for light scattering.

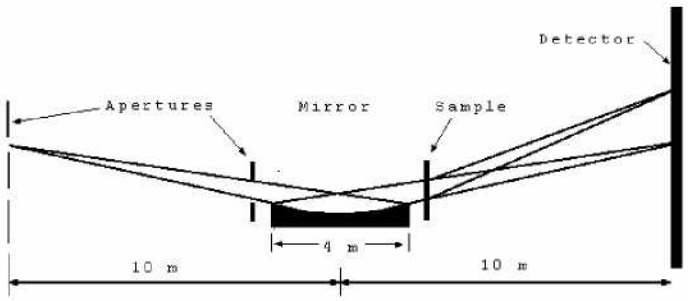



**Figure 8.7**: Scheme of the focusing SANS instrument KWS-3.

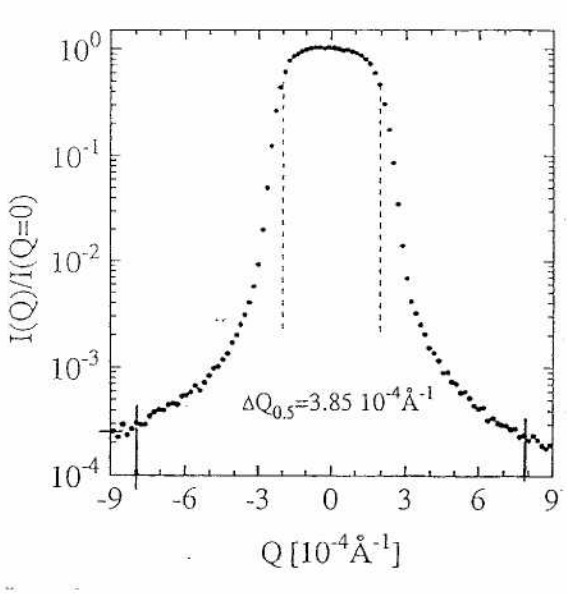



**Figure 8.8**: Footprint of the primary beam of the focusing SANS. The width of this curve $\Delta Q_{0.5}$ is the resolution at zero scattering angle. The residual intensity at $2\Delta Q_{0.5}$ is much higher than for the conventional SANS instrument.

The intensity at the sample position is given by the same concepts as for neutron lenses:

$$\Delta I_0 = L_{\text{luminosity}} \cdot \frac{d_E^2}{L_C^2} \cdot \frac{d_S^2}{L_D^2} \cdot L_D^2 \quad \propto \quad L_{\text{luminosity}} \cdot \left(\frac{\Delta Q}{k}\right)^2 \cdot \gamma_C^2 \cdot L_D^2 \tag{8.12}$$

The break even point for the focusing SANS instrument in comparison to the pin-hole setup appears for $Q$ in the $10^{-3}$Å$^{-1}$ region. The focusing SANS concept has been known for a long time, but only recent developments of high quality mirrors made this instrument possible. An example of a primary beam measurement is shown in Fig. 8.8. The mirrors originate to a development of X-ray satellites, and were successfully transferred for the purposes of neutron scattering.

### 8.3.4. Double Crystal Diffractometer

This double crystal diffractometer (DCD), or this Bonse-Hart diffractometer has the highest resolution in comparison with the other SANS instruments. A scheme of this instrument is given in Fig. 8.9. The essential parts are two perfect silicon single crystals mounted on an optical bench. The reflectivity $R(y)$ of a perfect crystal is described by the Darwin curve:

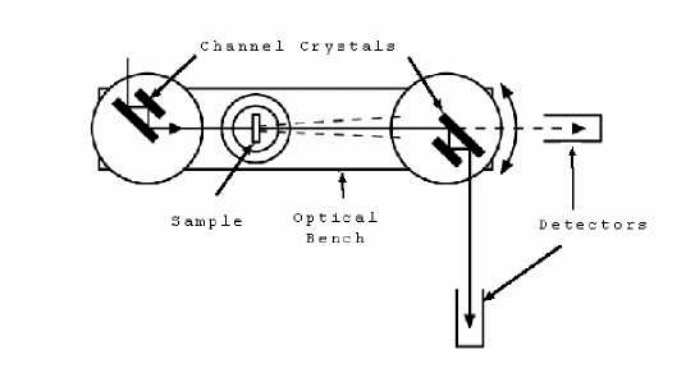



**Figure 8.9**: Schematic design of a double crystal diffractometer

$$R(y)=\begin{cases}1 & |y|\le 1\\ 1-(1-y^{-2})^{0.5} & |y|>1\end{cases} \tag{8.13}$$

The ideal Darwin curve is depicted in Fig. 8.10. The Bragg angle is called $\Theta$, and the parameter $y$ is the deviation of the scattering angle $\Delta\Theta$ normalized with respect to the Darwin width $\Delta\Theta_C$, i.e. $y = \Delta\Theta / \Delta\Theta_C$. So for smaller deviating angles than the Darwin width all neutrons are reflected.

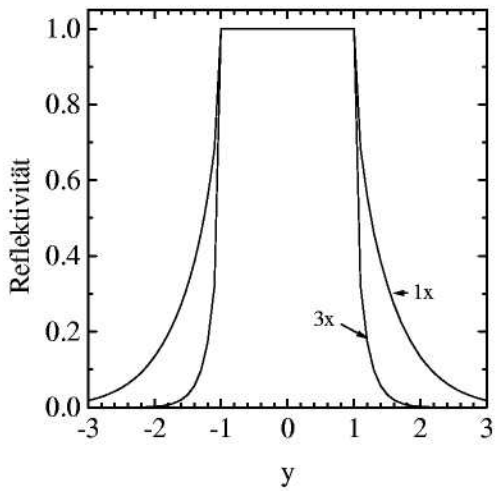



**Figure 8.10**: Ideal Darwin curve of a single crystal (indicated by 1x). After three reflections the Darwin curve is much sharper (indicated by 3x, i.e. the third power of the original curve).

The analyzing crystal is rotated with respect to the first one by an angle $\delta$. The resulting intensity as a function of $\delta$ arises from the convolution of two Darwin curves as given by eq. 8.13 and Fig. 8.10. This convolution is depicted in Fig. 8.11. At an angle $\delta = 0$ the lattice planes of both crystals are oriented parallel, the two Darwin curves overlap totally, and the maximum intensity is obtained. With a finite rotation $\delta$ the two Darwin curves overlap only partially, and the reflected intensity is reduced. The width of this convolution function $\Delta\delta$ is characteristic for the minimum scattering angle $Q_{min}$, and is given by the Darwin width $\Delta\delta \approx \Delta\Theta_C$, which in turn is given by:

$$\Delta\Theta_C = \frac{b_C\, e^{-W} |F| N \lambda^2}{4\pi \cdot \sin(2\Theta)} \qquad (8.14)$$

For the (331) lattice planes of a Silicon single crystal and neutrons with a wavelength of $\lambda$ = 1.8Å the Bragg angle of diffraction is about 45° and the half width of the resolution curve is $\Delta\Theta_C$ = 3.2μrad, which corresponds to an angle of slightly more than half a second of arc or a scattering vector of $Q = 1.12 \cdot 10^{-5}$ Å$^{-1}$ (the missing symbols are the scattering length $b_C$ of silicon, the Debye-Waller factor exp(-$W$), the structure factor $F$, and the atom number density $N$). So this diffractometer opens access to smallest scattering angles, which demands protections against mechanical vibrations, fluctuations of temperature, and much patience from experimentalist.

The strength of this instrument is its very high resolution, which is even better than of light and its relatively simple and cheap design in comparison with most other neutron scattering instruments. This instrument can also be successfully operated at smaller research reactors. Disadvantages are (i) the slit geometry, which needs a special deconvolution formula for isotropic samples, (ii) the sequential scanning of different $Q$-vectors, which is time consuming, and (iii) a rather low intensity, which needs good background conditions. Improvements are possible by a special design of the crystals: The relatively high background near the primary beam can be strongly suppressed by a 'channel cut' in the crystals, which separates the crystal volumes of each reflection, and interference of guided waves within the crystal are reduced. A nearly ideal triple reflection is obtained as indicated by Figs. 8.9 and 8.10. The resulting resolution function is depicted in Fig. 8.11 with highly suppressed tails. Experimentally, this change from single-single to triple-triple reflections was verified as shown in Fig. 8.12. The multiple reflections clearly lead to a sharper resolution and a strongly suppressed background next to the primary beam. The background level of $10^{-4}$ is sufficient for many samples since the observed objects are large anyways, and thus scatter strongly.

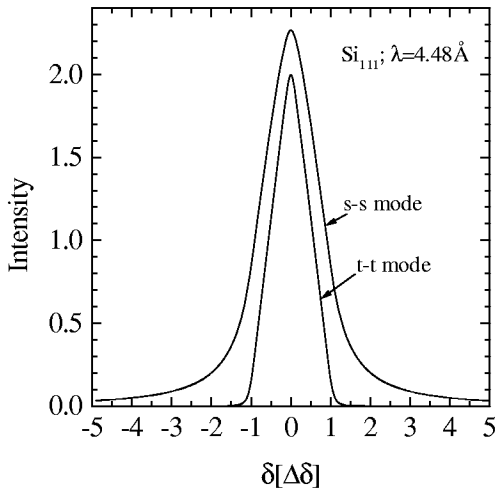



**Figure 8.11**: Theoretical resolution curves of a double crystal diffractometer as obtained from the self-convolution of a Darwin curve (Fig. 8.10). The two different curves represent the modes of a single-single (s-s) and a triple-triple (t-t) reflection. Clearly, the resolution is improved, and the background suppressed. The angle $\delta$ is given in relative units of the Darwin width $\Delta\delta$.

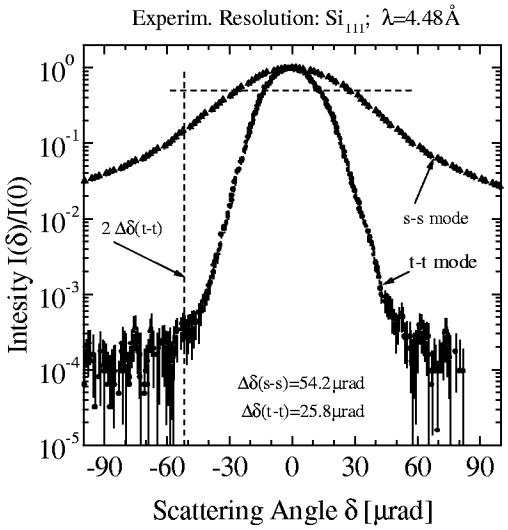



**Figure 8.12**: An experimental resolution of a double crystal diffractometer for the two modes of a single-single and triple-triple reflection. The 'channel cut' in the crystal was necessary to obtain a much more ideal result, since guided waves within the crystal are suppressed.

### 8.4. Important Elements of Small Angle Scattering

Important elements of a small angle neutron scattering diffractometer are: (i) the neutron guides transport the neutrons from the cold source to the instrument, and are used to bridge distances within the collimation; (ii) the velocity selector selects mechanically the wavelength of the neutrons (or crystals are used for the DCD); (iii) the position sensitive detector allows for the allocation of intensities to scattering angles in one snapshot.

#### 8.4.1. Neutron Guide

Neutron guides transport neutrons over long distances without large losses. As we have already seen in the discussion of intensities of focusing SANS instruments (eqs. 8.11 and 8.12) an essential parameter is the maximum divergence, which is transported by the neutron guide. It is tightly connected with the angle of total reflection, which reads:

$$\gamma_C = \lambda \, (\rho / \pi)^{0.5} \tag{8.15}$$

The coherent scattering length density is given by $\rho = b_C \cdot N$. Already natural nickel is a good choice for the coating to reach large angles of total reflection. An even better choice is the isotope nickel 58 because of the large coherent scattering length. The total angle of reflection is $\gamma_C = 6' \cdot \lambda[\text{Å}]$ and $\gamma_C = 7.1' \cdot \lambda[\text{Å}]$ for natural and pure nickel. Some 40 years ago neutron guides were invented at the research reactor in Munich. Neutron guides made neutron scattering instruments more popular since many more instruments can be placed around the reactor. The intensity is still high far away from the reactor core.

An advanced technique to transport neutrons with an even higher critical angle is connected to the super mirrors. Alternating layers of two different metals with sufficiently different scattering length densities and a continuous range of layer thicknesses leads to Bragg scattering over a larger continuous range of angles. The total angle of reflection can be increased my more than a factor of two with respect to $^{58}$Ni (this is called the m-factor). The disadvantage is a slightly reduced reflectivity close to the smallest angles, which means considerable neutron losses over longer distances (and this radiation has to be absorbed).

Another application of the super mirrors is a curved neutron guide. The curvature can be made rather large when the m-factor is large. The bender guides can have one or many channels. Super mirrors in a constant magnetic field can also serve as polarizer either in reflection or in transmission.

### 8.4.2. Velocity Selector

A rotor of a velocity selector is depicted in Fig. 8.13. In the vacuum housing the rotor can rotate with a speed of up to 30,000 rpm. The selector lets neutrons with the right speed pass through the rotating lamellae. The wavelength distribution of the monochromatized neutrons is shown in Fig. 8.14. The wavelength is inversely proportional to the rotation speed. The slower and faster neutrons are absorbed in the lamellae, which contain either lithium or boron.




**Figure 8.13**: The rotor of the velocity selector of KWS-3 built at the FZ-Jülich.

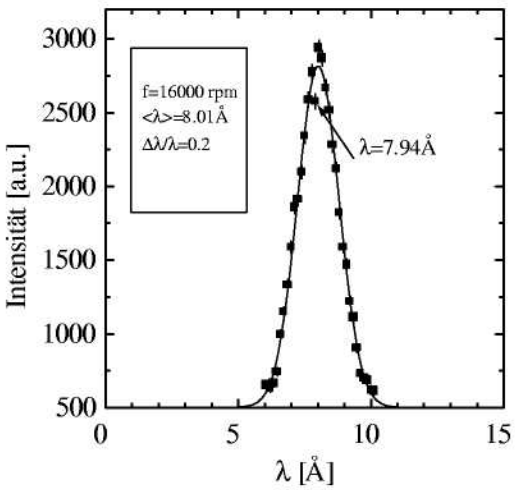



**Figure 8.14**: Time-of-flight spectrum of a velocity selector. By measuring the flight time with a triggered chopper, the velocity and the wavelength are determined. Due to the Bragg scattering of the bismuth filter the wavelength can be calibrated by the small dip at 7.94Å.

### 8.4.3. Position Sensitive Detectors

Position sensitive detectors can collect much information by one snapshot, which reduces the measurement times dramatically (compared to the DCD for instance). The spatial resolution of pin-hole SANS detector is typically 0.5 to 1cm, and the focusing (lens and mirror) SANS needs a spatial resolution of 0.5 to 1mm. The number of channels ranges from 64x64 over 128x128 to 256x256. Usually the spatial resolution is much better than required by the experimental resolution (as given by eqs. 8.6 and 8.7). There are gas- and scintillation-detectors available which all base on a nucleus reaction with the neutron.

#### 8.4.3.1. Gas Detector

$^3$He gas detectors are frequently used for neutron scattering experiments. The neutron is absorbed by the helium atom and decays according to

$$^3\mathrm{He} + \mathrm{n} \rightarrow {}^3\mathrm{H} + {}^1\mathrm{H} + 0.77\mathrm{MeV} \qquad (8.16)$$

in two ionic particles with kinetic energies of 0.573Mev and 0.191Mev for the proton and the $^3$H (tritium), respectively. As shown in Figure 8.15, this 'primary ionization' generates free electrons. The free electrons are accelerated by the electric field and produce further charges by the 'secondary ionization' process. The acceleration of the electrons dominates due to their smaller mass, and finally a full avalanche of electrons generates a measurable current at the anode for the detector electronics.

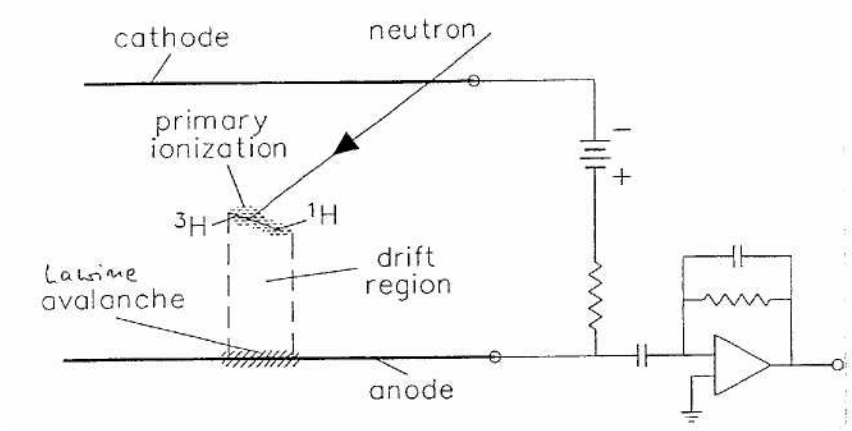



**Figure 8.15**: Circuit of the $^3$He gas detector and the movement of charges inside

In a one-dimensional position sensitive detector tube the electric pulses are measured at both ends of the tube. The ratio of these pulses is related to the exact position of the original detection. In a two-dimensional detector there are two meander-wires with perpendicular orientation. By coincidental measurements of the pulses, even the position of the detected neutron on the area can be determined.

Gas detectors have a low sensitivity to $\gamma$-radiation which is good in the presence of neighboring instruments. Not all detectors have an efficiency close to 100%. A single gas detector is slower compared to scintillation detectors, but a large number of one-dimensional parallel $^3$He tubes can process high count rates if the intensity is evenly distributed.

#### 8.4.3.2. Scintillation Detector

The scintillation detectors use a solid state material for the primary detection. The underlying radioactive reaction is:

$$^6\text{Li} + \text{n} \rightarrow {}^4\text{He} + {}^3\text{H} + 4.79\text{MeV} \qquad (8.17)$$

A lithium glass with 6.6% $^6$Li is mixed with cerium (Ce). Again, by the nuclear reaction two ionic nuclei are formed, which interact with the cerium and produce per neutron about 4000 photons of 400nm wavelength. In the disperser the photons form a light cone with an opening angle of about 90° as depicted in Fig. 8.16. The air gap between the scintillatior and the disperser (total reflection) and the thickness of the disperser are rendered in a way, that the light cone covers two photo multipliers (per dimension). The single multiplier has a diameter of 8cm, and the array of 8x8 photomultipliers covers an area of ca. 60x60 cm$^2$.

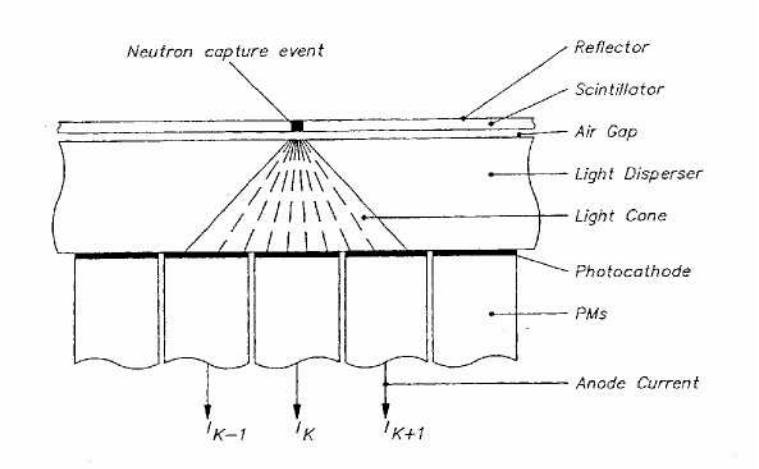



**Figure 8.16**: Geometry of a $^6$Li scintillation detector with its detection light cone

Due to a subtle computer algorithm the position of the detected neutron can be specified within 0.5cm. First, the photo multiplier with the mayor intensity determined. In a second step, by the distribution of light on the neighbored photomultipliers the position of the original process can be calculated within a precision of 0.5cm.

An important advantage of this detector is the large atomic density of the absorbing material and its consequently large detection probability. A 1mm thick scintillation material has a detection probability of 93% for 7Å neutrons. Such a detector (Anger camera) was developed at the Forschungszentrum Jülich and is used for our KWS-1 and KWS-2 small angle instruments.

**Acknowledgement:**

This lecture bases on material of D. Schwahn, who generously supported this lesson.

**References:**

Books:

[1] J.S. Higgins und H.C. Benoit, *Polymers and neutron scattering*. Clarendon Press, Oxford (1994)

[2] C.G: Windsor, *Pulsed Neutron Scattering*. Taylor & Francis, London(1981)

[3] P. Convert and J.B. Forsyth (eds.), *Position-Sensitive Detection of Thermal Neutrons*. Academic Press, London (1983)

Articles:

[4] W. Schmatz, T. Springer, T. Schelten and K. Ibel, *J. Appl. Cryst.* **7**, 96 (1974)

[5] J. Skov Pedersen, D. Posselt, K. Mortensen, *J. Appl. Cryst.* **23**, 321 (1990)

[6] D.F.R. Mildner, *J. Appl. Cryst.* **38**, 488 (2005)

[7] D. Schwahn, A. Miksovsky, H. Rauch, E. Seidl and G. Zugarek, *Nucl. Instrum. Methods* **A239**, 229 (1985)

[8] B. Alefeld, H.J. Fabian, D. Schwahn and T. Springer, *Physica* **B156&157**, 602 (1989)

[9] D.Schwahn, G.Meier and T.Springer, *J. Appl. Cryst.* **24**, 568 (1991)

[10] M. Heiderich, R. Reinartz, R. Kurz and J. Schelten, *Nucl. Instrum. Methods* **A305**, 423 (1991)

# 9

# Inelastic Crystal Spectrometers

Joachim Wuttke

# 9. Inelastic Crystal Spectrometers

Joachim Wuttke

Here and in the following chapter, we will consider *inelastic* scattering. While elastic scattering experiments yield information about *structure* or *texture* of a sample, inelastic scattering is used to investigate its *dynamics*. More specifically, one studies atomic and molecular motion, as well as magnetic and crystal field excitations.

In inelastic scattering, scattering intensity is measured as function of energy. As in other areas of physics, a data set of the form intensity-versus-energy is called a *spectrum*. An instrument that resolves inelastic scattering is therefore called a *spectrometer*.

In this chapter, we will get acquainted with two important neutron spectrometers: the triple-axis-spectrometer, and the backscattering spectrometer. Both of them use Bragg reflection from crystals for selecting (and thereby measuring) neutron energies. This method is essentially based on the neutron's wave nature. In contrast, the time-of-flight method presented in the next chapter treats the neutron as a classical particle.

## 9.1 Inelastic Scattering, Triple-Axis Spectrometer

Figure 9.1 shows the basic design of an inelastic neutron spectrometer. A *monochromator* (also called *primary spectrometer*) selects neutrons of a certain energy $E_\mathrm{i}$. The neutron flux that reaches the sample is measured by a *monitor* (a neutron counter with high transmission). In the *secondary spectrometer*, scattered neutrons are registered as function of scattering angle $2\theta$ and energy $E_\mathrm{f}$.

To see how different methods of energy selection are related to each other, we use the first de Broglie equation,

$$\mathbf{p} = \hbar\mathbf{k}\,, \tag{9.1}$$

and insert it in the kinetic energy

$$E = \frac{m}{2}v^2 = \frac{p^2}{2m} \tag{9.2}$$

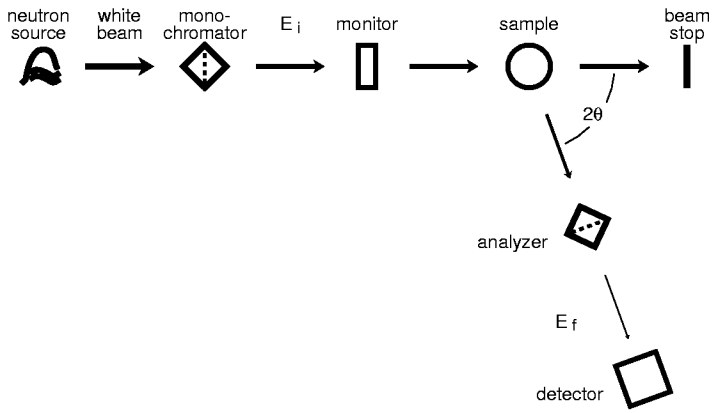



*Figure 9.1: Basic design of an inelastic neutron spectrometer.*

to obtain the *dispersion relation* of the free neutron:

$$E = \frac{\hbar^2}{2m}k^2 = \frac{\hbar^2 c^2}{2mc^2}k^2 = 2.07\text{meV}\,\text{Å}^2\,k^2 \tag{9.3}$$

(note in passing the expansion by $c^2$ which is a useful trick once one has memorised some basic constants in *atomic units*: $\hbar c = 1973\text{eVÅ}$ and $m_n c^2 = 940$ MeV). In time-of-flight methods, neutron energies are selected and measured via the velocity $v$. In crystal spectrometers, energies are selected according to the wavelength $\lambda = 2\pi/k$, using Bragg reflection from crystals:

$$n\lambda = 2d_{hkl}\sin\Theta \tag{9.4}$$

where $d_{hkl}$ is the interplanar distance of lattice planes with Miller indices $h$, $k$, $l$, and $\Theta$ is the glancing angle of reflection from these planes. The integer $n$ indicates that along with a fundamental wavelength $\lambda_1$, integer fractions $\lambda_n = \lambda_1/n$ are transmitted as well. To suppress these unwanted higher orders, experimental setups include either a mechanical neutron velocity selector, or a beryllium filter. Table 9.1 lists some frequently used monochromator materials. Figure 9.2 shows a monochromator used at FRM-II.

The triple-axis-spectrometer (TAS) owes its name to its main degrees of freedom. Neutron paths are always horizontal; the three axes are vertical. Figures 9.3 and 9.4 show two typical instruments. The first axis goes through the monochromator crystal. Incident

| material | structure | $[hkl]$ | $d_{hkl}$ | used e. g. at |
|---|---|---|---|---|
| Si | diamond | 111 | 3.14 Å | backscattering: SPHERES |
| C | graphite | 002 | | thermal TAS: PUMA |
| Cu | | 002 | | thermal TAS: PUMA |

*Table 9.1: Frequently used monochromator materials.*



*Figure 9.2: Pyrolythic graphite PG(002) monochromator of PUMA, the Göttingen-München thermal triple-axis-spectrometer at FRM-II.*

energies are selected by orienting the monochromator towards the appropriate Bragg angle $\Theta_i$. Simultaneously, the entire downstream instrument is moved on air cushions so that the incident beam is deflected by the appropriate angle $2\Theta_i$. The second axis goes through the sample. The downstream part of the instrument is positioned so that scattering is observed under the chosen scattering angle $2\theta$. The sample orientation needs also to be controlled. The third axis goes through the analyzer crystal. The crystal is oriented at angle $\Theta_f$, according to the chosen final energy. The neutron detector is positioned at angle $2\Theta_f$. Obviously, routine measurements require computer control to coordinate the movements of crystals and axes.

For a quantitative description of inelastic scattering, some formalism must be agreed upon. The second de Broglie equation relates the kinetic energy to a frequency or angular

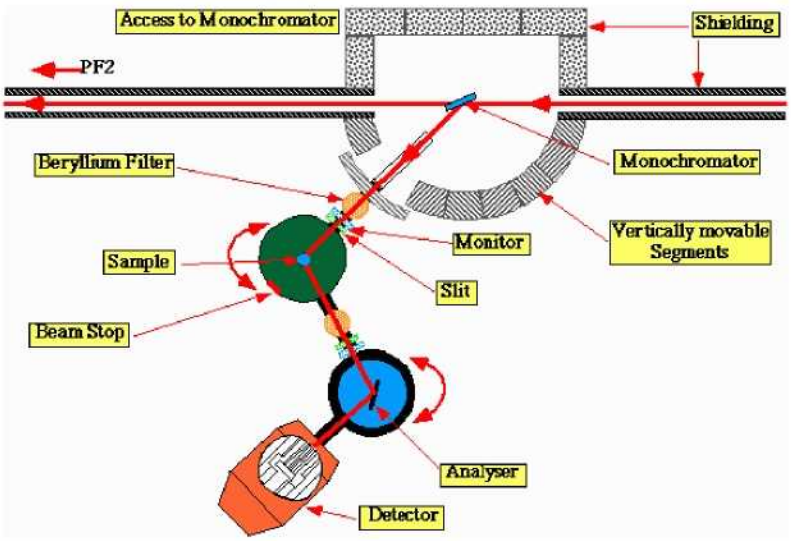



*Figure 9.3: Layout of the triple-axis spectrometer IN12. The instrument is located on a cold neutron guide at the ILL; it is jointly operated by JCNS and by the French CEA.*

frequency: $E = 2\pi\hbar\nu = \hbar\omega$. However, it is convention in neutron scattering to reserve the expression $\hbar\omega$ for the *energy loss* of the neutron in the scattering process,

$$\hbar\omega = E_\mathrm{i} - E_\mathrm{f}\,. \tag{9.5}$$

Theoretical formulæ, for instance the relation between double differential cross section and scattering law,

$$\frac{\partial^2\sigma}{\partial\Omega\partial\omega} = \frac{\sigma}{4\pi}\frac{k_\mathrm{f}}{k_\mathrm{i}}S(\mathbf{Q},\omega)\,, \tag{9.6}$$

are almost always written in terms of $\omega$. However, actual numeric values are rarely given in $\mathrm{s}^{-1}$; most often, energy transfers are expressed in meV or THz. It is not unusual that an axis is labelled $\omega$, though values are reported in energy or frequency units.[1]

[1]Even worse things happen in biophysics where energy transfers are sometimes expressed as *wave numbers*. This comes from *light scattering* where the dispersion relation, in contrast to (9.3), is linear so that energy differences are proportional to wave number differences. In order to be understood by biologists for whom inelastic neutron scattering is quite exotic, a neutron scattering event is described by the wave number change a photon would experience if it underwent the same energy change as the neutron.

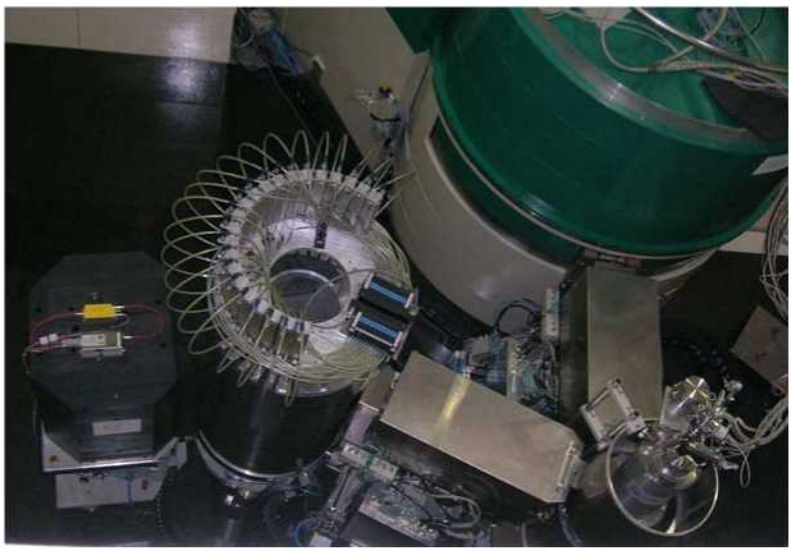


*Figure 9.4: View from the gallery onto the triple-axis spectrometer TRISP, located in the FRM-II reactor building, build and operated by the Max-Planck-Gesellschaft. The beam path before and after the sample is protected by a mu-metal housing because the instrument has a spin-echo option that greatly enhances its energy resolution.*

The letter $\mathbf{Q}$ is commonly used to designate the wave number change of the scattered neutron,

$$\mathbf{Q} = \mathbf{k}_\mathrm{i} - \mathbf{k}_\mathrm{f} \,. \tag{9.7}$$

Correspondingly, $\hbar\mathbf{Q}$ is the momentum transfer in the scattering event.

From conservation laws it is clear that an energy or momentum loss of the scattered neutron is accompanied by an opposite gain of the sample. In the literature as well as in the practice at neutron scattering institutes, there is no general agreement over the *sign* of the energy and momentum transfer. The conventions (9.5), (9.7) are, however, highly recommendable because they emphasize the physics of the sample over the physics of the spectrometer: *positive* values of $\omega$ and $Q$ mean that the *sample* has *gained* energy and momentum.

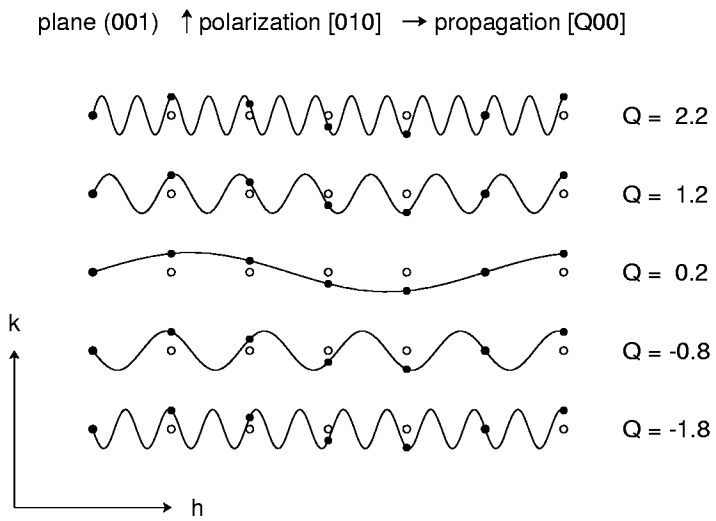



*Figure 9.5: A square lattice, representing the (001) plane of a cubic lattice. Open circles: equilibrium positions of the atoms. Solid circles: momentary positions when atoms take part in a transverse lattice oscillation. The lines show that the same oscillation can be described by different sine functions. Their wave numbers $Q$ agree up to an arbitrary integer. More generally, the propagation vector $\mathbf{Q}$ can be written as $\mathbf{G}+\mathbf{q}$ where $\mathbf{G}$ is a reciprocal lattice vector, and $\mathbf{q}$ is located in the first Brillouin zone. In this example $q = [0.2, 0, 0]$.*

## 9.2 Phonon Scattering

Let us start with a mechanical picture of neutron scattering. Suppose neutrons are scattered by particles of mass $M$. These particles are allowed to have arbitrary thermal velocity distributions. Since the sample as a whole is at rest, we just require $\langle v \rangle = 0$. In a scattering event, a sample particle takes up a momentum $\mathbf{P} = \hbar\mathbf{Q}$. A short calculation shows that this momentum transfer is accompanied on average by an energy transfer of $P^2/(2M)$. This, however, is not compatible with the existence and dominance of *elastic* neutron scattering which by definition has *zero* energy transfer.

The only escape is to let $M$ become macroscopically large. In this limit, the recoil of the scattered neutron is taken up not by individual scattering centers, but by the entire sample. This leads to a new reading of the Bragg condition for elastic scattering: a crystal lattice can take up a momentum $\hbar\mathbf{Q}$ iff $\mathbf{Q}$ coincides with a reciprocal lattice vector $\mathbf{G}_{hkl}$.

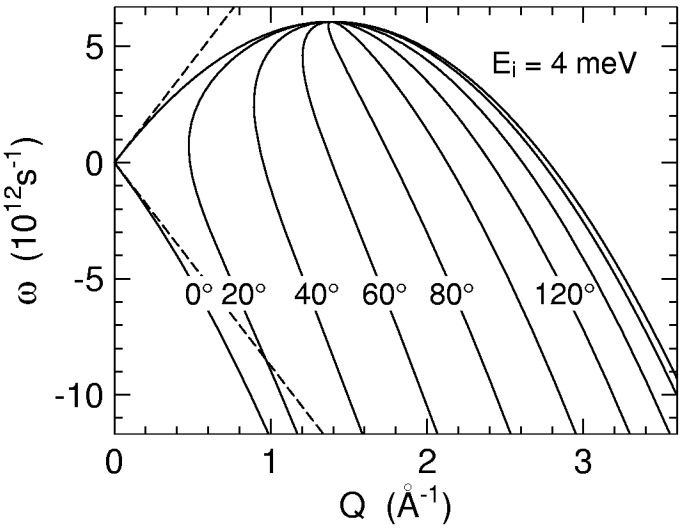



*Figure 9.6: $\omega$–$Q$–range accessible for inelastic scattering for a given incident neutron energy of 4 meV. Solid lines correspond to fixed scattering angles $2\theta$ from 0° to 180°. The initial slope of the 0° lines, indicated by the dashed lines, is given by the incident neutron velocity $v_\mathrm{i}$, in this example 875 m/s.*

Inelastic scattering happens if some excess momentum $\hbar\mathbf{q}$ with $\mathbf{q} = \mathbf{G}_{hkl} - \mathbf{Q}$ is taken up by emitting or absorbing a phonon with wave vector $\mathbf{q}$. This exchange of momentum is accompanied by an exchange of energy $\hbar\omega_\mathbf{q}$ where $\omega_\mathbf{q}$ is the phonon's angular frequency, as given by its dispersion relation.

An alternative explanation of inelastic scattering is the Doppler shift a wave experiences when reflected by a moving wall. In order to apply this picture to neutron scattering by phonons, the moving wall must be replaced by a stack of oscillating lattice planes. Significant scattering intensity is observed iff the spatial periodicity of the excursions agrees with the scattering vector $\mathbf{Q}$. The real-space representation of a phonon in Figure 9.5 shows that this periodicity is only determined up to a shift by $\mathbf{G}_{hkl}$; again, it is found that the condition for inelastic scattering depends only on the excess wave number $\mathbf{q} = \mathbf{G}_{hkl} - \mathbf{Q}$ which may always be chosen within the first Brillouin zone.

Equivalently, we may say that phonon dispersions are invariant under translation by reciprocal lattice vectors, $\omega_\mathbf{q} = \omega_{\mathbf{q}+\mathbf{G}}$. This allows us to choose freely the Brillouin zone

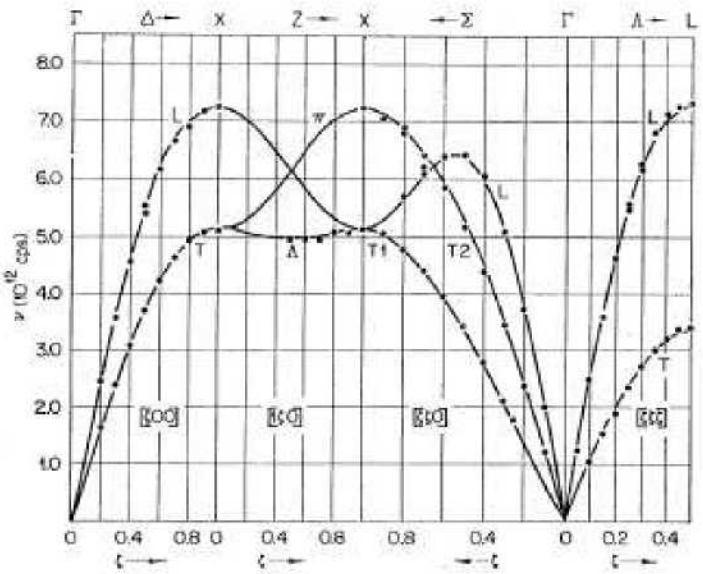



*Figure 9.7: Phonon dispersion curves for copper at 49 K in the main symmetry directions. Lines are fits with a force model that takes into account up to sixth nearest neighbours [1]. As usual, wave numbers are expressed in relative units. Copper crystallises in a fcc lattice with $a = 3.61$ Å. The vertical axis shows frequency, not angular frequency.*

in wich phonons can be measured best. This is hardly ever the first Brillouin zone. To understand why, consider Figure 9.6. The lines show which combinations of $Q$ and $\omega$ can be accessed by inelastic neutron scattering. Different lines correspond to different scattering angles. In practice, scattering angles near 0° are contaminated by the unscattered part of the incident beam; in general, they are blocked by a beamstop. For obvious geometrical reasons, scattering angles close to 180° are also inaccessible. Therefore, on any real spectrometer the accessible $Q$ $\omega$ range is even more restricted than the figure shows.

Figure 9.6 has been produced for one particular incident energy $E_\mathrm{i}$. The lines, however, are scale invariant. Changing $E_\mathrm{i}$ changes the numbers on the two axes, but not the shape of the lines. Unless we go to very high neutron energies, high frequencies at low wave numbers remain inaccessible. Unfortunately, this is just the region we would need for scattering from first Brillouin zone phonons. To see this, compare Figure 9.6 *quantitatively*

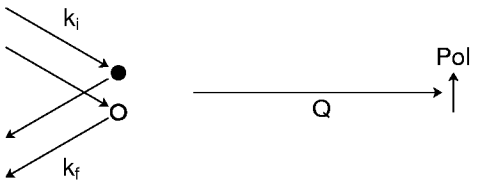



*Figure 9.8: Atomic displacement perpendicular to* $\mathbf{Q}$ *does not change the path length of scattered neutrons. Therefore, it does not change the interference pattern of the scattered neutron waves. In consequence, phonons with transverse polarisation cannot be observed in the first Brillouin zone.*

with a typical phonon dispersion curve, as shown in Figure 9.7. The initial slope of the acustic phonons is the macroscopic *sound velocity*. Compare this with the initial slope of the 0°-curve in Fig. 9.6 which is given by the incident neutron velocity: in order to measure phonons in the first Brillouin zone, neutrons must be considerably faster than the sound in the sample. This requires very high incident energies. Choosing such energies would deteriorate the energy resolution to inacceptable widths.[2]

Figure 9.8 explains a second reason why we must move freely through different Brillouin zones in order to measure full phonon dispersions: phonons are not observable if their polarisation vector is perpendicular to the scattering vector $\mathbf{Q}$. This is in particular the case for transverse phonons in the first Brillouin zone. More generally, the scattering intensity is proportional to the scalar product of $\mathbf{Q}$ and the phonon's polarisation vector. Therefore, in order to measure a specific phonon branch, one chooses the Brillouin zone so that $\mathbf{Q}$ is about perpendicular to the polarisation. This is explained by some examples in Figure 9.9

In order to measure one particular phonon dispersion branch, one chooses a sequence of $\mathbf{Q}$ vectors, ranging from the center to the surface of a Brillouin zone. For each $\mathbf{Q}$, one measures scattering intensity as function of $\omega$ (constant $\mathbf{Q}$ scan). Figure 9.10 shows results of such scans. The scattering intensity is peaked where $\omega$ agrees with a phonon frequency

[2]When studying sound in disordered materials one has actually no choice but to measure in the first Brillouin zone — there are no other zones. Such experiments cannot be done on triple-axis spectrometers; they require a very sophisticated small-angle, high-$E_i$, high-resolution setup at a time-of-flight spectrometer.

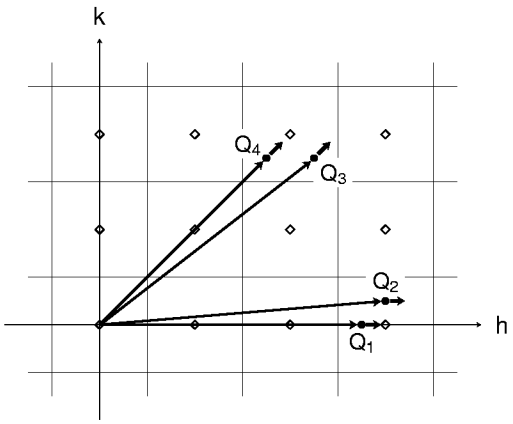



*Figure 9.9: A 001 plane in the reciprocal space of a cubic lattice. Examples show how* $\mathbf{Q}$ *is chosen in order to measure specific phonon spectra:* $\mathbf{Q}_1$ *is used to measure a longitudinal phonon with propagation vector* $[-\frac{1}{2},0,0]$*,* $L_{-\frac{1}{2},0,0}$ *for short.* $\mathbf{Q}_2$ *sees a transverse phonon with propagation vector* $[0,\frac{1}{2},0]$ *and polarisation* $[100]$*, abbreviated* $T[100]_{0,\frac{1}{2},0}$*.* $\mathbf{Q}_3$ *and* $\mathbf{Q}_4$ *are used to measure* $T[110]_{-\frac{1}{2},\frac{1}{2},0}$ *and* $L_{-\frac{1}{2},-\frac{1}{2},0}$*, respectively.*

$\omega_{\mathbf{q}}$. The peaks have finite widths because of (1) the finite lifetime of the phonon, and (2) the finite resolution of the spectrometer.

## 9.3 Resolution of Crystal Spectrometers

So far, we have considered *ideal* monochromators which select exactly one well defined wave vector $\mathbf{k}_\mathrm{i}$ out of the incident spectrum, and transform it into an equally well defined $\mathbf{k}_\mathrm{f}$. A spectrometer based on such monochromators would have perfect resolution, but zero count rates. We better accept finite wave vector distributions.

The resolution of a crystal spectrometer may be limited by any of the following causes: (1) absorption in the monochromator crystal, (2) imperfections of the monochromator crystal, (3) especially *mosaicity* (non-parallelity) of the Bragg planes, (4) finite apertures for incoming and outgoing beam.

Cause (1) is physically unavoidable. Its effect can be described by a finite width $\delta\mathbf{G}$ of the Bragg vector $\mathbf{G}_{hkl}$. Cause (4) is also unavoidable if nonzero intensities shall be obtained.

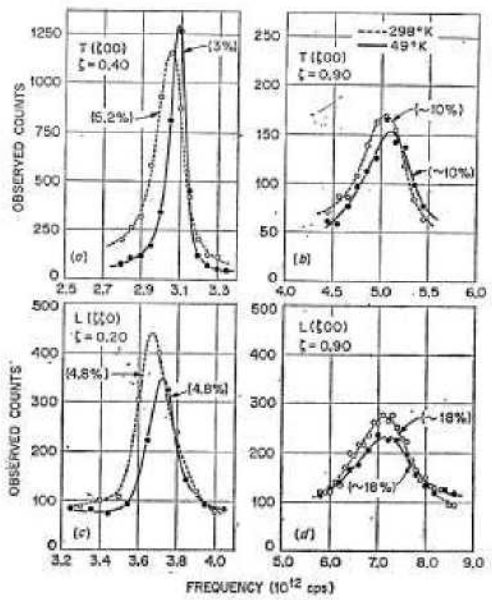



*Figure 9.10: Some of the constant-**Q**-scans that led to the dispersion curve shown in Fig. 9.7. Open circles have been measured at 298 K, filled circles at 49 K. Percentages in parentheses indicate relative line widths. Line widths are in part due to finite instrumental resolution [1].*

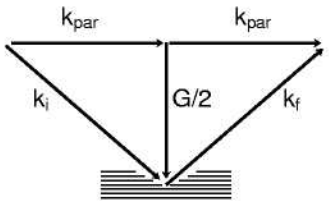



*Figure 9.11: Bragg scattering by a perfect crystal: the vector components of $\mathbf{k}_\mathrm{i}$ and $-\mathbf{k}_\mathrm{f}$ that are perpendicular to a lattice plane $[hkl]$ must equal half a reciprocal lattice vetor $\mathbf{G}_{hkl}$; the parallel components of $\mathbf{k}_\mathrm{i}$ and $\mathbf{k}_\mathrm{f}$ must be equal.*

The combined impact of (1) and (4) on the wave number $k = k_\mathrm{i} = k_\mathrm{f}$ can be estimated by differentiating the Bragg equation. A particularly simple starting point is the form

$$k = \frac{G}{2\sin\Theta} \tag{9.8}$$

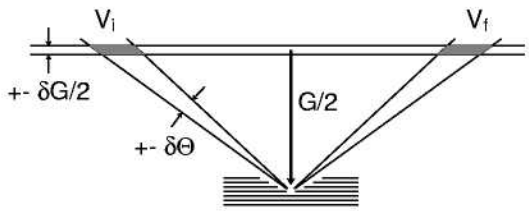



*Figure 9.12: In a real monochromator, incident neutrons are accepted from a finite angular range $\pm\delta\Theta$. Neutron absorption and certain crystal imperfections lead to a finite width $\delta G$ of the reciprocal lattice vector. As a result, Bragg scattering is possible for neutrons from a finite phase-space volume $V_\mathrm{i}$. This volume is symmetrically mapped onto an outgoing phase-space volume $V_\mathrm{f}$.*

which leads to

$$\frac{\delta k}{k} = \frac{\delta G}{G} + \cot\Theta\,\delta\Theta\,. \tag{9.9}$$

Usually, the first summand can be neglected against the second. Except for extreme angles, the resolution is then essentially given by the aperture $\delta\Theta$.

To visualise these and other resolution effects, Figure 9.11 gives a geometric interpretation of the Bragg equation (9.8). Figure 9.12 shows that a Bragg reflection in the presence of (1) and (4) maps a $\mathbf{k}_\mathrm{i}$-volume to a $\mathbf{k}_\mathrm{f}$-volume without changing its shape.

This symmetry can be broken by using mosaic crystals. Figure 9.13 explains how such crystals act as *phase-space transformers*. For a given incident aperture they accept a relatively wide range of incident wavelengths. In the outgoing beam this phase-space volume is transformed to one with wider angular spread, but narrower wavenumber distribution. This transform »from white to wide« is employed in many spectrometers to improve the resolution-intensity balance.

Of course wave vector distributions are not produced by rectangular cut-off functions. Insofar the shaded areas in Figs. 9.12–9.13 are inappropriate representations; actually the intensity fall off smoothly at the edges of these areas. This is even more the case when the $\mathbf{k}_\mathrm{f}$ distribution of the monochromator and the $\mathbf{k}_\mathrm{i}$ distribution of the analyser are convoluted to yield the distribution that describes how accurately the wave vector $\mathbf{Q}$ of the scattering event in the sample is resolved by the instrument. Consequently,

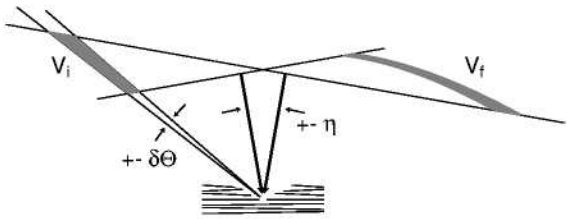



*Figure 9.13: A crystal with mosaic spread $\eta$ turns a »white« incoming phase-space volume $V_i$ into a volume $V_f$ with a comparatively »wide« angular distribution, and a comparatively narrow wavelength distribution.*

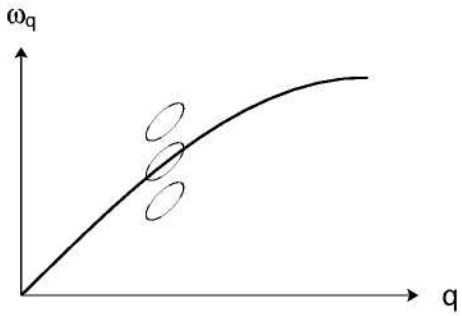



*Figure 9.14: Constant* **Q** *scan with resolution ellipsoids optimally oriented with respect to an acoustic phonon branch.*

this distribution is well approximated as an ellipsoid. Depending on the setup of the entire triple-axis spectrometer, different orientations of this ellipsoid can be achieved. Furthermore, Bragg zones and **q** vectors can be chosen so that the long axis of the ellipsoid is approximately parallel to the dispersion curve (Figure 9.14).

## 9.4 Backscattering

In backscattering ($2\Theta \simeq 180°$), the $\cot\Theta$ in (9.9) goes to zero. In this case, the wavelength spread of the Bragg reflected beam depends mainly on $\delta G/G$, besides a $(\delta\Theta)^2$ term. In a backscattering spectrometer, both monochromator and analyser are operated under backscattering conditions. Relative energy resolutions between $10^{-3}$ and $10^{-4}$ are routinely obtained. The Jülich backscattering spectrometer SPHERES uses 2.08 meV neutrons from the Si(111) reflection, and achieves a resolution (full width at half maxi-

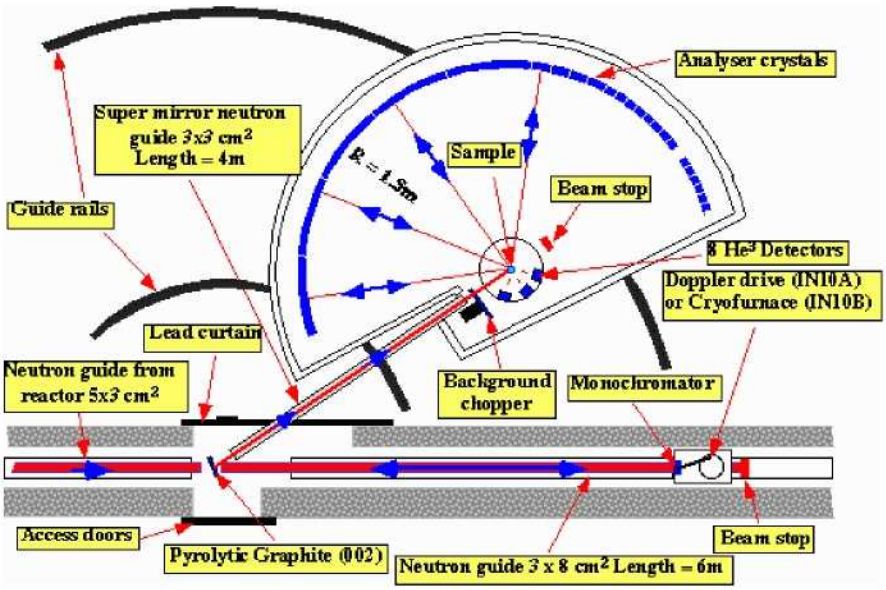



*Figure 9.15: Layout of the backscattering spectrometer IN10 at the ILL.*

mum) of 0.65 $\mu$eV. With such a resolution one can study processes that are considerably slower than phonons: side group rotations, including tunneling phenomena at low temperatures; jump diffusion; relaxation in viscous liquids; chain motion in polymers; dynamics of membranes and proteins.

While the basic operation principle is the same as for a triple-axis spectrometer, the design of a backscattering spectrometer is quite different. Figure 9.15 shows the classical layout of a first-generation instrument. Besides the three axis (monochromator, sample, analyser) there are two more elements in the beam path. They are required to cope with the very special $2\Theta = 180°$ geometry. Obviously, the sample cannot be placed in the incoming beam. Therefore, (1) a *deflector* is needed to redirect the backscattered beam into the secondary spectrometer which is placed in a separate housing outside the primary beam casemate.

Furthermore, neutrons that are backscattered from an analyser have to traverse the sample a second time before they reach the detector. This geometry exposes the detector to neutrons that are scattered directly from the sample into the detector, without being energy analysed. These uninformative neutrons have to been discounted. Therefore, every

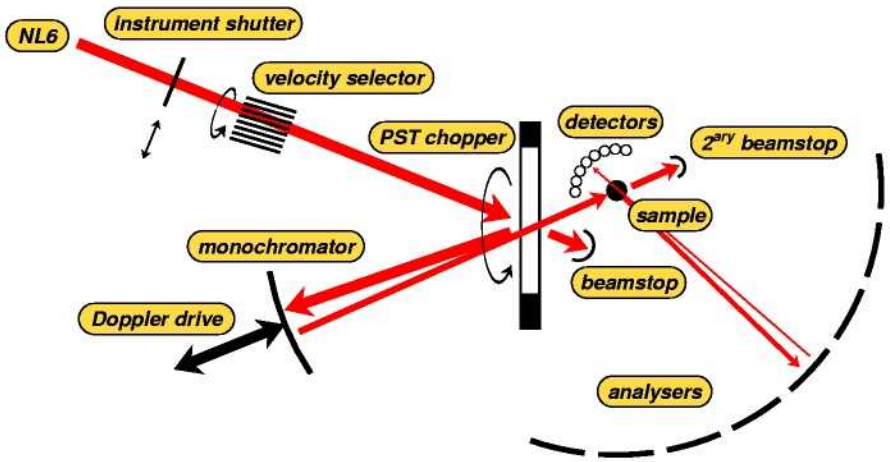



*Figure 9.16: Layout of the Jülich backscattering spectrometer SPHERES at FRM-II. The central component is the phase-space transforming chopper. Half of its circumference is covered with deflecting graphite crystals.*

backscattering instrument needs (2) a *chopper* to pulse the incoming beam. Analysed and unanalysed neutrons are then distinguished by their different time of flight.

A third fundamental difference between triple-axis and backscattering spectroscopy concerns the way energies are scanned. In triple-axis spectroscopy this is done by varying Bragg reflection angles in monochromator or/and analyser. In backscattering, this is no option, as even a few degrees deviation from $2\Theta = 180°$ would ruin the energy resolution. Instead, two other methods are used to vary $\hbar\omega = E_\mathrm{i} - E_\mathrm{f}$: (a) Varying the lattice constant of the monochromator by cooling/heating. Used on two instruments at the ILL: IN13, and as an option at IN10. (b) Doppler shift of $E_\mathrm{i}$ by periodic motion of the monochromator. Used on all other backscattering spectrometers.

Fourthly, keeping the Bragg angles fixed facilitates simultaneous measurements at different scattering angles: backscattering spectrometers are always built as multi-detector instruments.

However, using several detectors is only a weak antidote against the notoriously low count rates of backscattering instruments. At the first-generation instruments BSS (Jülich) and IN10 (ILL), the neutron flux at the sample was/is only (1 to 2)$\cdot 10^4$ n/cm$^2$/s. In the

second-generation instrument IN16 (ILL), the intensity was increased by focussing optics, taking advantage of phase-space transformation by a deflector with high mosaicity. In the third-generation instruments HFBS (NIST, USA) and SPHERES (Jülich at FRM-II), the intensity is further increased by integrating deflector and chopper into *one* component, the *phase-space transform chopper* (Figure 9.16). This chopper carries mosaic crystals on half of its circumference. Thereby, it both pulses the primary beam and deflects it towards the monochromator. The fast motion of the deflector crystals (ideally 300 m/s) improves the efficiency of the phase-space transform.

# References

[1] R. M. Nicklow, G. Gilat, H. G. Smith, L. J. Raubenheimer, and M. K. Wilkinson: Phonon Frequencies in Copper at 49 and 298°K. Phys. Rev. 164, 922–928 (1967).

## Exercises and Problems

1. Express an energy transfer of 1 meV in THz and in $\mathrm{cm}^{-1}$ (light scattering wave number).

2. In triple-axis-spectrometers, polycrystalline beryllium, cooled to the temperature of liquid nitrogen, is placed before sample and monitor to suppress higher order Bragg reflections from the monochromator. How does that work? Name at least two properties that make beryllium the optimum material for this purpose.

3. Which degrees of freedom are varied in a constant-**Q**-scan?

4. Explain how a Z-shaped double monochromator facilitates scans with variable $\mathbf{k}_\mathrm{i}$.

5. Derive without explicit calculation of $Q(\omega)$ how the axis in Fig. 9.6 must be rescaled so that the lines remain unchanged when the incident neutron energy is changed.

6. Use the law of cosines

$$Q^2 = k_\mathrm{i}^2 + k_\mathrm{f}^2 - 2k_\mathrm{i}k_\mathrm{f}\cos 2\theta \tag{9.10}$$

to find an analytic expression for $Q$ as function of $\omega$, $E_\mathrm{i}$, and $2\theta$. Verify that the slopes $\mathrm{d}\omega/\mathrm{d}Q$ at $2\theta = 0$ and $\omega \to 0$, as shown by the dashed lines in Fig. 9.6, are indeed equal to $\pm v_\mathrm{i}$.

7. Why does the resolution deteriorate if high incident energies are chosen? Does this hold for any type of spectrometer?

8. Determine the speed of sound in copper from Fig. 9.7, and check against a handbook value.

9. Name the two main reasons why phonons have finite lifetimes.

10. Reconsider the derivation of the Bragg equation for a crystal with finite penetration depth. Assume that every lattice plane absorbs a given fraction of a traversing neutron beam.

11. The phase-space transform »from white to wide« is quite useful. Yet it is a compromise. A transform »from white and wide to monochromatic and narrow« would be much more useful. Any idea, how such a transform could be achieved, or why it has proved so difficult?

# 10

# Time-of-flight spectrometers including NSE

Michael Monkenbusch

# 10. Time-of-flight spectrometers including NSE

Michael Monkenbusch

## 10.1 Introduction

The information that may be extracted from a neutron scattering experiment can be expressed in terms of the *scattering function* $S(\underline{Q},\omega)$. All properties accessible by these kinds of scattering experiments are contained in $S(\underline{Q},\omega)$. The resulting intensity represents the double differential cross section:

$$\frac{d^2\sigma}{d\Omega dE'} = N\,\frac{k'}{k}b^2 S(\underline{Q},\omega) \tag{10.1}$$

where $k'$, $k$ is the modulus of wavevectors the scattered and incoming neutrons respectively. $N$ denotes the number of atoms in the sample and $b$ is the *scattering length.* [1]. The energy transfer during scattering is $\hbar\omega = (E - E')$, thereby $E$ , $E'$ denotes the energies of the incoming and scattered neutrons respectively. The variables of the scattering function depend on $\underline{k}$, $\underline{k}'$; $\underline{Q} = \underline{k} - \underline{k}'$ is the momentum transfer and

$$\hbar\omega = (\hbar^2/2m_n)(k^2 - k'^2) \tag{10.2}$$

the energy transfer that occured during the scattering process. Since the modulus of the wavevector $\underline{k}$ of the neutron is related as well to the neutron velocity, $\underline{v}$ (momentum) as to the wavelength (1/wavenumber):

$$\underline{v}m_n = \hbar\underline{k} \tag{10.3}$$

$$\frac{2\pi}{\lambda} = k \tag{10.4}$$

it is possible to determine the energy transfer (10.2) as well –by employing the wave proerties of the neutron– by analysis of the wavelength $\lambda'$ as –by using the particle character– by measurement of the velocity $v'$ of the scattered neutrons. The first method is applied in crystal-spectrometers like the classical **triple-axis-spectrometer** or the **backscattering-($\pi$)-spectrometer**. The second method leads to the spectrometer types that are the topic of this chapter, namely different variants of **time-of-flight (TOF)-spectrometers**. Also the **neutron spin-echo spectrometer, NSE** employs –somewhat

[1] For compounds containing different types of atoms (elements or isotopes) the corresponding expression consists of the sum of partial structure factors multiplied by the corresponding scattering lengths $b_i b_j$ in bilinear combination. For the discussion of instruments the simple version is sufficient.

less obvious– the velocity **change** of the neutrons to infer the energy transfer. The generic geometry of a scattering experiment in reciprocal (i.e. velocity, momentum or wavevector) space is illustrated in Fig. 10.1. The scattering triangle consisting of the incoming

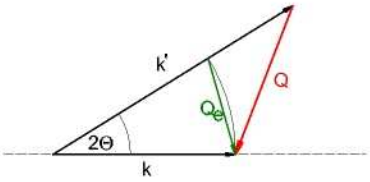



Figure 10.1: Scattering triangle.

wavevector $\underline{k}$, the wavevector of the scattered neutrons $\underline{k'}$ and the resulting momentum transfer ($\div\hbar$), $\underline{Q}$, the figure shows the general situation of inelastic scattering (here: energy gain of the neutron). $2\Theta$ is the scattering angle, $\underline{Q}_e$ indicates the momentum transfer for elastic scattering (i.e. **without** energy transfer).

A nuclear research reactor as neutron source basically yields a thermal (Maxwellian) spectrum of neutron velocities, the temperature of the moderator ($D_2O$-cooling water apporx. $60^0C$) determines the temperature of the neutron cloud. Many facilities contain additional small moderators of different temperature that supply single beam tubes with neutrons of a different spectral distribution (different temperature). In particular the so called "cold sources" have to be mentioned, which typically consist of a volume filled with liquid liquid $H_2$ or $D_2$ corresponding to a temperature of 20 K. On the other hand some ractors are also equipped with a "hot source", e.g. an vacuum isolated block of graphite that is heated by the nuclear radiation inside the moderator tank. The following table enables a quick survey over the average values of the corresponding neutron spectra.

| $T_{\text{Moderator}}/K$ | $\sqrt{v^2}$/m/s | $\lambda$/nm | $\hbar\omega$/eV | $\nu = \omega/2\pi/\text{s}^{-1}$ |
|---|---|---|---|---|
| 2000 | 7060 | 0.056 | $170 \times 10^{-3}$ | $42 \times 10^{12}$ |
| 330 | 2870 | 0.14 | $28 \times 10^{-3}$ | $6.87 \times 10^{12}$ |
| 20 | 706 | 0.56 | $1.7 \times 10^{-3}$ | $0.42 \times 10^{12}$ |

For specific experiments of course also neutrons of deviating velocities within a band around the average are employed. However, with increasing deviation from the optimum wavelength the flux drops strongly. Typical neutron velocities are in the order of 1000 m/s the corresponding time-of-flight per meter is 1 ms/m, i.e. such neutrons need a couple of milliseconds for their journey through a spectrometer.

The energy resolution –respectively resolution in $\omega$– of time-of-flight (TOF) instruments depends strongly on the used wavelength ($\Delta\omega \propto 1/\lambda^3$). But also the different techniques used to detect differences in neutron energy determine the available resolution. TOF instruments perform the energy transfer measurement by neutron velocity measurements.

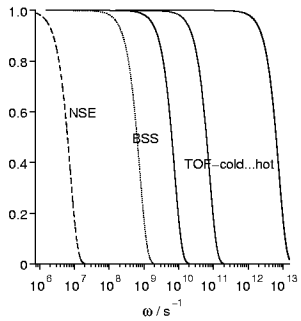



Figure 10.2: Range of resolution widths.

The range spanned by combining different wavelengths and experimental methods spans about $7 \cdots 8$ decades in energy resolution, as illustrated in figure 10.2.

## 10.2 The classic time-of-flight spectrometer

Basically there are two types of classic time-of-flight (TOF) spectrometer types, which use at least TOF-techniques either to analyze the velocity distribution after the sacttering process or tag the incoming velocity by the time.

### 10.2.1 Normal Geometry TOF-spectrometer

Figure 10.3 illustrates the generic setup of a classical time-of-flight (TOF) instrument.

From the thermal spectrum of the neutron beam entering from the left a monochromator (of any type) filters a limited wavelength band $\lambda \pm \Delta\lambda$, thereby typically a bandwidth of $\Delta\lambda/\lambda \approx 10^{-2}$ is achieved. The thus monochromatized beam enters a so-called chopper which opens the beam path periodically for a short moment. Typical frequencies are between 20 and 400 Hz, the ratio of time-open:time-closed is around 1:100. The resulting pulse widths are of the order of several (tens) of microseconds. After an – as short as – possible flight path the neutron bunches hit the sample and are scattered according to the double differential cross section of the sample material, thereby some neutrons exchange kinetic energy with excitations in the sample, i.e. change their velocities. After scattering into different directions the neutrons transverse the flight space between sample and the detectors. The path length between sample and detector is usually kept the same for all detectors placed at the periphery of the flight space. The detectors most often consists of $^3$He ($\simeq$10 bar) filled counting tubes of $30 \cdots 40$ cm length. Up to 1000 (and more) tubes are used in some installations to cover as much solid angle as possible.

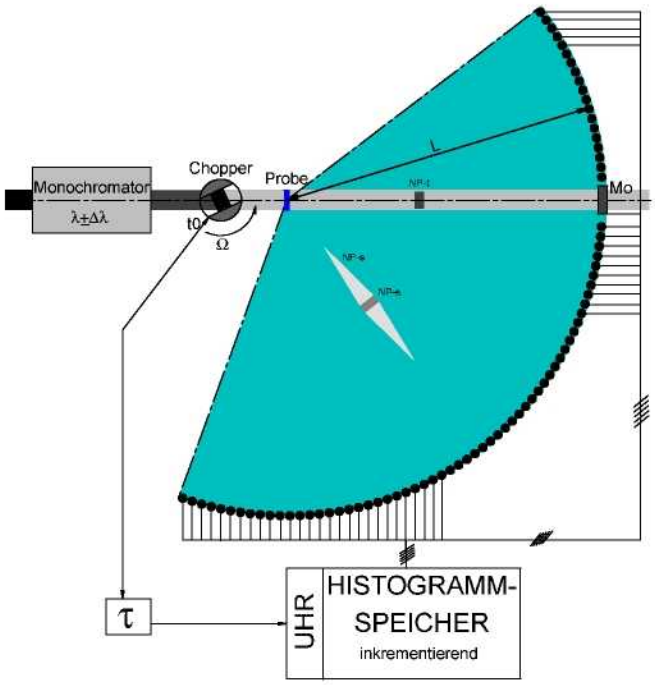



Figure 10.3: Generic setup of a classical TOF instrument.

The elastically scattered neutrons (like those from the direct beam) reach the detectors after the time $t_{CP} + t_0 = d_{\text{chopper-sample}}/v_0 + L/v_0$, those scattered inelastically arrive earlier (energy gain of the neutron) or later (energy loss of the neutron). Each pulse from a counting tube causes via the associated electronics an increment of one cell in the histogrammic memory. The address of this cell is derived from the time difference between chopper opening and arrival time of the neutron (pulse), i.e. TOF, and the detector number ($\rightarrow$ scattering angle). Thus the distribution of flight times evolves as a histogram of $512 \cdots 2048$ channels with a width of around $10\mu$s each. For each detector (resp. group of detectors) such an histogramm vs. time is obtained. A monitor (Mo) in the direct beam serves to normalize the histograms to the incoming neutron flux. [2]

The neutron path-time diagram that corresponds to the scattering situation in this type of TOF instruments is show in figure 10.4.

[2] A "monitor" is a detection device (counting "tube") that covers the beam cross section and has a high transmission for neutrons ($> 90\%$) and low detection probability ($10^{-3} \cdots 10^{-7}$). In the figure only one monitor behind the sample is shown for clarity. Generally another monitor (more important) is located between chopper and sample, it measures the incoming flux without the influence of the sample transmission.

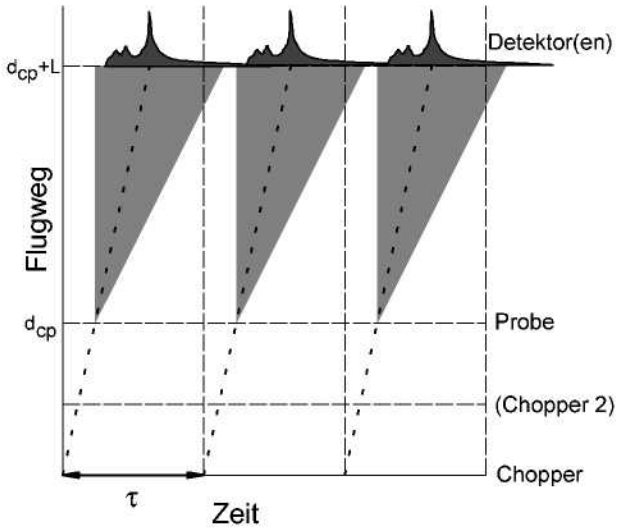



Figure 10.4: Path-time diagram of neutrons in a normal geometry TOF instrument..

### 10.2.2 Inverted Geometry TOF-spectrometer

In the spectrometer type described above the sample was "illuminated" by pulses of neutrons with a single defined wavelength (velocity) which have been prepared by a chopper-monochromator combination. The analysis of the velocities of the scattered neutrons was effected by TOF-measurement.

It is also possible to **invert** this sequence, the incoming velocity (i.e. wavelength, energy, $k$) is determined by the TOF between chopper (pulsed source) and sample. Then –to obtain a defined energy and momentum transfer– only scattered neutrons of a given final wavelength that may pass an analyzer are detected. Neutrons emerging the pulsed source fly according to their individual velocity in direction of the sample, the associated pathes are indicated by the grey triangle. The intensity within the range of this triangle is of course not uniform but depends on the spectral properties of the source. [3] Neutrons that have been elastically scattered by the sample (path 2) pass the analyzer/filter M/F and lead to the elastic line in the TOF-histogram. Neutrons that loose energy (path 1) are faster before the sample scattering and arrive earlier at the detector than the elastically scattered ones. Analogously path 3 represents neutrons that gained energy during scattering. Compared to a "normal" TOF instrument the energy gain and energy loss sides of the histogram are reversed. Therefore also high energy excitations that are thermally not occupied may be measured. Figure 10.5 shows a corresponding setup.

The pulse at the chopper contains neutrons from a broad velocity distribution (Maxwellian

[3] In particular overlap of the triangles ("frame overlap") may happen, which may be suppressed by filters tayloring the incoming spectrum.

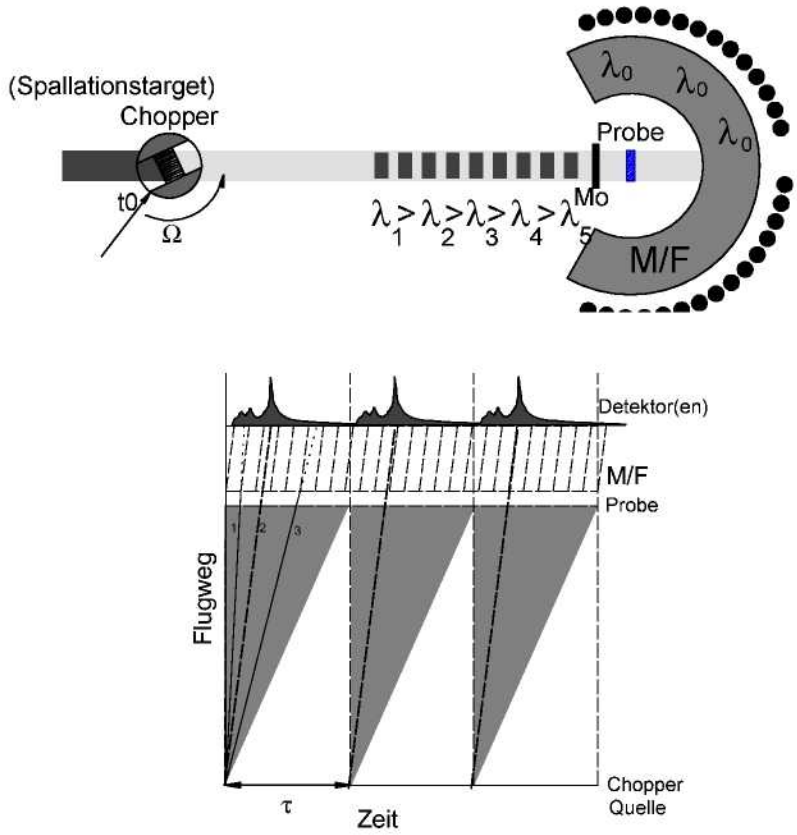



Figure 10.5: Setup and path-time diagram of a TOF spectrometer with inverted geometry.

spectrum at moderator temperature). During the path from chopper (pulsed source) to sample this pulse separates into different wavelengths $\lambda$, resp. different incident energies, that arrive at different times at the sample. Since a wavelength selection (to $\lambda_0$) is performed between sample and detectors, all detected neutrons have the same velocity and the distance sample-detector adds a constant offset to the TOF. To be able to correct the TOF-histograms with respect to the spectral distribution of the incoming pulse, it is important to detected the incoming neutron flux by a monitor (Mo) located close to the sample position accumulated in a separate TOF-histogram. This type of TOF-spectrometer is preferentially used at pulsed sources, ideally it may be possible to omit the first chopper by taking the pulse as generated by the pulsed source (spallation target). [4] All neutrons from the pulse (flying into the right direction) are utilized. This method has a few specific advantages and disadvantages, advantages are:

- The pulse contains neutrons with high incident energy that may perform energy loss scattering, the resolution at high energy loss is relatively good, especially if the pulsed source supplies very short pulses at high neutron energies.

The utilization of the full spectrum has however also disadvantages:

1. The full "white" pulse enters the shielded sample detector space. Any parasitic scattering and any imperfection of the analyzing filters or failure to absorb neutrons of "unused" final wavelength or direction leads to increased background. In addition the background depends on the sample which makes correcting subtractions difficult.

2. Samples are hit by a higher integral flux and therfore become more radioactive.

In general also "normal" TOF instruments perform better on a pulsed source in comparison with a reactor (if the average fluxes are equal) since by synchronizing source and chopper only a small part of the generated neutrons (with the desired wavelength) are not used. The distance source-chopper may serve at the same time as TOF-monochromator. In total the efficiency is comparable with the inverted type because in both cases on one side of the sample the spectrum is restricted by filters/monochromators and on the other side the full spectrum is utilized and sorted according to the TOF. Energy transfer analysis without filter on any side is impossible.

### Analysis by filters

The analyzer that is indicated by the grey segement labelled M/F in fig. 10.5 may either consist of an array of crystals reflecting scattered neutrons of the selected wavelength

[4] To suppress background or to prevent "frame overlap" it may be nevertheless advisable to use an additional chopper.

$\lambda_0$ onto the assocaiated detectors or of a filter. Especially in the early days of neutron scattering filters made from polycrystalline blocks of Be , BeO etc. were used. These filters are transparent only for neutrons with energies below the "Bragg-edge", i.e. for wavelengths larger than twice the largest lattice spacing. All faster neutrons will be reflected by some crytallite in the block. By integrated absorbing plates the thus reflected neutrons are removed. For the filter to be sufficiently transparent below the Bragg-edge the used material may only have a very low absorption cross section. In addition the thermal diffuse scattering by fluctuating lattice deformations (phonons) has to be suppressed by cooling (liquid nitrogen). Below the Bragg-edge these filters transmit all neutrons from nearly zero energy to the edge energy of a few meV. For the spectroscopy of high energy excitation this is accceptable since the energy transfer is then determined by the incident energy of a few 100 meV. High resolution quasielastic scattering has to be done with other instruments. By employing the difference between data obtained with two different filters (e.g. Be and BeO) the effective window of final energies may be narrowed, however two measurements are needed and the final signal is obtained from a small difference of two larger counting signals with the corresponding statistical errors. Modern versions of inverted TOF spectrometers also have narrower filters for analysis. In particular with the introduction of the new high intensity spallation sources spectrometers of the inverted TOF geometry with Bragg scattering crystals in (near) backscattering geometry were build. Short pulses in combination with a long flight path ($\simeq 100\,\mathrm{m}$) allow to get a resolution in the range of $\mu$eV for the incoming neutrons, the scattered neutrons are then analyzed by (perfect) crystals in backscattering geometry.

### 10.2.3 Transforms

Since the physics of the systems under investigation is usually expressed in terms of $S(Q,\omega)$, transformation of the raw data $I(2\Theta,t)$ into the $(Q,\omega)$-space are needed. The following is formulated for the normal TOF geometry, however, the expressions for the inverted geometry are analogous. With $t = L/v'$ and $t_0 = L/v$ inserted in Eqn. 10.2 yields

$$\omega(t) = \frac{m_n}{2\hbar} L^2 \frac{t^2 - t_0^2}{t^2 t_0^2} \tag{10.5}$$

and

$$Q = \frac{m_n}{\hbar} L \sqrt{\frac{t^2 + t_0^2 - 2cos(2\Theta)t_0 t}{t_0^2 t^2}} \tag{10.6}$$

The nonlinear mapping from channels to energy given by Eqn. 10.5 also causes a strongly varying energy-width of TOF-channels, $K$.

$$I(2\Theta,K) \propto \int_{(K-1)\Delta\tau}^{K\Delta\tau} \frac{k'}{k} 4\pi b^2 S(\underline{Q},\omega(t)) \frac{d\omega}{dt} dt \tag{10.7}$$

or somewhat simpler (but **not** applicable if $\delta(\hbar\omega)$-contributions or quasi- or inelastic components with intrinsic width comparable or smaller than a time channel):

$$I(2\Theta, K) \propto \frac{k'}{k} 4\pi b^2 S(\underline{Q}, \omega(K\Delta\tau)) \frac{d\omega}{dt} \Delta\tau \tag{10.8}$$

with

$$\frac{k'}{k} = \frac{t_0}{t} \tag{10.9}$$

and

$$\frac{d\omega(t)}{dt} = \frac{m_n}{\hbar} L^2 \frac{1}{t^3} \tag{10.10}$$

the result

$$I(2\Theta, K) \propto S(\underline{Q}, \omega(K\Delta\tau)) \ \frac{1}{t^4} \tag{10.11}$$

is obtained, all constant factors are omitted and lumped into a still undetermined proportionality factor [5]. Note the factor $t^{-4}$ between $S$ and $I$ which causes a significant intensity enhancement for the early arriving time channels, however, intimately connected with a corresponding loss of energy resolution.
Finally the true TOF raw data are only obtained if the resolution of the instrument is accounted for. The simplest basic assumption is a constant broadening on the time-of-flight scale. Thus

$$I_{raw}(2\Theta, K) \simeq \sum_{K'} R(K - K') I(2\Theta, K') \tag{10.12}$$

where $R(K)$ is the normalized TOF "spectrum" of an elastic resolution sample (e.g. Vanadium).

**Remark:** application of a coordinate transform (here $(Q,\omega) \rightarrow (2\Theta, K)$ resp. $(Q,\omega) \leftarrow (2\Theta, K)$) requires –besides the observation of the (nonlinear) coordinate dependence– the application of a Jacobian determinant as factor to preserve "volume". For the time-frequency part this is also done here ($t^{-4}$-factor). The transform $2\Theta \rightarrow Q$, however is performed without Jacobian due to an asymmetry in definitions of $S(Q,\omega)$, namely $d\sigma(2\Theta)/d\Omega = S(Q(2\Theta))$ !

## 10.3 Neutron Spin-Echo Spectrometers

### 10.3.1 The Resolution versus Intensity Trap

In order to improve the resolution of the above TOF spectrometers e.g. by a factor 0.1 this factor has to be applied as well to the monochromatization as to the pulse length (chopper opening time). This would on the one hand increase the resolution accordingly by a factor

[5] For practical purposes the proportionality factor is determined by an absolute calibration using a standard sample, e.g. vanadium which is a purely incoherent elastic scatterer.

of about 10 but at the same time the intensity is reduced by $0.1_{monoch.} \times 0.1_{chopper} = 10^{-2}$. Still other necessary measures to preserve the increased resolution as the reduction of sample size (definition of flight path) are not contained in this reduction factor. In general an improvement of the spectral resolution requires the narrowing of the filter transmission functions **before** and **after** the sample scattering by the desired improvement factor. This implies an intensity reduction by the square of the resolution improvement factor. However, the problem of vanishing intensity if one would try to further increase the resolution by narrowing velocity/wavelength bands can be overcome using a technique that is able to detect the tiny velocity differences due to scattering of neutrons within a broad velocity distribution.

### 10.3.2 The Spin-echo Knack

The attempt to increase the resolution of the TOF instruments far beyond the $\Delta E/E \approx 1\%$ of the present realizations would lead to an unacceptable loss of intensity (as expressed in terms of detector count rate). However, this situation would immeadiately improve, if it would be possible to equip each neutron with an individual stop watch which could be read in a way that the run time difference between test tracks before and after the sample is obtained at detection. If this stop watch has a sufficient time resolution it would be possible to observe very small velocity changes even if a beam with a wide range of initial neutron velocities is used. This would allow to escape the intensity trap.
With some restrictions (with important consequences for the application) it is indeed possible to use the neutron spin directions as kind of individual stop watch pointers. The clockwork of this watch is then effected by the precession of the neutron spins in an external magnetic field. [6] The restrictions affecting application are caused by the fact that the "spin-stop watch" can only be read up to an unknown integer number of complete precession turns. The reading is performed by the cosine type transmission function of an analyzer and yields only ensemble averages and not individual rotation angles. The intensity at the detector is modulated accordingly.
In addition the scattering function $S(Q,\omega)$ as a rule is not such that there is only one defined velocity change induced but $\Delta v$ is distributed according to $S(Q,\omega \approx k\Delta v)$. The detector signal is then proportional to the integral of precession-angle-cosine modulated intensity contributions with weight according to the $\Delta v$ from $S(Q,\omega)$. Therefore the signal of the NSE spectrometer –as explained in this chapter– is completely different from the TOF histogramms of classical TOF-spectrometers. Instead it is proportional to the

[6] It is somewhat involved to extract this analogy starting from a quantum mechanical view with spin eigenstates and eigenvalues. Implicitly we are talking about the behaviour of the ensemble average of the spin vectors which obeys the "classical" Bloch equation concerning its precession in the magnetic field. As long as the kinetic energy of the neutrons is much bigger than the magnetic level splitting the classical picture is completely sufficient and much easier to visualize to understand the NSE spectrometer than a quantum mechanical treatment.

cosine-Fourier transform of $S(Q,\omega)$, i.e. the intermediate scattering function $S(Q,t)$. A detailed derivation and discussion is given below. But first of all a concrete setup of an NSE spectrometer is presented.

## 10.4 Setup and function

The upper part of figure 10.6 shows the directions of the spin expectation value during the passage of a neutron through the spectrometer.

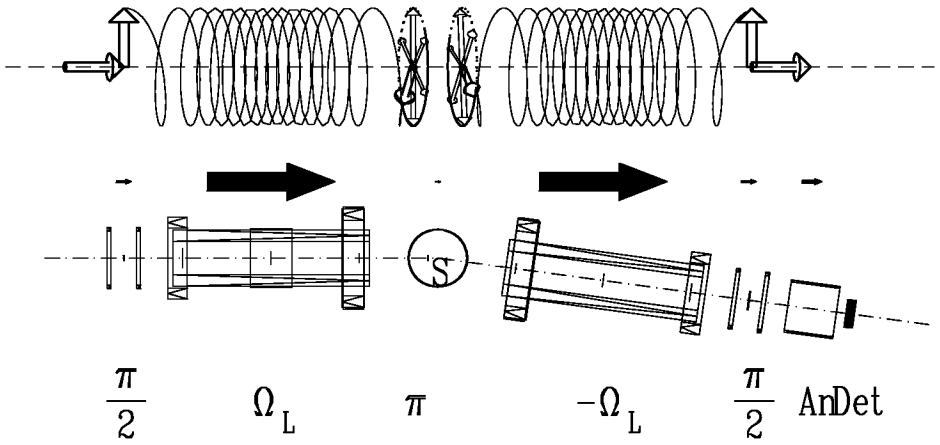



Figure 10.6: Spin roatations and setup of a generic NSE-spectrometer. Upper part: Spin rotrtation, middle part: magnitude of the magnetic field, lower part: schematic setup of the Jülich NSE-spectrometer.

Longitudinally polarized neutrons [7] (i.e. spin expectation value parallel to the beam direction) enter the spectrometer from the left. In the first so-called $\pi/2$-flipper the spin is rotated such that on exit it is orthogonal to the longitudinal magnetic field of the precession path. That defines the start of the "spin stop watch", immediately after the flipper a precession of the spins around the axial magnetic field begins. The precession frequency increases during the approach of the center of the main precession solenoid, where it reaches its maximum of up to a few MHz. The accumulation of precession angle

[7] The polarized neutron beam is obtained by reflection by a magnetic multilayer mirror. The layer stack consists of alternating nonmagnetic (e.g. Fe, Si or Ti) and magnetic (Fe or Co) layers. The effective index of refraction of the magnetic layers depends on the relative orientation of magnetization and spins of the neutrons such that there is a modulation of index of refraction for neutrons in one spin state only. Those neutrons are reflected, the others are transmitted. For layer distances of $5\cdots10$nm reflection angles of a few degrees result for wavelengths around 10Å. Both the reflected and the transmitted beam are polarized (with opposite spin directions).

continues –with decreasing frequency– until the neutrons reach the $\pi$-flipper close to the sample (S). The total precession angle at that point is:

$$\Psi \;=\; \frac{\gamma}{v}\int_l |B|dl \;=\; n2\pi + \alpha \tag{10.13}$$

where $\gamma = 2\pi \times 2913.06598 \times 10^4 \mathrm{s}^{-1}/\mathrm{Tesla}$ is the gyromagnetic ratio of the neutrons ($\rightarrow$ rad/sec !) and $|B|$ is the modulus of the magnetic induction along the path l.

The "stop watch" does not proceed uniformly but with a position dependend frequency that is proportional to the local magnetic field along the neutron path, see fig. 10.6. This may also be considered as a field dependend distance streching, which releases e.g. the mechanical positioning accuracy requirements for the flippers since they are located in low field regions. The total number of precessions a neutron spin undergoes on passage through one arm of the spectrometer lies between 10 and some $10^4$.

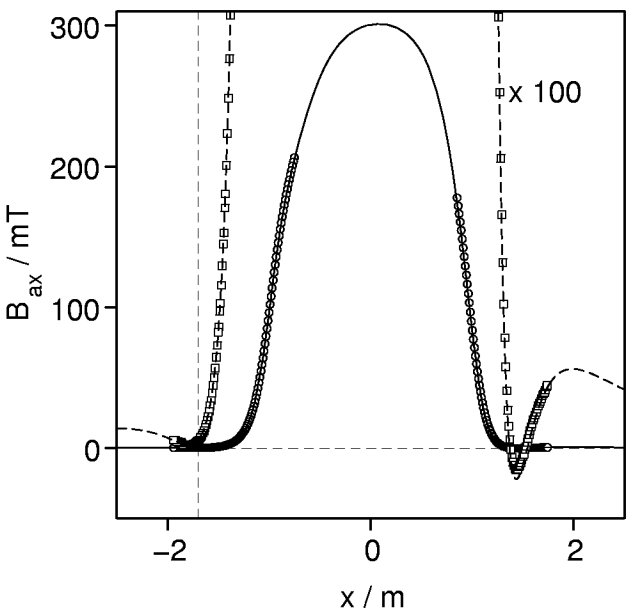



Figure 10.7: Field along the axis of a main precession coil.

Close to the sample (ideal: at the sample position) the so-called $\pi$-flipper is located, it rotates the spins by $180^0$ around a vertical axis, thereby the total precession angle is transformed to $\Psi_1 = n2\pi + \alpha \rightarrow n2\pi - \alpha$. The parameters $n$ and $\alpha$ are –according to eqn. 10.13 – extremely dependend on velocity and therefore very different for different neutrons in a

beam with finite width of the wavelength distribution. As a consequence the spin vectors at the sample position ($\pi$-flipper) are evenly distributed on a disc orthogonal to the field direction. If no velocity change occurs during scattering at the sample (elastic scattering) each neutron enters the secondary arm of the spectrometer with unchanged velocity. The precession field and path length of the secondary arm exactly match the corresponding elements of the primary arm before the sample ($\pi$-flipper). Accordingly the precession accumulated in the secondary arm is $\Psi_2 = n2\pi + \alpha$ and the total precession angle at the second $\pi/2$-flippers is $\Psi_1 + \Psi_2 = (n+n)2\pi - \alpha + \alpha = 2n2\pi$. I.e. all spins –irrespective of their initial velocity– reassemble at the same vertical position they had at the start point, the rotation imposed by the second $\pi$-flipper converts this back to the initial logitudinal polarization that is fully restored. The flippers limit the the two race tracks and realize "start", "time reversal" and "stop" of the "spin stop watches". The second $\pi/2$-flipper is the last element used to manipulate the spins it converts the average precession angle to a longitudinal polarisation component. Since the field after the second $\pi/2$-flipper is again longitudinal, further precessions do not influence the analyzed longitudinal polarization component (the stop watch is stopped!). The analyzer consists –like the polarizer– of mgnetic multilayer mirrors which only reflect neutrons of one longitudinal spin state into the detector. After ensemble averaging this means that the count rate at the detector is proportional to $(1 \pm \cos(\overline{\Psi}))/2$, [8] where $\overline{\Psi}$ is the expectation value of the angle between spin and axial direction.

## 10.5 The detector signal

As mentioned above the detector signal results from the cosine-of-net-precession-angle shaped transmission function of the analyzer in combination of the distribution of net precession angles due to the distribution of velocity changes during scattering. The velocity distribution is proportional to the spectral part of $S(Q,\omega)$. The intensity on the detector is proportional to the cos-modulated distribution. In the following this is derived in terms of mathematical expressions. First the field integrals along the primary and secondary pathes of precession are defined:

$$J_1 = \int_{l((\pi/2)_1)}^{l(\pi)} |B| dl \tag{10.14}$$

$$J_2 = \int_{l(\pi)}^{l((\pi/2)_2)} |B| dl \tag{10.15}$$

[8] The sign in front of the cosine depends on the technical realization of polarizer and analyzer (both reflecting, transmitting, one reflecting one transmitting) and on the orientation of flippers. It may be selected by choosing the signs of the flipper currents.

for a symmetric setup $J_1 = J_2$; $l(\pi, (\pi/2)_{1,2})$ denotes the positions of the corresponding flippers. The precession angle accumulated on a path is

$$\Psi_i \;=\; \frac{\gamma J_i}{v} \tag{10.16}$$

where $v$ is the neutron velocity (typically several 100 m/s). Because the $\pi$-flipper inverts the sign of $\Psi_1$ (i.e. of the part $\Psi_1 \mathrm{mod}\, 2\pi$), a total precession angle of

$$\Psi_{1,2} \;=\; -\frac{\gamma J_1}{v} \;+\; \frac{\gamma J_2}{v+\Delta v} \;+\; 4n\pi \tag{10.17}$$

results, where $\Delta v$ is the velocity change of the neutron during scattering and $n$ is an integer. The transmission function of an (assumed ideal) analyzer is

$$T_a \;=\; \frac{1}{2}\left[1 + \cos(-\frac{\gamma J_1}{v} \;+\; \frac{\gamma J_2}{v+\Delta v})\right] \tag{10.18}$$

From that the detector intensity

$$I \;=\; \eta S(Q) \iint \frac{1}{2}\left[1 \pm \cos(-\frac{\gamma J_1}{v} \;+\; \frac{\gamma J_2}{v+\Delta v})\right] w_\omega(\Delta v) w_\lambda(v)\; d\Delta v\; dv \tag{10.19}$$

results, where $\eta$ is an irrelevant calibration factor and $w_\omega$ resp. $w_\lambda$ are normalized distribution functions. $w_\omega$ represents the spectrum of the sample as found in the scattering function and $w_\lambda$ takes account for the fact that the NSE spectrometers usually are operated with a broad incoming wavelength distribution ($\Delta\lambda_{FWHM}/\lambda = 10 \cdots 20\%$). Observing the linear dependences of $k$, $\lambda$ and $v$ and series expansion of the squares in Eqn. 11.2 and insertion into Eqn. 10.19 leads to:

$$I = \eta \iint \frac{1}{2}\left[1 \pm \cos(-\frac{\gamma J_1}{(h/m_n)\lambda^{-1}} + \frac{\gamma J_2}{(h/m_n)\lambda^{-1} + \lambda\omega/2\pi})\right] S(Q,\omega) w_\lambda(\lambda)\; d\omega\; d\lambda \tag{10.20}$$

.

### 10.5.1 Symmetric case

At the point of symmetry $J_1 = J_2 = J$ it is possible to collect the $\lambda$-dependend terms in Eqn. 10.20 and to write them as series expansion for small $\omega$:

$$-\frac{1}{\lambda^{-1}} + \frac{1}{\lambda^{-1} + \lambda(m_n/h)\omega/2\pi} \approx -\lambda^3 \frac{m_n \omega}{h 2\pi} \tag{10.21}$$

To see the salient features of the spectrometer signal more clearly the finite wavelength distribution is temporarily ignored

$$I \;=\; \eta\frac{1}{2}\left[S(Q) + \int \cos(\underbrace{\gamma J \frac{m_n^2}{h^2 2\pi}\lambda^3}_{t}\;\; \omega) S(Q,\omega) d\omega\right] \tag{10.22}$$

The underbraced product has the unit "time", the integral in Eqn. 10.22 represents the cos-Fourier transform of $S(Q,\omega)$ with respect to $\omega$, the resulting function is called **intermediate scattering function,** $S(Q,t)$ [9] From Eqn. 10.22 it is further reckognizable that the time parameter $t = \gamma J(m_n^2)/(h^2 2\pi)\lambda^3$ depends on the third power of the wavelength $\lambda$ (i.e. long wavelength $\rightarrow$ very long Fourier times). In addition $t \propto J$, i.e. mainly proportional to the current throught the main precession solenoids. This current usually is the parameter used to stepwise scan the Fourier time during an experiment to get a table of $S(Q,t)$ vs. $t$.

### 10.5.2 Elastic scattering of a finite width wavelength distribution

For a transmitted beam or elastically scattered neutrons from a reference sample $\omega = 0$ holds, i.e $S(Q,\omega) = \delta(\omega)$. With that Eqn. 10.20 becomes

$$I = \frac{1}{2}\int \left[1 \pm \cos(\lambda \underbrace{\gamma(m_n/h)\{J_2 - J_1\}}) \right] w_\lambda(\lambda) d\lambda \tag{10.23}$$

For this case the intensity is proportional to the Fourier transform of the wavelength distribution, thereby the underbraced part is the external control parameter. It contains the difference between the field integrals along the primary and secondary pathes $J_2 - J_1$. This difference is easily controllable by sending a current through an auxiliary coil of a few windings around one of the precession solenoids. For a Gaussian wavelength distribution the envelope of the Fourier transform is again a Gaussian the width of which is inversely proportional to the width of the wavelength distribution. Since $w_\lambda$ is centered at a finite nominal wavelength $\lambda_0$ the envelope is multiplied by a cosine with a period $\propto 1/\lambda_0$. This function follows immediately from Eqn. 10.23 if $w_\lambda = \delta(\lambda)$ is assumed. Figure 10.8 displays the results of a extensive measurement using the attenuated direct beam with a central wavelength of $\lambda_0 = 0.7$nm and $\Delta\lambda_{FWHM}/\lambda_0 = 0.1$ compared to a calculation (fit) assuming a Gaussian wavelength distribution.

At the echo point (=perfect symmetry) at a phase coil current close to 1.5 A the count rate has a minimum. Ideally the rate there should be zero, but because all elements that contribute to the polarization manipulation and analysis are imperfect a residual intensity is left that has to be determined by calibration measurements. From the function intensity vs. phase current it is possible to determine the wavelength distribution.

[9] Strictly this is only true for a $S(Q,\omega)$ that is symmetric with respect to $\omega$. For any practical problems however this is well fulfilled since the minute energy transfers corresponding to the NSE time scale are very small compared to $k_B T$.

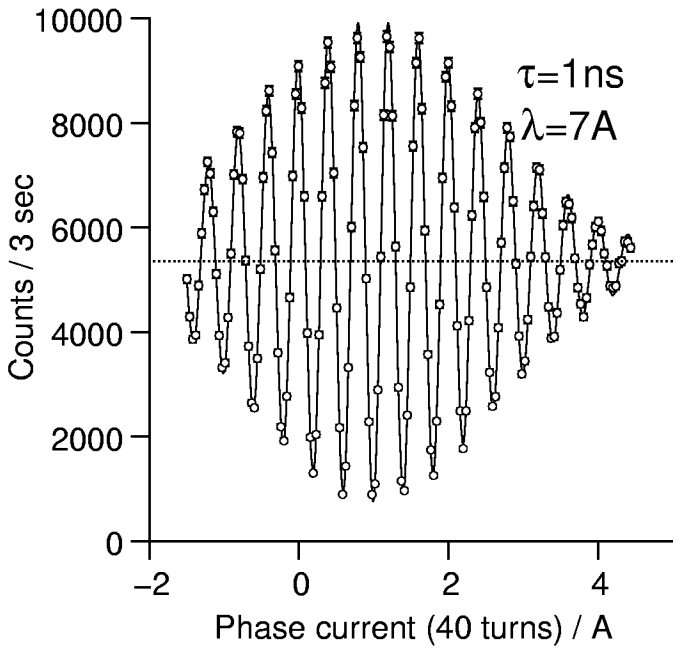



Figure 10.8: Echoform: count rate as function of the magnetic symmetry ($\propto$ phase coil current).

## 10.6 Experimental procedures and evaluation

In principle the information on $S(Q,t)$ according to Eqn. 10.22 is contained in the ratio of the intensities at the symmetry point and the average intensity $(\eta/2)\ S(Q)$. However there are practical reasons that prevent the reliable setting of the symmetry point alone. The location of the symmetry point (i.e. phase zero current in the phase coil) is extremely sensitive to tiny variations of the magnetic environment caused e.g. by displacement of larger iron parts at neighbouring instruments, movement of the crane and/or thermal displacements of coils ... . Therefore the position of the symmetry point has to be measured as well as the intensitiy each time. In fig. 10.9 the minimum of single countings is indicated, intensity must be determined for 3 points $P_1 \cdots P_3$ separated by a symmetry change corresponding to a quarter precession each. From these 3 values it is possible to extract the average intensity $I(Q,0)$, the echo amplitude $I(Q,t)$ and the exact symmetry point location. This also holds if any disturbance shifted the location as indicated by the three hollow circles in the figure.

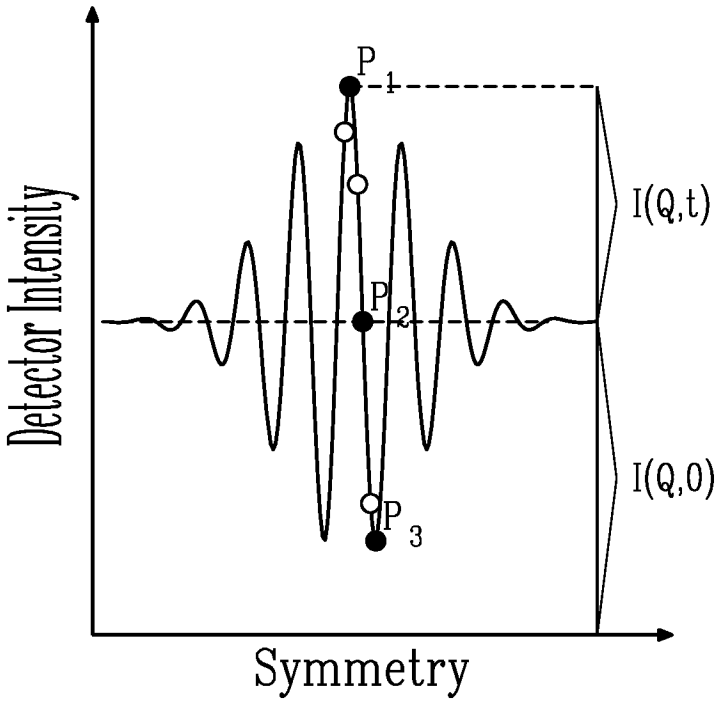



Figure 10.9: Schematic echo form, idealized.

For an ideal spectrometer $I(Q,t)/I(Q,0) = S(Q,t)/S(Q)$ would be the desired value of the normalized intermediate scattering function. In reality resolution effects and polarization losses reduce the value of $I(Q,t)/I(Q,0)$ compared to $S(Q,t)/S(Q)$.

## 10.7 Field integral homogeneity and resolution

Besides the decay of $S(Q,t)$ as a consequence of the dynamical processes in the sample the measured echo amplitude suffers a further reduction due to resolution effects (different from the above mentioned depolarization effects) that must be accounted for in the data evaluation. These effects result from residual differences of the path integral over the magnetic field along various paths connecting the beam apertures. They are quantified by a measurement with a purely elastic scattering reference sample. Resolution correction may then be performed by division of the echo-amplitudes by those of the reference sample.

## 10.8 Practical aspects, peculiarities

From the above description it follows that the NSE spectrometer measures the Fourier transform $S(Q,t)$ of the spectral part of $S(Q,\omega)$ directly. As a consequence the average count rate at the detector corresponds to half of all neutrons scattered from the sample into the soild angle of the detector (Fourier**integral**). Therefore weak spectral features are buried under the noise due to counting statistics. However the method is perfectly adapted to relaxations that are performed by most of the scattering structure since the realxation functions are measured in the time domain directly and resolution correction consists of a division instead a deconvolution in the frequency space. One very important field for NSE investigations are "soft matter" problems. These comprise polymer melts and solutions and other complex fluids. The NSE methods opens a dynamics window in the SANS regime. Since in that regime the dynamics is determined by the balance between elastic (entropic) forces and friction and in comparison inertial forces are negligible the observed fluctuations are pure relaxations and well suited for investigation by NSE. In addition SANS scattering is coherent and usually intense compared to scattering at large angles.

The spin incoherent scattering is caused by the dependence of the scattering length on the relative orientation of nuclear and neutron spins. The fluctuating part of the scattering length due to random spin orientation contains no interference of scattering from different nuclei, i.e. the scattering intensity distributes evenly over $4\pi$ solid angle and is "diluted" accordingly. The intensity is very small compared to typcial SANS intensities. The dynamics of the incoherent scattering reflects the one-particle motion (self correlation). For the NSE method it is important to note that the spin-dependend scattering flips 2/3 of the neutron spins. This means that a considerable loss of polarization is encountered, only 1/3 of the neutrons contribute to the echo signal the rest is background. This 1/3 stems form the spin flipped neutrons, i.e. the echo amplitude is also inverted (negative). If coherent and incoherent scattering contributions are present this may lead to peculiar effects since the amplitudes may cancel each other depending on their –potentially different– dynamics.

## 10.9 Scattering cross section and time-of-flight spectra for some basic systems

In this chapter the scattering from a number of very basic physical systems is presented and the corresponding features of the neutron time-of-flight spectra are discussed. It should help the reader to gain a feeling of what kind of effects determine the shape of TOF

spectra in different energy and resolution regime and for samples in various states of aggregation. The expressions of scattering functions mainly follows the textbooks of Marshall & Lovesey [Marshall and Lovesey(1971)] and Doi & Edwards [Doi and Edwards(1994)], which are recommended as reference books for the field of neutron scattering respectively polymer dynamics.
We start from the high energy side where scattering results in broad spectral distributions.

### 10.9.1 Ideal monoatomic Gas

As a starting point for the discussion of general features of TOF spectra we consider the simple gas model as alredy presented in chapter 5 first. We deal with scattering centers (atoms) with totally uncorrelated mutual distances. Therefore on average all interference terms from the superposition of partial waves cancel and –as for incoherent scattering– the observed cross section represents the (Maxwellian) velocity distribution. Figure 10.10 shows spectra which may be obtained with a hot source or an "eV" spectrometer at a pulsed source, they are dominated by the recoil shifted velocity(momentum) distribution. Please note that in the following figures the intensity data are plotted versus the neutron wavelength which is synonym, respecttively direct proportional to the time-of-flight!

The gas scattering obtained with thermal incident energy is shown in figure 10.11 which also reveals the fact that only a part of the $[Q, \omega]$-space is kinematically accessible.

The scattering function for a gas is given by:

$$S(Q,\omega) \;=\; \sqrt{\frac{\beta M}{2\pi\hbar^2 Q^2}}\;\exp\left[-\frac{\beta M}{2\hbar^2 Q^2}(\hbar\omega - \frac{\hbar^2 Q^2}{2M})^2\right] \tag{10.24}$$

where $M$ is the particle mass, $\beta = (k_B T)^{-1}$ and $\hbar^2 Q^2/(2M)$ is the recoil energy. At high $Q$, i.e. at high incident neutron velocity a significant shift of the center of neutron velocity is encountered which depends on the mass of the scattering particle. The width of the neutron spectrum reflects the momentum distribution (here Maxwellian velocity distribution) of the ensemble of scatterers of this mass. Note that $S(Q,\omega)$ in this regime is assymetric with respect to $\omega$.

### 10.9.2 Ensemble of Harmonic Oscillators

An interesting insight into the interrelation of recoil and incorporation of the scatterers in a condensed matter system is obtained by consideration of a particle in a harmonic potential (i.e. Einsteins model of a solid), which is the next example to be discussed.

For an ensemble of particles in identical spatially uncorrelated isotropic harmonic poten-

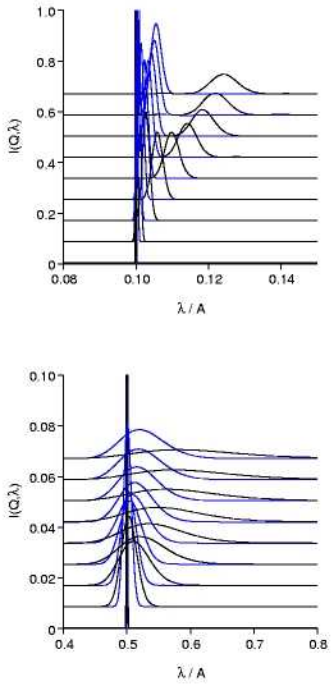



Figure 10.10: Computed time-of-flight spectra from monoatomic gases with atomic weight 1 (wide recoil peaks) and 4 (narrow recoil peaks) at $T = 300K$. The incident neutron wavelength is $\lambda_0 = 0.1$Å (left) and $\lambda_0 = 0.5$Å (right) the scattered wavelength $\lambda$ is proportional to the time of flight. The series of curves correspond to equidistant scattering angles between $1^0$ and $161^0$. Observe the mass dependent loss of average energy of the neutron due to the recoil effect, visisble at larger scattering angle.

tials the scattering function is [Marshall and Lovesey(1971)]:

$$S(Q,\omega) = \exp\left[-\frac{\hbar Q^2}{2M\omega_{osz}}\coth(\hbar\omega_{osz}\beta/2)+\hbar\omega\beta/2\right]\times \sum_{n=-\infty}^{\infty}\delta(\hbar\omega-n\hbar\omega_{osz})I_n(\frac{\hbar Q^2}{2M\omega_{osz}\sinh(\hbar\omega_{osz}\beta/2)}) \qquad (10.25)$$

the corresponding spectrum is shown in figs. 10.12, 10.13, 10.14, where the $\delta$-function has been replaced by a narrow Gaussian. As is seen from the figures the oscillator frequency may easily be inferred by the spacing between the excitation lines. Their positions do not depend on $Q$, but their intensities that reflect the form factor due to the oscillator eigenfunctions weighted by their thermal occupation do so. The varying spacing of lines in the TOF-diagrams $I(\lambda,\theta)$ results from the nonlinear tranformation from experimental TOF representation to $S(Q,\omega)$.

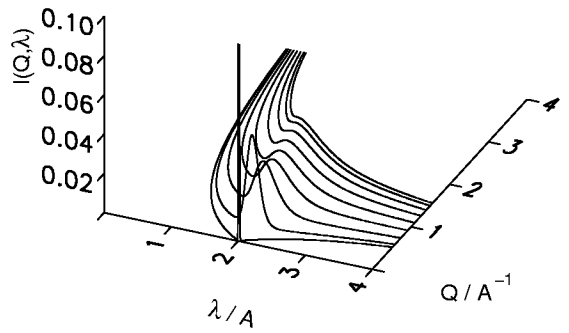



Figure 10.11: Gas ($m = 4$) scattering displayed as intensity vs $Q$ and $\lambda$ for an equidistant series of scattering angles. The incident wavelength is $\lambda_0 = 2$Å. As is visible only a part of the $[Q, \omega = \hbar/(8\pi^3 m_n)(\lambda^{-2} - \lambda_0^{-2})]$ space is kinematically accessible.

As a dense line spacing of the oscillator illustrates that at low resolution ,i.e. high enough incident neutron energy, the intensity distribution is such that the oscillator scattering approaches that of a gas of free particles (short time behaviour), see fig. 10.15. This is another way to state that for high energy neutrons and at short times the particle in a (shallow) potential looks very similar to a free particle.
However, why don't we see more effects from recoil? In particular in high resolution spectroscopy this would even at low $Q$ lead to significant energy shifts. A closer look to the oscillator spectra reveals the answer. There is always a line at $\omega = 0$ separated by the oscillators excitation energy from the closest inelastic lines. Only the envelope over the line intensities displays the trace of the recoil. The physical explanation is that observation for longer times ($\omega$ small) reveals that the particle is bound and attached to the (immovable, "infinitely" heavy) background (e.g. a macroscopic crystal) and therefore the recoil energy becomes infinitely small. If the neutron transfers more energy and exites higher oscillator states the effect more and more resembles a kick to the confined particle that leaves a localized oscillating distribution within the potential. For the short effective interaction time of the neutron this more and more resembles the collision with a free particle, as the illustration of fig. 10.15 corroborates.

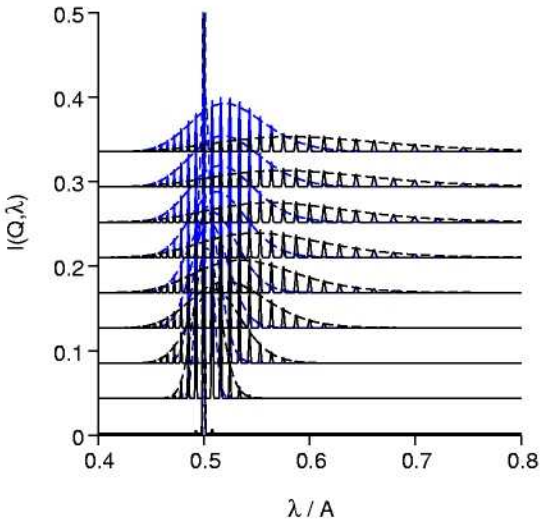



Figure 10.12: Computed time-of-flight spectra from particles of mass 1 (black) and 4 (blue) in a harmonic potential (such that $\hbar\omega_{osz} = 10\,\mathrm{meV}$) at $T = 300K$. The incident neutron wavelength $\lambda_0 = 0.5\text{Å}$ (right) the scattered wavelength $\lambda$ is proportional to the time of fligth. The dashed lines correspond to the gas scattering shown in fig. 10.10.

### Phonon density of states

Whereas the "Einstein solid" gave some insights and may be the right model for localized optical modes, e.g. realized by hydrogen in metals, the dominant atomic motions in a normal solid can be described as sound-like phonons.

The simplest model of the phonon density of states of a solid is the Debye spectrum which assumes sound waves with linear dispersion up to a cut-off frequency $\omega_D$. Then the density of states is

$$Z(\omega) = \frac{3\omega^2}{\omega_D^3} \tag{10.26}$$

The Bose factor that describes the temperature dependent occupation of phonon states is

$$n(\omega) = \frac{1}{e^{\hbar\omega\beta} - 1} \tag{10.27}$$

and with

$$\gamma(t) = \int_{-\infty}^{\infty} \frac{Z(\omega)}{\omega}\, n(\omega) \exp(-i\omega t)\, d\omega \tag{10.28}$$

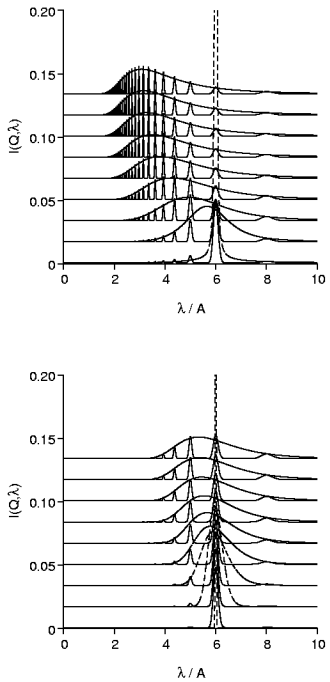



Figure 10.13: Comparison of time-of-time of flight spectra computed for a gas (m=4) and an ensemble of oscillators (m=4) at $T = 300K$ and $T = 30K$ for an incident wavelength of $\lambda = 6$Å. The series of curves correspond to equidistant scattering angles between $1^0$ and $161^0$.

the Debye-Waller factor is

$$\exp(-2W(q)) \quad \text{with} \quad 2W(q) = \frac{\hbar q^2}{2M}\gamma(0) \tag{10.29}$$

with that the phonon scattering (in incoherent approximation, e.g. by decorating protons) is

$$\frac{d^2\sigma}{d\Omega dE'} = Nb^2\frac{k'}{k}\frac{1}{2\pi\hbar}\int_{-\infty}^{\infty} exp[-i\omega t - 2W(q) + \frac{\hbar q^2}{2M}\gamma(t)]dt \tag{10.30}$$

this may be expanded by using the series expansion of $exp[\frac{\hbar q^2}{2M}\gamma(t)]$ as series of 0-, 1- and multiple phonon scattering contributions.

$$\frac{d^2\sigma}{d\Omega dE'} \simeq Nb^2\frac{k'}{k}\, e^{-2W(q)} \left[\delta(\hbar\omega) + \frac{\hbar^2 q^2}{2M}\frac{Z(\omega)}{\omega}\{1 + n(\omega)\} + \cdots\right] \tag{10.31}$$

Equation 10.31 shows a way how the density of states $Z(\omega)$ may be derived from the results of a TOF-experiments on a solid.

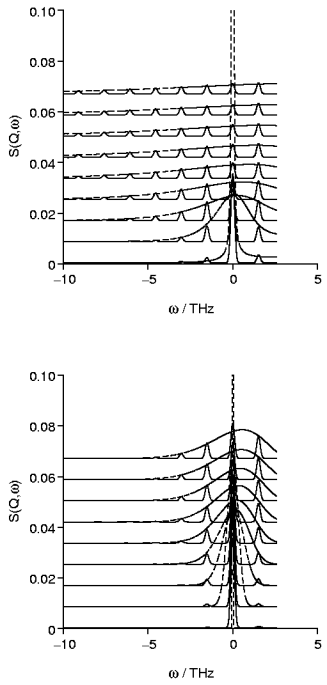



Figure 10.14: Comparison of scattering function corresponding to figure 10.13.

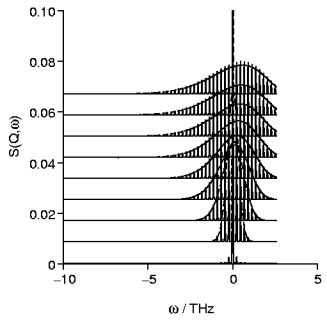



Figure 10.15: Comparison of scattering functions of a gas compared to an oscillator with narrow spacing at $T = 30K$.

**Note**

Strictly speaking the above expression is only valid for a simple monoatomic solid in incoherent approximation. I.e. either composed of incoherent scatterers (like Vanadium) or measured in powder average

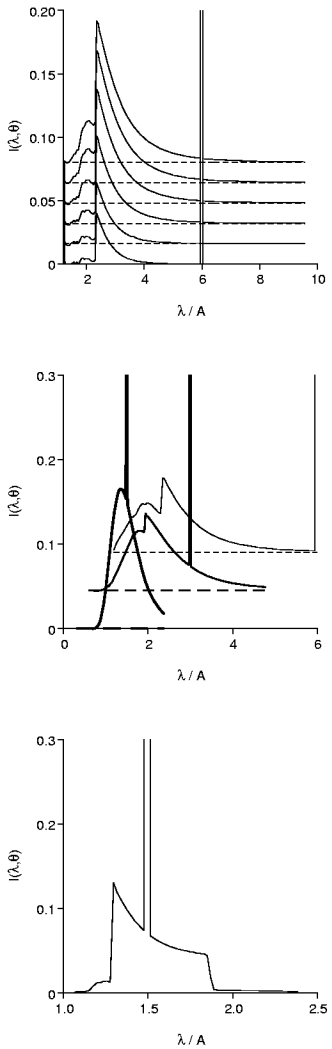



Figure 10.16: Multiphonon spectra of a Debye solid with a Debye temperature of 150. The effective mass was taken as 1 amu. Upper left: TOF spectra computed for an incident wavelength of 6 Å for scattering angles $10^0 \cdots 150^0$ at $T = 100\,\mathrm{K}$. Upper right: TOF spectra at $90^0$ scattering angle and $T = 300\,\mathrm{K}$ for incoming wavelengths $\lambda = 1.5$, 3, 6 Å. Note the approach to the free gas scattering with increasing incident energy. Lower curve: situation that allows to estimate the one phonon spectrum $Z(\omega)$ at the low scattering angle of $15^0$ even with $\lambda = 1.5$ Å $T = 300\,\mathrm{K}$.

at large $Q$ such that coherent effects are averaged out. For more complex structures a amplitude and scattering length weighted density of states is obtained rather than the plain $Z(\omega)$. The exact treatment

becomes more involved.

As far as the single phonon scattering dominates $Z(\omega)$ directly follows from Eq. 10.31 by separating the elastic scattering ($\delta(\hbar\omega)$) and multiplication of the rest with $\omega/(1+n(\omega))$. However, care must be taken to avoid the effects of multiphonon scattering. As the occurence of multiple excitation with the simple oscillator also here the nonlinearity in the exponential functions of displacement $\times$ $Q$ lead to multiphonon contributions. The effect is large at high $Q$ and $T$ as can be read from fig. 10.16. Similar to the ensemble of decoupled oscillators also the Debey solid approaches the response of a gas of "free" particles if the energy/momentum transfer is large. I.e. to plan an experiment to extract $Z(\omega)$ from TOF-data one should select low $Q$ values and low $T$, which unfortunately contradicts the quest for high intensity of the desired signal.

## 10.10 Measured Spectra

In fig. 10.17 several spectra as they are accumulated in the histograammatic memory are displayed. The time-of-flight scale of the horizontal axis refers to the distance $L$ between sample and detectors. This time-of-flight is directly proportional to the wavelength $\lambda'$ of the scattered neutrons as is indicated by the diagonal representing this linear relation using the right hand vertical scale. This diagonal straight line intersects the level $\lambda_0 = 6$Å at the location of the "elastic channel" where neutrons are collected that did not change their velocity during scattering. Since in liquid water which was the sample all moelcules may diffuse without restriction only a so called **quasielastic** line is observed which corresponds to a Lorentzian with a width proportional to $Q^2$. The maximum of intensity is nevertheless at the elastic channel ($\rightarrow$ quasielastic).

The difference between a solid with atoms/molecules fixed at lattice sites and a liquid is illustrated by the right part of the figure. Imidazole in the solid state exhibits an intense line at the elastic channel with a width corresponding to the instrumental resolution, the small inelastic intensity around the elastic line can be associated with a Debye solid like density of states, which at larger energy transfer, however, displays different structures according to the phonon dispersion of the imidazole crystal. Also multiphonon contribute there.

In contrast molten imidazole (especially for the relatively large scattering angle displayed here $\rightarrow$ large $Q$) shows only a broad quasielastic intensity distribution. At shorter times-of-fligth corresponding to larger energy transfers (gains) structures in the spectra are visible that stem from molecular and lattice virbrations. Note the second left scale in combination with the dashed line that illustrates the strongly nonlinear relation between energy and time-of-flight. For energy gains $\Delta E \gg k_B T$ the scattering energy dies out due to the exponential Boltzmann factor. At ambient temperature $k_B T$ is equivalent to 25meV. Well above that energy gain the unavoidable virtually constant background due

to "frame overlap" may be determined.

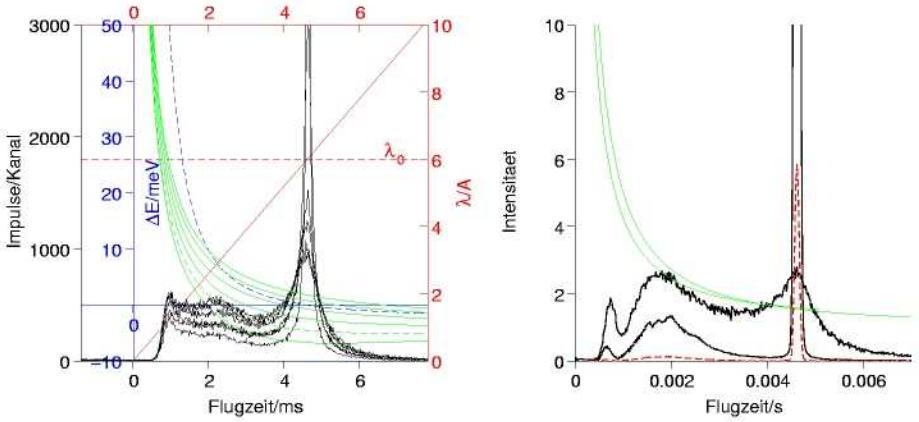



Figure 10.17: Left: TOF-spectra from liquid water at ambient temperature for different scattering angles between $30^0$ and $140^0$. Parameters: $\lambda_0 = 0.6$nm, $\Delta\tau = 18\mu$s, $L = 3.05$m, $N = 512$. Right: TOF-spectrum from imidazole ($C_4H_4NH$) as crystalline solid at 300K (the dashed lines displays the same data scaled by $\times 0.1$) and as melt at 403K at a scattering angle of $95^0$.

That corresponds to the situation of the scattering triangle as depicted in fig. 10.1. $\underline{Q}$ (depending on energy transfer) for elastic and inelastic scattering have to be assigned to the different time channels of the histogram from one specific detector. That applies as well for the modulus $Q$ as for the direction of $\underline{Q}$. The sequence of curves in the left figure 10.17 shows the values of $Q$ as function of scattering angle (different curves) and time channel. The property that the values become very similar for large energy gains –also expressed by the similar intensity distribution of that part of the spectra for different angles– follows from the fact that the main contribution to $Q$ at high energy gain stems from the length difference of $k$ and $k'$ (see fig. 10.1). The variation of $|\underline{Q}|$ may be compensated within certain limits by combining the data from different detectors (angles), however that does not apply for the direction change of $\underline{Q}$. Therfore TOF-instruments –in contrast to triple-axis spectrometers– are better suited for isotropic samples (liquids, powders, amorhpous substances) than for single crystals or other highly oriented samples.

### Conversion to $S(Q,\omega)$

Application of the transforms Eqns. 10.5 and 10.11 allows for a display of the spectra in terms of $S(2\Theta,\omega)$. Figure 10.18 shows a corresponding $S(2\Theta,\omega)$ derived from the water data (medium angle data in fig. 10.17).

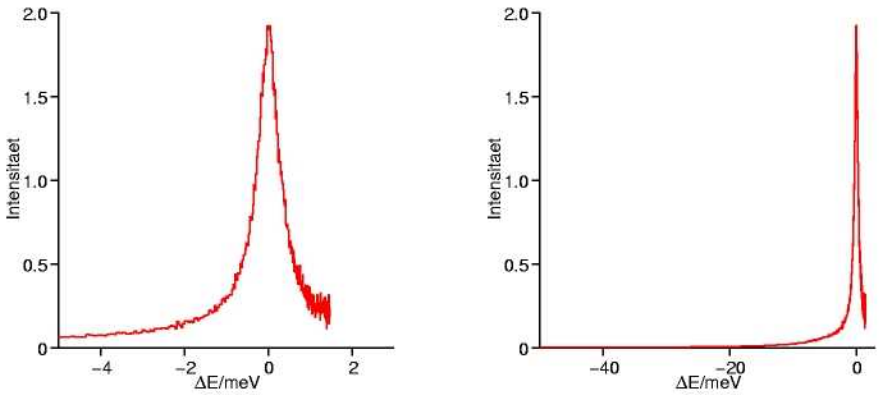



Figure 10.18: TOF spectrum from liquid water (see fig. 10.17) converted to $S(2\Theta, \omega)$ displayed over two different energy ranges.

The diffusion is easily reckognizable but the structur due to (internal) vibrations is lost in this type of representation. As soon as a model for $S(Q, \omega)$ is available, it is in most cases more advantageous to apply the inverse transform to that model to compute $I(2\Theta, K)$ and to compare this result with the raw TOF data. This procedures also allows for a simpler more direct application of resolution corrections.

**NSE Experiment Data**

The single chain structure factor of a linear polymer in the melt in terms of the standard NSE data representation as $S(Q,t)/S(Q)$ for a series of different $Q$-values is shown in figure 10.19. The sample was a melt of polyethylethylene with 10% protonated chains in 90% deuterated chains of the same chemical architecture.
Flexible linear polymer chains in solution follow a different universal behaviour due to the long range hydrodynamic coupling between different segments of the same chain. The corresponding model is called ZIMM model, within the so-called preavaeraging approximation it has the same structure as that of the Rouse model (see [Doi and Edwards(1994)]). Please refer to chapter 13 for further details. In the universal regime the decay rate is $\propto Q^3$ instead of $Q^4$ as in the Rouse model. Except "trivial" temperature factors, the only parameter that determines the decay rates is the solvent viscosity. Figure 10.20 shows results from a measurement of a linear polymer solution the fitted viscosity coincides within 10% with the known solvent viscosity.

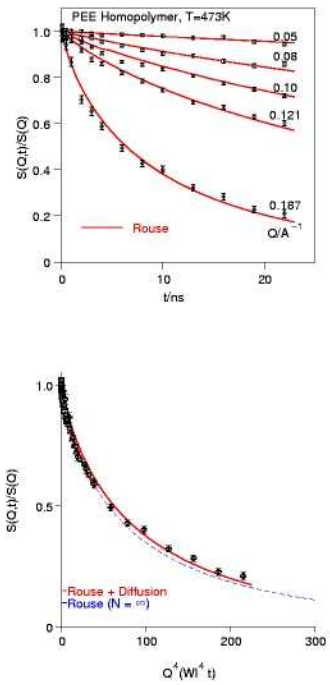



Figure 10.19: Single chain scattering from a a PEE-polymer melt in standard representation for NSE data as $S(Q,t)/S(Q)$ (right). On the left a scaling plot of the same data is shown. Curves correspond to a (one parameter) fit to the Rouse model. They show nearly pure Rouse scaling (i.e. rate $\propto Q^4$) following the master function given in chapter 13 with marginal distortion due to the centre-of-mass motion.

## 10.11 Resolution and Intensity

### 10.11.1 TOF

For TOF-spectrometers –unlike for triple-axis instruments– for many applications mainly/only the energy resolution is important since the scattering intensity has to be collected and accumulated in a large solid angle anyway to yield a sufficient number of counts. The energy resolution is determined by the accuracy of the TOF-measurement and by the width of the incoming (or analyzed) wavelength band. The latter is given by the beam divergence in combination with the mosaik width of the crystals (see also chapter on triple-axis spectrometres). The TOF-uncertainity is given by the chopper pulse length and the accuracy of the flight path. The flight path cannot be defined with arbitrary accuracy, since finite sample size of cm and a detection position uncertainity of some

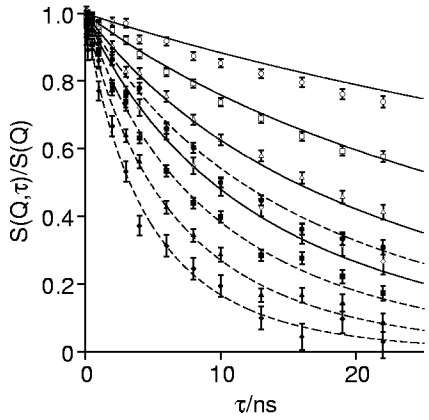



Figure 10.20: $S(Q,t)/S(Q)$ of a 2.5 % polymer solution with a fit to the Zimm model that theoretically describes $S(Q,t)$ for a dilute polymer solution. The data have been measured using the area detector at only two angluar positions of the secondary spectrometer arm within 8 h time. The hollow symbols habe been obtained at an arm setting of $\bar{Q} = 0.05\text{Å}^{-1}$ and correspond to $Q/\text{Å}^{-1} = 0.038, 0.05, 0.061, 0.072$. The filled symbols were measured at $\bar{Q} = 0.08\text{Å}^{-1}$ and correspond to $Q/\text{Å}^{-1} = 0.067, 0.08, 0.09, 0.102$.

mm in the detectors. [10] If all timing uncertainities are lumped into $\Delta t$, a classical TOF instruments has the following resolution:

$$\Delta\omega = \sqrt{(\frac{\partial\omega}{\partial t}\Delta t)^2 + (\frac{\partial\omega}{\partial\lambda}\Delta\lambda)^2} \tag{10.32}$$

From Eqns. 10.2 - 10.5 follows:

$$\Delta\omega = \sqrt{(\frac{m_n L}{\hbar t^3}\Delta t)^2 + (\frac{4\pi^2\hbar}{m_n\lambda^3}\Delta\lambda)^2} \tag{10.33}$$

Because $\lambda' \propto 1/v' \propto t$ and close to the elastic line ($\lambda' \approx \lambda$) it follows that $\Delta\omega \propto 1/\lambda^3$, i.e. the most efficient measure to increase the "elastic" resolution is the use of a long neutron wavelength/ For a matched setup the relative timing uncertainity $\Delta t/t_0$ and the relative wavelength width $\Delta\lambda/\lambda$ should be about equal. Eqn.10.33 shows in addition that the timing uncertainity term $\propto \Delta t$ dominates the resolution width for short time $t$, i.e. large energy gain of the neutron. If path uncertainities $\Delta L$ are treated separately, $\Delta t$ represents only the chopper opening and Eqn. 10.33 reads:

$$\Delta\omega = \sqrt{(\frac{m_n L}{\hbar t^2}\Delta L)^2 + (\frac{m_n L}{\hbar t^3}\Delta t)^2 + (\frac{4\pi^2\hbar}{m_n\lambda^3}\Delta\lambda)^2} \tag{10.34}$$

[10] For sample in form of thin plates the path uncertainity due to scattering position in the sample may be reduced for (only) one scattering angle (region) to the plate thickness.

For the inverted spectrometer the expressions stay the same expect for the exchange of $\lambda$ and $\lambda'$.

### 10.11.2 NSE

For NSE spectrometers the high energy resolution is not realized directly but comes as large (Fourier)time, $t$, in the intermediate scattering function $S(Q,t)$. Again the relative $Q$-resolution is less important for many applications. However, the range of interest often is located at small $Q$ where the large structures of typical "soft"-matter samples contribute to the scattering intensity. This implies that the covered solid angle is more limited than for the TOF instruments described above. The resolution in terms of maximum Fouriertime is either limited by the product $t = \lambda^3 \int |B| dl$ or by the field integral inhomogeniety within the paths in the neutron beam. The first limitation is given by the spectrum of the neutron source and the technical ability to increase the magnetic field. The second limitation depends on the ability to maintain equal field integrals by sufficiently accurate coils and correction elements. Currently the latter factor is the limiting one. High resolution NSE requires relative field integral of less than $10^{-5} \cdots 10^{-6}$. The effect of loss of resolution due to inhomgenieties is a strong reduction of the echo amplitude even for a perfectly elastic reference scatterer. An echo reduction by a factor of $\simeq 2$ marks the approximate resolution limit.

### 10.11.3 Intensity Issues

The available neutron sources are rather weak compared to sources of electromagnetic radiation (laser, synchrotron), they emit neutrons in form of a thermalized gas with a broad distribution of velocities and into all directions. Preparation of collimated and monochromatic beams is only possible by selection, i.e. removing all unwanted neutrons. The resulting beams –even at high flux reactors– contain only relatively few neutrons. [11] For this reason the available neutrons have to be utilized as efficient as possible. Even if an increase in resolution may be achieved by stricter wavevector $\underline{k}$ selection (velocity, direction) and by reduction of the chopper pulse length, it is often not advisable to enhance all elements of the resolution up to the technological limits because this goes along with a drastic loss of intensity (detector count rate). Design of (neutron)-spectrometers means the search for the best compromise between resolution and intensity. The optimum depends on the nature of the problem, i.e. the features and structures expected in $S(Q,\omega)$. TOF-spectrometer as described in this chapter are preferentially used to investigate isotropic to weakly anisotropic samples with only weak structures in $S(Q)$.

[11] The typical neutron flux in front of the chopper of a classical TOF instrument is in the order of $10^7$n/cm$^2$s, after chopping only $10^5$n/cm$^2$s hit the sample and are available for scattering. In comparison a beam of a small 1 mW HeNe laser is strictly collimated and monochromatic and represents an integral flux of $3 \times 10^{15}$Photonen/s with a cross section of maybe $1mm^2$, i.e. $3 \times 10^{17}$photons/cm$^2$s.

This enables the utilization of a large solid angle for detection which compensates for the losses caused by energy analysis. In the schematics of the spectrometers this is already indicated by the large number of detectors. Modern TOF instruments contain more than 1000 single counting tubes covering a detecting area of $30 \times 1\text{cm}^2$ each. The total area coverd by 1000 detectors is about $3\text{m}^2$, for a fligth path of 3 m this corresponds to a solid angle of 0.333 or 1000 degrees squared. Thereby an intensity gain of a factor 500 is obtained compared to a triple axis spectrometer with a detecting area of 2 degrees squared, the loss caused by the fact that the chopper opens only for about 1% of the time is more than compensated. In addition the TOF instrument has a multiplex advantage: all energy transfers are detected simultaneously and not sequentially as in the case of a triple-axis spectrometer. However it is seldom useful to sum the data of ALL detectors into one spectrum but different scattering angle regions have to be evaluated separately. Still they are measured all at the same time! Generally the TOF instruments is more efficient than a triple-axis spectrometer for isotroic samples. As soon as single crystals or very anisotropic samples with a strong dependence of the spectra on $\underline{Q}$ are to be investigated the conventional triple-axis spectrometers are better suited.

Since many NSE problems –as the NSE tecniques– do not allow to increase the solid angle to very large values, the intensity loss of high energy resolution must be recovered by other means. As it is explained above the NSE method decouples the incident beam enregy width from the energy transfer detection limit, it is possible to operate NSE spectrometers with 10% to 20% incident wavelength width. Thereby intense incoming beams may be employed. The reduction in $Q$-resolution associated with the wavelength width is often tolerable as in the typical SANS experiments. Even then the data collection efficiency of an NSE instrument can be boosted by empoying an area detector to cover an angular range of several degrees in horizontal and vertical direction.

Both TOF and NSE methods have resolutions that depend on $\lambda^3$ and therfore it is tempting to use this factor to increase resolution. But in the regime of long wavelength all available sources (even the cold sources) suffer from a $\lambda^{-5}$ dependence of intensity, which sets a practial limit of $\lambda = 15 \cdots 20\,\text{Å}$ for virtually all applications.

# Bibliography

[Marshall and Lovesey(1971)] W. Marshall and S. W. Lovesey, *Theory of Thermal Neutron Scattering* (Oxford University Press, London, 1971).

[Doi and Edwards(1994)] M. Doi and S. Edwards, *The Theory of Polymer Dynamics*, vol. 73 of *International Series of Monographs on Physics* (Oxford University Press, Oxford, 1994).

# Contents


10.1 Introduction . . . . . 1
10.2 The classic time-of-flight spectrometer . . . . . 3
10.2.1 Normal Geometry TOF-spectrometer . . . . . 3
10.2.2 Inverted Geometry TOF-spectrometer . . . . . 5
10.2.3 Transforms . . . . . 8
10.3 Neutron Spin-Echo Spectrometers . . . . . 9
10.3.1 The Resolution versus Intensity Trap . . . . . 9
10.3.2 The Spin-echo Knack . . . . . 10
10.4 Setup and function . . . . . 11
10.5 The detector signal . . . . . 13
10.5.1 Symmetric case . . . . . 14
10.5.2 Elastic scattering of a finite width wavelength distribution . . . . . 15
10.6 Experimental procedures and evaluation . . . . . 16
10.7 Field integral homogeneity and resolution . . . . . 17
10.8 Practical aspects, peculiarities . . . . . 18
10.9 Scattering cross section and time-of-flight spectra for some basic systems . 18
10.9.1 Ideal monoatomic Gas . . . . . 19
10.9.2 Ensemble of Harmonic Oscillators . . . . . 19
10.10 Measured Spectra . . . . . 26
10.11 Resolution and Intensity . . . . . 29
10.11.1 TOF . . . . . 29
10.11.2 NSE . . . . . 31
10.11.3 Intensity Issues . . . . . 31

# 11

# Structure determination

Gernot Heger

# 11. Structure determination

G. Heger

## 11.1 Introduction

The analysis of crystal structures and magnetic ordering is usually based on diffraction phenomena caused by the interaction of matter with X-rays, neutrons, or electrons. Even though electron microscopy can achieve atomic resolution, more detailed information on the 3-dim. atomic arrangement of crystals with its symmetry and chemical bonding, as well as 3-dim. magnetic structures and spin densities, requires diffraction methods. The basic theory of diffraction is the same for all types of radiation. Complementary information is achieved due to the different character of X-rays, neutrons and electrons, and hence their different interactions with matter and further practical aspects.

Considering only X-rays and thermal neutrons one finds that their wavelengths are similar (0.5 Å < λ < 2.4 Å). While the electromagnetic X-ray radiation yields the total electron density distribution, the nuclear scattering of neutrons probes the density distribution of the nuclei and the magnetic neutron scattering determines the spin density of unpaired electrons.

X-ray diffraction using conventional laboratory equipment and/or synchrotron installations is the most important method for structure analyses. The purpose of this paper is to discuss special cases, for which, in addition to this indispensable part, neutrons are required to solve structural problems. Even though the huge intensity of modern synchrotron sources allows in principle the study of magnetic X-ray scattering, the investigation of magnetic structures is still one of the most important applications of neutron diffraction.

## 11.2 Structure factor and Bragg intensities

The characteristic feature of the crystalline state consists of its periodic order, which may be represented by a (translation) lattice. In the 3-dim. case three basis vectors $\underline{a}$, $\underline{b}$, and $\underline{c}$ define a parallelepiped, called unit cell. The general lattice vector

$$\underline{\tau} = u\underline{a} + v\underline{b} + w\underline{c} \qquad (1)$$

results from a linear combination of the basis vectors with coefficients $u$, $v$, and $w$ being positive or negative integers (incl. 0). According to their point-symmetry properties seven crystal systems are distinguished:

*Triclinic*, *Monoclinic*, *Orthorhombic*, *Tetragonal*, *Trigonal*, *Hexagonal*, and *Cubic*.

IN addition to the seven primitive lattices, with only one lattice point per unit cell, multiple lattices with centred unit cells are possible. In this way a total of 14 Bravais lattices is defined.

The position of atom j in the unit cell is given by the vector

$$\underline{r}_j = x_j\underline{a} + y_j\underline{b} + z_j\underline{c}. \quad (2)$$

The coefficients $x_j$, $y_j$, and $z_j$ are called atomic coordinates ($0 \le x_j < 1$; $0 \le y_j < 1$; $0 \le z_j < 1$).

Lattice planes (that means a set of parallel planes containing lattice points) defined by three integers (*hkl*), called Miller indices, have the characteristic interplanar spacing $d_{hkl}$.

For scattering studies of crystals the concept of the reciprocal lattice with the basis vectors $\underline{a}^*$, $\underline{b}^*$, and $\underline{c}^*$ was developed. In crystallography, the lattice vector of the reciprocal lattice is defined by

$$\underline{H} = h\underline{a}^* + k\underline{b}^* + l\underline{c}^*. \quad (3)$$

In solid state physics, instead of $\underline{H} = 1/d_{hkl}$, normally used is the scattering vector

$$\underline{Q} = 2\pi\underline{H}. \quad (4)$$

### 11.2.1 Nuclear scattering

In the kinematical approximation, assuming that the magnitude of the incident wave amplitude is the same at all points in the specimen (this implies a small sample size, weak scattering intensities, no multiple diffraction and neglecting of absorption), the diffracted intensity is proportional to the square of the amplitude of the scattered wave for each individual reflection; it can be regarded as a weight ascribed to the reciprocal-lattice nodes

$$I(\underline{H}) \sim |F(\underline{H})|^2. \quad (5)$$

The structure factor $F(\underline{H})$, in terms of the Fourier transform, contains the complete information on the distribution of the scattering density in the unit cell, including the atomic coordinates $x_j$, $y_j$, and $z_j$,

$$F(\underline{H}) = \sum_j b_j \exp[2\pi i(\underline{H}\cdot\underline{r}_j)]\cdot T_j(\underline{H}) = |F(\underline{H})|\cdot\exp[i\varphi(\underline{H})]. \quad (6)$$

In the case of nuclear scattering of neutrons the structure factor has the dimension of a length, as has the scattering length $b_j(\underline{H}) = b_j$ = const. of nucleus j. $T_j(\underline{H})$ is the Debye-Waller factor which takes into account dynamical and static displacements of the nucleus j from its average position $\underline{r}_j$ (see Eq. 2) in the unit cell. With the fractional coordinates $x_j$, $y_j$ and $z_j$ the scalar product in the exponential function can be written as

$$\underline{H}\cdot\underline{r}_j = hx_j + ky_j + lz_j. \quad (7)$$

**Important:** The measured Bragg intensities $I(\underline{H})$ from diffraction experiments yield only the modulus of the structure factors, $|F(\underline{H})| \propto \sqrt{I(\underline{H})}$, and not their phases $\varphi(\underline{H})$ (see Eq. 6), which would be required for the inverse Fourier transform of the data (Fourier synthesis) to give directly the arrangement of the atoms in the unit cell. The lack of the phase information is known as the phase problem of crystallography.

In a diffraction experiment normally only relative Bragg intensities are measured. A SCALE factor is assumed to be rigorously the same for all reflections of one data set. For merely nuclear neutron scattering and single crystals the integrated relative intensities are given by

$$I(\underline{H}) = \text{SCALE} \cdot L \cdot A \cdot |F(\underline{H})|^2. \tag{8}$$

The Lorentz factor L is instrument specific. The absorption correction A depends on the geometry and linear absorption coefficient of the sample.

The geometrical diffraction conditions and hence the reciprocal lattice yield the periodicity of a crystal. Information on the crystal system, the Bravais lattice type and the basis vectors $\underline{a}$, $\underline{b}$, $\underline{c}$ of the unit cell (lattice constants a, b, c, $\alpha$, $\beta$, $\gamma$) may be directly deduced from the reciprocal lattice. The $|F(\underline{H})|^2$ values associated as weights to the nodes of the reciprocal lattice give the diffraction symbol and hence valuable information on the space-group symmetry. Here systematic absences (zero structure factors) can be related to the choice of a non-primitive Bravais lattice, or to the presence of non-symmorphic symmetry operations (symmetry operations with translation components).

### 11.2. 2 Magnetic scattering

The dipolar interaction between the neutron magnetic moments and the magnetic moments of atoms/ions (and nuclei) $\underline{m}_j$ leads to the magnetic neutron scattering in addition to the nuclear contribution. In the case of an ordering of the magnetic moments over the whole crystal (periodic magnetic structure) the magnetic structure factor is given by

$$F_M(\underline{H}) = \sum_j b_{Mj}(\underline{H}) \cdot \exp[2\pi i(\underline{H} \cdot \underline{r}_j)] \cdot T_j(\underline{H}) \tag{9}$$

with the magnetic scattering amplitude

$$b_{Mj}(\underline{H}) = (e^2\gamma/2m_ec^2) \cdot f_{Mj}(\underline{H}) \cdot \sigma \cdot \underline{m}_{\perp j}(\underline{H}). \tag{10}$$

$\frac{1}{2}\sigma$ is the neutron spin operator and $\underline{m}_{\perp j}(\underline{H})$ the projection of the magnetic moment $\underline{m}_j$ onto the scattering plane (*hkl*). The magnetic form factor $f_{Mj}(\underline{H})$ is the Fourier transform of the normalised magnetisation density $M_j(\underline{r})$ of the atom or ion j:

$$f_{Mj}(\underline{H}) = \int_V M_j(\underline{r}) \cdot \exp[2\pi i(\underline{H} \cdot \underline{r})] \cdot d\underline{r} \qquad (11)$$

with $f_M(0) = \int_V M_j(\underline{r}) \cdot d\underline{r} = 1$.

This is a function of the reciprocal lattice vector $\underline{H}$, whereas the atomic scattering factor $f_j$ of X-ray diffraction

$$f_j(|\underline{H}|) = \int_V \rho_j(r) \cdot \exp[2\pi i(\underline{H} \cdot \underline{r})] \cdot d\underline{r}, \qquad (12)$$

for a spherical electron density $\rho_j(r)$, depends only on the length of $\underline{H}$.

The intensity of magnetic and nuclear neutron scattering is of the same order of magnitude. For unpolarised neutrons the Bragg intensity of nuclear and magnetic neutron diffraction is simply an incoherent superposition

$$I(\underline{H}) = I_N(\underline{H}) + I_M(\underline{H}) \sim |F_N(\underline{H})|^2 + |F_M(\underline{H})|^2. \qquad (13)$$

For polarised neutrons on the other hand the coherent superposition gives

$$[|F(\underline{H})|^2]^{\pm} = |F_N(\underline{H}) \pm F_M(\underline{H})|^2 \qquad (14)$$

with the interference terms $\pm\ 2 \cdot |F_N(\underline{H}) \cdot F_M(\underline{H})|$ according to the two possible directions of polarisation (+ and -). In measuring the flipping ratio at superimposed Bragg reflections, that means the ratio of the intensities for the two polarisations up and down, even small magnetic structure factors can be determined quite accurately.

The analysis of a magnetic structure starts with the determination of its periodicity with respect to that of the crystal structure. The identification of magnetic reflections is usually accomplished by a careful comparison of powder diagrams recorded below and above the magnetic phase transition temperatures. A more detailed study of the scattering vectors, e.g. for incommensurate structures, may require also single-crystal experiments. The nuclear structure factors $F_N(\underline{H})$ can be calculated from the known crystal structure. In this way the SCALE factor of the data set can be obtained and the absolute values of the magnitudes of the magnetic structure factors $|F_M(\underline{H})|$ can be determined. The individual orientations of the magnetic moments $\underline{m_j}$ with respect to the basis vectors of the crystal lattice and their magnitudes are then to be calculated.

### 11.3 Contrast variation

Neutron diffraction can be used for an experimental distinction of atoms/ions with almost equal X-ray scattering amplitudes. In the case of mixed systems it is furthermore possible to determine a fractional site occupation. Another application of neutron diffraction is the

determination of accurate atomic parameters (positional and thermal parameters, site occupations) of lighter elements in the presence of heavy ones.

The contrast in conventional X-ray diffraction is directly related to the ratio of the number of electrons $Z_j$ of the different atoms or ions j involved. The atomic scattering factor $f_j$ in the structure-factor formula, which represents the Fourier transform of the atomic electron density distribution, is proportional to $Z_j$ ($f_j = Z_j$ for $\sin\theta/\lambda = 0$). Standard X-ray techniques can hardly differentiate between atoms/ions with a similar number of electrons, and only an average structure - including a total occupation probability of mixed occupied sites - may be obtained in such cases.

For neutrons the atomic scattering factor $f_j$ is replaced by the nuclear scattering length (or coherent scattering amplitude) $b_j$, which is of the same order of magnitude for all nuclei but varies from nucleus to nucleus in a non-systematic way. $b_j$ values, which can be either positive or negative, depend on the isotopes and nuclear spin states of the element j. A nucleus of an isotope with spin I may have two different neutron scattering lengths: one for the combined spin state $J = I + ½$ and one with $J = I - ½$. An important and fundamental example is provided by the simplest of all nuclei, the proton with spin $I = ½$. The two spin states, $J = 1$ (triplet) and $J = 0$ (singlet), with statistical weights ¾ and ¼ respectively, have the scattering lengths for a *free* proton:

$b^s_H = -23.7$ fm, $b^t_H = +5.38$ fm, $b_{freeH} = ¼b^s_H + ¾b^t_H = -1.89$ fm (with $10^{-15}$ m = 1 fm).

The value for the *bound* proton in a crystal structure, which is to be used in the structure-factor calculations, amounts to $b_H = 2 \cdot b_{freeH} = -3.741$ fm.

The natural isotope mixture and a statistical spin-state distribution lead to the commonly used general formula $b_j = \alpha \cdot b_{j\alpha} + ß \cdot b_{jß} + \gamma \cdot b_{j\gamma} + \ldots$ with the sum of the different isotope fractions $\alpha + ß + \gamma + \ldots = 1$ ($b_{j\alpha}$, $b_{jß}$, $b_{j\gamma}$ being the individual scattering lengths of the different isotopes of the element j). The natural nickel isotopes, for instance, have extremely different coherent scattering amplitudes:

$b(^{58}Ni) = +14.4$ fm, $b(^{60}Ni) = +3.0$ fm, $b(^{61}Ni) = +7.6$ fm, $b(^{62}Ni) = -8.7$ fm, $b(^{64}Ni) = -0.37$ fm resulting in an overall scattering length $b_{Ni} = +10.34$ fm.

Neutron experiments frequently make use of compounds containing single isotope elements, like fully deuterated samples. Incoherent scattering due to a statistical distribution of isotopes and nuclear spin states is not discussed here. It may influence the effective absorption and the background conditions of neutron diffraction studies.

### 11.3.1 Example of contrast variation:

**Crystal structure and magnetic ordering of $(Mn_{1-x}Cr_x)_{1+\delta}Sb$**

A special possibility of contrast variation, the combination of X-ray and neutron diffraction information, is demonstrated for the example of the intermetallic compounds $(Mn_{1-x}Cr_x)_{1+\delta}Sb$, with $0 \leq x \leq 1$ [1]. This solid solution system is of special interest due to its magnetic properties: competing magnetic interactions with isotropic ferromagnetic behaviour for $Mn_{1+\delta}Sb$ and an uniaxial antiferromagnetic structure for $Cr_{1+\delta}Sb$. It crystallises in the hexagonal NiAs-type structure (space group: $P6_3/mmc$) with some additional partial occupation ($\leq 0.14$) of the interstitial site 2(d) (see Fig. 1):

Ni: 2(a) - 0,0,0; 0,0,1/2 and As: 2(d) - 2/3,1/3,3/4; 1/3,2/3,1/4.

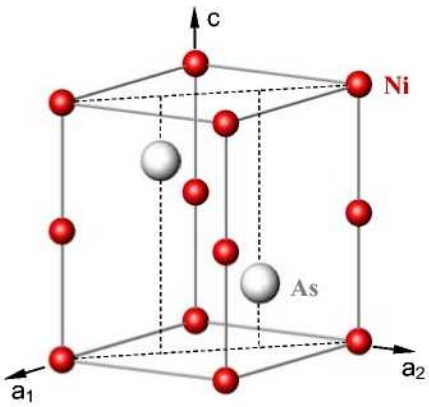



Fig. 1(a). NiAs structure

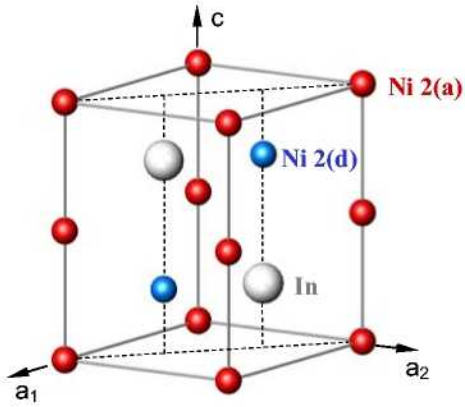



Fig. 1(b). $Ni_2In$ structure (filled NiAs-type)

Conventional X-ray diffraction cannot differentiate between chromium ($Z_{Cr}$= 24) and manganese ($Z_{Mn}$= 25) on these sites but yields important information on their overall occupation probabilities M = (Mn,Cr): $M_aM_dSb$, where $M_a$ stands for the occupation probability of site 2(a) and $M_d$ for that of site 2(d). The Sb position is assumed to be fully occupied, thus serving as an internal standard.

The corresponding nuclear scattering lengths of neutron diffraction are extremely different with a negative sign for manganese: $b_{Cr}$ = +3.52 fm and $b_{Mn}$ = -3.73 fm.

**Remember:** A positive value of $b_j$ means that there is a phase shift of 180° between the incident and scattered neutron waves as a consequence of predominant potential scattering. The few negative $b_j$ values - no phase change - result from resonant scattering.

The knowledge of the overall occupation probabilities $M_a$ and $M_d$ - from conventional X-ray studies - allows the evaluation of the Cr : Mn ratios of the different sites 2(a) and 2(d) from the corresponding effective scattering lengths determined by neutron diffraction. In the structure analyses based on the neutron data $b_{eff} = b_{Mn} \cdot PP$ is obtained individually for the two sites ($PP_a$ and $PP_d$ stands for refined pseudo-occupation probabilities). According to

$$b_{eff}(2a) = M_a[(1-y) \cdot b_{Mn} + y \cdot b_{Cr}] \quad \text{and} \quad b_{eff}(2d) = M_d[(1-z) \cdot b_{Mn} + z \cdot b_{Cr}]$$

we can calculate (with replacing $M_a = a$ and $M_d = d$)

$$y = [b_{eff}(2a)/a - b_{Mn}] \,/\, [b_{Cr} - b_{Mn}] \quad \text{and} \quad z = [b_{eff}(2d)/d - b_{Mn}] \,/\, [b_{Cr} - b_{Mn}].$$

The detailed site occupations lead to the general formula

$$(Mn_{1-y}Cr_y)_a(Mn_{1-z}Cr_z)_dSb$$

site 2(a) site 2(d)

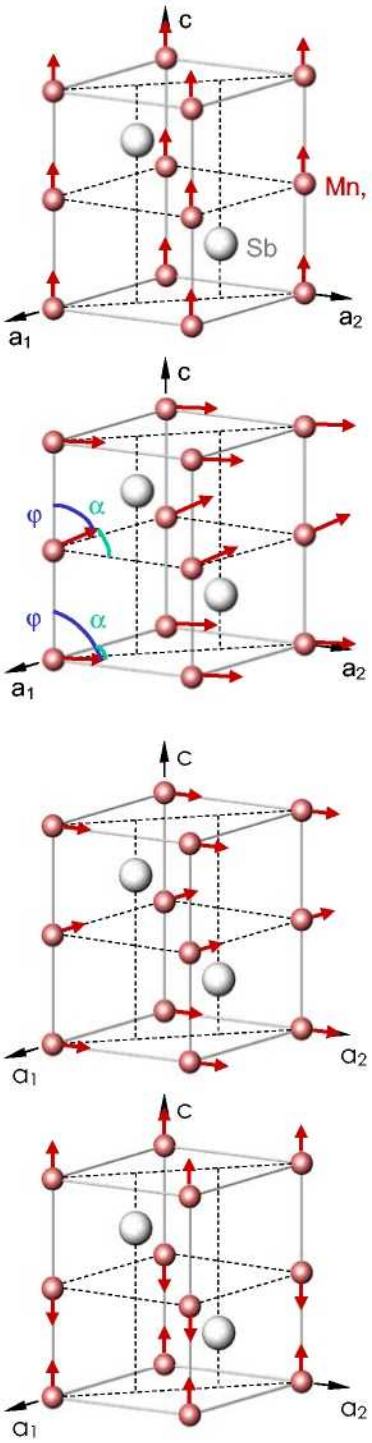
corresponding to a chemical composition of $Mn_{[(1-y)a + (1-z)d]}Cr_{[ya + zd]}Sb$.

It is evident, that the individual (Cr,Mn) distributions on the two crystallographically different sites 2(a) and 2(d) are not accessible merely by a chemical analysis. For most of the samples studied, the site 2(a) was found to be fully occupied: $a \approx 1.0$. But the formula $(Mn_{1-x}Cr_x)_{1+\delta}Sb$ used normally is only correct for the special case of equal Cr : Mn ratios on both sites:

$$x = y = z \quad \text{and} \quad 1 + \delta = a + d.$$

The detailed information on the (Cr,Mn) distribution is needed to explain the magnetic properties of these intermetallic compounds, for which only the spins localised on the 2(a) sites are involved in the magnetic ordering leading to a complex magnetic phase diagram of the MnSb – CrSb system (see Fig. 3). An overall Cr : Mn ratio from chemical analysis is not sufficient. The ferromagnetic $Mn_{1+\delta}Sb$ changes its axis of easy magnetisation from parallel to the hexagonal c-axis at high temperatures to $\perp$c at low temperatures. The magnetic spins of the uniaxial antiferromagnetic $Cr_{1+\delta}Sb$ are oriented parallel (or antiparallel) to c. For solid solutions $(Mn_{1-x}Cr_x)_{1+\delta}Sb$ between the pure end members there exist various ferro- and antiferromagnetic states with inclined spin orientations, with non-colinear magnetic arrangements, and regions with co-existing magnetic ordering. Several magnetic structures of the intermetallic MnSb – CrSb system are shown in Fig. 2.

| |
|---|
| In general, a statistical occupation of one crystallographic site with three kinds of scatterers - e.g. Mn, Cr, and "vacancies" - requires at least two independent and sufficiently different experimental data to determine the fractional occupancies. |




Ferromagnetism:
spin orientation ‖c

Canted magnetic structure
(weak ferromagnet):
the spins are turned away from [001]
by an angle φ and within the (001) planes
with an antiphase rotation around c by α

Canted magnetic structure:
canting angle α = 60°
all spins lie in (001) planes

Antiferromagnetism:
spin orientation ‖c

Fig. 2. Various types of magnetic structures in the intermetallic system $(Mn_{1-x}Cr_x)Sb$ (NiAs structure type)

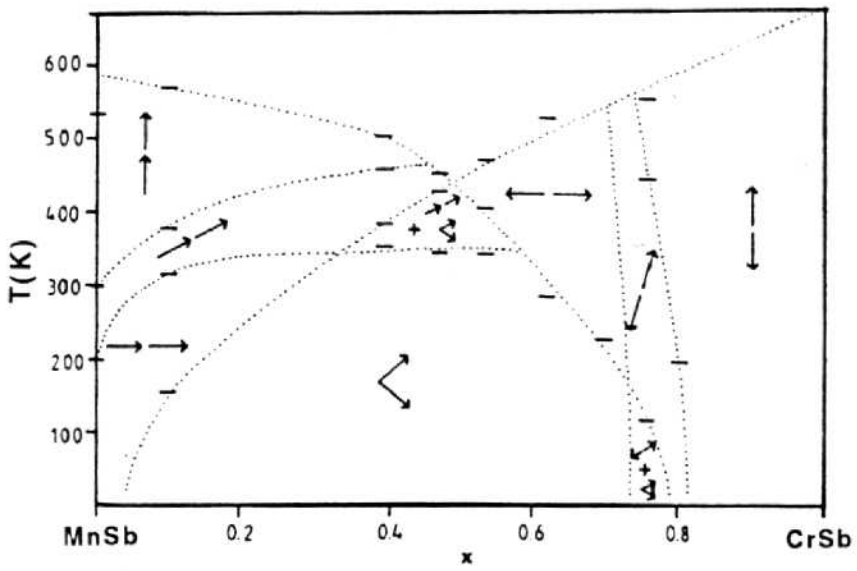



Fig. 3. Magnetic phase diagram of the intermetallic system MnSb – CrSb. The vectors indicate the spin orientations in the different magnetic structures.

**11.4 The hydrogen problem in structure analysis**

The determination of the structure parameters of hydrogen atoms is a special problem involving different aspects of X-ray and neutron diffraction. It is obvious that H/D atoms with Z = 1 give only a small contribution to the electron density and, therefore, they are hardly visible in X-ray structure analyses. This holds especially when heavy atoms are present. But there is a more general problem: the single electron of H/D is engaged in the chemical bonding and is not localised at the proton/deuteron position. This position, however, is of importance when hydrogen bonds - possibly related to the lattice dynamics or structural phase transitions - are discussed.

X-ray studies of electron densities of simple molecular crystals, for which theoretical calculations for isolated molecules are possible, are of special interest in order to compare experimental and theoretical results for a better understanding of chemical bonding in crystalline solids. Molecular crystals consist normally of light atoms often including hydrogen. A combination with neutron diffraction experiments is important to determine the structure parameters of the H/D atoms properly. More generally, the structure analysis by neutron diffraction yields separately and independently from the X-ray data the structure parameters of all atoms including the mean square displacements due to static and dynamic (even anharmonic) effects. This complete information can be used in a so-called X-N

synthesis to obtain experimental electron deformation densities from the measured X-ray Bragg intensities.

### 11.4.1 Example of the determination of H/D positions:

**Study of hydrogen bonds in $Na_2S{\cdot}9D_2O$**

One of the most important fields of application of neutron diffraction is the determination of H/D sites and of their Debye-Waller factors. As an example of a study of a variety of hydrogen bonds, where the structure model was established by conventional X-ray analysis and where neutron diffraction served especially to localise the hydrogen atoms, the case of fully deuterated $Na_2S{\cdot}9D_2O$ was chosen [2]. Its crystal structure (non-centrosymmetric, space group $P4_122$ or $P4_322$) is dominated by discrete $[Na(D_2O)_5]$ and $[Na(D_2O)_4]$ spiral chains of $Na(D_2O)_6$ octahedra (see Fig. 4). There are five different water molecules (see Fig. 5) with O-D distances between 0.949 Å and 0.983 Å, and D-O-D angles from 104.6° to 107.5°. These water molecules are furthermore involved in six different O-D...S bridges to the $S^{2-}$ ions. Details of the various O-D...O/S hydrogen bonds (given in Table I) were combined with results from Raman spectroscopy from which the uncoupled O-D(H) stretching frequencies could be reasonably well assigned to the nine different O-D(H) groups of the crystal structure.

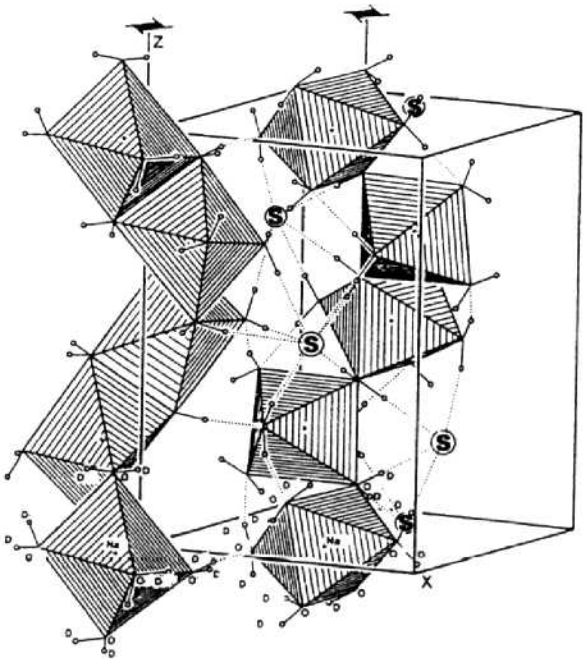



Fig. 4. $Na_2S{\cdot}9D_2O$: A partial view of the crystal structure

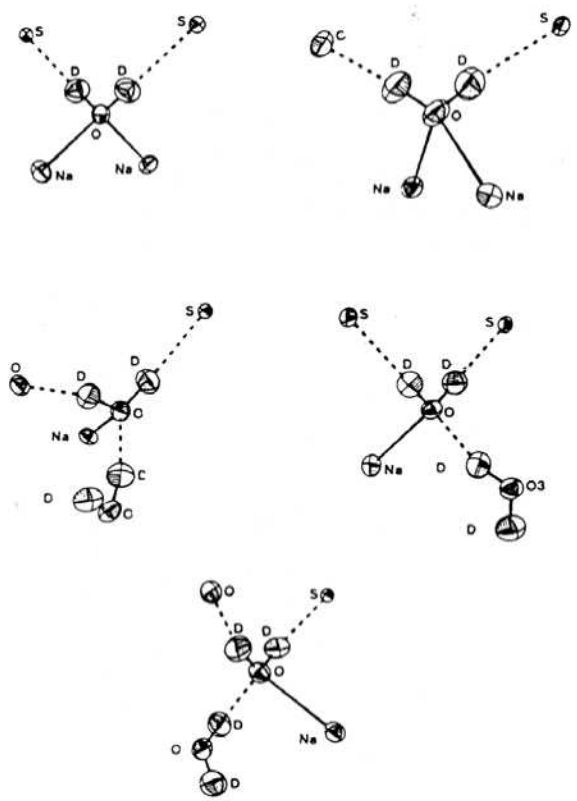


Fig. 5. Coordination of the $D_2O$ molecules in $Na_2S{\cdot}9D_2O$.

| A | B | C | A-B | B-C | A-C | ∠BAC | ∠ABC | ∠BAB' | ∠CAC' | L | A-L | ∠LAL' |
|---|---|---|---|---|---|---|---|---|---|---|---|---|
| O(1) | -D(1)...S | | 0.961(7) | 2.359(5) | 3.319(5) | 1.4(4) | 178.0(6) | 106.3(7) | 103.4(2) | Na(1) | 2.411(4) | 116.1(2) |
| | -D(1')...S | | 0.961(7) | 2.359(5) | 3.319(5) | 1.4(4) | 178.0(6) | | | Na(1') | 2.411(4) | |
| O(2) | -D(21)...O(5) | | 0.964(7) | 1.793(7) | 2.752(7) | 4.9(4) | 172.4(6) | 106.1(7) | 111.5(2) | Na(2) | 2.588(5) | 97.6(2) |
| | -D(22)...S | | 0.962(7) | 2.550(6) | 3.506(5) | 5.2(4) | 172.8(6) | | | Na(2') | 2.380(5) | |
| O(3) | -D(31)...S | | 0.977(7) | 2.311(5) | 3.284(5) | 4.7(4) | 173.3(5) | 107.5(7) | 116.9(2) | Na(1) | 2.397(5) | 104.8(2) |
| | -D(32)...O(4) | | 0.953(7) | 1.797(7) | 2.730(7) | 9.6(4) | 165.3(6) | | | O(5) | 2.768(7) | |
| O(4) | -D(41)...S | | 0.983(7) | 2.294(5) | 3.274(4) | 3.4(4) | 175.1(5) | 104.6(6) | 104.1(2) | Na(2) | 2.418(5) | 105.5(2) |
| | -D(42)...S' | | 0.973(7) | 2.359(5) | 3.333(5) | 0.3(4) | 179.6(5) | | | O(3) | 2.730(7) | |
| O(5) | -D(51)...O(3) | | 0.949(7) | 1.838(7) | 2.768(7) | 9.2(4) | 166.1(6) | 105.5(6) | 103.4(2) | Na(1) | 2.485(5) | 101.7(2) |
| | -D(52)...S | | 0.967(7) | 2.441(5) | 3.401(5) | 5.7(4) | 172.1(5) | | | O(2) | 2.752(7) | |
| mean values | | | 0.965 | | | | | 106.0 | 107.9 | <Na-O> | 2.447 | |
| mean values O-D...O | | | 0.955 | 1.809 | 2.750 | | 167.9 | | | | | |
| mean values O-D...S | | | 0.970 | 2.386 | 3.353 | | 175.2 | | | | | |

Table I. Interatomic distances (Å) and angles (°) of the hydrogen bonds in $Na_2S{\cdot}9D_2O$.

**Remember:** The scattering lengths of the proton and the deuteron are $b_H$ = -3.74 fm and $b_D$ = +6.67 fm, respectively. Their magnitudes are comparable with the average of all $b_j$ magnitudes and, therefore, H/D can be considered as "normal" atoms for neutron diffraction. The different signs of $b_H$ and $b_D$ may be of interest in Fourier maps for contrast reasons. Experimental conditions like background and effective absorption are strongly affected by the huge and exceptional incoherent neutron scattering cross-section of hydrogen ($\sigma_{inc}(H)$ = 79.7 barns as compared to $\sigma_{inc}(D)$ = 2.0 barns).Very often deuterated compounds are preferred in order to profit from the larger $b_D$ value, but mainly to reduce the background from incoherent scattering. This volume-dependent background may become crucial for neutron powder diffraction experiments, for which normally sample volumes of more than 1 $cm^3$ are required.

### 11.4.2 Example of a study of H/D ordering:

**Ferroelectric phase transition in $RbH_2PO_4$ (RDP)**

The hydrogen problem in crystal structure analysis is of special importance for structural phase transitions driven by proton ordering. $KH_2PO_4$ (KDP) is the most well-known representative of hydrogen-bonded ferroelectrics. A characteristic feature of its crystal structure consists of a three-dimensional network of $PO_4$-groups linked by strong hydrogen bonds (Fig. 6).

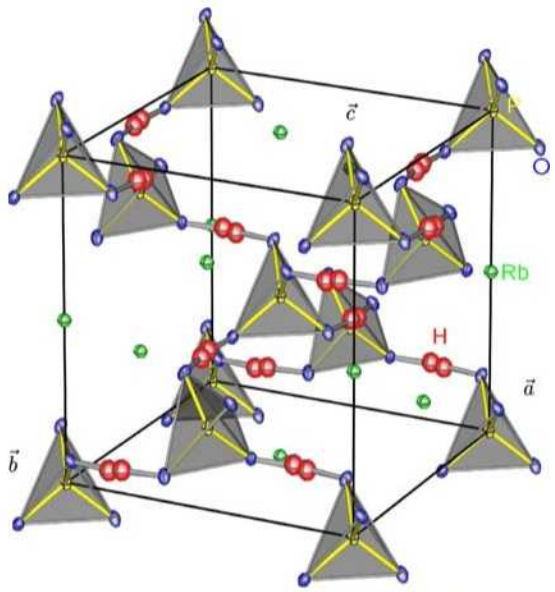



Fig. 6. Crystal structure of the paraelectric phase of $RbH_2PO_4$ (RDP) with a split-model representation of the hydrogen disorder

The temperature of the ferroelectric phase transition is extremely different for protonated KDP, $T_C$(KDP) = 122 K, and deuterated $KD_2PO_4$ (DKDP), $T_C$(DKDP) = 229 K. This huge H/D-isotope effect proves that hydrogen ordering is the major factor for this phase transition. Another type of H/D-isotope effect was found for $Tl(H,D)_2PO_4$ (TDP/DTDP) and $Rb(H,D)_2PO_4$ (RDP/DRDP), where a different polymorphism between the protonated and deuterated phases exists.

In the paraelectric phase at room temperature KDP crystallises in the tetragonal space group I $\bar{4}$2d, where the H-atoms are dynamically disordered in symmetric O···H···O bonds, which are almost linear with short O–O distances, typically in the range of 2.5 Å. The disordered H-distribution may be interpreted as corresponding to a double-well potential [3]. Results of crystal structure analyses on the rubidium compound RDP, isotypic to KDP, are presented here (Fig. 6, 7, 8) [4].

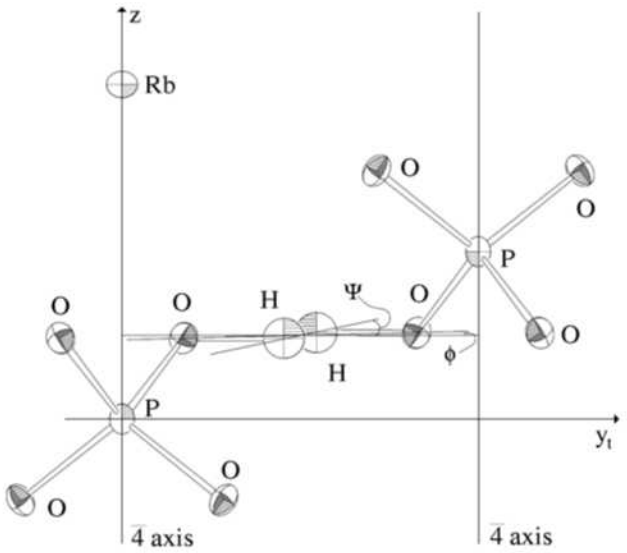



Fig. 7. Hydrogen disorder (split-model description) in the $PO_4$···H-H···$PO_4$ hydrogen bond of RDP at $T_C$ + 4 K (atoms are represented by their mean-square displacement ellipsoids).

At $T_C$ = 147 K, RDP transforms to a ferroelectric phase of orthorhombic symmetry (space group: Fdd2) in which the protons order in short asymmetric O-H···O bonds (Fig. 9). The $PO_4$-tetrahedra show a characteristic deformation with two shorter and two longer P-O

distances due to a transfer of electron density to the covalent O–H bonds. The electrical dipole moments are oriented ||z which give rise to a polarisation in c-direction.

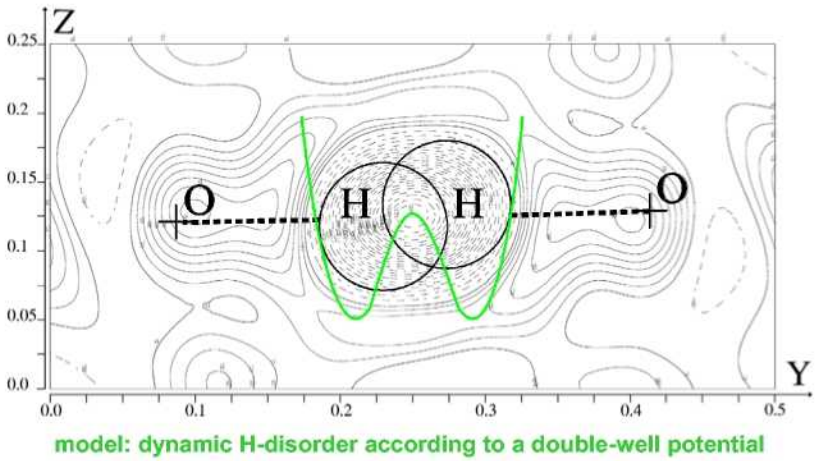



Fig. 8. Difference-Fourier-plot of the negative proton density in the hydrogen bond of Fig. 7 indicated by broken contour lines.

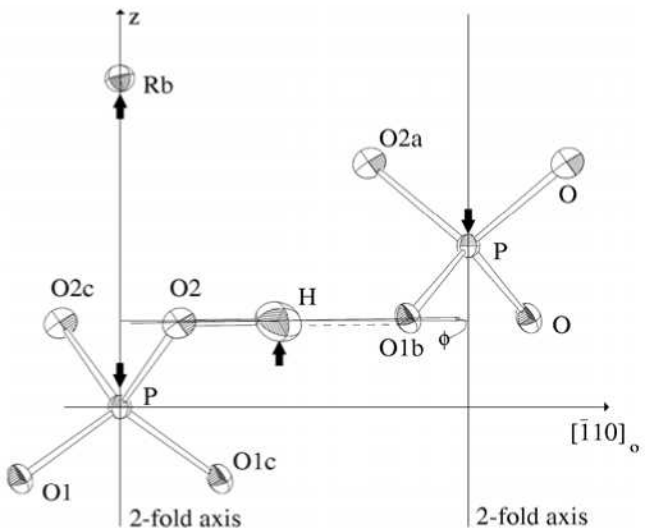



Fig. 9. Ferroelectric deformed structure (indicated by arrows) of RDP close to the phase transition at $T_C - 1$ K (presentation as in Fig.7).

.

### 11.5 Molecular disorder

Disordered structures and pseudosymmetries related to dynamical reorientation and/or structural phase transitions are of great current interest. In principal, the dynamical disorder of molecules is due to the fact that the intramolecular bonds are very much stronger than the external ones between the molecular groups and the surrounding crystalline frame. It is obvious that the chemical bonding scheme determines the symmetry of a crystal structure, and not the other way around. We can state, however, that in the case of an incompatible point-group symmetry of a molecule with respect to its site symmetry in the crystal structure, molecular disorder is the necessary consequence. In order to model the atomic density distributions correctly in a way to obtain physically meaningful potentials, very accurate Bragg intensities over a large $\sin\theta/\lambda$ range are required. X-ray experiments are generally more restricted than neutron studies because of the decrease of the atomic scattering factor $f_j$ with $\sin\theta/\lambda$.

#### 11.5.1 Example of molecular disorder:

**Almost free rotation of $NH_3$ groups in the crystal structure of $Ni(NH_3)_6I_2$**

As an example, related to the H/D problem, the dynamical disorder of the $NH_3$ group in the cubic high-temperature phase of the metal hexamine halide $Ni(NH_3)_6I_2$ (space group: Fm3m) is presented. The corresponding crystal structure is shown in Fig. 10.

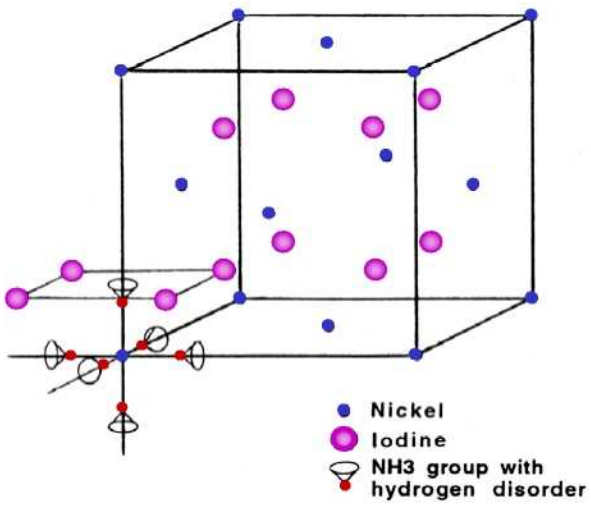



Fig. 10. High-temperature structure of $Ni(NH_3)_6I_2$, the hexamine coordination is shown only for the Ni atom at the origin.

With the $NH_3$ tetrahedra (3m symmetry) on crystallographic sites of 4mm symmetry it is obvious that they must be orientationally disordered. At 19.7 K, $Ni(NH_3)_6I_2$ undergoes a first-order phase transition to a probably ordered rhombohedral low-temperature modification [5].

Single-crystal neutron diffraction experiments of $Ni(NH_3)_6I_2$ have been performed at 295 K and 35 K [6] in order to study the proton density distribution. Fig.11 shows a Fourier density map of a [110] section with the negative proton density of the $NH_3$-group represented by broken contour lines.

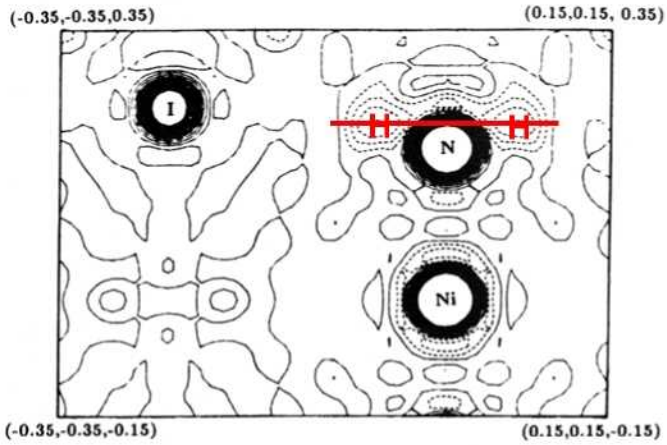



Fig. 11. Fourier map ([110] section) of the nuclear density of $Ni(NH_3)_6I_2$. The negative proton contributions of the amine-group are represented by broken contour lines, its orientation perpendicular to the fourfold axis is indicated by a horizontal beam.

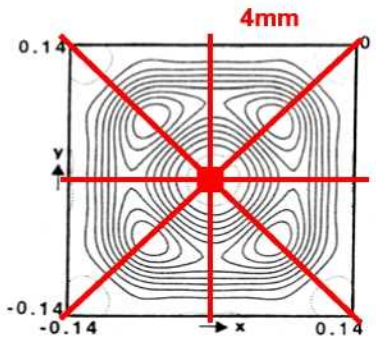



Fig. 12. Proton density of $Ni(NH_3)_6I_2$ at 295 K, (001) section at z = 0.23 (represented by continuous contour lines). The four maxima are directed towards adjacent iodines (N–H···I hydrogen bonds).

The H-density of a [001]-section perpendicular to the fourfold axes (corrected for contributions of the neighbouring nitrogen) reveals the 4mm symmetry (Fig. 12). Its four maxima are directed towards the adjacent iodines according to the influence of N-H···I hydrogen bonding. This proton density can be explained as a consequence of a coupled rotational-translational motion of the amine-group. The experimental results obtained at 295 K and 35 K are perfectly reproduced by corresponding model calculations (see Fig. 13).

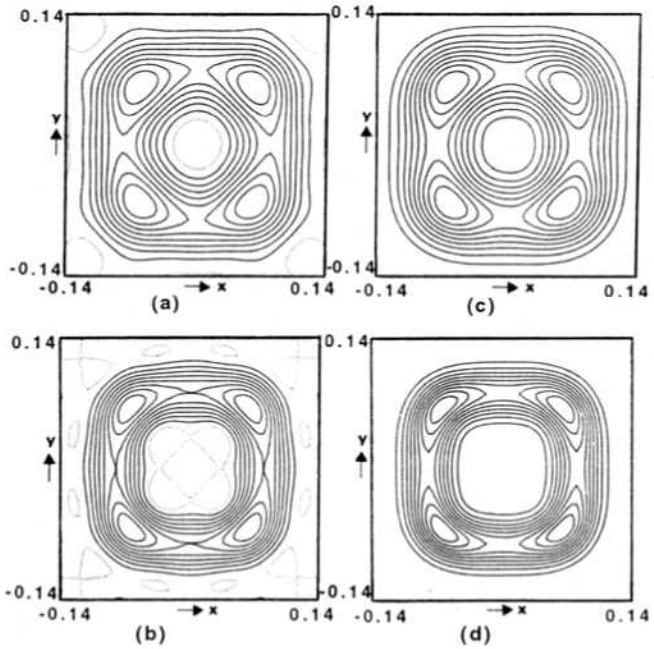



Fig. 13. $Ni(NH_3)_6I_2$: Proton density in a (001) section at z = 0.23;
(a) and (b) experimental results at 295 K and 35 K,
(c) and (d) calculated densities at 295 K and 35 K.

### 11.6 Example for a spin density study in magnetic molecular compounds:

### *p*-NPNN, an organic ferromagnet,

### β-4,4,5,5-tetramethyl-2-*p*-(nitro-phenyl)-3-oxido-4,5-dihydro-imidazolium 1-oxyl

Molecular magnetic compounds are of great actual interest due to both, applicational perspectives and fundamental research. The spin density distribution is an essential information for the understanding of the magnetic properties of these materials; it yields the localisation of the magnetic electrons and gives rise to the microscopic magnetic interactions. Polarised neutron diffraction on single crystals is presently the most powerful tool for

determining the spin densities in molecular compounds [7]. For ferromagnetic or paramagnetic single crystals with magnetic moments aligned by an external magnetic field, the spin density can be determined by the so-called flipping ratio method. The intensity of reflections is measured with polarization of the neutrons parallel and antiparallel to the magnetisation direction. From their ratio can be calculated the magnetic structure factors.

In this way, the spin density of the purely organic ferromagnet β-4,4,5,5-tetramethyl-2-*p*-(nitro-phenyl)-3-oxido-4,5-dihydro-imidazolium 1-oxyl (*p*-NPNN) was investigated. *p*-NPNN has an orthorhombic crystal structure with the non-centrosymmetric space-group Fdd2 (Fig.14).

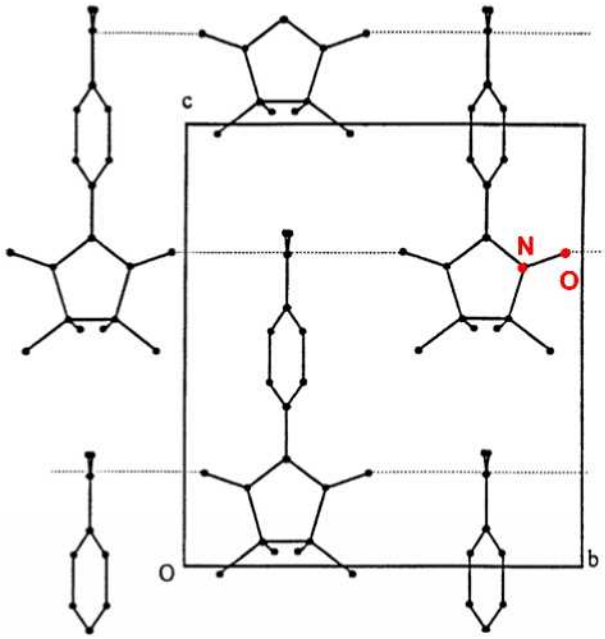



Fig. 14. Relative arrangement of the molecules in the crystal structure of .*p*-NPNN, one of the N-O groups is specially marked. Possible magnetic interactions are indicated by dotted lines.

Results obtained from a data treatment by the maximum-entropy reconstruction method are presented in Fig. 15 for the purely organic ferromagnet, β-4,4,5,5-tetramethyl-2-*p*-(nitro-phenyl)-3-oxido-4,5-dihydro-imidazolium 1-oxyl (*p*-NPNN) [8]. It is remarkable that the major spin density contributions are displaced off the N-O bond above and below the molecular plane.

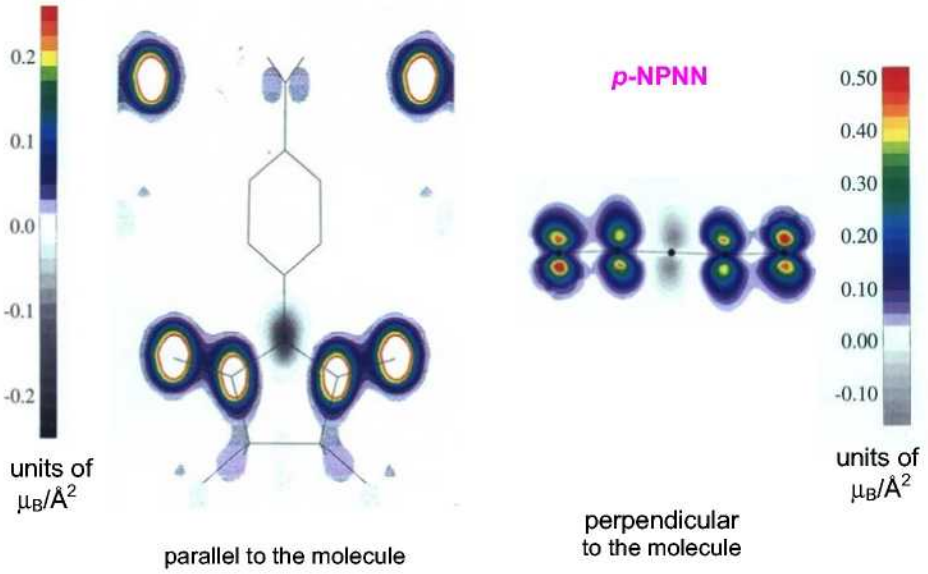



Fig. 15. Spin density distribution of *p*-NPNN
(magnetization density reconstructed by MAXENT).

**References**


1. W. Reimers, E. Hellner, W. Treutmann and G. Heger, J. Phys. C: Solid State Phys. **15**, 3597 (1982).
2. A. Preisinger, K. Mereiter, O. Baumgartner, G. Heger, W. Mikenda and H. Steidl, Inorg. Chem. Acta **57**, 237 (1982).
3. R. J. Nelmes, W. F. Kuhs, C. J. Howard, J. E. Tibballs and T. W. Ryan, J. Phys. C: Solid State Phys. **18**, L711 (1985).
4. S. Mattauch, G. Heger, and K. H. Michel, Cryst. Res. Technol. **39**, 1027 (2004)
5. J. Eckert and W. Press, J. Chem. Phys. **73**, 451 (1980).
6. P. Schiebel, A. Hoser, W. Prandl, G. Heger and P. Schweiss, J. Phys. I France **3**, 987 (1993).
7. J. Schweizer, Physica B **234-236**, 772 (1997).
8. P. Schleger, A. Puig-Molina, E. Ressouche, O. Rutty and J. Schweizer, Acta Cryst. **A53**, 426 (1997).


**Textbooks**


8. G. E. Bacon, Neutron Diffraction, Clarendon Press, Oxford (1975).
9. HERCULES: Neutron and Synchrotron Radiation for Condensed Matter Studies, Vol. I and II (edited by J. Baruchel, J. L. Hodeau, M. S. Lehmann, J. R. Regnard and C. Schlenker), Les Editions de Physique, Les Ulis & Springer-Verlag, Berlin (1993-1994).
10. L. Dobrzynski and K. Blinowski, Neutrons and Solid State Physics, Ellis Horwood Series in Physics and its Applications, New York (1994).

# 12

# Inelastic neutron scattering: phonons and magnons

Markus Braden

# 12. Inelastic neutron scattering : phonons and magnons

Markus Braden
II. Physikalisches Institut, Universität zu Köln,
Zülpicher Str. 77, D-50937 Köln
braden@ph2.uni-koeln.de

## 12.1 Interaction and scattering law

### 12.1.1 Basic concepts of scattering experiments

Scattering experiments are performed with almost all types of radiation on various systems (solids, liquids, gases, atoms, nuclei, ...). The radiation with well defined initial properties ( wavevector $\underline{k}$; energy E) hits the sample, gets scattered and may be detected again with well defined final properties (wavevector $\underline{k'}$; energy E') in the angular segment $r^2 d\Omega$, the schematic picture of the scattering arrangement is drawn in figure 1. Aim of any scattering experiment is to obtain information on the states of the sample by use of the knowledge of the interaction between the radiation (for example neutrons) and the particles forming the sample. In this chapter we deal with the inelastic neutron scattering in solids which is till today the most efficient way to study dispersion relations of lattice vibrations and magnetic excitations. We give examples of simple phonon and magnon dispersions studied in the early days of neutron scattering as well as results of recent research on complex materials.

The initial and final states of the neutron may be denoted by $\sigma_i$ and $\sigma'$, those of the sample by $\lambda_i$ and $\lambda'$. $\sigma_i$ is characterized by the wavevector $\underline{k}$ and the energy $E = \frac{\hbar^2}{2m}k^2$, $\sigma'$ respectively. The momentum transferred to the sample crystal, $\underline{Q}$, and the energy transfer, $E = \hbar\omega$, have to fulfill the conservation laws, $\underline{Q} = \underline{k} - \underline{k'}$ and $\omega = \hbar(\frac{1}{2m})^2(k^2 - k'^2)$. The probability to observe a scattered neutron in the angular segment $d\Omega$ and in the energy interval $dE'$ is described by the partial differential cross section which may be obtained within the Born-approximation. This is a perturbation theory of first order, i.e. one considers the interaction between radiation and sample crystal to be small.

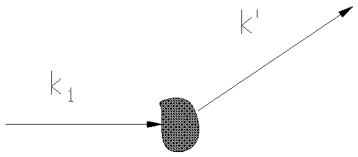



**Figure1** Schematical drawing of a general scattering experiment.

$$\frac{d^2\sigma}{d\Omega dE'} = (k'/k)(m/2\pi)^2 \sum_{\lambda_i,\sigma_i} P_{\lambda_i} P_{\sigma_i} \sum_{\lambda',\sigma'} \qquad (12.1)$$
$$| < \sigma'\lambda' | \int d^3r \; exp(i\underline{k}' \cdot \underline{r}) \hat{V}(r) exp(i\underline{k} \cdot \underline{r}) | \sigma_i \lambda_i > |^2$$
$$* \delta(\omega + E' - E)$$

The cross section in equation (12.1) is given by the sum of the transition matrix elements between initial states $\sigma_i\lambda_i$ and the final states $\sigma'\lambda'$ weighted by the probabilities of the initial states. In order to calculate the cross section and the observable intensity distribution, one needs the interaction potential $\hat{V}(\underline{r})$ and detailed knowledge of the states in the sample $\lambda_i$. In the inverse way one may use a measured intensity distribution in order to characterize the sample states, for example the phonons. This is the usual way to interpret any scattering experiment. The sample states may be characterized by specific parameters, for example the frequencies and the polarization patterns in case of phonons, which with the aid of equation (12.1) will be deduced from the experimental intensity distribution.

### 12.1.2 Nuclear interaction – phonons

The nuclear interaction between the neutron and the core of the atoms is characterized by an extension of $10^{-5}$Å, which is small in comparison to the wavelength of thermal neutrons. Therefore, the scattering is isotrope and may be described by only one parameter, the scattering length. The interaction with the entire crystal is given by the sum over the atoms :

$$\hat{V}(\underline{r}) = \frac{2\pi}{m} \sum_j b_j \delta(\underline{r} - \underline{R}_j) \qquad (12.2),$$

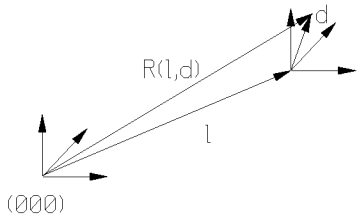



**Figure 2** Schematic drawing of the vectors determining the position of an atom in the crystal lattice.

where $b_j$ and $\underline{R}_j$ are the scattering length and the position of the j-th atom. The mixing of different isotopes at the same atom site in the crystallographic lattice yields a further complication, since different isotopes have different scattering lengths. This means that the interaction potential (12.2) does not show the full translation symmetry of the crystal lattice. The local variation of the scattering length splits the differential cross section into two contributions :

$$\frac{d^2\sigma}{d\Omega dE'} = (\frac{d^2\sigma}{d\Omega dE'})_{coh.} + (\frac{d^2\sigma}{d\Omega dE'})_{incoh.} \qquad (12.3).$$

The coherent contribution is determined by the mean scattering length, whereas the incoherent contribution is given by the root mean square deviation to the averaged scattering length.

In order to calculate the differential cross section in (12.1) it is necessary to know the states in the sample or at least to parameterize them. The sum over the states $\lambda_i$ in (12.1) may be transformed to the correlation function, in which one has to introduce the parameterized Eigen-states of the system. In order to achieve this transformation in case of the phonons we consider the vibrations of a crystal in harmonic approximation.

*Description of lattice dynamics in harmonic approximation* A crystal consists of N unit cells with $n$ atoms within each of them, the equilibrium position of any atom is given by the position of the unit cell to which it belongs, $\underline{l}$, and by the position of the atomic site in the unit cell, $\underline{d}$. At a certain time the atom may be displaced from its equilibrium position by $\underline{u}(\underline{l},\underline{d})$. The instantaneous position is hence given by $\underline{R}_{\underline{l},\underline{d}} = \underline{l} + \underline{d} + \underline{u}(\underline{l},\underline{d})$ (see figure 2).

For simplification we consider first a lattice with only one atom in the unit cell, $\underline{d} = \underline{0}$; $\underline{l}$ describes then the equilibrium position of the atom. The interaction potential between

two atoms $\underline{l}$ and $\underline{l'}$, $\Phi(\underline{l},\underline{l'})$, may be expanded at the equilibrium position in terms of $\underline{u}(\underline{l})$=$\underline{u}(\underline{l'})$=0. The constant term does not give any contribution to the equations of movement, it is relevant only for the total energy of the crystal structure. Since at the equilibrium position the atom should not experience any forces, terms of first order are not allowed. In harmonic approximation one assumes the expansion till the second order to be sufficient. This assumption is essential for the following analysis, because the presence of third order terms already prohibits one to solve the equations of movement in the general case. In most solids, anharmonic contributions to the potential are, however, small justifying the assumption. If the anharmonic effects have to be taken into consideration (for example close to the melting of the crystal lattice), perturbation theory is the usual technique.

Using the definition :

$$D_{\alpha,\beta}(\underline{l},\underline{l'}) = \frac{d^2\Phi(\underline{l},\underline{l'})}{du_\alpha(\underline{l})du_\beta(\underline{l'})} \qquad (12.4)$$

one obtains the equations of movement ($\alpha,\beta = x,y,z$) to :

$$M\ddot{u}_\alpha(\underline{l}) = -\sum_{\beta,\underline{l'}} D_{\alpha,\beta}(\underline{l},\underline{l'})u_\beta(\underline{l'}) \qquad (12.5).$$

The displacement of the atom $\underline{l'}$ in $\beta$-direction yields a force on the atom $\underline{l}$ in $\alpha$-direction of strength $D_{\alpha,\beta}(\underline{l},\underline{l'})u_\beta(\underline{l'})$, $D_{\alpha,\beta}(\underline{l},\underline{l'})$ are therefore called the force-constants. The real problem in treating lattice dynamics consists in the large number of these equations, there are 3N equations to be solved with N being of the order of $10^{23}$. In order to avoid this complexity one makes the Ansatz of plane waves : the movements of all atoms are given by the displacement in one unit cell at time zero propagating in time and space as a plane wave :

$$u_\alpha(\underline{l}) = e_\alpha M^{-1/2} \cdot exp(i\underline{q}\underline{l} - \omega_0 t) \qquad (12.6).$$

Figure 3 shows the displacement pattern of a plane wave characterized by the wave vector $\underline{q}$, reflecting the propagation of the wave (planes perpendicular to $\underline{q}$ are always identically displaced), the vibration frequency $\omega_0$ of each atom and the direction of the oscillation given by the polarization vector $\underline{e} = (e_x, e_y, e_z)$. In the single atom lattice there are only acoustic modes, they are called longitudinal (LA) if $\underline{q}$ is parallel to $\underline{e}$ and

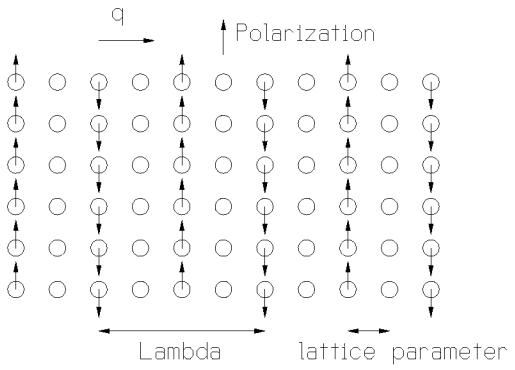



**Figure 3** Scheme of the displacements in a transversal plane wave.

transversal (TA) for $\underline{q}$ perpendicular to $\underline{e}$.

The plane wave Ansatz (12.6) for the equations of movement yields a system of three equations for each $\underline{q}$-value :

$$\omega_0^2 e_\alpha = 1/M \sum_{\underline{l},\beta} D_{\alpha,\beta}(\underline{l},0) exp(-i\underline{q}\underline{l}) e_\beta \qquad (12.7).$$

Here we use that the force constants depend only on the distance in real space $(\underline{l}-\underline{l'})$ and not on the particular values of $\underline{l}$ and $\underline{l'}$. With (12.7) one obtains an easily solvable system; the original complexity of the problem is transferred to the number of these 3-dimensional problems. For a complete solution of the crystal dynamics one would need to solve the problem (12.7) for each of the N$\sim 10^{23}$ allowed $\underline{q}$-values. In reality, however, one has to analyze only a few different $\underline{q}$-values. In general it is sufficient to study only $\underline{q}$-values within the first Brillouin-zone.

We may define the dynamical matrix as

$$\bar{D}_{\alpha,\beta}(\underline{q}) = 1/M \sum_{\underline{l},\beta} D_{\alpha,\beta}(\underline{l},0) exp(-i\underline{q}\underline{l}) \qquad (12.8),$$

which allows to rewrite the equations (12.7) in matrix form :

$$\omega_0^2 \underline{e} = \bar{D} \cdot \underline{e} \qquad (12.9).$$

The system (12.9) is just a three-dimensional Eigen-value problem.

For fixed $\underline{q}$ one has to determine the three Eigen-vectors $\underline{e}_j$, $j$=1,2,3, together with the three corresponding Eigen-values, $\omega_j(\underline{q})$. This may be achieved with the standard numerical techniques. The dependence of the Eigen-frequencies on the wave-vector, $\omega_j(\underline{q})$ with $j = 1, 2, 3$, is called the dispersion relation.

The extension to a system with $n$ Atoms in the primitive cell can be easily done, one gets for each $\underline{q}$ an Eigen-value problem in $3n$ dimensions. The Eigen-vectors have the dimension $3n$ and the dynamical matrix is $3n * 3n$ dimensional. For each $\underline{q}$ one finds hence $3n$ Eigen-modes, therefore the complete phonon dispersion consists of $3n$ branches, three of which have zero frequency for $q \to 0$. The latter branches are called acoustic since they are associated with the propagation of sound. The upper part of Figure 4 shows the typical presentation phonon frequency, $\omega$, against wave-vector $\underline{q}$ for the phonon dispersion of elementary aluminum, whereas the lower part shows the result of a recent study on the phonon dispersion in $CuGeO_3$. In the latter material, there are 10 atoms in the primitive unit cell yielding a phonon dispersion with 30 branches. In order render the presentation clearer, one has to separate the phonon modes according to their symmetry following group theory. The symbols denote the frequencies determined by inelastic neutron scattering and the line give the calculation with a shell model [7].

The plane waves including Eigen-frequencies and Eigen-vectors for each of the allowed $\underline{q}$-values form a complete set of functions for the displacements of the N times $n$ atoms in the crystal. Any distortion can be represented as a linear combination of these plane waves. Obviously it is rather favorable to use this set for calculating the differential apply quantum mechanics to the lattice vibrations, the corresponding quasi-particle is called a phonon. A one-phonon process is shown in the schematic figure 5. The momentum transfer $\underline{Q} = \underline{k} - \underline{k'}$ consists of the sum of a reciprocal lattice vector $\underline{\tau}$ and the wave-vector $\underline{q}$, which lies within the first Brillouin-zone. Only $\underline{q}$ determines the wave vector of the contributing phonons, however $\underline{Q}$ determines the differential cross section, i.e. the intensity.

The exact scattering may be deduced from the correlation function. In the following we only want to discuss the meaning of the different terms in the cross section :

$$(\frac{d^2\sigma}{d\Omega dE'})^{\pm} = (k'/k)\frac{(2\pi)^3}{2v_0}\sum_{\underline{\tau}}\sum_{j,\underline{q}} \qquad |G_j(\underline{q},\underline{Q})|^2 \qquad (12.10.a)$$

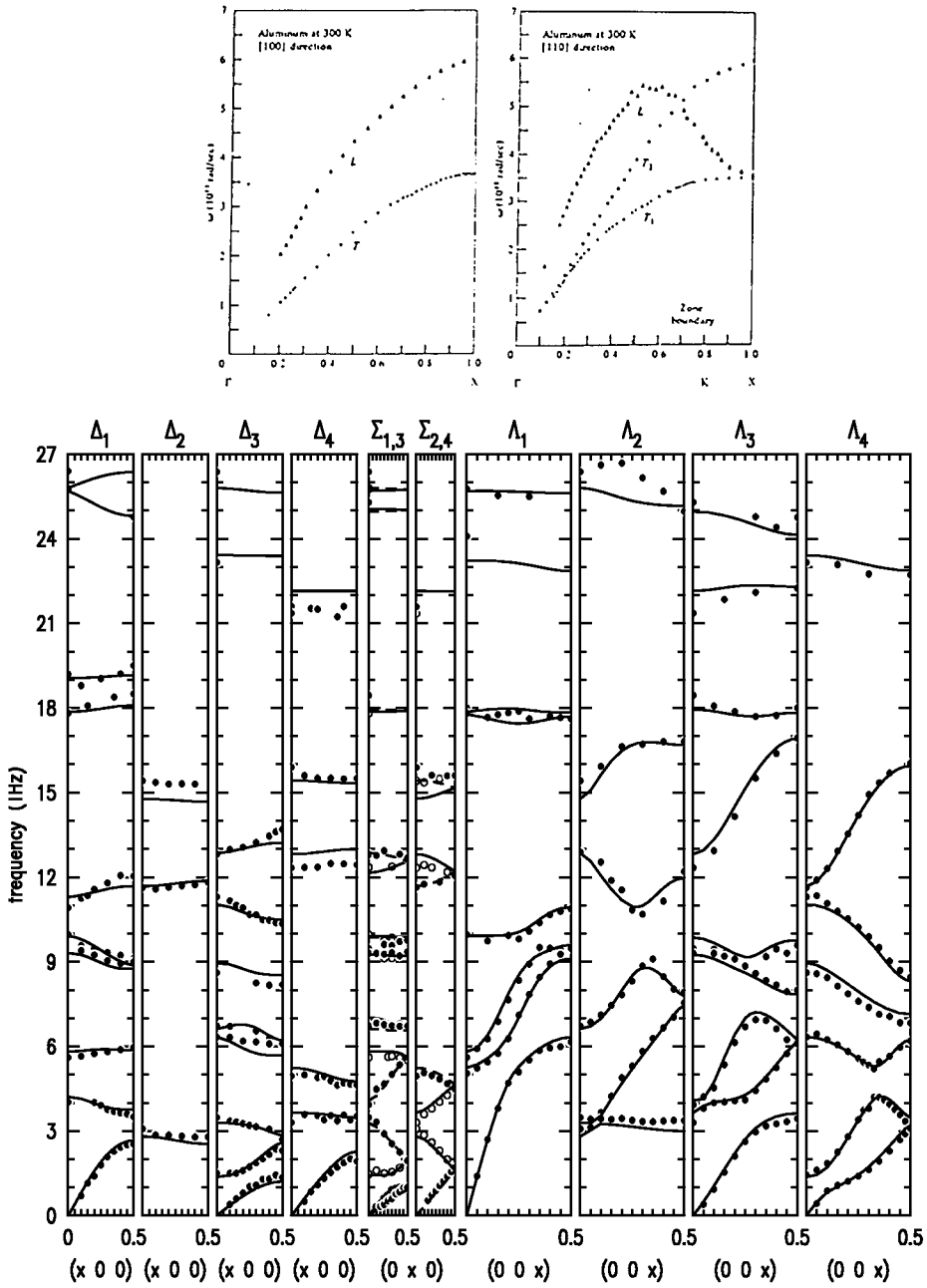



**Figure 4** Upper part :Phonon dispersion of Al along the [100] and [011]-directions (from reference [1]); lower part : Phonon dispersion of $CuGeO_3$, a material with 10 atoms in the primitive unit cell and accordingly 30 phonon branches, which are separated following the group theory analysis [7].

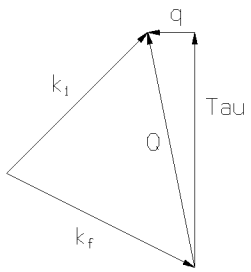



**Figure 5** Scattering triangle corresponding to the observation of a phonon mode with wave vector $\underline{q}$ at the reciprocal lattice vector $\underline{\tau}$.

$$\cdot\frac{1}{\omega_j(\underline{q})} \qquad (12.10.b)$$

$$\cdot(n(\omega_j(\underline{q})) + 1/2 \pm 1/2) \qquad (12.10.c)$$

$$\cdot\delta(\omega \mp \omega_j(\underline{q})) \cdot \delta(\underline{Q} \mp \underline{q} - \underline{\tau}) \quad (12.10.d),$$

with $v_0$ the volume of the reciprocal unit cell. Equation (12.10) describing the intensity of a one-phonon measurement at specific $\underline{Q}$ closely resembles the elastic structure factor of the Bragg reflection intensity, a part of expression (12.10) is called dynamic structure factor. The intensity is given by the sum over all reciprocal lattice and all wave vectors; however only the combination $\underline{q}+\underline{\tau} = \underline{Q}$ may contribute due to the $\delta$-function in (12.10.d). The second $\delta$-function in (12.10.d) reflects the law of energy conservation, however, one has to take into account that the scattering processes may lead to a creation as well as to an annihilation of a single phonon, corresponding to the upper and the lower signs respectively. There are two more general factors determining the intensity of the phonon observation by neutron scattering. The term (12.10b) indicates, independently of all other terms, that the intensity is inversely proportional to the frequency of the mode. High energy modes are always more difficult to observe than the low-lying ones. Since neutron experiments suffer from the low flux of the existing sources, this effect frequently prohibits the study of the high-energy part of the phonon dispersion. The term (12.10.b) results from the quantum mechanics of a single harmonic oscillator : the square of the amplitude is proportional to $\frac{1}{\omega_j(\underline{q})}$.

The term (12.10.c) results from the Bose-statistics of the phonon mode with frequency $\omega_j(q)$ , the occupation number is given by the Bose-function:

$$n(\omega_j(\underline{q})) = \frac{1}{exp(\frac{\hbar\omega_j(\underline{q})}{kT}) - 1} \qquad (12.11).$$

$n(\omega_j(\underline{q}))$ tends for $T \to 0$ towards zero, the phonons are frozen. For $T \to \infty$, $n(\omega_j(\underline{q}))$ approaches $(\frac{\hbar\omega_j(\underline{q})}{kT})$, i.e. the classical relation. The term (12.10.c) indicates that the Bose-function is increased by +1 only in case of phonon creation. At low temperature where $n(\omega_j(\underline{q}))$ is close to zero, the phonon may be observed only in the creation mode, the cross section for the annihilation process vanishes since the phonon states are no longer occupied. At finite temperature the Bose-statistics further simplifies the observation of phonons with low frequencies.

The complex term in (12.10.a) is called the dynamical structure factor:

$$G_j(\underline{q}, \underline{Q}) = \sum_d \frac{b_d}{\sqrt{m_d}} \cdot exp(-W_d(\underline{Q}) + i\underline{Q}\underline{d}_d) \cdot (\underline{Q} \cdot \underline{e}_d^j(\underline{q})) \qquad (12.12),$$

where the sum extends over the atoms, numbered by $d$, in the primitive cell. The atoms possess the mass $m_d$ scattering length $b_d$ and a three-dimensional polarization vector $\underline{e}_d^j(q)$, the equilibrium position in the unit cell is given by $\underline{d}_d$. Without the last part equation (12.12) corresponds to the elastic structure factor, in particular one finds the same Debye-Waller-factor $exp(-W_d(\underline{Q}))$. The whole term in the exponential function determines whether the interference between atoms is constructive or destructive. In the dynamical structure-factor equation, there is in addition to the elastic one the polarization term (last parenthesis); for instance only those atoms may contribute whose polarization vector, $\underline{e}_d^j(\underline{q})$, possesses a component parallel to $\underline{Q}$. Since $\underline{Q}$ enters this term directly, the structure factor increases with $|Q|$; the intensity is proportional to $Q^2$. The interference and the polarization term in (12.12) cannot be separated in general, therefore one has to calculate the structure factors precisely.

In addition to the interpretation of the frequency data the prediction of the scattered intensity is an important result of model calculations. Only with the help of these predictions a neutron scattering experiment aiming at the lattice dynamics of a complex material can be performed in an efficient manner.

Some easy examples may illustrate the significance of the terms in (12.12). Let us

consider a longitudinal acoustic mode polarized in the [100]-direction; for this mode all $\underline{e}_d$ are parallel to [100]. The polarization term becomes maximum for $\underline{Q}$=(h+$\xi$ 0 0) and can be extracted from the sum. The remaining interference sum corresponds for small $\xi$ to the elastic structure-factor of (h00), The dynamic structure becomes hence strong for strong Bragg-reflections. In general, acoustic phonons have to be measured close to the strong Bragg-reflections. Since for optical modes the atoms may be displaced in opposite directions, the polarization term can change sign yielding a rather distinct sum of the interference term. In a simple two-atomic structure the optical mode has only a weak dynamical structure factor close to the strong Bragg-reflections (this argument is, however, no longer valid in case of negative scattering lengths).

Why does inelastic neutron scattering play such a dominant role in the study of lattice dynamics? The central advantage certainly concerns the similar masses of the atoms and of the neutron. This yields the possibility of elastic as well as that of inelastic scattering and renders the wave-vectors of thermal neutrons comparable to the wave-vectors of the phonons. Inelastic neutron scattering allows to determine the phonon dispersion over the whole Brillouin zone, whereas optical techniques (Raman and Infra-Red-scattering) yield only the analysis of modes at the zone center.

Recently, there are serious efforts to perform lattice dynamical studies using synchrotron radiation. In case of thermal neutrons the energies amount to 1–100 meV and correspond to the typical phonon energies. For comparison, $CuK_\alpha$-radiation has an energy of $8 \cdot 10^6$meV. In order to determine phonon frequencies, one needs a relative energy resolution of $10^{-6} - 10^{-7}$, which may be achieved only by extreme experimental effort. The concomitant loss of intensity permits these measurements only at powerful synchrotron sources, and even then the measurements remain slow. We have seen that the one-phonon process yields an intensity proportional to $Q^2$, this may be used in case of neutron scattering due to the nuclear interaction. In case of the x-rays the large $\underline{Q}$-range is not favorable, because the form-factor strongly reduces the interaction. In the closer future one may not expect, that inelastic x-ray scattering will supply results comparable to neutron studies concerning their efficiency. The x-ray measurements, however, may become valuable in cases where the neutron scattering is hampered either by sample size or by absorption.

### 12.1.3 Magnetic interaction – magnetic excitations

The neutron has a spin 1/2 which implies a coupling to the magnetic fields. The interaction operator is given by :

$$-\gamma_n \mu_N \hat{\sigma} \cdot \underline{H} \qquad (12.13);$$

here $\gamma_n$=1.913 is the magnetic moment of the neutron, expressed in $\mu_N$, the nuclear magneton, $\hat{\sigma}$ the Pauli-spin operator and $\underline{H}$ the magnetic field induced by the electrons in the sample. $\underline{H}$ may arise from the velocity of the electrons as well as from their magnetic moment. In the following we limit the discussion to the latter contribution.

Furthermore we assume, that the orbital moment has vanished. This assumption is justified in case of quenching by crystal fields or for a half-filled shell ($Mn^{2+}$, $Fe^{3+}$, $Gd^{3+}$).

The Fourier-component of the interaction potential is :

$$\hat{V}(\underline{Q}) = \frac{2\pi}{m} \frac{\gamma_n e^2}{M_e c^2} \hat{\sigma} \hat{D}_\perp(\underline{Q}) \qquad (12.14)$$

with

$$\hat{D}_\perp(\underline{Q}) = \sum_{\underline{l},d} (1/2) \gamma_d F_d(Q) \hat{\sigma} \hat{S}_\perp(\underline{l}, d) exp(i\underline{Q} \cdot \underline{R}_{\underline{l}d}) \qquad (12.15),$$

here $\gamma_d$ is the gyro-magnetic factor, $F_d(\underline{Q})$ the form-factor of the atom $d$ and $S_\perp(\underline{l}, d) = \underline{Q} \times (\hat{S}_{\underline{l}d} \times \underline{Q})$ with $\hat{S}(\underline{l}d)$ being the spin-operator of the atom.

There are two important differences between the magnetic and the nuclear interaction of the neutron with the atom. Due to the spatial extension of the electron cloud, which causes the magnetic moment, the interaction is non-local. Described by the form-factor, $F(Q)$, the interaction gradually decreases towards large $\underline{Q}$. The detailed dependence of $F(Q)$ is determined by the single ion. Rare earths show, due to the strong localization of the 4f-electrons, a less pronounced decrease when compared to the transition metal ions with more delocalized electrons. In the latter case the decrease may be quite strong limiting any measurement to the first Brillouin-zones. The Q-dependence of the magnetic signal due to the form-factor may be used to separate magnetic and nuclear contributions. Furthermore, the magnetic interaction is mediated by vector-operators. Only those magnetic moments may contribute to the interaction, which have a component perpendicular to $\underline{Q}$. This yields the possibility to determine not only the size but also the direction of magnetic moments.

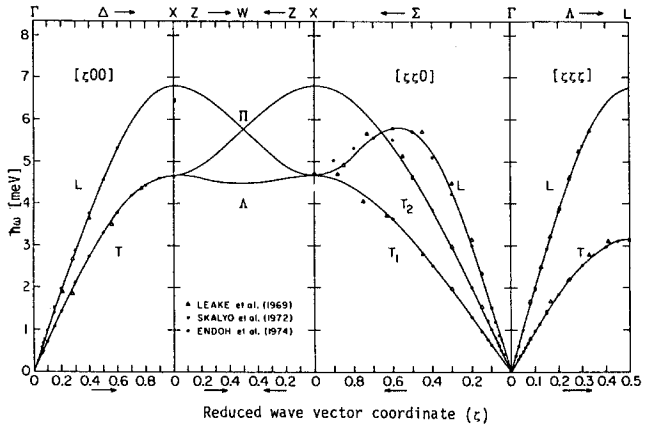



**Figure 6** Phonon dispersion of Ne along the three main symmetry directions (from Ref. [2]).

## 12.2 Analysis of lattice vibrations

### 12.2.1 Lattice dynamics in simple structures

For a simple crystal lattice one may determine the polarization patterns without detailed model calculations. The lattice dynamics of such a system may then be studied experimentally without particular effort.

In figure 6 we show the phonon dispersion of Ne in the three main symmetry directions, which according the common use are labeled $\Delta$, $\Sigma$ and $\Lambda$. Ne crystallizes in a fcc-lattice with only one atom in the primitive cell, therefore one expects only three acoustic branches per $\underline{q}$-value. One observes the three distinct branches only in the [xx0]-direction, whereas there are only single transverse branches along [x00] and [xxx]. In the [x00]-direction these acoustic polarization patterns may be easily understood. In the longitudinal mode atoms are vibrating in [100]-direction, i.e. parallel to the wave vector. The two transverse modes are characterized by displacements in [010] or in [001]-directions, i.e. perpendicular to the wave-vector. Since [100] represents a four-fold axis in the fcc lattice, the latter two modes cannot be distinguished; they are degenerate. The same situation is found along the [111]-direction which is a three-fold axis of the lattice. This behavior is a simple example of the general relation between crystal symmetry and the phonon dispersion. The crystal symmetry yields constraints for the phonon modes which may be necessarily degenerate at certain points or - like in the Ne-structure - along a direction. In the case of more

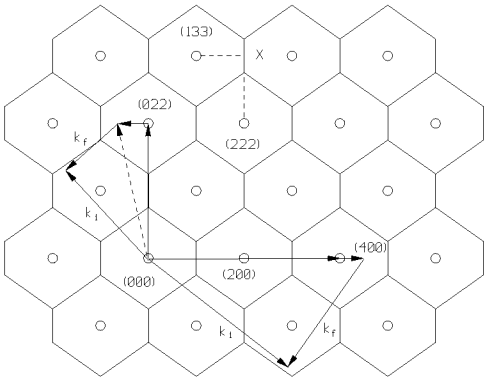



**Figure 7** The plane in reciprocal space spanned by the (100) and (011) vectors for a fcc-lattice; the scattering triangle indicates the observation of $\Delta$-modes.

complex structures it is essential to profit from symmetry analysis. The [110]-direction represents only a two-fold axis since [1-10] and [001] are not identical, as consequence the corresponding transverse acoustic branches are not equivalent.

In addition, figure 6 shows that at X=(100)=(011) $\Delta$ and $\Sigma$-branches are coinciding, which may be explained due to the shape of the Brillouin-zone. Figure 7 presents the plane of the reciprocal space spanned by (100) and (011); one recognizes that starting at the zone-center, $\Gamma$, in the figure (133), in the [100]-direction one will reach the zone-boundary at (233)$\equiv$(100)=X. Similar, one will reach this point when starting at the neighboring point (222) in [011]-direction. However, in this path one finds the border of the Brillouin-zone earlier and continues the last part on the zone boundary. (100) and (011) are equivalent points in reciprocal space; they are connected by a reciprocal lattice vector, (-1 1 1). For the phonon branches we conclude that $\Delta$- and $\Sigma$-branches have to coincide. The symmetry further determines which branches coincide : for example the longitudinal $\Sigma$-branch with the transversal $\Delta$-branch. Again, similar considerations in more complex systems may decisively contribute to the identification of the branches.

Figure 7 further shows how to measure the $\Delta$-branches. One may observe the longitudinal branch in the (400)-zone passing to (4+x 0 0) (the (400)-zone has to be preferred to (200) due to the larger value of $Q^2$), whereas one may determine the transverse frequencies in the (022)-zone at (x 2 2).

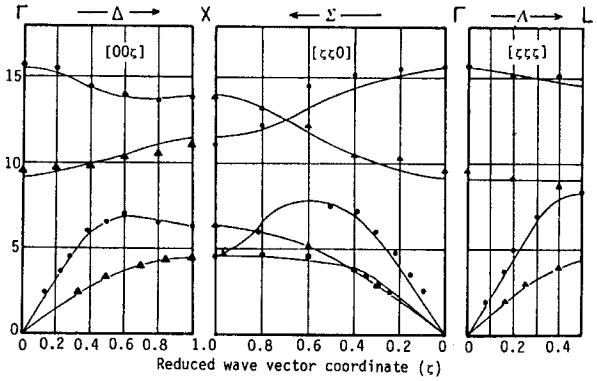



**Figure 8** Dispersion curves and crystal structure of FeO (from reference [2]).

– *NaCl-structure* – The NaCl-structure represents one of the most simple possible crystal structures with two atoms per primitive cell. It consists of two fcc-lattices shifted against each other by (0.5 0.5 0.5). The entire crystal structure possesses fcc-symmetry too. Figure 8 shows the dispersion curves of FeO.

The six branches expected for the two-atomic structure are observed only in [xx0]-direction. Like in case of the fcc Ne-lattice, the transverse $\Delta$- and $\Lambda$-branches are doubly degenerate. Also in other aspects, there is some resemblance with the Ne-phonon dispersion; in both cases LA-$\Delta$ and TA-$\Sigma$ branches coincide at the zone boundary.

A more detailed discussion is needed in order to understand the optical modes at $\Gamma$. The polarization pattern of an optical mode corresponds to an anti-phase axial movement of the ion pairs connected in [100], [010] or [001] direction. The three vibrations polarized in the crystal directions should, however, be degenerate due to the cubic symmetry; one might expect only one optical frequency. The optical vibration in the ionic lattice possesses a polar character, i.e. there is a local polarization due to the opposite shifts of cations and anions. For large wave-length, i.e. close to the zone-center, the local polarization adds to a macroscopic polarization only in case of the longitudinal mode. This macroscopic polarization requires an additional energy, the longitudinal optic (LO) mode is always higher in frequency than the trnaversal optic (TO) mode (note, that these modes are only defined as the limit for $\underline{q}$ tending to zero. The splitting between LO and TO-mode frequencies is called Lydane-Sachs-Teller (LST) splitting and is related by the LST-

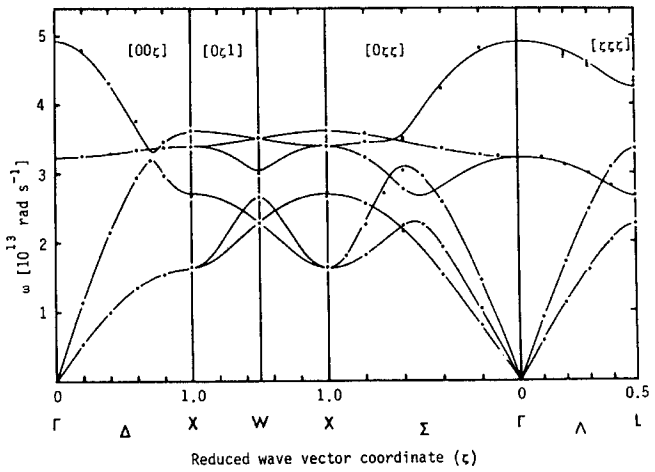



**Figure 9** Phonon dispersion of NaCl (from reference [2]).

relation to the dielectrical constant. Polar mode frequencies may be easily determined by Infra-Red techniques. Inelastic neutron scattering on this topic is frequently difficult, due to the unfavorable form of the resolution ellipsoid. In metallic materials electric fields are screened due to the free charge carriers at least for macroscopic distances. As a consequence, the LST-splitting disappears. The phonon dispersion may then give information on the efficiency of the metallic screening.

Figure 9 shows the phonon dispersion in NaCl, which is isostructural to FeO. Compared to the latter one recognizes the perturbation of the curves arising mainly from the lower optical frequencies. Within the Brillouin-zone it is no longer possible to separate optical and acoustic modes, the branches tend to cross each other but there is always a small gap between branches of the same symmetry. This represents a general property : branches of the same symmetry may not cross. By mixing the polarization patterns it is always possible to yield a gap reducing the total energy of the system. Whether this gap is small or large depends on the similarity between the polarization patterns of the two branches. Similar branches may induce larger gaps, they are called to strongly interact.

### 12.2.2 Model calculations

The examples discussed above are characterized through their simplicity, which permits to analyze the polarization patterns without detailed calculations. In actual topics

one has to deal with systems of more than 10 atoms per primitive cell, see lower part of figure 4, one may identify then the character of the phonon modes only with the aid by predictions of model calculations.

As discussed above the lattice dynamics is described by the $3n$-dimensional Eigen-value problem with the dynamical matrix :

$$\omega^2 \underline{e} = \bar{D}\underline{e} \qquad (12.16)$$

$$D_{\alpha,\beta}(d,d') = \frac{1}{(m_d m_{d'})^{1/2}} \sum_{\underline{l'}} \Phi_{\alpha,\beta}(\underline{0}d, \underline{l'}d') exp(i\underline{q}\underline{l'}) \qquad (12.17).$$

$\Phi_{\alpha,\beta}(0d, l'd')$ denote the force constants between the atoms $d$ and $d'$ in by $\underline{l}$ shifted cells. The determination of the force constants represents the real problem in lattice dynamics, in particular the question which constants are relevant.

Already by symmetry, the nine parameters per atom-pair are significantly reduced. Furthermore, one may reduce the analysis to the closer neighbors, as far as no long range force is involved. The next step consists in the development of potentials, from which one may obtain the force constants for many pairs inducing only a few free parameters.

Frequently it is sufficient to consider axial-symmetric potentials with $V(\underline{l}d, \underline{l'}d') = V(r)$, i.e. the potential depends only on the distance between the two atoms. Such a potential yields only two force constants, a radial and a transversal one :

$$\Phi_R(\underline{l}d, \underline{l'}d') = \frac{\partial^2 V}{\partial r^2}|_{r=r_o} \qquad (12.18),$$

$$\Phi_T(\underline{l}d, \underline{l'}d') = 1/r \frac{\partial V}{\partial r}|_{r=r_o} \qquad (12.19).$$

In the most simple model one may only introduce these radial and transverse force constants for the close neighbors (Born-von-Kàrmàn Model). However, extending more and more shells will rapidly increase the number of parameters. In particular the lattice dynamics of ionic compounds with the long range Coulomb-interaction, can only be poorly described by such a model.

Even when parameterizing the Coulomb-potential $V(r) \propto \frac{Z_d Z_{d'} e^2}{r}$ by the charges, $Z_d, Z_{d'}$, in order to deduce the respective force constants, the problem of the long range

persists. It is not possible to cut the sum at a certain distance, since the sums do not converge. The satisfying solution of this problem consists in the Ewald-method [1].

The Coulomb-potentials in an ionic crystal yields an attractive potential, which has to be compensated by a repulsive one. If the electron clouds of two ions of opposite charge start to overlap upon decrease of their distance, this repulsive potential will increase rapidly. One may describe this interaction by a Born-Mayer-potential $V(r) = B{\cdot}exp(-r/r_o)$, inducing only two parameters for one type of ionic pair, $B$ and $r_0$. Amongst the various extensions of this type of model, called "rigid ion", we mention only the shell model, where the polarizability of the ions is described by a separation between an electron cloud (the shell) and the cores. There are many different ways to couple the cores and the clouds by force constants.

In order to prepare an inelastic neutron scattering study on the lattice dynamics of a complex material, even a simple and un-adapted model may be helpful, as long as the crystal structure and, therefore, the symmetry is correctly entered. By symmetry, degenerations are fixed for certain points or even for lines in reciprocal space, and frequently the structure factors follow some inelastic extinction rules. In principle these predictions may also be found by a careful analysis through group theory; however, the use of a simple model which does not need to describe the frequencies well is much less time demanding. Some of these aspects have already been illustrated for the example of the NaCl structure. Concerning the dynamic structure factors one may add, that one will observe the optical modes close to $\Gamma$ best at the odd reciprocal lattice vectors (for example (333) ) independently of the forces involved.

### 12.2.3 Structural phase transitions and soft mode behavior

Structural phase transitions form still a topic of actual interest, where information about the underlying microscopic mechanism may frequently be achieved only by inelastic neutron scattering.

In figure 10 one finds the representation of a fictive structural phase transition in a two-dimensional crystal structure with two atoms in the primitive cell. In the high-symmetry high-temperature phase the black ion in the middle occupies a site with inversion symmetry. This symmetry is broken at the phase transition due to the displacement of the black ion. The right part of figure 10 shows the corresponding dispersion curve, here the polarization pattern of the $\Gamma$-mode corresponds to the static distortion below the transition

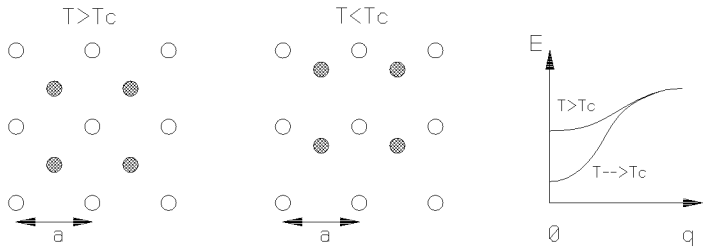



**Figure 10** Schematic picture of a displacive phase transition occuring at the zone center and the corresponding dispersion curve.

temperature, $T_c$. The phonon frequency of this mode softens upon approaching the phase transition and is, therefore, called a "soft-mode". The structural instability, however, can be also seen in the dispersion quite above $T_c$ : the frequency of the relevant mode at $\Gamma$ is lower than those of modes with $\underline{q}$-values in the Brillouin-zone.

In addition to the phonon softening one expects a broadening of the line width in frequency; finally the width of the phonon mode may surpass its frequency. Such overdamped modes may no longer be described in the harmonic approximation.

The best-studied example for a zone-center phase transition may be found in the ferroelectric transition in perovskites, for example $PbTiO_3$ see figure 11. In the low-temperature phase the anions are deplaced against the cations, Pb, Ti, the corresponding phonon frequency vanishes almost completely. This polarization pattern has a strong polar character and is connected to the dielectric constant through the LST-relation. The softening of the TO mode induces a divergence in the dielectric constant, which explains the interest of the phenomena for technical applications.

A structural phase transition may also lead to an enlargement of the unit cell. Here, the equivalent atoms in neighboring cells are not displaced identically; a schematic picture is given in figure 12, where neighboring black ions are shifting in opposite direction. The phonon mode associated with such a displacement pattern necessarily has a finite wave-vector, since the translation symmetry is broken. In case of figure 12, $\underline{q}$ is situated on the zone boundary. But like for the zone-center transition, one may find a softening for the zone-boundary mode too. The best-known example for such a transition can again be found amongst the perovskites $ABO_3$. The perovskite structure consists of $BO_6$ octahedra

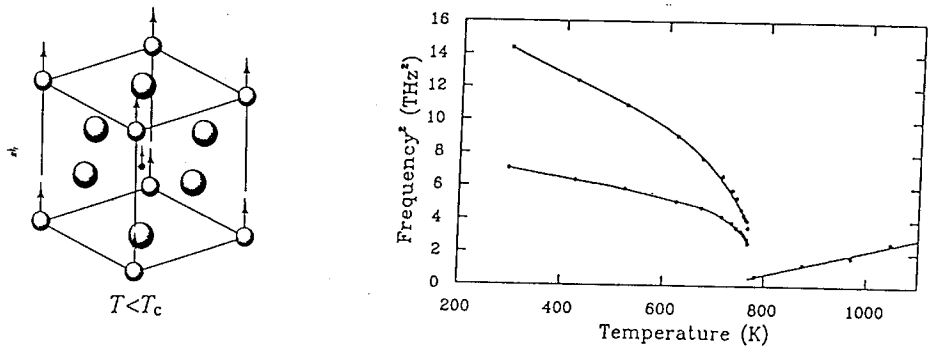



**Figure 11** Structure and displacement pattern of the ferrroelectric transition in the perovskite $PbTiO_3$ (left) small black dots in the center designate Ti the small and the large open spheres Pb and O respectively; square of the corresponding phonon frequency as function of temperature from reference [3] (right).

with partially covalent and quite hard bonds; the octahedra are connected only through their corners. Therefore, all these systems are more or less unstable against a rotation of the octahedra around an arbitrary axis. Only the strength of this instability and therefore the question whether a transition occurs or not, depends on the composition. For example the octahedron in $SrTiO_3$ below 105 K is rotated around a [100]-direction. The coupling of rotations around different directions leads to a variety of distinct low-temperature symmetries.

Recently the rotation phase transitions in the perovskites have regained interest, since they seem to be closely connected in the manganates to the electronic properties in particular their colossal-magneto-resistivity. Also the high-$T_c$-cuprates show similar transitions.

### 12.2.4 Electron phonon interaction

The study of the electron-phonon interaction represents an important field in lattice dynamics, which is analyzed almost exclusively by inelastic neutron scattering since the largest effects are expected in the Brillouin-zone.

The screening of the inter-atomic potentials through free charge carriers is determined by the topology of the Fermi-surface. In particular there are singularities in the electronic

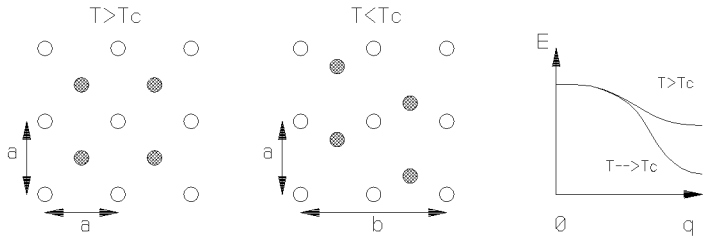



**Figure 12** Schematic picture of a displacive phase transition corresponding to a zone-boundary mode.

susceptibility when parts of the Fermi-surface are parallel and may, hence, be connected by a single nesting vector. The susceptibility at this vector will be essentially increased and may renormalize the phonon frequency of a mode just at this wave vector. In most cases this type of electron-phonon coupling leads to a reduction of the phonon frequency, which shows up as a dip in the dispersion curve, called a Kohn-anomaly. In particular the conventional superconductors, for example TaC in Figure 13, exhibit such effects. The phonon dispersion of TaC shows pronounced dips, which are not observed in the phonon dispersion of normal metals. The study and interpretation of similar anomalies in the high-$T_c$-cuprates is subject of present research. However, in this case the analysis gets rather complicated due to the large number of atoms in these systems.

## 12.3 Magnetic excitations

### 12.3.1 Spin waves in a ferromagnet

Like the crystal structure, magnetic order may be perturbed at finite temperature with the perturbation propagating through the crystal. In full analogy with the phonons, the quantisized excitations are called magnons.

The ground state of a ferromagnet results from the interaction between spins of neighboring atoms, which favors a parallel alignment. The energy of a neighboring pair, $\underline{S}_i, \underline{S}_j$, depending on the relative orientation of the spins is described within the Heisenberg-model by $e = -J\underline{S}_i \cdot \underline{S}_j$, where $J$ is the Heisenberg exchange constant. For a chain of coupled spins the energy of the magnetic interaction amounts to :

$$U = -2J \sum_{p=1}^{N} S_p \cdot S_{p+1} \qquad (12.20).$$

In the ground state all spins are parallel and $U_0 = -2NJS^2$, this corresponds to figure

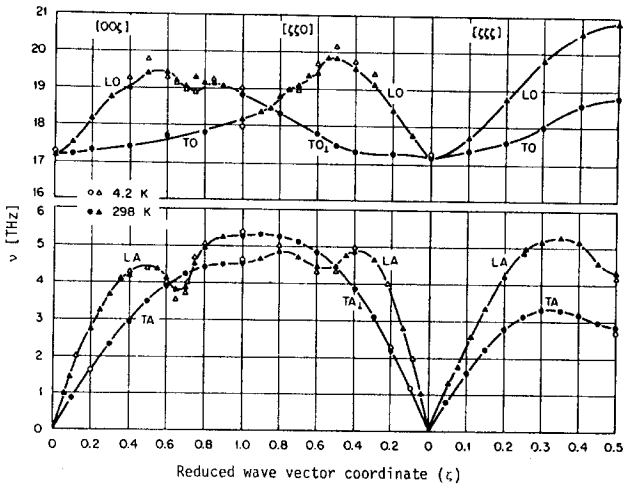



**Figure 13** Phonon dispersion of TaC, the dips, for example at (0 0 0.7) andd at (0.6 0.6 0), indicate modes renormalized through the electron phonon coupling, from reference [2].

14a. A possible excitation might consist in the flip of just one spin, like it is shown in figure 14b. This perturbation yields a finite increase in energy of $8JS^2$. However, the temperature dependence of several macroscopic properties like specific heat or magnetization does not correspond to an exponential law, as it has to be expected for a finite excitation energy. Spin waves (magnons) must have a much smaller energy than the single spin flip, like phonons may have lower energy than an ionic vacancy for instance.

The distortion of the magnetic order corresponds to a plane magnetic wave (with propagation vector $\underline{q}$ and frequency $\omega$) and is drawn in Figure 14c. Spins are precessing around the direction of magnetic order (here $z$) with components :

$$S_p^x = u \cdot exp[i(pqa - \omega t)] \qquad (12.21),$$

$$S_p^y = v \cdot exp[i(pqa - \omega t)] \qquad (12.22),$$

where $a$ designates the lattice constant and $b$ is numbering the spins.

Like in the case of the phonon dispersion one may deduce the magnon relation. In case of a simple chain one yields :

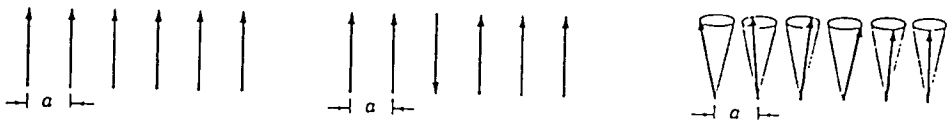



**Figure 14** Schematic drawing of a simple ferromagnet : a) ground state, b) one spin being flipped c) in a spin-wave the spins precess on cones (from reference. [4]).

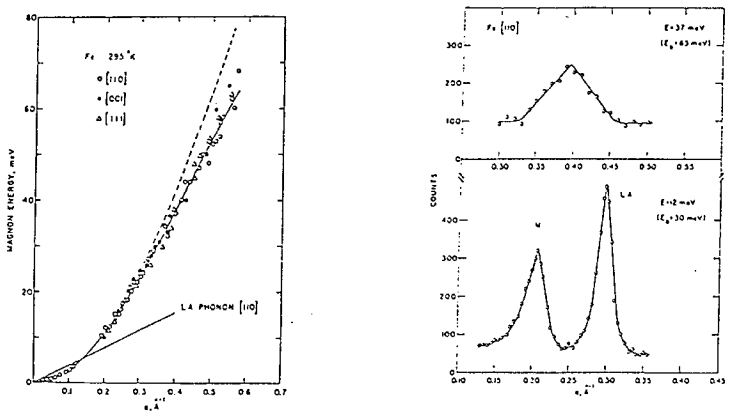



**Figure 15** Magnon- and phonon dispersion curves in Fe at room temperature and two $\underline{Q}$-scans at constant energy , reference [5].

$$\hbar\omega(q) = 4JS(1 - cos(qa)) \qquad (12.23),$$

which may be approximated for small $\underline{q}$ by $\hbar\omega(q) = 2JS(qa)^2$, i.e. a quadratic relation. In contrast, an acoustic phonon dispersion is always linear in that $\underline{q}$-range. Equation (12.23) may be extended to the three-dimensional case, in all cubic systems the relation $\hbar\omega(\underline{q}) = 2JS(qa)^2$ remains valid for small $q$.

Figure 15 shows the magnon dispersion measured in Fe, from which one may obtain the exchange constant $J$; for comparison the linear dispersion relation of the LA branch is added. One may note, that in the case of Fe the magnon frequencies extend to higher energies than those of the phonons. Due to the special form of the resolution ellipsoid in the triple axis spectrometer, it is favorable to perform scans at constant energy revealing both the phonon and the magnon, which exhibit approximately the same intensities, see right part of figure 15.

Since magnons are bosons, their occupation is given by Bose-statistics like that of the phonons, equation (12.11). Also for the differential cross section one may deduce a formula similar to equation (12.10) valid for phonons :

$$\begin{aligned}(\frac{d^2\sigma}{d\Omega dE'})^{\pm} = \quad & (k'/k) \cdot S \cdot const. \cdot exp(-2W(\underline{Q}))F^2(Q)(1 + \tfrac{Q_z^2}{Q^2}) \cdot \\ & \textstyle\sum_{\underline{\tau}\underline{q}}(n(\omega_{\underline{q}}) + 1/2 \pm 1/2) \cdot \delta(\omega \mp \omega_j(\underline{q})) \cdot \delta(\underline{Q} \mp \underline{q} - \underline{\tau}) \qquad (12.24).\end{aligned}$$

One recognizes the terms for momentum and energy conservation as well as the Bose-factor, which is increased by one in case of magnon creation. Furthermore the intensity is modulated by the same Debye-Waller-factor as the phonons. However, there is no term equivalent to the dynamic structure factor, the intensity is determined just by the spin $S$, the form factor $F(Q)$ and the direction of the momentum transfer.

Ferromagnetic materials are still of considerable interest due to their enormous technical potential in the context of data storage media. Attempts to optimize the technical properties lead to binary or ternary compounds, where the complexity of the magnetic order is considerably increased. In all cases the study of the magnon dispersion gives an almost unique insight to the microscopic coupling terms.

### 12.3.2 Antiferromagnetic Excitations

Antiferromagnetic order results from a negative exchange constant $J$ in $U = -2J \sum_p \underline{S}_p \cdot \underline{S}_{p+1}$. The anti-parallel alignment of neighboring spins ($\uparrow\downarrow\uparrow\downarrow\uparrow\downarrow\uparrow\downarrow$), however, leads to a magnetic cell which is larger than the nuclear one. A classical example is given by the antiferromagnetic order observed in MnO at 120 K (Shull et al. 1951). Again one may find excitations in an antiferromagnet, which have lower energy than the simple flip of a single spin. Again each spin deviates from the ordered position by a component given by a plane wave. The calculation of the antiferromagnetic dispersion more closely resembles that of the phonon case :

$$\omega^2(\underline{q}) = (\frac{4JS}{\hbar})^2(1 - cos^2(\underline{q} \cdot a)) \quad \omega(\underline{q}) = -\frac{4JS}{\hbar}|sin(\underline{q} \cdot a)| \qquad (12.25).$$

In contrast to the ferromagnetically ordered structure and in close similarity to the acoustic phonons, the frequency becomes linear in $\underline{q}$ for sufficiently small $\underline{q}$. Figure 16 shows the magnon dispersion observed in $RbMnF_3$ consisting of a single branch and the result of a recent study on the magnetic excitations of $La_{0.5}Sr_{1.5}MnO_4$ with several branches [8]. However, the magnon dispersions studied so far remain still less complex than what can be treated in terms of a phonon dispersion.

In general both dispersion relations (12.23) and (12.25) are not gaped, the magnon energy vanishes for $\underline{q}$ approaching the zone center, like in case of an acoustic phonon. For the acoustic phonon the zone-center limit corresponds to an infinitely small translation of the entire crystal which does not cost any energy, since no force constant is stretched. In case of the magnons the limit corresponds to a rotation of the ordered moment, which in the Heisenberg-model does not involve any energy shift (the interaction depends only on the relative orientation). However, in general this model is not sufficient, there are always interactions favoring the orientation of a certain spin direction. These interactions yield a finite gap in the excitation spectrum, however much smaller than the spin flip energy.

Antiferromagnetic materials have much less technical importance compared to ferromagnetism. However, antiferromagnetic correlations in metallic systems are often essential for the understanding of the electronic properties. For instance the physics of high-temperature cuprate superconductors seems to be determined by the closelyness of the antiferromagnetic order in the insulating parent compounds.

### 12.3.3 Crystal field excitations for rare earth ions

In the rare earth series one finds unpaired electrons in the 4f-shell, which are strongly

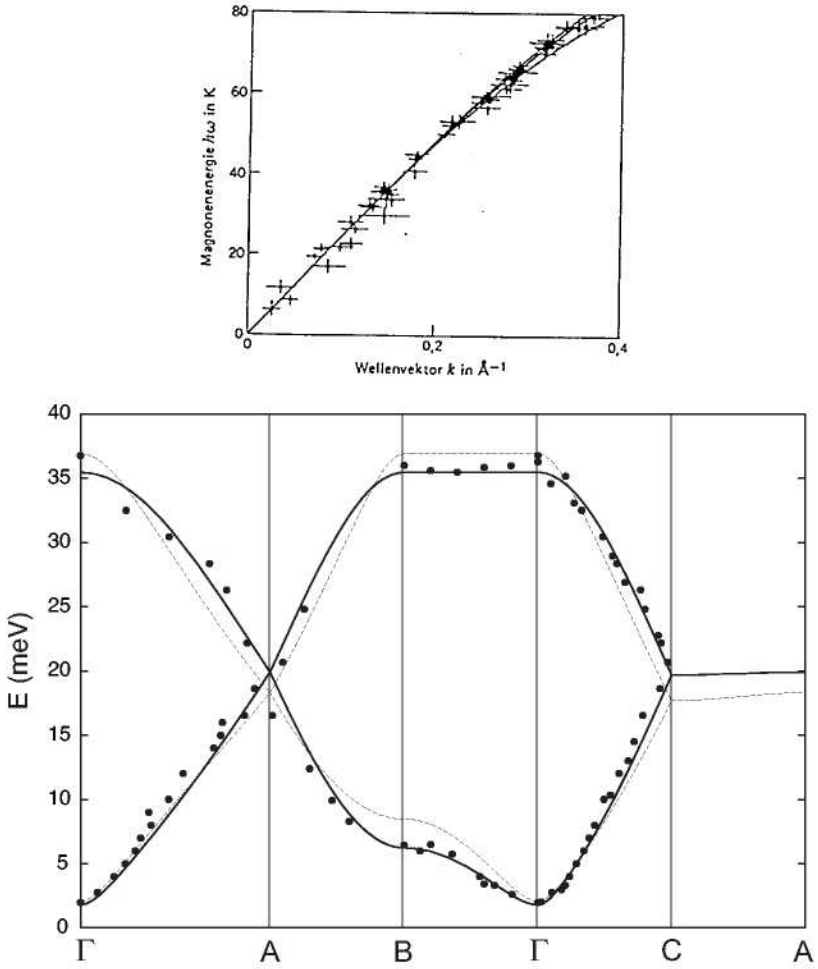



**Figure 16** Upper part : Magnon dispersion in $RbMnF_3$ (from reference [4]); lower part : Magnon dispersion in $La_{0.5}Sr_{1.5}MnO_4$ a material related to the colossal magneto-resistivity manganites, points denote experimental magnon frequencies and lines calculations within spin-wave theory [8].

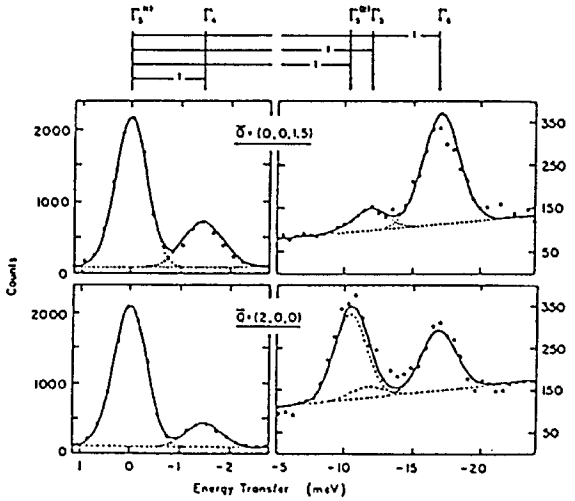



**Figure 17** Crystal field scheme and measured energy scans in $PrB_3$ (T=1.5 K), from reference [6].

localized and therefore screened from the surrounding ions. In consequence the total momentum $J$ remains a good quantum number. For a free ion the the ground state would be $(2J+1)$ times degenerate. In a crystal this degeneracy is partially lifted due to the – weak – Coulomb-fields of the surrounding ionic charges. The transitions between the single levels may be observed by inelastic neutron scattering. (This is valid for the crystal field splittings in transition metals too, but due to the larger overlap of the d-orbitals the excited levels in these compounds are usually to high in energy.) If the rare earth ions are sufficiently diluted, interactions amongst them may be neglected. The level frequencies show then no dispersion and may be studied with time of flight methods on a polycristalline sample.

In figure 17 we show the observed spectrum compared to the crystal field scheme for $PrB_3$. The levels of $Pr^{3+}$ with a $J$ of 4 may split into not more than 9 levels. The local symmetry of the site occupied by the ion in the lattice determines which levels may exist with which multiplicity. However, the symmetry cannot predict the sequence of the levels, for this purpose one needs a quantitative estimate for the surrounding fields. The single levels are designated according to the irreducible representations of the local symmetry

group by $\Gamma_i$. In close resemblance to equations (12.10) and (12.24) the differential cross section arises from the sum of transition probabilities $\Gamma_i \rightarrow \Gamma_j$; these matrix elements may be calculated within point-charge models.

### 12.4 Conclusions

Inelastic neutron scattering is almost the unique technique to observe lattice vibrations and magnetic excitations throughout the whole Brillouin-zone. The main part of our knowledge on these topics has indeed been achieved by inelastic neutron scattering studies.

Also the subjects of present interest, like high-$T_c$-superconductors, heavy fermions, quasi-crystals, $C_{60}$ and compounds with colossal magneto-resistivity demand a detailed analysis of their lattice dynamics as well as of their magnetism. Frequently the materials of current interest exhibit a larger complexity; therefore, their study requires a continuous development of the experimental facilities as well as of the analysis methods.

### References


**1** N.W. Ashcroft and N.D. Mermin, Solid State Physics, Holt-Saunders International Editions, Philadelphia (1976).

**2** H. Bilz and W. Kress, Phonon Dispersion Relations in Insulators, Springer Verlag, Berlin Heidelberg New-York (1979).

**3** M.T. Dove, Introduction to Lattice Dynamics, Cambridge University Press, Cambridge (1993).

**4** C. Kittel, Einführung in die Festkörperphysik, R. Oldenbourg Verlag, München (1983).

**5** G. Shirane, V.J. Minkiewiecz and R. Nathans, Journal of Appl. Physics 39, 3833 (1968).

**6** A. Furrer, Magnetic Neutron Scattering, World Scientific, Singapore (1995).

**7** M. Braden, W. Reichardt, B. Hennion, G. Dhalenne, and A. Revcolevschi Phys. Rev. B 66, 214417 (2002).

**8** D. Senff, F. Krger, S. Scheidl, M. Benomar, Y. Sidis, F. Demmel, and M. Braden Phys. Rev. Lett. 96, 257201 (2006).


further suggestions

- P. Brüesch, Phonons: Theory and Experiments I, II, III, Springer Verlag, Berlin Heidelberg New-York (1982).

- Landolt-Börnstein Band 13, Metalle, Phononenzustände, Elektronenustände and Fermiflächen, Springer Verlag, Berlin Heidelberg New-York (1981).

- E. Balcar and S.W. Lovesey, Theory of Magnetic Neutron and Photon Scattering, Oxford Science Publications, Clarendon Press, Oxford (1989).

- G.L. Squires, Thermal Neutron Scattering, Cambridge University Press, Cambridge (1978).

# 13

# Structure of Complex Fluids and Macromolecules

Henrich Frielinghaus

# 13. Structure of Complex Fluids and Macromolecules

Henrich Frielinghaus

## 13.1 Introduction

The method small angle neutron scattering (SANS) is widely used in the fields of conventional solid state physics, but more intensively in the field of soft matter research. This field embraces polymer melts, solutions, and rubbers, but also complex fluids such as microemulsions, colloidal dispersions, and micellar solutions. The complex fluids often also contain polymers, i.e. macromolecules. Finally the neighborhood to biological systems brings biophysical subjects close to neutron scattering techniques.

The typical length scale of a SANS experiment lies in the range of 1 to 100 nanometers (or 10 to 1000 Angstroems). The developments of ultra SANS enlarged the spatial region to 10 to 100µm. While the scattering techniques observe structures in the reciprocal space, all these length scales are also covered by microscopy techniques (transmission electron microscopy (TEM) and light microscopy). Advantages of SANS experiments will be made clear.

In the following some important properties of polymers shall be introduced and discussed. Then polymer blends and melts will be introduced connected with their typical scattering pattern. Finally, microemulsions are an interesting system where amphiphilic polymers can be added. These polymers modify the phase behaviour and the microscopic structure, which is studied by SANS experiments.

## 13.2 Homopolymers

Homopolymers are long linear chain molecules consisting of a single repeat unit, the monomer. While there is a local rigidity and a non-vanishing angular correlation of single carbon-carbon bonds, effective longer chain segments can be defined. The Kuhn segment embraces so many monomers that the angular correlation of these effective segments is lost. In the following we assume the polymer physics we want to describe take place on length scales larger than the Kuhn segment length $\ell_K$. Especially, the polymer itself is large compared to the single Kuhn element, of which it contains $N_K$ ($\gg 1$) segments. One important observable of a single polymer is the end-to-end distance, which simply is defined as:

$$\vec{R}_{ee} = \sum_{i=1}^{N_K} \vec{r}_i \tag{13.1}$$

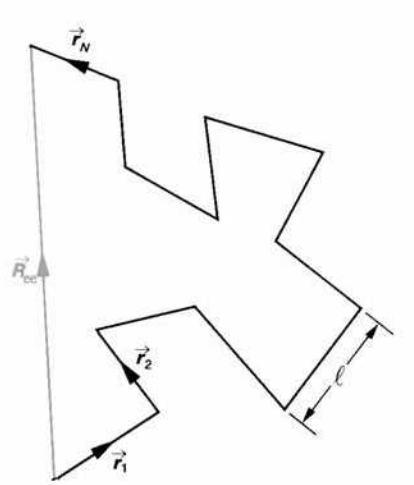



**Figure 13.1**: Schematic drawing of a chain with independent chain segments. The vectors $\vec{r}_i$ specify the individual segments. The segment length is $\ell_K$. The end-to-end vector $\vec{R}_{ee}$ is a measure for the size of the polymer.

The statistical average of this observable is simply zero, since each segment does not have a preferred orientation ($\langle \vec{r}_i \rangle = 0$), and so the whole polymer does not show a preference either. The next higher order moment of this observable is the second moment. We simply can arrange the square of a sum by:

$$\left\langle \vec{R}_{ee}^{\,2} \right\rangle = \sum_{i,j=1}^{N_K} \left\langle \vec{r}_i \cdot \vec{r}_j \right\rangle = \sum_{i=1}^{N_K} \left\langle \vec{r}_i^{\,2} \right\rangle + 2 \cdot \sum_{1 \le i < j \le N_K} \left\langle \vec{r}_i \cdot \vec{r}_j \right\rangle \tag{13.2}$$

The diagonal terms appear $N_K$ times and represent the length of a single Kuhn segment $\ell_K^2$. The off-diagonal terms would contribute if angular correlations were present. According to our assumptions this is not the case, and we finally obtain:

$$\left\langle \vec{R}_{ee}^{\,2} \right\rangle = N_K \cdot \ell_K^2 \quad \text{or:} \quad R_{ee} \equiv \sqrt{\left\langle \vec{R}_{ee}^{\,2} \right\rangle} = \sqrt{N_K} \cdot \ell_K \tag{13.3}$$

The radius of gyration is a similar measure for the size of the polymer, which is defined like the moment of inertia normalized to the total mass:

$$\left\langle \vec{R}_g^{\,2} \right\rangle = \frac{1}{N_K + 1} \cdot \sum_{i=0}^{N_K} \left\langle \vec{s}_i^{\,2} \right\rangle \tag{13.4}$$

The single vectors $\vec{s}_i$ specify the distance of a single segment from the centre of mass. It can be shown (as article C1 in reference 4) that the two typical sizes of a polymer are proportional for our assumptions ($N_K \gg 1$):

$$R_g \equiv \sqrt{\left\langle \vec{R}_g^2 \right\rangle} = \sqrt{\tfrac{1}{6} N_K} \cdot \ell_K = \sqrt{\tfrac{1}{6}} \cdot R_{ee} \tag{13.5}$$

In this sense, a polymer with negligible segment rigidity has only one length scale, given by either $R_g$ or $R_{ee}$. This typical size of the polymer is proportional to the length of a single Kuhn length $\ell_K$ and the square root of the segment number $N_K$. In practical equations, often some effective monomer length $\ell_{mon}$ and the real degree of polymerization N, which is the monomer number in a polymer, are used. For relatively rigid chains the monomer length can be larger than the real geometric length, since the equations hold for sizes on the polymer length scale.

### 13.3 Scattering of homopolymers

We now consider the scattering of a solution of homopolymers without interactions. The macroscopic scattering cross section $d\Sigma/d\Omega$ as a function of the scattering vector $\vec{Q}$ is defined rigorously as the squared amplitude of the individual phases of all atoms in the whole macroscopic volume $V$, and thus:

$$\frac{d\Sigma}{d\Omega}(\vec{Q}) = \frac{1}{V} \cdot \left| \sum_j b_j \exp\left(i\vec{Q}_j \vec{R}_j\right) \right|^2 \tag{13.6}$$

The scattering length $b_j$ determines the amplitude of the outgoing wave from a single atom $j$. with the position $R_j$. The symbol $i$ is now the imaginary unit. This elementary formula can be expressed in a handier way:

$$\frac{d\Sigma}{d\Omega}(\vec{Q}) = (\Delta\rho)^2 \cdot \phi \cdot \frac{v_K}{N_K} \cdot \left| \sum_j \exp\left(i\vec{Q}_j \vec{R}_j\right) \right|^2 = (\Delta\rho)^2 \cdot \phi \cdot \frac{1}{V_{pol}} \cdot \left| \int_{pol} \exp\left(i\vec{Q}\vec{R}\right) d^3R \right|^2 \tag{13.6}$$

The first assumption is, that we take all monomers of a Kuhn segment as one unit. This unit has a total volume $v_K$, and so a scattering length density can be defined $\rho_{pol} = (\sum b_j)/v_K$ being a measure of the polymer. In the same way one obtains the scattering length density of the solvent $\rho_{sol}$. The contrast, i.e. the scattering length density difference, appears when the sum focuses on the solute only. A remaining term considering the solvent as a homogenous matrix results in a delta function $\delta(Q)$, which does not contain information for the typical scattering experiment, and thus is neglected. The concentration $\phi$ is the volume fraction of the polymer in solution. It is proportional to the number of polymers, and thus the individual sum

in eq. 13.6 over index $j$ considers a single homopolymer only. All homopolymers contribute to the scattering independently without interference, which is true for dilute solutions. The second part of eq. 13.6 considers the polymer to be a worm with a finite volume, over which the integration is conducted. The new prefactor contains the volume $V_{pol} = v_K \cdot N_K$ of a single polymer. It is important to repeat, that we consider length scales above the Kuhn segment length, and atomic structures within the large molecule are neglected.

The chain statistics we have developed for homopolymers will be applied to this final scattering formula (eq. 13.6) now. For the scattering function $S(Q)$, i.e. the structure factor, we obtain now:

$$\begin{aligned} S(\vec{Q}) &= \frac{v_K}{N_K} \cdot \left\langle \left| \sum_j \exp\left(i\vec{Q}_j \vec{R}_j\right) \right|^2 \right\rangle \\ &= \frac{v_K}{N_K} \cdot \left\langle \sum_{j,k} \exp\left(i\vec{Q}(\vec{R}_j - \vec{R}_k)\right) \right\rangle \\ &= \frac{v_K}{N_K} \cdot \left( \sum_{j,k} 1 + \left\langle \sum_{j,k} i\vec{Q}(\vec{R}_j - \vec{R}_k) \right\rangle + \frac{1}{2} \left\langle \sum_{j,k} \left(i\vec{Q}(\vec{R}_j - \vec{R}_k)\right)^2 \right\rangle + \ldots \right) \end{aligned} \tag{13.7}$$

The vectors $\vec{R}_j$ specify the position of a segment relative to a fixed origin (contrary to $\vec{r}_i$ which is an individual segment vector). In the first transformation the complex conjugate was explicitly used, and all addends were combined in every possible form. The next transformation uses the Taylor expansion of the exponential function. The linear term has an expected value of zero, since again a first order momentum appears. So the quadratic term determines the $Q$-dependence of the structure factor, and one expresses the expansion as an exponential again:

$$S(\vec{Q}) = \frac{v_K}{N_K} \cdot \sum_{j,k} \exp\left\langle -\tfrac{1}{2} \left(\vec{Q}(\vec{R}_j - \vec{R}_k)\right)^2 \right\rangle \tag{13.8}$$

For independent chain segments - as we assumed anyhow - it can be shown, that all higher order terms of eq. 13.7 contribute consistently to the final expression of eq. 13.8. The averaging is carried out inside the exponential now, which simplifies the calculation strongly. For a random orientation relatively to the scattering vector $Q$, one obtains:

$$S(\vec{Q}) = \frac{v_K}{N_K} \cdot \sum_{j,k} \exp\left( -\tfrac{1}{6} Q^2 \left\langle (\vec{R}_j - \vec{R}_k)^2 \right\rangle \right) \tag{13.9}$$

The inner term $(\vec{R}_j - \vec{R}_k)^2$ specifies a chain part with $|j - k|$ segments. This chain part behaves like an ideal chain, and so its average length follows the formula of eq. 13.3. Furthermore, it

is helpful to express the sum as integrals, which is a good approximation on larger length scales. So one obtains:

$$S(\vec{Q}) = \frac{v_K}{N_K} \cdot \int_0^{N_K} dj \cdot \int_0^{N_K} dk \cdot \exp\left(-\tfrac{1}{6} Q^2 |j-k| \ell_K^2\right)$$
$$= V_{\text{pol}} \cdot f_D(Q^2 R_g^2) \qquad (13.10)$$
$$f_D(x) = \frac{2}{x^2}\left(\exp(-x) - 1 + x\right)$$

The Debye function $f_D(Q^2R_g^2)$ (see Fig. 13.2) is a monotonously decaying function with the maximum at $Q = 0$. There are two important limits of the structure factor. For small scattering vectors a Taylor series yields the Zimm approximation:

$$S^{-1}(\vec{Q}) = V_{\text{pol}}^{-1}(1 + \tfrac{1}{3} Q^2 R_g^2) \qquad (13.11)$$

The extrapolated forward scattering $S^{-1}(Q \rightarrow 0)$ is a measure for the single polymer volume. Of course, as described by eq. 13.6, the scattering contrast $(\Delta\rho)^2$ and the concentration $\phi$ have to be known beforehand. The slope of a Zimm-plot tells about the typical polymer size, i.e. the radius of gyration. At larger scattering angles (the considered length scales are still large compared to the segmental size $Q^{-1} \gg \ell_K$) another important scattering behaviour is obtained:

$$S(\vec{Q}) = 2 \cdot V_{\text{pol}} / (Q^2 R_g^2) \qquad (13.12)$$

Here the self similarity of a chain becomes dominant. On these intermediate scales chain parts still look like perfect chains. The corresponding fractal dimension of ideal chains is 2.

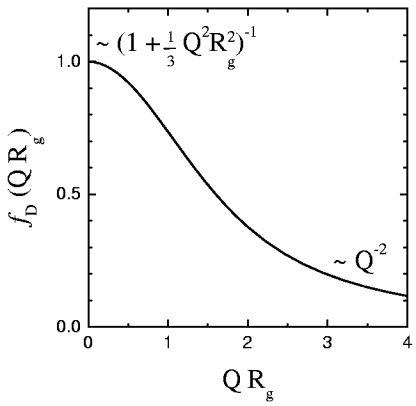



**Figure 13.2**: The Debye-Function as a function of the scaled scattering vector. Two important limits are given for small and large scattering vectors.

### 13.4 Scattering of Homopolymer Blends

The formula 13.10 was derived for dilute homopolymers in soultion without interactions. When describing homopolymer blends of two homopolymers, the assumptions of dilution and of negligible interactions do not hold anymore. The concept of the random phase approximation (RPA) bases on the undisturbed chain structure factor (eq. 13.10) and introduces high concentrations and interactions afterwards. Since this short lecture cannot go into details, we simply present the final expression of the RPA:

$$S_{RPA}^{-1}(Q) = \Delta\rho^2 / \frac{d\Sigma}{d\Omega}(Q) = \left(\phi_{pol1} V_{pol1} f_D(Q^2 R_{g1}^2)\right)^{-1} + \left(\phi_{pol2} V_{pol2} f_D(Q^2 R_{g2}^2)\right)^{-1} + \Gamma \qquad (13.13)$$

The reciprocal structure factor of a homopolymer blend is the sum of the reciprocal structure factors of the undisturbed homopolymers plus the Flory-Huggins interaction parameter $\Gamma$. In the limit of identical homopolymers (for instance a blend of protonated and deuterated polymers) and negligible interactions basically the undisturbed chain structure factor is obtained. An example of a real polymer blend is depicted in Fig. 13.3. The basic properties of the Debye function are preserved, but of course the Flory-Huggins interaction parameter is obtained by the detailed analysis. The scattering at small scattering vectors is maximal, which means that on large length scales the thermal composition fluctuations are maximal. The extrapolated forward scattering $S(Q=0)$ is the reciprocal susceptibility. The peak width is connected with the correlation length $\xi$ telling over which distance the local composition can be assumed constant. At high temperatures $S(0)$ and $\xi$ are small which is connected with a small or even negative interaction parameter $\Gamma$. When the interaction parameter comes close to the critical value $\Gamma = 2/V_{pol}$ the fluctuations become infinitely large, and $S(0)$ and $\xi$ diverge. At this moment the concept of the RPA breaks down, and the system behaves like a 3d-Ising system. This means that the point of criticality is shifted to slightly lower temperatures compared to the RPA estimation. The temperature shift is proportional to the Ginzburg number, which is a measure how strongly fluctuations influence the thermo-dynamics of the system [7].

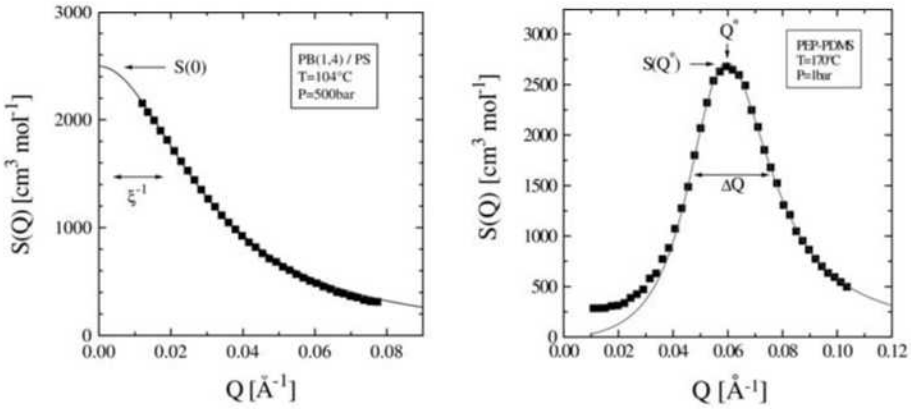



**Figure 13.3**: The scattering function $S(Q)$ as a function of the scattering vector. On the left the typical scattering of a homopolymer is shown. The sample is a polybutadiene(1,4) / polystyrene blend at 104°C and 500bar. On the right the typical scattering of a diblock copolymer is shown which is a poly-ethylene-propylene-poly-dimethylsiloxane at 170°C and 1bar.

### 13.4 Scattering of Diblock Copolymers

Diblock copolymers are chainlike molecules with two different kinds of monomers which are placed along the molecule at two different blocks. The RPA is capable to describe the scattering of diblock copolymers at high temperatures. The combination of Debye functions is just slightly more complex as in eq. 13.13, but the interaction parameter is added in the same way [8]. So we simply look on the scattering pattern of a diblock copolymer in Fig. 13.3. At small scattering vectors the ideal intensity vanishes at $Q = 0$ and increases like $Q^2$, which is due to the chemical connectivity of the two blocks. Fluctuations on large length scales ideally are impossible. Polydispersity of the block length ratio leads to some finite intensity at $Q = 0$. At large scattering vectors mainly chain parts are observed, and the connectivity of the blocks does not play a role anymore. Thus the same $Q^{-2}$ behaviour as for homopolymers is observed. At the intermediate $Q^*$ the pronounced intensity maximum indicates strong fluctuations on length scales $2\pi/Q^*$ similar to the radius of gyration. The peak width again is connected with the reciprocal correlation length, and the maximal intensity is the reciprocal susceptibility. When the temperatures are lowered the fluctuations become much stronger as for homopolymers, and deviations from the RPA concept become much more prominent. The corresponding Ginzburg numbers are much larger.

### 13.5 Scattering of Homopolymer / Diblock Copolymer blends

For mixtures of A and B homopolymers with an AB diblock copolymer (here polybutadiene and polystyrene) the scattering patterns of the two different systems compete [9]. For small diblock copolymer contents the strong scattering occurs at small scattering angles, while for larger diblock copolymer contents the strong scattering occurs at a finite scattering vector $Q^*$. For intermediate diblock copolymer contents there appears a wide plateau of strong scattering intensity ranging from zero to finite scatting angles. This high temperature phase is interesting by itself to study the critical behaviour of these extremely strong fluctuations.

At lower temperatures a phase separation occurs. While for the homopolymer-like systems with $Q^* = 0$ a phase separation takes place on macroscopic length scales (macrophase separation), for the diblock-like systems with finite $Q^*$ the phase separation leads to ordered structures (microphase separation). For the intermediate diblock copolymer contents discussed here the system forms a bicontinuous phase structure. This means that the A-rich phase forms a sponge-like structure with space for the B-rich phase. Each of the phases is continuously connected. The diblock copolymer acts as a surfactant and thus inhibits the macrophase separation.

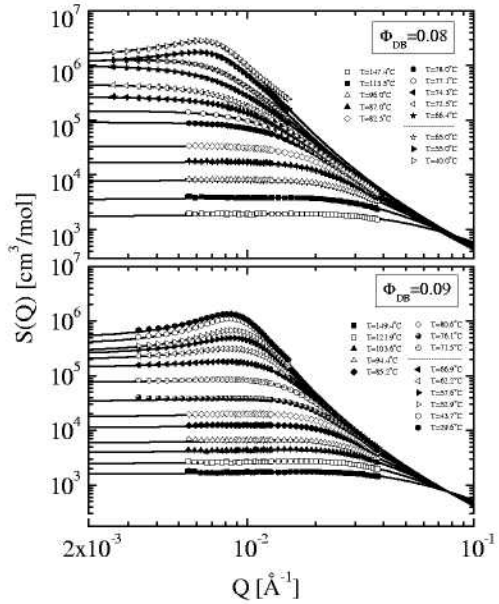



**Fig. 13.4:** The scattering function of an A/B/AB homopolymer / diblock copolymer blend. At higher temperatures the scattering is less intense, the plateau at small scattering angles is quite broad. At lower temperatures there is a phase transition to the microemulsion phase where a correlation peak appears.

The tailoring of homopolymer domains by small amounts of additives (here: diblock copolymers) is an interesting field of the current research. These systems resemble microemulsions since the mediating component has an A-philic and a B-philic segment. Some systems mimic the microemulsions better others worse. The still open mayor issue is to replace the costly diblock copolymers by less expensive polymers.

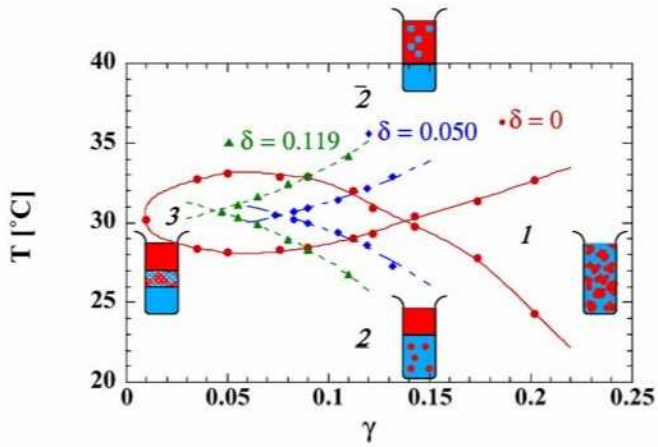



**Figure 13.5**: A typical fish-phase-diagram (red curve): temperature versus surfactant content for a symmetric water to oil ratio. At high surfactant contents a one-phase microemulsion (1) is observed, while for lower surfactant contents the three-phase coexistance (2) with a microemulsion phase, an excess oil and an excess water phase is found. At low and high temperatures (2 and $\bar{2}$) a two-phase coexistance occurs with excess oil or water phases. When adding aphiphilic diblock copolymers ($\delta$ measures the polymer content with respect to the amphiphile) the fish-tail moves to lower surfactant contents. The minimum amount of surfactant of the one-phase region is given by the fish-tail-point and is a measure for the efficiency of the amphiphile. The polymer increases the efficiency dramatically.

### 13.6 Microemulsions

Microemulsions consist of oil, water and a surfactant. While the microemulsion appears macroscopically homogenous, oil- and water-rich domains form on a microscopic level. The mediating surfactant forms a thin film between these domains. In the following we restrict ourselves to equal amounts of oil and water. A typical phase diagram is shown in Fig. 13.5 in the temperature versus surfactant content $\gamma$ representation [10]. The most interesting region is the one-phase region (1), where a bicontinuous microemulsion is found. The minimum amount of surfactant is connected to the fish-tail-point, and is a measure for the efficiency of

the surfactant. When adding amphiphilic diblock copolymer, the system becomes more efficient. The polymer amount δ is given in units relative to the total amphiphile, but in absolute units it is less than 0.5%. The dramatically increased efficiency bases on the polymer boosting effect which is described in the following.

By contrast variation measurements it was revealed where the polymer is placed in this four component system. Is was necessary to have each component in a normal protonated and a deuterated version, i.e. normal and heavy water, normal and deuterated decane and normal and deuterated $C_{10}E_4$ surfactant. The minor component polymer was always protonated. The bulk contrast was achieved by using heavy water and protonated components otherwise. Then the water domain is visible against the other components. For the film contrast also deuterated decane was used, and the surfactant film became visible. For the polymer contrast only the protonated polymer was visible. The macroscopic cross section of such a four component system can be written generally as:

$$\begin{aligned}\frac{d\Sigma}{d\Omega}(Q) = &(\rho_O - \rho_W)^2 S_{OO} + (\rho_F - \rho_W)^2 S_{FF} + (\rho_P - \rho_W)^2 S_{PP} \\ &+ (\rho_O - \rho_W)(\rho_F - \rho_W) S_{OF} + (\rho_F - \rho_W)(\rho_P - \rho_W) S_{FP} \\ &+ (\rho_O - \rho_W)(\rho_P - \rho_W) S_{OP}\end{aligned} \tag{13.14}$$

The first three terms are purely represented by the bulk, film, and polymer contrast ($S_{OO}$, $S_{FF}$, $S_{PP}$). But since the macroscopic cross section is a quadrature of the scattering amplitudes (see eq. 13.6) also cross terms appear. By measuring many contrasts close to the polymer contrast, also the other partial scattering functions ($S_{OF}$, $S_{FP}$, $S_{OP}$) are detectable. These cross terms arise due to a convolution of the real space structures, and thus relative positions of two components are measurable. This valuable information is unavailable by the diagonal terms or a single contrast condition.

For many measurements of macroscopic cross sections at different contrast conditions eq. 13.14 reads $d\vec{\Sigma}/d\Omega = \underline{\underline{\Delta\rho}} \cdot \vec{S}$. Usually, there are many more measurements than the six unknown partial scattering functions, and so the system is over-determined and the experimental noise is reduced. Formally, the inverse matrix of the scattering length densities can be calculated by the Sigular Value Decomposition method, and the partial scattering functions are obtained by $\vec{S} = \underline{\underline{\Delta\rho}}^{-1} \cdot d\vec{\Sigma}/d\Omega$. An example of a cross term $S_{FP}$ is shown in Fig. 13.6. The valuable information of the polymer relative to the surfactant membrane is obtained. The solid line is described by a diblock copolymer decorating the surfactant membrane. Each of the blocks is placed in its pleasant environment and the coils form a mushroom like object.

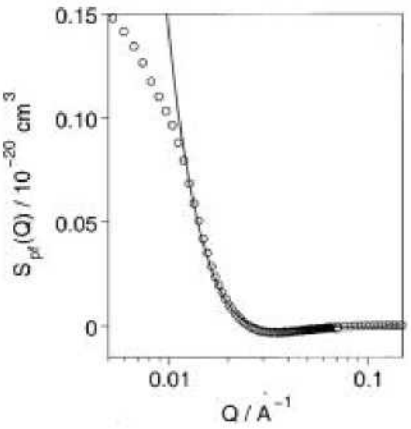



**Figure 13.6**: The partial polymer-film scattering function as a function of the scattering vector. The fitted function describes a polymer in the presence of a planar wall. The polymer shows a mushroom conformation.

### 13.7 Bulk Scattering and Phase Diagrams

The bulk scattering also reveals valuable information about the domain structure and finally about the thermodynamics of the microemulsion [11]. An example for the bulk scattering is shown in Fig. 13.7. The macroscopic cross section can be described by the Teubner-Strey theory which bases on a Ginzburg-Landau approach, which considers long wavelength fluctuations of the oil and water domains. The final formula reads:

$$\frac{d\Sigma}{d\Omega}(Q) = \frac{(\Delta\rho_{OW})^2 \cdot 8\pi\phi_W(1-\phi_W)/\xi}{((2\pi/d)^2+\xi^{-2})^2 - 2((2\pi/d)^2-\xi^{-2})Q^2+Q^4} \tag{13.15}$$

The dominator contains the total fraction of water $\phi_W$. Much more interesting are the two structural parameters $\xi$ and $d$ which are obtained as fitting parameters from the measurement. The domain size $d$ is to be understood as the average distance between two consecutive water parts. The correlation length $\xi$ is a measure for the regularity of alternating domains. As indicated in Fig. 13.7 the peak position is mainly given by the domain size $d$, and the peak width is mainly given by the correlation length $\xi$. In comparison to diblock copolymers the forward scattering of microemulsions is clearly non-zero. Thermal fluctuations of oil and water can take place easily on large length scales while for the diblock copolymer the bond between the block makes sure that the polymer looks homogenous on large length scales. Many similarities to the polymeric microemulsions become visible (see Fig. 13.4) where the domains become less pure by raising the temperature or the domains even turn to fluctuations at temperatures above the phase boundary.

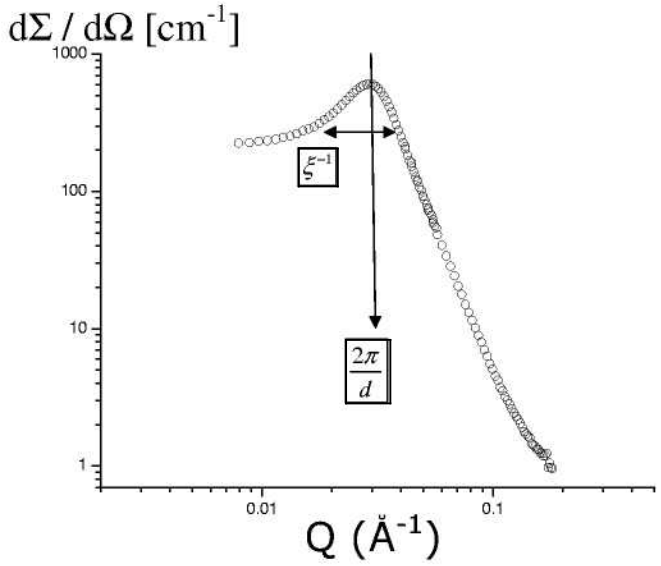



**Figure 13.7**: A typical scattering pattern of a bicontinuous microemulsion. The peak position is connected to the domain spacing *d*. The peak width is inversely proportional to the correlation length ξ. This kind of data is usually well described by the Teubner-Strey fitting function given in eq. 13.15.

While the structure is described by the concepts above, the thermodynamic properties of a microemulsion shall be discussed now. Phase diagram measurements and SANS measurements can be compared in a unique way. The Helfrich free energy assumes that the free energy of a microemulsion is dominated by the elastic properties of the surfactant film:

$$H = \int dS \left( \tfrac{1}{2} \kappa (c_1 + c_2)^2 + \bar{\kappa} c_1 c_2 \right) \tag{13.16}$$

The integral is conducted along the membrane surface. The two principal curvatures $c_1$ and $c_2$ are obtained by a tangential construction of two circles at each membrane point. The curvatures $c_i = 1/R_i$ are the reciprocal radii, and the two circles are perpendicular. The mean curvature $c_1 + c_2$ is connected with the first modulus, the bending rigidity κ. The Gaussian curvature $c_1 c_2$ is connected with the saddle splay modulus $\bar{\kappa}$. The moduli have the following dependence:

$$\begin{aligned} \frac{\kappa_R}{k_B T} &= \frac{\kappa_0}{k_B T} + 0.239 \cdot \ln \gamma + 0.214 \cdot \sigma (R_W^2 + R_O^2) \\ \frac{\bar{\kappa}_R}{k_B T} &= \frac{\bar{\kappa}_0}{k_B T} - 0.265 \cdot \ln \gamma - 0.167 \cdot \sigma (R_W^2 + R_O^2) \end{aligned} \tag{13.17}$$

The logarithmic spatial renormalization ($\ln \gamma$) lets the membrane appear flabbier on larger length scales. The connected intrinsic modulus ($\kappa_0$, $\bar{\kappa}_0$) is the extrapolated modulus for high surfactant contents ($\gamma \rightarrow 1$). The analytic theory of diblock copolymers [12] scales with the grafting density $\sigma$ and the end-to-end distances $R_{ee}$ of the oil- and water-soluble blocks. Please note, that for both moduli the correction terms are very similar except for the sign. As a rule of thumb, the saddle splay modulus $\bar{\kappa}_R$ is basically the negative value of the bending rigidity $\kappa_R$.

Now, both moduli are connected with experimentally accessible magnitudes. At the fish tail point of the phase diagram (see Fig. 13.5) the renormalized saddle splay modulus $\bar{\kappa}_R$ is a small constant, and, thus, changes of the minimal surfactant amount are connected with the polymer amount: $\Delta\bar{\kappa}_R / k_B T = -0.167 \cdot \sigma(R_W^2 + R_O^2) = +0.265 \cdot \Delta \ln \gamma$. In a real experiment the sensitivity $\hat{\Xi}$ (i.e. one coefficient) is measured besides the linear dependence, and, thus, $\Delta \ln \gamma = -\hat{\Xi} \cdot \sigma(R_W^2 + R_O^2)$. The bending rigidity is accessible through SANS experiments by the following trick: The Gaussian random field theory describes the statistics of a membrane by a random field, which defines the membrane at the zero of the random field. The fluctuations of the random field are controlled by a parameterized spectral density, which exactly has the appearance of eq. 13.15. In this way the structural parameters $d$ and $\xi$ are connected with the bending rigidity by $\kappa_R / k_B T = 0.85 \cdot \xi / d$. Again, the linear dependence is observed as a function of the scaled polymer amount by: $\Delta\kappa_R / k_B T = 0.85 \cdot \Delta(\xi / d) = \Xi \cdot \sigma(R_W^2 + R_O^2)$.

While this concept proved correct for amphiphilic diblock copolymers it remains to be tested for the newly synthesized sticker polymers. These polymers have only a short hydrophobic unit of 10 carbon atoms, and a polymeric hydrophilic block (90 ethylene oxide units). If all polymers are anchored at the surfactant membrane the same equations should hold, except for the oil soluble end-to-end distance, which simply can be set to zero. The obtained results are shown in Fig. 13.8. The dependencies are linear as predicted by the theory. The coefficients read $\hat{\Xi} = 1.64$ and $\Xi = 0.256$ which agrees exceptionally well with the coefficients of the diblock copolymers. This means, that the polymer boosting effect is successfully transferred to the new sticker polymers which are much easier to synthesize and therefore much cheaper to produce. This polymer is highly water soluble, which is important for formulations of powders. So this polymer is much better for applications than the initially well characterized diblock copolymer.

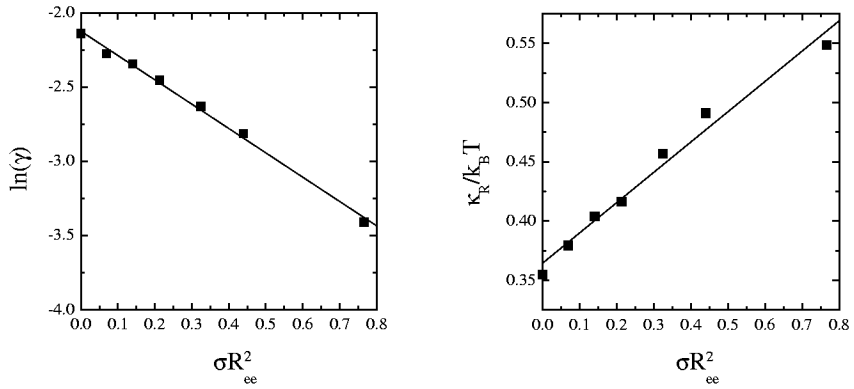



**Figure 13.8**: The minimum surfactant amount $\gamma$ as a function of the scaled polymer amount $\sigma \cdot R_{ee}$ for microemulsions with increasing amount of a sticker polymer $C_{12}E_{90}$. The decrease shows that the microemulsion becomes more and more efficient, i.e. the polymer boosting effect is successfully transferred to sticker polymers. On the right the bending rigidity $\kappa_R$ is plotted as a function of the scaled polymer amount. The increased bending rigidity explains why larger domain structures with a better surface to volume ratio can be formed. On a microscopic scale both diagrams are related through the Helfrich free energy. The polymer effect was described by Lipowsky.

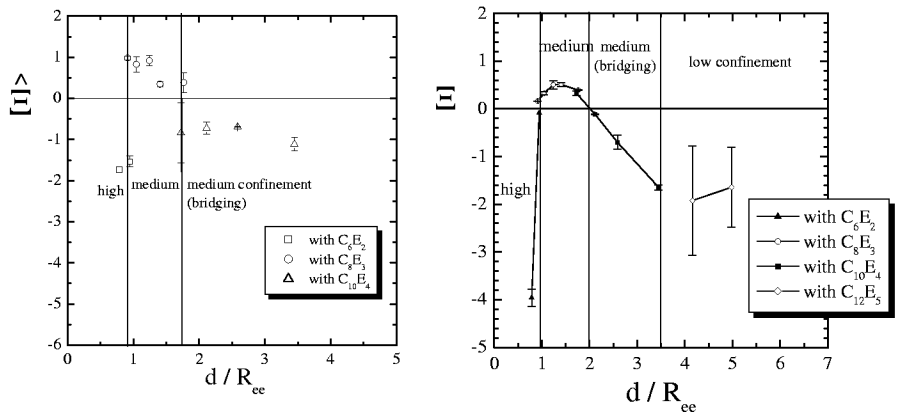



**Figure 13.9**: The sensitivities of the telechelic polymer on the phase diagram and the bending rigidity for different scaled domain sized $d / R_{ee}$. At low confinement (large $d$) a constant limit is reached (for $\Xi$). At medium confinement there is a region where bridging is continuously switched on (for $\Xi$) and a region where the sensitivity is almost constant. This constant sensitivity compares well with the confined diblock copolymer. At high confinement a reversed behaviour is found. For this degree of confinement homopolymers, diblock copolymers and telechelic polymers agree. The discontinuous change of $\hat{\Xi}$ at medium confinement might be interesting for applications.

Another aspect of possible additives is addressed with the telechelic polymer. This polymer has two hydrophobic end-groups at each end of the hydrophilic mid-block. So this polymer will connect two spots of the membrane, if both end-groups are anchored safely. This kind of connection can take place between neighbored points, or between opposite points, if the domains are small enough. For the full information of possible conformations, the domain size $d$ has to be changed with respect to the end-to-end distance $R_{ee}$ of the polymer. The sensitivities $\hat{\Xi}$ and $\Xi$ of the saddle splay modulus and the bending rigidity are shown as a function of the scaled domain size $d/R_{ee}$ in Fig. 13.9 (the reciprocal ratio $R_{ee}/d$ can be also interpreted as a degree of confinement). At large domain sizes a constant value is reached (at least for $\Xi$). Here only neighbored membrane points should be connected, and the dependence on the domain size should vanish. At medium domain sizes a continuous change of $\Xi$ indicates that more and more polymers bridge opposite membrane points. At even lower domain sizes a plateau value of $\Xi$ is reached, which is comparable for diblock copolymers in the same stage ($d/R_{ee}$). For these medium domain sizes $\hat{\Xi}$ changes discontinuously from negative to positive values. So the bridging does not affect the saddle splay modulus continuously, but the plateau value at lower domain sizes is comparable to diblock copolymers as for $\Xi$. The plateau value is a sign of medium confinement without differentiating between bridging and connecting neighbored points, since telechelic polymers and diblock copolymers are similar. At the lowest domain sizes a reversed behavior is found. This high confinement stage is universal for homopolymers, diblock copolymers and telechelic polymers. Here the polymer is reflected by the membrane many times, and the anchoring does only play a minor role.

The sudden change of $\hat{\Xi}$ at medium domain sizes is directly connected to the phase behavior, and should be interesting for applications. When dilution of microemulsions plays a role in an industrial process, the polymer supports the emulsification for a concentrated system and a phase separation upon dilution. In metal processing often microemulsions are used, which are cleaned and phase separated after the process in order to be reused for another cycle. The telechelic polymer acts as an intelligent additive which reacts on the environment and supports special purposes. Other polymer architectures may bear many other important properties, which should be uncovered and made suitable for applications. Furthermore, the synthetic polymers mimic biological proteins on cell membranes. The basic research on synthetic polymers thus reveals also valuable information about the functions of biological attachments on membranes, such as the cytoskeleton. Many interesting results are about to come.

### 13.6 Summary

Many new interesting aspects appear, when certain polymers are added to either polymer blends or microemulsions. All these new polymers are A-philic and B-philic at certain parts, and the architecture can vary. The aim of the polymer additives is always to modify the overall miscibility of the components A and B. Furthermore, the domain size and shape can be influenced by the polymer additive. While the miscibility often can be studies by visual inspection - it is a macroscopic property - the detailed analysis of the nano-scale domain structure is performed best by scattering experiments. The more components are used in the final formulation the more important is the method of contrast variation. This method inevitably leads to neutron scattering. In this way basic research will support the tailoring of next-generation materials.

### References


Text books:

[1] R.J. Roe, *Methods of x-ray and neutron scattering in polymer science*. Oxford University Press, Oxford 2000

[2] J.S. Higgins and H.C. Benoit, *Polymers and neutron scattering*. Clarendon Press, Oxford (1994)

IFF Spring Schools:

[3] 33. IFF-Ferienkurs 2002, *Soft Matter - Complex Materials on Mesoscopic Scales*, Schriften des Forschungszentrums Jülich, Jülich 2002

[4] 35th Spring School 2004, *Physics Meets Biology - From Soft Matter to Cell Biology*, Schriften des Forschungszentrums Jülich, Jülich 2004

[5] 38th Spring School 2007, *Probing the Nanoworld - Microscopies, Scattering and Spectroscopies of the Solid State*, Schriften des Forschungszentrums Jülich, Jülich 2007

[6] 22. IFF-Ferienkurs 1991, *Physik der Polymere*, Ferienkurse des Forschungszentrums Jülich, Jülich 1991 (written in German)

Articles:

[7] D. Schwahn *Adv. Polym. Sci.* **183**, 1 (2005)

[8] L. Leibler, *Macromolecules* **13**, 1602 (1980)

[9] V. Pipich, D. Schwahn, L. Willner *J. Chem. Phys.* **123**, 124904 (2005)

[10] H. Endo, M. Mihailescu, M. Monkenbusch, J. Allgaier, G. Gompper, D. Richter, B. Farago, T. Sottmann, R. Strey, I. Grillo, *J. Chem. Phys.* **115**, 580 (2002)

[11] D. Byelov, H. Frielinghaus, O. Holderer, J. Allgaier, D. Richter *Langmuir* **20**, 10433 (2004)

[12] C. Hiergeist, R. Lipowsky *J. Phys. II* **6**, 1465 (1996)

# 14

# Dynamics of Macromolecules

Dieter Richter

# 14. Dynamics of Macromolecules

D. Richter
Institut für Festkörperforschung, Forschungszentrum Jülich GmbH

## 14.1 Introduction

Polymeric materials are used because they are durable, cheaply to produce, easily to process and because they exhibit very favourable processing and mechanical properties. Polymers may behave like a viscous fluid or rubber elastic, very tough with high impact strength or even brittle. In the simplest case polymers are long linear chain molecules build from a repeating unit: the monomer. Such polymers are called linear homopolymers. Other than synthetic polymers, biopolymers are highly complex molecular structures with a sharp molecular weight and a uniquely defined sequence of building blocks. They are the molecular manifestations of life with a high variety of structure and specific function. Nevertheless, at least in their denaturated state they exhibit similarities with synthetic materials while in their folded state the specific function evolves. Also the general principles of selfassembly in structure formation are common to both species.

The diffusional motions of long flexible polymers constitute fascinating physics and at the same time represent one of the great challenges of modern material science. The drive towards the molecular understanding of the complex viscoelastic properties of polymer liquids is the focal point of rheology and connects the classical chemical engineering approach with modern physics [1]. There the tube model invented by Doi and Edwards [2] and de Gennes [3] has shown itself as the most successful molecular model describing the topological confinement imposed by the mutually interpenetrating polymer chains in the melt. In terms of this so called reptation model a theory of viscoelasticity has been developed that describes the main features of polymer melt rheology.

Large scale protein motions on the other hand are critical for proteins to coordinate precise biological function. Such dynamics are invoked in regulatory proteins, motor proteins, signalling proteins and structural proteins. Structural studies have documented the conformational flexibility in proteins accompanying their activity. Results from macroscopic

studies such as biochemical kinetics and single molecule detection have also shown the importance of conformational dynamics and Brownian thermal fluctuations within the proteins or protein complexes. However, the time dependent dynamic processes that facilitate such protein motions remain poorly understood and experimentally nearly untouched [4].

Neutron spin echo spectroscopy is the highest resolution neutron technique and provides time resolution in the 100ns range, enabling thereby the access to molecular motion on a mesoscopic time scale between the atomic picosecond scales and the macroscopic times [5]. At that scale the molecular motions of the polymers take place that underlie their macroscopic viscoelastic behaviour. Similarly, the large scale motions of bio molecules occur on similar space time frames.

This lecture aims to identify general principles of chain motion on a molecular scale which underpin the macroscopic properties and presents concepts and experimental results on these motional mechanisms in space and time. We will mainly address the dynamics of homopolymers and give one example for studies of the molecular dynamics of biopolymers.

### 14.2 Scattering and the large scale motion of macromolecules

Neutron scattering with its space time sensitivity on a molecular and atomic scale unravels the space time occurrence of the molecular motions we are interested in. Commencing at the scale of the single bond, where movements take place at a pace as in normal liquids quasielastic neutronscattering (QENS) provides insight into local relaxation processes. At larger length scales first the entropy driven Rouse motion and at even larger distances the effect of topological confinement due to the mutual interpenetrating chains come into the observation range. The most powerful technique suitable for these investigations, the neutron spin echo spectroscopy (NSE) operates in the time domain and uncovers a time range from about 2ps to 200ns and accesses a momentum transfer between about $0.01\text{Å}^{-1}$ and $3\text{Å}^{-1}$.

Coherent, quasi- and inelastic neutronscattering reveals the dynamic structure factor ($S(Q,t)$) or its Fourier transformed counter part $S(Q,\omega)$.

$$S(Q,t) = \frac{1}{N}\sum_{ij}\left\langle \exp\left(-i\underline{Q}\underline{r}_j(t)\right)\exp\left(-i\underline{Q}\underline{r}_i(0)\right)\right\rangle \tag{14.1}$$

Where $\underline{r}_j(t)$ and $\underline{r}_i(0)$ are the position vectors of the scatterers at time $t$ and time $t=0$ respectively. $N$ is the number of scatteres, $\hbar Q = \hbar 4\pi/\lambda * \sin(\theta/2)$ is the momentum transfer during scattering (for elastic or nearly elastic scattering) with $\theta$ the scattering angle and $\lambda$ the neutron wavelength. The brackets denote the thermal average. $S(Q,t)$ reflects the pair correlation function and relates to the collective properties of a material. In the neutron cross section it is weighted by the average scattering length $\left|\overline{b}\right|^2$.

Incoherent scattering is related to the scattering length disorder which may either result from spin dependent scattering lengths like in the case of hydrogen or from isotope mixtures of isotopes with different scattering properties. This disorder prevents constructive interference of partial waves scattered at different atoms and reveals the self correlation function . Eq.[14.1] provides the self correlation function if in the double sum only terms with $i=j$ are considered. In the cross section $S_{inc}(Q,t)$ is weighted by the average scattering length fluctuation $\left(\left\langle b^2\right\rangle - \left|\overline{b}^2\right|\right)$.

In Gaussian approximation which is commonly used for the calculation of neutron dynamic structure factors for polymer dynamics Eq.[1] is approximated by

$$S(Q,t) = \frac{1}{N}\sum_{ij}\exp\left[-\frac{Q^2}{6}\left\langle\left(\underline{r}_i(t)-\underline{r}_j(0)\right)^2\right\rangle\right] \tag{14.2}$$

**14.3 Entropy driven dynamics**

The dynamics of a generic linear Gaussian chain as described in the Rouse model [6] is the starting point for a standard description of the Brownian dynamics in polymer melts. In this model the conformational entropy of a chain acts as a resource for restoring forces for a chain conformation deviating from thermal equilibrium. In this chapter we deal with this entropy driven dynamics in terms of the Rouse model and present neutron spin echo (NSE) results on

the space time evolution of the Rouse relaxation. Thereby, we exemplify the mathematical treatment of chain dynamics problems. Therefore, we detail the description such that it may be followed in all steps. In the discussion of further models later on for details we refer to the relevant literature.

### 14.3.1 Gaussian chains

The conformation of a flexible linear polymer chain on scales somewhat larger than the main chain bond length $\ell_0$ assumes a random walk. The conformations of such a chain are described by a set of segment vectors $\{\underline{r}(n)\} = (\underline{R}(n) - \underline{R}(n\text{-}1))$ where $\underline{R}(n)$ is the position vector of segment $n$. Following the central limit theorem the length distribution of a vector $\underline{r}$ connecting segments that have a topological distance of $n$ steps is a Gaussian.

$$\phi(R,n) = \left(\frac{3}{2\pi n\ell^2}\right)^{3/2} \exp\left(-\frac{3R^2}{2n\ell^2}\right) \tag{14.3}$$

with $\ell$ the segment length. The Rouse model bases on a further idealization of the chain statistics assuming that the bond vector $\underline{\ell}$ of hypothetic connecting points along the chain also has a Gaussian distribution. With $\langle \ell^2 \rangle = b^2$. For simplicity throughout the lecture we will take $b^2 = \ell_0^2 C_\infty$. Keeping, however, in mind that the building block of a Gaussian chain may well contain a larger number of main chain bonds. $C_\infty$ is the characteristic ratio accounting for the local stiffness arising from the non-random bond angle distribution of the bonds of length $\ell_0$. The conformational probability of a conformation $\{\underline{r}(n)\}$ follows as

$$P\left(\{\underline{r}(n)\}\right) = \left(\frac{3}{2\pi\ell^2}\right)^{\frac{3}{2}N} \exp\left[-\sum_{n=1}^{N} \frac{3\left(\underline{R}(n) - \underline{R}(n-1)\right)^2}{2\ell^2}\right] \tag{14.4}$$

with $n$ counting the number of segments of the chain. The free energy of a Gaussian chain is entirely described by its conformational entropy

$$S = k_B \ell n \left[ P\left(\{r(n)\}\right) \right] \tag{14.5}$$

The Gaussian chain model yields a spring constant even for a single bond. $k = 3k_BT/\ell^2$ where $k_B$ is the Boltzmann constant. From Eq.[14.4] the chain extension between arbitrary points along the chain becomes $|n - m|\ell^2$.

### 14.3.2 The Rouse model

The Rouse model starts from a Gaussian chain representing a coarse grained polymer model where springs stand for the entropic forces between hypothetic beads [6] (Fig.1).



Figure 14.1: *Spring-bead model of a Gaussian chain as assumed in the Rouse model. The beads are connected by "entropic springs" and are subject to a frictional force $\zeta_0 \upsilon$, where $\upsilon$ is the bead velocity and $\zeta_0$ the bead friction coefficient*

We are interested in the motion of segments on a length scale $\ell < r < R_E$ where $R_E^2 = N\ell^2$ is the end to end distance of the chain. The segments are subject to an entropic force resulting from the derivative of Eq.[14.5] ($x$ components).

$$\frac{\partial}{\partial x(n)} \; S = \frac{k_B T}{\ell^2} \left[ x(n+1) - 2x(n) + x(n-1) \right] \tag{14.6}$$

And to a stochastic force $f_x(n,t)$ which fulfils $\langle f_x(n,t)\rangle = 0$ and $\left\langle f_\alpha(n,t)\ f_\beta(m,0)\right\rangle = 2k_BT\,\zeta_0\,\delta_{nm}\,\delta_{\alpha\beta}\,\delta(t)$. $\zeta_0$ denotes the friction coefficient and $\alpha,\beta$ the Cartesian components. Regarding the index $n$ as the continuous variable the Langevin equation for segment motion assumes the form

$$\zeta_0 \frac{\partial x}{\partial t} = \frac{3k_BT}{\ell^2} \frac{\partial x^2(n)}{\partial n^2} + f_x(n,t) \tag{14.7}$$

The boundary condition of force free ends requires $\frac{\partial^2 x(n)}{\partial n} \Big|_{n=0,N} = 0$. The partial differential equations are solved by Cosine Fourier transformation to normal coordinates fulfilling the boundary conditions. In normal coordinates the Langevin Eq.[7] becomes

$$\zeta_p \frac{\partial}{\partial t} \tilde{x}(p,t) = -k_p \tilde{x}(p,t) + \tilde{f}(p,t) \tag{14.8}$$

with $k_p = \frac{2\pi^2 p^2}{N} k$, $\zeta_p = 2N\zeta_0$. For the stochastic force we have

$$\left\langle f_\alpha(p,t)\ f_\beta(q,0)\right\rangle = 2\zeta_p\ k_BT\,\delta_{pq}\,\delta_{\alpha\beta}\,\delta(t) \tag{14.9}$$

Eq.[14.8] is readily solved by a single exponential

$$\tilde{x}(p,t) = \frac{1}{\zeta_p} \int_{-\infty}^{t} dt' \exp\left((t-t')/\tau_p\right) \tilde{f}(p,t') \tag{14.10}$$

Where the mode relaxation time $\tau_p$ is given by

$$\tau_p = \frac{\zeta_p}{k_p} = \frac{\zeta_0 N^2 \ell^2}{3\pi^2 k_BT\, p^2} = \frac{\tau_R}{p^2} = \frac{N^2}{W\pi^2 p^2};\ W = \frac{3k_BT}{\ell^2\zeta_0} \tag{14.11}$$

$\tau_r$ is the Rouse time – the longest time in the relaxation spectrum – and $W$ is the elementary Rouse rate. The correlation function of the normal coordinates is finally obtained to

$$\left\langle \tilde{x}(p,t)\ \tilde{x}(p,0)\right\rangle = \frac{N\ell^2}{6\pi^2 p^2}\exp\left(-\frac{t}{\tau_p}\right) \tag{14.12}$$

For the center of mass coordinate one finds

$$\left\langle \tilde{x}(0,t)\ \tilde{x}(0,0)\right\rangle = \frac{2k_BT}{N\zeta_0}t \tag{14.13}$$

Scattering experiments relate to mean square segment correlation functions which are obtained by back transformation of the normal coordinates

$$\begin{aligned} B(n,m,t) =& 3\left\langle \left(x(n,t) - x_m(0)\right)^2\right\rangle = 6D_Rt + |m-n|\ell^2 + \frac{4N\ell^2}{\pi^2} \\ &\times\sum_{p=1}^{N}\frac{1}{p^2}\cos\left(\frac{p\pi m}{N}\right)\cos\left(\frac{p\pi n}{N}\right)\left[1-\ \exp\left(-\frac{tp^2}{\tau_R}\right)\right] \end{aligned} \tag{14.14}$$

In order to arrive at Eq.[14.14] we have used $D_R = \frac{3}{6t}\left\langle \left(x(0,t) - x(0,0)\right)^2\right\rangle$; $D_R$: Rouse diffusion coefficient and $\sum_{p=1}^{\infty}\frac{1}{p^2}\left[\cos\left(\frac{p\pi m}{N}\right) - \cos\left(\frac{p\pi n}{N}\right)\right]^2 = \frac{\pi^2}{2N}|n-m|$. For the special case of the self correlation function ($n = m$) $B(n,n,t)$ reveals the mean square displacement of a polymer segment. For large $p$ the $\cos^2$ in Eq.[14.14] is a rapidly oscillating function which may be replaced by the mean value ½. With this approximation we convert the sum into an integral and obtain

$$B(n,n,t) = \left\langle r^2(t)\right\rangle = 2\ell^2\left(\frac{3k_BTt}{\pi\zeta_0\ell^2}\right)^{1/2} + 6D_Rt \tag{14.15}$$

Other than in normal diffusion in the segmental regime the mean square displacement does not grow linearly in time but with its square root. For the translational diffusion coefficient $D_R = \frac{k_B T}{N\ \zeta_0} = \frac{W\ell^4}{3N\ell^2} = \frac{W\ell^4}{3R_E^2}$ is obtained. $D_R$ is inversely proportional to the number of friction performing segments.

The self correlation function relates directly to the mean square displacement of the diffusing segments. In Gaussian approximation, inserting Eq.[14.15] into Eq.[14.2], for $t < \tau_R$ we have

$$S_{self}(Q,t) = \exp\left[-Q^2 D_R t\right]\ \exp\left\{-\frac{2}{\sqrt{\pi}}\left(\frac{k_B T \ell^2}{12\zeta_0} Q^4 t\right)^{1/2}\right\} \tag{14.16}$$

For coherent scattering observing the pair correlation function interferences from waves emanating from various segments complicate the scattering function

$$S_{chain}(Q,t) = \frac{1}{N}\exp\ \left[-Q^2 D_R t\right]\ \sum_{nm}\exp\ \left\{-\frac{1}{6}|n-m|\ Q^2\ell^2\right\}\ * \\ \exp\left\{-\frac{2}{3}\frac{R_E^2 Q^2}{\pi^2}\ \sum_p \frac{1}{p^2}\ \left\{\cos\left(\frac{p\pi m}{N}\right)\ \cos\left(\frac{p\pi n}{N}\right)\ \left(1-\exp\ \left(-\frac{tp^2}{\tau_R}\right)\right)\right\}\right\} \tag{14.17}$$

For small $Q(QR_E < 1)$ the second and third terms are negligible and $S_{chain}(Q,t)$ describes the center of mass diffusion of the chain

$$S_{self}(Q,t) = S_{chain}\ (Q,t) = \exp\left(-D_R Q^2 t\right) \tag{14.18}$$

For $Q\,R_E > 1$ and $t < \tau_R$ the internal relaxations dominate. For $t = 0$ we have $S_{chain}(Q,t) = S_{chain}(Q)$ i.e. the structure factor corresponds to a snapshot of the chain structure

$$S_{chain}(Q) = \frac{1}{N}\sum_{n,m}\exp\left(-\frac{1}{6}Q^2|n-m|\ell^2\right) \tag{14.19}$$

Replacing the summation by integrals and observing the relation $R_g^2 = \frac{1}{6} N \ell^2$ for the radius of gyration Eq.[14.19] immediately leads to the well known Debye function.

$$S_{chain}(Q) = N f_{Debye}\left(Q^2 R_g^2\right)$$
$$f_{Debye}(x) = \frac{2}{x^2}\left(e^{-x} - 1 + x\right) \qquad (14.20)$$

The shape of the Debye function corresponds to the uppermost curve in Figure 14.2.

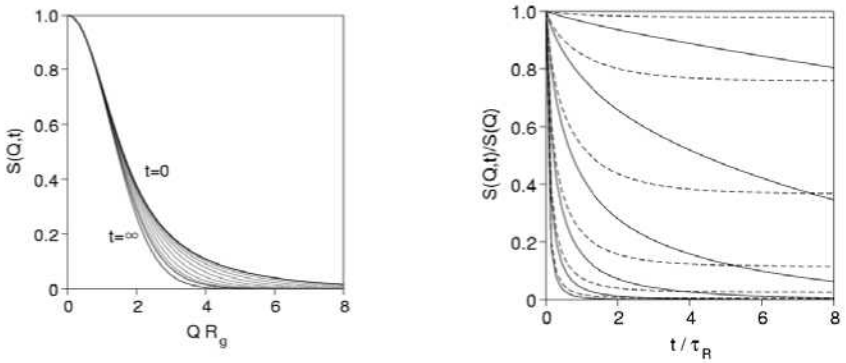



Figure 14.2: *Development of $S_{chain}$ (Q,t) for different times (left) and the normalized relaxation function $S_{chain}(Q,t)/S(Q)$ (right) for $QR_g$ = 1, 2, ... 6. The dashed lines contain only the intra-chain relaxation, whereas the solid lines include the center-of-mass diffusion. Note that for short chains, respectively for small Q the translational diffusion dominates the observed dynamics.*

Important scaling properties are revealed by an approximate computation of the high/$Q$ behaviour of $S_{chain}(Q,t)$ (Eq.[14.17]). Replacing sums by integrals and performing some simplifications we get

$$S_{chain}(Q,t) = \frac{12}{Q^2 \ell^2} \int_0^\infty du \exp\left\{-u - \left(\Omega_R t\right)^{1/2} h\left(u\left(\Omega_R t\right)^{-1/2}\right)\right\}$$
$$h(y) = \frac{2}{\pi} \int_0^\infty dx \, \frac{\cos(xy)}{x^2}\left(1 - \exp\left(-x^2\right)\right) \qquad (14.21)$$

Note that this equation only depends on one variable: the Rouse variable.

$$(\Omega_R t)^{1/2} = \frac{Q^2}{6}\sqrt{\frac{3k_B T\,\ell^2 t}{\zeta_0}} = \frac{Q^2\ell^2}{6}\sqrt{Wt} \tag{14.22}$$

The Rouse model does not contain an explicit length scale. Therefore for different momentum transfers the dynamic structure factors are predicted to collapse to a single master curve if they are represented as a function of the Rouse variable.

Further note, that for $t = 0$ Eq.[14.21] does not resemble the Debye function but yields its high $Q$ limiting behaviour $\approx Q^{-2}$. The approximation is only valid for $QR_g \gg 1$. In that regime the form of $\Omega_R$ immediately reveals that the intrachain relaxation increases $\approx Q^4$ in contrast to normal diffusion $\approx Q^2$. Finally, Eq.[14.2] illustrates the time development of the structure factor.

### 14.3.3 Neutron spin echo results

Recently it became possible to observe directly the incoherent cross section from a protonated chain, thereby measuring the self correlation function. Figure 14.3 displays the time dependent mean square displacement obtained from a high molecular weight ($M_w = 80000$) monodisperse polyethylene-propylene (PEP) melt at 492K [7]. In Gaussian approximation for negligible translational diffusion Eq.[14.16] yields

$$\left\langle r^2(t)\right\rangle = -\frac{6}{Q^2}\ell n\, S_{self}(Q,t) \tag{14.23}$$

As may be seen from Figure 14.3 the mean square displacement (MSD) follows with high accuracy the predicted square root law in time. Since neutron quasielastic scattering resolves dynamic processes in space and time these measurements give direct information about the segment displacement at a given time. E.g. at 10ns the MSD amounts to 620Å$^2$ i.e. the average proton has travelled about 25Å during this time interval.

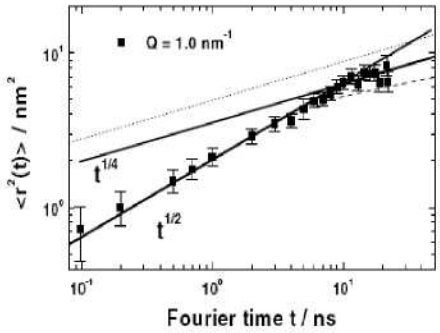



Figure 14.3: *Time dependent mean square displacement of a PEP segment in the melt at 492K. The solid line indicates the prediction of the Rouse model. The slowing down at longer times is an indication of a cross over to local reptation (see ref [7]).*

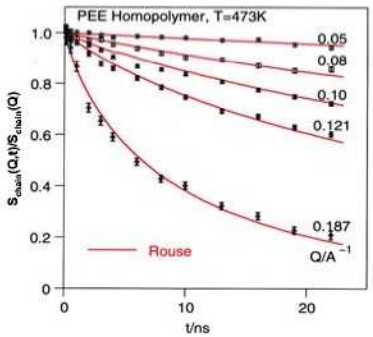



Figure 14.4: *Single chain structure factor from a PEE melt at 473K. The numbers along the curves represent the experimental Q-values in [Å$^{-1}$]. The solid lines are a joint fit with the Rouse model (Eq.[14.21]).*

The pair correlation function arising from the segment motion within one given chain is observed if some protonated chains are dissolved in a deuterated matrix. Figure 14.4 displays the observed spectra for polyethylethylene (90% dPEE, 10% hPEE) with the molecular weight of $M_w^h = 21.5kg/mol$; $M_w^d = 24.5kg/mol$ and a narrow molecular weight distribution [8]. The solid lines give the predictions of the dynamic structure factor of Eq.[14.17]. Obviously very good agreement is achieved.

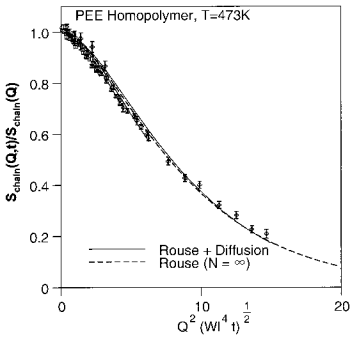



Figure 14.5: *Single chain structure factor from PEE melts as a function of the Rouse scaling variable. The dashed line displays the Rouse prediction for infinite chains, the solid lines incorporate the effect of translational diffusion. The different symbols relate to the spectra displayed in Figure 4.*

We now use these data in order to investigate the scaling prediction inherent in Eq.[14.21]. Figure 14.5 presents a plot of the data of Figure 14.4 now as a function of the Rouse scaling variable (Eq.[14.22]). With satisfactory precision the data follow the scaling prediction. The small deviations are related to the translational diffusion of the chains. This becomes evident from Figure 14.6 where the obtained relaxation rates $\Omega_R(Q)$ are plotted vs. $Q$ in a double logarithmic fashion. The dashed line gives the Rouse prediction $\Omega_R \approx W\ell^4Q^4$ while at larger momentum transfer the experimental results follow very well this prediction, towards lower $Q$ a systematic relative increase of the relaxation rate is observed. Including translational diffusion we have

$$\Omega_R(Q) = Q^2\left[D_R + Q^2\frac{W\ell^4}{6}\right] = Q^2W\ell^2\left[\frac{\ell^2}{3R_E^2} + \frac{Q^2\ell^2}{6}\right] \qquad (14.24)$$

The solid lines in Figure 14.6 represent the predictions of Eq.[14.24] - perfect agreement is obtained. The above expressions provide a universal description of the dynamics of a Gaussian chain and are valid for real linear polymer chains on intermediate length scales. The specific properties of a polymer enter only in terms of two parameters: $N\ell^2 = R_E^2$ and $\ell^2/\zeta_0$. The friction parameter is governing the Rouse variable (Eq.[14.22]). As alluded to in

Eq.[14.24] also the center of mass diffusion coefficient may be expressed in these terms. Since the Rouse model does not contain an inherent length scale the parameter $N$ (chain length) and $\ell^2$ (segment length squared) are somewhat arbitrary as long as the physical values $\ell^2/\zeta_0$ and $R_E^2$ are constant. The NSE experiments measure directly the friction coefficient/length$^2$.

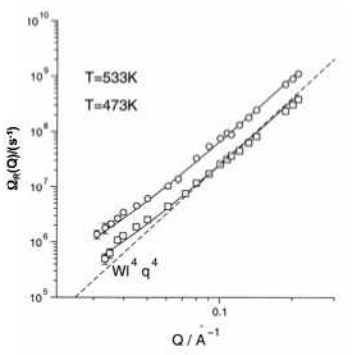



Figure 14.6: *Relaxation rates from PEE melts vs. Q for two different temperatures. The dashed line represents the $\Omega_R \sim Q^4$ prediction of the Rouse model. The solid lines include the contribution from translational diffusion (Eq.[14.24]).*

### 14.4 Topological confinement: Reptation

The dynamic modulus of a polymer melt is characterized by a plateau in frequency which broadens with increasing chain length. In this plateau regime the polymer melt acts like a rubber where the elastic properties are derived from the entropy elasticity of the chains between permanent cross links. The modulus of a rubber is inversely proportional to the mesh size and proportional to the temperature. In analogy, it is suggestive to assume that the entanglement or topological interactions between the chains in a melt lead to the formation of a temporary network which displays rubber elastic properties. Other than in a rubber for long times the chains may disentangle and the melt flows. This flow process is characterized by a melt viscosity $\eta \approx N^{3.2\ldots3.6}$ and the translational chain diffusion coefficient $D \approx N^{2\ldots2.3}$ [9]. Using the analogy to the modulus of a rubber we may estimate the distances between entanglement points from the value of the plateau modulus $G_N^0$. For different polymers they

come out to be between 30Å and 100Å. On the basis of such assumptions a number of theories of viscoelasticity have been developed [2,9,10]. The most famous among them is the reptation model by de Gennes [3] and Doi and Edwards [2]. In this model the dominating chain motion is a reptile like creep along the chain profile. The lateral restrictions by the interpenetrating other chains are modelled by a tube with a diameter $d$ parallel to the chain profile. $d$ relates to the plateau modulus of the melt

$$d^2 = \frac{4}{5}\frac{\mathrm{R}_E^2}{M}\frac{k_B T}{G_N^0} \tag{14.25}$$

The restrictions of the motion by the presence of the other chains are not effective on a monomer scale but rather permit lateral freedom on intermediate length scales. The experimental observations for viscosity and diffusion can be made directly comprehensible in this simple model.

The viscosity relates to the longest relaxation time in a system. If we consider Rouse diffusion along the tube with a Rouse diffusion coefficient $D_R \approx 1/(N\zeta_0)$ then an initial tube configuration is completely forgotten when the mean square displacement along the tube $\langle r^2(t)\rangle_{\text{tube}}$ = (contour length $L$)$^2$. Thus, for the longest relaxation time we obtain

$$\tau_\eta \approx \frac{L^2}{D_R} \approx N^3\zeta_0 \tag{14.26}$$

The diffusion coefficient is found by considering that during this time in real space the MSD just amounts to the end to end distance of the chain squared. Thus, we obtain

$$D_{rep} = \frac{R_E^2}{\tau_\eta} \approx \frac{N}{N^3\zeta_0} \approx \frac{1}{N^2\zeta_0} \tag{14.27}$$

### 14.4.1 Mean square displacements

We now consider the predictions of the reptation model for the mean square displacements of the chain segments. For short times when the chain segments have not yet realized the topological constraints ($r^2 < d^2$) we expect unrestricted Rouse motion $\langle r^2(t)\rangle \approx t^{1/2}$ (Eq.[14.15]). Experimentally this was the case for PEP (Figure 14.4) where for an entangled chain for times up to 20ns and displacements up to 30Å Rouse dynamics was observed. At a time $\tau_E$, $\tau_E = d^4/(\pi^2 W\ell^4)$ the mean square displacement reaches the order of the tube diameter. $\tau_E$ is derived as the Rouse time for polymer strand spanning the tube. Then motional restrictions are expected.

For times $t > \tau_e$ one dimensional curve linear Rouse motion along the tube needs to be considered. Displacements along the tube are described by Eq.[15] where we have to change real space coordinates to coordinates $s(t)$ along the tube. If a segment is displaced along the tube by $\langle (s_n(t) - s_n(0))^2\rangle$ then the mean square displacement in 3-d real space is $d\left\langle \left(s_n(t) - s_n(0)\right)^2 \right\rangle^{1/2}$. With that we obtain

$$\left\langle r^2(t)\right\rangle = \begin{cases} 2d\left(\dfrac{k_B T \ell^2 t}{\zeta_0 \pi}\right)^{1/4} & \tau_e < t < \tau_R \\ \\ 2d\left(\dfrac{k_B T t}{N\zeta_0}\right)^{1/2} & \tau_R < t < \tau_d \end{cases} \tag{14.28}$$

In Figure 14.7 the two situations correspond to the second and the third process. The second process where the chain performs Rouse motion along the tube is called local reptation while the creep like diffusion along the tube which eventually leads to a complete tube renewal is also termed pure reptation. The terminal time $\tau_d$ after which the chain has left its original tube determines to a large extend the viscosity of the melt ($\tau_d \approx \tau_\eta$ see Eq.[14.27]). Beyond that time reptation diffusion prevails.

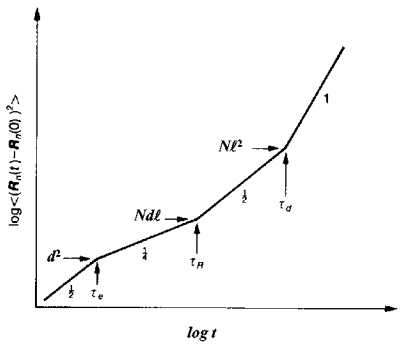



Figure 14.7: *Mean-square displacement of a chain segment in the reptation model.*

### 14.4.2 Self correlation function

In Gaussian approximation the self correlation function of a reptating chain directly relates to the MSD's of chapter 4.1. This supposes that the widths of the Gaussian function after a diffusion time $t$ of the single segment distribution along the 1-dimensional tube contour may be taken for the time dependent displacement. Projecting this on the Gaussian contorted tube then would again correspond to a Gaussian sublinear diffusion in real space.

However, as Fatkullin and Kimmich have shown [11], the real process has to be modelled by projecting the segment probability distribution due to the linear Rouse motion with the curve linear coordinate $s$ on the random walk like contour path of the contorted tube. This leads to a non-Gaussian probability distribution of the segment at times $t > \tau_e$,

$$S_{self}(Q,t > \tau_e) = \exp\left[\frac{Q^4 d^2}{72}\frac{\langle r^2(t)\rangle}{3}\right] erfc\left[\frac{Q^2 d}{6\sqrt{2}}\sqrt{\frac{\langle r^2(t)\rangle}{3}}\right] \qquad (14.29)$$

invalidating the Gaussian approximation for times longer than $\tau_e$. We note that Eq.[29] is strictly valid only for $t \gg \tau_e$ when $\langle r^2(t)\rangle \gg d^2$. The effect on the scattering function is that if (wrongly) interpreted in terms of the Gaussian approximation the cross over to local reptation

appears to occur a significantly lower values of $\tau_e$. A generic asymptotic $t^{1/4}$ law remains untouched.

In the sense of Eq.[14.29] the MSD of a chain segment may be directly observed by incoherent quasielastic scattering. In the local reptation regime we expect to observe the predicted cross over of the MSD from a $t^{1/2}$ to a $t^{1/4}$ law (Eq.[14.29]). Experiments were performed on PE and PEP samples at temperatures where also the dynamic structure factors were studied [7]. Figure 14.9 displays these data in terms of an effective mean square displacement (Eq.[14.23]), thereby assuming implicitly the Gaussian approximation.

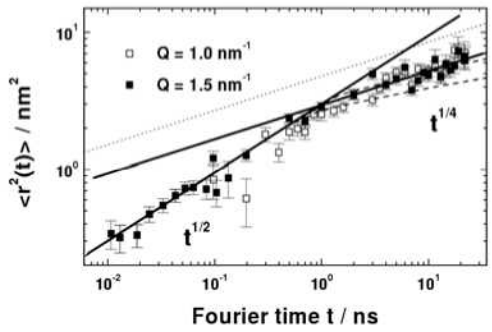



Figure 14.8: *NSE data obtained from the incoherent scattering of a fully protonated PE-melt in a representation of -6ℏn[$S_{self}(Q,t)$]/$Q^2$ which is the mean-square displacement* $\langle r^2(t)\rangle$ *as long as the Gaussian approximation holds. Solid lines describe the asymptotic power laws* $\langle r^2(t)\rangle \propto t^{1/2}, t^{1/4}$. *Dotted lines: prediction form the Gaussian approximation, dashed lines: see text.*

Inserting the Rouse rate for PE at 509K, $W\ell^4 = 7 \pm 0.7\text{nm}^4/\text{ns}$ obtained from single chain dynamic structure factor measurements into Eq.[14.16] the solid line $\approx t^{1/2}$ is obtained. It quantitatively corrobates the correctness of the Rouse descriptions at short times. The data also reveal clearly a transition to a $t^{1/4}$ law, though Eq.[14.28] would predict the dotted line. The discrepancy explains itself in considering the non-Gaussian character of the curve linear Rouse motion (Eq.[14.29]). Fixing also the value of the tube diameter to that obtained from single structure factor measurements (see later),b the dashed line in Figure 14.8 presents the

prediction of the non-Gaussian treatment. For $Q = 0.1\text{Å}^{-1}$ the unrestricted Rouse regime ($t < \tau_e$) as well as the local reptation regime is perfectly reproduced.

### 14.4.3 Single chain dynamic structure factor

Now we turn to the single chain dynamic structure factor $S_{chain}(Q,t)$ which is also strongly effected by the topological tube constraints. Qualitatively, we would expect the following behaviour:

(i) At short times $t < \tau_e$ the chain will perform unrestricted Rouse motion and the dynamic structure factor of Eq.[14.17] and [14.21] should well describe the dynamics. This e.g. has been exemplified in earlier measurements of the Rouse dynamic structure factor of entangled PDMS melts - in these materials $d$ is large [12].

(ii) In the regime of local reptation the chain has already explored the tube laterally and further density fluctuations of the labelled chain will only be possible via Rouse relaxation along the tube. Under such circumstances the structure factor to a first approximation will mirror the formfactor of the tube $S_{chain}(Q,\tau_R > t > \tau_e)/S_{chain}(Q) \approx \exp\left(-Q^2d^2/36\right)$. In this regime the experiment should reveal the size of the topological constraints without applying any detailed model.

(iii) In the creep regime $t > \tau_R$ the memory of the tube confinement will be gradually lost and the dynamic structure factor should reveal the fraction of the still confined polymer segments.

(iv) Finally, in the diffusive regime at very small $Q$ ($QR_g \ll 1$) an equivalent to Eq.[14.18] will be valid where now the reptation diffusion coefficient will be measured. de Gennes [13] and Doi and Edwards [9] have formulated attractable analytic expressions for the dynamic structure factor. Thereby, they neglected the initial Rouse regime i.e. the derived expression is valid only for $t > \tau_e$ ones confinement effects become important. The dynamic structure factor is composed from two contributions $S^{loc}$ and $S^{esc}$ reflecting local reptation and escape processes from the tube.

$$\frac{S_{chain}(Q,t)}{S_{chain}(Q)} = \left[1 - \exp\left(-\frac{Q^2d^2}{36}\right)\right] S^{loc} + \exp\left(-\frac{Q^2d^2}{36}\right) S^{esc} \qquad (14.30)$$

The local reptation part was calculated as

$$S^{loc}(Q,t) = \exp\left(\frac{t}{\tau_0}\right) erfc\left(\sqrt{\frac{t}{\tau_0}}\right) \tag{14.31}$$

Where $\tau_0 = {}^{36}\!/\!_{\left(W\ell^4Q^4\right)}$ a more general expression for $S^{esc}(Q,t)$ due to pure reptation was given by Doi and Edwards [9]. For short times $S^{chain}(Q,t)$ decays mainly due to local reptation (first term) while for longer times (and low $Q$) the second term resulting from the creep motion is important. The ratio of the two relevant time scales $\tau_0$ and $\tau_d$ is proportional to $N^3$. Therefore, for long chains at intermediate times a pronounced plateau in $S_{chain}(Q,t)$ is predicted. Such a plateau is a generic signature for confined motion. Beside the reptation model also other models for the description of entanglements have been brought forward.

1. In generalized Rouse models the effect of topological hindrance is described by a memory function. In the boarderline case of long chains the dynamic structure factor can be explicitly calculated in the time domain of the NSE experiment [14].
2. Rubber like models take entanglements as local stress points acting as temporary cross links. de Cloiseaux [15] has proposed such a model where he considered infinite chains with spatially fixed entangled points at intermediate times.
3. Recently in a mode coupling approach a microscopic theory describing the polymer motion in entangled melts has been brought forward. While this theory describes well the different time regimes for a segmental motion, unfortunately as the consequence of the necessary approximations, the dynamic structure factor could not yet been derived [16].

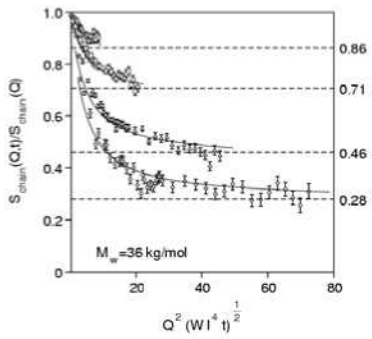



Figure 14.9: *Scaling presentation of the dynamic structure factor from a $M_w$ = 36000 PE-melt at 509K as a function of the Rouse scaling variable. The solid lines are a fit with the reptation model (Eq.[14.30]). The Q-values are from above $Q = 0.05,\ 0.077,\ 0.115,\ 0.145 Å^{-1}$. The horizontal dashed lines display the prediction of the Debye-Waller factor estimate for the confinement size (see text).*

Figure 14.9 displays the dynamic structure factor from a $M_w = 36$kg/mol PE-melt as a function of the Rouse variable $Q^2\ell^2\sqrt{Wt}$ (Eq.[14.22]). Other than in Figure 14.5, where the scaled data followed a common master curve, here they split into different branches which only at small values of the scaling variable are coming close together. This splitting is a consequence of the existing dynamic length scale invalidating the Rouse scaling properties. We note that this length is of purely dynamical character and cannot be observed in static equilibrium experiments.

In the spirit of Eq.[14.30] and neglecting the ongoing decay of $S_{chain}(Q,t)$ due to local reptation from the heights of the achieved plateaus we may obtain a first estimate for the amount of confinement. Identifying the plateau levels with a Debye Waller factor description of the confinement, we get $d = 46$Å, a value which is a lower estimate for the two tube diameter since $S^{loc}$ is not fully relaxed. The horizontal lines in Figure 14.9 are the predictions from this Debye-Waller factor estimate.

In Figure 14.10 the same data are presented linearly as a function of time. The figure compares the data with the predictions of the various models. It is evident that these data clearly favour the reptation model. We note that the fits with the reptation model were done

with only one free parameter, the entanglement distance $d$. The Rouse rate $W\ell^4$ was determined earlier through NSE data taken for $t < \tau_e$. With this one free parameter quantitative agreement over the whole range of $Q$ and $t$ using the reptation model with $d = 46 \pm 1.0$Å was found.

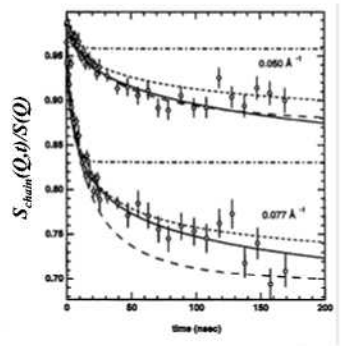



Figure 14.10: *Plot of $S_{chain}(Q,t)$ vs. t at $Q = 0.050$ and $0.077$Å$^{-1}$ [17] with a comparison between the predictions of reptation (solid lines) [31], local reptation (dotted lines) [30], the model of des Cloiseaux [15] (dashed lines) and the Ronca model [14] (dot-dashed lines).*

### 14.5 Large scale dynamics in biopolymers

While the study of the dynamics of synthetic polymers has reached some maturity, the next challenge will be the investigation of the large scale motion of biopolymers. The goal there will be to find out to what extend these dynamics play a role in bio function. On local scales some insight into the conformational dynamics has been gained e.g. by time dependent crystallography [18]. On the other hand, the large scale dynamics such as protein domain motions remain basically untouched experimentally, because of the lack of techniques to study these large scale correlated motions. In this lecture we present a first study on such dynamics on the example of alcohol dehydrogenase (ADH [19]) . The alcohol dehydrogenases are enzymes that are important for many organisms allowing the interconversion between alcohols and ketones. In humans ADH is present as a dimer and catalyzes the oxidation of ethanol allowing thereby the consumption of alcohol in beverages. In yeast on the hand it is at the basis of the fermentation process converting acetaldehyde into

ethanol. In the process the cofactor Nicotinamide Adenine Dinucleotide (NAD) is needed assisting the oxidation reaction at the zinc catalytic side.

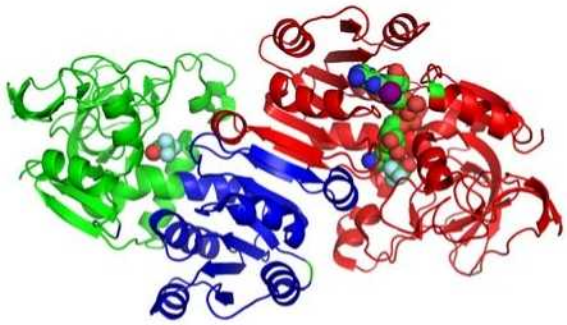


Figure 14.11: *Dimer of alcohol dehydrogenase. The molecule presented by spherical caps is the NAD cofactor used in the chemical reaction.*

Figure 14.11 displays a schematic structure of the dimer based on crystallographic data. The two monomeric units are clearly visible. Each monomer is build from two domains, the catalytic and the binding domain with a small opening in between, where the cofactor NAD is placed. ADH from yeast forms a tetrameric structure. The crystallographic data suggest a crossed arrangement of the two dimers.

In order to verify whether in solution a similar tetrameric aggregate is present it is important to perform neutron small angle scattering (SANS) experiments. Figure 14.12 presents SANS data at different concentrations. Included is a comparison with a number of models for solution structures. Let us commence with the insert.

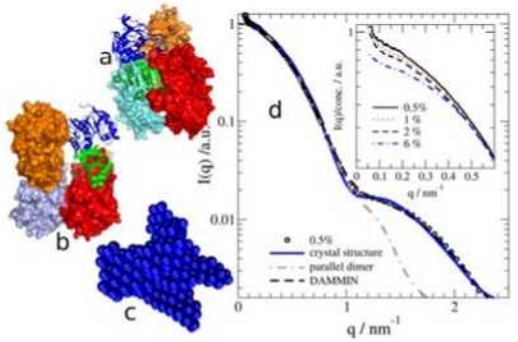



Figure 14.12: *SANS results on ADH solutions of different concentration (d). Insert: concentration dependent results. The different curves in the main figure display modelling results for various dimer arrangements a) solid line: crystal structure; b) thin solid line: DAMMIN result c) dashed dotted line: planar dimers at close contact.*

Here for different concentrations the low $Q$ data are presented and there with increasing concentration we observe a decrease of the SANS intensities. This observation results from the repulsive interaction between different tetramers giving rise to an inter tetramer structure factor causing the reduced intensity at low $Q$.

In the main figure the low concentration data are presented over the full $Q$ range and are compared with different structural models. The solid line reflects the crystal structure which appears to be in a very good agreement with the SANS data. Testing the sensitivity of the SANS approach, we compare with a configuration where two dimers form a planar configuration at close contact. The results are presented by the dashed line which in particular at high momentum transfers leads to a significant underestimation of the scattering intensities. Furthermore, a model independent approach was used in applying the program DAMMIN [20]. This program builds SANS scattering profiles from an arrangement of small mesoscopic spheres considering the proper scattering length densities. This program leads to a perfect fit of the experimental data (results superimpose with the crystal results) and confirms the crystal based perpendicular arrangements of the two planar structures. Thus, we may conclude that as in the crystal the ADH tetramer in solution is present in a crossed dimer configuration.

The dynamics in solution is importantly influenced by the overall translational diffusion of the molecular aggregate. Therefore, in the next step the translational diffusion coefficient needs to be studied. Dynamic light scattering is the proper tool since it investigates the overall dynamics on the proper length scale. Figure 14.13 displays light scattering results for different ADH concentrations as a function of momentum transfer squared. We note that apparently for all concentrations we observe identical translational diffusion coefficients. At 5°C it amounts to $D_{DLS} = 2.35 \pm 0.2 \times 10^{-2}\text{nm}^2/\text{ns}$.

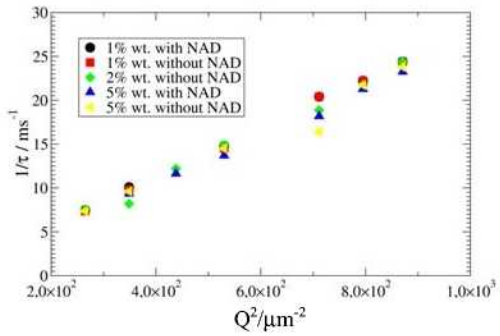



Figure 14.13: *Dynamic light scattering results on the translational diffusion of tetrameric ADH in water solution at different concentrations. The characteristic rates* $1/\tau = D*Q^2$ *are plotted vs.* $Q^2$.

In order to approach the internal dynamics of such an aggregate one has to increase the $Q$ range such that $1/Q$ roughly corresponds to the molecular or aggregate size. This may be achieved implying neutron spin echo spectroscopy to the ADH solutions. Figure 14.14 displays NSE results in a logarithmic fashion for a large number of different momentum transfers $Q$. The data are presented in a log linear fashion showing directly the single exponential decay observed in all cases. Fits with single exponential decays are included by straight lines. We note however, that at intermediate $Q$ ($Q = 0.68\text{nm}^{-1}$) small but systematic deviations appear indicating a two component structure.

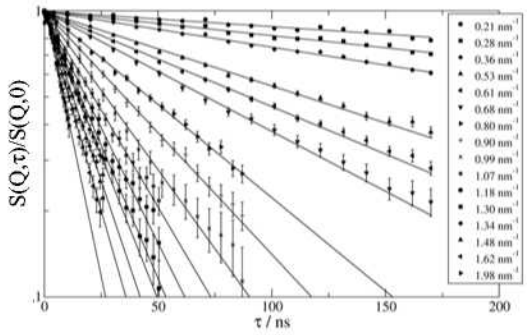



Figure 14.14: *Neutron spin echo results on a 5% ADH resolution at 5 °C with cofactor for various momentum transfers.*

Comparing the covered $Q$ range with the SANS data (Figure 14.12) we realize that the range of the structure factor, where intermolecular interactions are important as well as the regime of internal structure are covered. Now we consider that all data may be described in terms of a single exponential decay. Therefore, we may approximate the spectra in terms of a first cumulant expansion

$$\ell n\frac{S(Q,t)}{S(Q)} = -\Gamma(Q)t + \frac{1}{2}K_2t^2 \qquad \text{(a)} \qquad (14.32)$$

The decay rate of the dynamic structure factor, also called initial slope, is

$$\Gamma(Q) = -\lim_{t\to 0}\frac{\partial}{\partial t}\,\ell n\left[S(Q,t)\right] \qquad \text{(b)} \qquad (14.33)$$

Using the decay rates $\Gamma(Q)$ we may define an effective diffusion coefficient

$$D_{eff}(Q) = \frac{\Gamma(Q)}{Q^2} \qquad \text{(c)} \qquad (14.34)$$

For the case of a translational diffusion $D_{eff}(Q)$ would be a constant and giving the translational diffusion coefficient.

Figure 14.15a displays the thus obtained effective diffusion coefficients as a function of $Q$ for the different concentrations with and without the cofactor NAD. The line at low $Q$ indicates the level of the light scattering results.

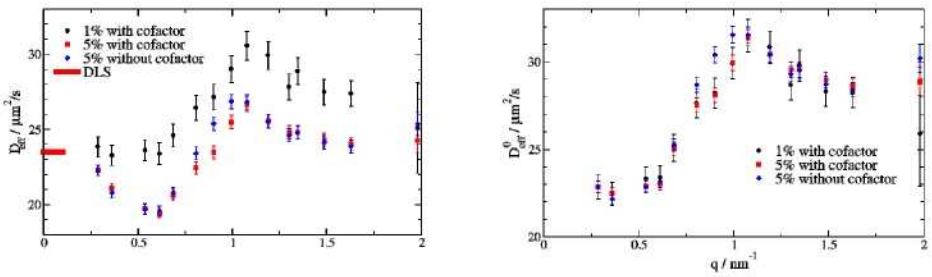



Figure 14.15: *(a) Effective diffusion coefficient $D_{eff}(Q)$ for 3 different solutions of ADH, (b) comparison of $D_{eff}(Q)$ corrected for S(Q) with different models (see text).*

The experimental results show a strong $Q$ modulation with a maximum around $Q = 1\text{nm}^{-1}$. Furthermore, we realize that at low $Q$ the data are in agreement with the concentration independent light scattering results. We also see that beyond the statistical error in the low $Q$ flank of the 5% data the relaxation without the cofactor NAD is faster than that including the cofactor. We may conclude that in the dynamics of the ADH tetramer on the scale of the aggregate itself we observe significant contributions beyond translational diffusion.

We now want to interpret the data and commence with the low $Q$ data which are affected by the interactions between the molecules. Then the effective diffusion coefficient relates to the diffusion coefficient $D_0$ at infinite dilution by

$$D_{eff}(Q) = D_0 \frac{H(Q)}{S(Q)} \tag{14.35}$$

where $H(Q)$ is the hydrodynamic factor and $S(Q)$ is the interparticle structure factor. The structure factor may be extracted from the SANS data in dividing the concentration dependent results by the lowest concentration results ($C = 0.25\%$). With this experimental structure factor the data may be corrected. This correction removes the low $Q$ increase of the 5% data but leaves the results at higher $Q$ untouched (see Figure 14.15b). The hydrodynamic factor cannot be measured directly. A first approximation in terms of a Percus-Yevick model shows that (i) at a 1% level the correction factor $H(Q)/S(Q)$ leaves the experimental data practically

untouched and (ii) at 5% the correction is somewhat weaker than the experimentally observed effect. Nevertheless, beyond $Q = 0.6\text{nm}^{-1}$ the ratio of $H(Q)/S(Q)$ remains constant. Thus, the observed higher $Q$ structure is entirely determined by intra aggregate effects.

The prime reason for a $Q$ dependent structure in $D_{eff}(Q)$ are rotational motions of the molecule. In a first cumulant approximation (see Eq.[14.34]) the effective diffusion coefficient of a rigid boy undergoing translational and rotational diffusion has the form [21]

$$D_{eff}(Q) = \frac{k_B T}{Q^2} \times \frac{\sum_{jK} \left\langle b_j e^{i\underline{Q}\underline{r}_j} \begin{pmatrix} \underline{Q} \\ \underline{Q} \times \underline{r}_j \end{pmatrix} \vec{H} \begin{pmatrix} \underline{Q} \\ \underline{Q} \times \underline{r}_K \end{pmatrix} b_K e^{-i\underline{Q}\underline{r}_K} \right\rangle}{\sum_{jK} \left\langle b_j e^{i\underline{Q}\underline{r}_j} \; b_K e^{-i\underline{Q}\underline{r}_K} \right\rangle} \tag{14.36}$$

Here $\underline{r}_j$ and $\underline{r}_k$ are the atomic coordinates, $b_i$ and $b_k$ the corresponding neutron scattering length and $\vec{H}$ the mobility tensor. The sum runs over all atoms of the molecule or molecular aggregate and the pointed brackets indicate an ensemble average. The denominator is the aggregate formfactor. The mobility matrix $\vec{H}$ is a 6×6 tensor involving translational ($\vec{T}$) rotational ($\vec{R}$) parts including a translational rotational coupling ($\overrightarrow{TR}$). For the simplest case of an isotropic particle $T = D_{trans}/k_B T$ and $R = D_{rot}/k_B T$. The evaluation of Eq.[14.36] is importantly complicated by the hydrodynamic interaction between the different parts of the molecule. In the biophysical literature one finds the computer code HYDROPRO which was developed by the group around Garcia de la Torre [22]. In this code a complicated molecule is approximated by a rigid aggregate of little spheres. Its diffusional motion including the hydrodynamic interaction is then calculated by a proper superposition of the motion of the rigidly connected spheres. The calculations with HYDROPRO need as an input the crystallographic coordinates of all atoms.

In Figure 14.15b all data sets for $D_{eff}(Q)$ at the different concentrations with and without cofactor are compared. After rescaling with the diffusion coefficients at different concentrations in the region above $Q = 0.6\text{nm}^{-1}$ all data sets are consistent. We furthermore note that the data at 5% solution are of significantly higher statistical significance. The solid line in Figure 14.15b displays the result of the HYDROPRO calculations for a rigid molecule. While the line describes the general form of the effective diffusion coefficient data reasonably

well, we observe significant deviations at smaller momentum transfers. These differences between the rotational diffusion expectation for a rigid aggregate and the experimental data are displayed in Figure 14.16. We note that at $Q$ values below the peak of the rigid body rotational diffusion coefficient significantly faster effective diffusion takes place. This result indicates the presence of internal motion within the molecule which must involve mainly those atoms which are placed in the outer regions of the tetramer emphasizing more strongly the larger distances and within the molecule and therefore giving rise to extra dynamics at low $Q$.

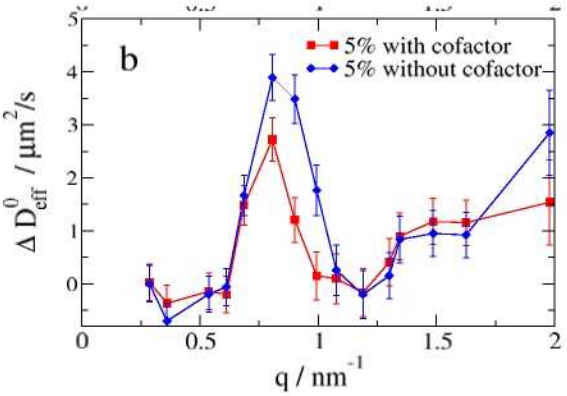



Figure 14.16: *Differences between the measured effective Q- dependent diffusion coefficient and expectation from rigid body motion. The lines are guides to the eye.*

A first interpretation of this result may be carried out in terms of a normal mode analysis. For this purpose an elastic network model is used where the complicated bonded and non-bonded interactions are replaced by a pair wise Hookian potential controlled by a single parameter. As has been shown, such a simple formulation is sufficient to describe the anomalous low frequency motion of large proteins [23].

In this model two close enough atoms are connected by a spring, if the equilibrium distance between them is sufficiently small. The elastic forces acting on the particles obey Hookes law and depend only on the change in the distances between them. If $\underline{R}^0_i$ are the equilibrium

positions of the particles and $\underline{R}_i(t)$ are their actual coordinates the Hookean Potential has the form

$$E_H = f\sum_{i,j} A_{ij}\left(\left|\underline{R}_i - \underline{R}_j\right| - \left|\underline{R}_i^0 - \underline{R}_j^0\right|\right)^2 \tag{14.37}$$

$A$ is the adjacency matrix with the elements, $A_{ij} = 1$ if $\left|\underline{R}_i^0 - \underline{R}_j^0\right| < \ell_0$ and $A_{ij} = 0$ otherwise. In principle the dynamics of such an elastic network is nonlinear because the distances $\left|\underline{R}_i - \underline{R}_j\right|$ are nonlinear functions of the coordinates. Close to the equilibrium the equations of motions can however be linearized yielding to an equation of motion

$$m_i \ddot{\underline{r}}_i = -\sum_j \Lambda_{ij}\,\underline{r}_j \tag{14.38}$$

where $\Lambda$ is the $3N \times 3N$ dynamical matrix obtained by the linearization process. In this linear approximation the motions are described by a sum of independent oscillating normal modes.

$$\underline{r}_i(t) = \sum_\alpha k_\alpha \underline{e}_i^\alpha \sin\omega_\alpha t \tag{14.39}$$

With $\omega_\alpha^2$ and $\underline{e}_i^\alpha$ representing nonzero eigenvalues and the respective eigenvectors of the matrix $\Lambda$ and $k_\alpha$ the amplitude factor of the mode. The large scale slow motions we are interested in, are dominated by the soft modes with small eigenvalues. In the case of overdamped modes which are seen in the experiment the oscillating part needs to be replaced by an exponential $\left(e^{(-\lambda_\alpha t)}\right)$. The relaxation rates $\lambda_\alpha$ contain the unknown friction factors within the molecule and with the surrounding water molecules.

A first approximation for the dynamic structure factor may be obtained in terms of a one phonon approximation of the cross section. In this approximation the dynamic structure factor reads

$$S(Q,t)_{1-phon} \simeq \sum_{k,\ell} b_k b_e \left\langle e^{i\underline{Qr}_k} e^{-i\underline{Qr}_e} \right\rangle$$
$$+\sum_{\alpha} \frac{k_B T}{\omega_\alpha^2} e^{-\lambda_\alpha t} \sum_{k,\ell} \frac{b_k b_e}{\sqrt{m_k m_l}} \left\langle e^{i\underline{Qr}_k} e^{-i\underline{Qr}_e} \left(\underline{Q}\,\underline{e}_k^{\alpha}\right)\left(\underline{Q}\,\underline{e}_\ell^{\alpha}\right) \right\rangle \tag{14.40}$$

In first cumulant approximation (Eq.[14.33]) we have to take the logarithmic derivative with respect to time at time equal zero. Subtracting the translational and rotational part we finally obtain

$$\Delta D_{eff}(Q) = \frac{\sum_{\alpha} \lambda_\alpha \frac{k_B T}{\omega_\alpha^2} \sum_{k,\ell} \frac{b_k b_e}{\sqrt{m_k m_l}} \left\langle e^{i\underline{Qr}_k} e^{-i\underline{Qr}_e} \left(\underline{Q}\,\underline{e}_k^{\alpha}\right) \times \left(\underline{Q}\,\underline{e}_\ell^{\alpha}\right) \right\rangle}{Q^2 \sum_{k,\ell} b_k b_e \left\langle e^{i\underline{Qr}_k} e^{i\underline{Qr}_e} \right\rangle} \tag{14.41}$$

describing the dynamic formfactor of the eigenmodes. Finally, Figure 14.17 presents the outcome of such a harmonic analysis for the tetrameric aggregate of ADH with and without the cofactor. In an exemplary way we present the contributions from the modes 7, 9 and 11 with and without the cofactor. In all cases the low eigenmodes exhibit a formfactor with the strong peak around $Q = 1\text{nm}^{-1}$ comparing with Figure 14.16 qualitatively the experimental observation and the results of the normal mode analysis resemble each other.

Quantitatively the observed experimental feature is shifted towards smaller $Q$ indicating a more pronounced motion of the outer atoms. This difference is not yet fully understood but may result from the anharmonicity of the dynamics or the effect inhomogenously distributed friction within the molecule or both.

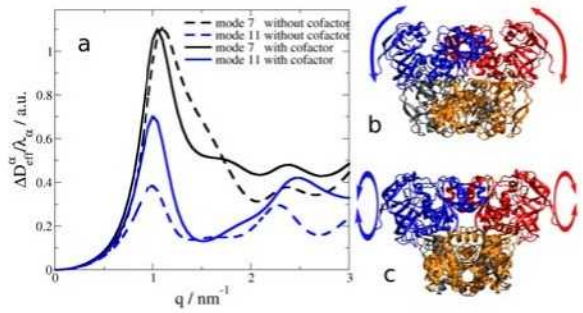



Figure 14.17: *Diffusion form factor of the normal modes 7 and 11 for the protein configuration with and without cofactor.* ***b****, Motional pattern of mode 7: Without cofactor the exterior domain (catalytic domain) tilts outwards and opens the cleft. The inner domain with connection points between the monomers remains stiff.* ***c****, Motional pattern of mode 11: With and without bound cofactor the monomers within a dimer exhibit torsional motion around the long dimer axis (in the image plane), which is more pronounced without the cofactor.*

### 14.6 Conclusion and outlook

We have presented some representative results from neutron spin echo spectroscopy on the dynamics of macromolecules. In the case of synthetic polymers we have displayed recent results on the universal dynamics of flexible polymers from the entropy driven Rouse dynamics to confinement and reptation including reptation limiting processes. In the case of biopolymers we have displayed some first experiments on the intra aggregate motion of alcohol dehydrogenase an important enzyme for fermentation and the oxidation of ethanol. The lecture attempted to transmit a flavour of what can be achieved with high resolution neutron spin spectroscopy which permits to access the molecular motion simultaneously in space and time.

The lecture commenced with a description of the standard model of polymer motion, the entropy driven dynamics covered by the so called Rouse model. In the spatial range where the Rouse approximations are valid, the NSE measurements have confirmed most of the predictions of the Rouse model both for the self- and pair correlation function. We also have shown limitations related to the inter chain interactions which reveal themselves in the center of mass selfdiffusion at short times.

Towards larger scales topological interactions resulting from the mutually interpenetrating chains gain dominating influence and confine the chain motion to a tube along the chain profile. We have presented measurements on the dynamic structure factor of a reptating chain which unequivocally confirm the picture of local reptation i.e. Rouse relaxation along the contorted tube. A measurement of the self correlation function corrobates the picture.
Compared to the investigations of the dynamics of synthetic polymers the study of the large scale relaxation dynamics of biopolymers is still in its early stages. We have presented some first experimental data on the collective inter aggregate fluctuations of a tetrameric aggregate formed by alcohol dehydrogenase. It became possible to directly measure the $Q$ dependent effective diffusion coefficient which bears information on the detailed rotational diffusion dynamics. Furthermore, additional dynamics appears at low momentum transfers which is related to motions of the outer more flexible parts of each dimer. Employing normal mode analysis these dynamical features have been attributed to the slow large scale collective fluctuations of the domains.

These experiments are a first attempt to directly observe the collective internal dynamics of proteins or protein complexes. In the future experiments will be needed in order to resolve the internal dynamics or further proteins, in order to try to resolve the different relaxation modes. Such experiments need to be accompanied by computer simulations in order to enhance the level of interpretation. Furthermore, the experiments need to address proteins where domain motion is functionally important. We hope that in the future such NSE studies will make an important contribution to a better understanding of protein function based not only on the structure but also on the dynamics.

**References**


[1] For a recent review see: D. Richter, M. Monkenbusch, A. Arbe, J. Colmenero, Adv. Polymer Sci. 174, Springer, Berlin, Heidelberg, New York (2005)
[2] M. Doi, S.F. Edwards, J. Chem. Soc. Farad. Trans. 274, 1789; 274, 1802; 275, 38 (1978)
[3] P.G. de Gennes, J. Chem. Phys. 55, 572 (1971)
[4] Z. Bu, R. Biehl, M. Monkenbusch, D. Richter, J.E. Callaway, PNAS 102, 17646 (2005)
[5] F. Mezei (Ed.), Neutron spin echo lecture notes in physics 128, Springer, Berlin, Heidelberg, New York (2005)
[6] P.R. Rouse, J. Chem Phys. 21, 1272 (1953)
[7] A. Wischnewski, M. Monkenbusch, L. Willner, D. Richter, B. Farago, G. Kali, Phys. Rev. Lett. 90, 058302 (2003)
[8] H. Montes, M. Monkenbusch, L. Willner, S. Rathgeber, L.J. Fetters, D. Richter, J. Chem. Phys. 110, 10188 (1999)
[9] M. Doi, S.F. Edwards, The theory of polymer dynamics, Clarendon Oxford (1986)
[10] P.G. de Gennes, Scaling concepts in polymer physics, Cornell University Press, Ithaca (1979)
[11] N. Fatkullin, R. Kimmich, Phys. Rev. E 52, 3273 (1995)
[12] D. Richter, A. Baumgärtner, K. Binder, B. Ewen, J.B. Hayter, Phys. Rev. Lett. 47, 109 (1981)
[13] P.G. de Gennes, J. Phys. (Paris) 42, 735 (1981)
[14] G.J. Ronca, J. Chem. Phys. 79, 79 (1983)
[15] J. des Cloiseaux, Macromolecules 23, 3992 (1990)
[16] K.S. Schweitzer, J. Chem. Phys. 91, 5802; 5822 (1989)
[17] P. Schleger, B. Farago, A. Kollmar, C. Lartigue, D. Richter, Phys. Rev. Lett. 81, 124 (1998)
[18] F. Schotte, M. Lim, T.A. Jackson, A.V. Smirnov, J. Soman, J.S. Olson, G.N. Jr Philips, M. Wulf, P.A. Aminfrud, Science 300, 1944 (2003)
[19] R. Biehl, B. Hofmann, M. Monkenbusch, P. Falus, S. Prevost, R. Merkel, D. Richter, submitted
[20] D.I. Svergun, Biophysics J. 76, 2879 (1999)
[21] N. Brown, Dynamic Light Scattering, Monographs of the Physics and Chemistry of Materials, Oxford Science Publications, Oxford 49 (1993)
[22] J. Garcia de la Torre, M.L. Huertas, B. Carrasco, Biophysics J. 78, 719 (2000)
[23] M.M. Tirion, Phys. Rev. Lett. 77, 1905 (1996)

# 15

# Correlated electrons in complex transition metal oxides

Thomas Brückel

# 15. Correlated electrons in complex transition metal oxides

Thomas Brückel, IFF, Forschungszentrum Jülich

## 15.1 Introduction

Materials with strong electronic correlations are materials, in which the movement of one electron depends on the positions and movements of all other electrons due to the long-range Coulomb interaction. With this definition, one would naively think that all materials show strong electronic correlations. However, in purely ionic systems, the electrons are confined to the immediate neighborhood of the respective atomic nucleus. On the other hand, in ideal metallic systems, the other conduction electrons screen the long-range Coulomb interaction. Therefore, while electronic correlations are also present in these systems and lead for example to magnetism, the main properties of the systems can be explained in simple models, where electronic correlations are either entirely neglected (e. g. the free electron Fermi gas) or taken into account only in low order approximations (Fermi liquid, exchange interactions in magnetism etc.). In highly correlated electron systems, simple approximations break down and entirely new phenomena appear, possibly with related novel functionalities. These so-called *emergent phenomena* cannot be anticipated from the local interactions among the electrons and between the electrons and the lattice [1]. This is a typical example of *complexity*: the laws that describe the behavior of a complex system are qualitatively different from those that govern its units [2]. This is what makes highly correlated electron systems a research field at the very forefront of condensed matter research. The current challenge in condensed matter physics is that we cannot reliably predict the properties of materials with strong electronic correlations. There is no theory, which can handle this huge number of interacting degrees of freedom. While the underlying fundamental principles of quantum mechanics (Schrödinger equation or relativistic Dirac equation) and statistical mechanics (maximization of entropy) are well known, there is no way at present to solve the many-body problem for some $10^{23}$ particles. Some of the exotic properties of strongly correlated electron systems and examples of emergent phenomena and novel functionalities are:

- *High temperature superconductivity*; while this phenomenon was discovered in 1986 by Bednorz and Müller [3], who received the Nobel Prize for this discovery, there is still no commonly accepted mechanism for the coupling of electrons into Cooper pairs, let alone a theory which can predict high temperature superconductivity or its transition temperatures. This lack of understanding is the more surprising, the more we consider the large number of solid-state physicists worldwide, which are trying to solve this problem. High temperature superconductivity has already some applications like in so-called SQUID (Superconducting Quantum Interference Device) magnetic field sensors, superconducting generators or motors, high field magnets etc but might in the future have even further applications for loss-free energy storage or -transport.
- *Colossal magnetoresistance effect CMR*, which was discovered in transition metal oxide manganites and describes a large change of the electrical resistance in an applied magnetic field [4]. This effect can be used in magnetic field sensors and could eventually replace the giant magnetoresistance field sensors[1], which are employed for example in the read heads of magnetic hard discs.

[1] The giant magnetoresistance effect [5] is an effect that occurs in artificial magnetic thin film multilayers. It was discovered independently by P. Grünberg and A. Fert, who received the Nobel Prize in 2007 for their discovery.

- *The magnetocaloric effect* [6], which describes a temperature change of a material in an applied magnetic field and can for example, be used for magnetic refrigeration without moving parts or a cooling fluid.
- *The multiferroic effect* [7], which describes the simultaneous occurring of various ferroic orders in one material. This could be ferromagnetism, ferroelectricity or ferroelasticity. If the respective degrees of freedom are strongly coupled, one can switch one of the orders by applying the conjugate field of the other order. In certain multiferroic materials, the application of a magnetic field can switch the ferroelectric polarization or the application of an electric field can switch the magnetization of the material. Future applications of multiferroic materials in computer storage elements are apparent. One could either imagine elements, which store several bits in form of a magnetic- and electric polarization, or one could apply the multiferroic properties for an easier switching of the memory element.
- Metal-insulator-transitions as observed e. g. in magnetite (Verwey transition [8]) or certain vanadites are due to strong electronic correlations and could be employed as electronic switches.
- Negative thermal expansion [9] is just another example of the novel and exotic properties that these materials exhibit. It is likely that many more such emergent phenomena will be discovered in the near future. This huge potential is what makes research on highly correlated electron systems so interesting and challenging: this area of research is located right at the intersection between fundamental science investigations, striving for basic understanding of the electronic correlations, and technological applications, connected to the new functionalities [10].

## 15.2 Electronic structure of solids

In order to be able to discuss the effects of strong electronic correlations, let us first recapitulate the textbook knowledge of the electronic structure of solids [11]. The description of the electron system of solids always starts with the *adiabatic or Born-Oppenheimer approximation*. The argument is made that the electrons are moving so quickly compared to the nuclei that the electrons can instantaneously follow the movement of the much heavier nuclei and thus see the instantaneous nuclear potential. This approximation serves to separate the lattice- and electronic degrees of freedom. Often one makes one further approximation and considers the nuclei to be at rest in their equilibrium positions. The potential energy seen by a single electron in the averaged field of all other electrons and the atomic core potential is depicted schematically for a one dimensional system in figure 15.1.

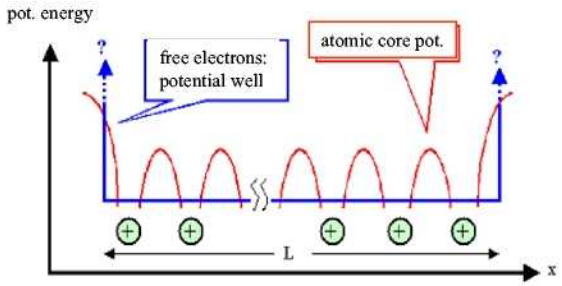



***Fig. 15.1:*** *Potential energy of an electron in the solid; once in the case of free electrons, where the electron is described as moving in a potential well with infinitely high walls; and once taking into account the potential arising from the Coulomb interaction with the atomic cores, which is periodic in the infinite solid.*

The following simple models are used to describe the electrons in a crystalline solid:

- *Free electron Fermi gas*: here a single electron moves in a 3D potential well with infinitely high walls corresponding to the crystal surfaces. All electrons move completely independent, i. e. the Coulomb interaction between the electrons is not considered explicitly, only the Pauli exclusion principle.
- *Fermi liquid*: here the electron-electron interaction is accounted for in a first approximation by introducing quasiparticles, so-called dressed electrons, which have a charge e, and a spin ½ like the free electron, but an active mass m*, which can differ from the free electron mass m.
- *Band structure model*: this model takes into account the periodic potential of the atomic cores at rest i. e. the electron moves in the average potential from the atomic cores and from the other electrons.

Considering the strength of the long-range Coulomb interaction, it is surprising that the simple models of Fermi gas - or better Fermi liquid - already are very successful in describing some basic properties of simple metals. The band structure model is particularly successful to describe semiconductors. But all three models have in common that the electron is described with a single particle wave function and electronic correlations are only taken into account to describe phenomena like magnetism due to the exchange interaction between the electrons or BCS superconductivity [12], where an interaction between electrons is mediated through lattice vibrations and leads to Cooper pairs, which can undergo a Bose-Einstein condensation.

What we have sketched so far is the textbook knowledge of introductory solid state physics courses. Of course there exist more advanced theoretical descriptions, which take into account the electronic correlations. The strong Coulomb interaction between the electrons is taken into account in density functional theory in the so-called "LDA+U" approximation or in so-called dynamical mean field theory DMFT or a combination of the two in various degrees of sophistication [13]. Still, all these extremely powerful and complex theories often times fail to predict even the simplest physical properties, such as whether a material is a conductor or an insulator.

Let us come back to the band structure of solids. In the so-called tight binding model one starts from isolated atoms, where the energy levels of the electrons in the Coulomb potential of the corresponding nucleus can be calculated. If such atoms are brought together, the wave functions of the electrons from different sites start to overlap, leading to a broadening of the atomic energy levels, which eventually will give rise to the electronic bands in solids. The closer the atoms are brought together, the more the wave functions overlap, the more the electrons will be delocalized, and the broader are the corresponding bands. This relationship is depicted graphically in figure 15.2.

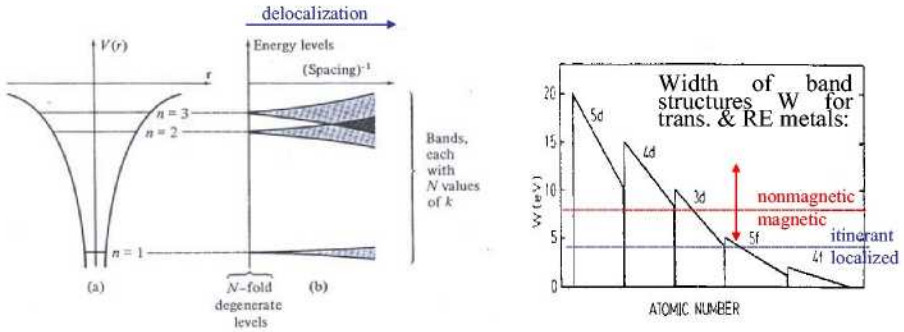



***Fig. 15.2:*** *Left: The figure on the left shows the atomic potential of an electron interacting with the atomic core and the corresponding level scheme, which consists of sharp energy levels. The figure in the middle shows how these atomic energy levels broaden into bands, the more the wave functions of neighboring atoms overlap. Right: The figure on the right shows schematically the band width as a function of atomic number for the rare-earth- and transition metals. Underneath a certain width, the electrons remain localized. For partially filled shells such electrons can be magnetic. But even itinerant electrons can remain magnetic up to a certain band width. At band width over typically 8 eV, the electrons will be itinerant (the material will be metallic) and non-magnetic.*

If electronic correlations are not too strong, the electronic properties can be described by a band structure, which allows one to predict, whether a material is a metal, a semiconductor or an insulator. This is shown in figure 15.3. At T = 0 all electronic states are being filled up to the Fermi energy. At finite T the Fermi-Dirac distribution describes the occupancy of the energy levels. If the Fermi energy lies somewhere in the middle of the conduction band, the material will be metallic. If it lies in the middle between valence band and conduction band and these two are separated by a large gap significantly larger than the energy equivalent of room temperature, the material will show insulating behavior. Finally, if the gap is small enough to allow thermal excitations of electrons from the valence band to the conduction band, we have semiconducting behavior. But again, this band structure model describes the electrons with single particle wave functions. Where are the electronic correlations?

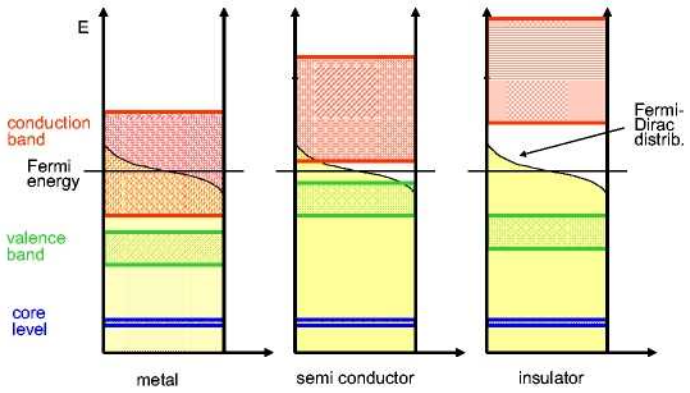



***Fig. 15.3:*** *Schematic band structure for a simple metal, semiconductor and insulator.*

## 15.3 Electronic correlations

It turns out that electronic correlations are particularly important in materials, which have some very narrow bands. This occurs for example in transition metal oxides or transition metal chalcogenides[2] as well as in some light rare earth intermetallics (heavy fermion systems). Let us chose CoO as a typical and simple example of a transition metal oxide. CoO has the rock salt structure depicted in figure 15.4.

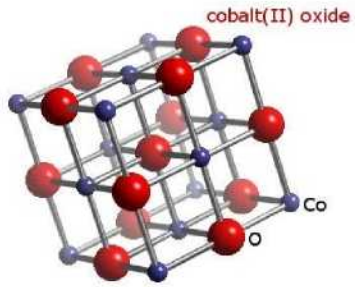



***Fig. 15.4:*** *CoO crystallizes in the rock salt structure.*

The unit cell depicted in figure 15.4 is face centered cubic fcc and contains four formula units. The primitive unit cell of the fcc lattice, however, is spanned by the basis vectors

$$\underline{a}' = \frac{1}{2}a\left(\hat{\underline{e}}_x + \hat{\underline{e}}_y\right) \; ; \; \underline{b}' = \frac{1}{2}a\left(\hat{\underline{e}}_y + \hat{\underline{e}}_z\right) \; ; \; \underline{c}' = \frac{1}{2}a\left(\hat{\underline{e}}_z + \hat{\underline{e}}_x\right) \qquad (15.1)$$

Here a is the lattice constant, and $\hat{\underline{e}}_x$ , $\hat{\underline{e}}_y$ , $\hat{\underline{e}}_z$ are the unit basis vectors of the original fcc unit cell. Therefore the primitive unit cell contains exactly one cobalt and one oxygen atom. The electronic configurations of these atoms are: Co: [Ar]$3d^7 4s^2$; O: [He]$2s^2 2p^4$. In the solid, the atomic cores of Co and O have the electronic configuration of Ar and He, respectively. These electrons are very strongly bound to the nucleus and we need not consider them on the usual energy scales for excitations in the solid state. We are left with nine outer electrons for the Co and six outer electrons for the O atom in the solid, so that the total number of electrons per primitive unit cell is 9 + 6 = 15. Therefore we have an uneven number of electrons in the primitive unit cell. According to the Pauli principle, each electronic state can be occupied by two electrons, one with spin up and one with spin down. Therefore with an uneven number of electrons, we must have at least one partially filled band and according to figure 15.3, CoO must be a metal.

What does experiment tell us? Well, in fact, CoO is a very good insulator as the resistivity at room temperature amounts to $\rho \sim 10^8$ Ωcm. This value can be compared to a good conductor like iron, which has a resistivity of about $10^{-7}$ Ωcm. The resistivity of CoO corresponds to activation energies of about 0.6 eV or a temperature equivalent of 7000 K, which means there is a huge band gap making CoO a very good insulator. To summarize these considerations: the band theory breaks down already for a very simple oxide consisting of only one transition metal and one oxygen atom!

[2] Chalcogenides are compounds of the heavier chalcogens (group VI elements of the periodic table, particularly sulfides, selenides, tellurides). Even so, oxygen is in the same group of the periodic table, oxides are usually not considered chalcogenides.

In order to understand the reason for this dramatic breakdown of band theory, let us consider an even simpler example: the alkali metal sodium. It has the electronic configuration: Na: $[Ne]3s^1=1s^2 2s^2 2p^6 3s^1$. Following our argumentation for CoO, sodium obviously has a half-filled 3s band and is therefore a metal. This time our prediction was correct: the electrical resistivity at room temperature is about $5 \cdot 10^{-6}$ Ωcm. However, what happens if we pull the atoms further apart and increase the lattice constant continuously? Band theory predicts that for all distances sodium remains a metal, since the 3s band will always be half-filled. This contradicts our intuition and of course also the experiment: at a certain critical separation of the sodium atoms, there must be a transition from a metal to an insulator. It was Sir Nevill Mott (Nobel Laureate in physics of 1977), who predicted this metal-to-insulator transition, which is therefore called the Mott-transition [14]. The physical principle can be made clear with the illustration in figure 15.5.

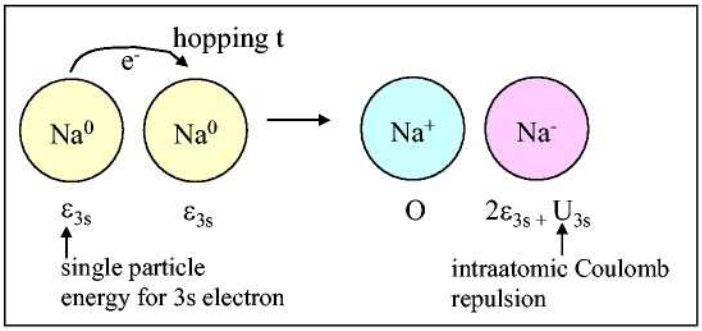



***Fig. 15.5:*** *Illustration of the hopping process of an electron between two neutral sodium ions leading to charge fluctuations.*

On the left of figure 15.5, two neutral sodium atoms are depicted. The atomic energy levels of the outer electrons correspond to an energy $\varepsilon_{3s}$. The wave functions of the 3s electrons will overlap giving rise to a finite probability that an electron can hop from one sodium atom to the other one. Such a delocalization of the electrons is favored according to the Heisenberg uncertainty principle

$$\Delta p \cdot \Delta x \geq \frac{\hbar}{2} \tag{15.2}$$

(15.2) shows that we can gain kinetic energy, if the electrons become more delocalized. Figure 15.5 on the right shows the situation after the electron transfer. Instead of neutral atoms, we have one $Na^+$ and one $Na^-$ ion. However, we have to pay a price for the double occupation of the 3s states on the $Na^-$ ion, namely the intra-atomic Coulomb repulsion between the two electrons denoted as $U_{3s}$. While this is a very simplistic picture, where we assume that the electron is either located on one or the other Na atom, this model describes the two main energy terms by just one parameter: the hopping matrix element t, connected to the kinetic energy, and the intra-atomic Coulomb repulsion U, connected with the potential energy due to the Coulomb interaction between the two electrons on one site. In this simple model, we have replaced the long range Coulomb potential proportional to $1/r$ with its leading term, an onsite Coulomb repulsion U. More realistic models would have to take higher order terms into account but already such a simple consideration leads to very rich physics. We can see from figure 15.5 that electronic conductivity is connected with charge fluctuations and that such charge transfer costs energy, where U is typically in the order of 1 or 10 eV. Only if the gain in kinetic energy due to the hopping t is larger than the penalty in potential energy U can we

expect metallic behavior. If the sodium atoms are now being separated more and more, the intra-atomic Coulomb repulsion U will maintain its value, while the hopping matrix element t, which depends on the overlap of the wave functions, will diminish. At a certain critical value of the lattice parameter a, potential energy will win over kinetic energy and conductivity is suppressed. This is the physical principle behind the Mott transition.

More formally, this model can be cast into a model Hamiltonian, the so-called *Hubbard model* [15]. In second quantization of quantum-field theory, one can write down the so-called single band Hubbard Hamiltonian:

$$\mathbf{H} = -t \sum_{\substack{j,l \\ \text{en.N.}}} \sum_{\sigma} (\mathbf{c}^{+}_{j\sigma}\mathbf{c}_{l\sigma} + \mathbf{c}^{+}_{l\sigma}\mathbf{c}_{j\sigma}) + U \sum_{j} \mathbf{n}_{j\uparrow}\mathbf{n}_{j\downarrow} \tag{15.3}$$

The operator $\mathbf{c}^{+}_{j\sigma}$ creates an electron in the tight binding (Wannier)-state $\Phi(\underline{r} - \underline{R}_j)|\sigma\rangle$, $\mathbf{n}_{j\sigma}$ is the occupation operator $\mathbf{c}^{+}_{j\sigma}\mathbf{c}_{j\sigma}$ of the corresponding Wannier state; U is the Coulomb repulsion in one orbital at one site:

$$U = \int dr_1 \int dr_2 \frac{e^2 \left|\Phi(\underline{r}_1 - \underline{R}_j)\right|^2 \left|\Phi(\underline{r}_2 - \underline{R}_j)\right|^2}{4\pi\varepsilon_0 \left|\underline{r}_1 - \underline{r}_2\right|} \tag{15.4}$$

t is the hopping amplitude

$$t = \int d\underline{r} \Phi(\underline{r} - \underline{R}_1) \frac{e^2}{4\pi\varepsilon_0 \left|\underline{r} - \underline{R}_2\right|} \Phi(\underline{r} - \underline{R}_2) \tag{15.5}$$

The Hubbard model is a so-called "*lattice fermion model*", since only discrete lattice sites are being considered. It is the simplest way to incorporate correlations due to the Coulomb interaction since it takes into account only the strongest contribution, the onsite Coulomb interaction. Still there is very rich physics contained in this simple Hamiltonian like the physics of ferromagnetic- or antiferromagnetic metals and insulators, charge- and spin density waves and so on [15]. A realistic Hamiltonian should contain many more inter-site terms due to the long range Coulomb interaction and it is quite likely that additional new physics would be contained in such a more realistic model.

The most direct consequence of the onsite Coulomb interaction is that additional so-called Hubbard bands are created due to possible hopping processes. This is illustrated in figure 15.6.

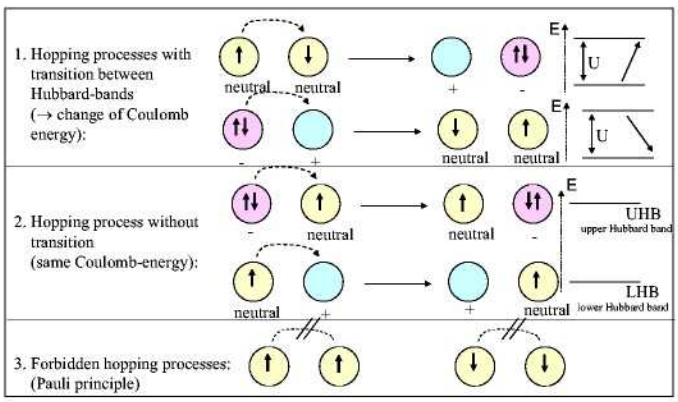



***Fig. 15.6:*** *Illustration of hopping processes between neighboring atoms together with their corresponding energy scales.*

The first row in figure 15.6 shows hopping processes, which are connected with a change of the total Coulomb energy. The second row shows hopping processes without transition. The last row shows hopping processes, which are forbidden due to the Pauli principle. From figure 15.6 we can identify two different energy states. Configurations for which the onsite Coulomb repulsion comes into play have an energy which is higher by the onsite Coulomb repulsion U as compared to such configurations where the electrons are not on the same atom. In a solid these two energy levels will broaden into bands (due to the delocalization of the electrons on many atoms driven by the hopping matrix element t), which are called the *lower Hubbard band* and the *upper Hubbard band*. If these bands are well separated, i. e. the Coulomb repulsion U dominates over the hopping term t, we will have in insulating state, since only the lower Hubbard band is occupied. If the bands overlap, we will have a metallic state. Note however that lower and upper Hubbard band are totally different from the usual band structure of solids as they do not arise due to the interaction of the electrons with the atomic cores but due to electronic correlations. As a result the existence of the Hubbard bands depends on the electronic occupation. Figure 15.6 illustrates how in correlated electron systems the energy terms for simple hopping processes depend of the occupation of neighboring sites and how hopping transports spin information. The apparently simple single electron operator gets complex many body aspects.

### 15.4 Example: doped CMR manganites

In what follows we will discuss one example of highly correlated electron systems, the mixed valence manganites (see e.g. [16]). Their stoichiometric formula is $A_{1-x}B_xMnO_3$, where A is a trivalent cation (A= La, Pr, Nd, Sm, Eu, Gd, Tb, Dy, Ho, Er, Y, Bi) and B is a divalent cation (B = Sr, Ca, Ba, Pb). The doping with divalent cations leads to a mixed valence on the manganese sites. If we neglect covalency[3] and describe these compounds in a purely ionic model, charge neutrality requires that manganese exists in two valence states: $Mn^{3+}$ and $Mn^{4+}$ according to the respective doping levels:

$$A_{1-x}B_xMnO_3 \rightarrow \left[A^{3+}_{1-x}B^{2+}_x\right]\left[Mn^{3+}_{1-x}Mn^{4+}_x\right]O_3 \qquad (15.6)$$

This is why one speaks of mixed valence manganites as Mn exists in two valence states with the following electronic configurations:

$Mn^{3+}$: $[Ar]3d^4$ / $Mn^{4+}$: $[Ar]3d^3$ (15.7)

The structure of these mixed valence manganites is related to the perovskite structure depicted in figure 15.7.

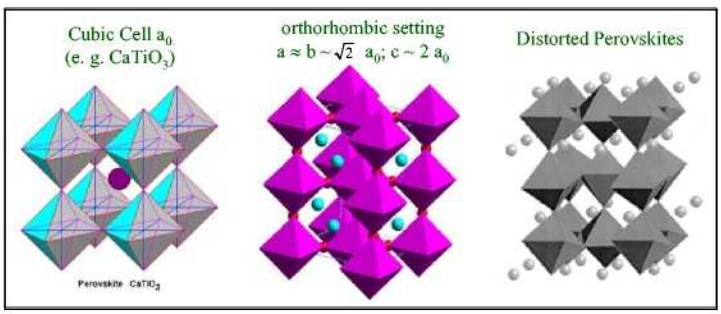



***Fig. 15.7:*** *The perovskite structure. Left: The ideal cubic structure; middle: the cubic structure in orthorhombic setting; right: the distorted perovskite structure with rotated and tilted oxygen octahedra.*

[3] an assumption which is often made but certainly wrong in this class of materials!

Perovskite is a mineral $CaTiO_3$, which has a cubic crystal structure, where the smaller $Ca^{2+}$ metal cation is surrounded by six oxygen atoms forming an octahedron; these corner sharing octahedra are centered on the corners of a simple cubic unit cell and the larger $Ti^{4+}$ metal cation is filling the interstice in the centre of the cube. This ideal cubic perovskite structure is extremely rare. It only occurs when the sizes of the metal ions match to fill the spaces between the oxygen atoms ideally. Usually there is a misfit of the mean ionic radii of the A and B ions, which leads to sizeable tilts of the oxygen octahedra. The resulting structure is related to the perovskite structure as illustrated in figure 15.7: in the middle of figure 15.7 the cubic perovskite structure is shown in a different, orthorhombic setting. The usually observed perovskite structure is related to this structure by a tilting of the corner shared oxygen octahedra as shown on figure 15.7 on the right. Such an orthorhombic structure is for example realized in $LaMnO_3$ with space group Pbnm. Orthorhombic or rhombohedral structures occur if the so-called *tolerance factor T*, which is the measure for the misfit of the ionic radii deviates significantly from the value 1, where T is defined as:

$$T = \frac{1}{\sqrt{2}} \frac{\langle R_{A,B} \rangle + \langle R_O \rangle}{\langle R_{MN} \rangle + \langle R_O \rangle} \tag{15.8}$$

For the manganites the octahedral surrounding of the Mn ions leads to so-called crystal field effects. To explain these we stay in the ionic model and describe the oxygen atoms as $O^{2-}$ ions. The outer electrons of the Mn ions, the 3d electrons, experience the electric field created by the surrounding $O^{2-}$ ions of the octahedral environment. This leads to a splitting of the electronic levels as depicted in figure 15.8, the so-called *crystal field splitting*. Those 3d orbitals, which have loops of the electron density pointing towards the negatively charged oxygen ions, will have higher energies with respect to those 3d orbitals, where the loops point in directions between the oxygen atoms. This leads to a splitting of the d-electron levels into three so-called $t_{2g}$ and two so-called $e_g$ crystal field levels. For the manganites this crystal field splitting is typically in the order of 2 eV. If we now consider a $Mn^{3+}$ ion, it depends on the ratio between the crystal field splitting and the intra-atomic exchange, how the electrons will occupy these crystal field levels. According to Hunds' rule, electrons tend to maximize the total spin i. e. occupy energy levels in such a way that the spins of all electrons are parallel as far as Pauli principle permits. This is a consequence of the Coulomb interaction within a single atom and is expressed by the Hunds' rule energy $J_H$. If the crystal field splitting is much larger than Hunds' coupling, a *low spin state* will result where all electrons are in the lower $t_{2g}$ level and two of these $t_{2g}$ orbitals are single occupied, while one orbital is double occupied. Due to Pauli principle the spins in the doubly occupied orbital have to be antiparallel giving rise to a total spin S = 1 for this low spin state. Usually, however, in the manganites Hunds' rule coupling amounts to about 4 eV, and is stronger than the crystal field splitting. In this case the *high spin state* shown in figure 15.8 is realized, where four electrons with parallel spin occupy the three $t_{2g}$ levels plus one of the two $e_g$ levels. The high spin state has a total spin of S = 2 and the orbital angular momentum is quenched[4]. This state has an orbital degree of freedom. The $e_g$ electron can either occupy the $3z^2$-$r^2$ or the $x^2$-$y^2$ orbital. Nature does not like such degenerate states. The $MnO_3$ octahedra will undergo a geometric distortion that removes this degeneracy and lowers the overall energy of the complex. This is called the *Jahn-Teller effect*, which is depicted in figure 15.8 as a further splitting of the d-electron levels. For the case shown in the figure, the c-axis of the octahedron has been elongated thus lowering the energy of the $3z^2$-$r^2$ orbital with respect to the energy level of the $x^2$-$y^2$ orbital. The Jahn-Teller splitting in the manganites has a magnitude of typically some 0.6 eV.

[4] i.e. vanishes: L=0

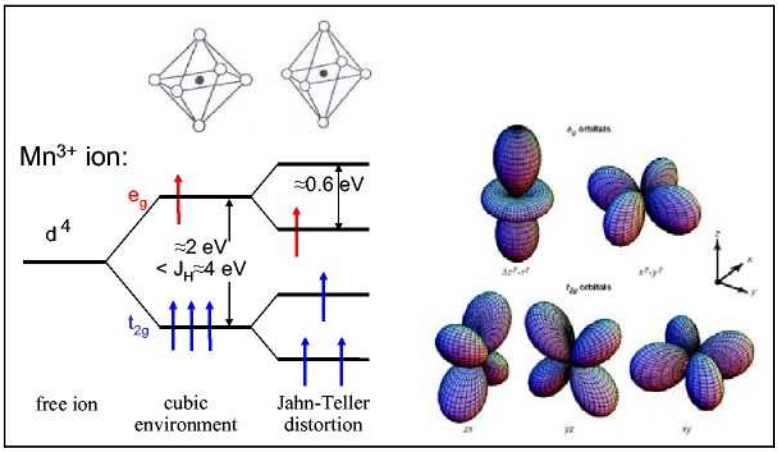



***Fig. 15.8:*** *Energy level diagram for a $MnO^{3+}$ ion in an oxygen octahedron. For the free ion, the four 3d electron levels are degenerate. They split in a cubic environment into $t_{2g}$ and $e_g$ levels. If Hunds' rule coupling is stronger than crystal field splitting, a high spin state results. The degeneracy of the $e_g$ level is lifted by a Jahn-Teller distortion, which results in an elongation of the oxygen octahedra. On the right of the figure, the 3d orbitals corresponding to the different orbital magnetic quantum numbers are depicted.*

The Jahn-Teller effect demonstrates nicely how in these transition metal oxides electronic degrees of freedom and lattice degrees of freedom are coupled. Only the $Mn^{3+}$ ion with an even number of electrons (the so-called *Kramer ion*) exhibits the Jahn-Teller effect, while the $Mn^{4+}$ ion with only three d electrons does not. A transfer of charge between neighboring manganese ions is accompanied with a change of the local distortion of the oxygen octahedron: a so-called lattice polaron. Due to the Jahn-Teller effect, charge fluctuations and lattice distortions become coupled in these mixed valence transition metal oxides.

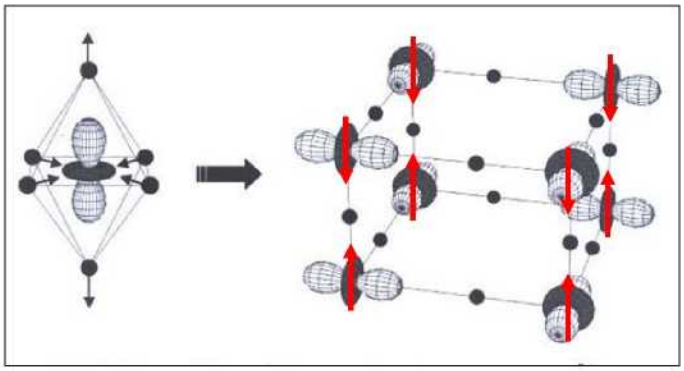


***Fig. 15.9:*** *Orbital order in $LaMnO_3$. Below the Jahn-Teller transition temperature of 780 K, a distinct long range ordered pattern of Jahn-Teller distortions of the oxygen octahedra occurs leading to orbital order of the $e_g$ orbitals of the $Mn^{3+}$ ions as shown. Also shown is the antiferromagnetic spin order which sets in below the Néel temperature $T_N \sim 145$ K. Oxygen atoms are represented by filled circles, La is not shown.*

Having explained the Jahn-Teller effect, we can now introduce an important type of order occurring in these transition metal oxides: *orbital order*. Let us look at the structure of the $LaMnO_3$ parent compound. Here all manganese are trivalent and are expected to undergo a Jahn-Teller distortion. In order to minimize the elastic energy of the lattice, the Jahn-Teller distortions on neighboring sites are correlated. Below the Jahn-Teller transition temperature $T_{JT}$ ~780 K, a cooperative Jahn-Teller transition takes place, with a distinct pattern of distortions of the oxygen octahedra throughout the crystal lattice as shown in figure 15.9. This corresponds to a long range orbital order of the $e_g$ electrons, which should not be confused with magnetic order of an orbital magnetic moment. In fact, the orbital magnetic moment is quenched i. e. totally suppressed by the crystal field surrounding the $Mn^{3+}$ ions. Orbital ordering instead denotes a long range ordering of an anisotropic charge distribution around the nuclei. As the temperature is further lowered, magnetic order sets in at the Néel temperature of 145 K. In $LaMnO_3$ the spin degree of freedom of the $Mn^{3+}$ ion orders antiferromagnetically in so-called A-type order: spins within the a-b plane are parallel, while spins along c are coupled antiferromagnetically. This d-type orbital ordering and A-type antiferromagnetic ordering results from a complex interplay between structural-, orbital- and spin degrees of freedom and the relative strengths of the different coupling mechanisms in $LaMnO_3$.

The situation becomes even more complex for doped manganites, where the charge on the manganese site becomes an additional degree of freedom due to the two possible manganese valances $Mn^{3+}$ and $Mn^{4+}$. In order to minimizes the Coulomb interaction between neighboring manganese sites, so-called *charge order* can develop. This is shown for the example of half-doped manganites in figure 15.10.

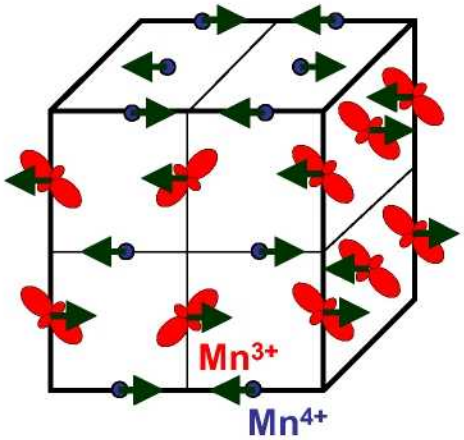



***Fig. 15.10:*** *Charge-, orbital- and spin-order in the half-doped manganite* $\left[La^{3+}_{1/2}Sr^{2+}_{1/2}\right]\left[Mn^{3+}_{1/2}Mn^{4+}_{1/2}\right]O_3$

These half-doped manganites show antiferromagnetic spin order, a checkerboard-type charge order with alternating $Mn^{4+}$ and $Mn^{3+}$ sites and a zigzag orbital order of the additional $e_g$ electron present on the $Mn^{3+}$ sites. This is only one example of the complex ordering phenomena that can occur in doped mixed valence manganites. These ordering phenomena result from a subtle interplay between lattice-, charge-, orbital-, and spin degrees of freedom and can have as a consequence novel phenomena and functionalities like the colossal magnetoresistance effect.

How are these ordering phenomena related with the macroscopic properties of the system? To answer this question, let us look at the resistivity of doped Lanthanum-Strontium-Manganites, see figure 15.11.

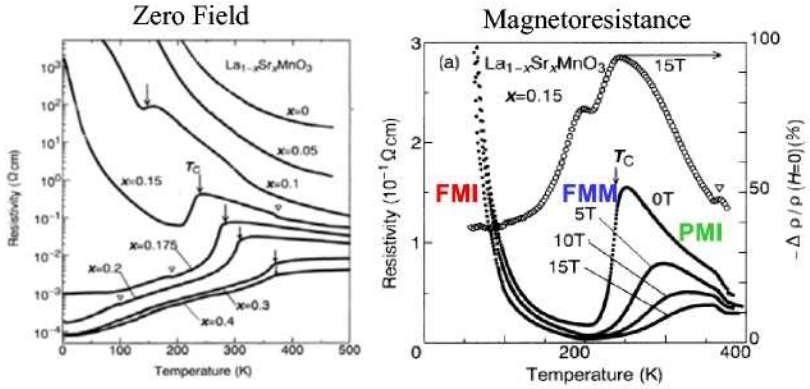



***Fig. 15.11:*** *Resistivity in the $La_{1-x}Sr_xMnO_3$ series, taken from [17]. Left: resistivity in zero field for various compositions from x = 0 to x = 0.5. Right: resistivity for x = 0.15 in different magnetic fields as well as the magnetoresistance defined as the change in resistivity relative to its value for field equal zero.*

The zero field resistance changes dramatically with composition. The x = 0 compound shows insulating - or better semiconducting - behavior as the resistivity increases with decreasing temperature. The higher doped compounds e. g. x = 0.4 are metallic as the resistivity decreases with decreasing temperature. Note however that the resistivity of these compounds is still about three orders of magnitude higher than for typical good metals. At an intermediate composition x = 0.15, the samples are insulators at higher temperatures down to about 250 K, then a dramatic drop of the resistivity indicating an insulator-to-metal transition and again an upturn below about 210 K with typical insulating behavior. The metal-insulator transition occurs at a temperature, where the ferromagnetic long-range order sets in. Around this temperature we also observe a very strong dependence of resistivity on external magnetic field. This is the so-called *colossal magnetoresistance effect*. In order to appreciate the large shift in the maximum of the resistivity curve with field shown in figure 15.11, one should remember that the energy scales connected with the Zeeman interaction of the spin ½ electron in an applied magnetic field are very small: the energy equivalent of 1 Tesla for a spin ½ system corresponds to 0.12 meV, which in turn corresponds to a temperature equivalent of 1.3 K.

Can we understand this strong dependence of the resistance on an external field in simple terms? Indeed there is a mechanism for a magnetic exchange interaction which can give rise to a ferromagnetic order and at the same time is connected with conductivity. This mechanism is called *double exchange* and is depicted schematically in figure 15.12. This exchange interaction can only occur between transition metals of different valences. In the case depicted in figure 15.12, an $e_g$ electron from a $Mn^{3+}$ ion hops into the oxygen 2p orbital while the other oxygen 2p electron hops on the $Mn^{4+}$ site. Since $e_g$ and $t_{2g}$ electrons are strongly coupled through the Hund's rule coupling, this transfer of an electron from $Mn^{3+}$ to $Mn^{4+}$ can only occur if the spins of the $t_{2g}$ electrons are parallel.

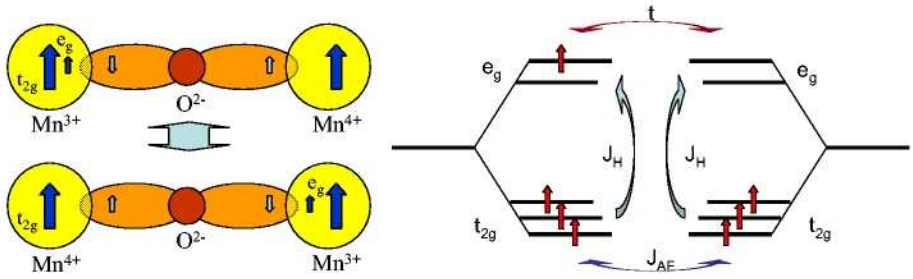



***Fig. 15.12:*** *Schematic representation of the double exchange interaction. On the left, the transfer of an $e_g$ electron through the intervening 2p orbitals from a $Mn^{3+}$ to a $Mn^{4+}$ ion is shown. On the right, this process is illustrated in an energy level diagram for the manganese atoms. There is an antiferromagnetic exchange interaction $J_{AF}$ between the $t_{2g}$ electrons. Within the Mn atoms, Hund's rule coupling $J_H$ is assumed to be larger than the crystal field splitting. t represents the hopping term between the two Mn sites. Only if the $t_{2g}$ spins of both Mn atoms are parallel can the $e_g$ electron hop between the two sites. If the $t_{2g}$ spins are anti-parallel, hopping is suppressed by the strong Hund's rule coupling between $e_g$ and $t_{2g}$ spins. As double exchange is stronger than $J_{AF}$, the Mn spins tend to align parallel.*

For an anti-parallel orientation of the $t_{2g}$ spins hopping is suppressed due to the penalty of the Hund's rule coupling energy $J_H$. Therefore the double exchange between $Mn^{3+}$ and $Mn^{4+}$ ions is ferromagnetic and this ferromagnetic exchange is connected with conductivity. In terms of the double exchange mechanism, we can now explain the insulator-to-metal transition occurring at $T_C$: in the paramagnetic states, the spins of the $t_{2g}$ electrons fluctuate, thus suppressing the hopping of the $e_g$ electron due to Hund's rule coupling. The system behaves like an insulator. As soon as ferromagnetism sets in, hopping between neighboring manganese sites can occur and the resistivity drops. An applied external field aligns the Mn spins even above the Curie temperature. This induced magnetization permits an increased hopping of the $e_g$ electrons and thus to a decrease of resistivity. Thus in this simple model of the double exchange interaction, magnetoresistance can be explained qualitatively. However, it has been shown [18] that the double exchange interaction alone gives the wrong magnitude for the magnetoresistance effect. Other effects, such as the electron-phonon interaction, have to be taken into account. It is also clear that our entire discussion starting from ionic states is only a crude approximation to the real system. Therefore we now have to pose the question how can we determine the true valence state? Or more general, which experimental methods exist to study the complex ordering and excitations of the charge-, orbital-, spin- and lattice- degrees of freedom in these complex transition metal oxides?

### 15.5 Experimental techniques: Neutron and x-ray scattering

In this chapter we will give a first glimpse into how these various ordering phenomena can be studied experimentally. Obviously we need probes with atomic resolution which interact as well with the spins as with the charges in the system. Therefore neutron and x-ray scattering are the ideal microscopic probes to study the complex ordering phenomena and their excitation spectra. The lattice and spin structure can be studied with neutron diffraction from a polycrystalline or single crystalline sample as detailed in chapter 11 "Structure determination"

of this course. Figure 15.13 shows as an example a powder spectrum of a $La_{7/8}Sr_{1/8}MnO_3$ material.

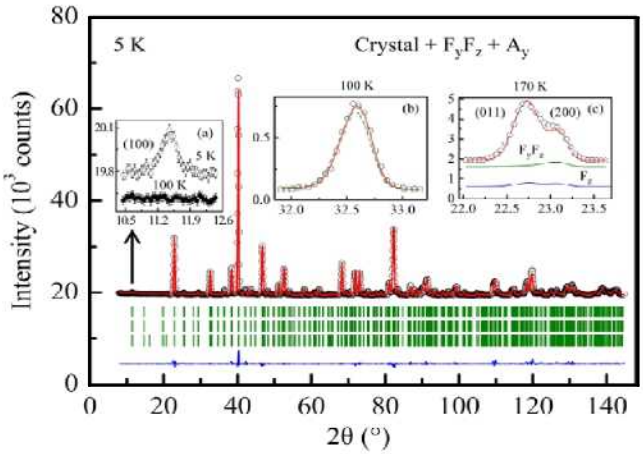



***Fig. 15.13:*** *High resolution neutron powder diffractogram of a powdered single crystal of $La_{7/8}Sr_{1/8}MnO_3$. Circles are the data points, the solid line is the result of the structural refinement. Structural and magnetic Bragg reflections are located at the 2θ values indicated by the vertical lines below the spectrum. The solid line underneath shows the difference between the observed and simulated spectrum. Inserts show details in certain 2θ regions e. g. a magnetic Bragg reflection at very low Q.*

Preferably the structure determination from polycrystalline material is done by a simultaneous refinement of neutron and x-ray powder diffraction spectra, as the two probes have different contrast mechanisms. For example an x-ray spectrum contains less precise information on the structural parameters for the oxygen atoms, since these rather light atoms scatter much weaker than the heavier metal atoms. Neutrons have the added advantage of a vanishing form factor for nuclear scattering and therefore give information up to larger momentum transfer. Neutrons also allow one to determine the magnetic structure from a powder diffraction pattern. As a result of such a refinement, one can show that the low temperature structure of this compound is monoclinic or even triclinic[5], e.g. there exists an additional distortion from the Pnma structure introduced in chapter 15.4. Ferromagnetic order becomes visible by intensity on top of the structural Bragg peak. Antiferromagnetic order is usually (but not always!) connected with an increase in the unit cell dimension, which in turn shows up in the diffractogram by additional superstructure reflections between the main nuclear reflections. It is beyond the scope of this lecture to discuss the experimental and methodological details of such a structure analysis or to present detailed results on specific model compounds. For this we refer to the literature, e.g. [16]. We just want to mention that with detailed structural information, we cannot only determine the lattice- and spin structure, but also the charge- and orbital order and can relate them to macroscopic phenomena such as the CMR effect. At first sight it might be surprising that neutron diffraction is able to give us information about charge order. We have learnt in the introductory chapters that neutrons interact mainly through the strong interaction with the nuclei and through the magnetic dipole interaction with the magnetic induction in the sample. So how can neutrons give information about charge order?

[5] Highest resolution synchrotron x-ray powder diffraction is best suited to solve the problem of the metric of the low temperature structure, as peak splitting can be detected much better with this method than with laboratory x-ray- or neutron powder diffraction which has generally less resolution

Obviously charge order is not determined directly with neutrons. However in a transition metal-oxygen bond, the bond length will depend on the charge of the transition metal ion. The higher the positive charge of the transition metal, the shorter will be the bond to the neighboring oxygen, just due to Coulomb attraction. This qualitative argument can be quantified in the so-called *bond valence sum*. There exists an empirical correlation between the chemical bond length and the bond valence:

$$s_{ij} = \exp\left(\frac{R_0 - R_{ij}}{B}\right) \tag{15.9}$$

Here, the $R_{ij}$ are the experimentally determined bond lengths, B is a constant (B = 0.37 according to [19]) and $R_0$ are tabulated values for the cation-oxygen bonds see e. g. [19]. Table 15.1 reproduces some of these values.

| Ions | $La^{3+}$ | $Pr^{3+}$ | $Nd^{3+}$ | $Sm^{3+}$ | $Eu^{3+}$ | $Gd^{3+}$ | $Tb^{3+}$ | $Dy^{3+}$ | $Er^{3+}$ |
|---|---|---|---|---|---|---|---|---|---|
| $R_0$ | 2.172 | 2.138 | 2.105 | 2.090 | 2.074 | 2.058 | 2.032 | 2.001 | 1.988 |
| Ions | $Tm^{3+}$ | $Yb^{3+}$ | $Y^{3+}$ | $Ca^{2+}$ | $Sr^{2+}$ | $Ba^{2+}$ | $Mn^{3+}$ | $Mn^{4+}$ | |
| $R_0$ | 1.978 | 1.965 | 2.019 | 1.967 | 2.118 | 2.285 | 1.760 | 1.753 | |

***Tab. 15.1***: *$R_0$ values of cation-oxygen bonds in manganese perovskites needed for the bond valence calculation (15.9); taken from [19].*

Finally the valence or oxidation state of the cation can be determined by the sum of the bond valences around the respective atom i according to:

$$V_i = \sum_{ij} s_{ij} \tag{15.10}$$

Even though this method to determine the valence state is purely empirical, it proves to be rather precise, if compared to other techniques. The values of the valences found with this method differ significantly from a purely ionic model. Instead of integer differences between charges on different transition metal ions, one finds more likely differences of a few tenth of a charge of an electron.

Just like charge order, orbital order is not directly accessible to neutron diffraction techniques since orbital order represents an anisotropic charge distribution and neutrons do not directly interact with the charge of the electron. However, we have seen in the discussion of the Jahn-Teller effect (figure 15.8 and figure 15.9) that an orbital order is connected with a distortion of the local environment visible in different bond lengths within the anion complex surrounding the metal cation. In this way, by a precise determination of the structural parameters from a combined neutron and x-ray powder diffraction experiment, one can determine in favorable cases the ordering pattern of all four degrees of freedom: lattice, spin, charge and orbitals.

One can ask, whether there is not a more direct way to determine charge- and orbital order. The scattering cross section of x-rays contains the atomic form factors, which are Fourier transforms of the charge density distribution of an atom. Naively one would think therefore that charge and orbital order can be easily determined with x-ray scattering. However, as discussed in the last paragraph on bond valence sums, it is usually only a fraction of an

elementary charge, which contributes to charge- or orbital ordering. If we take the case of the Mn atom, the atomic core has the Ar electron configuration i. e. 18 electrons are in closed shells with spherical charge distributions. For the $Mn^{4+}$ ion, three further electrons are in the $t_{2g}$ levels. Since in scattering, we measure intensities and not amplitudes, these 21 electrons contribute $21^2 r_0^2$ to the scattered intensity[6]. If the difference in charge between neighboring Mn ions amounts to 0.2e, this will give an additional contribution to the scattered intensity of $0.2^2 r_0^2$. The effect of charge ordering in x-ray scattering is therefore $\frac{0.2^2}{21^2} \sim 1 \cdot 10^{-4} = 0.1‰$. In this simple consideration, we have completely ignored the scattering from all the other atoms, so that detection of charge- or orbital ordering becomes even more difficult in reality. There is, however, a way to enhance the scattering from non-spherical charge distributions, the so-called *anisotropic anomalous x-ray scattering*. It was first discussed by Templeton and Templeton [20] and applied for orbital order in manganites by Murakami et al. [21]. The principle of this technique is shown in figure 15.14.

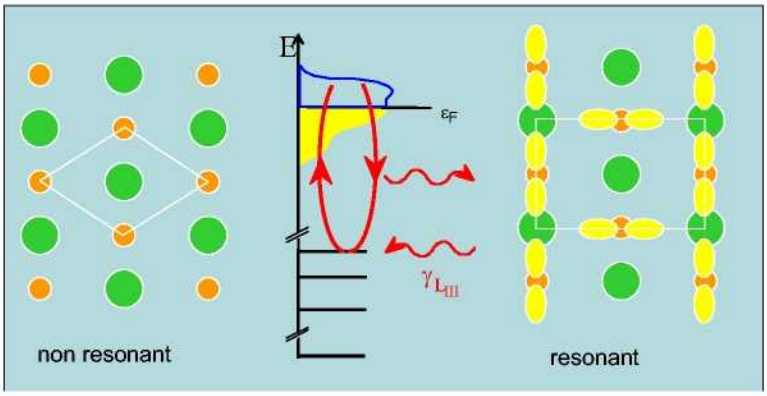



***Fig. 15.14:*** *Illustration of the principle of anisotropic anomalous x-ray scattering for a hypothetical 2-dimensional compound consisting of two atoms with different number of electrons. On the left a possible reconstruction of the charge distribution from a laboratory x-ray source is shown. Non resonant x-ray scattering is sensitive mainly to the spherical charge distribution and a unit cell as shown by the white lines is being deduced from this experiment. In the middle the principles of a resonance x-ray scattering is depicted in an energy level diagram (see text). On the right, the charge distribution deduced from such an anomalous x-ray scattering experiment is shown. Now an orbital ordering pattern becomes apparent, which could not be detected with non-resonant x-ray scattering. The unit cell is evidently larger, giving rise to superstructure reflections which appear at resonance.*

The figure shows scattering from a hypothetical two dimensional compound consisting of two atoms with different number of electrons. Non resonant x-ray scattering as it can be done on a laboratory x-ray source is sensitive mainly to the spherical charge distribution. A reconstruction of the charge distribution done from such an experiment might look schematically as shown on the left of figure 15.4. The corresponding crystal structure can be described with a primitive unit cell indicated by the white lines. In order to enhance the

[6] The classical electron radius $r_0=e/mc^2=2.82$ fm is the natural unit for the scattering amplitude of x-ray Thomson scattering

scattering from the non spherical part of the charge distribution, an experiment can be done at a synchrotron radiation source. There the energy of the x-rays can be tuned to the energy of an absorption edge as shown in the middle of figure 15.4. Now second order perturbation processes can occur, where a photon induces virtual transitions of an electron from a core level to empty states above the Fermi energy and back with re-emission of a photon of the same energy as the incident photon. Since second order perturbation processes have a resonant denominator, this scattering will be largely enhanced close to an absorption edge. If the intermediate states in this resonant scattering process are somehow connected to orbital ordering, scattering from orbital ordering will be enhanced. Thus in the resonant scattering experiment, orbital order can become visible as depicted schematically on the right of figure 15.14. With the shown arrangement of orbitals, the true primitive unit cell of this hypothetical compound is obviously larger than the unit cell that was deduced from the non resonant scattering experiment (shown on the left), which was not sensitive enough to determine the fine details of the structure. An increase of the unit cell dimensions in real space, however, is connected with a decrease of the distance of the reciprocal lattice points, i. e. an increase in the number of Bragg reflections. Therefore orbital order is visible by a resonant scattering process in the appearance of additional superstructure reflections. The intensity of these reflections has strong energy dependence as we would expect for a second order perturbation process. This type of scattering experiment is called anisotropic anomalous x-ray scattering, since it is sensitive to the anisotropic local charge distribution around an atom.

Figure 15.15 shows data from such a resonant scattering experiment [22] together with its interpretation in terms of an orbital polaron lattice [23].

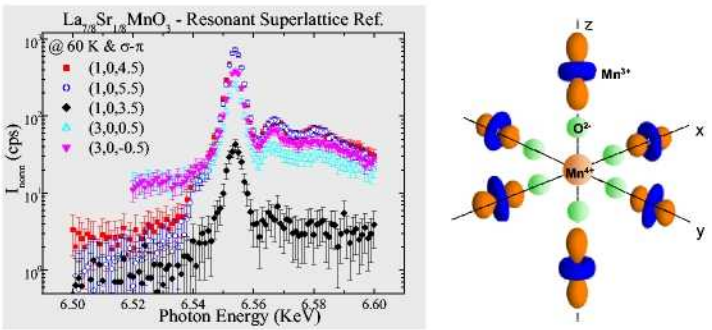



***Fig. 15.15:*** *The figure on the left shows the dependence of the intensity of resonant superlattice reflections from $La_{7/8}Sr_{1/8}MnO_3$ as a function of the energy of the incident photons. Clearly visible is the strong resonant enhancement at the K-absorption edge of Mn (note the logarithmic intensity scale). Several reflections with half indices along c become visible at resonance. The interpretation of this experiment is given in real space on the right of the figure. There is an alternating arrangement of $Mn^{3+}$ and $Mn^{4+}$ ions. The additional electron of the $Mn^{3+}$ ion occupies an $e_g$ orbital, which points towards the $Mn^{4+}$ ion. This arrangement is called an orbital polaron. In the ferromagnetic insulating phase of $La_{7/8}Sr_{1/8}MnO_3$ below 155 K, these orbital polarons arrange into a long ranged ordered orbital polaron lattice.*

The figure gives a nice example of how anisotropic anomalous x-ray scattering gives detailed information on charge- and orbital ordering in solids. Its advantage is that it is element specific (due to the different absorption edge energies for the different elements) and that it

combines diffraction and spectroscopy. This can also be seen in figure 15.15: there is a distinct fine structure in the resonance above the absorption edge, which gives information about the density of states of the unoccupied orbitals above the Fermi level.

So far we have discussed some powerful experimental techniques to determine the various ordering phenomena in complex transition metal oxides. Scattering can give much more information than just on the time averaged structure. Quasielastic diffuse scattering gives us information on fluctuations and short range correlations, i. e. short range correlations of polarons above the phase transition, magnetic correlations in the paramagnetic state, local dynamic Jahn-Teller distortions above the Jahn-Teller transition etc. Studying these correlations and fluctuations help us to understand what drives the respective phase transitions into long range order. The relevant interactions, which give rise to these ordering phenomena, can be determined from inelastic scattering experiments as we have learnt in chapter 12 on "Inelastic neutron scattering". For example, one can determine the exchange interactions from measurements of the spin wave spectra and compare with models for superexchange interactions and double exchange in order to verify or falsify the simple model explanations for the CMR effect discussed in chapter 15.4. Since there is a huge amount of such experiments on highly correlated transition metal oxides and chalcogenides, a review of these experiments definitely goes far beyond the scope of this introductory lecture.

## 15.6 Summary

This chapter gave a first introduction into the exciting physics of highly correlated electron systems, restricted to the complex transition metal oxides and -chalcogenides. The main message can be summarized in figure 15.16.

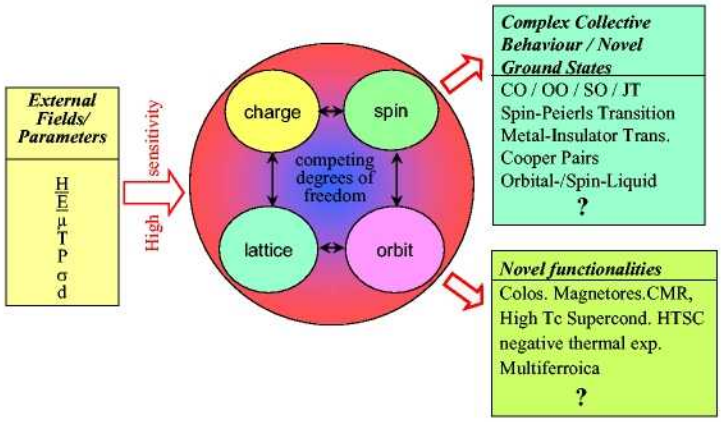



***Fig. 15.16:*** *Illustration of complexity in correlated electron systems. Meaning of the symbols is: H, E: magnetic and electric field, respectively; μ: chemical potential (doping); T: temperature; P: pressure; σ: strain (epitaxial growth); d: dimensionality (e. g. bulk versus thin film systems); CO: charge order; OO: orbital order; SO: spin order; JT: Jahn-Teller transition.*

The complexity in these correlated electron systems arises from the competing degrees of freedom: charge, lattice, orbit and spin. The ground state is a result of a detailed balance between these different degrees of freedom. This balance can be easily disturbed by external fields or other thermodynamical parameters, giving rise to new ground states or complex

collective behavior. Examples are the various ordering phenomena discussed, Cooper pairing in superconductors, so-called spin Peierls transitions in one dimensional systems etc. This high sensitivity to external parameters as well as the novel ground states of the systems gives rise to novel functionalities, such as the colossal magnetoresistance effect, high temperature superconductivity, multiferroic behavior and many more. A theoretical description of these complex systems starting from first principles, like Schrödinger equation in quantum mechanics or the maximization of entropy in statistical physics, is bound to fail due to the large number of strongly interacting particles. Entirely new approaches have to be found to describe the emergent behavior of these complex systems. Therefore highly correlated electron systems are a truly outstanding challenge in modern condensed matter physics. We have shown in this lecture that neutron and x-ray scattering are indispensable tools to disentangle this complexity experimentally. They are able to determine the various ordering phenomena as well as the fluctuations and excitations corresponding to the relevant degrees of freedom. No other experimental probe can give so much detailed information on a microscopic level as scattering experiments.

## References


[1] R.B. Laughlin and D. Pines; *The theory of everything*; PNAS 97 (2000), 28

[2] T. Vicsek; *The bigger picture*; Nature 418 (2002), 131

[3] J.G. Bednorz, K.A. Müller; *Possible high $T_C$ superconductivity in the Ba-La-Cu-O system*; Z. Phys. B 64 (1986), 189

[4] A-M. Haghiri-Gosnet1 and J-P. Renard; *CMR manganites: physics, thin films and devices (TOPICAL REVIEW)*; J. Phys. D: Appl. Phys. 36 (2003) R127

[5] G. Binasch, P. Grünberg, F. Saurenbach, and W. Zinn, *Enhanced magnetoresistance in layered magnetic structures with antiferromagnetic interlayer exchange;* Phys. Rev. B 39, (1989), 4828
and
M.N. Baibich, J.M. Broto, A. Fert, F. Nguyen van Dau, F. Petroff, P. Eitenne, G. Creuzet, A. Friederich, and J. Chazelas; *Giant magnetoresistance of (001)Fe/(001)Cr magnetic superlattices;* Phys. Rev. Lett. 61 (1988), 2472

[6] MH. Phan, SC. Yu; *Review of the magnetocaloric effect in manganite materials*; JMMM 308 (2007), 325

[7] M. Fiebig; *Revival of the magnetoelectric effect*; J. Phys. D: Appl. Phys. 38 (2005), R123

[8] E. J. W. Verwey; *Electronic conduction of magnetite ($Fe_3O_4$) and its transition point at low temperatures*; Nature 144 (1939), 327

[9] G.D. Barrera, J.A.O. Bruno, T.H.K. Barron et al.; *Negative thermal expansion*; J. Phys-Condens. Mat. 17 (2005), R217

[10] E. Dagotto; *Complexity in strongly correlated electronic systems*; Science 309 (2005), 257

[11] see e.g.
N.W. Ashcroft, N.D. Mermin; *Solid state physics*; Holt, Rinehart and Winston, 1976
or
H. Ibach, H. Lüth; *Solid-state physics: An introduction to principles of materials science*; Springer, 2003

[12] J Bardeen, L. N. Cooper & J. R. Schrieffer; *Nobel Prize in Physics 1972 for their jointly developed theory of superconductivity, usually called the BCS-theory*; http://nobelprize.org/nobel_prizes/physics/laureates/1972/index.html

[13] e.g. K. Held, O.K. Andersen, M. Feldbacher, A. Yamasaki, Y.F. Yang; *Bandstructure meets many-body theory: the LDA + DMFT method*; J. Phys. – Condens. Mat. 20 (2008), 064202

[14] N.F. Mott; *Metal-insulator transition*; Rev. Mod. Phys. 40 (1968), 677

[15] a good introduction into the physics of correlated electrons and the Hubbard model is provided by:
P. Fazekas; *Lecture notes on electron correlation and magnetism (Series in Modern Condensed Matter Physics, Vol. 5)*; World Scientific, 2003

[16] T. Chatterji (Ed.); *Colossal magnetoresistive manganites*; Kluwer Academic, 2004

[17] A. Urushibara, Y. Moritomo, T. Arima, A. Asamitsu, G. Kido, Y. Tokura; *Insulator-metal transition and giant magnetoresistance in* $La_{1-x}Sr_xMnO_3$; Phys. Rev. B 51 (1995), 14103

[18] A.J. Millis, P.B. Littlewood, B.I. Shraiman ; *Double exchange alone does not explain the resistivity of* $La_{1-x}Sr_xMnO_3$ Phys. Rev. Lett. 74 (1995), 5144

[19] G.H. Rao, K. Bärner & I.D. Brown; *Bond-valence analysis on the structural effects in magnetoresistive manganese perovskites*; J. Phys.: Condens. Matter 10 (1998), L757

[20] D. H. Templeton, L. K. Templeton, J. C. Phillips & K. O. Hodgson; *Anomalous scattering of x-rays by caesium and cobalt measured with synchrotron radiation*; Acta Cryst. A 36 (1980), 436

[21] Y. Murakami, J. P. Hill, D. Gibbs, M. Blume, I. Koyama, M. Tanaka, H. Kawata, T. Arima, Y. Tokura, K. Hirota & Y. Endoh; *Resonant x-ray scattering from orbital ordering in* $LaMnO_3$; PRL 81 (1998), 582

[22] Y. Su, Th. Brückel et al., unpublished results

[23] J. Geck, B. Wochner, S. Kiele, R. Klingeler, P. Reutler, A. Revcolevschi & B. Büchner; *Orbital polaron lattice formation in lightly doped* $La_{1-x}Sr_xMnO_3$; PRL 95 (2005), 236401

Schriften des Forschungszentrums Jülich
Reihe Schlüsseltechnologien / Key Technologies

1. **Soft Matter**
   From Synthetic to Biological Materials
   Lecture manuscripts of the 39th IFF Spring School March 3 – 14, 2008
   Jülich, Germany
   edited by J.K.G. Dhont, G. Gompper, G. Nägele, D. Richter, R.G. Winkler (2008),
   c. 1000 pages
   ISBN: 978-3-89336-517-3

2. **Structural analysis of diblock copolymer nanotemplates using grazing incidence scattering**
   by D. Korolkov (2008), III, 167 pages
   ISBN: 978-3-89336-522-7

3. **Thermal Nonequilibrium**
   Thermal forces in fluid mixtures
   Lecture Notes of the 8th International Meeting on Thermodiffusion,
   9 – 13 June 2008, Bonn, Germany
   edited by S. Wiegand, W. Köhler (2008), 300 pages
   ISBN: 978-3-89336-523-4

4. **Synthesis of CMR manganites and ordering phenomena in complex transition metal oxides**
   by H. Li (2008), IV, 176 pages
   ISBN: 978-3-89336-527-2

5. **Neutron Scattering**
   Lectures of the JCNS Laboratory Course held at the Forschungszentrum Jülich and the research reactor FRM II of TU Munich
   edited by Th. Brückel, G. Heger, D. Richter and R. Zorn (2008), c. 500 pages
   ISBN: 978-3-89336-532-6

Band | Volume 5
ISBN 978-3-89336-532-6

JÜLICH
FORSCHUNGSZENTRUM